ABSTRACT

Title of Dissertation:

PETROLOGIC AND GEOCHRONOLOGIC CONSTRAINTS ON THE THERMAL AND STRUCTURAL EVOLUTION OF PALEO-SUBDUCTION INTERFACES

Kayleigh May Harvey, Doctor of Philosophy, 2020

Dissertation directed by: Professor Sarah C. Penniston-Dorland
Department of Geology

In subduction zones, the interface between the downgoing slab and overriding plate controls a number of important dynamic processes. Both the rheologic behavior and thermal structure of the interface influence fluid release and transport, melt generation, seismic phenomena and viscous coupling between the downgoing and overriding plates. In this dissertation I present field, petrologic and geochronologic observations of paleo-subduction interface rocks from the Catalina Schist (Santa Catalina Island, CA) and Rio San Juan Complex (Dominican Republic). Methods including trace element thermometry, elastic barometry and Sm-Nd garnet geochronology are used to place constraints on spatial and temporal scales of deformation and to understand long-term changes in thermal

structure. The applicability of new thermobarometric methods to reconstruct the pressure-temperature evolution of a sample are also assessed.

Mélange, a block-in-matrix structure, is an important constituent of the subduction interface. Blocks within mélange can be mechanically and metasomatically mixed over several kilometers along the subduction interface, likely as a result of rheologic contrasts in the matrix. In the Catalina Schist amphibolite-facies mélange zone, blocks record up to 7 million years of variation in peak metamorphic age, placing constraints on the timescale over which the zone developed prior to underplating and rapid cooling of the system. This mixing process fundamentally changes the composition of the interface and may be an important driver of seismic phenomena including episodic tremor and slip.

Changes in the thermal structure of the subduction interface can be constrained by thermobarometry of exhumed metamorphic rocks and the timescales of those changes can be constrained by geochronology. Here, new age constraints on the timing of amphibolite-facies metamorphism of the Catalina Schist are presented as well as the first evidence of an earlier eclogite-facies metamorphic event that is approximately coeval with the earliest records of subduction in related exhumed terranes. Finally, trace element and elastic thermobarometers are compared to major element thermobarometry and phase equilibria modeling in order to assess the utility of trace element and elastic thermobarometry to reconstructing the metamorphic history of a sample using an eclogite from the Rio San Juan Complex as a type-example.

PETROLOGIC AND GEOCHRONOLOGIC CONSTRAINTS ON THE THERMAL AND STRUCTURAL EVOLUTION OF PALEO-SUBDUCTION INTERFACES

by

Kayleigh May Harvey

Dissertation submitted to the Faculty of the Graduate School of the
University of Maryland, College Park, in partial fulfillment
of the requirements for the degree of
Doctor of Philosophy
2020

Advisory Committee:
Professor Sarah C. Penniston-Dorland, Chair
Associate Professor Ricardo Arevalo
Assistant Professor Besim Dragovic
Professor Matthew J. Kohn
Research Scientist Dr. Philip M. Piccoli
Professor Alice Mignerey, Dean's Representative

Foreword

Portions of the research presented in this dissertation were completed in collaboration with other researchers. I made substantial contributions to the development of each project and performed the majority of the work to implement and interpret each study. A summary of each author's contributions is provided below.

Chapter 2:

Harvey, K.M., Penniston-Dorland, S.C., Kohn, M.J., and Piccoli, P.M. (in revision). Assessing *P-T* variability in mélange blocks from the Catalina Schist: Is there differential movement at the subduction interface? *Journal of Metamorphic Geology*.

K. Harvey performed the majority of the analytical work, interpreted the data and wrote the manuscript. S. Penniston-Dorland provided funding and assisted with field work, experimental design, collection of the Zr-in-rutile data, and with the writing of the manuscript. M. Kohn assisted with field work, collection of the quartz-in-garnet data, method development for interpreting the quartz-in-garnet data, and with the writing of the manuscript. P. Piccoli assisted with all data collection by electron probe microanalysis and with the writing of the manuscript.

Chapters 3 and 4:

K. Harvey performed the majority of the sample preparation and clean laboratory work (mineral separation, partial dissolutions, column chemistry), collected all major and trace element data by EPMA and LA-ICP-MS, interpreted the data and wrote the chapters. E.

Baxter provided the analytical resources for Sm-Nd garnet geochronology for both chapters. TIMS data were primarily collected by S. Walker and P. Starr with assistance from K. Harvey and M. Tappa. S. Penniston-Dorland provided funding, aided in sample collection, assisted with experimental design and provided feedback for each chapter. M. Kohn assisted with field work and experimental design for both projects. P. Piccoli and R. Ash assisted with data collection by EPMA and LA-ICP-MS, respectively.

Chapter 5:

K. Harvey performed all of the analytical work, interpreted the data and wrote the chapter. B. Dragovic provided the pseudosection models and aided in experimental design. S. Penniston-Dorland provided funding and assisted with experimental design. Samples were provided by Hans Peter-Schertel.

Acknowledgements

I would first like to thank my advisor, Dr. Sarah Penniston-Dorland. I am incredibly grateful to have had the opportunity to learn from and work with Sarah, and I truly could not have made it through this process without her constant encouragement, support and dedication. I will be forever grateful for the opportunities that she has given me, including the fantastic scientists that she has introduced me to, the numerous chances to attend international conferences and workshops, and (of course) all of the field seasons on Santa Catalina Island. Sarah not only taught me how to be a scientist, but also about how to be an effective mentor. Second, I would like to thank Dr. Phil Piccoli for his guidance and mentorship throughout my PhD and for all of his assistance with my analytical work. I would also like to extend my appreciation to all of my collaborators, including Dr. Matt Kohn, Dr. Ethan Baxter, Dr. Besim Dragovic, Dr. Stephanie Walker, Dr. Paul Starr, Dr. Peter van Keken, and Dr. Ikuko Wada. Thank you for the numerous opportunities that you have all given me –from allowing me to be a visiting researcher in your laboratory to mentoring me in the field, and all of the fun and interesting chats about science along the way. Finally, I would like to extend my gratitude to Dr. Ricardo Arevalo for serving on my committee, and to Dr. Alice Mignerey for her role as the Dean's Representative.

This project has been supported by NSF grants EAR-1419871 and EAR-1850786 to S. Penniston-Dorland and two GSA Graduate Student Research Grants (awarded to K. Harvey). Funding for travel to conferences was also provided through the University of Maryland's Earth System Science Interdisciplinary Committee (ESSIC), Goldhaber Award and International Conference Student Support Award, as well as through the Geological Society of America and the Mineralogical Society of America.

I would like to thank the Santa Catalina Island Conservancy for their logistical support during three field seasons on Santa Catalina Island. In particular, I would like to extend my gratitude to Rebecca Rudy, who assisted with organizing our last two field seasons. I would also like to thank Frank the Buffalo (who is, in fact, a bison) for always keeping an eye on us, even if sometimes he got a little too close.

Thank you to past and present members of my research group, Nivea Magalhães, Will Hoover, Christiana Hoff and the numerous undergraduate students for all of the fun discussions about science and for indulging my obsession with mélange.

To my friends -I don't really know where to begin. Thank you to all of you for keeping me sane and happy, I certainly would not have survived the last five years without you. Thank you in particular to my riding instructor, Astrid Dalley, who has not only provided fantastic horses for me to ride but has also served as my life coach, therapist and friend. I would also like to thank my closest friends, Erin Deans, Mara Miller, Jordan Frick, and Paige Gustafson, for being my rocks (even though none of you actually like rocks). Thank you to all of my housemates over the years, especially Joe and Angela putting up with me throughout the COVID-19 Pandemic. And of course, thank you to all of my fellow graduate students, past and present, for sharing this journey with me and for all of the fun memories.

I would like to thank Suzanne Martin, Todd Karwoski, Michelle Montero, Deborah Yeagley, Joanne Patterson, and Dorothy Brown for all of their administrative and technical support.

And finally -my family. Thank you, mom. Thank you for supporting me for the past 26 years, for being there for me through the good and the bad, and for always loving me.

Thank you for always telling me that I am good enough and to never give up. Thank you to the rest of my family, although there are too many of you to list. Thank you Rox, you have been by my side through it all. And last, but not least, thank you dad. Thank you for teaching me to love the outdoors and for always encouraging and enabling my inquisitiveness and passion for science –life is good.

Table of Contents

List of Tables

List of Figures

Chapter 1: Introduction

In subduction zones, dynamically evolving pressure-temperature-fluid conditions drive a complex feedback between chemical, mineralogic and rheologic changes in rocks. This in turn influences a number of processes including generation of some of Earth's largest and deadliest earthquakes, production of arc magmatism, and long-term geochemical exchange including recycling of volatiles such as H_2O and CO_2. Understanding the earthquake cycle and arc volcanism is critical for accurately assessing and mitigating the societal risk associated with these hazards. Similarly, long-term geochemical cycling has profound effects on climate change and the availability of natural resources.

There are a number of ways by which researchers can both directly and indirectly study processes occurring within subduction zones. These include geophysical observations of active subduction zones (e.g., Abers et al., 2006; Audet and Bürgmann, 2014; Freymueller et al., 2013; Naif et al., 2015; Schmandt and Humphreys, 2010), geochemical and petrologic observations of both active and paleo-volcanic arcs (e.g., Kelemen et al., 2007; Newcombe et al., 2020; Nielsen and Marschall, 2017; Plank and Langmuir, 1998), experimental constraints on mechanical and geochemical rock properties (e.g., French and Zhu, 2017; Grove et al., 2012; Hirschmann, 2006; Holland and Powell, 2003) and analog and numerical geodynamic models (e.g., Behn et al., 2011; Billen and Hirth, 2007; Gerya et al., 2002; Kincaid and Griffiths, 2004; van Keken et al., 2011; Wada et al., 2015). The final way that we can study subduction is by petrologic, geochemical and

geophysical observations of metamorphic rocks exhumed from paleo-subduction zones. These exhumed rocks provide the only direct record of processes occurring at depth within subduction systems and can be used to refine geophysical and geochemical models of modern subduction. Metamorphic rocks record nearly the entire subduction cycle, including early sea-floor hydrothermal alteration (e.g., Alt et al., 2013; Cooperdock et al., 2018; Kodolányi et al., 2012; Ranero et al., 2003), shallow processes occurring along the megathrust (e.g., Bachmann et al., 2009; Fisher and Byrne, 1990; Kimura et al., 2012; Sakakibara et al., 2007; Vrolijk et al., 1988) and deeper processes from the brittle/ductile transition to sub-arc conditions and beyond (e.g., Cloos, 1986; Rubatto and Angiboust, 2015; Spandler et al., 2008; Whitney et al., 2014). As a result, paleo-subduction terranes can be used to directly investigate any number of processes including fluid, melt and mass transport mechanisms recorded by vein and shear zone networks (e.g., John et al., 2012; Penniston-Dorland et al., 2010; Taetz et al., 2018), structural and rheologic changes recorded at both the mineral and outcrop scales (e.g., Behr et al., 2018; Hayman and Lavier, 2014; Rowe et al., 2013; Whitney et al., 2014) and the thermo-tectonic evolution of subduction zones at geologic timescales (e.g., Palin et al., 2020; Penniston-Dorland et al., 2015).

The metamorphic rock record has the potential to address a number of outstanding questions of interest to the broader subduction zone research community. Among these are questions about the geochemical and structural evolution of the plate interface and secular changes in the thermal structure of the system. The thermal structure of the subducting slab is a dominant control on a number of processes, including the size of the seismogenic zone,

when and where fluids are released and where magma is generated. Similarly, the plate interface controls mass flux and geochemical exchange between the downgoing slab and overriding plate and influences the rheologic and seismic behavior of the system. Throughout this dissertation, I examine how the metamorphic rock record can be utilized to understand the evolution of the subduction interface by combining field observations with petrology, thermobarometry and geochronology. The dissertation can largely be divided into two themes: the structural evolution of mélange and temporal variations in pressure-temperature conditions. Each of these themes is discussed briefly below.

1.1 Structural evolution of the subduction interface

Mélange, where competent cm- to sub-km-scale blocks of various lithologies are encapsulated within a deforming and hydrated finer-grained matrix, is thought to be an important constituent of the plate interface. This block-in-matrix structure is observed in exhumed terranes from a wide range of depths, including shallow sediment-dominated (e.g., sandstone, shale) mélanges associated with the megathrust region of the interface (e.g., Fisher and Byrne, 1987; Kimura et al., 2012), and more evolved and hybridized mélanges (a mixture of sedimentary, mafic and ultramafic material) from depths relevant to episodic tremor and slip (c. 30-50 km) and intermediate depth seismicity (c. 60-70 km). Hybridization during subduction is thought to occur by a combination of metasomatism of and mechanical mixing between the mélange components (e.g., Bebout and Barton, 2002; Penniston-Dorland et al., 2014; Figure 1.1) and is important for several reasons. First, the weak and permeable mélange matrix appears to be a particularly efficient pathway for transporting fluids released from the downgoing slab, which facilitates geochemical exchange between the downgoing slab and overriding plate (e.g., Bebout and Penniston-

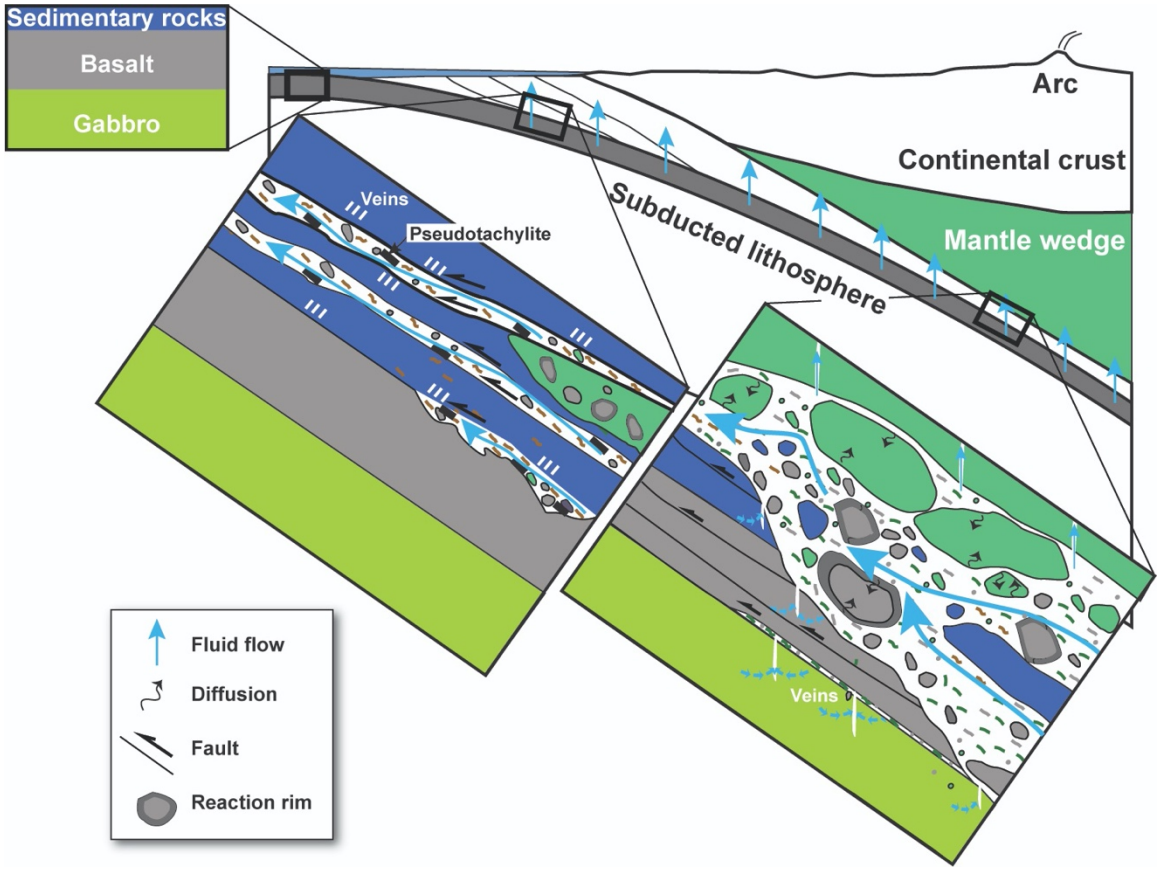

Figure 1.1 Conceptual model of the structure of the subduction interface as informed by rocks exhumed from shallow and deep portions of the interface. Pervasive fluid flow through mélange matrix and metasomatism of blocks are indicated by blue and black arrows respectively. Modified from Bebout and Penniston-Dorland (2016).

Dorland, 2016) and allows for transfer of volatiles such as H_2O and CO_2 (e.g., Ague and Nicolescu, 2014; Bebout and Barton, 1993; Penniston-Dorland et al., 2012) and oxidation potential (e.g., Gerrits et al., 2019). Fluid transport has been implicated in a number of deep seismic phenomena such as slow slip events, episodic tremor and slip, and intermediate-depth seismicity (e.g., Audet and Bürgmann, 2014; Broadwell et al., 2019; Brown et al., 2005; French and Zhu, 2017; Hacker et al., 2003; Tarling et al., 2019). The hybrid composition can also explain unique geochemical signatures of arcs which cannot be explained by more traditional "MASH" (melting-assimilation-storage-homogenization) melt transport models (e.g., Cruz-Uribe et al., 2018; Marschall and Schumacher, 2012; Nielsen and Marschall, 2017). This, in conjunction with field-based evidence for partial

melting of mélange (i.e., restite and leucosomes/melanosomes, pegmatite veins; Garcia-Casco et al., 2007; Marocchi et al., 2010; Sorensen and Barton, 1987), indicates that mélange is likely an important contributor to arc volcanism. Finally, rheology of material at the subduction interface controls slip partitioning and influences a number of processes including seismic phenomena and viscous coupling between the downgoing slab and overriding plate (e.g., Agard et al., 2018; French and Condit, 2019). Hybridization of mafic, ultramafic and metasedimentary components fundamentally alters the mineralogy and, thus, rheology of mélange matrix. Matrix observed in exhumed terranes is often dominated by sheet silicates including chlorite and talc (e.g., Bebout and Barton, 2002; Nielsen and Marschall, 2017), which deform differently than any of the individual mélange components and may change how slip is partitioned within the slab (e.g., French and Condit, 2019). The rheologic contrast between the weak matrix and juxtaposed competent blocks has also been implicated as a potential source of seismic phenomena including episodic tremor and slip, whereby steady creep within the matrix coincides with brittle failure of the blocks (e.g., Beall et al., 2019; Hayman and Lavier, 2014; Kano et al., 2018).

Although mélange appears to be a geochemically and structurally important constituent of the downgoing slab, the mechanisms by which it forms and deforms are widely debated. This is largely due to the variety of tectonic and sedimentary settings where this block-in-matrix structure is observed. For example, olistostromal mélanges, which originate by slumping of unconsolidated submarine sediments, can form at the trench and be subsequently subducted (e.g., Festa et al., 2019). This contrasts with tectonic mélange, which forms through metasomatism and mechanical disaggregation of material at the plate

interface (e.g., Penniston-Dorland et al., 2014) or within intraslab shear zones (e.g., Angiboust et al., 2012, 2011). Because these two types of mélange are both associated with subduction, it is often difficult to distinguish between sedimentary and tectonic processes in exhumed terranes. As a result, a number of exhumed mélange zones have been interpreted by some researchers as having a tectonic origin (e.g., Cloos, 1982; Cloos and Shreve, 1988a, 1988b; Shreve and Cloos, 1986; Ukar and Cloos, 2014) while others have interpreted the same features as having a sedimentary origin (e.g., Platt, 2015; Raymond, 2016; Wakabayashi 2011, 2012). There is also community debate about how mélange deforms at the subduction interface. Some researchers argue that the deformation does not necessarily mix material over significant length-scales (e.g., Wakabayashi, 2012), while others argue that blocks can be chaotically mixed over tens or even hundreds of kilometers (e.g., Gerya et al., 2002; Penniston-Dorland et al., 2018). These contrasting deformation styles have significantly different implications for mass transport and geochemical cycling as well as the rheologic behavior of the plate interface.

Throughout this dissertation, two primary questions relating to the formation of mélange at the subduction interface are addressed. In Chapter 2, the question "*what controls the spatial scales of mixing within mélange?*" is examined by comparing the length-scales of mixing recorded by high-grade mélange from various structural units of a single exhumed terrane, the Catalina Schist (Santa Catalina Island, CA). This research incorporates field observations with pressure-temperature (*P-T*) estimates from 25 mélange blocks in addition to a coherent (non-mélange) unit of the terrane to ascertain the depths to which these blocks were subducted prior to mixing with lower-grade material. The results

are then compared to prior temperature estimates of blocks from the terrane (Penniston-Dorland et al., 2018) in order to assess variations in mixing. Scenarios to explain these observations, including post-metamorphic faulting, sedimentary mélange, underplating, and mélange flow are then explored. The scenarios which best-explain the observations are a combination of mélange flow and underplating.

In Chapter 3, the question "*over what temporal scales does tectonic mélange form?*" is then addressed by assessing age variations of mélange blocks from the same structural unit of the Catalina Schist. There are relatively few mélange zones where the timing of peak metamorphism has been constrained for multiple blocks. In this chapter, Sm-Nd garnet geochronology is used to estimate the timing of peak metamorphism for 5 mélange blocks which record c. 100°C variations in temperature (Penniston-Dorland et al., 2018). These ages are compared to previous age estimates for the terrane and the tectonic implications are discussed. The results demonstrate that there are resolvable age differences within the mélange zone and that the zone is younger than the structurally lower coherent unit indicating that the contact between the units is non-conformable. The data are best explained by mélange development over c. 12 million years which was followed by underplating of the mélange zone and partial exhumation of the lower coherent unit.

1.2 Thermal evolution of the subduction interface

The temperature of the downgoing slab is perhaps the most important intensive variable in subduction zone dynamics. Temperature controls both where metamorphic reactions occur and the rheologic behavior of materials, thereby influencing seismicity, the

extent of geochemical cycling, where fluids are released and how they are transported, the depth at which magma is generated, and the deformational behavior of the downgoing slab. Because temperature controls all of these processes, it is important to accurately model thermal structure. Temperature conditions can be estimated in several ways, both using information from active subduction zones and from paleo-subduction terranes. In active subduction zones, temperatures are commonly modeled based on forearc heat flow measurements and seismic attenuation (e.g., Syracuse et al., 2010) or estimated via

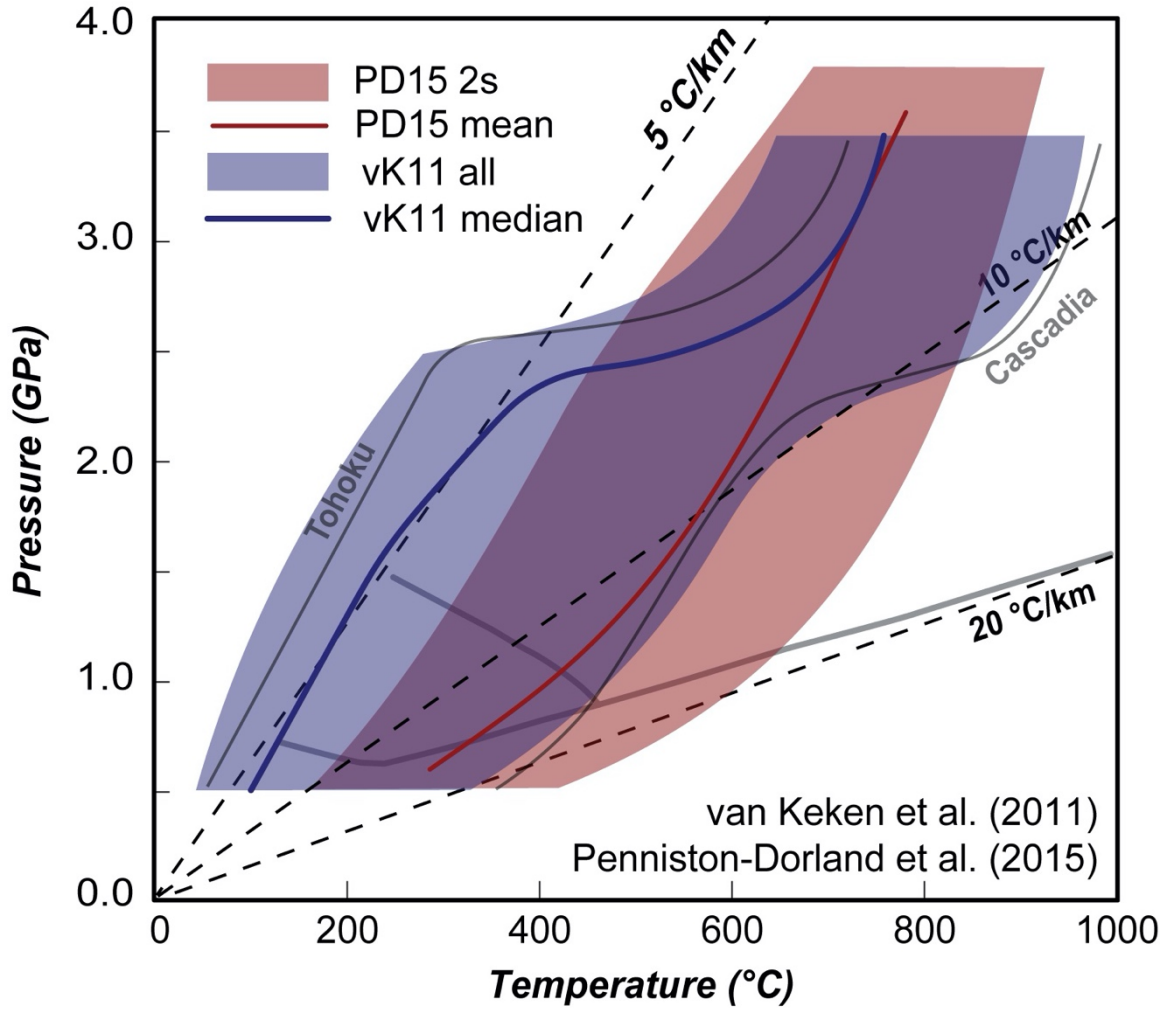

Figure 1.2 Comparison of global compilation of *P-T* estimates from exhumed metamorphic rocks and slab-top geothermal gradients predicted by 2-D geodynamic models. Modified from Penniston-Dorland et al. (2015) and van Keken et al. (2011).

thermometry on melt inclusions hosted in phases erupted at the volcanic arc (e.g., H_2O/Ce thermometry; Cooper et al., 2012). Alternatively, thermal structure can be estimated from the exhumed rock record by determining the *P-T* conditions at which the rocks recrystallized (e.g., via equilibrium thermodynamics; Lanari and Engi, 2017). This is particularly important for relating processes inferred from the rock record to observations of active subduction zones.

However, *T* estimates from the exhumed rock record are, on average, 200-300°C hotter than predictions from 2-D kinematic models for modern subduction zones (Penniston-Dorland et al., 2015; van Keken et al., 2011; Figure 1.2). There have been multiple explanations for this discrepancy, including preferential exhumation at the beginning and end of subduction when conditions are hotter (e.g., Agard et al., 2009; van Keken et al., 2018) and incorporation of additional model parameters such as the effect of shear heating of the interface (e.g., Kohn et al., 2018) which is often not included in geodynamic models because the effect is considered minimal (see Syracuse et al., 2010). Other explanations include the potential for equilibrium thermodynamics, which has been a long-standing tool utilized by the metamorphic petrology community to estimate the *P-T* conditions of exhumed rocks, to either under- or over-estimate temperature conditions because of disequilibrium processes (e.g., Kohn and Penniston-Dorland, 2017; Kohn and Spear, 2000; Lanari and Duesterhoeft, 2019; Pattison et al., 2011; Spear and Pattison, 2017), 3-D geometry effects which cause the system to depart from steady-state conditions including toroidal mantle flow from oblique subduction or slab tears/holes/windows (e.g., Menant et al., 2016; Plunder et al., 2018; Wada et al., 2015) and mantle upwelling from

delamination or slab rollback (e.g., Göğüş and Pysklywec, 2008; Kincaid and Griffiths, 2004; Stegman et al., 2006; Wells and Hoisch, 2008). Additionally, some exhumed terranes have been linked to subduction of sea floor features such as seamounts or ridges, which are expected to perturb the system (e.g., DeLong et al., 1979; Iwamori, 2000; Santosh and Kusky, 2010; Spinelli and Harris, 2011). Critically assessing each of these potential contributing factors both in the rock record and at active subduction zones will not only enhance our understanding of the controls on the thermal structure of the subducting slab, but also improve our understanding of the relationship between paleo- and modern subduction zones.

In this dissertation, four primary questions relating to the thermal structure of the subduction interface are addressed. In Chapter 4, the questions *"can the duration of high-T metamorphism in a terrane inform us about the driving processes of such metamorphism?*" and, similarly *"how can along-strike and temporal variations in temperature conditions inform us about high-T metamorphism?"* are examined. The highest-grade units of the Catalina Schist record temperature conditions that are anomalously hot even in terms of the metamorphic rock record. To-date, there have been multiple explanations for these temperature conditions; however, none have fully reconciled both petrologic and chronologic constraints on when and where the units formed. In this chapter, Sm-Nd garnet geochronology is used to determine the timing of peak metamorphic conditions for three samples from the Catalina Schist which span the range of high-grade metamorphic conditions recorded by the terrane as determined in Chapter 2 (eclogite- to amphibolite-facies). These new age constraints are the earliest

records of metamorphism in the terrane to-date and provide new insight into the timing and duration of high-*T* metamorphism. The data are compared to prior age constraints both for the Catalina Schist and related exhumed terranes to the north (the Franciscan Complex, Oregon) and south (Baja California) in order to assess which processes may contributed to the formation of the terranes.

In Chapter 5, the utility of new and emerging methods, which require few or no assumptions about chemical equilibrium, is explored to reconstruct *P-T* paths of exhumed metamorphic rocks. To do this, the questions "*are these methods self-consistent?*" and "*how do the results compare to P-T estimates from more traditional methods?*" are examined. In this chapter, Zr-in-rutile thermometry and both quartz-in-garnet and zircon-in garnet elastic barometry are used on inclusions hosted within individual growth zones of a large eclogite-facies garnet porphyroblast from the Rio San Juan Complex (Dominican Republic) to estimate prograde, peak and retrograde conditions associated with garnet growth. The results are then compared to prior estimates for the sample using major element thermobarometry and new phase equilibria models. While the results from trace element and elastic thermobarometry are consistent with each other and largely consistent with phase equilibria modeling, they predict a different *P-T* path than previously estimated for the sample.

Chapter 2: Assessing *P-T* variability in mélange blocks from the Catalina Schist: Is there differential movement at the subduction interface?

Harvey, K.M., Penniston-Dorland, S.C., Kohn, M.J., and Piccoli, P.M. (in revision) Assessing *P-T* variability in mélange blocks from the Catalina Schist: Is there differential movement at the subduction interface? *Journal of Metamorphic Geology*.

2.1 Abstract

In subduction-related tectonic mélange, thermobarometry on individual blocks can in principle constrain the scale of lithologic mixing along the subduction interface. Previous thermobarometric investigation of the tectonic amphibolite-facies mélange unit in the Catalina Schist, Santa Catalina Island, California, U.S.A., has suggested relatively limited mixing among blocks (≤12 km). Here we further investigate scales of mixing among metamorphically disparate ("exotic") blocks within epidote-amphibolite and lawsonite-blueschist facies mélange of the Catalina Schist using field and petrographic observations, Zr-in-rutile thermometry, and quartz-in-garnet elastic barometry. A new statistically-based method is presented for calculating elastic barometry maximum pressures.

The exotic blocks record peak metamorphic temperatures between 580 and 735°C and peak pressures between 1.16 and 1.65 GPa. Temperatures primarily fall in between those recorded by rocks in the amphibolite-facies and epidote amphibolite-facies units (643-735°C and 553-596°C, respectively). The pressure estimates encompass those

recorded by blocks from the amphibolite-facies mélange (1.34-1.44 GPa), although the exotic blocks record a much larger range of pressures. The large range of recorded temperatures and pressures suggests that blocks within the epidote amphibolite unit were sourced from and mixed along a 20-30 km region of the subduction interface while an exotic block from the lawsonite blueschist-facies unit appears to have been sourced from at least 70 km deeper than the unit it is hosted in. Meter- to km-scale variations in matrix mineral rheology likely control strain partitioning at the interface and permit differential transport of mélange blocks over variable length scales.

2.2 Introduction

Subduction zones are the location of many crucial and catastrophic processes, including the generation of some of Earth's largest and deadliest earthquakes and volcanic eruptions, production of new crust by arc volcanism, and recycling of crustal material and volatiles into the Earth's interior. Physico-chemical interaction between the downgoing slab and overriding plate is thought to influence all of these processes, but our understanding of this interaction is limited because it cannot be directly observed. High-*P*/low-*T* metamorphic rocks exhumed from paleo-subduction zones are commonly employed to infer processes occurring during subduction. Often, these exhumed terranes have mappable regions of blocks surrounded by a fine-grained matrix (i.e., mélange). These mélange zones appear to form at various depths within the subduction zone, ranging from low-grade block-in-matrix structures that are commonly associated with seafloor and subduction megathrust processes to high-grade blueschist-, eclogite- and amphibolite-facies mélange zones that record much deeper processes. Many studies have used such high-grade mélange to understand fluid flow, mass transport, and thermal structure at the

subduction interface (see reviews by Agard, Plunder, Angiboust, Bonnet, & Ruh, 2018; Bebout & Penniston-Dorland, 2016; Marschall & Schumacher, 2012; Penniston-Dorland, Kohn, & Manning, 2015). Thus, high-grade mélange represents a key rock type for interpreting geochemistry and petrology of subduction zones.

In exhumed terranes, mélange commonly occurs as high-P/low-T metamorphic blocks surrounded by a highly-deformed fine-grained metamorphic matrix (e.g., Cowan, 1985; Festa, Pini, Dilek, & Codegone, 2010; Festa, Pini, Ogata, & Dilek, 2019 and references therin). Given that mélange can be derived by both tectonic and sedimentary processes, the origin of many of these high-P/low-T mélange zones is debated. Tectonic mélange is thought to form by fluid-mediated mechanical disaggregation and shearing of material both along the interface between the down-going slab and overriding mantle wedge (see Bebout & Penniston-Dorland, 2016) or at smaller-scale shear zones developed elsewhere within the subduction system (e.g., intra-slab shear zones observed within the Monviso Ophiolite, Western Alps; see Angiboust et al., 2011). In contrast, sedimentary mélange associated with subduction zones is thought to form by slumping or sliding of unconsolidated submarine sediments, i.e., they are olistostromes. Sedimentary mélanges display a range of fabrics, but are commonly distinguished by the presence of cross-bedding, an unstrained or fossiliferous matrix, or undeformed and/or angular clasts (e.g., Festa et al., 2019 and references therein). Some serpentine and mud-matrix mélanges, such as rocks of the Franciscan Complex, California, exposed at San Simeon, Ring Mountain, and Jenner, have been interpreted by some researchers to have a tectonic origin (e.g., Cloos, 1982; Cloos & Shreve, 1988a, 1988b; Shreve & Cloos, 1986; Ukar & Cloos, 2014) and by

others to have a sedimentary origin (e.g., Platt, 2015; Raymond, 2016; Wakabayashi, 2011, 2012).

The presence of high-grade 'exotic' blocks juxtaposed with a lower-grade matrix has proved difficult to explain unequivocally in HP/LT mélange. In sedimentary models, exotic blocks are emplaced within a lower-grade matrix by exhumation to the seafloor followed by erosion of the high-grade rocks to form an olistostromal mélange (Festa et al., 2010, 2019). This sedimentary body is then re-subducted, causing the matrix to recrystallize, and the high-grade blocks to be overprinted at lower metamorphic conditions (e.g., Wakabayashi, 2012). Alternately, some tectonic models suggest that return flow at the subduction interface can chaotically mix blocks of disparate grades and lithologies (Cloos, 1982; Cloos & Shreve, 1988a, 1988b; Gerya, Stöckhert, & Perchuk, 2002; Penniston-Dorland, Kohn, & Piccoli, 2018; Shreve & Cloos, 1986). In this model, narrowing of the subduction interface at depth forces material at the slab interface up-dip, juxtaposing materials that experienced different peak metamorphic conditions. Identifying whether sedimentary vs. tectonic processes dominate the formation of mélange in a given geologic setting will not only lead to a clearer understanding of that locality, but also provide a better context for understanding the nature of the subduction plate interface.

The Cretaceous-age Catalina Schist subduction complex consists of both thrust slices of coherent rock units and mélange zones, which range in metamorphic grade from lawsonite-albite to amphibolite facies (Figure 2.1). The amphibolite-facies mélange has been described most extensively (e.g., Bebout & Barton, 2002; Penniston-Dorland,

Gorman, Bebout, Piccoli, & Walker, 2014; Page et al., 2019; Penniston-Dorland et al., 2018; Sorensen & Barton, 1987; Sorensen & Grossman, 1989). Unlike the serpentinite- and mud-matrix mélanges observed elsewhere in the Franciscan Complex and other subduction complexes (e.g., Cloos, 1986; Draper & Nagle, 1991), the matrix is dominated by mixed mafic and ultramafic material, similar to the dominant lithologies of the blocks (Bebout & Barton, 2002). This unique composition is best explained by mixing of material derived by metasomatically altering and mechanically disaggregating mafic and ultramafic blocks at the subduction interface (e.g., King, Bebout, Moriguti, & Nakamura, 2006; Penniston-Dorland et al., 2014). These processes imply that the high-grade mélange in the Catalina Schist has a tectonic origin. Prior investigation of the amphibolite-facies mélange within the Catalina Schist found that blocks record similar peak metamorphic temperatures as the surrounding matrix (i.e., they are isofacial); however, the blocks have resolvably different peak metamorphic temperatures from each other, spanning from 650°C to 730°C (±2-16°C for estimates from a single rock; Penniston-Dorland et al., 2018). This range in temperatures was interpreted as evidence for relatively small-scale (≲12 km) differential movement along the subduction interface.

Based on geochemical observations, mélanges throughout the lower-grade units of the Catalina Schist have also been generally interpreted as tectonic (Bebout & Barton, 1993; King et al., 2006). However, whereas the amphibolite-facies mélange is isofacial (amphibolite-facies blocks occur in amphibolite-facies matrix), metamorphic grades in lower-grade mélange can differ between blocks and matrix (Platt, 1975). Notably, high-grade blocks of garnet-bearing blueschist and amphibolite occur within epidote

amphibolite- and lawsonite-blueschist-facies matrix (Figure 2.1). For simplicity, we refer to these high-grade blocks as "exotic," although their pressure-temperature (*P-T*) history relative to the surrounding mélange has not been specifically determined. The presence of apparently exotic blocks in the lower grade units raises the question of whether these units were derived primarily by sedimentary or tectonic processes. Differentiating between these models is crucial for interpreting geochemical, petrologic and rheologic processes observed throughout these units and, more generally, in subduction-related mélange worldwide.

In this paper we contribute to understanding the origin of these blocks in a number of ways. We use field relationships to characterize the contact between blocks and matrix as well as the structural position with respect to mapped thrust faults. We also use zirconium-in-rutile trace element thermometry and quartz-in-garnet elastic barometry to quantify *P-T* conditions of exotic and isofacial blocks. These *P-T* conditions are compared among blocks and between blocks and associated matrix. Variations in *P-T* conditions are used to estimate the scale of mixing among blocks. Finally, the data are combined to evaluate competing models for the formation of mélange and to speculate on the causes of different scales of mixing.

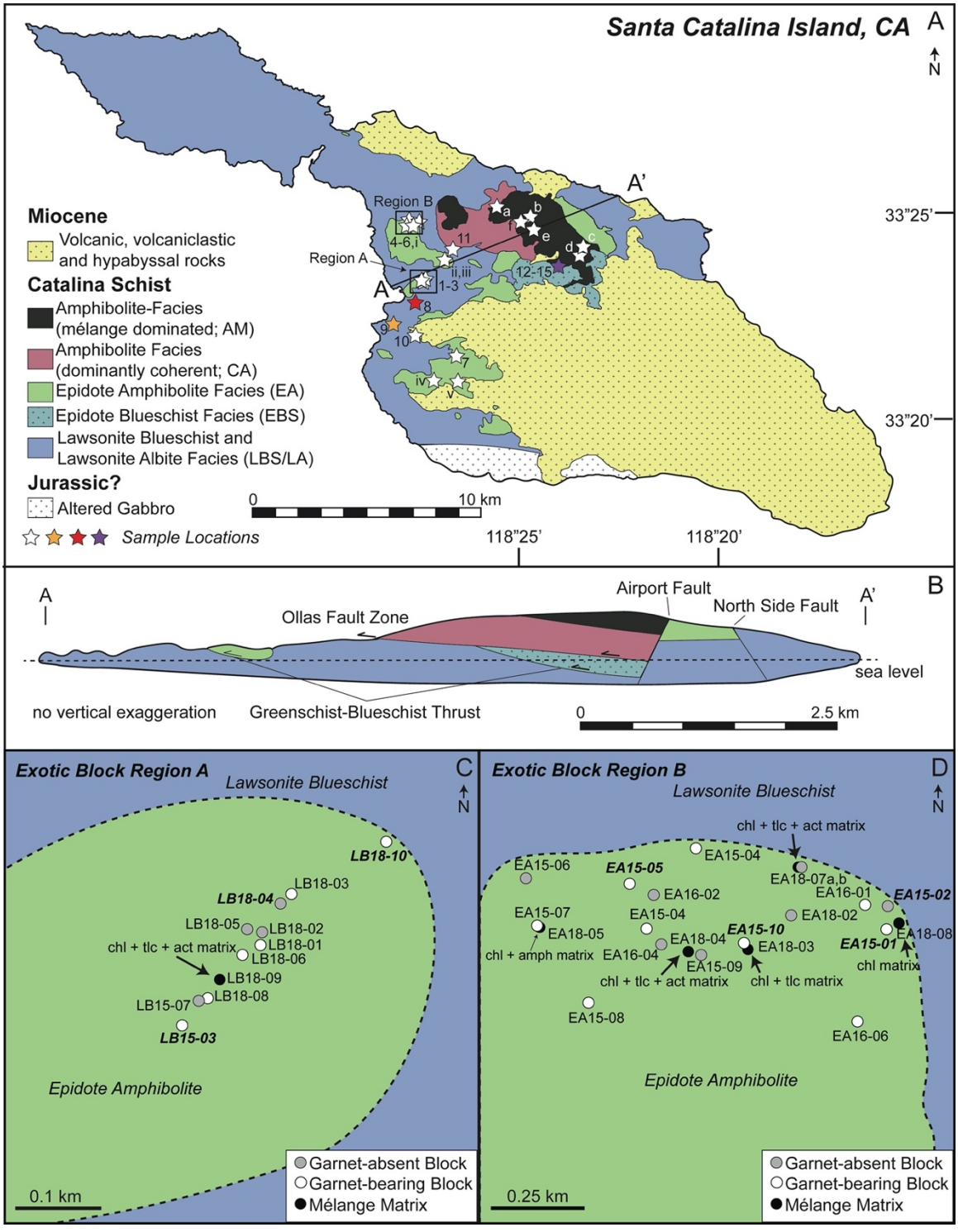
Santa Catalina Island, CA
A
N
A'
Region B
Region A
33"25'
33"20'
118"25'
118"20'
Miocene
Volcanic, volcaniclastic and hypabyssal rocks
Catalina Schist
Amphibolite-Facies (mélange dominated; AM)
Amphibolite Facies (dominantly coherent; CA)
Epidote Amphibolite Facies (EA)
Epidote Blueschist Facies (EBS)
Lawsonite Blueschist and Lawsonite Albite Facies (LBS/LA)
Jurassic?
Altered Gabbro
Sample Locations
0
10 km
B
Airport Fault
North Side Fault
Ollas Fault Zone
sea level
no vertical exaggeration
Greenschist-Blueschist Thrust
0
2.5 km
Exotic Block Region A
Lawsonite Blueschist
C
LB18-10
LB18-03
LB18-04
LB18-05
LB18-02
chl + tlc + act matrix
LB18-01
LB18-06
LB18-09
LB18-08
LB15-07
LB15-03
Epidote Amphibolite
0.1 km
Garnet-absent Block
Garnet-bearing Block
Mélange Matrix
Exotic Block Region B
Lawsonite Blueschist
D
chl + tlc + act matrix
EA15-06
EA15-05
EA15-04
EA18-07a,b
EA16-02
EA16-01
EA15-02
EA15-07
EA15-04
EA18-02
EA18-05
EA15-10
EA18-08
chl + amph matrix
EA16-04
EA18-04
EA18-03
EA15-01
EA15-09
chl matrix
chl + tlc + act matrix
chl + tlc matrix
EA15-08
EA16-06
Epidote Amphibolite
0.25 km
Garnet-absent Block
Garnet-bearing Block
Mélange Matrix

Figure 2.1: (A) Map and (B) cross-section (A-A') of the Catalina Schist exposed on Santa Catalina Island, California, USA. Stars show locations of samples discussed in this study. Colored stars indicate regions where block-in-matrix structures are preserved. *Exotic block locations:* (1) LB15-03B (2) LB18-04 (3) LB18-10 (4) EA15-10A (5) EA15-05B (6) EA15-01A (7) WB16-03A (8) LB/A14-01 (red star) (9) GB (gold star) (10) A14-71 (11) MR16-01 (12) CC16-14B (13) CC16-14D (purple star) (14) CC16-14C (15) CC16-14E *Isofacial epidote-amphibolite locations:* (i) EA15-02Ba (ii) 79841A, appx. (iii) 77842, appx. (iv) EA13-07g (v) EA13-12 *Isofacial amphibolite-facies locations:* (a) E2718C (b) A15-01A (c) A15-22 (d) A15-21A (e) A15-07A (f) CA15-06. Map after Platt (1975, 1976) with modifications after Grove and Bebout (1995). Sample locations for 79841A and 77842 were approximated based on unpublished maps by S. Sorensen. (C) Map of Exotic Block Region A showing sample locations. (D) Map of Exotic Block Region B showing sample locations. Bolded and italicized sample numbers in (C) and (D) are samples considered in this study.

2.3 Geologic Background

The Catalina Schist subduction complex consists of multiple km-scale tectonic slices separated by sub-horizontal thrust faults. These slices form an inverted metamorphic stack (Figure 2.1), and range in metamorphic grade from lawsonite-albite to upper-amphibolite facies (Grove et al., 2008; Platt, 1975, 1976). These tectonometamorphic units have been described extensively (see especially Grove et al., 2008; Grove & Bebout, 1995; Platt, 1975, 1976), and are only briefly discussed here. Each unit consists of both coherent rock sequences (including metasedimentary and metamafic rocks) and mélange zones which appear to be intercalated with the coherent rock units (Bebout and Barton, 1993). In the coherent rock sequences, the relative proportion of sedimentary protoliths (primarily graywacke, with small proportions of mudstone, conglomerate, chert, and sandstone) decreases with increasing metamorphic grade (Grove & Bebout, 1995; Grove et al., 2008). Similarly, metasedimentary rocks dominate block lithologies in the lawsonite-albite and lawsonite-blueschist facies mélange zones, whereas metamafic and ultramafic rocks dominate rock lithologies in the epidote amphibolite- and amphibolite-facies mélange zones (Grove & Bebout, 1995). Mélange matrix throughout the units is heterogeneous but generally consists of varying proportions of chlorite, talc, biotite, actinolite, anthophyllite

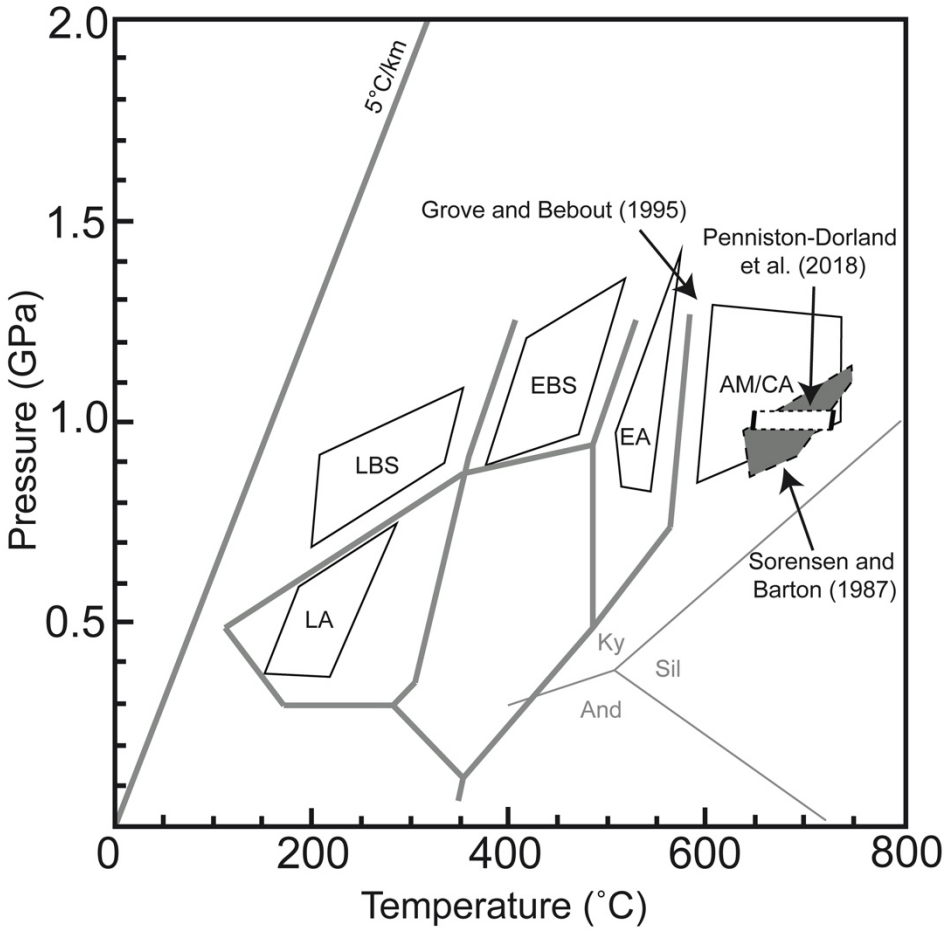

Figure 2.2. Previous pressure-temperature estimates for the tectono-metamorphic units of the Catalina Schist (Grove and Bebout, 1995; Sorensen and Barton, 1987; Penniston-Dorland et al., 2018). Symbology from Figure 2.1.

and enstatite depending on its composition and metamorphic grade. The mélange zones all record similar O isotopic values, which has been interpreted as evidence for large-scale homogenization by infiltrating fluids (Bebout & Barton, 2002). Locally, the amphibolite-facies mélange also records isotopic and geochemical evidence for partial homogenization of its mafic and ultramafic components by mechanical mixing (Bebout, 1997; Bebout & Barton, 2002; King et al., 2006; King, Bebout, Grove, Moriguti, & Nakamura, 2007).

Each unit appears to record a restricted range of *P-T* conditions (Figure 2.2), and the amphibolite-facies units record the highest peak metamorphic temperatures of ~600-

750°C at 0.7-1.2 GPa (Grove & Bebout, 1995; Penniston-Dorland et al., 2018; Platt, 1975; Sorensen & Barton, 1987). The thermal gradient required to produce these *P-T* conditions (~20°C/km) is anomalously high relative to current models of subduction zone thermal structures (e.g., Gerya et al., 2002; Syracuse, van Keken, & Abers, 2010). It is also hot relative to *P-T* conditions of other exhumed subduction complexes (e.g., Penniston-Dorland et al., 2015), and the lower-grade units within the Catalina Schist (Grove et al. 2008; Platt 1975). Multiple hypotheses have been offered to explain these high temperatures.

Platt (1975) hypothesized that high temperatures were achieved through nascent subduction, which requires metamorphism prior to or coeval with earliest magmatism. The pluton belt associated with the Catalina Schist, the Peninsular Ranges Batholith, initiated at ca. 140 Ma (Morton et al., 2014; Shaw, Todd, Grove, & Johnson, 2003; Suppe & Armstrong, 1972), at least 25 million years prior to amphibolite-facies metamorphism at ca. 115-110 Ma (Anczkiewicz, Platt, Thirlwall, & Wakabayashi, 2004; Mattinson, 1986). This age disparity suggests that subduction was initiated well before amphibolite-facies metamorphism. High-temperature amphibolite-facies rocks of the Catalina Schist might alternatively have formed via thrusting of forearc material beneath the Peninsular Ranges batholith during tectonic shortening (Grove et al., 2008). In this model they were later juxtaposed against younger (c. 100-97 Ma; Grove et al., 2008; Suppe & Armstrong, 1972) lower-grade units that formed at the colder subduction interface by subduction erosion. High temperatures such as these may be possible along the subduction interface for other

reasons, although the mechanism for producing sub-arc temperatures at such low pressures (~1 GPa) has not been explored for this terrane.

Platt (1975) first recognized amphibolite-facies exotic blocks in the epidote-amphibolite-facies unit (Figure 2.1). Because they occur close to the boundary between blueschist-facies and epidote amphibolite-facies units, the study proposed that they were located along a thrust (the Greenschist-Blueschist thrust) and derived from the amphibolite-facies mélange zone along post-metamorphic thrust faults. It is important that the blocks are all either amphibolite- or epidote amphibolite-facies. No blueschist-facies blocks are observed, although the proposed fault bounds this unit. Grove and Bebout (1995) proposed an alternative model for a garnet-bearing blueschist block in the lawsonite blueschist unit. In this model, the block, which appears to pre-date the amphibolite-facies units (Anczkiewicz et al., 2004; Grove et al., 2008; Grove & Bebout, 1995), was entrained in the mantle wedge and later juxtaposed with the lower grade rocks at the subduction interface. The tectonic interpretation of the Catalina Schist depends on the origin of these blocks (e.g., Grove and Bebout 1995; Grove et al. 2008), but their relationship to the coherent regions and isofacial mélange zones of the terrane is largely unconstrained.

2.4 Methods

2.4.1 Trace Element Thermometry

The zirconium-in-rutile thermometer (Zr-in-rutile) was used to determine the peak metamorphic temperature recorded by each rock. The recently updated combined experimental-empirical calibration of Kohn (2020) is adopted in this study, but results of

the commonly used Tomkins, Powell, & Ellis (2007) calibration are reported for comparison. For 16 samples, the concentration of Zr was measured using the JEOL JXA 8900R Electron Probe Microanalyzer (EPMA) at the University of Maryland. Measurements were made using a 20 kV accelerating voltage, a beam current of 120 nA, and a beam diameter of 5 μm. Zr was measured simultaneously on three spectrometers. For the first two spectrometers, the peak was counted for 300 seconds and the background for 150 seconds. On the third spectrometer, the peak was counted for 240 seconds and the background for 120 seconds. The data were processed using a ZAF correction scheme (Armstrong, 1988), and the quality was assessed using the secondary standard K13-02 (natural rutile, [Zr] ~273 ppm; see Appendix S1). Uncertainties from counting statistics typically range from 2-15%. One sample was additionally analyzed by laser ablation inductively coupled plasma mass spectrometry (LA-ICP-MS). The results from the two methods were not appreciably different, so the data were combined to calculate a final temperature. Additional details on the method, as well as a comparison between LA-ICP-MS and EPMA, can be found in Appendix S1.

For each sample 8-44 rutile grains were analyzed, depending on grain size and abundance, with 1-4 analyses per grain. The center of each grain was targeted to measure the highest Zr concentration, and additional points were measured across the grains to assess heterogeneity. Both matrix rutile and rutile inclusions in garnet and hornblende were analyzed. To account for phase boundary effects and micro-inclusions of quartz or zircon, analyses with Si > 300 ppm were excluded (see Zack, Moraes, & Kronz, 2004).

The mean maximum zirconium method (Penniston-Dorland et al., 2018) was used to estimate the maximum Zr content of rutile in each sample, which is assumed to represent the peak metamorphic Zr content and consequently temperature. This approach is preferred for defining the peak metamorphic conditions of samples where rutile grains record a wide range of Zr concentrations. Variations in Zr concentration amongst rutile grains may reflect growth throughout the metamorphic history of the sample or a number of secondary processes. These secondary processes include variation in the activities of quartz and zircon, diffusion or exsolution of Zr out of rutile, recrystallization, and diffusion-limited exchange at low temperatures. The majority of processes expected to occur in amphibolite-facies mafic and metasedimentary rocks (lowering a_{Qtz}, diffusion, exsolution) lower the observed Zr concentration, making the peak conditions more difficult to recover. The only process that might increase the observed Zr concentration during prograde metamorphism is $a_{Qtz} <1$, either in quartz-absent rocks or from diffusion-limited transport of SiO_2 along grain boundaries (or both). Because of the ubiquity of quartz in the samples, an $a_{Qtz} < 1$ is unlikely, and even in quartz-absent rocks from amphibolite-facies blocks of the Catalina Schist, amphibole chemistry implies $a_{Qtz} \sim 1$ (calculated range = 0.94 to 1.07; Penniston-Dorland et al., 2018). Also, diffusion-limited exchange has been proposed to occur only during cooling at temperatures ≤ ~550 °C (Kohn et al., 2016). From a more practical perspective, microinclusions of zircon could also cause spuriously high Zr analyses, through either direct ablation during LA-ICP-MS analysis (e.g., see Chalmers, Spear, & Cheney, 2007) or fluorescence during EPMA analysis. Within the context of these considerations, the approach is as-follows:

1) Using the maximum Zr concentration recorded by each grain, we identify a high-Zr population of statistically overlapping rutile compositions (i.e., indistinguishable within uncertainty) that includes the highest-Zr analysis.
2) If the population contains 4 or more analyses, the population is assumed to represent the peak Zr composition, The maximum Zr content and uncertainty are calculated from that population using a mean and standard deviation about the mean. A cutoff of 4 analyses is consistent with common practice in interpreting other types of geochemical data such as detrital zircon data, where a minimum of 3 analyses (but more typically 4 or more) are used to define significant age peaks (e.g., Dickinson & Gehrels, 2009). Fewer analyses are considered outliers.
3) If the population that includes the highest-Zr analysis contains fewer than 4 analyses, the 4 analyses with highest Zr are averaged and a standard deviation calculated. Here, the philosophy is to acknowledge the possibility of either analytical artifacts or low a_{Qtz}, without discarding any measurements. The temperature and its uncertainty are calculated from the mean and standard deviation of these 4 analyses.

In general, the "mean max method" predicts similar results to using an upper-quartile concentration (e.g., EA15-10A in Figure S1.5), which has been used by others (e.g., Tomkins et al., 2007). However, there are some notable exceptions. In samples where two (or more) distinct rutile populations were analyzed (e.g., rutile inclusions in garnet and matrix rutile), upper-quartile Zr concentrations are systematically lower than the mean

maximum Zr concentrations (WB16-03A in Figure S1.5). We attribute this discrepancy to retrogression of matrix rutile, which skews the population towards lower Zr concentrations. This effect is mitigated by using a mean maximum Zr concentration.

2.4.2 Quartz-in-garnet elastic barometry

Peak metamorphic pressures were determined using the quartz-in-garnet elastic barometer (QuiG; Angel, Alvaro, Miletich, & Nestola, 2017; Angel, Mazzucchelli, Alvaro, & Nestola, 2017; Enami, Nishiyama, & Mouri, 2007; Kohn, 2014; Thomas & Spear, 2018). The following sections outline our procedure.

2.4.2.1 Measurements

Raman spectra of encapsulated quartz inclusions were collected *in situ* using the Jobin Yvon Horiba LabRAM HR Evolution Raman microscope equipped with a 532 nm laser at the Department of Materials Science and Engineering, Boise State University. The instrument was calibrated daily using a silica wafer. Spectra were collected using a 100x optical objective,1800 gr/mm grating, and a neutral density filter between 25 and 50%. For the optics of this system, the analytical spot has a diameter of approximately 1 μm. Three 10-second accumulations on a single spot were averaged to produce a spectrum for each inclusion. Samples were analyzed immediately following analysis of unstressed natural quartz to account for any instrumental drift. Only near-spherical quartz inclusions that were more than 3x the radius of the inclusion to any free surface (i.e., grain boundaries or fractures, another inclusion, the surface of the thin section) were analyzed to avoid elastically-relaxed inclusions (see Campomenosi et al., 2018; Mazzucchelli et al., 2018).

The radius of most inclusions was between 5 and 10 µm. Any mutually proximal inclusions were also avoided because they can exhibit excess pressure compared to isolated inclusions (Bonazzi, Tumiati, Thomas, Angel, & Alvaro, 2019). Between 6 and 18 inclusions were analyzed for each sample, depending on the number of suitable inclusions present in the thin section. No preference was given to individual zones of garnet, although some inclusion-rich garnet cores were not suitable for analysis.

Raman spectra were fit using a mixed Gaussian-Lorentzian function with the Matlab program ipf.m (https://www.mathworks.com/matlabcentral/fileexchange/23452-ipf-arg1-arg2-arg3-arg4). The drift-corrected external reproducibility of the unstressed natural quartz standard was typically <0.10 cm^{-1}, <0.15 cm^{-1} and <0.10 cm^{-1} for the 128 cm^{-1}, 206 cm^{-1} and 464 cm^{-1} peaks, respectively. This reproducibility is significantly larger than any uncertainty associated with fitting the Raman spectra, and is therefore used as a conservative estimate of uncertainty in the peak positions. These uncertainties propagate to uncertainties in the three peak shifts (sample minus standard, $\Delta\omega$) of 0.14 cm^{-1}, 0.21cm^{-1} and 0.14 cm^{-1} respectively.

2.4.2.2 Calculations of inclusion pressure (P_{inc})

In a quartz inclusion, Raman peak position shifts relative to a standard are sensitive to strain. Residual strain on each inclusion was calculated from $\Delta\omega$ using the phonon-mode Grüneisen tensor for quartz (Murri et al., 2018) in the program stRAinMAN (Angel, Murri, Mihailova, & Alvaro, 2019). Reported uncertainties for the independent strain components (ε_{1+2}, ε_3) reflect both uncertainty in $\Delta\omega$ and in fitting the strain components (see Angel et

al., 2019). Because volume strain ($\varepsilon_v = 2\varepsilon_1+\varepsilon_3$) often overestimates inclusion pressures (Bonazzi et al., 2019), the independent strain components were converted to average stress (or inclusion pressure; P_{inc}) using the elastic tensor for quartz (*C*; Wang, Mao, Jiang & Duffy, 2015), where $\sigma_i = C_{ij}\varepsilon_j$ and $P_{inc} = -\frac{1}{3}\sum_{i=1}^{3}\sigma_i$.

2.4.2.3 Identification of maximum P_{inc}

Ultimately, we seek to use the values of P_{inc} to calculate an entrapment isomeke (an isopleth in *P-T* space along which there is no deviatoric volume change between the host and inclusion, i.e., at which an inclusion could have been fully entrapped in a host). Inclusions can be susceptible to reequilibration adjacent to even tiny fractures, with a decrease in P_{inc} for moderate- to high-pressure rocks (Enami et al., 2007), so many researchers seek the maximum P_{inc} value for estimating peak entrapment pressure. Insofar as we know, no statistically robust method has been proposed to identify a maximum P_{inc} and ascertain its errors from multiple measurements.

In this study, the Isoplot data processing tool (Ludwig, 2012) was used to identify whether the data were consistent with measurements of one or more unique P_{inc} values. Importantly, our approach provides an alternative to other studies that have not considered uncertainties and instead focused on raw maximum inferred P_{inc} (e.g., Kouketsu, Nishiyama, Ikeda, & Enami, 2014; Spear, Thomas, & Hallett, 2014), sometimes for a single measurement. If uncertainties are large, the highest P_{inc} may not be statistically different from lower, more precise P_{inc} values. In this case a robust estimate of P_{inc} may be lower than assumed. Conversely, a cluster of P_{inc} values may appear to form a single population when in fact reproducibilities are sufficiently good to warrant separation into

different, overlapping clusters. In this case, a robust estimate of P_{inc} is higher than assumed. These retrieved values are referred to here as "best-fit P_{inc} values" to distinguish them from an "individual P_{inc}", which refers to a single measurement. Isoplot's "unmix" routine (Sambridge and Compston, 1994) was applied iteratively to identify whether the data were consistent with a single best-fit P_{inc} or multiple best-fit P_{inc} values. Noting that unmix must return at minimum two P_{inc} values, our possible outcomes were evaluated as follows:

1. Two identical best-fit P_{inc}'s (LB15-03B, A15-07A, A15-21A). All data were combined to calculate a weighted mean, its uncertainty, and an MSWD. Note that unmix must return at minimum two P_{inc} values. Although the values of both P_{inc} values are the same in this case, unmix does not calculate an uncertainty for a combined single P_{inc}. Combining all data into a simple weighted mean accurately represents its uncertainty.
2. A cluster of data at high P_{inc} and a single low- P_{inc} outlier (GB, EA15-10A, A15-01A). The low- P_{inc} outlier was eliminated and a weighted mean, its uncertainty, and an MSWD were calculated for the cluster. In unmixing a set of data, each analysis affects each best-fit P_{inc}, even if only slightly. The philosophy here is that if data are clearly distinct, they should be treated independently.
3. A cluster of data at low P_{inc} and a single high- P_{inc} outlier (A15-22). Choosing either the cluster or the outlier does not change our interpretations. Considering that an inclusion can be overpressured because of proximity to other inclusions (Bonazzi et al., 2019), the high- P_{inc} outlier was eliminated, and a weighted mean, its uncertainty, and an MSWD were calculated for the cluster. Other studies might favor the outlier.

4. Multiple clusters that cannot be separated into specific subsets of analyses (A14-71, E2718C). The output of the unmix routine was used directly, selecting the maximum best-fit P_{inc} for interpretation.

The uncertainty in a best-fit P_{inc} value can be surprisingly small. For example, the median uncertainty in individual P_{inc} values for this dataset was ±0.083 GPa, whereas the median uncertainty in the maximum best-fit P_{inc} was ±0.027 GPa. This reduction in uncertainty reflects averaging of statistically indistinguishable measurements. For weighted means, the data are assumed to derive from repeatedly measuring the same (best-fit) P_{inc} from multiple inclusions with varying magnitudes of uncertainty. If there is a single value of P_{inc}, multiple measurements will reduce the uncertainty in its value. The same principle holds for unmixing. Although there will be more than one best-fit P_{inc}, each is supported by multiple analyses, reducing its uncertainty.

We emphasize that statistical approaches should be applied cautiously, with special consideration for spatial distributions of inclusions and P_{inc}. If, for example, pressure was decreasing during garnet growth, the highest P_{inc} values from inclusions in the core of the garnet have no relevance to the peak P-T conditions, even if high P_{inc} values are statistically well-defined. Similarly, different values of P_{inc} may correlate with chemical zoning (Viete et al., 2018), and should be interpreted separately. For the samples considered here, there is no spatial dependence to P_{inc} values.

Note that averaging multiple individual P_{inc} values implies that some must be higher than the (averaged) best-fit P_{inc}. This deviation can be large if the uncertainty in an individual P_{inc} is large. In fact, in the current dataset, some of the highest individual P_{inc} values have the largest uncertainties, in several cases >0.2 GPa (e.g., in A14-71 and GB). While these individual P_{inc} values might superficially imply a higher entrapment pressure, the uncertainty is large, and they cannot be distinguished from lower entrapment pressures. These individual P_{inc} values represent clear cases where indiscriminate use of the highest P_{inc} should be avoided. Although unmixing should identify statistically different outliers, the consistency of the highest individual P_{inc} values with the best-fit P_{inc} value was double-checked to ensure they were truly statistically indistinguishable.

2.4.2.4 Calculation of isomekes

After P_{inc} values were determined for each inclusion and for the best-fit P_{inc} and its 95% confidence limits, entrapment pressure isomekes were calculated between 500 and 800°C in the module EOS-FitPinc (http://www.rossangel.com/text_eosfit.htm) using the most recent equations of state for quartz (Angel et al., 2017a,b; verified experimentally by Thomas and Spear, 2018) and almandine (Milani et al., 2015). Uncertainties in host garnet composition do not significantly affect calculated isomekes for QuiG (<0.1 GPa; Kohn, 2014). For best-fit P_{inc} and its 95% confidence limits, the best-fit isomeke and a band corresponding to the 95% confidence limits on that isomeke are shown.

2.4.3 Calculation of *P-T* conditions

For each sample with both Zr-in-rutile and QuiG analyses (n=9), the intersection between the Zr isopleth and pressure isomeke was assumed to represent the peak metamorphic condition. This assumption is supported by petrographic observations: rutile coexists with quartz inclusions in garnet for all of the samples. The maximum uncertainty defined by the intersection of the error envelopes (i.e., the upper NE and lower SW corners of the intersection polygon) for the QuiG isomeke and Zr isopleth is reported as the final uncertainty for these samples. For samples without QuiG pressure estimates (n=10), a pressure of 1.4 GPa was used to estimate the peak metamorphic temperature based on QuiG estimates from the amphibolite-facies mélange zone. The thermometer's dependence on pressure is ~5°C/0.1 GPa, so uncertainties of even ±0.25 GPa propagate to relatively small errors in temperature. The uncertainties reported here apply only for inter-comparison of samples using the same thermometer/barometer. The calibration uncertainty of the Zr-in-rutile thermometer is around 10°C (Kohn, 2020). The calibration uncertainty of QuiG has not been studied extensively, but data from Bonazzi et al. (2019) show consistency between QuiG and experimental pressures to within 0.04±0.05 and 0.10±0.03 GPa.

2.5 Results

2.5.1 Field Observations

As documented by Platt (1975, 1976), most exotic blocks within the epidote amphibolite and lawsonite blueschist units occur close to the boundary between these units, either as observed directly in the field or as projected from regional structure. All blocks contain garnet, which should not be stable for most bulk compositions if peak

metamorphism of the blocks occurred at the same *P-T* conditions as the surrounding epidote amphibolite- and lawsonite blueschist-facies rocks (Grove & Bebout, 1995). These blocks typically occur in clusters or regions surrounded by and interspersed with apparently lower-grade rocks. Five of these regions are described below and shown on Figure 2.1. Of these, Regions A and B occur within the epidote amphibolite unit, sample LB/A14-01 and the garnet blueschist block occur within the lawsonite blueschist unit, and the Ollas Fault Zone separates amphibolite-facies units from epidote amphibolite and epidote blueschist units. More detailed descriptions follow.

2.5.1.1 Region A

This ~0.5 x 0.5 km region within the epidote-amphibolite facies unit contains mélange with blocks of amphibolite, mafic garnet-amphibolite, and metagraywacke (Figure 2.1C). Amphibolite blocks are generally foliated and closely resemble the mafic portion of the coherent amphibolite unit, which primarily contains garnet-absent foliated rocks with green hornblende, epidote and plagioclase. In contrast, the mafic garnet-bearing blocks are non-foliated and resemble mafic blocks observed throughout the amphibolite-facies mélange zone. These contain brown hornblende and garnet that often statically overgrow inherited compositional layering or an older foliation. A chlorite + talc + actinolite matrix is exposed locally, but no matrix was observed in direct contact with the blocks. Lower-grade material (i.e., lawsonite blueschist) was not observed within the region.

2.5.1.2 Region B

This ~1 km x 0.5 km region within the epidote-amphibolite facies unit contains mélange with mafic, unfoliated blocks of garnet amphibolite and epidote amphibolite (Figure 2.1D) with no systematic spatial arrangement. Several exposures of matrix, some in direct contact with blocks, consist of either talc + actinolite or are chlorite-rich. The region occurs to the north of a large package of coherent epidote amphibolite-facies metasedimentary rocks (Platt, 1975), although the contact between these units is not clearly exposed. Lawsonite blueschist-facies rocks occur both to the north, west and east of the unit (Figure 2.1); however, none were observed within the region. The contact between the lawsonite blueschist and epidote amphibolite units in this region is not preserved.

2.5.1.3 LB/A14-01

Outcrop LB/A14-01 (red star, Figure 2.1A; outcrop photograph in Appendix S1) consists of a rounded garnet amphibolite block encapsulated by mafic-ultramafic matrix (physically above) and lawsonite-blueschist facies metasedimentary rock (physically below). Centimeter-scale micro-blocks –likely chlorite or serpentine– occur in the matrix. The contact between the block and both the matrix and metasedimentary rock is sharp, with no intercalation. A ~4 cm thick actinolite + chlorite reaction rind separates the core of the block from the surrounding mafic-ultramafic matrix. Previous studies have interpreted this outcrop to represent the contact between the epidote amphibolite and lawsonite blueschist units (Platt, 1976). However, the relationship between the two units at this location is ambiguous. While the lower portion of the contact is clearly lawsonite blueschist-facies material, the matrix structurally above the block is not indicative of either facies. There are

also no clear field relationships between the block and epidote amphibolite-facies rocks. Therefore, we tentatively interpret the block as occurring within the lawsonite blueschist-facies unit, although we cannot rule out that it is a rare example of the contact between the epidote amphibolite and lawsonite blueschist units. The block does not contain rutile, so *P-T* conditions were not determined. However, this exotic amphibolite block represents a rare example where the contact with matrix is clearly visible.

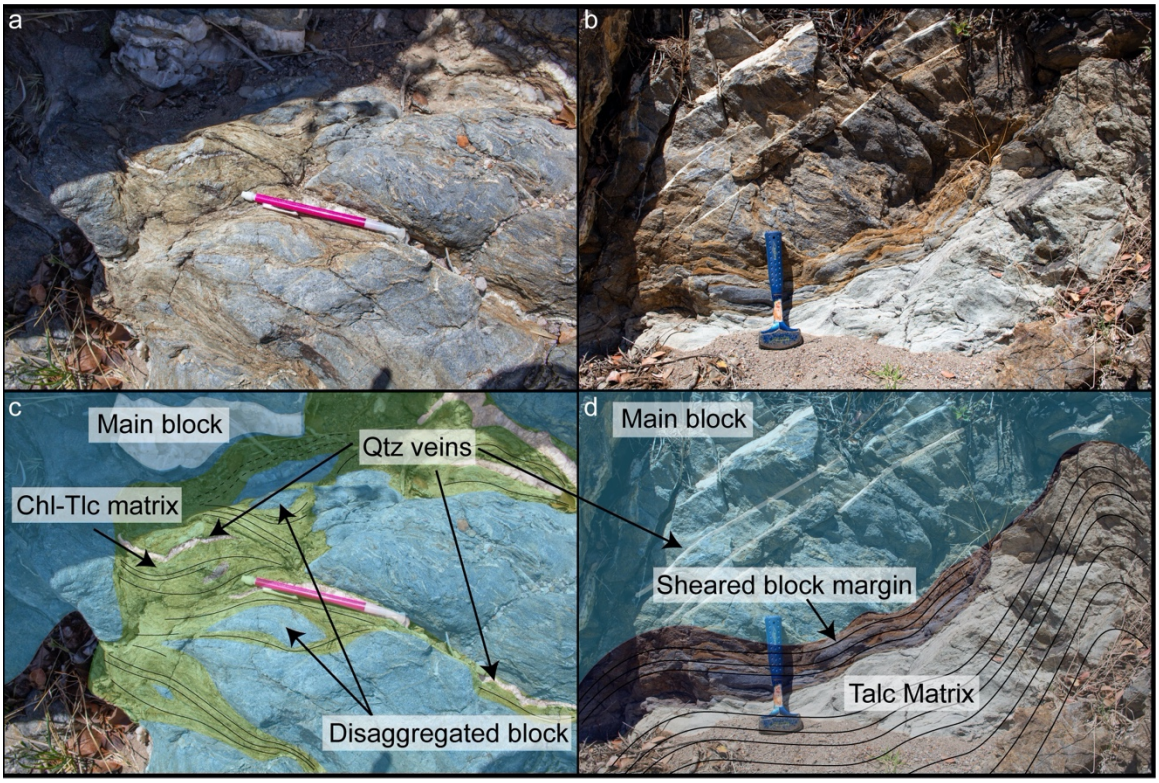

Figure 2.3. Outcrop photos and simplified sketches of mélange matrix in contact with the base of the garnet blueschist exotic block. (a, c) matrix with quartz veins and boudinaged garnet blueschist (b, d) matrix at base of the garnet blueschist block, showing a foliation subparallel to the sheared block margin.

2.5.1.4 Garnet blueschist block

This ~100 m x 50 m mafic block (gold star, Figure 2.1A) occurs within the lawsonite blueschist facies unit and is variably foliated and compositionally heterogeneous. Two types of contacts with mélange matrix were observed. The first matrix, a fine-grained

mafic-ultramafic chlorite + talc phyllite/phyllonite, is commonly intercalated with block material at its edge and cross-cut by quartz veins. The second matrix is fine-grained, gray, talc-dominated, and foliated subparallel to the sheared block margin, but it is not intercalated with the block and lacks quartz veins (Figure 2.3b). $^{40}Ar/^{39}Ar$ and Rb-Sr ages of the garnet blueschist are >135 Ma (Grove and Bebout, 1995; Grove et al., 2008) are significantly older than the surrounding lawsonite blueschist-facies rocks (<97 Ma; Grove et al., 2008).

2.5.1.5 Ollas Fault Zone

The Ollas fault zone (purple star in Figure 2.1a) has previously been interpreted as a low-angle thrust fault that juxtaposed amphibolite-facies rocks with lower grade units during exhumation (Platt, 1975, 1976). The fault is locally ≤ ~0.15 km thick where it outcrops between the epidote blueschist and coherent amphibolite units. Within the fault zone, ~ 0.5 m mafic blocks are entrained within a heterogenous matrix (Figure 2.4). Garnet-bearing blocks are rare. A highly-deformed actinolite-dominated matrix (likely a sheared reaction zone) and a talc + biotite matrix occur at the base of the hanging wall. Both are foliated sub-parallel to the contact, which is oblique to the primary foliation of the coherent amphibolite unit. The footwall of the fault zone in this area consists of a ~10 m-thick, epidote blueschist-facies, highly-strained metachert composed primarily of quartz + glaucophane + garnet. The metachert is underlain by a foliated mafic blueschist with

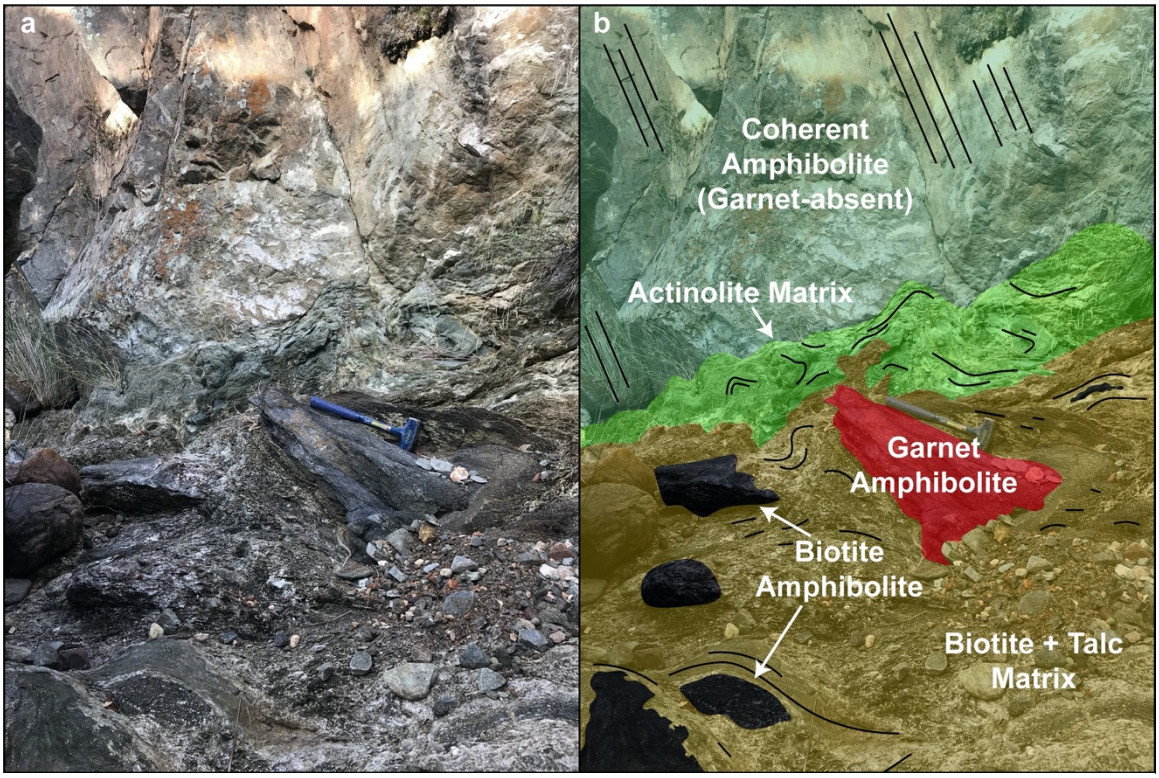

Figure 2.4. A) Contact between the base of the coherent amphibolite unit and Ollas fault zone exposed in Cottonwood Canyon (locations 12-16 in Figure 2.1) showing two matrix lithologies and blocks hosted within biotite-talc matrix. B) Simplified sketch showing the foliation of the coherent amphibolite and two matrix compositions as well as the relationship between the fault zone blocks and matrix.

epidote porphyroblasts. More detailed descriptions of the epidote blueschist-facies rocks can be found in Appendix S1.

2.5.2 Rock samples and mineralogy

Twenty-four samples were chosen for analysis. Of these, eleven are from exotic blocks, five are isofacial epidote amphibolite-facies rocks, five are isofacial amphibolite-facies rocks, one is from the coherent amphibolite unit, and two are mélange matrix. Sample lithologies are summarized in Table 2.1 and locations are shown in Appendix S1. Six major lithologies were analyzed: mafic amphibolite, garnet-bearing blueschist, garnet quartzite, metapelite, metagraywacke, and mélange matrix adjacent to exotic blocks.

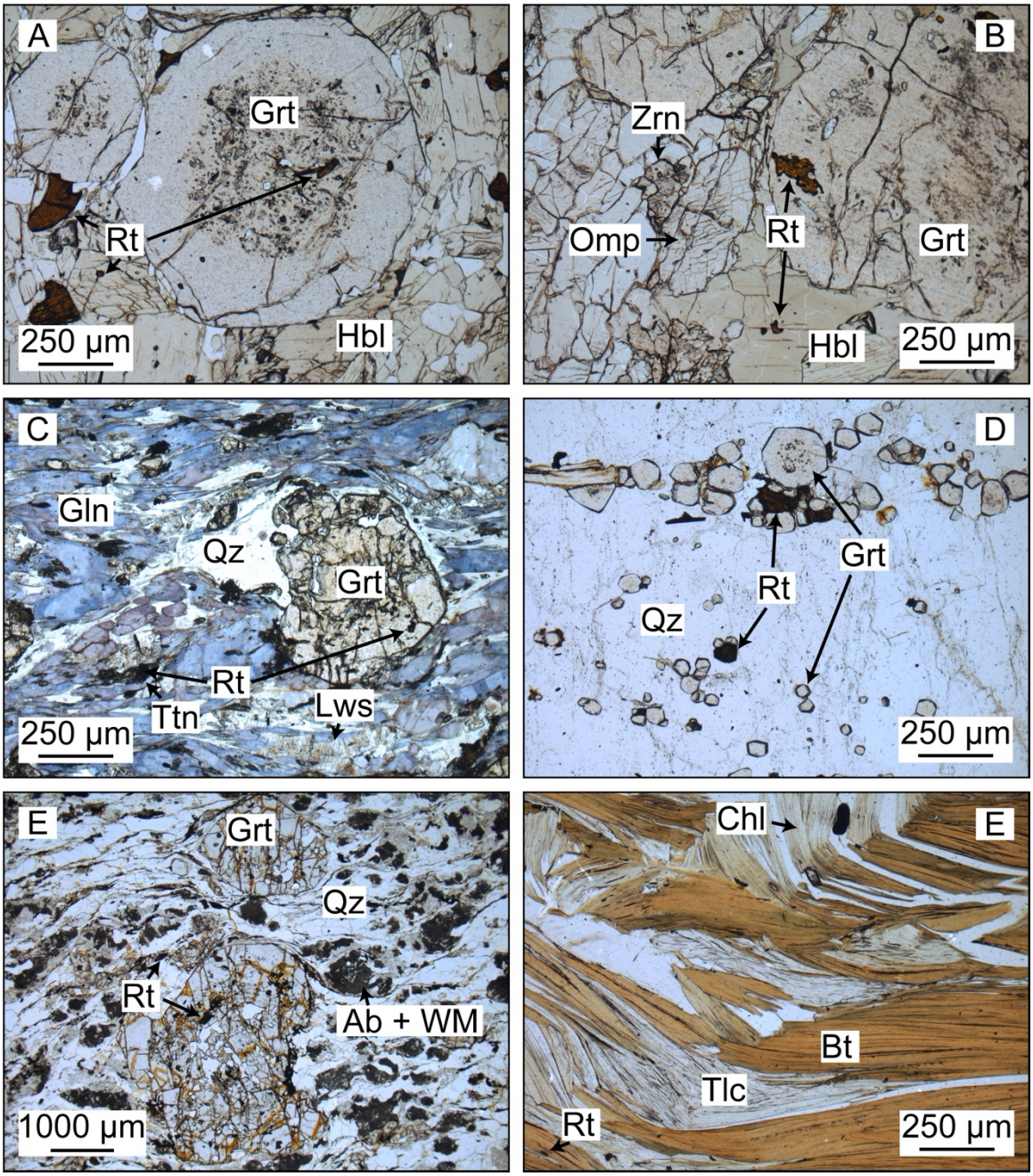

Figure 2.5. Representative photomicrographs of rocks from the Catalina Schist a) amphibolite-facies mélange block showing subhedral garnet with rutile inclusions and adjacent matrix rutile b) exotic block (A14-71) showing matrix omphacite associated with garnet porphyoblast as well as hornblende, zircon and rutile which occur both as inclusions and matrix phases. c) exotic block (GB) showing showing a pervasive blueschist-facies overprint. Lawsonite occurs in the matrix and within fractures in garnet. d) metachert (A15-01A) from the amphibolite-facies mélange zone. e) metagraywacke exotic block (LB15-03B) showing fractured garnet pophyroblasts as well as albite + white mica symplectite. f) Mélange matrix (CC16-14E) from the Ollas fault zone showing intergrowth of biotite and chlorite as well as talc and rutile. Mineral abbreviations after Whitney and Evans (2010). Ab = albite; Bt = biotite; Chl = chlorite; Gln = glaucophane; Grt = garnet; Hbl = hornblende; Lws = lawsonite; Qz = quartz; Rt = rutile; Zrn = zircon.

The amphibolites all contain hornblende with varying amounts of garnet and/or epidote (Figure 2.5a). Plagioclase is often replaced by an albite + zoisite + white mica symplectite (Kohn, Penniston-Dorland, & Ferreira, 2016). Minor amounts of chlorite commonly occur in the matrix or partially replacing garnet. Quartz, rutile and/or titanite, zircon, and ilmenite occur as accessory phases. Rutile occurs in the matrix and as inclusions in hornblende and garnet. When titanite and rutile coexist, titanite generally rims rutile. Omphacite occurs rarely in some amphibolite-facies mélange zone blocks (see Sorensen & Barton, 1987), and in one exotic block (sample A14-71; Figure 2.5b). Biotite occurs in one amphibolite exotic block (CC16-14B). In general, mafic mélange blocks are generally not foliated and often preserve compositional layering. The coherent amphibolite preserves a primary foliation defined by hornblende and epidote.

The garnet-bearing blueschist block primarily consists of sodic amphibole and garnet with varying amounts of quartz. Unlike many other mafic mélange blocks, the sample preserves a strong foliation defined by glaucophane and lawsonite. Both glaucophane and lawsonite occur as a late-stage phases in the matrix (Figure 2.5c) and lawsonite has been observed within cracks in garnet (Alder-Ivanbrook, Hampton, Esparaza Limon, Lackey, & Page, 2018). Rutile occurs as inclusions in garnet and is almost completely replaced by titanite in the matrix. Zircon and apatite occur as accessory phases.

The garnet quartzites consist primarily of quartz with fine-grained garnet (Figure 2.5d) and generally preserve compositional layering defined by thin (<1 mm) garnet-rich

bands. Rutile and zircon occur both as inclusions within garnet and in the matrix. Trace amounts of allanite, chlorite and ilmenite also occur.

The metapelites and metagraywackes are all foliated and contain varying amounts of feldspar, quartz, chlorite, and (in higher-grade rocks) porphyroblastic garnet (Figure 2.5e). Rutile occurs both in the matrix and as inclusions in garnet. Fine-grained albite + white mica + zoisite symplectite is commonly observed in the high-grade rocks. Accessory phases include rutile, zircon, graphite and ilmenite.

One of the matrix samples from the Ollas fault zone is dominated by biotite and talc (Figure 2.5f), the other by actinolite and minor biotite. Rutile, zircon and quartz occur as accessory phases in both samples.

Because rutile is found both in the matrix of the rock samples and as inclusions in the peak metamorphic mineral assemblage, it is interpreted to have grown over a range of metamorphic conditions that included peak temperatures. Zircon and quartz are proximal to or touching rutile, but show no reaction textures (e.g., zircon rimming rutile; Ewing, Hermann, & Rubatto, 2013). Garnet with quartz inclusions suitable for quartz-in-garnet barometry occurs in four exotic blocks and all amphibolite-facies mélange zone blocks.

2.5.3 Zr-in-rutile thermometry

Zirconium concentrations in rutile show no obvious systematic distribution within and among grains (Figure 2.6; see complete data set in Appendix S1). Profiles across some

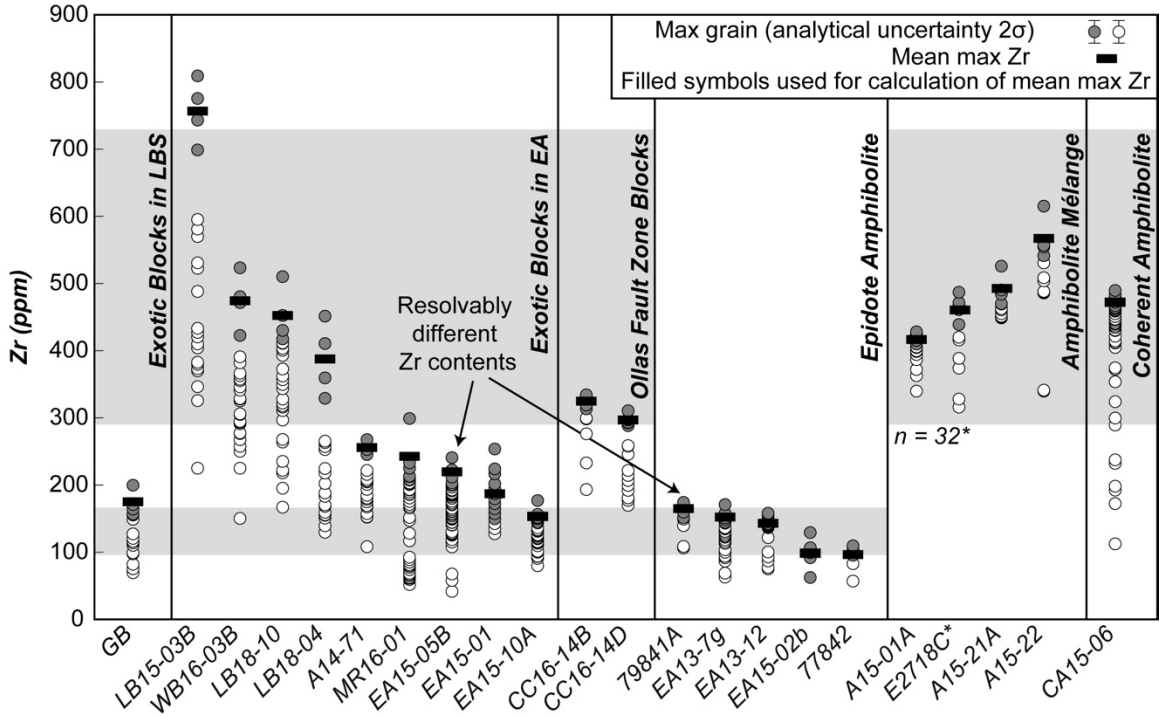

Figure 2.6. Zirconium concentrations in rutile for exotic blocks from the lawsonite blueschist, epidote amphibolite facies and Ollas fault zone, epidote amphibolite rocks (mélange blocks and coherent metasedimentary rocks), amphibolite-facies mélange blocks, and coherent amphibolite. Each column displays the range of zirconium concentrations measured in rutile throughout the samples and the mean-maximum concentration for each. The filled circles represent grains used to calculate the mean-maximum concentration, which is shown as a black rectangle. The average analytical uncertainty for EPMA is shown in the legend. The grey bars represent the range of Zr concentrations measured throughout the isofacial amphibolite and epidote amphibolite units. Data for sample E2718C are from Penniston-Dorland et al. (2018).

grains are nearly homogeneous or show a change in concentration only at the rims. Other grains show decreasing Zr concentrations towards rims. In some samples, rutile inclusions in garnet record higher Zr concentrations than those in the matrix; however, in most samples there is no systematic compositional difference between inclusions and matrix grains (see Appendix S1 for examples of both inter- and intra-grain Zr variability observed in the exotic block samples). Mean maximum Zr concentrations are reported in Table 2.1.

Table 1. Summary of sample lithology, location, Zr content in rutile, and peak metamorphic conditions

Sample Number and Location in Figure 1		Lithology	Mean Max Zr (ppm)	T (°C) Kohn (2020)	T (°C) Tomkins et al. (2007)	P_{inc} (GPa)	P_{trap} (GPa)
Region A: Amphibolite Facies Exotic Blocks in Epidote Amphibolite-Facies Unit							
LB15-03B	1	Metagraywacke	757 ± 94	735 ± 12	745 ± 11	0.347 ± 0.021	1.30 ± 0.05
LB18-04*	2	Grt Amphibolite	388 ± 108	671 ± 19	688 ± 17		
LB18-10*	3	Metagraywacke	452 ± 82	686 ± 13	702 ± 12		
Region B: Amphibolite Facies Exotic Blocks in Epidote Amphibolite-Facies Unit							
EA15-10A	4	Grt Amphibolite	153 ± 20	579 ± 10	606 ± 9	0.363 ± 0.027	1.16 ± 0.06
EA15-05B*	5	Grt Amphibolite	219 ± 32	619 ± 9	642 ± 8		
EA15-01A*	6	Grt Amphibolite	185 ± 61	605 ± 19	629 ± 17		
Region B: Epidote-Amphibolite Facies Blocks in Epidote Amphibolite-Facies Unit							
EA15-02Ba*	i	Ep Amphibolite	95 ± 36	553 ± 19	581 ± 17		
Other Epidote-Amphibolite Facies Rocks in Epidote Amphibolite-Facies Unit							
79841A*	ii	Metapelite	167 ± 22	596 ± 7	621 ± 7		
77842*	iii	Metapelite	98 ± 23	555 ± 12	583 ± 11		
EA13-07g	i	Ep Amphibolite	152 ± 26	589 ± 9	614 ± 9		
EA13-12*$^{+}$	v	Ep Amphibolite	144 ± 19	584 ± 9	610 ± 8		
Other Exotic Blocks in Epidote Amphibolite-Facies Unit							
WB16-03A*	7	Grt Amphibolite	475 ± 83	691 ± 13	706 ± 11		
A14-71	10	Grt Amphibolite	255 ± 22	636 ± 10	658 ± 9	0.47 ± 0.057	1.47 ± 0.11
MR16-01*	11	Grt Amphibolite	243 ± 77	628 ± 19	650 ± 18		
Exotic Blocks in Lawsonite Blueschist-Facies Unit							
LB/A14-01	8	Grt Amphibolite					
GB	9	Grt Blueschist	173 ± 34	611 ± 15	635 ± 14	0.608 ± 0.042	1.65 ± 0.10
Ollas Fault Zone Blocks (Amphibolite Facies)							
CC16-14B*	12	Bt Amphibolite	325 ± 20	654 ± 4	673 ± 4		
CC16-14D*	13	Grt Amphibolite	297 ± 15	646 ± 3	666 ± 3		
Ollas Fault Zone Matrix (Amphibolite Facies)							
CC16-14C*	14	Act Matrix	344 ± 43	660 ± 8	678 ± 7		
CC16-14E*	15	Bt-Tlc Matrix	129 ± 17	576 ± 7	602 ± 6		
Amphibolite Facies Blocks in Amphibolite Facies Mélange Zone							
E2718C**	a	Metagraywacke	461 ± 39	689 ± 10	705 ± 9	0.387 ± 0.041	1.42 ± 0.08
A15-01A	b	Grt Quartzite	417 ± 22	676 ± 7	693 ± 6	0.35 ± 0.03	1.34 ± 0.06
A15-22	c	Grt Quartzite	567 ± 66	707 ± 11	721 ± 9	0.325 ± 0.01	1.36 ± 0.03
A15-21A	d	Grt Quartzite	493 ± 48	697 ± 10	712 ± 8	0.391 ± 0.026	1.44 ± 0.06
A15-07A***	e	Grt Amphibolite				0.341 ± 0.025	1.26-1.47
Coherent Amphibolite							
CA15-06*	f	Paragneiss	470 ± 21	690 ± 3	705 ± 3		

**T estimated at 1.4 GPa; **Zr concentration from Penniston-Dorland et al. 2018; $^{+}$analyzed by LA-ICP-MS and EPMA; ***P estimated from 650-730˚C. Grt = garnet; Ep = epidote; Bt = biotite; Act = actinolite; Tlc = talc*

In the amphibolite-facies mélange zone, mean maximum Zr concentrations in rutile from 30 mélange blocks and 1 matrix sample range from 290 to 720 (± 10-40) ppm (Figure 2.6; Penniston-Dorland et al., 2018; this study). Calculated at 1.4 GPa (see discussion below; recalculated temperatures are shown in Appendix S1), these Zr concentrations correspond to peak metamorphic temperatures of 643°C to 735°C (± 4-28°C; Penniston-

Dorland et al., 2018 using the new calibration by Kohn, 2020; this study). Concentrations of Zr in rutile from the coherent amphibolite unit (470 ± 21 ppm) fall within the range that is observed for the amphibolite-facies mélange zone and imply T = 690 ± 3°C (at an assumed pressure of 1.4 GPa). In epidote amphibolite facies rocks, rutile records significantly lower Zr concentrations between 98 and 167 (± 22-26) ppm, corresponding with temperatures of 553-596°C (± 9-19°C).

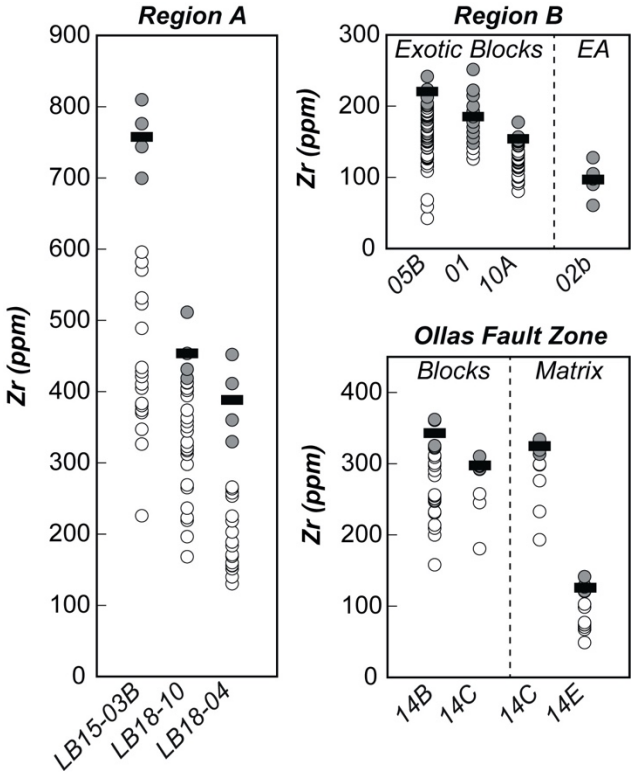

Figure 2.7. Zirconium concentrations for rutile in blocks from Regions A and B and both blocks and mélange matrix from the Ollas fault zone. Symbology and uncertainty follow Figure 2.6. Prefixes for sample numbers from Region B and the Ollas Fault Zone are EA15- and CC16- respectively.

In exotic blocks from the epidote amphibolite unit, rutile records mean maximum Zr concentrations between 153 and 757 (± 20-108) ppm (Figure 2.6), which corresponds to peak metamorphic temperatures between 579 and 735°C (±9-19°C). In general, rutile from Region A records the highest Zr concentrations (388 to 758 ± 82-108 ppm; Figure 2.7), the highest temperatures (671 to 735°C ± 11-17°C), and the largest temperature difference between blocks (~60 °C; samples LB18-04 and LB15-03B). In exotic blocks

within Region B, rutile records lower Zr concentrations (153 to 219 ± 20-60) ppm and peak metamorphic temperatures (579 to 619°C ± 9 to 19°C). Rutile from an epidote amphibolite block within the region records the lowest Zr concentration (95 ± 36 ppm) and temperature (553 ± 19°C).

In the two blocks within the Ollas thrust fault, rutile records mean maximum Zr concentrations of 297 ± 15 ppm and 325 ± 20 ppm respectively, corresponding to peak metamorphic temperatures of 646 to 654°C (±3-4°C). Rutile from the actinolite mélange matrix within the fault zone records a similar Zr concentration of 344 ± 43 ppm (660 ± 8°C). In contrast, rutile from the adjacent talc-biotite mélange matrix records a significantly lower Zr concentration of 129 ± 17 ppm, implying a relatively low temperature of 576 ± 7°C.

In the garnet blueschist block from the lawsonite blueschist unit, rutile records a mean maximum Zr concentration of 173 ± 34 ppm. This concentration corresponds to a peak metamorphic temperature of 635 ± 14°C at a pressure of 1.65 GPa (see Section 4.4 for constraints on pressure).

In the two blocks within the Ollas thrust fault, rutile records mean maximum Zr concentrations of 297 ± 15 ppm and 325 ± 20 ppm respectively, corresponding to peak metamorphic temperatures of 646 to 654°C (±3-4°C). Rutile from the actinolite mélange matrix within the fault zone records a similar Zr concentration of 344 ± 43 ppm (660 ± 8°C). In contrast, rutile from the adjacent talc-biotite mélange matrix records a significantly

lower Zr concentration of 129 ± 17 ppm, implying a relatively low temperature of 576 ± 7°C.

In the garnet blueschist block from the lawsonite blueschist unit, rutile records a mean maximum Zr concentration of 173 ± 34 ppm. This concentration corresponds to a peak metamorphic temperature of 635 ± 14°C at a pressure of 1.65 GPa (see Section 4.4 for constraints on pressure).

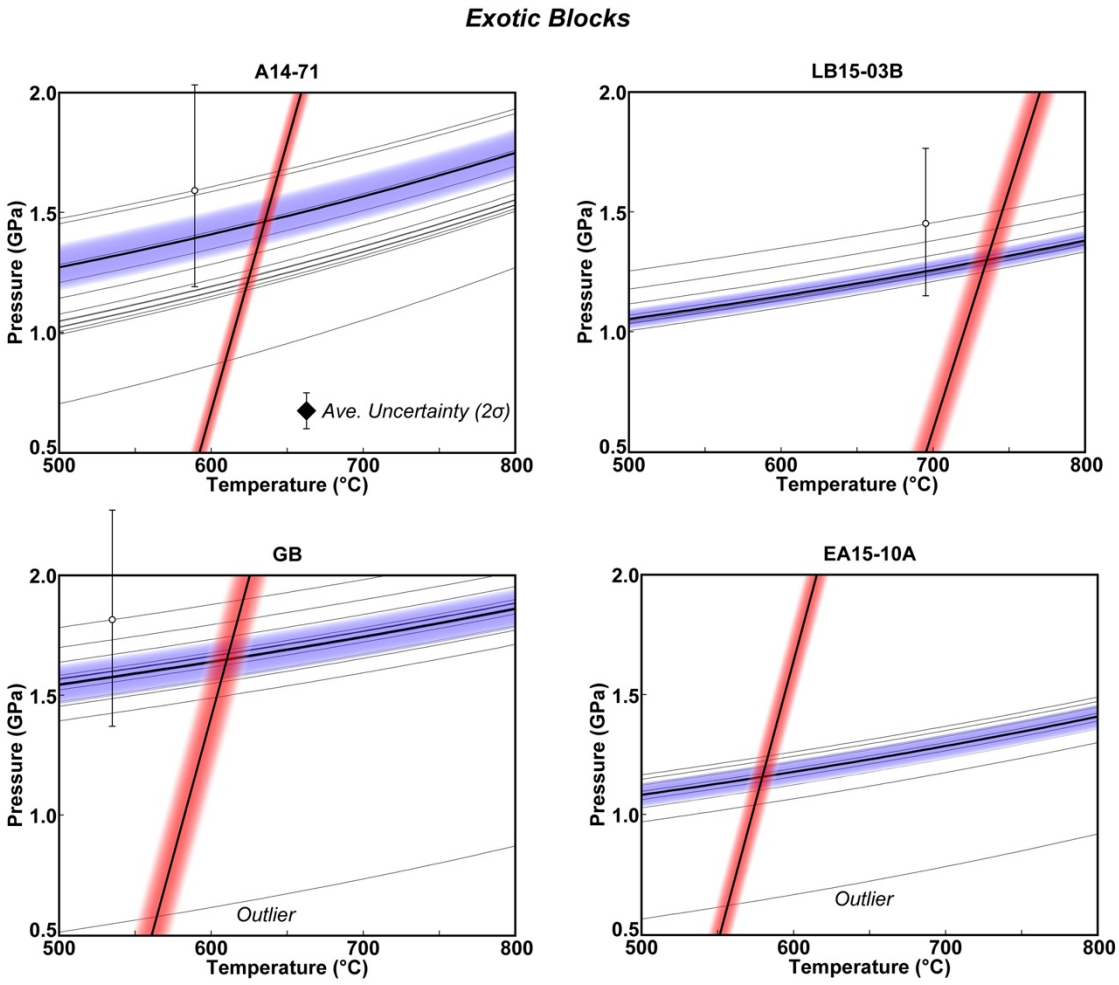

Figure 2.8. Pressure-temperature estimates for exotic blocks from the lawsonite blueschist- (GB) and epidote amphibolite-facies (A14-71, LB15-03B, EA15-10A) mélange zones determined using the intersection between the Zr-in-rutile temperature isopleths and QuiG isomekes. Individual analyses for quartz inclusions in garnet shown as grey isomekes. Mean maximum Zr-in-rutile isopleth and best-fit P_{trap} isomeke shown as solid black lines with 95% confidence intervals. White circles with error bars on maximum P_{trap} isomekes show that the large uncertainties for these specific measurements overlap the much tighter cluster defined by multiple, more resolved analyses. The average uncertainty (± 0.15 GPa) for individual analyses is shown as a black diamond with error bars.

2.5.4 Quartz-in-garnet barometry

Quartz-in-garnet barometry was used to estimate peak pressures for four exotic blocks and five amphibolite-facies mélange zone blocks. Figures 2.8-10 and Table 2.1 summarize the results of QuiG barometry. Appendix S1 lists Raman shifts, calculated strains, and inclusion pressures for each analyzed inclusion. Best-fit P_{inc} ranges from 0.33 to 0.39 ± 0.01-0.04 GPa for amphibolite-facies mélange blocks which corresponds to entrapment pressures between 1.34 and 1.44 GPa. A15-07A contains no rutile, so P_{trap} was calculated assuming the range of temperatures recorded by rutile-bearing blocks across the unit (643-735°C; recalculated from Penniston-Dorland et al., 2018; this study). This assumption implies a P_{trap} between 1.26-1.47 GPa, which is consistent with estimates for the other four amphibolite-facies mélange blocks. Because the dominant Ti-bearing phase in the block is titanite, it is likely that the block is lower-grade than the rutile-bearing amphibolite-facies mélange blocks. The stability of rutile versus titanite is primarily sensitive to pressure and composition (see Zack and Kooijman, 2017; Kohn, 2017) and is expected to be between 1.1 and 1.3 GPa for mafic lithologies. The exotic blocks within the epidote amphibolite unit record best-fit P_{inc}'s between 0.34 and 0.47 ± 0.02 – 0.04 GPa, corresponding to entrapment pressures between 1.16 and 1.47 GPa. The garnet blueschist block records a higher best-fit P_{inc} of 0.61 ± 0.04 GPa, which corresponds to a peak pressure of 1.65 ± 0.10 GPa. There is no obvious systematic variation between inclusions hosted in garnet cores versus rims of these samples, precluding resolving multiple garnet growth events. Because P_{inc} is substantially greater than 0, this consistency is not related to

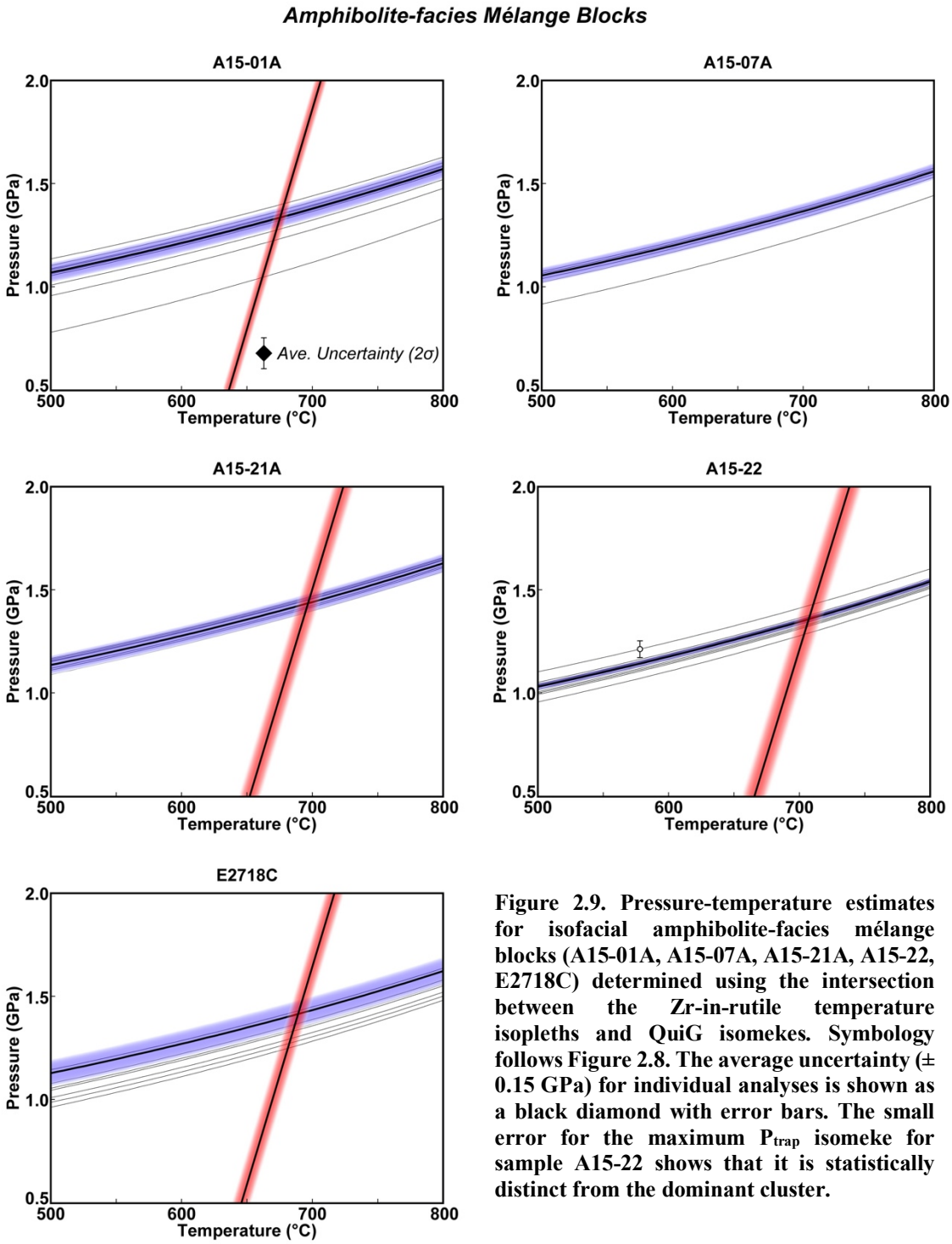

Figure 2.9. Pressure-temperature estimates for isofacial amphibolite-facies mélange blocks (A15-01A, A15-07A, A15-21A, A15-22, E2718C) determined using the intersection between the Zr-in-rutile temperature isopleths and QuiG isomekes. Symbology follows Figure 2.8. The average uncertainty (± 0.15 GPa) for individual analyses is shown as a black diamond with error bars. The small error for the maximum P_{trap} isomeke for sample A15-22 shows that it is statistically distinct from the dominant cluster.

complete relaxation of inclusions to room conditions, for example adjacent to cracks or near free surfaces (which were avoided).

2.6 Discussion

2.6.1 Revisiting *P-T* estimates

Zirconium-in-rutile thermometry and quartz-in-garnet barometry are applicable to a range of lithologies and metamorphic grades and provide a common basis for comparing *P-T* estimates. At the *P-T* conditions relevant to the Catalina Schist, the Zr-in-rutile thermometer is not likely to be significantly influenced by retrograde reequilibration by diffusion (Ewing et al., 2013; Kohn et al., 2016), increasing the likelihood that the peak metamorphic temperature is recoverable. There is some potential for the quartz-in-garnet elastic barometer to be partially reequilibrated by viscous relaxation of the garnet host (see Zhong, Moulas, & Tajčmanová, 2020). However, viscous relaxation has the largest impact on prograde inclusions in garnet, which reequilibrate at peak conditions above ~600°C, and is not likely to affect estimates of peak *P*.

Our new temperature estimates for isofacial amphibolite-facies mélange blocks and coherent amphibolite rocks (~676-707°C) fall within the broad ranges estimated in older studies (~600-750°C; , and overlap completely with recently published Zr-in-rutile thermometry (~643-735°C; recalulated from Penniston-Dorland et al., 2018, for the calibration of Kohn, 2020, at peak pressures estimated from QuiG). The consistency of results across these studies provides a robust basis for comparison with the exotic blocks.

QuiG barometry for five isofacial amphibolite-facies mélange blocks indicates pressures that tightly cluster at 1.26-1.44 GPa (Figure 2.10) at temperatures of 676-707°C. These pressures are higher than previous estimates (0.8 to 1.1 GPa) that were based on

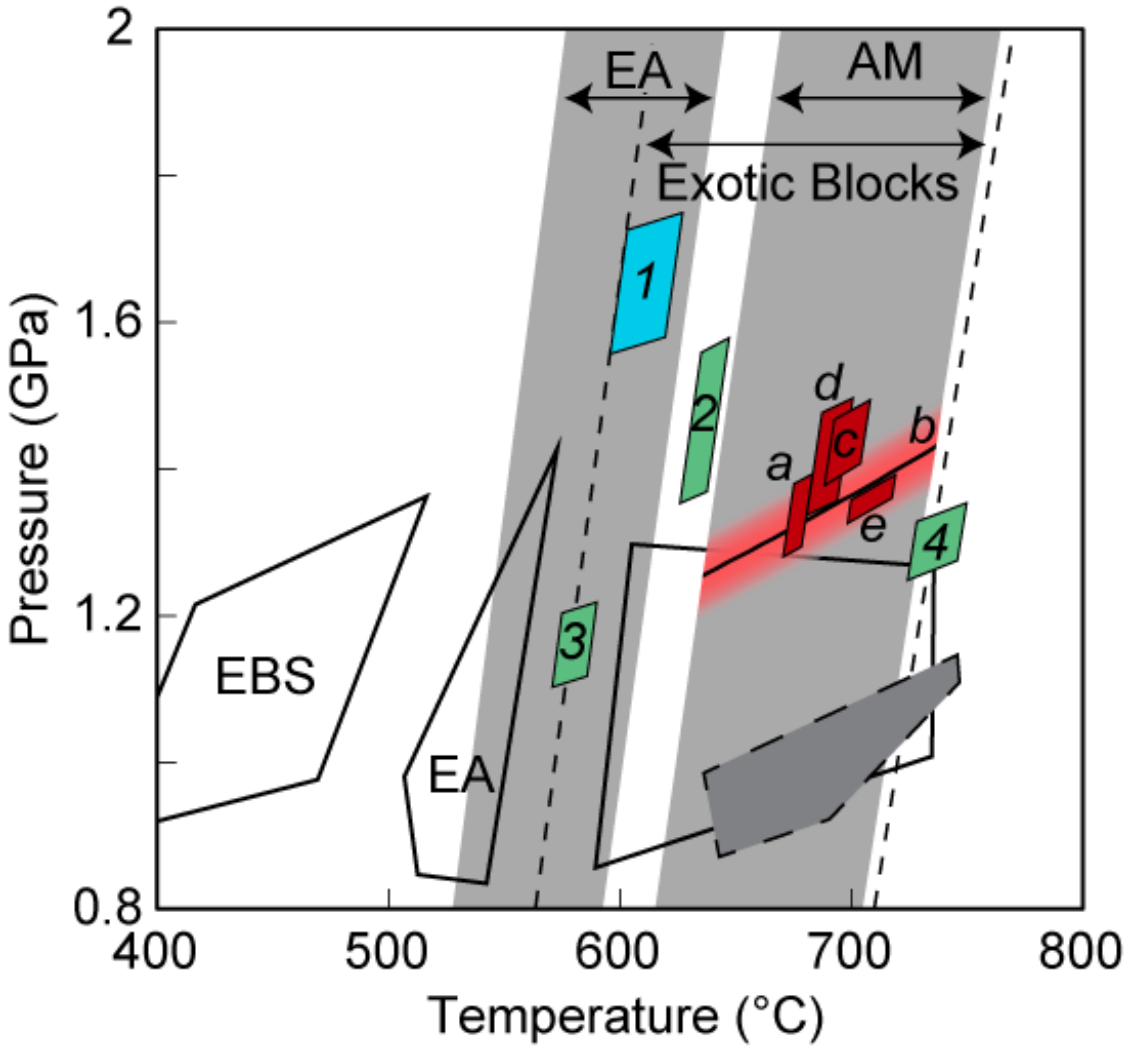

Figure 2.10. Summary of pressure-temperature estimates for exotic blocks, epidote amphibolite rocks, and isofacial amphibolite blocks. Blue, green and red polygons represent the intersection of the QuiG barometry isomeke and Zr-in-rutile thermometry isopleth for exotic blocks in the lawsonite blueschist (blue) and epidote amphibolite (green) units as well as isofacial amphibolite-facies mélange blocks (red) as shown in Figures 2.7 and 2.8. The red isomeke is for sample A15-07A, which is a metamafic block from the isofacial amphibolite-facies mélange and does not have an independent temperature estimate. The grey lines represent isopleths for the range of temperatures observed in the isofacial epidote amphibolite unit (EA) and amphibolite facies units (AM). The dashed lines represent isopleths for the range of temperatures observed in exotic blocks from the epidote amphibolite unit without independent P estimates. The white and dark grey fields represent previous estimates by Grove and Bebout (1995) and Sorensen and Barton (1987; see also Figure 2.2). Sample labels: (1) GB (2) A14-71 (3) EA15-10A (4) LB15-03B (a) A15-01A (b) A15-07A (c) A15-21A (d) A15-22 (e) E2718C.

fluid inclusions and simplified phase equilibria (Grove & Bebout, 1995; Sorensen & Barton, 1987). We view the QuiG estimates as more accurate because they do not depend on assumed mineral associations and compositions, and because the density of fluid

inclusions can readily reset to post-peak metamorphic conditions (e.g., Touret, 2001). Overall, *P-T* conditions among blocks are remarkably consistent at ~690 ± 40°C and 1.39 ± 0.1 GPa, although resolvable differences in peak metamorphic temperature do occur (see Penniston-Dorland et al., 2018).

Temperatures for both the coherent epidote amphibolite-facies metasedimentary rocks and epidote amphibolite mélange blocks are lower than for isofacial amphibolite-facies mélange blocks (as expected), but higher than previous estimates. Mélange blocks and coherent metapelites both record temperatures between 553 and 596°C (± 9-19°C) at 1.4 GPa, which are consistently higher than temperatures that have been calculated using generalized phase equilibria (500-550°C; Grove & Bebout, 1995), although the estimates overlap at lower pressures (Figure 2.10). It is likely that these samples reflect the highest-pressure rocks within the unit, since in general rutile is stable at higher-*P* conditions than other Ti-bearing phases which are commonly observed in rocks throughout the unit (i.e., titanite; Zack & Kooijman, 2017).

The exotic blocks record a near continuum of temperatures from the highest-T amphibolite facies units (~735°C) down to the upper end of the epidote amphibolite facies rocks (~605°C). Blocks within Regions A and B record temperature variations of 64°C ± 23°C and 67°C ± 21°C respectively, which are similar to variations observed within the amphibolite-facies mélange (~90°C; recalculated from Penniston-Dorland et al., 2018).

Of the four exotic blocks for which we have both pressure and temperature estimates, two differ resolvably from the amphibolite-facies mélange zone rocks in both peak pressure and peak temperature. The garnet blueschist block records a peak temperature of 611 ± 10°C, which is lower than any temperature estimate from the amphibolite-facies mélange zone (643-735°C; recalculated from Penniston-Dorland et al., 2018), yet a higher pressure of 1.65 ± 0.10 GPa. Similarly, sample EA15-10A records both a lower pressure of 1.16 ± 0.06 GPa and temperature of 579 ± 10°C. The other two exotic blocks overlap with the amphibolite-facies mélange zone in both peak pressure and temperature. Sample LB15-03B records peak conditions of 735 ± 12°C at 1.30 ± 0.05 GPa and just overlaps with the highest temperatures and lowest pressures recorded in the amphibolite-facies mélange zone. In contrast, sample A14-71 records peak conditions of 636 ± 10°C at 1.47 ± 0.11 GPa and just overlaps with the lowest temperatures and highest pressures recorded in the mélange zone.

2.6.2 Source of exotic blocks

New temperature estimates for the garnet-bearing and non-garnet bearing rocks within the epidote amphibolite and lawsonite blueschist facies units are consistent with mixing of higher-grade 'exotic' blocks with lower-grade material. The exotic blocks found within the epidote amphibolite unit record a near continuum of temperatures up to 140°C higher than the associated lower-grade rocks. Similarly, the garnet blueschist block records a peak metamorphic temperature >300°C higher than *T* estimates for the enclosing lawsonite blueschist unit (Grove & Bebout, 1995).

Pressure-temperature estimates for the exotic blocks from the epidote amphibolite unit suggest that they were sourced from a large region along the subduction interface. Assuming a maximum thermal gradient of 16°C/km based on the *P-T* results presented here, an average lithospheric density of 3,000 kg/m^3 and a slab dip of 20°, which is broadly representative of shallow portions of the subduction interface (Hayes et al., 2012), blocks in Regions A and B must have each been sourced over a minimum distance of 12 km along the subduction interface in order to explain the observed temperature variations. Pressure variations suggest that the source region for the exotic block population is even larger. Peak pressure estimates for the exotic blocks from the epidote amphibolite unit correspond to burial depths between ~40 and 50 km. Assuming a slab dip of 20°, these estimates suggest that the exotic blocks were sourced from a minimum of ~30 km distance along the subduction interface. This is likely a more accurate estimate of the source region for exotic blocks within the epidote amphibolite facies because it does not require any assumptions about the thermal structure of the subduction interface, which is variable within the slab. This is a significantly larger source region than inferred for the amphibolite-facies mélange zone using similar assumptions (~12 km; Penniston-Dorland et al., 2018 and supported by P estimates in this study).

Pressure estimates for the garnet blueschist block correspond to a burial depth of ~ 56 km. Given prior constraints on the *P-T* conditions associated with the lawsonite blueschist unit (~0.7-1.0 GPa; Grove and Bebout, 1995), this indicates that the block was sourced from ~25 km deeper than the surrounding lawsonite blueschist-facies material. Using the same calculations presented above, this corresponds to a distance of ~70 km

along the subduction interface. This is a substantially larger than the source regions recorded by the epidote amphibolite- and amphibolite-facies mélange zones. Because the block appears to be substantially older than the rest of the terrane (see Awalt et al., 2013; Grove and Bebout, 1995; Grove et al., 2008), it is possible that it was emplaced by a different mechanism than the exotic blocks found within the epidote amphibolite unit.

2.6.3 The Ollas Fault Zone

New *T* estimates for both blocks and matrix within the Ollas fault zone can be used to distinguish between previously proposed tectonic models which explain the anomalously high-*T* conditions recorded by the amphibolite-facies units. Blocks within the Ollas fault zone between the amphibolite facies unit and epidote blueschist unit record similar peak metamorphic temperatures to each other and to the actinolite matrix (646-660°C ±3-8°C). The talc-biotite matrix within the fault zone records a significantly lower temperature (576°C ± 7°C); however, it still records amphibolite facies conditions.

The subduction erosion model (Grove et al., 2008) hypothesizes that the amphibolite and epidote amphibolite facies rocks formed within a forearc thrust system and were later juxtaposed with the epidote blueschist, lawsonite blueschist and lawsonite albite facies rocks by subduction erosion. In this model, the contact between the epidote blueschist and amphibolite units is expected to have developed at blueschist- to sub-blueschist-facies conditions. If instead the amphibolite-facies rocks formed at the subduction interface (e.g., Platt, 1975; Penniston-Dorland et al., 2018) the contact is not necessarily required to record blueschist facies conditions –especially if the units were

juxtaposed by progressive underplating. This model best explains the amphibolite-facies conditions recorded by both the blocks and the matrix within the Ollas fault zone.

2.6.4 Models for making mélange

There are four general models for the juxtaposition of mélange blocks of diverse metamorphic grades within a single rock unit: post-metamorphic faulting (Platt, 1975), sedimentary mélange (e.g., Hsü, 1968; Page, 1978; Wakabayashi, 2012), underplating (e.g., Angiboust, Glodny, Oncken, & Chopin, 2014), and mélange flow (e.g., Cloos, 1982; Gerya et al., 2002). Of these four models, three (post-metamorphic faulting, underplating, mélange flow) explain juxtaposition of exotic blocks primarily through structural and

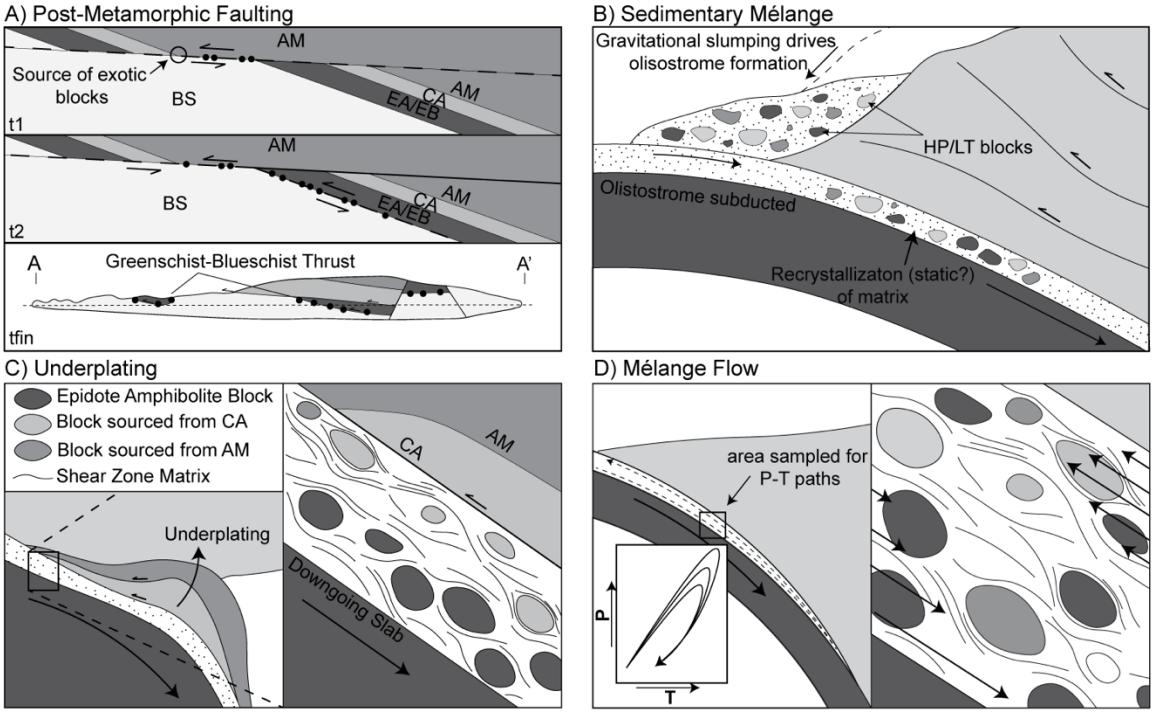

Figure 2.11. Possible scenarios for exotic block emplacement. (A) blocks are transported along post-metamorphic thrust faults from the amphibolite-facies mélange to the lower grade units (after Platt 1975) between time steps 1 (t1) and 2 (t2) before final exhumation (tfin). (B) exhumed high-grade rocks are eroded into an olistostromal mélange within the accretionary prism and are re-subducted (after Festa 2010). (C) Material from the downgoing slab is underplated to the overriding plate, moving the slab interface downwards. A shear zone between the underplated material and the downgoing slab juxtaposes non-coeval blocks (after Angiboust et al. 2014). (D) Mélange flow results from narrowing of the subduction interface, which forces flowing materials up-dip and juxtaposes blocks of disparate lithology and metamorphic grade (after Cloos 1982, Gerya et al. 2002).

geodynamic processes, while the fourth (sedimentary mélange) explains juxtaposition by sedimentary processes. Mélange flow and underplating are not necessarily mutually exclusive, rather they form a structural continuum, but one process may play a larger role in emplacement. Each model predicts different *P-T* relationships between the exotic blocks and the surrounding rocks and is discussed below.

2.6.4.1 Post-metamorphic faulting

Platt (1975) proposed that garnet amphibolite exotic blocks found intermingled with epidote amphibolite-facies rocks were emplaced along post-metamorphic thrust faults during exhumation. In this model (Figure 2.11a), blocks from the amphibolite-facies mélange were transported along a shear zone developed between the epidote-amphibolite and lawsonite blueschist units ("Greenschist-Blueschist Thrust" in Figure 2.1) during exhumation. In this scenario, the metamorphic grade of exotic blocks is expected to be the same as (or, at a minimum, record similar thermal gradients as) the isofacial amphibolite-facies mélange blocks, and to occur between the epidote amphibolite and lawsonite blueschist units. It also implies that the shear zones between the units formed at blueschist-facies (or colder) conditions. Finally, although not explicitly stated by Platt (1975), a fault that contains blocks would likely contain material that was sourced both from the footwall (the lawsonite blueschist unit) and hanging wall (the epidote amphibolite and amphibolite units). In this case, it is expected that material from all three units would be juxtaposed within the shear zone.

Many exotic blocks occur proximal to mapped thrust faults, with the exception of the garnet blueschist block (Figure 2.1). However, the exotic blocks generally record lower temperatures than the amphibolite facies units (median temperatures are 636°C and 700°C respectively). In addition, a t-test and F-test of Zr contents (excluding the garnet blueschist block) for our data versus Penniston-Dorland et al. (2018) both yield p-values of 0.001, indicating that it is very unlikely that the two populations share the same mean, variance, or, consequently, rock sources. These comparisons indicate that the exotic blocks are unlikely to have been sourced from either the base of the coherent amphibole unit or from the amphibolite-facies mélange zone as the post-metamorphic thrusting model suggests. Furthermore, material within the Ollas fault zone, which divides the coherent amphibolite and epidote blueschist unit, records temperatures between ~580-650°C. Such high temperatures suggest that the contact developed at near-to-post peak metamorphic conditions. This interpretation does not preclude re-activation of the fault at lower-temperature conditions, but unequivocally demonstrates that the fault is not post-metamorphic in origin. Finally, lawsonite blueschist-facies material was not observed within either exotic block Regions A or B, indicating that there was no mixing between the lawsonite blueschist-facies unit and amphibolite units while this shear zone was actively deforming. While the post-metamorphic faulting model explains the structural relationship between the tectonometamorphic units, it ultimately does not reconcile the generally lower continuum of temperatures recorded by the exotic blocks, the lack of clear mixing between the epidote amphibolite and lawsonite blueschist units, or the amphibolite-facies conditions recoded by material within the Ollas fault zone.

2.6.4.2 Sedimentary mélange

In this model, material is exhumed from the subduction zone, eroded at the seafloor into an olistostromal mélange, and then re-subducted. Exhumation might occur by diverse processes, including as a tectonic sliver and within serpentinite diapirs (see summary by Festa et al., 2010). Blocks exhumed from different depths or times throughout the lifespan of the subduction zone could be eroded into a single mélange.

The olistostrome model (Figure 2.11b) has been proposed for a variety of mélanges, including both mud and serpentinite mélanges in the Franciscan Complex (e.g., Platt, 2015; Raymond, 2016; Wakabayashi, 2011, 2012). Although discriminating tectonic vs. sedimentary mélanges is not always straightforward, matrix composition may aid in differentiating between the two processes. Matrices derived by sedimentary or hydrothermal processes at the seafloor are expected to be either pelitic or ultramafic (i.e., serpentinite).

Pelitic and serpentinite matrix compositions are rarely observed throughout the terrane, more often the matrix is an intermediate mafic-ultramafic composition. This composition, characterized by the presence of chlorite and/or talc (± actinolite, anthophyllite, biotite and glaucophane), has been interpreted to reflect tectonic and chemical mixing at the subduction interface (Bebout & Barton, 2002; King et al., 2006), and would be difficult to derive by sedimentary processes. This type of matrix has been observed in all exotic block "patches" and in direct contact with LB/A14-01, GB and blocks within the Ollas fault zone, and suggests a tectonic mechanism.

2.6.4.3 Underplating

A shear zone that develops between underplated material and the down-going slab may also form mélange. When material is underplated, it is detached coherently from the down-going slab and laminated to the over-riding plate. This mechanism of juxtaposing tectonic slices of varying metamorphic grades has been proposed for other localities, for example the Tsaté Complex in the Western Alps (Angiboust et al., 2014). Development of a shear zone between the underplated material and the down-going slab could juxtapose mélange blocks of different metamorphic grades without requiring differential transport of blocks within the shear zone matrix. In this model (Figure 2.11c), a new slab interface develops below the underplated material, where blocks from both surfaces can become incorporated into a single shear zone by fluid-mediated mechanical disaggregation (e.g., Penniston-Dorland et al., 2014). Secular changes in the thermal structure of the slab could cause blocks sourced from the slab to preserve different peak metamorphic conditions than blocks sourced from the underplated material. The model in a pure end-member scenario where no mélange flow occurs predicts a bimodal mixture of blocks sourced from a spatially discrete area at the contact, with one population reflecting the *P-T* conditions of a discrete portion of underplated material and the other reflecting the *P-T* conditions of a discrete portion of the down-going slab. In the case that the underplated material has multiple block sources (i.e., if the units are oblique to the newly-developed subduction interface, similar to the field relationships shown in Figure 2.11A), then the number of block sources may increase; however, the blocks should still fall within discrete populations.

The underplating model readily explains the broad structural and temporal relationships between the tectonometamorphic units. Progressive underplating in conjunction with secular cooling of the subduction interface is expected to produce an inverted metamorphic sequence, with the oldest and hottest material structurally above younger and colder material. This is consistent with both structural observations (Figure 2.1b; Platt, 1975, 1976) and the age progression from amphibolite-facies metamorphism between ~115-110 Ma (Anczkiewicz et al., 2004; Grove et al., 2008; Suppe & Armstrong, 1972) to blueschist-facies metamorphism from ~100-97 Ma (Grove et al., 2008; Suppe & Armstrong, 1972). The model also explains the distribution of peak metamorphic temperatures recorded by material within the Ollas fault zone for reasons discussed above.

However, for reasons similar to the post-metamorphic thrust faulting model, the underplating model does not readily explain all of the observations. Specifically, the *P-T* conditions recorded by the exotic blocks suggest that the blocks were sourced over a range of depths rather than from a bi- (e.g., epidote amphibolite + amphibolite) or trimodal (e.g., blueschist + epidote amphibolite + amphibolite) population. Because underplating alone predicts mixing of discrete populations rather than the continuum of conditions observed, an additional mechanism is needed to fully explain exotic block emplacement.

2.6.4.4 Mélange flow

Cloos (1982) proposed that transport of rigid blocks within a flowing matrix at the subduction interface could chaotically mix materials of different lithologies and

metamorphic grades. In the model, narrowing of the wedge-shaped subduction interface at depth forces convection, returning material up-dip at velocities on the order of the convergence rate (Figure 2.11d; Gerya et al., 2002). Similar to the underplating model, blocks are thought to be derived throughout subduction by fluid-mediated mechanical disaggregation of the downgoing slab and overriding plate (e.g., Penniston-Dorland et al., 2014). The degree of differential movement of mélange blocks resulting from mélange flow is thought to be dependent on several factors, including the degree of hydration and the density contrast between the mélange matrix and the overriding plate, but primarily controlled by the matrix viscosity (Cloos, 1982; Gerya et al., 2002). The mélange flow model predicts that juxtaposed blocks may be sourced from a range of spatially or temporally distinct regions of the subduction interface, with adjacent material in 2-D dynamic models recording differences in burial depth up to ~60 km in the most extreme cases (Gerya et al., 2002).

Differential movement resulting from mélange flow was proposed to have occurred over relatively small, yet resolvable, scales in the amphibolite-facies mélange zone (~12 km along the slab interface; Penniston-Dorland et al., 2018). This restricted scale of mixing relative to other exhumed terranes was attributed to the high proportion of amphiboles, including anthophyllite and actinolite, observed throughout the mélange matrix (Bebout & Barton, 2002), which are hypothesized to increase the matrix viscosity and inhibit differential transport of material (Penniston-Dorland et al., 2018). Numerical models predict that lower matrix viscosity has the potential to result in mélange flow, whereas higher viscosity results in more coherent behavior (Gerya et al., 2002). Temperature

variations observed among the exotic blocks from the epidote amphibolite-facies are as large as ~150°C with pressure variations up to 0.5 GPa. These variations require a much larger scale of differential transport than observed within the amphibolite-facies mélange zone, on the order of ~30 km along the slab interface. Rheologic contrasts within the matrix may reconcile these two scales of mixing. Regardless, mélange flow best explains the presence of the garnet-bearing 'exotic' blocks within the lower grade units of the Catalina Schist. Mélange flow likely occurred in conjunction with underplating, since the underplating model best explains the structural relationships between the tectonometamorphic units, and the *T* variations with the Ollas fault zone.

2.6.5 Mechanisms of mélange flow

The exact mechanism of mixing within mélange at the subduction interface is not well-constrained. Both Cloos (1982) and Gerya et al. (2002) model this process with the primary driving force for return flow, and thus mixing, being narrowing of the subduction interface at depth. However, these models employ a large wedge-shaped interface that is often larger than 20-30 km at its widest point. In contrast, geophysical observations of active subduction zones suggest that the subduction interface is no more than 5-10 km-thick (e.g., Calvert, 2004) and field observations of exhumed terranes suggest that the interface is most likely between 300 and 500 m (e.g., Rowe, Moore, & Remitti, 2013; Agard et al., 2018). The latter is consistent with the thickness of mélange zones observed throughout the Catalina Schist, which never exceed ~500 m (Platt, 1976). Because the force required for up-dip flow increases as the width of the interface decreases, large-scale return flow may not be feasible for narrow subduction interfaces (Gerya et al., 2002), suggesting that this mechanism alone may not fully explain mixing within mélange.

An additional mechanism that can explain mixing of disparate materials at the subduction interface is stress amplification and strain localization as a result of rheologic heterogeneities either between blocks and matrix or between two matrix compositions (e.g., Fagereng & Sibson, 2010; Beall, Fagereng & Ellis, 2019). In contrast to large-scale return flow, where the primary driving force for mixing is narrowing of the interface at depth, strain localization causes deformation to be focused within m- to hm-scale regions of the subduction interface, driving shearing and mixing between components (Beall et al., 2019). This mechanism has been proposed to drive mixing at shallower depths between metasedimentary and mafic lithologies within a relatively narrow interface (tens to hundreds of meters; Fagereng, Hillary & Diener, 2014) and likely works either in conjunction with or as an alternative to large-scale mélange flow as described in the previous section.

2.6.6 Mineralogy and rheology

Mineralogy is expected to exert a strong control on the mechanical behavior of the matrix. Blocks recording significantly different peak metamorphic conditions and *P*-*T* paths are commonly observed in terranes with serpentinite or mud matrices, such as the Franciscan Complex (e.g., Ukar & Cloos, 2014), the Rio San Juan Complex (Krebs et al., 2008; Krebs, Schertl, Maresch, & Draper, 2011) and the Sistan suture (e.g. Bonnet et al., 2018). This observation suggests that when sheet silicates such as serpentine, chlorite, and talc are the dominant matrix phases at the subduction interface, materials may be transported differentially over large scales. In contrast, where matrices have large proportions of amphiboles and pyroxenes, blocks record a more restricted range of *P*-*T*

conditions (Penniston-Dorland et al., 2018). This observation suggests that amphibole- and pyroxene-rich matrix may have a higher effective viscosity than sheet silicates, restricting flow.

Geochemical and mineralogical matrix heterogeneities in the amphibolite unit are thought to have resulted from incomplete mechanical homogenization of the end-member matrix components (mafic and ultramafic rocks with minor sedimentary input at amphibolite-facies conditions; Bebout & Barton, 2002). Two dominant compositions have been observed: siliceous matrix with abundant anthophyllite or enstatite, and aluminous matrix that is dominated by chlorite, talc and biotite. These two compositions appear to be intercalated at a variety of scales, from <1 to 100's of meters, within the amphibolite-facies mélange unit (Bebout & Barton, 2002), and are expected to have contrasting rheological properties (e.g., Bystricky & Mackwell, 2001; Kronenberg, Kirby, & Pinkston, 1990; Shelton, Tullis, & Tullis, 1981; see also summary of Bürgmann & Dresen, 2008).

If strain is partitioned within layers and lenses where sheet silicates are concentrated, blocks within those regions may be differentially transported over larger scales than blocks encapsulated by a less-deformable chain-silicate dominated matrix. These rheologically weak layers, if spatially extensive enough, may juxtapose blocks of disparate lithologies and/or that experienced different peak metamorphic conditions. A conceptual model is presented in Figure 2.12. In the model, geochemical heterogeneities within the mélange matrix create regions where sheet silicates, including chlorite and talc, are the primary matrix phase. These regions are intercalated with regions where chain

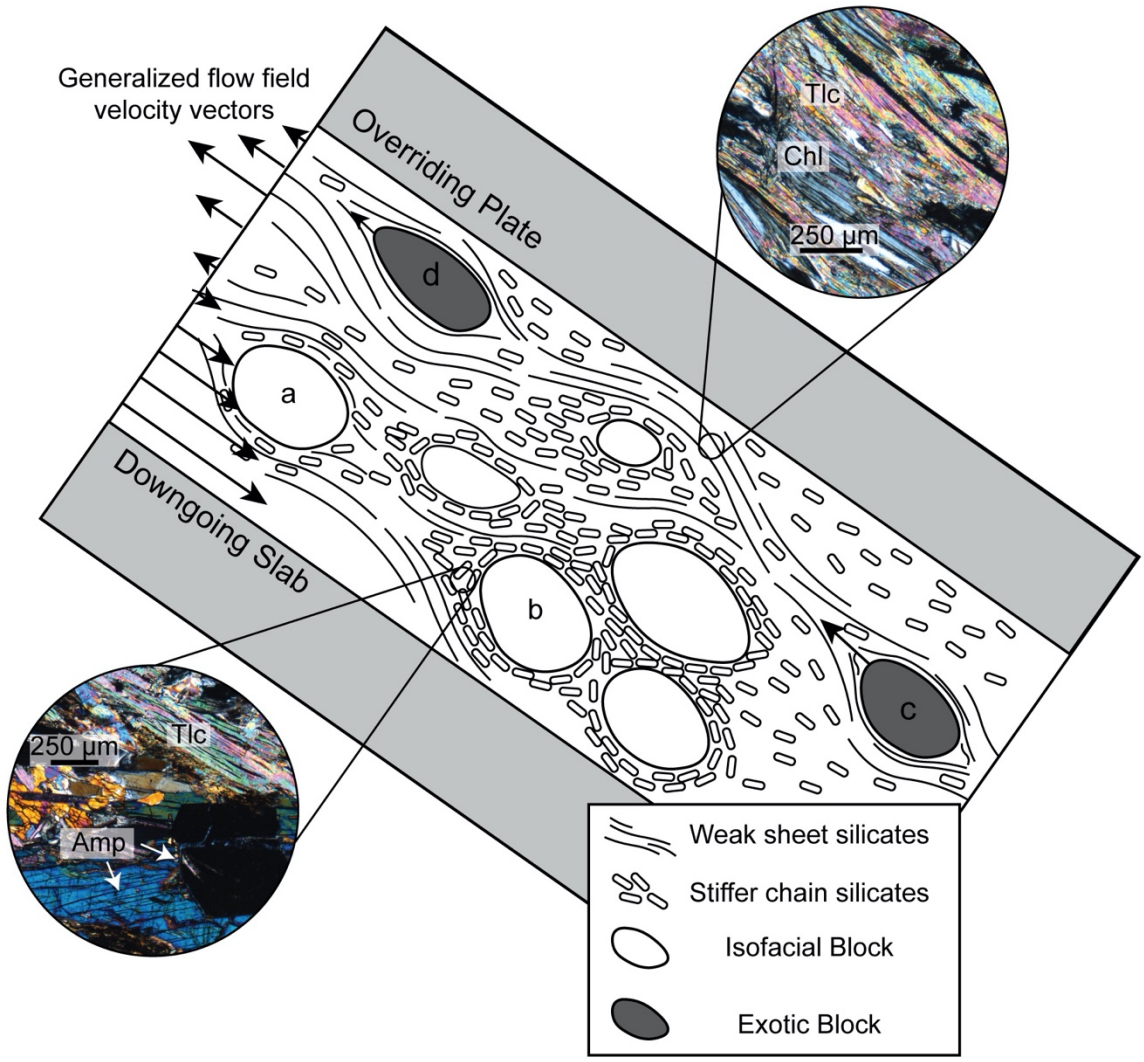

Figure 2.12. Conceptual model for differential movement. (a) progressive metamorphism causes amphiboles and pyroxenes to start forming in the matrix, (b) amphiboles and pyroxenes become the dominant matrix phase, inhibiting block mobility, (c) layers of chlorite and talc accommodate strain, blocks within them are transported based on generalized flow field velocity vectors, (d) the scale of differential movement is controlled by spatial extent of weak layers/lenses. Photomicrographs show examples of chain silicate- and sheet silicate-dominated matrices. Amp = amphibole, Chl = chlorite, Tlc = talc.

silicates are the primary matrix phase, which is consistent with field observations of the Catalina Schist. If the sheet silicates are mechanically weaker than the chain silicates, then it is expected that slip and deformation should partition into the weaker layers (e.g., Beall et al., 2019; French & Condit, 2019). In contrast, the regions composed dominantly of chain silicates behave as largely undeformed aggregate “rafts”. Intercalation of a sheet-

silicate matrix deforming faster and over larger length-scales with an adjacent undeforming chain silicate matrix could juxtapose blocks from different depths. Up-dip transport by mélange flow (Figure 2.12) will juxtapose blocks from deeper in the system with shallower blocks. In this scenario, the scale of mixing would be limited by the connectivity and spatial extent of sheet silicates, which provides a mechanism for different scales of mixing recorded within a single terrane and even within a single unit of the terrane.

2.7 Conclusions

New *P-T* estimates for the isofacial amphibolite-facies mélange zone of the Catalina Schist reveal that the unit reached peak metamorphic conditions of 640-740°C between 1.34-1.44 GPa. While new *T* estimates agree well with prior estimates, *P* estimates by quartz-in-garnet barometry indicate the unit experienced higher peak-*P*. New *T* estimates for the epidote amphibolite facies rocks range from 553-596°C and are higher than previous estimates. These estimates likely represent the upper end of the range of conditions experienced by rocks of the epidote amphibolite unit. Blocks and mélange matrix from the Ollas thrust fault zone dividing the amphibolite facies units from the epidote blueschist unit record temperatures between 576-660°C, indicating that the fault developed at near-peak metamorphic conditions, likely as a result of underplating of the amphibolite-facies units at the subduction interface. Garnet-bearing 'exotic' blocks found within the epidote amphibolite unit record a near continuum of temperatures from 579-735°C. Pressure estimates for three of the exotic blocks are between 1.16 and 1.47 GPa. A garnet-bearing blueschist block from the lawsonite blueschist unit records a similar peak metamorphic temperature of 635°C although at a higher pressure of 1.65 GPa.

The ‘exotic’ high-grade blocks found within the epidote amphibolite mélange units of the Catalina Schist have previously been interpreted to have been sourced along post-metamorphic thrust faults (Platt,1975). Zr-in-rutile thermometry and quartz-in-garnet barometry along with field and petrographic observations suggest that these blocks were sourced from a 20-30 km region of the subduction interface and are spatially (and perhaps temporally) distinct from the amphibolite-facies units, precluding this mechanism of emplacement. Instead, we propose that these blocks represent a continuum of mixing of material along the subduction interface. Variations in the scale of mixing of mélange blocks within the subduction complex may be explained by mineralogic and, therefore rheologic heterogeneities within the matrix, whereby layers and lenses of weaker minerals preferentially accommodate strain and allow for larger length-scales of deformation than adjacent regions dominated by stronger minerals like pyroxene and amphibole.

2.8 Acknowledgements

This work was supported by NSF grant EAR-1419871 to SPD and grants EAR-1419865, OIA-1545903 and EAR-1450507 to MJK. We thank Guillaume Bonnet and John Platt for their thoughtful and constructive reviews and Donna Whitney for her handling of the manuscript. We also thank John Platt for showing us sample locations. Undergraduate researcher Jenna Reimer is thanked for her contribution to the results presented. We acknowledge the support of the Maryland NanoCenter and its AIMLab. Finally, we thank the Santa Catalina Island Conservancy for logistics and support of sample collection of the Catalina Schist.

Chapter 3: A mélange of subduction ages: evidence for rapid shear zone development and underplating at the subduction interface

3.1 Abstract

The Catalina Schist (Santa Catalina Island, CA) amphibolite-facies mélange zone is interpreted to represent a paleo-subduction interface. Blocks throughout the mélange zone all record amphibolite-facies metamorphic conditions with resolvable (up to 90°C), differences in peak metamorphic temperatures. The spatial distribution of these temperatures throughout the zone is non-systematic and appears to indicate that material was chaotically mixed at the subduction interface through a combination of metasomatism and localized deformation, although the scale of mixing is small relative to other exhumed tectonic mélange zones such as regions of the Franciscan Complex. If this scenario is correct, blocks would be expected to record different peak metamorphic ages. In this chapter, I assess age variations within the amphibolite-facies mélange zone using Sm-Nd garnet geochronology. Five garnet amphibolite tectonic blocks with a wide range of peak metamorphic temperatures (643-735°C; estimated using Zr-in-rutile thermometry) were selected. Ages for the five blocks range from 108 to 115 Ma and do not appear to correlate with the peak metamorphic temperature recorded by each block, favoring the mélange flow model previously proposed to explain the non-systematic temperature distribution. A median age of 110 Ma suggests that the rate of mixing may have increased between c. 111 and 108 Ma. These ages overlap with previous estimates for the unit between 111 and 114 Ma but are predominately younger than an estimate for the structurally lower coherent amphibolite unit of c. 115 Ma. Hornblende Ar/Ar and U-Pb rutile ages suggest that the unit rapidly cooled to 500-550°C before 105 Ma. Collectively, these results demonstrate that

mélange development occurred over 7 Myr from 114 to 108 Ma and was followed by underplating and rapid cooling to 500-550°C between 108 and 105 Ma. The age discrepancy between the mélange zone and the underlying coherent amphibolite unit is best explained by partial exhumation of the coherent amphibolite either synchronous with or following the underplating event.

3.1 Introduction

Mélange at the subduction interface controls many important physico-chemical processes, including mass transport between the downgoing slab and overriding plate, large-scale channelization of fluids, and the rheologic evolution of the plate interface. Both fluid transport at the subduction interface and the mechanical behavior of rigid blocks within a deforming matrix have recently been indicated as potential catalysts of seismic phenomena occurring below the megathrust including episodic tremor and slip (ETS; e.g., Audet and Bürgmann, 2014; Beall et al., 2019; French and Zhu, 2017; Tarling et al., 2019), which occurs at depths between c. 30 and 50 km. Understanding the controlling factors on the formation and evolution of mélange will help elucidate how feedbacks between metamorphism, deformation and fluid release at the subduction interface contribute to the seismic cycle and the dynamic evolution of subduction zones. Field-based observations in paleo-subduction terranes are particularly important for understanding how variations in controlling factors such as composition, thermal structure and timescale of deformation influence the mechanical behavior of the subduction interface.

While subduction-related mélange can form by a variety of both tectonic and sedimentary processes, tectonic mélange is thought to develop by feedbacks among

mechanical mixing, metasomatism and progressive metamorphism, whereby cm-m scale blocks sourced from the downgoing slab and overriding plate are mechanically incorporated into a fine-grained metasomatic matrix (e.g., Bebout and Penniston-Dorland, 2016). Metasomatism of these blocks drives the formation of hydrated reaction rinds, which can be mechanically ablated and incorporated into the matrix (e.g., Penniston-Dorland et al., 2014), creating a unique matrix composition that is geochemically and isotopically distinct from its end-member components (Bebout and Barton, 2002; King et al., 2006, 2007). Geochemical, petrologic and geodynamic evidence suggests that tectonic mélange development occurs throughout prograde and peak metamorphism (e.g., Gerya et al., 2002; Penniston-Dorland et al., 2014), as shearing between mélange components mixes materials of disparate lithologies and metamorphic grade.

The Catalina Schist amphibolite-facies mélange zone provides an opportunity to understand the relationship between spatial and temporal scales of tectonic mélange development and mixing at conditions relevant to ETS. Blocks and matrix throughout the mélange zone all record amphibolite-facies metamorphic conditions with resolvable (up to 90°C; Penniston-Dorland et al., 2018) differences in peak metamorphic temperature. The spatial distribution of these temperatures throughout the zone is non-systematic and appears to indicate that the material was mixed through a combination of metasomatism and localized deformation at the subduction interface. Interestingly, the scale of mixing based on this temperature disparity is small relative to other exhumed subduction-related mélange zones, such as regions of the Franciscan Complex and the Rio San Juan Complex, which record up to c. 400°C differences in peak metamorphic temperature between blocks

(e.g., Krebs et al., 2011; Krohe, 2017; Tsujimori et al., 2006). Currently, there is little understanding of how the spatial scale of mixing is controlled by factors such as matrix rheology and the timescale over which the mélange zone develops. Penniston-Dorland et al. (2018) related limited scales of mixing in the Catalina Schist to development of rheologically strong phases in the matrix, such as amphibole and pyroxene, as a result of prograde metamorphism. This is supported by geodynamic models that demonstrate that rheologically weak matrix minerals permit larger scales of mixing than strong matrix minerals (Gerya et al., 2002). Another possibility is that the amphibolite-facies mélange zone developed over a much shorter period of time than those that record larger temperature disparities.

Few studies have quantified the timescale of tectonic mélange formation, especially in relation to the recorded spatial scale of mixing. Elucidating this timescale is particularly important in the context of interpreting the tectonic and geochemical evolution of mélange zones, including observations of mass transport processes (e.g., Sorensen and Grossman, 1989; Bebout and Barton, 1993; Penniston-Dorland et al., 2012, 2014), tectonic mixing processes (e.g., Bebout and Baron, 2002; King et al., 2006, 2007; Penniston-Dorland et al., 2018) and for understanding timescales of deformation relative to processes such as underplating (e.g., Agard et al., 2018). Here, Sm-Nd garnet geochronology is used to assess temporal variations in the timing of peak metamorphism of mélange blocks throughout the amphibolite-facies mélange zone of the Catalina Schist. These data are compared to geochronologic data from prior studies to understand the relationship between spatial and temporal scales of mixing within the mélange zone. The results also have implications for

understanding structural relationships between the mélange zone and other tectonometamorphic units of the Catalina Schist, and specifically address the temporal relationship between the mélange zone and underlying coherent amphibolite unit. Importantly, this work contributes to understanding various controls on mélange formation and development, including how feedbacks between matrix rheology and the timescale over which a mélange zone develops affect the degree of tectonic mixing.

3.2 Geologic Background

The Catalina Schist, best exposed on Santa Catalina Island (California, USA), consists of several tectonometamorphic units separated by subhorizontal thrusts. These thrust sheets form an inverted metamorphic sequence ranging in grade from lawsonite

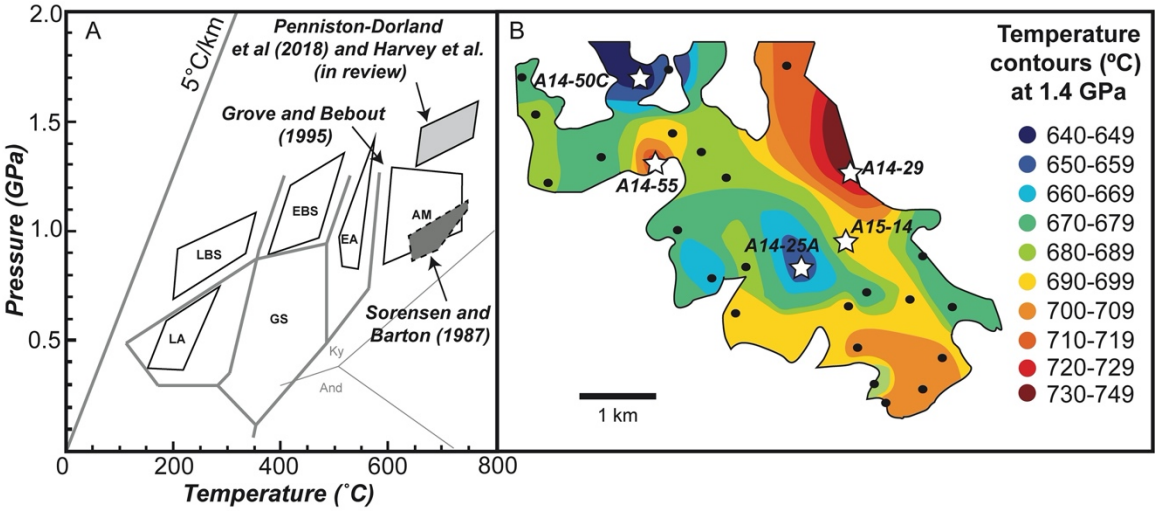

Figure 3.1. (A) pressure-temperature estimates for the tectonometamorphic units of the Catalina Schist modified after Grove and Bebout (1995). Estimates shown for the amphibolite-facies units are based on generalized phase equilibria modeling (Grove and Bebout, 1995), multi-phase thermobarometry and fluid inclusions (Sorensen and Barton, 1987), and zirconium-in-rutile thermometry and quartz-in-garnet elastic barometry (Penniston-Dorland et al., 2018; K. Harvey et al., in revision). (B) contour map showing the distribution of peak metamorphic temperatures recorded by blocks and matrix throughout the amphibolite-facies mélange zone determined by Zr-in-rutile thermometry and estimated at 1.4 GPa (modified from Penniston-Dorland et al., 2018 with updated temperature estimates from K. Harvey et al., in revision). The locations of samples considered in this study are shown as white stars.

albite to upper amphibolite facies (see Figure 3.1; Platt, 1975, 1976; Grove and Bebout, 1995). Each thrust sheet consists of both structurally coherent units and mélange. Within the mélange zones, sub-cm to 100-m sized metasedimentary, mafic and ultramafic blocks are encapsulated within a deformed, fine-grained heterogeneous matrix. This matrix is a chemical and isotopic mixture of the mafic, ultramafic and metasedimentary materials that comprise the mélange zone (Bebout and Barton, 2002, 1993, 1989; Sorensen, 1984; Sorensen and Barton, 1987). Pressure-temperature estimates for the units have been determined using a combination of multi-phase thermobarometry (e.g., Platt, 1975; Sorensen and Barton, 1987), generalized phase equilibria modeling (Grove and Bebout, 1995), Zr-in-rutile thermometry (Penniston-Dorland et al., 2018; K. Harvey et al., in revision; see Chapter 2), and quartz-in-garnet elastic thermobarometry (K. Harvey et al., in revision; see Chapter 2), and are summarized in Figure 3.1. Previous constraints using Lu-Hf garnet and U-Pb titanite geochronology place the timing of amphibolite-facies metamorphism between c. 115 and 110 Ma (Anczkiewicz et al., 2004; Mattinson, 1986). The lower grade units are younger, and range in age from c. 109 to 97 Ma based on K-Ar and $^{39}Ar/^{40}Ar$ white mica and hornblende geochronology as well as U-Pb detrital zircon (Grove and Bebout, 1995; Grove et al., 2008; Suppe and Armstrong, 1972).

The amphibolite-facies mélange zone is the highest-grade unit in the Catalina Schist. It is primarily composed of garnet amphibolite and serpentinite blocks (with rare metasedimentary rocks including metachert and metagraywacke) encapsulated within a heterogeneous matrix. The matrix can broadly be subdivided into two distinct mafic-ultramafic compositions with different deformation features (see Bebout and Barton,

2002). The first is a siliceous matrix composed of radiating anthophyllite or enstatite plus talc. This matrix is generally associated with massive serpentinite blocks and often shows little evidence of deformation. The second matrix composition observed within the zone is an aluminous matrix composed primarily of folded or crenulated sheet silicates including chlorite, biotite and talc, which often has minor amounts of clinoamphiboles such as hornblende or actinolite. This matrix is most often associated with the mafic blocks and appears to record more evidence of deformation than the siliceous matrix. The two matrix compositions appear to intercalated at the sub-km scale (Bebout and Barton, 2002).

Blocks throughout the zone record temperatures between 640-740°C (Penniston-Dorland et al., 2018; K. Harvey et al., in revision) and pressures of 1.3-1.4 GPa (K. Harvey et al., in revision). These conditions require thermal gradients that are much higher than average conditions recorded by other exhumed subduction terranes (see compilation by Penniston-Dorland et al., 2015). Multiple mechanisms have been suggested to reconcile these anomalously high temperature conditions, including nascent subduction and that the amphibolite units may have formed in a forearc thrust system (e.g., Grove et al., 2008; Platt, 1975). However, geochronologic evidence has shown that the unit post-dates subduction initiation in the region (Grove et al., 2008), while petrologic evidence suggests that the unit still formed at the subduction interface (Penniston-Dorland et al., 2018; K. Harvey et al., in revision).

Multiple lines of evidence suggest that the amphibolite-facies mélange zone formed by progressive tectonic and metasomatic mixing at the subduction interface rather than by

sedimentary processes. In particular, the unique hybrid matrix compositions observed throughout mélange zone are difficult to explain by sedimentary processes (Bebout and Barton, 2002; King et al., 2006). Additionally, geochemical and petrologic evidence from metasomatic reaction rinds found at the contact between blocks and matrix suggest that the matrix was formed by progressive alteration and ablation of the blocks throughout prograde and peak metamorphism (i.e., Penniston-Dorland et al., 2014). There are also numerous high-strain features observed throughout the mélange zone, including mylonitization of mafic blocks (see Appendix S2.1), suggesting that deformation was hosted within the mélange zone. Finally, the matrix records similar peak metamorphic conditions to the blocks (see Penniston-Dorland et al., 2018), making a sedimentary origin unnecessary.

3.4 Methods

3.4.1 Sm-Nd Garnet Geochronology

Garnet separates were prepared from a representative fraction of each sample by hand crushing using steel and agate mortar and pestles, magnetic separation and hand picking. Each separate was then hand crushed using an agate mortar and pestle to between 75 and 100 μm for chemical preparation. Powder fractions (grain sizes <75 μm) were also collected for analysis and are indicated in the results by "Pwd". Aliquots between 40-130 mg of the garnet and garnet powder separates were chemically leached in 2 mL of 7 N nitric acid for two hours followed by 20-150 μL of concentrated hydrofluoric acid in 2 mL of H_2O for two hours. The procedure was repeated with varying concentrations of hydrofluoric acid until the samples reached a mass loss between 70 and 90%. This partial dissolution procedure, outlined in Baxter et al. (2002), Dragovic et al. (2012) and

Pollington and Baxter (2011) removes any recalcitrant microinclusions such as apatite, epidote and hornblende. Leachates were collected from garnet separates following the final stages of partial dissolution for analysis and are indicated in the results by "Lch". Following partial dissolution, each sample was fully dissolved using a combination of concentrated nitric acid, hydrofluoric acid and hydrochloric acid.

Whole rock separates were also prepared for analysis. A representative fraction (30-50 g) of each sample was hand crushed and then powdered using a ball mill. Between 30 and 100 mg of each whole rock powder was then fully dissolved using a combination of HNO_3, HF and HCl.

After full dissolution, all samples were spiked with an in-house mixed ^{147}Sm-^{150}Nd spike prior to chemical separation by column chromatography (J. Harvey and Baxter, 2009). Samples were first loaded in a cation exchange column using AG50w-X4 resin with HCl to remove Fe. The rare earth elements (REEs) were then isolated using Eichrom TRU spec resin with HNO_3. Finally, Sm and Nd were separated using AG50w-X4 resin with in-house distilled 2-methyl lactic acid (MLA). Full-procedure and 3-column blanks were run alongside the samples. Blank concentrations for the lab were all <5 pg Nd.

Samples were analyzed at the Boston College Center for Isotope Geochemistry using an IsotopX Phoenix Thermal Ionization Mass Spectrometer (TIMS). For each sample, 1.7-16.3 ng of NdO was loaded onto outgassed rhenium filaments in Ta_2O_5 activator slurry, and 1.7-46 ng of Sm was loaded in HNO_3 onto tantalum center filaments.

In-house standard solutions of Sm and Nd (AMES metal) were used to assess long-term reproducibility. For Nd, 4ng loads of the standard solution yielded $^{143}Nd/^{144}Nd$ = 0.512151±9 (17.3 ppm, 2sd; *n* = 226). For Sm, 20 ng loads of the standard solution yielded $^{147}Sm/^{152}Sm$ of 0.560869±41 (72ppm, 2sd; *n* = 145).

3.4.2 Garnet major and trace element compositions

Garnet major element compositions were determined by wavelength dispersive spectroscopy (WDS) using the JEOL JXA 8900R Electron Probe Microanalyzer (EPMA) housed in the AIMLab at the University of Maryland. Measurements were made using a 15 kV accelerating voltage, a beam current of 25 nA, and a beam diameter of 1 μm. Analyses were standardized using natural mineral standards and processed using a ZAF correction scheme (Armstrong, 1988). Select garnets in each sample were additionally chosen for WDS X-Ray maps to fully assess major element zoning. X-Ray maps were collected using a 15 kV accelerating voltage, a beam current of 250 nA and a beam diameter between 5 and 20 μm.

Trace element zoning was determined by laser ablation inductively coupled plasma mass spectrometry (LA-ICP-MS) using the Thermo-Fisher Element 2 magnetic sector mass spectrometer coupled to a Nu-Wave UP213 solid state Nd:YAG laser ablation system housed in the Plasma Laboratory at the University of Maryland. Analyses were collected using 55 μm spots, a repetition rate of 7 Hz, and a fluence of 3-5 J/cm^{-2}. Data were processed using Iolite v4. Raw counts were standardized against the glass standard

NIST612 (Jochum et al., 2011) and normalized to ^{29}Si. BHVO-2g glass (Jochum et al., 2005) was used as a secondary standard to assess data reproducibility.

3.4 Results

Five mafic garnet amphibolite blocks from the amphibolite-facies mélange zone were analyzed. The blocks vary slightly in composition, but generally contain garnet, magnesio-hornblende, plagioclase, epidote, rutile and chlorite with accessory phases including zircon, apatite and quartz. Garnet porphyroblasts range in diameter from ≤ 0.3 mm to c. 8 mm, and are generally sub-to-euhedral, although some are partially resorbed or replaced by chlorite. The peak metamorphic temperature for each sample was determined

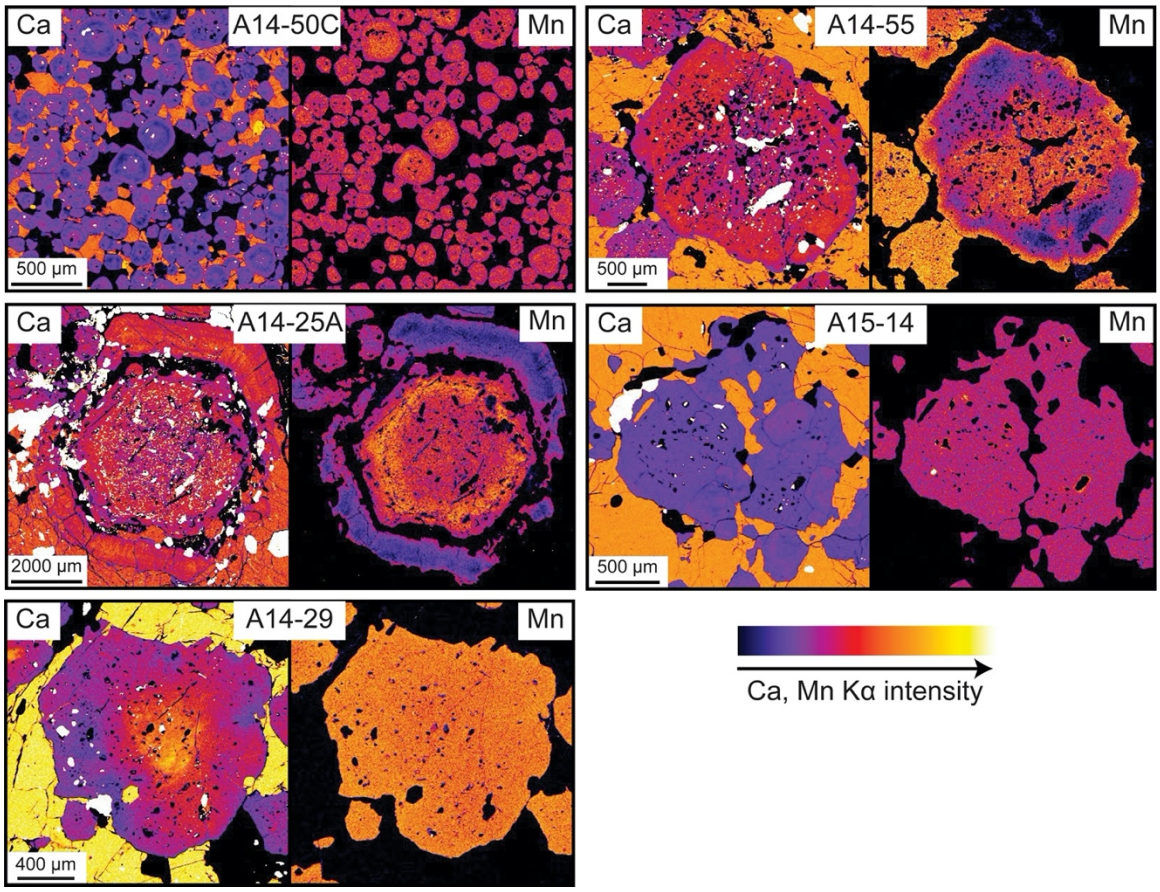

Figure 3.2. Kα X-ray maps of garnet porphyroblasts for samples A14-50C, A14-25A, A15-14, A14-55 and A14-29 showing zoning in Ca and Mn for each sample.

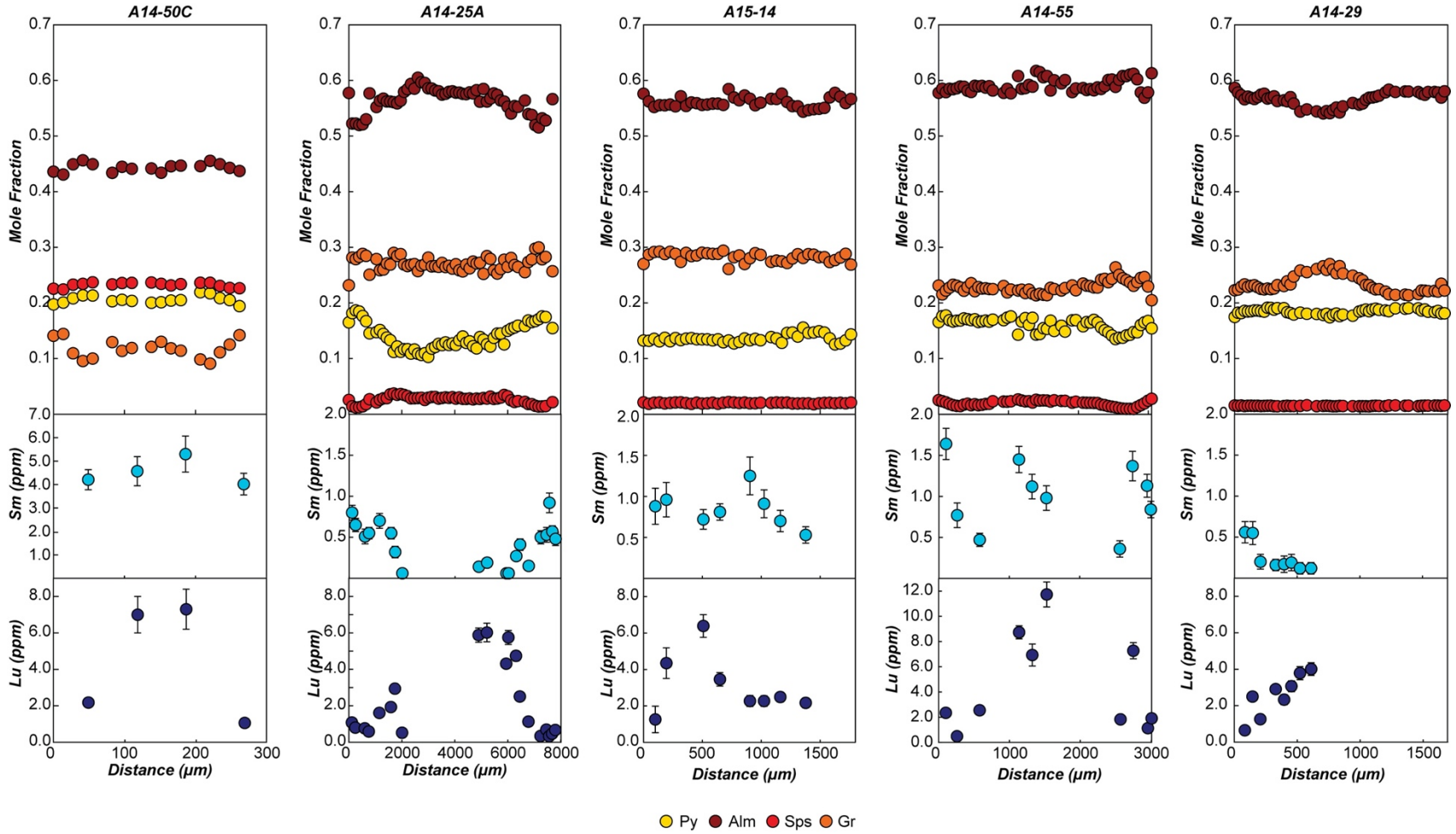

Figure 3.3. Major and trace element zoning in garnet for samples A14-50C, A14-25A, A15-14, A14-55 and A14-29 showing changes in garnet chemistry from rim to rim.

by Zr-in-rutile thermometry by Penniston-Dorland et al. (2018) and updated using the most recent thermometer calibration (Kohn, 2020) by K. Harvey et al. (in revision). Figure 3.1 shows peak temperatures estimated at 1.4 GPa for the samples relative to other blocks in the mélange zone (see Penniston-Dorland et al., 2018 for methods and sample locations). These five blocks span the range of peak metamorphic temperatures observed throughout the mélange zone.

3.4.1 Major and trace element zoning in garnet

Major element zoning in garnet for each sample was determined by EPMA. WDS X-ray maps of Ca and Mn are shown in Figure 3.2 and traverses are shown in Figure 3.3 (see Appendix S2.2 for full data set). Major element zoning is variable. In samples A14-50C, A14-55 and A14-25A Mn decreases from core to rim, consistent with growth during prograde metamorphism (Hollister, 1966), although there is a Mn "spike" either at the mantle/rim boundary (A14-50C and A14-25A) or at the rim of the grain (A14-55). Ca shows the opposite trend for all three samples. Sample A14-29 does not preserve any obvious zoning in Mn while Ca decreases gradually from core to rim. Sample A15-14 records little systematic major element zoning.

Trace element compositions were determined by LA-ICP-MS. Sm and Lu zoning in garnet for each sample is shown in Figure 3.3, other trace elements including Nd and Hf are reported in Appendix S2.2. Samples A14-50C, A14-25A and A14-29 record rare earth element (REE) zoning typical of prograde metamorphism (i.e., heavy REE-enrichment in garnet cores and middle REE-enrichment in garnet rims; e.g., Cheng et al., 2018, 2010, 2008; Kohn, 2009; Lapen et al., 2003; Skora et al., 2006; Smit et al., 2013), although there

is no resolvable zoning in Sm in sample A14-50C. A14-55 records similar zoning in HREEs but preserves a depletion in MREEs (c. 1 ppm decrease in Sm) at the mantle/rim boundary which corresponds to a decrease in Mn from $X_{Sps} = 0.02$ to $X_{Sps} = 0.01$. Sample A15-14 preserves asymmetrical zoning in both Sm and Lu, where Sm is enriched towards the geometric center of the grain while Lu is enriched towards the geometric mantle.

3.4.2 Sm-Nd garnet geochronology

Sm and Nd concentrations in garnet determined by TIMS show good agreement with LA-ICP-MS analyses for all samples except for A14-29. Garnet porphyroblasts in sample A14-29 are poikiloblastic, so it is possible that the difference in concentrations reflects contamination of the LA-ICP-MS data by microinclusions. A comparison between Sm and Nd concentrations in garnet determined using the two methods is shown in Appendix S2.3. Whole rock concentrations determined by TIMS range from 1-66 ppm Sm and 5-364 ppm Nd. Two whole rock separates (A14-55 and A14-50C) record usually high Sm and Nd concentrations. These concentrations were externally verified by ICP-MS to rule out contamination (see Appendix S2.4) and are consistent with REE enrichment via metasomatism which was previously reported for the terrane (Sorensen and Grossman, 1989).

Isotopic data determined by TIMS are reported in Table 3.1. Garnet, garnet powder and garnet leachate $^{147}Sm/^{144}Nd$ ratios range from 0.45-2.1. The majority of the separates record $^{147}Sm/^{144}Nd$ ratios ≥ 0.99, suggesting that garnet separates were sufficiently cleansed to determine an accurate age. The whole rock record typical $^{147}Sm/^{144}Nd$ ratios between

Table 3.1. Sm-Nd isotopic data for garnet and whole rock separates. Grt = garnet, Pwd = powder, Lch = leachate, WR = whole rock. * = excluded from isochron (see discussion)

	% Mass Loss	Nd (ppm)	Sm (ppm)	$^{147}Sm/^{144}Nd$	±2σ	$^{143}Nd/^{144}Nd$	±2σ	$^{143}Nd/^{144}Nd$ (internal, ppm, 2σ)	$^{150}Nd/^{144}Nd$
A14-50C									
Grt1	91	1.866	5.526	1.79115	0.00097	0.513596	0.000009	10.5	0.93
Grt2	76	1.946	5.497	1.708788	0.00092	0.513548	0.000011	21.4	0.89
Grt Pwd	69	1.638	3.688	1.362176	0.00074	0.51327	0.000009	16.3	1.03
WR	-	363.921	66.021	0.109738	0.00006	0.512378	0.000009	12	0.72
A14-25A									
Grt2	73	0.243	0.626	1.55808	0.00076	0.513931	0.000011	21.2	1.67
Grt2		0.194	0.62	1.93807	0.00105	0.51418	0.000015	16	1.39
Grt3	81	0.197	0.625	1.91618	0.00105	0.514166	0.000009	29.2	1.37
Grt4	84	0.176	0.591	2.025	0.00074	0.514227	0.000015	40.8	1.49
Grt Pwd	90	0.172	0.583	2.05405	0.00109	0.514263	0.000021	22.5	1.69
Grt2 Lch	-	0.212	0.557	1.58819	0.00111	0.513939	0.000012	50.6	1.89
WR	-	37.248	13.117	0.21301	0.00086	0.512923	0.000026	15.6	4.77
A15-14									
Grt1	78	0.484	0.891	1.1138	0.0006	0.51349	0.000014	27.3	1.67
*Grt2**	82	0.511	1.023	1.21129	0.00065	0.51367	0.000017	33.1	1.39
Grt3	79	0.307	0.595	1.17452	0.00063	0.51455	0.000011	21.4	1.37
Grt4	77	0.455	0.903	1.19914	0.00065	0.51353	0.000011	22.3	1.49
Grt Pwd	87	0.194	0.561	1.74763	0.00094	0.51394	0.000009	16.3	1.69
Grt Lch	-	0.429	0.638	0.89964	0.00049	0.51333	0.000008	15	0.94
WR	-	221.621	36.775	0.10045	0.00005	0.51277	0.000009	12.9	1.89
A14-55									
Grt1	82	0.379	0.85	1.35773	0.00073	0.513772	0.000009	10.9	1.54
*Grt2**	79	0.341	0.69	1.224904	0.00066	0.513587	0.000014	27.2	1.67
Grt3	78	0.367	0.851	1.403425	0.00076	0.513788	0.000009	16.5	1.16
Grt4	81	0.366	0.834	1.379144	0.00074	0.513775	0.000011	21.8	1.17
Grt Pwd	84	0.307	0.663	1.308267	0.00071	0.513738	0.000009	17.5	1.55
WR	-	46.45	13.549	0.176423	0.0001	0.512874	0.000009	11.5	1.12
A14-29									
Grt1	80	0.49	0.801	0.989847	0.00053	0.513503	0.000009	13.1	0.98
Grt2	78	0.645	0.814	0.763681	0.00041	0.513318	0.000009	12	0.84
Grt Lch1	-	0.576	0.426	0.447618	0.00024	0.513104	0.000009	10.8	0.57
Grt Lch2	-	0.59	0.782	0.801251	0.00043	0.513349	0.00001	20	0.9
WR	-	5.256	1.206	0.138829	0.00007	0.512897	0.000009	15.6	0.63

0.11 and 0.21. Isochrons were calculated using IsoplotR (Vermeesch, 2018), and are shown in Figure 3.4. The bulk garnet ages for the five samples range from 108.0-115.2 Ma, with a median age of c. 110 Ma and two-sigma uncertainties of 0.9 to 2.0 Ma (i.e., age differences are significant). One garnet separate (Grt2) from sample A14-55 falls below the isochron defined by the remaining 4 separates plus whole-rock (Figure 3.4). The separate records similar Sm and Nd concentrations to other separates from the sample (see

Table 3.1) and there are no obvious analytical reasons to exclude the analysis (e.g., high praseodymium interferences, reverse fractionation, few cycles, over- or underspiked); however, it does not appear to be from the same population of garnet as the other four separates and as such it was excluded from the calculations. A two-point isochron between A14-55-Grt2 and the whole rock gives an anomalously young age of 103.9 ± 2.4 Ma. Similarly, Grt2 from sample A15-14 falls above the isochron. This separate again records similar Sm and Nd concentrations to other garnet separates from the sample and there are

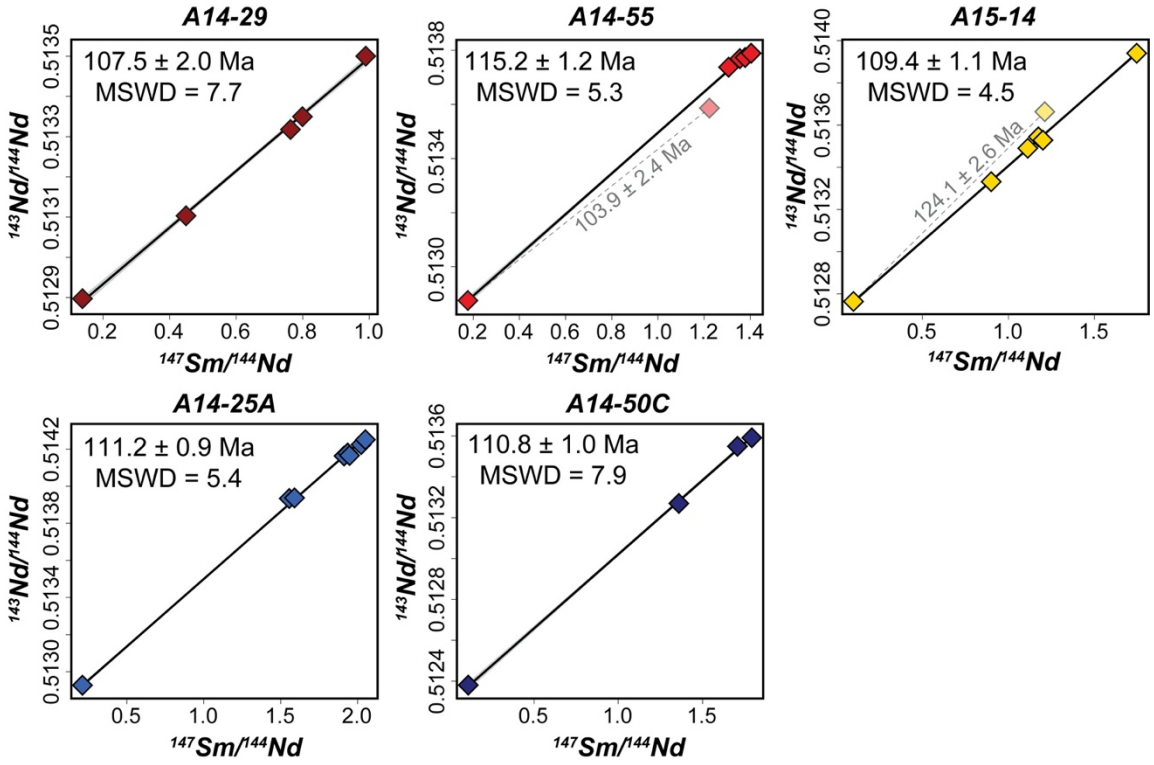

Figure 3.4. Garnet-whole-rock Sm-Nd isochrons for samples A14-50C, A14-25A, A15-14, A14-55 and A14-29. Errors are reported as 2σ uncertainty and are smaller than the symbols.

no analytical reasons to exclude the analysis. A two-point isochron between A15-14-Grt2 and the whole rock gives an anomalously old age of 124.1 ± 2.6 Ma.

3.5 Discussion

3.5.1 Interpreting bulk garnet ages

The effect of REE-bearing inclusions which are not in isotopic equilibrium with the whole rock such as zircon, apatite, epidote and monazite on skewing calculated Sm-Nd ages is well-documented (e.g., Baxter and Scherer, 2013; Scherer et al., 2000). For example, phases with low $^{147}Sm/^{144}Nd$ ratios such as apatite or re-equilibrated high Sm-Nd phases such as zircon will lower the observed $^{143}Nd/^{144}Nd$ ratio, causing the model isochron age to be younger than the actual age of garnet growth. Similarly, high $^{147}Sm/^{144}Nd$ phases such as zircon will increase the observed $^{143}Nd/^{144}Nd$ ratio, causing the model isochron to be older than the actual age of garnet growth. This problem was primarily mitigated through careful hand picking of garnet separates to remove any obvious inclusions followed by partial dissolution to remove any recalcitrant inclusions.

While the samples have moderate MSWDs (3.7-13), reflecting some scatter in the isotopic data, it is unlikely that this reflects contamination by inclusions. The moderate-to-high $^{147}Sm/^{144}Nd$ ratios recorded by garnet, garnet powder and garnet leachate separates, and the generally good agreement between LA-ICP-MS and TIMS Sm and Nd concentrations both support that the separates were sufficiently cleansed. Instead, the moderate MSWDs likely reflect real variations in garnet crystallization age.

Since light rare earth elements (LREEs) are generally enriched in garnet rims relative to garnet cores, bulk garnet Sm-Nd ages are often interpreted to reflect growth of garnet approaching peak metamorphic conditions (Baxter and Scherer, 2013). Of the five

samples considered here, two record Sm enrichment in garnet rims (A14-25A, A14-29) and one (A14-50C) does not record any systematic zoning in Sm. Sample A15-14 appears to record Sm enrichment in the geometric center of the crystal, although the zoning is not symmetrical. The fifth sample, A14-55, preserves Sm enrichment in the garnet core and rim, with a c. 1 ppm depletion in the mantle that corresponds with Mn depletion annuli which likely represent garnet overgrowth following a resorption event (e.g., Ague and Carlson, 2013; Carlson, 2012). These data imply that the reported Sm-Nd ages likely represent the peak age of each sample, although this interpretation is slightly ambiguous for samples A14-50C and A15-14 where there is no obvious enrichment in the Sm towards the garnet rims.

3.5.2 Impact of REE Diffusion

Diffusion of Nd in garnet as a result of long durations of high-temperature metamorphism or post-peak thermal pulses can reset the Sm-Nd isotopic system, resulting in recorded ages that are significantly younger than the true timing of peak metamorphic conditions. Although diffusion of REEs in garnet is slow relative to major elements such as Mn (e.g., Carlson, 2006; Chakraborty and Ganguly, 1992; Tirone et al., 2005), diffusional modification is expected at the peak metamorphic conditions reached by these samples (e.g., Baxter and Scherer, 2013; Bloch and Granguly, 2015; Bloch et al., 2020; Smit et al., 2013). The degree of diffusional resetting is primarily dependent on three factors: the size of the garnet grains, the maximum temperature and the duration of the metamorphic event. Small grains (0-1 mm) like those observed in sample A14-50C can be partially reset at 700°C in as little as 1000 kyr and fully reset in 1-10 Myr (Baxter and Scherer, 2013). In contrast, larger grains (c. 5 mm) like those observed in A14-25A require

durations of metamorphism on the order of 100 Myr at 700°C to completely reset the Sm-Nd system.

While it is likely that these samples experienced some diffusional modification, the degree of modification is difficult to quantify. Retention of Mn zoning in samples A14-25A, A14-50C and A14-55 favors the interpretation that the duration of amphibolite-facies metamorphism was relatively short (e.g., Carlson, 2006; Chakraborty and Ganguly, 1992). In that case, significant modification of Sm-Nd systematics is not expected. Samples A14-29 and A15-14, on the other hand, do not preserve any significant zoning in Mn, which may suggest that these two samples experienced more diffusional modification of the Sm-Nd system. In the case of significant diffusional modification, it is also expected that the smallest garnet grains would experiences the highest degree of modification and thus record the youngest ages. There is no obvious correlation between garnet grain size (see Figure 3.2) and the age recorded by each sample, again suggesting limited diffusional resetting. It is possible that the single garnet separate that falls above the isochron for sample A15-14 reflects an early metamorphic event at c. 124 Ma which was largely reset to c. 109 Ma (Figure 3.4).

Diffusion modeling of either REE or major elements in garnet could be used to elucidate the timescale of metamorphism (e.g., Ague and Baxter, 2007; Caddick et al., 2010). However, in order to utilize an element as a geospeedometer it is necessary to estimate the initial distribution of the element in the mineral, which is often difficult to constrain for all but the simplest of systems (e.g., a 2-phase system such as garnet +

omphacite; see Bloch et al., 2020). Elements commonly used for geospeedometry in garnet are Lu and Mn. Both are thought to partition into garnet under equilibrium conditions by Rayleigh distillation (e.g., Hollister et al., 1966; Kohn et al., 2009; Bloch et al., 2020), which is described in Eqn. 3.1:

$$Eqn\ 3.1\ C_i^M = \alpha_i C_{i,o}^R f^{\alpha_i - 1}$$

In this equation, C_i^M is the concentration of Mn or Lu in garnet, α_i is the partition coefficient of the element between garnet and the whole rock, $C_{i,o}^R$ is the initial concentration in the whole rock and $f^{\alpha_i - 1}$ is the fraction of Lu or Mn remaining in the whole rock following

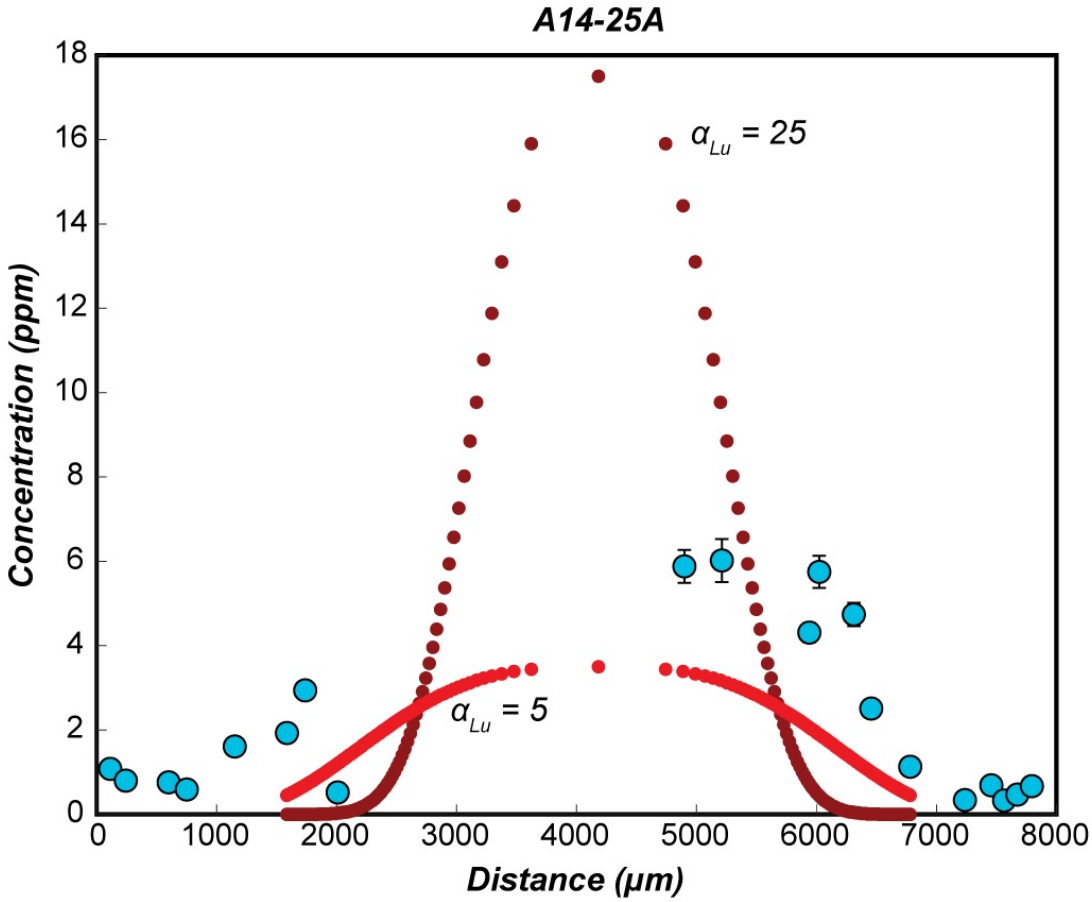

Figure 3.5. Rayleigh distillation models showing the predicted initial distribution of Lu in garnet for sample A14-25A following Hollister (1966) and Kohn et al. (2009). This model shows how uncertainty in the partition coefficient for Lu in garnet (α_{Lu}) affects the predicted starting conditions, which would significantly alter estimates of the timescale of metamorphism based on Lu diffusion geospeedometry.

garnet growth. Reported partition coefficients for Lu in mafic rocks vary in the literature from 5 to 500 (e.g., Bloch et al., 2015; Bloch and Ganguly, 2015; Cheng et al., 2018, 2010, 2008; Kohn, 2009; Lapen et al., 2003; Sassi et al., 2000; Skora et al., 2006), although the majority of reported literature values range between 20 and 50.

Unfortunately, the large uncertainty in this partition coefficient makes the initial zoning difficult to constrain. For example, Figure 3.5 shows two Rayleigh distillation models for sample A14-25A compared to Lu zoning determined by LA-ICP-MS. The first model uses a partition coefficient of 25, which is similar to values reported for a variety of amphibolites (e.g., Kohn, 2009; Cheng et al., 2010, 2018). The second uses a partition coefficient of 5, which is the lowest value reported in the literature (Lapen et al., 2003). These models would result in drastically different diffusive timescales for sample A14-25A. While α_{Lu} = 5 appears to underpredict Lu concentrations, a partition coefficient between 5 and 10 would likely explain the observed Lu zoning without requiring any significant diffusional modification. In contrast, α_{Lu} = 25 predicts significantly higher concentrations of Lu in the garnet core, likely requiring >10 million years of high-*T* metamorphism to diffusively relax Lu to the observed concentrations, even with a fast diffusion mechanism (e.g., Bloch and Gangully, 2015; Bloch et al., 2020; Tirone et al., 2005). In this case, it is expected that the Sm-Nd system would be largely reset, and the observed age would not correspond to any significant metamorphic event. It is also possible that in natural samples, incorporation of Lu into garnet is limited by its mobility in the rock matrix (Skora et al., 2006), in which case a Rayleigh distillation model would not be appropriate. While diffusion-limited REE uptake profiles are reported in blueschist-facies

mafic rocks (e.g., Lagos et al., 2007), it is not clear if this type of model applies at amphibolite-facies conditions, especially in a mélange-type setting where fluid is readily available.

Because of the current challenges associated with attempting to quantify the degree of diffusive resetting, the ages reported here are tentatively interpreted to representative the timing of peak metamorphism. This interpretation is supported by the preservation of Mn zoning in all but two samples and the lack of correlation between age and grain size, suggesting that the timescale of metamorphism was relatively short. The implications for this are discussed below.

3.5.3. Age and temperature variations within the amphibolite-facies mélange zone

Non-systematic temperature variations within a single tectonic mélange zone can be broadly explained in three ways. The first is by chaotic mixing via mélange flow throughout prograde and peak metamorphism, as was previously hypothesized for the amphibolite-facies mélange zone and the lower-grade units of the Catalina Schist (Penniston-Dorland et al., 2018; K. Harvey et al., in revision). In this model, blocks sourced from various depths are juxtaposed through a combination of forced up-dip transport from narrowing of the subduction interface at depth and shearing between mélange components with contrasting rheologic behavior. The model does not require any systematic variation between the peak metamorphic temperature and age recorded by blocks and may even predict no resolvable differences in age if the timescale of mixing was short. The second possible explanation is that the mélange zone developed in conjunction with rapid cooling

of the subduction zone. This scenario may be expected in nascent subduction zones, where subduction into an unrefrigerated mantle produces high thermal gradients at the subduction interface; however, as the mantle wedge becomes hydrated and steady state conditions are reached the interface rapidly cools (e.g., Ishizuka et al., 2011; Plunder et al., 2015; Wakabayashi and Dilek, 2003). It may also be expected following a temperature perturbation (e.g., as the result of a subducting seamount, etc.) as the subduction zone returns to steady-state conditions. In this case, progressive cooling of the subduction interface throughout shear zone development would produce a positive correlation between mélange block age and temperature, whereby the hottest blocks are expected to be the oldest and the coldest the youngest. This model does not necessarily require mélange flow, although the two scenarios are not mutually exclusive. The third and final scenario is that the subduction interface is heating during shear zone development. This scenario could be expected as a result of a variety of non-steady state tectonic processes, including upwelling of hot mantle as a result of either slab rollback or a slab hole/window (e.g., Abratis and Wörner, 2001; Menant et al., 2016; Thorkelson et al., 2011) or subduction of a seamount or ridge (e.g., DeLong et al., 1979; Iwamori, 2000; Santosh and Kusky, 2010; Spinelli and Harris, 2011), and is expected to produce a negative correlation between block age and temperature. Again, this model and mélange flow are not mutually exclusive. Pressure estimates for individual blocks could help differentiate between these models. However, temperature estimates suggest that the unit was sourced over a c. 12 km region of the subduction interface (Penniston-Dorland et al., 2018), which corresponds to a difference in burial depth of c. 4 km. This would produce lithostatic pressure variations of <0.15 GPa, which are unlikely to be resolvable.

Garnet amphibolite blocks throughout the amphibolite-facies mélange zone record peak metamorphic ages between 108-115 Ma, with a median age of c. 110 Ma. There does not appear to be any systematic correlation outside of uncertainty between Sm-Nd garnet ages and Zr-in-rutile peak metamorphic temperatures (Figure 3.6). Of the five blocks considered in this study, the oldest block (A14-55; 115.2 ± 1.2 Ma; 2σ) records a temperature of 721 ± 11°C. The other four blocks record a range of peak metamorphic temperatures, between 643-735°C, yet do not have resolvably different ages. The block that appears to be the youngest of the five (A14-29; 108.0 ± 2.6 Ma; 2σ) records the highest temperature of 735 ± 8°C. These results suggest that the mélange zone developed over c. 7 Myr and suggest that mélange flow was the primary mechanism by which blocks with different peak metamorphic temperatures were juxtaposed throughout the mélange zone. This age difference is significantly shorter than other mélange zones, which record age disparities between blocks within individual mélange zones on the order of 30-40 million years (e.g., Krebs et al., 2008; Mulcahy et al., 2018), suggesting that the mélange zone

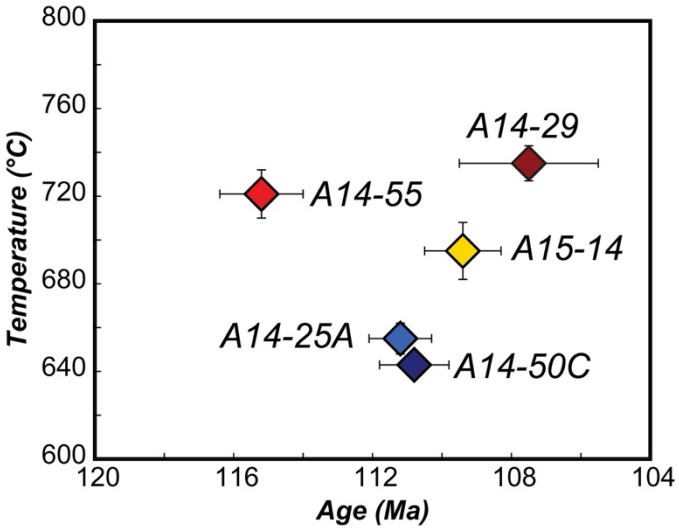

Figure 3.6. Peak metamorphic temperature for each mélange block determined by Zr-in-rutile thermometry (Penniston-Dorland et al., 2018; recalculated by Harvey et al., in revision) versus peak metamorphic age determined by Sm-Nd garnet geochronology. There is no obvious systematic relationship between age and temperature recorded by the blocks.

either developed rapidly prior to exhumation or that mixing ceased following development of rheologically strong matrix phases including amphiboles and pyroxenes.

3.5.4 Comparison with previous chronologic constraints

The timing of amphibolite-facies metamorphism for the Catalina Schist has been previously estimated using a variety of methods. A comparison of these previous estimates to our new estimates is shown in Figure 3.7 and discussed below.

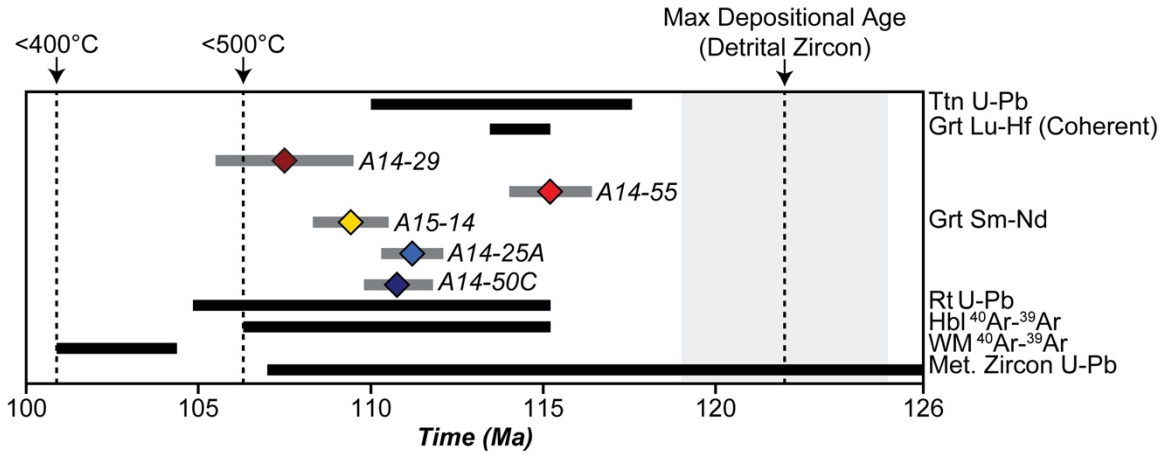

Figure 3.7. Summary of geochronologic data for the amphibolite-facies units of the Catalina Schist. Age estimates from this study are ordered based on peak metamorphic temperature. All other metamorphic ages are shown as black rectangles. The maximum depositional age of metasedimentary blocks from the amphibolite mélange zone based on detrital U-Pb zircon ages (Grove et al., 2008) is shown as a dashed line with uncertainty shown as a gray band. Cooling ages based on Ar diffusion in hornblende ($T_c \sim 500°C$) and white mica ($T_c \sim 400°C$) are shown as dashed lines. Other data Sources: Anczkiewicz et al. (2004), Grove (1993), Grove and Bebout (1995), Grove et al. (2008), Suppe and Armstrong (1972).

Three studies to-date have placed constraints on the prograde and peak metamorphic history of the amphibolite-facies units. These estimates include U-Pb ages from detrital and metamorphic zircon (Grove et al., 2008) and titanite (Mattinson, 1986) from mélange blocks and a Lu-Hf garnet age from the underlying coherent amphibolite unit (Anczkiewicz et al., 2004). Detrital zircon from metagraywacke blocks within the mélange zone record a large range of U-Pb ages from Proterozoic to Early Cretaceous

(Grove et al., 2008). A weighted mean age of the youngest detrital zircon grains provides a maximum depositional age for the protolith of the metagraywackes of 122 ± 3 Ma. Metamorphic zircon from the same rocks records U-Pb ages between 107 and 126 Ma (Grove et al., 2008). This may provide an upper constraint on the earliest stages of mélange zone development, although it is difficult to assess whether the metamorphic zircon ages reflect prograde or peak metamorphism (see Kohn et al., 2015). A garnet amphibolite block from the mélange zone (sample HGB-2 from Sorensen, 1988 and Z5-129-2a from Zack et al., 2004) records a U-Pb titanite-garnet-hornblende-clinopyroxene isochron age of 111.7 ± 1.5 Ma (Mattinson, 1986). Although this has previously been interpreted as a peak metamorphic age and falls within the range of observed Sm-Nd garnet ages, it most likely represents a post-peak metamorphic age, since titanite in the block is found only in the matrix partially replacing rutile (see Zack et al., 2004). Finally, a garnet amphibolite from the structurally lower coherent amphibolite unit (PG5) records a Lu-Hf garnet age of 114.5 ± 0.6 Ma (Anczkiewicz et al., 2004). Interestingly, this is older than all but one of the amphibolite-facies mélange blocks considered in this study. This age relationship and its relevance for the structural evolution of the Catalina Schist are discussed in the following section.

Two additional studies have placed constraints on the cooling history of the amphibolite-facies mélange zone. K-Ar and $^{40}Ar/^{39}Ar$ ages for hornblende from amphibolite-facies rocks ranges from 108-115 Ma (Grove, 1993; Suppe and Armstrong, 1972). Whether these ages are from mélange blocks or the underlying coherent amphibolite unit is not specified; however, since the closure temperature for Ar diffusion in hornblende

is relatively low (c. 500-550°C; Baldwin et al., 1990; Lister and Baldwin, 1996), these ages suggest that some or all of the unit had cooled to epidote-amphibolite facies conditions by c. 108 Ma. $^{40}Ar/^{39}Ar$ white mica ages from both the mélange zone and coherent amphibolite are even younger, between c. 105-100 Ma (Grove and Bebout, 1995). This suggests that both units cooled to below the closure temperature for Ar diffusion in white mica (c. 400-425°C; Harrison et al., 2009) before 100 Ma, which is synchronous with the timing of epidote blueschist-facies metamorphism (Grove and Bebout, 1995; Grove et al., 2008). This requires a relatively rapid cooling rate on the order of 30-40°C/Ma.

3.5.5 Rapid shear zone development and underplating

Few studies to-date have specifically quantified the timescale over which tectonic mélange develops. In some terranes, age estimates from blocks within a single mélange zone span tens-of-millions of years. For example, blocks from the Tiburon Peninsula in the Franciscan Complex record metamorphic ages ranging from 176 to 145 Ma (Anczkiewicz et al., 2004; Catlos and Sorensen, 2003; Firsov and Dobretsov, 1970; Mulcahy et al., 2018; Suppe and Armstrong, 1972). Similarly, blocks from Berkeley Hills, also part the Franciscan Complex record metamorphic ages between 163 and 129 Ma (Anczkiewicz et al., 2004; Mulcahy et al., 2018; Suppe & Armstrong, 1972). Mélange blocks from the Rio San Juan Complex (Dominican Republic) record comparable age disparities, with metamorphic ages between 104 and 62 Ma (Krebs et al., 2008). In both the Franciscan Complex and the Rio San Juan Complex, the age disparities are associated with large differences in metamorphic grade including blueschists, eclogites and amphibolites. In contrast, some mélange zones record no apparent differences in age between blocks, even when the blocks record resolvably different metamorphic histories. For example, age

estimates from Sistan suture (Eastern Iran) based on $^{39}Ar/^{40}Ar$ white mica and hornblende ages are all c. 86 Ma (Bonnet et al., 2018). This similarity was interpreted as representing coeval detachment and tectonic mixing during exhumation, as opposed to mixing during subduction as is the case with the Catalina Schist (see Bebout and Barton, 2002; Penniston-Dorland et al., 2014). In all of the localities mentioned above, large disparities in either metamorphic age or history have been attributed by one or more studies to large-scale mixing of tectonic blocks within a deforming matrix (see Bonnet et al., 2018; Cloos, 1982; Gerya et al., 2002; Krebs et al., 2008).

Blocks from the amphibolite-facies mélange zone of the Catalina Schist record a relatively narrow range of both peak metamorphic temperatures, from c. 643 to 735°C (Penniston-Dorland et al., 2018; Harvey et al., in revision), and peak metamorphic ages, from c. 115 to 108 Ma. The small, but resolvable, difference in peak metamorphic temperatures has previously been interpreted to have resulted from limited mixing as a result of crystallization of rheologically stiff mélange matrix phases including anthophyllite and enstatite (Penniston-Dorland et al., 2018). Two mechanisms could potentially explain both the limited spatial scale of mixing and the narrow range of ages recorded by the unit. The first is that mixing largely ceased following development of chain silicates in the matrix. Jamming of mélange at the subduction interface has been predicted to greatly reduce deformation, resulting in episodic brittle deformation events similar to those observed during episodic tremor and slip (Beall et al., 2019; Webber et al., 2018). While this mechanism is consistent with the observed spatial and temporal scales of mixing, as well as with field observations, it does not fully explain the structural and

chronologic relationships between the mélange zone and coherent amphibolite unit. The second possibility is that the unit was underplated, causing localized deformation within the mélange zone to cease. This mechanism has been proposed in other exhumed terranes that preserve similar structural and chronologic features (i.e., an inverted metamorphic

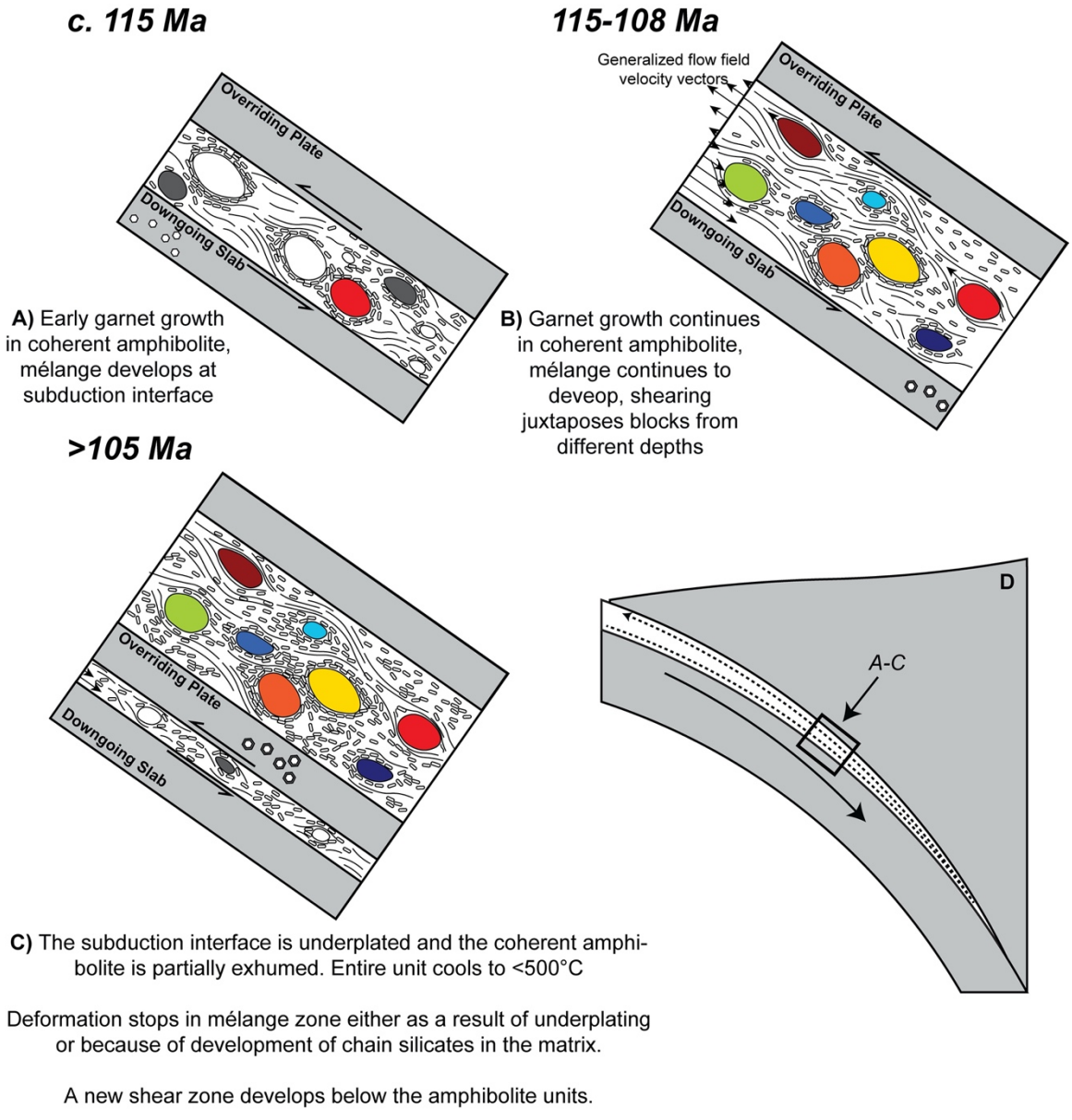

Figure 3.8. A-C. Proposed model for the development of the amphibolite-facies mélange zone of the Catalina Schist showing the evolution of the shear zone from early development at c. 115 Ma to underplating and cooling after c. 105 Ma. D. Sketch of subduction zone interface showing narrowing of interface at depth and resultant return flow.

sequence where the units become progressively older towards the top of the sequence; Angiboust et al., 2014). Underplating best explains the structural relationship between the amphibolite-facies units and the lower grade units (see Figure 2.1) and the chronologic relationship between the units (Grove et al., 2008), and provides a mechanism for the limited spatial and temporal timescales of mixing recorded by the amphibolite-facies mélange zone. However, given the large proportion of chain silicates observed within the mélange zone we cannot rule out that jamming of the shear zone also contributed to the limited scale of mixing. Given that rheologic changes at the subduction interface has been specifically proposed to cause underplating (Agard et al., 2009), these two mechanisms likely acted in a structural continuum.

I propose the following scenario, shown as a conceptual model in Figure 3.8, to explain both the temperature and age variations among mélange zone blocks and the coherent amphibolite unit. *[1] The mélange zone begins developing at amphibolite-facies conditions at or around c. 115 Ma*. This appears to be synchronous with early garnet growth in the coherent amphibolite (recorded by Lu-Hf; Anczkiewicz et al., 2004). *[2] Between c. 115-108 Ma, return flow resulting from narrowing of the subduction interface at depth (Figure 3.8D) in conjunction with shearing between mélange components juxtaposes blocks with different peak metamorphic conditions.* Given a median Sm-Nd garnet age of 110 Ma, the rate of mixing may not have been constant throughout the evolution of the mélange zone. Instead, it appears that a higher proportion of blocks reached peak metamorphism near the end of mélange zone development, between c. 111 and 108 Ma. *[3] The mélange zone is underplated at some point between 108-105 Ma,*

causing deformation to cease. Underplating may have been catalyzed by changes in the rheology of the mélange matrix, where crystallization of amphiboles and pyroxenes strengthened the matrix. The coherent amphibolite is then partially exhumed. A new shear zone, the epidote amphibolite and epidote blueschist units, develops between the downgoing slab and underplated material. The amphibolite units cool to <500°C by c. 105 Ma and <400°C by c. 100 Ma.

3.6 Conclusion

New Sm-Nd garnet ages for blocks from the amphibolite-facies mélange zone of the Catalina Schist reveal that the mélange zone developed over at least 7 Myr from 115 to 108 Ma, which is rapid compared to age disparities as large as 40 million years recorded within other tectonic mélange zones (e.g., Krebs et al., 2008; Mulcahy et al., 2018). During this time, progressive tectonic mixing via mélange flow in conjunction with shearing between matrix components juxtaposed blocks from different depths. The c. 90°C variation in peak metamorphic temperature recorded by blocks throughout the mélange zone suggests that the scale of mixing was limited. Previous studies attributed this limited scale of mixing to rheologically stiff matrix phases which inhibit differential movement of blocks (Penniston-Dorland et al., 2018). These new results show that the mélange zone developed over a relatively short period of time, which likely also contributed to the small scale of mixing observed. Based on $^{39}Ar/^{40}Ar$ cooling ages from hornblende and white mica, the mélange zone appears to have been underplated between 108-105 Ma, causing deformation and therefore mixing within the zone to cease and the unit to rapidly cool from amphibolite facies conditions to <400-425°C by 100 Ma.

3.7 Acknowledgements

This work was funded primarily by NSF grant EAR-1419871 to SPD with additional support from the Geological Society of America's Graduate Student Research Grant (2018, 2019) to KMH. Laboratory work was supported in part by the Center for Isotope Geochemistry at Boston College. Thank you to Steph Walker and Paul Star (Boston College) for laboratory training and assistance with sample analysis.

Chapter 4: Protracted amphibolite-facies metamorphism of the Catalina Schist: Implications for along-strike variations in the thermal structure of the Farallon plate

4.1 Abstract

The role of non-steady-state tectonic processes in the formation and exhumation of many exhumed paleo-subduction terranes is poorly understood. Constraining this role is crucial for understanding the relationship between processes inferred from exhumed terranes and observations of active subduction zones. The Catalina Schist (Santa Catalina Island, CA) is interpreted to be a fossilized subduction interface. It consists of km-scale sub-horizontal thrust sheets ranging in metamorphic grade from lawsonite-albite to upper amphibolite facies. While the thermal gradients recorded by the lower grade units (c. 10-12°C/km) are broadly consistent with those observed in other exhumed terranes and with some benchmark thermal models for young oceanic crust and the early stages of subduction, the anomalously high temperatures recorded by the amphibolite-facies units is difficult to reconcile with steady-state subduction. Mélange blocks throughout the terrane record different peak metamorphic conditions that may be related to long-term or punctuated changes in the thermal structure of the subducting slab. In this chapter, Sm-Nd garnet geochronology was used to determine the ages of three blocks that span the range of high-grade (eclogite- and amphibolite-facies) metamorphic conditions recorded by the terrane. The peak metamorphic conditions of these blocks were estimated using Zr-in-rutile thermometry and quartz-in-garnet elastic barometry and range from 635 to 745°C at 1.30 to 1.65 GPa. A garnet blueschist block that records peak metamorphic conditions that approach eclogite facies records a peak age of c. 186 Ma and a subsequent overprint, likely

at blueschist-facies conditions, at c. 152 Ma. This is the oldest age estimate for the terrane. Two amphibolite-facies blocks record ages of c. 120 Ma and 115 Ma respectively. These are some of the earliest constraints on the timing of amphibolite-facies metamorphism in the terrane. These results in conjunction with previous age estimates for the terrane suggest that amphibolite-facies metamorphism occurred for at least 12 million years from 120 to 108 Ma and provide new insight into the thermo-tectonic evolution of the Catalina Schist. When compared to related exhumed terranes along the western coast of North American, it appears that this high-*T* metamorphic event was unrelated to other high-grade metamorphic events recorded by the exhumed terranes. Simultaneous blueschist-facies metamorphism south of the Catalina Schist indicates that the event was also relatively localized. There are multiple tectonic scenarios that may explain the localized and relatively protracted amphibolite-facies metamorphism of the Catalina Schist, although shallow toroidal mantle flow possibly as a result of a slab tear best explains both the petrologic and geochronologic constraints.

4.2 Introduction

The thermal structure of subducting slabs plays a crucial role in volatile release, magma generation and rheologic changes along the slab interface. Paleo-subduction terranes record a wide range of thermal gradients, with temperature differences as high as 400°C at a given depth even within a single terrane (see compilations by Brown and Johnson, 2018; Holder et al., 2019; Palin et al., 2020; Penniston-Dorland et al., 2015). Multiple processes have been invoked to explain these temperature variations including preferential exhumation of higher-temperature rocks following nascent subduction (Agard et al., 2009; van Keken et al., 2018), variations in the age of the incoming plate (Agard et

al., 2009), changes in slab geometry (Plunder et al., 2018; Wada et al., 2015), thermal perturbations from subduction of seamounts or ridges (e.g., DeLong et al., 1979; Iwamori, 2000; Santosh and Kusky, 2010; Spinelli and Harris, 2011) and mantle upwelling from slab tears/windows, delamination and slab rollback (e.g., Göğüş and Pysklywec, 2008; Kincaid and Griffiths, 2004; Menant et al., 2016; Stegman et al., 2006; Wells and Hoisch, 2008).

Recent geochronologic compilations for paleo-subduction terranes related to subduction of the Farallon Plate during the late-Jurassic/early-Cretaceous have shown that amphibolite-facies rocks occurred periodically throughout the lifespan of the subduction zone, and apparently simultaneously with colder eclogite- and blueschist-facies rocks (Mulcahy et al., 2018). The terranes included in this compilation, such as the Sixes River in Oregon, the Franciscan Complex in northern California, the Catalina Schist in southern California and Baja California (Mexico), occur over c. 2,000 km along the western coast of North America and represent an expansive record of Farallon subduction. For simplicity, these terranes will be collectively referred to as early-Farallon terranes, in that they all represent subduction of the Farallon plate prior to flat-slab subduction around c. 80 Ma (e.g., DeCelles, 2004; Saleeby, 2003). However, it is important to note that there are differences in both the timing and metamorphic/dynamic history across the terranes and as such they should not be treated as a single subduction complex.

There are no obvious mechanisms to explain how amphibolite-facies metamorphism was sustained across the Farallon plate from as early as c. 190 Ma in the northern regions of the Franciscan Complex (see compilation by Mulcahy et al., 2018) to

as young as 108 Ma in the Catalina Schist (see Chapter 3). Many of the amphibolite-facies rocks are younger than the associated arc plutonism (e.g., the Peninsular Ranges Batholith formed around c. 140 Ma; Morton et al., 2014; Shaw et al., 2003; Suppe and Armstrong, 1972) or supra-subduction ophiolite complexes (e.g., the Coast Range Ophiolite formed between 170 and 165 Ma; Shervais et al., 2005), suggesting that nascent subduction alone may not fully explain their occurrence. Similarly, plate reconstruction models suggest that the incoming plate was relatively old, between 60 and 120 Myr (Müller et al., 2016), and therefore not expected to be particularly hot or buoyant.

While detailed chronologic records of the metamorphic history of the northern early-Farallon terranes, principally the Franciscan Complex, provide a fairly comprehensive history of the region, there are relatively few constraints on the timing and duration of amphibolite-facies metamorphism in the southern terranes such as the Catalina Schist and Baja California. Assessing along-strike variations in high-grade (amphibolite- and eclogite-facies) metamorphism may provide insight into which processes dominantly controlled the formation and, perhaps, exhumation of these early-Farallon terranes. Here I present new geochronologic constraints on the formation of the Catalina Schist, including the first evidence for Jurassic eclogite-facies metamorphism. This work addresses the timing and duration of amphibolite-facies metamorphism in the terrane and also places new constraints on the thermal regime prior to amphibolite-facies metamorphism. The results are compared to previous age constraints for the terrane, and the tectonic implication is discussed. The chronologic record of the Catalina Schist is then compared to other early-Farallon terranes in order to assess potential mechanisms for amphibolite-facies

metamorphism across the terranes. This work contributes to understanding how the thermal structure of the Farallon plate evolved along-strike following closure of the Cache Creek plate in the early Jurassic until the onset of flat-slab subduction in the late Cretaceous. In particular, this compilation questions the long-standing association between amphibolite-facies metamorphism and subduction initiation.

4.3 Geologic Background

The Catalina Schist, best exposed on Santa Catalina Island (CA), is interpreted as an exhumed subduction interface that formed during Cretaceous subduction of the Farallon Plate beneath the North American Plate. It is broadly related to a series of paleo-subduction terranes spanning the western coast of North and Central America, including both the Franciscan Complex (CA) to the north and Baja California (Mexico) to the south. The terrane consists of an inverted sequence of tectonometamorphic thrust sheets ranging in metamorphic grade from lawsonite albite to upper amphibolite facies (see Figures 2.1, 2.2; Section 2.3). Zr-in-rutile thermometry and quartz-in-garnet barometry suggest that the amphibolite-facies rocks reached peak metamorphic conditions between 580 and 735°C at 1.2 to 1.5 GPa (Penniston-Dorland et al., 2018; Harvey et al., in revision). These conditions are anomalously hot relative to other exhumed terranes (see Penniston-Dorland et al., 2015) and to estimates of modern subduction zone thermal structures (e.g., Syracuse et al., 2010; van Keken et al., 2011). However, there is not currently an explanation for these conditions that explains both geochronologic constraints on the timing of subduction initiation relative to formation of the terrane (see Grove et al., 2008) and the observations that suggest that

the terrane formed at the subduction interface as opposed to within a forearc thrust system (see Section 2.3; Harvey et al., in revision).

Prior chronologic constraints on the timing of amphibolite-facies metamorphism have primarily focused on the two amphibolite units: the coherent amphibolite and the amphibolite-facies mélange zone. The coherent amphibolite appears to have reached peak metamorphic conditions around c. 115 Ma (Anczkiewicz et al., 2004), while the mélange zone records a range of ages from c. 115 to 108 Ma (see Section 3; Harvey et al., in prep; Mattinson, 1986). In contrast, there are few constraints on the ages of exotic high-grade blocks interspersed throughout the epidote amphibolite and lawsonite blueschist facies units, which are critical to multiple tectonic interpretations of the terrane (Platt, 1975; Grove et al., 2008; Harvey et al., in revision; Chapter 2). These exotic blocks record a range of peak metamorphic conditions from eclogite to upper amphibolite facies and have been interpreted to have been sourced via tectonic mixing from a 20-60 km region of the subduction interface (Harvey et al., in revision), although other interpretations exist (see Platt, 1975). Existing prior chronologic constraints on a single exotic block suggest that the exotic blocks may be temporally distinct from the amphibolite-facies units. Three age estimates for the garnet blueschist block found within the lawsonite blueschist unit (sample GB from Section 2) show that it is older than the amphibolite units. These include an ^{39}Ar-^{40}Ar white mica plateau age between 160 and 145 Ma (Grove and Bebout, 1995), a model Rb-Sr age of 135 Ma (2-point isochron between Na-amphibole and white mica; Grove et al., 2008) and a U-Pb titanite age of 155 ± 8 Ma (Awalt et al., 2013). Given this apparent age discrepancy between the garnet blueschist block and the amphibolite units, and because

the exotic blocks record a much larger range of *P-T* conditions than the amphibolite units, it is possible that these exotic blocks may provide broader insights, both spatially and temporally, into the metamorphic history of the Catalina Schist.

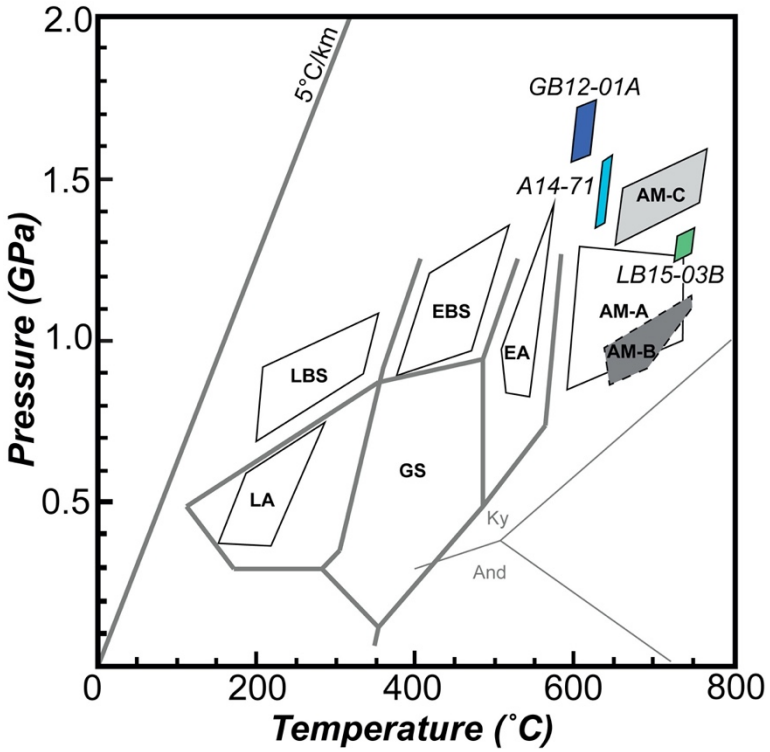

Figure 4.1. Summary of pressure-temperature estimates for each tectonometamorphic the Catalina Schist and for the three exotic blocks considered in this study. LA = lawsonite albite; LBS = lawsonite blueschist; EBS = epidote blueschist; AM = amphibolite; GS = greenschist (not observed). Data sources: white polygons and AM-A after Grove and Bebout (1995); AM-B from Sorensen and Barton (1987); AM-C: Harvey et al. (in revision).

4.4 Sample Descriptions

To constrain the timing and duration of amphibolite-facies metamorphism, three exotic blocks which span the range of high-*T* thermal gradients recorded by the terrane were chosen for analysis. The peak metamorphic conditions of these samples were previously estimated by Harvey et al. (in revision) and are summarized in Figure 4.1.

Major element zoning in garnet for each sample was determined by wave dispersive spectroscopy (WDS) using the JEOL JXA 8900R Electron Probe Microanalyzer (EPMA) in the AIMLab at the University of Maryland. Measurements were made using a 15 kV accelerating voltage, a beam current of 25 nA, and a beam diameter of 1 μm. Analyses

were standardized using natural mineral standards and processed using a ZAF correction scheme (Armstrong, 1988). WDS X-Ray maps were used to fully assess major element zoning. X-Ray maps were collected using a 15 kV accelerating voltage, a beam current of 250 nA and a beam diameter between 5 and 20 µm. WDS traverses across garnet are shown in Figure 4.2 and select X-ray maps are shown in Figure 4.3 (see Appendix S3.1 for full data set).

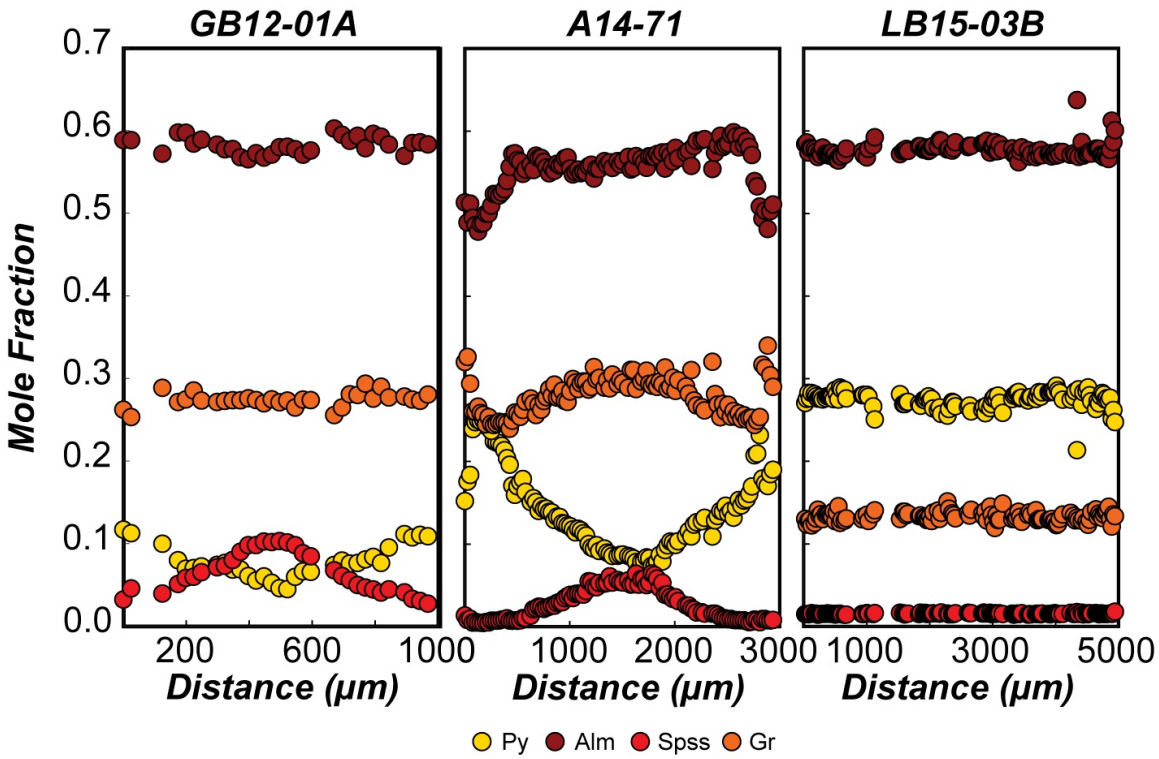

Figure 4.2. WDS traverses for samples GB12-01A, A14-71 and LB15-03B showing distribution of Mg, Fe, Mn and Ca in garnet as mole fractions pyrope, almandine, spessartine and grossular respectively.

Sample GB12-01A (eqv. to GB in Chapter 2) is a sheared garnet-bearing blueschist block found within the lawsonite blueschist facies mélange zone. The mineral assemblage of the block includes garnet + glaucophane + lawsonite + quartz + rutile + titanite + zircon. Garnet occurs within two primary textural domains: within glaucophane + lawsonite-

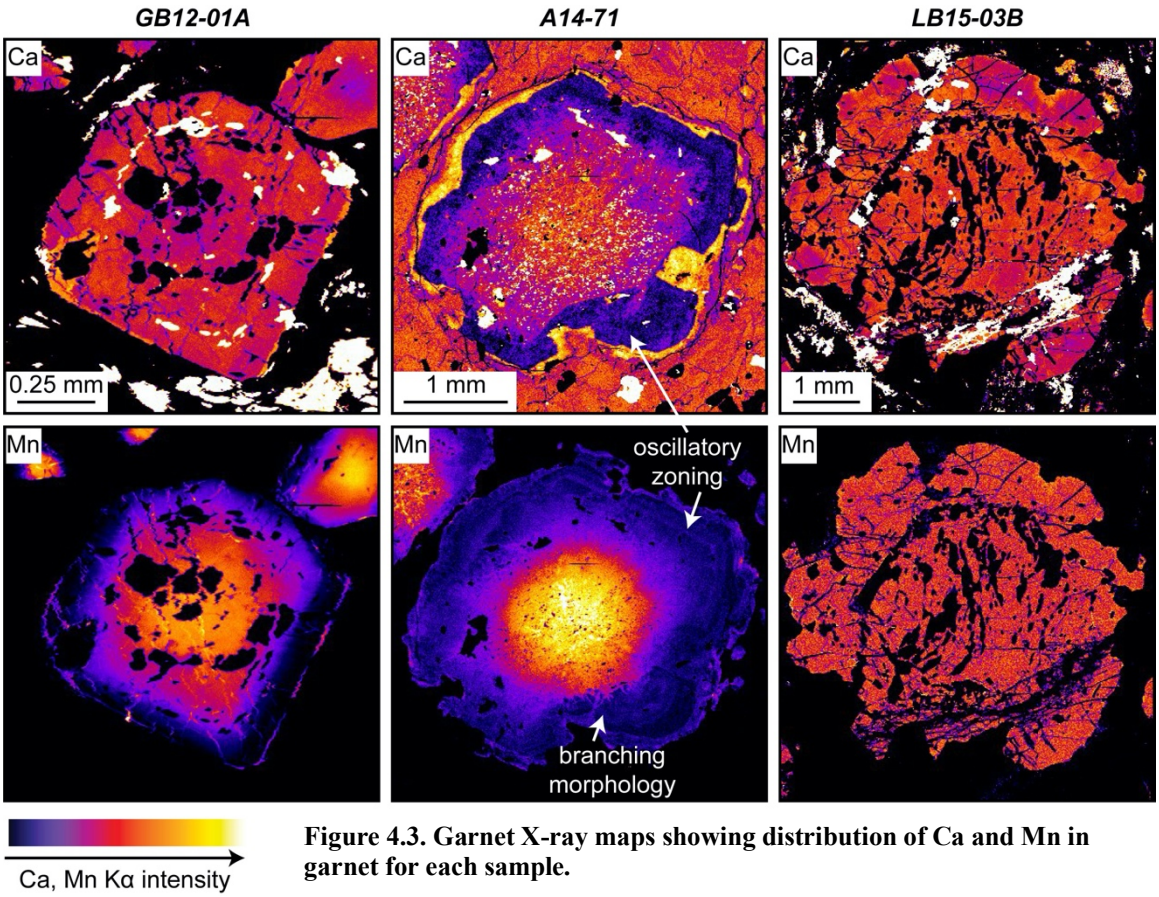

Figure 4.3. Garnet X-ray maps showing distribution of Ca and Mn in garnet for each sample.

dominated shear bands as highly-fractured c. 0.5 mm porphyroblasts (Figure 4.4A) and as small (c. 50-70 µm) un-fractured porphyroblasts within quartz ± lawsonite shear bands and veins (Figure 4.4B, C). Larger garnet porphyroblasts are zoned in all major elements, although the degree of zoning is variable (Figures 4.2 and 4.3). Mg increases from a core value around $X_{Py} = 0.04$ to a rim value of $X_{Py} = 0.12$. Mn is inversely zoned relative to Mg, with core concentrations around $X_{Sps} = 0.10$ and rim concentrations around $X_{Sps} = 0.03$. Ca and Fe are less strongly zoned, with concentrations ranging from $X_{Grs} = 0.26$ to 0.29 and $X_{Alm} = 0.57$ to 0.59. High-Mn re-healed fractures occur throughout the garnet porphyroblasts (Figure 4.3). Textural evidence suggests that the blueschist facies assemblage (Na-amphibole + lawsonite) occurred as a pervasive overprint at post-peak conditions and may be associated with late-stage deformation and shearing. Zr-in-rutile

thermometry and quartz-in-garnet barometry *P-T* estimates for the block place peak metamorphic conditions around eclogite facies at 611 ± 15°C and 1.65 ± 0.10 GPa (Harvey et al., in revision). Previous chronologic constraints between 145 and 160 Ma based on U-Pb titanite and ^{39}Ar-^{40}Ar white mica geochronology (Awalt et al., 2013; Grove and Bebout, 1995) for the block suggest that it is older than the amphibolite-facies rocks.

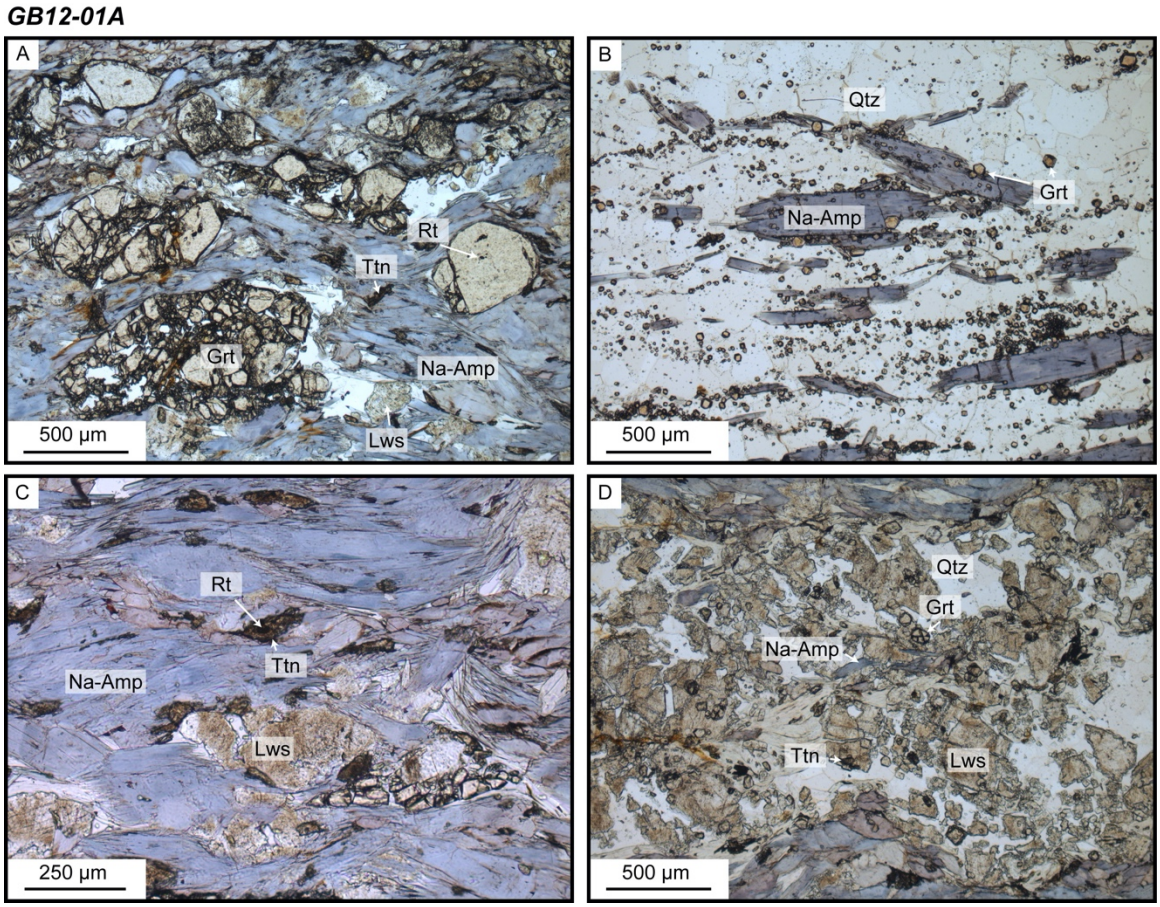

Figure 4.4. Photomicrographs of sample GB12-01A showing different textural domains and garnet populations observed in the block. A) Photomicrograph showing deformed garnet porphyroblasts with rutile inclusions and quartz pressure shadows. Na-amphibole, lawsonite and titanite occur in the matrix. B) Textural domain showing quartz-rich band with small euhedral garnet porphroblasts and glaucophane C) Photomicrograph showing textural relationship between rutile and titanite. Titanite occurs in the matrix replacing rutile. D) Quartz-rich textural domain showing textural relationship between small garnet porphyroblasts, lawsonite, titanite and Na-amphibole. Grt = garnet; Na-Amp = sodic amphibole; Rt = rutile; Ttn = titanite; Lws = lawsonite; Qtz = quartz.

A14-71 is an omphacite-bearing garnet amphibolite exotic block found within the epidote amphibolite facies. It is composed primarily of garnet + hornblende + omphacite + rutile + apatite + quartz + zircon (see Figure 2.5B). Garnet occurs as c. 3 mm garnet porphyroblasts with relatively strong major element zoning. The core and inner mantle regions of garnet are characterized by strongly zoned Ca, Mn and Mg (Figure 4.2). Ca decreases from core to mantle from X_{Grs} = 0.32 to 0.25. Mn follows a similar trend with X_{Sps} = 0.06 to 0.01. Mg is inversely zoned relative to Ca and Mn, with X_{Pyp} increasing from 0.08 to 0.18. Fe shows a slight increase in concentration from core to inner mantle, with concentrations ranging between X_{Alm} = 0.54 to 0.59. The outer mantle of the garnet appears to display a branching crystal chemistry characteristic of fast disequilibrium garnet growth (e.g., Wilbur and Ague, 2006) corresponding with oscillatory zoning in Mn and, to a lesser degree, Ca (Figure 4.3). The garnet rim is characterized by a sharp increase in Ca, Fe and Mn and a decrease in Mg. The block records peak conditions of 636 ± 10°C and 1.47 ± 0.11 GPa (Harvey et al., in revision).

LB15-03B is a metagraywacke exotic block found within the epidote amphibolite facies that preserves peak metamorphic conditions of 735 ± 12°C and 1.30 ± 0.05 GPa. The block is primarily composed of quartz + feldspar + garnet + rutile + chlorite with fine-grained rhomb-shaped groundmass composites composed of albite + white mica ± zoisite (see Figure 2.5E). These groundmass composites have previously been interpreted as reflecting plagioclase breakdown at peak conditions (Harvey et al., in revision); however, similar textures in other terranes have been interpreted to represent lawsonite breakdown following prograde blueschist facies metamorphism (e.g., Keiter et al., 2004). Garnet

occurs as c. 5 mm porphyroblasts with s-type quartz inclusion trails. There is little variability in major element concentration (Figure 4.2), with a slight decrease in Fe from core to mantle (X_{Alm} = 0.58 to 0.56) and a slight increase in Mg (X_{Pyp} = 0.25 to 0.28). There is a more significant change in Fe and Mg concentration at the garnet rim, with X_{Alm} increasing to 0.61 and X_{Pyp} decreasing to 0.24. There is no significant variability in either Ca or Mn, with X_{Grs} ~ 0.13 and X_{Sps} ~ 0.02.

4.5 Sm-Nd Garnet Geochronology

Ages for each sample were determined using Sm-Nd garnet geochronology. Garnet, garnet powder and whole rock fractions were prepared for analysis using an IsotopX Phoenix Thermal Ionization Mass Spectrometer (TIMS) at Boston College following the procedure outlined in Section 3.3.1. Measurements of full-procedure and 3-column blanks for the lab are all <5 pg Nd. For each sample, 2.0-68.8 ng of Nd was loaded onto outgassed rhenium filaments in Ta_2O_5 and 0.87-25.3 ng of Sm was loaded in HNO_3 onto tantalum center filaments. Repeated measurements of in-house standard solutions of Nd and Sm (AMES metal) yield long-term reproducibility of 17.3 ppm (2 RSE, $^{143}Nd/^{144}Nd$ =

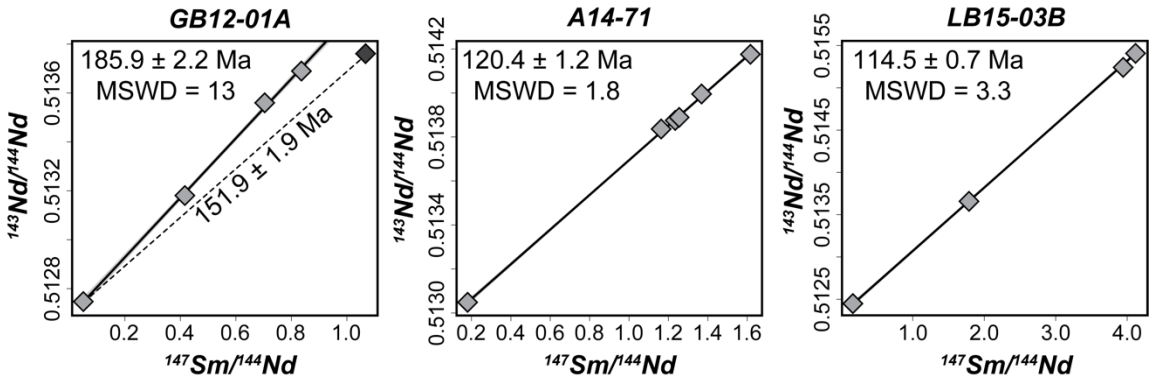

Figure 4.5. Garnet-whole rock isochrons for samples GB12-01A, A14-71 and LB15-03B. Errors are reported as 2σ uncertainty and are smaller than the symbols.

0.512151±9, n = 226) and 72 ppm (2 RSE, $^{147}Sm/^{152}Sm$ = 0.560869±41, n = 145), respectively.

Table 4.1. Sm-Nd isotopic data for garnet and whole rock separates. Gt = garnet, Pwd = powder, WR = whole rock. * = not included in isochron (see text)

	% Mass Loss	Nd (ppm)	Sm (ppm)	$^{147}Sm/^{144}Nd$	±2σ	$^{143}Nd/^{144}Nd$	±2σ	$^{143}Nd/^{144}Nd$ (internal, ppm, 2σ)	$^{150}Nd/^{144}Nd$
GB12-01A									
*Gt1**	75	0.4965	0.8774	1.068941	0.00058	0.513757	0.000009	13.6	0.95
Gt-Pwd1	80	0.4921	0.3388	0.416522	0.00022	0.51318	0.000018	35.1	1.1072
Gt-Pwd	63	0.4925	0.6817	0.837341	0.00045	0.51369	0.000009	12.1	1.0251
Gt2	79	0.6713	0.7823	0.704911	0.00038	0.51356	0.000009	15.6	0.792
WR	-	69.4481	5.827	0.050754	0.00003	0.512745	0.000009	11.7	0.453
A14-71									
Gt1	51	0.4058	0.8288	1.235445	0.00067	0.513877	0.00001	19.3	0.768
Gt2	68	0.3697	0.8372	1.369798	0.00074	0.513996	0.000018	35.1	0.816
Gt3	32	0.4723	0.9112	1.167128	0.00063	0.513836	0.00001	19.9	0.696
Gt4	40	0.4229	0.877	1.254433	0.00068	0.513889	0.000013	25.5	0.741
Gt5	80	0.3505	0.9366	1.616449	0.00087	0.514176	0.000009	14.7	1.268
WR	-	20.433	15.4678	0.18191	0.0001	0.513048	0.000009	14.4	
LB15-03B									
Gt1	-	0.5353	1.5791	1.784242	0.00096	0.513651	0.00003	58.4	0.961
Gt2	68	0.1893	1.2897	4.12205	0.00223	0.515416	0.000012	23.8	2.244
Gt3	75	0.1689	1.0997	3.939192	0.00213	0.515243	0.000026	50.5	1.294
WR	-	3.1439	0.8701	0.167421	0.00019	0.512449	0.000013	26.3	4.82

Isotopic data determined using TIMS are summarized in Table 4.1. Garnet and garnet powder separates yield moderate to high $^{147}Sm/^{144}Nd$ ratios between 0.41 and 4.1. The majority of the separates (n = 9 out of 12) record $^{147}Sm/^{144}Nd$ ratios > 1, suggesting that they were sufficiently cleansed via partial dissolution to determine an accurate age. Whole rock $^{147}Sm/^{144}Nd$ ratios range from 0.05-0.18. Bulk garnet-whole rock isochrons were calculated using IsoplotR (Vermeesch, 2018) and are shown in Figure 4.5.

Sample GB12-01a produced a 4-point isochron with an age of 185.9 ± 2.2 Ma (2σ, MSWD = 13). One garnet separate falls below the isochron. A two-point isochron (dashed line in Figure 4.5**)** between this separate and the whole rock yields an apparent age of 151.9 ± 1.9 Ma. LB15-03B produced a 4-point isochron with an age of 114.5 ± 0.7 Ma (2σ, MSWD = 3.3). A14-71 produced a 6-point isochron with an age of 120.4 ± 1.2 Ma (2σ, MSWD = 1.8). Given the complex metamorphic histories of these samples, the moderate MSWDs are interpreted to reflect real variations in garnet crystallization age as opposed to contamination by recalcitrant inclusions (see Section 3.5.1).

4.6 Discussion

4.6.1 Age Interpretation

Sample GB12-01a yielded an anomalously old age of 185.9 ± 2.2 Ma. While similar ages have been reported in association with subduction initiation across the early-Farallon terranes (see Gonzalez and Baldwin, 2019; Mulcahy et al., 2018; Page et al., 2003), this is significantly older than expected given the prior chronologic constraints on the block. U-Pb titanite and ^{40}Ar-^{39}Ar white mica ages for the block range from c. 160 to 145 Ma (Awalt et al., 2013; Grove and Bebout, 1995). Peak metamorphic conditions were estimated using

Zr-in-rutile thermometry and quartz-in-garnet barometry (Harvey et al., in revision) to be c. 610°C and 1.65 GPa. This is well above the closure temperature for Ar diffusion in white mica (c. 400-425°C; Harrison et al., 2009), so it is not surprising that the ^{40}Ar-^{39}Ar white mica age is younger than the Sm-Nd garnet age. Textural evidence also indicates that garnet pre-dates titanite in the rock. The likely peak-metamorphic Ti-bearing phase is rutile, which is found both in the matrix and as inclusions in garnet (Figure 4.4A). Titanite is found in the matrix replacing rutile, suggesting that it post-dates both garnet and rutile (Figure 4.4A, C). Interestingly, one garnet separate records a model Sm-Nd age of c. 152 Ma that is apparently consistent with previous age estimates. This may reflect a second generation of garnet growth associated with a blueschist-facies overprint around that time. Finally, a ^{40}Ar-^{39}Ar white mica thermal overprint around c. 110 Ma suggests that the block was entrained in the subduction system during amphibolite-facies metamorphism (Grove and Bebout, 1995), although given the substantial gaps in its metamorphic history the possibility that the block was exhumed and then re-subducted (e.g., Wakabayashi, 2012) cannot currently be ruled out.

While an age of 120.4 ± 1.2 Ma for sample A14-71 overlaps with both detrital and metamorphic U-Pb zircon ages from the amphibolite-facies melange zone (Grove et al., 2008), it is resolvably older than any estimates of the timing of peak metamorphism for both the amphibolite-facies melange zone and lower coherent amphibolite unit (c. 115-108 Ma; Chapter 3; Anczkiewicz et al., 2004; Mattinson, 1986).. Given the moderate grain size (c. 3 mm), relatively cold peak metamorphic temperature (c. 640°C at 1.5 GPa; Harvey et al., in revision) and retention of sharp major element zoning (Figure 4.3), this age is

unlikely to have been modified significantly by diffusion of Nd and is therefore interpreted as a peak metamorphic age (e.g., Baxter and Scherer, 2013).

In contrast, sample LB15-03B yielded an age of 114.5 ± 0.7 Ma, which is coeval with the coherent amphibolite unit (114.5 ± 0.6 Ma; Anczkiewicz et al., 2004) and the oldest amphibolite-facies mélange zone block (115.2 ± 1.2 Ma; sample A14-55 from Chapter 3). This age is currently interpreted to represent peak metamorphism; however, diffusive resetting cannot currently be ruled out given the lack of major element zoning and relatively high-temperature peak metamorphic conditions of c. 740°C at 1.30 GPa. Regardless, the block is still older than all but one of the amphibolite-facies mélange blocks and as such this does not significantly affect the implications for the duration of amphibolite facies metamorphism or the tectonic evolution of the Catalina Schist and early-Farallon terranes.

4.6.2 Implications for the tectonic evolution of the Catalina Schist

The exotic blocks found throughout the Catalina Schist, and in particular the garnet amphibolite blocks found within the epidote amphibolite facies, were previously interpreted by Harvey et al. (in revision) to represent a continuum of mixing along the subduction interface between higher-*T*/deeper garnet-bearing amphibolite and lower-*T*/shallower epidote amphibolite rocks. The model was supported by two primary observations: 1) the garnet-bearing exotic blocks record a large (c. 580-740°C) and nearly continuous, rather than a bi-modal, range of peak metamorphic temperatures spanning from just overlapping with the epidote amphibolite rocks to the highest temperatures recorded

by the amphibolite-facies mélange zone and 2) the exotic blocks record a wider range of pressures than those recorded by the amphibolite-facies mélange zone, indicating that they were sourced from a larger region of the subduction interface. Although these blocks as a whole appear to have been sourced from a larger region (c. 20-30 km for the exotic blocks in the epidote amphibolite unit) of the subduction interface, the scales of mixing observed within any given exotic block region were observed to be comparable to the scale of mixing interpreted for the amphibolite-facies mélange zone (c. 12 km along the subduction interface; Penniston-Dorland et al., 2018). Additional observations that support this model include geochemical and isotopic evidence of mechanical mixing between mélange components at every metamorphic grade (Bebout and Barton, 2002; King et al., 2006, 2007). The work presented in Chapter 3 elaborates on the tectonic mixing model, providing chronologic constraints on the timing of underplating relative to formation of the amphibolite-facies mélange zone. This work demonstrated that peak metamorphism of blocks within the amphibolite-facies mélange zone is younger than the coherent amphibolite unit and developed over c. 7 million years from 115 to 108 Ma. Both units appear to have been underplated between 108 and 105 Ma, corresponding with rapid cooling of the thrust slices to <500°C.

Interestingly, the two amphibolite-facies exotic blocks considered in this study are both older than the median age of the amphibolite-facies mélange zone (c. 110 Ma; see Chapter 3) and are either coeval with (LB15-03B) or older than (A14-71) the coherent amphibolite unit. This is somewhat surprising because the epidote amphibolite unit overlaps with but is predominately younger than the amphibolite-facies mélange zone (c.

109-97 Ma; see Grove et al., 2008); although given the relatively small number of both exotic blocks and amphibolite-facies mélange blocks with age constraints it is difficult to assess whether the exotic blocks are truly systematically older. Regardless, these results are likely still reconcilable with the tectonic models proposed by Harvey et al. (in revision) and in Chapter 3.

4.6.3 Implications for the timing and duration of amphibolite-facies metamorphism

Previous studies have invoked nascent subduction to explain the anomalously high-*T* conditions recorded by the amphibolite-facies rocks of the Catalina Schist (Platt, 1975). As highlighted by Grove et al. (2008), more recent constraints on the timing of arc plutonism in the region show that subduction initiated >140 Ma, precluding nascent subduction as a possibility (Morton et al., 2014; Shaw et al., 2003; Suppe and Armstrong, 1972). This is further corroborated by new age estimates for the garnet blueschist block which show that it is at least 186 Ma. However, there is still upwards of 30 to 45 million years of unaccounted for history between the blueschist-facies overprint of the block between 160 and 145 Ma and amphibolite-facies metamorphism. Sample A14-71 records the earliest evidence for amphibolite-facies metamorphism in the terrane. The block yields an Sm-Nd garnet age of c. 120 Ma, which is 5.2 (± 1.7) million years older than any other current peak metamorphic age estimates for the amphibolite-facies units. The peak *P*-*T* conditions recorded by the block overlap with the amphibolite-facies mélange zone, although it appears to fall along a somewhat colder geothermal gradient (Figure 4.1).

Combining all current chronologic constraints for the Catalina Schist, amphibolite-facies metamorphism post-dates subduction initiation yet was sustained for at least 12 million years between 120 and 108 Ma. This observation can rule out several processes. For example, delamination, seamount subduction or slab gaps are expected to produce localized and punctuated thermal pulses (e.g., Beall et al., 2017; Cloos, 1993; Fisher, 2003; Kay and Mahlburg Kay, 1993; Király et al., 2020; Spinelli and Harris, 2011) which would likely last for a significantly shorter amount of time than 12 million years given the timescales at which these types of perturbations occur. Alternatively, ridge subduction is expected to be protracted (e.g., DeLong et al., 1979; Iwamori, 2000); however, it is likely to last for far longer than 12 million years (see Iwamori, 2000). There are multiple other mechanisms that may explain both the petrologic and chronologic observations, including a slab tear or window (e.g., Abratis and Wörner, 2001; Menant et al., 2016; Thorkelson et al., 2011), oblique subduction (e.g., Plunder et al., 2018; Wada et al., 2015) or slab rollback (e.g., Čížková and Bina, 2013). These possibilities are further explored in the context of along-strike variations in metamorphic conditions across the Farallon plate.

4.4.6 Comparison to other early-Farallon subduction localities

Age constraints across early-Farallon terranes including Sixes River (Oregon), the Franciscan Complex (Northern California), the Catalina Schist (Southern California) and Baja California (Mexico) were recently compiled by Mulcahy et al. (2018). Based on this compilation, the study argued that amphibolite-facies rocks across the terranes do not just occur in association with subduction initiation, but rather dispersed throughout the lifespan of early-Farallon subduction. While this observation has been similarly interpreted by previous studies (Page et al., 2007), it largely contradicts the long-standing view that within

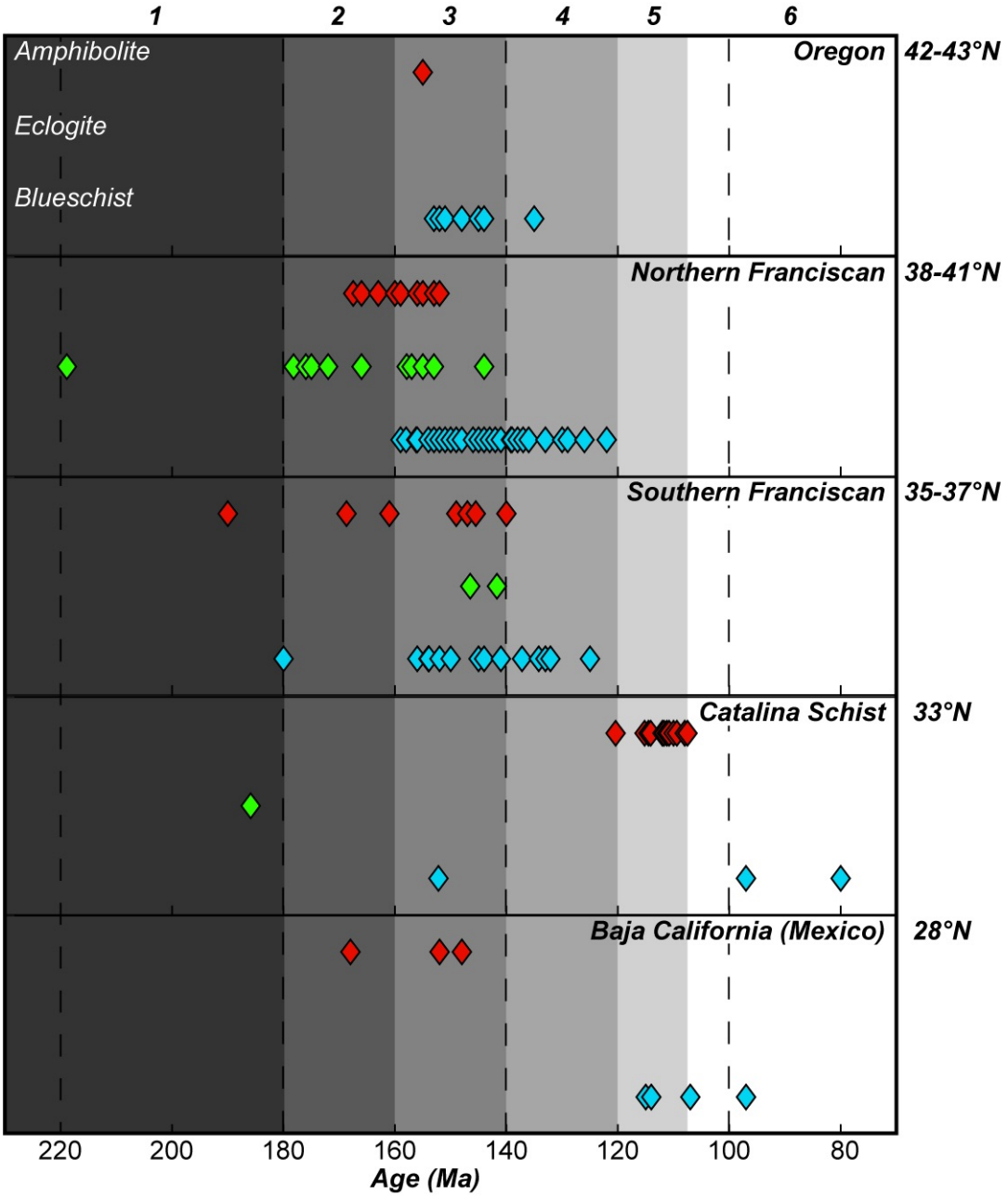

Figure 4.6. Compilation of age estimates for early-Farallon terranes showing distribution of amphibolite- (red), eclogite- (green) and blueschist-facies (blue) metamorphic events recorded along-strike. Data sources are reported in Appendix S3.2 and the full data repository can be found in Mulcahy et al. (2018). Grey bands show interpreted series of metamorphic events. 1) Subduction of the Cache Creek plate from >220 Ma to c. 180 Ma. 2) Subduction (re)initiation of the Farallon plate between 180 and 160 Ma indicated by occurrence of high-grade metamorphism. 3) Slow cooling of the subduction interface from c. 160 to 140 Ma indicated by co-occurrence of high-grade and blueschist-facies metamorphism. 4) Blueschist-facies metamorphism of the northern Farallon terranes between c. 140 and 120 Ma. The last occurrence of metamorphism in the northern terranes occurs at c. 120 Ma. 5) Amphibolite-facies metamorphism of the Catalina Schist between c. 120 and 108 Ma which occurs simultaneously with blueschist-facies metamorphism of Baja California. 6) Blueschist facies metamorphism of the Catalina Schist and Baja California terranes, a transition to flat-slab subduction occurs around c. 80 Ma.

the Franciscan Complex in particular high-grade amphibolites are remnants of nascent subduction (e.g., Anckiewicz et al., 2004; Krogh et al., 1994; Wakabayashi, 1990)

While the compilation by Mulcahy et al. (2018) certainly demonstrates that amphibolite-facies metamorphism occurred throughout the lifespan of the early-Farallon terranes, it does not take into account possible along-strike variations in thermal structure. This is especially important for considering the potential effect of asynchronous subduction initiation along the length of the plate boundary (Anczkiewicz et al., 2004) and for assessing other potential mechanisms for amphibolite-facies metamorphism. Figure 4.6 shows this compilation separated by the along-strike position of the localities. In lieu of precise *P-T* estimates for the majority of the localities, data were broadly separated into amphibolite, eclogite and blueschist facies. The Oregon localities include Sixes River, Roseburg, Big Craggies and Bandon (see Coleman and Lanphere, 1971). Because of the size of the Franciscan Complex, it was subdivided into northern and southern regions. The northern region includes all localities within and north of San Francisco (e.g., Berkeley Hills, Junction School, Jenner, Hull Mountain, Laytonville, etc.) while the southern region includes Goat Mountain, Mt. Hamilton, Pacheco Pass, Panoche Pass and San Simeon. Baja California (Mexico) includes localities on Cedros Island and East San Benito Island. Published whole rock argon ages were not considered (see Dumitru et al., 2010). The data sources for this compilation can be found in Appendix S3.2 and the full repository can be found in Mulcahy et al. (2018). Additional data sources that were not included in the original compilation but included in the figure include Gonzalez and Baldwin (2019) as well as the data presented in Chapter 3 and this study.

This updated compilation highlights several important considerations. First, it shows that high-grade metamorphism (eclogite- and amphibolite-facies) occurred across all of the early-Farallon terranes from c. 180 to 140 Ma. This suggests that subduction initiation occurred along the entire plate boundary at or earlier than 180 Ma. While chronologic constraints for the southern terranes (the Catalina Schist, Baja California) between 180 and 140 Ma are far more sparse than the Franciscan Complex, there does not appear to be any systematic variation in the timing of early amphibolite-facies metamorphism along-strike (i.e., Baja California is coeval with the northern terranes). This demonstrates that amphibolite-facies metamorphism of the Catalina Schist is not associated with asynchronous subduction initiation migrating from north-to-south, as was hypothesized by Anczkiewicz et al. (2004) to explain the age discrepancy between the Catalina Schist and the Franciscan Complex. Blueschist-facies metamorphism is also largely synchronous and is not overly prevalent until after c. 160 Ma. The timing of the blueschist-facies overprint of the garnet blueschist block appears to be coeval with blueschist-facies metamorphism in the northern early-Farallon terranes. Again, this is consistent with subduction occurring across the entire plate boundary at this time. There is a 20-million-year period between c. 160 and 140 Ma where amphibolite-, eclogite- and blueschist-facies rocks all coexist, but following which only blueschist-facies rock occur with the exception of the Catalina Schist.

Collectively, these observations favor slow cooling across the subduction zone from amphibolite to blueschist facies at a rate of c. 15°C/Myr between 160 and 140 Ma,

similar to the model proposed by Anczkiewicz et al. (2004). What is not apparent is if this truly represents cooling following subduction initiation. Because the Coast Range Ophiolite formed between c. 170 and 160 Ma (Shervais et al., 2005), most prior studies have suggested that the onset of amphibolite-facies metamorphism around that time represents nascent subduction. However, there are records of subduction in both the Franciscan Complex and the Catalina Schist between 220 and 170 Ma, the former of which were interpreted by Mulcahy et al. (2018) as evidence that subduction initiated prior to formation of the ophiolite. It is likely that some of these early ages represent subduction of the Cache Creek plate, which closed asynchronously from c. 200 to 180 Ma (see plate reconstruction model by Müller et al., 2016) with a triple junction point between the Cache Creek, Farallon and North American plates migrating northward. If Farallon subduction initiation occurred in conjunction with final closure of the Cache Creek system, then it may be expected that high-grade metamorphism would young northwards. This does not appear to be the case, although the metamorphic record between c. 220 and 180 Ma is sparse, precluding any definite conclusions. Formation of the Coast Range Ophiolite, while maybe not indicative of subduction initiation *sensu stricto*, likely represents some major change in and resetting of the geodynamics of the subduction system, such as collision of the island arc associated with an earlier west-dipping subduction zone between the Cache Creek plate and Farallon plate. This evidence suggests that the amphibolite-facies rocks observed across the early-Farallon terranes are potentially representative of subduction re-initiation following some major perturbation that resulted in formation of the Coast Range Ophiolite. The Catalina Schist, which has much younger ages of amphibolite-facies metamorphism, is a notable exception to this interpretation.

While this interpretation seems to reconcile the metamorphic record and formation of the associated supra-subduction ophiolite, it does not fully explain the duration of high-temperature metamorphism across the early-Farallon terranes. Most models of subduction initiation suggest that cooling is relatively rapid (<10 to 15 million years; e.g., Peacock, 1990; Kelemen et al., 2003); however, amphibolite-facies metamorphism in both Baja California and the Franciscan Complex appears to have been sustained for upwards of 20 to 40 million years. The source of heat required for this long duration of high thermal gradients across the entire subduction system is not immediately obvious. The age of the incoming plate is not anomalously young, as is the case with modern "hot" subduction zones such as Cascadia (see Syracuse et al., 2010). Other mechanisms for producing high thermal gradients, such as a slab tear, are likely to be relatively localized and therefore cannot fully explain amphibolite-facies metamorphism in both the southern and northern regions of the system. Other potential factors such as convergence velocity or the role of shear heating would be best considered in the context of numerical models. Nonetheless, the metamorphic rock record in conjunction with the timing of the Coast Range Ophiolite seem to suggest that the amphibolite-facies rocks that formed across the early-Farallon terranes between c. 180 and 140 Ma represent subduction initiation and/or re-initiation as described in the previous paragraph.

Because, with the exception of the Catalina Schist, there are no apparent along-strike variations in the timing of amphibolite-facies metamorphism from Oregon to Baja California, the asynchronous subduction initiation model of Anczkiewicz et al. (2004)

cannot explain amphibolite-facies metamorphism of the Catalina Schist. This is in agreement with chronologic constraints on the timing of the Peninsular Ranges batholith as discussed in Grove et al. (2008) and Section 4.6.3. So then, if all other amphibolite-facies rocks in the early-Farallon terranes appear to have resulted from some form of subduction (re?)-initiation, what drove the formation of the Catalina Schist? There are no records of metamorphism in the northern Farallon terranes after c. 120 Ma, which is coeval with the onset of amphibolite-facies metamorphism in the Catalina Schist. In contrast, there are records of blueschist-facies metamorphism in Baja California as early as 115 Ma (see Gonzalez and Baldwin, 2019), suggesting that the high-*T* thermal event was somewhat localized. Because the onset of this amphibolite-facies metamorphic event appears to coincide with the last record of metamorphism in the Franciscan Complex, one purely speculative possibility is that the two events are related. That is to say, whatever mechanism drove the final exhumation and accretion of the Franciscan Complex also perturbed the system and provided the heat source for amphibolite-facies metamorphism of the Catalina Schist.

Other possibilities that could explain a localized yet relatively protracted (12 million year) thermal event include a slab tear (e.g., Menant et al., 2016) or oblique subduction (e.g., Plunder et al., 2018; Wada et al., 2015). In the case of subduction obliquity, the curvature of the slab drives toroidal flow and concentrates heat either at the edges of the slab (for convex slabs) or in the center (for concave slabs). However, appreciable heating from oblique subduction is only expected to occur below the viscous coupling depth (see models in Plunder et al., 2018). In modern subduction zones, the depth

of viscous coupling is remarkably consistent at around 70-80 km (e.g., Wada and Wang, 2009). Because the amphibolite-facies rocks of the Catalina Schist formed at shallower depths (between 40 and 50 km; Harvey et al., in revision; see Chapter 2), it is unlikely that subduction obliquity can explain their formation. Alternatively, in slab tears toroidal mantle flow occurs through the tear, concentrating heat and causing lateral variations in subduction interface temperature. This has the potential to effectively reset the system at shallower depths by re-heating the serpentinized "cold nose" region of the mantle wedge (e.g., Menant et al., 2016) that refrigerates the system following subduction initiation.

Although there is currently no other independently proposed evidence for a slab tear in the region, it seems like a reasonable candidate for explaining the relatively protracted yet isolated amphibolite-facies metamorphism of the Catalina Schist. The mechanism does not require subduction initiation or that the amphibolite-facies units formed in a separate tectonic setting than the lower-grade units, as proposed by Grove et al. (2008), and therefore satisfies petrologic, geochemical and geochronologic constraints on the formation of the terrane. Similar mechanisms have been invoked to explain high-*T* metamorphism and magmatism in a number of paleo-subduction complexes including portions of the eastern Mediterranean (e.g., Dilek and Altunkaynak, 2009; Menant et al., 2016).

4.7 Conclusions

New age constraints for a garnet blueschist exotic block within the lawsonite blueschist unit of the Catalina Schist place peak eclogite-facies metamorphism of the block at c. 186 Ma. This was followed by a subsequent blueschist-facies overprint between 160

and 145 Ma, 30-45 million years prior to metamorphism of the amphibolite-facies mélange zone and coherent amphibolite unit. This is one of the earliest records of metamorphism within the early-Farallon terranes and suggests that subduction was underway prior to amphibolite-facies metamorphism of the Catalina Schist. A garnet amphibolite exotic block found within the epidote amphibolite facies records an age of c. 120 Ma, which is c. 5 million years older than any current age estimates for the amphibolite-facies units. This provides new constraints on the timing of amphibolite-facies metamorphism, which appears to have occurred for at least 5 million years longer than previously recognized from c. 120 to 108 Ma. A second garnet-bearing exotic block from the epidote amphibolite unit records an age of c. 115 Ma, which is coeval with the coherent amphibolite unit and the earliest age recorded by the amphibolite-facies mélange zone.

These new age constraints were compiled with existing data for early-Farallon terranes in order to assess along-strike variations in the subduction zone thermal structure. This compilation demonstrates that the main pulse of high-grade (eclogite- and amphibolite-facies) metamorphism occurred between c. 180 and 140 Ma and appears to be synchronous across all terranes. This is interpreted by previous studies to indicate slow cooling following initiation of subduction between the Farallon and North American plates. Amphibolite-facies metamorphism of the Catalina Schist occurred significantly later than the primary high-grade metamorphic event and blueschist-facies metamorphism of the northern early-Farallon terranes. The event was coeval with blueschist-facies metamorphism of Baja California to the south, suggesting that it was a localized event. One possible explanations for this is toroidal mantle flow as a result of a slab tear, which

potentially explains both the duration of amphibolite-facies metamorphism (c. 12 Myr) and the localized heating.

4.8 Acknowledgements

This work was funded by NSF grant EAR-1419871 to SPD with additional support from the GSA Graduate Research Fellowship (2018) to KMH. Thank you to Steph Walker and Paul Star at the Center for Isotope Geochemistry at Boston College for laboratory training and assistance with sample analysis.

Chapter 5: Comparison of single-phase thermobarometers and their application to reconstructing the tectonometamorphic history of the Rio San Juan Complex (Dominican Republic)

5.1 Abstract

Trace element and elastic thermobarometers have the potential to precisely reconstruct the pressure-temperature (*P-T*) histories of metamorphic rocks. For example, the zirconium-in-rutile trace element thermometer and quartz-in-garnet elastic barometer have been successfully applied in tandem to infer peak metamorphic conditions for a number of metamorphic terranes. These methods require relatively few or no assumptions about chemical equilibrium and can be applied to a range of lithologies, making them more widely applicable than traditional major element equilibrium thermobarometers. However, use of the Zr-in-rutile thermometer is limited to moderately high-temperature rocks (>450-500°C) where rutile is in equilibrium with quartz and zircon, precluding application of the thermometer to many blueschist- and eclogite-facies rocks found in exhumed subduction terranes. The zircon-in-garnet elastic barometer has recently emerged as a promising tool for such samples, although there are currently few empirical observations and no experimental validations of the barometer. Furthermore, these single phase thermobarometers have historically only been applied to estimate peak metamorphic conditions primarily because of uncertainty related to either mechanical or chemical reequilibration of the phases. Here, I investigate the accuracy of the zircon-in-garnet elastic barometer by comparing it to both the Zr-in-rutile thermometer and quartz-in-garnet barometer. I also assess the applicability of all three thermobarometers to reconstructing both prograde, peak and post-peak metamorphic conditions recorded by a c. 1 cm garnet

in an ecolgite from the Rio San Juan Complex (Dominican Republic). These results are compared to prior estimates using major element equilibrium thermobarometry and phase equilbria modeling. The single phase thermobarometers predict that garnet nucleation occurred at 530°C and 0.67 GPa. Peak conditions of 660°C and 1.76 GPa are recorded by the garnet mantle. A subsequent post-peak garnet rim records colder conditions of 600°C and 1.74 GPa, consistent with a counter-clockwise *P-T* path proposed by prior studies. These estimates show good agreement with new phase equilibria models for both prograde, peak and post-peak metamorphic conditions, suggesting that single phase thermobarometers can be applied to define a large portion of the metamorphic history of a sample. However, these estimates differ somewhat from estimates made using major element equilibrium thermobarometry and phase equilibria modeling. This discrepancy is primarily attributed to methodological differences in phase equilibria modeling and potential disequilibrium among the phases used in prior studies to estimate peak metamorphic conditions (garnet, omphacite, phengite). I assert that the results reported here more accurately represent the metamorphic history of the sample, although additional investigation into this discrepancy may be warranted.

5.2 Introduction

The pressure-temperature (*P-T*) evolution of subduction zones controls many important processes, including the size of the seismogenic zone, where fluids and melt are produced, and the rheology of the plate interface. Accurately estimating the *P-T* history of exhumed metamorphic rocks is therefore critically important for linking processes inferred from the rock record to processes occurring during active subduction. Historically, *P-T*

conditions have been estimated using equilibrium thermodynamics, which is based on the formation of one phase at the expense of another (net transfer reactions) or the exchange of cations between phases (exchange reactions). Classic examples of equilibrium thermobarometers involve net transfer or exchange of major elements. These include the garnet-biotite Fe^{2+}-Mg exchange thermometer (e.g., Ferry and Spear, 1978; Holdaway et al., 1997; Kohn and Spear, 2000) and the garnet-aluminosilicate-silicate-plagioclase (GASP; e.g., Holdaway, 2001) barometer, which have been widely applied to metamorphic rocks from a variety of tectonic settings.

However, there are numerous challenges associated with these thermobarometers. Perhaps the greatest challenge is the requirement that all phases involved in the exchange or net transfer reaction are both *present* and *in equilibrium*. The former of these requirements greatly limits the applicability of these thermometers across various lithologies and metamorphic grades. For example, the GASP barometer is largely only applicable to metapelitic rocks. To circumvent this problem, studies will commonly employ a number of major element thermobarometers to reconstruct the metamorphic history of a suite of samples. However, this cross-thermobarometer comparison amplifies calibration uncertainties and often results in prohibitively large errors (>50°C, 0.3 GPa). The latter requirement, that all phases involved in the reaction are in equilibrium, is often difficult, if not impossible, to verify. Any number of processes can affect equilibrium between phases, including reaction overstepping (e.g., Pattison et al., 2011; Spear and Pattison, 2017), retrograde reequilibration (e.g., Kohn and Spear, 2000), and diffusion-limited exchange (e.g., Kohn and Penniston-Dorland, 2017; Lanari and Duesterhoeft,

2019). Generally, the textural relationship between phases can be used to identify whether disequilibrium is likely; however, textural relationships are not always clear and do not necessarily provide information about processes described above. Finally, the phases involved in these reactions often have complex solid solution series with non-ideal mixing. This necessitates using activity-composition (*a*-X) models to accurately estimate equilibrium constants (e.g., Spear, 1993; Holland and Powell, 2003), which introduce an additional and often significant source of uncertainty.

To circumvent the challenges associated with major element equilibrium thermobarometers, many researchers have turned to utilizing phase equilibria modeling, or pseudosections. Pseudosections can be used to predict stable mineral assemblages for a given bulk rock composition by either minimizing Gibbs Energy (e.g., Connolly, 2005; de Capitani and Petrakakis, 2010) or by solving a set of non-linear equilibrium equations (e.g., Powell et al., 1998; Powell and Holland, 1994, 1988). Generally, these two approaches produce nearly identical results. By comparing the predicted mineral assemblages and mineral chemistry to petrologic observations of the sample (i.e., matrix and inclusion assemblages, mineral compositions, reaction textures, etc.) it is possible to reconstruct the *P-T* history of the sample. In addition to predicting how mineral modes/abundances change throughout prograde metamorphism, pseudosections can be used to inform a number of petrologic and geochemical processes including where fluids are produced along a *P-T* path (e.g., Dragovic et al., 2015, 2012; van Keken et al., 2011), changes in density (e.g., Behn et al., 2011; Palin et al., 2020), and the evolution of oxygen fugacity (e.g., Walters et al., 2020). For these reasons, pseudosections are widely utilized for petrologic,

geochemical and even geodynamic modeling. However, there are a number of factors that limit our ability to accurately model natural samples. First, pseudosections assume chemical equilibrium and cannot necessarily account for processes such as reaction overstepping (e.g., Castro and Spear, 2017; Pattison et al., 2011; Pattison and Tinkham, 2009; Spear et al., 2014; Spear and Pattison, 2017; Waters and Lovegrove, 2002), diffusion-limited variations in the reactive bulk composition (e.g., Carlson, 2002; Carlson et al., 2015; Carlson and Gordon, 2004; Lanari et al., 2019; Lanari and Engi, 2017; Meth and Carlson, 2005) and changes in the reactive bulk composition due to fractionation of elements during growth of large porphyroblasts (e.g., Dragovic et al., 2015, 2012; Evans, 2004; Gaidies et al., 2008; Konrad-Schmolke et al., 2008a, 2008b; Marmo et al., 2002). Phase equilibria modeling is also highly sensitive to fO_2 (i.e., Fe^{3+}/Fe_{tot}), fluid abundances and compositions (H_2O, CO_2) and the accuracy of the solid solution models used to describe element partitioning within and between phases, especially for elements such as Mn. Because of all of the variables associated with pseudosection modeling and the lack of community standardization regarding thermodynamic databases and solution models, it is also difficult to fully assess the uncertainty associated with any given model. Regardless of these limitations, phase equilibria modeling provides important information that cannot be obtained with any other thermobarometry method. However, these models are best-paired with external estimates of *P-T* conditions in order to validate the assumptions required to construct them and to assess their accuracy.

Over the past two decades, trace element thermometers such as Zr-in-rutile, Ti-in-quartz and Zr-in-titanite have emerged as powerful tools to use either in conjunction with

or as an alternative to major element thermobarometers and phase equilibria modeling (e.g., Hayden et al., 2008; Huang and Audétat, 2012; Kohn, 2020; Tomkins et al., 2007; Wark and Watson, 2006; Zack et al., 2004). Unlike major element thermobarometers, trace element thermometers generally involve minerals without major element solid solution series (quartz, rutile, zircon). Because of this and because trace element substitution follows Henry's Law, the phases involved in the reactions can be treated as a buffering assemblage. For example, the Zr-in-rutile thermometer involves a simple substitution of Zr for Ti in rutile (tetrahedral TiO_2), where quartz (SiO_2) and zircon ($ZrSiO_4$) act as a buffering assemblage:

$$(Eqn\ 5.1)\ ZrSiO_4 \leftrightarrow SiO_2 + ZrO_2$$

If all three phases occur in the rock, then the activities of SiO_2 in quartz and $ZrSiO_4$ in zircon can be treated as approximately 1. Therefore, the equilibrium constant of the reaction is simply equivalent to the concentration of Zr in rutile times its activity coefficient, which is assumed to be equal to 1. Trace element thermometers are advantageous for two reasons. First, whereas multi-phase thermobarometers by definition require analyzing several phases, trace element thermometers require analysis of only a single phase. This significantly reduces uncertainty related to identifying which phases are in textural equilibrium. Second, the phases are common across a wide range of lithologies and metamorphic grades. For example, zircon is nearly ubiquitous in both metamafic and metasedimentary rocks, quartz is nearly ubiquitous in metasedimentary rocks and common in metamafic rocks, and rutile is the dominate Ti-bearing phase in both lithologies at

moderate-to-high pressures (Zack and Kooijman, 2017). Given the analytical challenges associated with the Ti-in-quartz thermometer and diffusion kinetic effects at low- to moderate-*T* (<600°C) associated with the Zr-in-titanite thermometer (Cruz-Uribe et al., 2018; Harvey et al., in revision), the Zr-in-rutile thermometer is generally the most appropriate trace element thermometer to apply to subduction-related metamorphic rocks. The slope of the Zr-in-rutile isopleth in *P-T* space is steep, making it an ideal tool to estimate metamorphic temperatures even when pressure is not well-defined (Figure 5.1). For a number of reasons, the Zr-in-rutile trace element thermometer has traditionally only been applied to estimate peak metamorphic conditions. However, there is some relatively unexplored potential to apply the thermometer to inclusions in other phases (e.g., garnet) in order to reconstruct a prograde metamorphic history.

A second method which shows promise as being widely applicable to metamorphic rocks is elastic barometry, which requires no *a priori* assumptions about chemical equilibrium. When an inclusion becomes entrapped in its host at some external pressure (P_{ext}), the host and inclusion are in mechanical equilibrium and as such the deviatoric volume change (*dV/dP*) between the two phases is the same. However, during exhumation the host and inclusion may expand differentially depending on their thermal expansivity and compressibility such that *dV/dP* of the inclusion no longer equals the *dV/dP* of the host. Where the expansivity of the inclusion is sufficiently different from the host, and the host resists the differential expansion or contraction (i.e., the host does not fracture or plastically deform), the inclusion will develop a residual strain. If the thermoelastic properties of the host and inclusion are well-constrained, then this residual strain can be utilized to back-

calculate an entrapment isomeke, or a curve in *P* vs.*T* space along which *dV/dP* equals zero (e.g., Angel et al., 2017a, 2017b; Enami et al., 2007; Kohn, 2014; Rosenfeld and Chase, 1961). The slope of this isomeke depends on the inclusion-host pair. For example, the quartz-in-garnet isomeke has a shallow slope making it a useful geobarometer (Figure 5.1). In contrast, the zircon-in-garnet isomeke has a relatively steep slope making it more sensitive to changes in temperature.

Strain on an inclusion causes a phonon shift, which can be directly measured *in situ* by spectroscopic methods including Raman spectroscopy and X-ray diffraction (XRD).

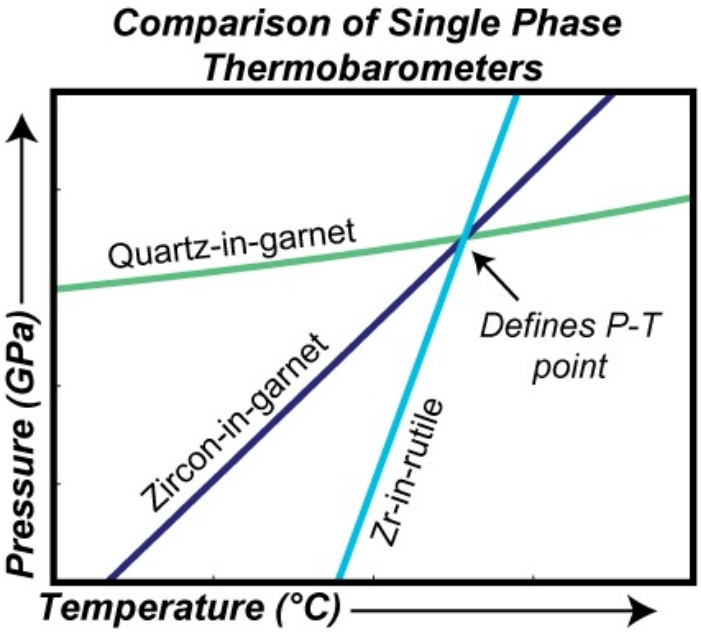

Figure 5.1. Examples of single phase thermobarometers showing the relative slopes of the quartz-in-garnet and zircon-in-garnet isomekes compared to the Zr-in-rutile isopleth. The intersection of one or more thermobarometers can be used to define a single *P-T* point if the phases are in equilibrium.

Elastic barometry is advantageous for several reasons. First, similar to trace element thermometry, elastic barometry requires analysis of only a single phase. Second, this approach could potentially be applied to several different inclusion-host pairs, permitting reconstruction of a large portion of the metamorphic history of a sample using a single technique. And finally, elastic barometry should in theory be applicable at any temperature so long as the host is not plastically deforming, although this has not been rigorously tested.

This makes the method more applicable at low temperatures than equilibrium thermobarometers, which often become problematic as a result of mineral stability fields and kinetic effects.

While there is potential to utilize several different inclusion-host pairs, currently the only pair that has been both empirically and experimentally calibrated as an elastic barometer is quartz-in-garnet. Garnet can be treated as elastically isotropic, making it an ideal host. While quartz is uniaxial and anisotropic, both its equation of state (EOS) and elastic tensor are well-constrained (Angel et al., 2017a, 2017b; Wang et al., 2015), as is the relationship between strain on the inclusion and the resultant phonon shift (Murri et al., 2018). The barometer has also been experimentally verified by two independent studies (Bonazzi et al., 2019; Thomas and Spear, 2018). However, similar to the Zr-in-rutile thermometer, the quartz-in-garnet barometer has historically only been successfully applied to estimate peak metamorphic conditions (e.g., Alvaro et al., 2020; Castro and Spear, 2017; Harvey et al., in revision). The primary reason for this is that inclusions are susceptible to elastic resetting for a number of reasons including both plastic and brittle deformation of the host. Plastic deformation of the host during prograde and peak conditions has the potential to elastically reset a prograde inclusion at higher-*P* conditions, obscuring the prograde history (Zhong et al., 2020). In contrast, brittle deformation causes the inclusion to elastically relax to lower inclusion pressures (e.g., Campomenosi et al., 2018; Enami et al., 2007; Mazzucchelli et al., 2018). Re-healing of fractures following the brittle deformation event may obscure any petrologic evidence of their existence, making the latter phenomena difficult to account for. However, variations in phonon shifts have

been reported in association with changes in chemical zoning in garnet (Viete et al., 2018) suggesting that there is some potential to resolve the pressure evolution during prograde metamorphism.

While quartz is common in subduction-related metamorphic rocks, it is not ubiquitous, especially in mafic lithologies. Zircon, however, is found in almost all metamafic and metasedimentary rocks. This makes the zircon-in-garnet elastic barometer an ideal tool to use either in conjunction with or as an alternative to other elastic or trace element thermobarometers. However, the barometer is still relatively untested and as such there are few empirical and no experimental observations to validate or refine it (Ehlers et al., in prep; Kohn et al., 2016b; Zhong et al., 2019). The thermoelastic properties of zircon are the primary reason that this barometer has not yet been widely applied. The equation of state is difficult to constrain because repulsion of Zr and Si along {001} results in zircon being approximately two times stiffer along the c-axis than axes perpendicular to {001}; however, this same repulsion results in a higher thermal expansivity along {001} (see Stangarone et al., 2019). Recently, two equations of state for zircon have been proposed (Ehlers et al., in prep; Zhong et al., 2019) which predict significantly different isomeke slopes. Empirical observations in well-characterized samples will aid in refining this elastic barometer and in assessing its applicability to metamorphic rocks.

In this chapter, I apply the Zr-in-rutile, quartz-in-garnet and zircon-in-garnet thermobarometers to rutile, quartz and zircon inclusions in a c. 1 cm garnet in a well-characterized eclogite from the Rio San Juan Complex (Dominican Republic) in order to

address two outstanding questions in thermobarometry. First, I assess the applicability of the newly-developed zircon-in-garnet elastic barometer by comparing the barometer to the more-refined Zr-in-rutile thermometer and quartz-in-garnet barometer. These empirical observations will aid in refining the barometer, allowing greater confidence when applying it to less well-characterized samples. Then, I assess whether single-phase thermobarometers can be applied to inclusions in zoned garnet porphyroblasts in order to reconstruct both the prograde and peak metamorphic history of a sample. I compare pressure-temperature estimates from these methods to prior constraints using multi-phase equilibrium thermobarometry (Krebs et al., 2011) and to new phase equilibria models (pseudosections) in order to fully characterize the metamorphic history of the sample and assess the uncertainties associated with each approach.

5.3 Geologic Background

The Rio San Juan Complex is an exhumed subduction terrane exposed on the northern coast of Hispaniola in the Dominican Republic. The terrane forms the basement complex of the Cordillera Septentrional and consists of both metamorphic and igneous rocks associated with subduction throughout the mid-late Cretaceous to mid-Eocene (see Draper and Nagle, 1991; Escuder-Viruete et al., 2013; Krebs et al., 2008). Serpentinite-matrix mélange zones found within the northern province of the terrane contain blocks of variable metamorphic grades, including blueschist-, greenschist-, eclogite-, and amphibolite-facies rocks. Previous work suggests that these blocks record much of the tectonometamorphic history of the terrane (Krebs et al., 2008, 2011; Escuder-Viruete et al., 2013), making them particularly useful for reconstructing the *P-T* evolution of the downgoing slab.

5.3.1 Prior pressure-temperature-time estimates of mélange blocks

The complex pressure-temperature time history of the Jagua Clara mélange zone has been extensively characterized by prior studies using multi-phase thermobarometry, pseudosection modeling, and multiple geochronometers including Lu-Hf (garnet), Rb-Sr (white mica, amphibole), ^{39}Ar-^{40}Ar (white mica), and U-Pb (zircon). The results of these

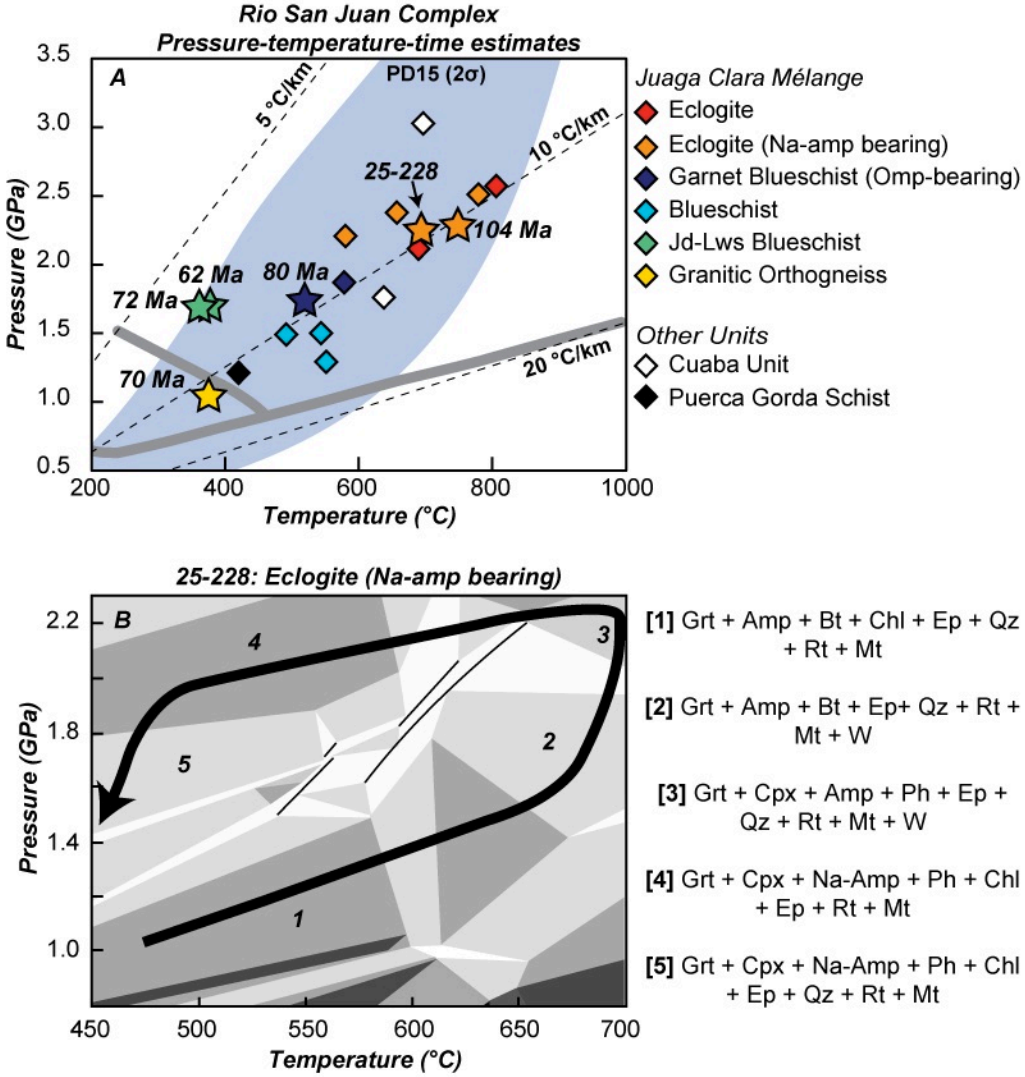

Figure 5.2. (A) Pressure-temperature plot showing prior constraints on the peak metamorphic conditions of mélange blocks from the Juaga Clara Mélange zone compared to other units within the Rio San Juan Complex and to the average conditions recorded by exhumed metamorphic rocks (2σ; Penniston-Dorland et al., 2015). Data sources: Krebs et al. (2008), Krebs et al. (2011), Escuder-Viruete and Pérez-Estaún (2013). (B) Pseudosection for sample 25-228 showing the counter-clockwise evolution of the sample. Predicted prograde, peak and retrograde mineral assemblages are numbers. Mineral abbreviations after Whitney and Evans (2010).

studies are summarized in Figure 5.2A. Blueschist and eclogite blocks throughout the mélange zone record large disparities in both metamorphic age and pressure-temperature history. Blocks record both clockwise and counter-clockwise *P-T* paths and reached peak conditions between 1.7-2.4 GPa and 300-800°C (Escuder-Viruete and Pérez-Estaún, 2013; Krebs et al., 2011). Current chronologic constraints suggest that there is a positive correlation between the age and peak metamorphic conditions of the blocks, where the highest-grade blocks record ages coeval with the earliest stages of subduction between c. 110 and 104 Ma while the lowest-grade blocks record much younger ages between 80 and 62 Ma (Krebs et al., 2008; Escuder-Viruete et al., 2013). The metamorphic history of the mélange zone has been interpreted to indicate progressive mixing and exhumation within a tectonic serpentinite mélange at the subduction interface (Escuder-Viruete et al., 2013; Escuder-Viruete and Pérez-Estaún, 2013; Krebs et al., 2011, 2008).

5.3.2 Sample 25-228

25-228 is an eclogite block from Jagua Clara mélange. The metamorphic history of the block has been previously characterized by Krebs et al. (2011), and the results are described briefly here. It is predominately composed of garnet and omphacite, with variable amounts of phengite, epidote/clinozoisite, rutile, titanite, albite, chlorite, apatite and zircon. Krebs et al. (2011) defined a nine-point counter-clockwise *P-T* path for the sample using multi-phase thermobarometry in the program THERMOCALC (Holland and Powell, 1998) and pseudosection modeling in the K_2O-Na_2O-CaO-FeO-Fe_2O_3-MgO-Al_2O3-SiO2-TiO_2-H_2O (KNCFMASHTO) system (Figure 5.2B). Initial garnet growth was predicted at 1.0 ± 0.2 GPa and 477 ± 66°C based on the assemblage Grt + Amp + Bt + Chl

+ Ep + Qz + Rt + Mt (Phase field 1 in Figure 5.2A; mineral abbreviations follow Whitney and Evans, 2010). Subsequent peak metamorphic conditions were estimated to be 701 ± 66°C and 2.3 ± 0.2 GPa based on equilibrium between garnet, omphacite and phengite and defined by the assemblage Gt + Omp + Amp + Ph + Ep + Qtz + Rt + Mt + W (Field 3, Figure 5.2A). A subsequent blueschist-facies overprint occurred between 450 and 495°C at 1.5 to 2.0 GPa (Fields 4 and 5, Figure 2A), which is defined by replacement of Ca-Na amphibole by Na-amphibole.

Both the mineralogy of the block and the previously characterized metamorphic history make it an ideal sample to assess the applicability of single phase thermobarometers for reconstructing its metamorphic history. In particular, rutile, quartz and zircon are predicted to be stable throughout prograde and peak conditions, and all occur as inclusions in garnet. The size of the garnet porphyroblasts (c. 1 cm) is also ideal for testing if the thermobarometers can be applied to inclusions within individual growth zones in garnet to determine the prograde metamorphic history of the block.

5.4 Methods

5.4.1 Mineralogy and major element chemistry

The sample was characterized by standard optical methods and using the Zeiss Auriga field emission Scanning Electron Microscope (SEM) equipped with a backscattered electron detector and an Oxford Instruments X-Max 80 energy dispersive spectroscopy (EDS) system housed in the Geophysical Laboratory at Carnegie Institution for Science. Major element zoning in garnet was determined using the Electron Probe Microanalyzer

(EPMA) at the University of Maryland following the methods outlined in section 3.4.2. Wavelength dispersive spectroscopy (WDS) maps were collected to semi-quantitatively assess major element zoning throughout the garnet porphyroblast. Major element zoning was further constrained by WDS spot analyses across the garnet from rim-to-rim.

5.4.2 Phase equilibria modeling

Forward thermodynamic modeling using bulk rock and matrix compositions was performed by B. Dragovic to predict stable mineral assemblages over the range of conditions that the rock is expected to have experienced. Growth of large garnet porphyroblasts fractionates components including Si, Al, Fe, Mg, Ca and Mn, effectively changing the reactive bulk composition of the system (e.g., Dragovic et al., 2015, 2012; Evans, 2004; Gaidies et al., 2008; Konrad-Schmolke et al., 2008a, 2008b; Marmo et al., 2002). To account for this, two models were constructed based on the compositions shown in Table 5.1. The first simulates initial garnet growth using the bulk rock composition (from Krebs et al., 2011) and the second simulates mantle and rim growth using a "matrix" composition (whole rock minus garnet; e.g., Dragovic et al., 2012, 2015). Pseudosection models were constructed in Perple_X (Connolly, 2009) in the MnO-K_2O-Na_2O-CaO-FeO-Fe_2O_3-MgO-Al_2O3-SiO2-TiO_2-H_2O (MnNCKFMASHTO) system using the internally consistent thermodynamic database of Holland and Powell (1998). Solid solution models included garnet (White et al., 2000), omphacite (Diener and Powell, 2012; Green et al., 2007), clinoamphibole (Diener et al., 2011), chlorite (Holland and Powell, 1998), feldspar (Fuhrman and Lindsley, 1988), epidote (Holland and Powell, 1998), chloritoid (White et al., 2000), ilmenite (White et al., 2000), pumpellyite (Massonne and Willner, 2008), carpholite (Smye et al., 2010), white mica (Auzanneau et al., 2010; Coggon and Holland,

2002), stilpnomelane (Massonne and Willner, 2008), and biotite (Tajčmanová et al., 2009; Tinkham et al., 2001). Quartz, rutile, titanite and lawsonite were considered as pure phases. Because phosphate (0.36 wt%) was not modeled, 0.47 wt% Ca was removed from both the bulk rock and matrix compositions to stoichiometrically account for apatite. These models assume chemical equilibrium and closed-system behavior.

Table 5.1. Whole rock and matrix (WR-garnet core) compositions used for phase equilibria modeling compared to compositions reported by Krebs et al. (2011). *Fe^{3+} reduced from titration value **0.47 wt% Ca removed to account for phosphates

	Reported by Krebs et al. (2011)	***Whole Rock Model***	***Matrix Model***
SiO_2	43.43	43.43	44.26
TiO_2	1.77	1.77	1.98
Al_2O_3	17.76	17.76	17.22
Fe_2O_3	2.81	1.93*	7.65
FeO	9.05	9.84	2.19
MnO	0.27	0.27	0.08
MgO	8.23	8.23	8.77
CaO	9.41	8.94**	8.97
Na_2O	2.82	2.82	3.20
K_2O	0.91	0.91	1.03
P_2O_5	0.36	-	-
Total	96.82		
H_2O	3.16	*Saturated*	*Saturated*
CO_2	0.05	-	-

5.4.3 Zr-in-rutile thermometry

The zirconium-in-rutile (Zr-in-rutile) thermometer was used to determine both the peak metamorphic temperature of the block and the range of temperatures recorded by rutile inclusions in garnet. The thermometer calibration of Kohn (2020) was adopted for this study. The concentration of Zr in rutile was measured by EPMA at the University of Maryland. Measurements were made using the conditions outlined in Section 2.4.1.

A total of 24 rutile inclusions in garnet were analyzed. The center of each inclusion was targeted to measure the highest Zr concentration (for examples of Zr zoning in rutile see Penniston-Dorland et al., 2018; Harvey et al., in revision) and to avoid secondary fluorescence of the garnet host. Where the inclusions were large enough (>10μm), 1-3 additional points across the inclusions were analyzed to assess intragrain variability. 7 matrix grains were similarly analyzed in order to assess if there are any systematic variations between rutile inclusions in garnet and matrix rutile. Analyses with Si > 300 ppm were excluded following Section 2.4.1. The concentration of Zr at peak metamorphic conditions was determined using the mean maximum concentration method (Penniston-Dorland et al., 2018). Rutile inclusions in garnet were then subdivided into regions based on garnet major element zoning and a mean maximum concentration was calculated for each region. Mean maximum Zr concentrations for the whole rock and each garnet zone were used to calculate an isopleth of Zr content in *P-T* space. Reported uncertainties follow Section 2.4.1.

5.4.4 Quartz-in-garnet elastic barometry

Metamorphic pressures were determined using the quartz-in-garnet elastic barometer (QuiG; Angel et al., 2017a, 2017b; Enami et al., 2007; Kohn, 2014; Thomas and Spear, 2018). Raman spectra of quartz inclusions were collected *in situ* using the Yvon Jobin LabRam ARAMIS confocal Raman microscope equipped with a 532 nm laser housed in the Surface Analysis Center in the Department of Chemistry and Biochemistry at the University of Maryland. The instrument was calibrated prior to each analysis session using a silica wafer. Spectra were collected using a 100x optical objective, 1800 gr/mm

and a neutral density filter between 25-50%. Three 10-second accumulations were averaged to produce a single spectrum for each inclusion. Samples were immediately analyzed following analyses of Herkimer Diamond, an unstressed natural quartz standard, to account for any instrumental drift. Inclusions were selected for analysis based on the parameters outlined in Section 2.4.2.1.

Raman spectra were fit using a mixed Gaussian-Lorentzian function with the Matlab program ipf.m (https://www.mathworks.com/matlabcentral/fileexchange/23452-ipf-arg1-arg2-arg3-arg4). The drift-corrected external reproducibility (2σ) of the Herkimer Diamond was 0.04 cm^{-1} for the 128cm^{-1} peak, 0.07 cm^{-1} for the 206 cm^{-1} and 0.08 cm^{-1} for the 464 cm^{-1} peak. Because the reproducibility of these peaks is larger than any uncertainty related to fitting the spectra, it is used as a conservative estimate of the uncertainty in the peak positions. This propagates to uncertainties in the three peak shifts (sample minus standard, $\Delta\omega$) of 0.04 cm^{-1}, 0.10 cm^{-1} and 0.19 cm^{-1} respectively. Independent strain components (ε_{1+2}, ε_3) were determined from the Raman peak shifts using the program stRAinMAN (Angel et al., 2019) and converted to average stress (or inclusion pressure; P_{inc}) using the elastic tensor for quartz (Wang et al., 2015). Reported uncertainties reflect both the uncertainty in $\Delta\omega$ and in the independent strain components (see Angel et al., 2019).

Best-fit P_{inc} values were determined using the program Peak Explorer for the whole rock and for each region in the garnet porphyroblast following the method described in Section 2.4.2.3. Details on Peak Explorer can be found in Appendix S4.1. Entrapment

isomekes were calculated for each inclusion and the best-fit P_{inc} values and associated 95% confidence limits in the module EOS-FitPinc using the most recent equation of state (EOS) for quartz (Angel et al., 2017a,b; verified experimentally by Thomas and Spear, 2018). For consistency with the zircon-in-garnet barometer (see Section 5.4.5), the EOS for pyrope (Milani et al., 2015) was used for the garnet host. Uncertainty in the host garnet composition does not significantly affect the position of the quartz-in-garnet isomeke (Kohn, 2014).

5.4.5 Zircon-in-garnet elastic barometry

Metamorphic conditions were also estimated using the recently calibrated zircon-in-garnet elastic barometer (ZiG; Ehlers et al., in prep). Like the QuiG barometer, the ZiG barometer relies on the contrasting elastic properties between a zircon inclusion and its garnet host. The slope of the isomeke in *P-T* space is steeper than the QuiG isomeke yet markedly shallower than the Zr-in-rutile isopleth (Figure 5.1), making the ZiG barometer a complementary tool to pair with either method in order to define a *P-T* point. Zircon is nearly ubiquitous in metasedimentary and metamafic rocks, making the barometer particularly useful to use in rocks where SiO_2 is undersaturated (e.g., metagabbros) such that quartz is not present/abundant, or in rocks that form at conditions outside of the stability field of rutile (most blueschist-facies rocks, low-pressure amphibolite-facies rocks). However, there is still significant uncertainty regarding the EOS for zircon (Zaffiro et al., 2018; Zhong et al., 2019; Ehlers et al., in prep; Figure 5.3A) and no experimental validation of the method. Empirical observations where *P-T* conditions can be externally verified using other approaches, such as this study, are important for refining the barometer and assessing its applicability to natural samples.

Raman spectra of zircon inclusions were collected using the Yvon Jobin LabRam ARAMIS confocal Raman microscope equipped with a 532 nm laser housed in the Surface Analysis Center in the Department of Chemistry and Biochemistry at the University of Maryland. Spectra were collected using a 100x optical objective, 1800 gr/mm and a neutral density filter of 25% to prevent heating of the inclusion. Three 10-second accumulations were averaged to produce a single spectrum for each inclusion. Samples were immediately analyzed following analyses of Mud Tank zircon, an unstressed and non-metamict natural zircon standard, to account for any instrumental drift. Inclusions were selected for analysis following the same criteria as quartz inclusions.

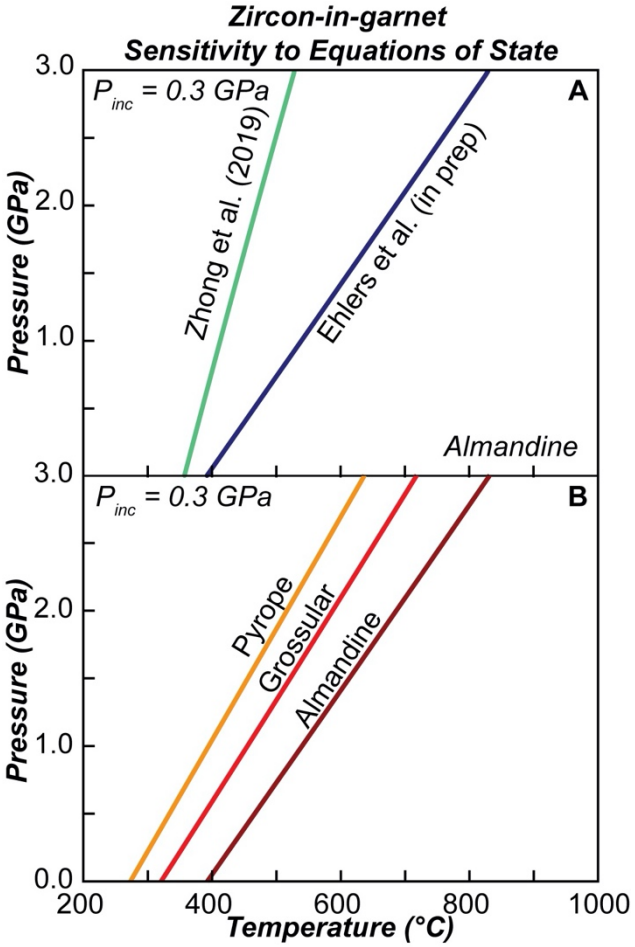

Figure 5.3. (A) Zircon-in-garnet isomekes (almandine garnet) calculated using the calibration of Zhong et al. (2019) compared to the most recent EOS for zircon Ehlers et al. (in prep) at a P_{inc} of 0.3 GPa. (B) Zircon-in-garnet isomekes calculated using different garnet endmember compositions (Milani et al., 2015; 2016) and the zircon EOS of Ehlers et al. (in prep) at a P_{inc} of 0.3 GPa.

Raman spectra were fit using a mixed Gaussian-Lorentzian function with the Matlab program ipf.m. The reproducibility of the 214 cm^{-1}, 224 cm^{-1}, 354 cm^{-1}, 440 cm^{-1}, 975 cm^{-1} and 1008 cm^{-1} peaks are 0.10 cm^{-1}, 0.10 cm^{-1}, 0.12 cm^{-1}, 0.10 cm^{-1}, 0.08 cm^{-1} and 0.09 cm^{-1} respectively. These values are used as a conservative estimate of the uncertainty and propagate to uncertainty in $\Delta\omega$ of 0.14 cm^{-1}, 0.14 cm^{-1}, 0.17 cm^{-1}, 0.14 cm^{-1}, 0.11 cm^{-1} and 0.13 cm^{-1} respectively. Independent strain components (ε_{1+2}, ε_3) were determined from the Raman peak shifts using the program stRAinMAN (Angel et al., 2019) using the Grüneisen tensor for zircon (Stangarone et al., 2019). Strains were converted to P_{inc} using the most recent elastic tensor for zircon (Zaffiro et al., 2018). Best-fit P_{inc} was determined for the whole rock and each garnet zone using Peak Explorer following the method outlined in Sections 2.4.2.3, 5.4.4 and Appendix S4.1.

Zircon-in-garnet entrapment isomekes and associated 95% confidence limits were calculated in the module EOS-FitPinc. Unlike the quartz-in-garnet elastic barometer, the zircon-in-garnet barometer is quite sensitive to the host garnet composition. Figure 5.3B shows zircon-in-garnet isomekes calculated using the equations of state for pyrope (Milani et al., 2015), grossular (Milani et al., 2017) and almandine (Milani et al., 2015) with the most recent EOS for zircon (Ehlers et al., in prep). The zircon-in-almandine barometer predicts conditions c. 140°C higher than zircon-in-grossular and c. 220°C higher than zircon-in-pyrope. This discrepancy is primarily attributed to uncertainty in the equations of state for zircon and the garnet end-member compositions. Because of the larger suite of experimental data for pyrope than the other garnet end-members, it likely has the best-constrained EOS (Milani et al., 2015). The zircon-in-pyrope barometer also predicts

conditions closest to the expected entrapment conditions. For these reasons, the zircon-in-pyrope barometer is adopted here, although it is important to note that the host garnet in this study is predominately almandine (X_{Alm} = 0.55; X_{Gr} = 0.25; X_{Py} = 0.16; X_{Spss} = 0.04).

5.5 Results

5.5.1 Garnet Chemistry

Major element zoning in garnet was determined by EPMA. WDS X-ray maps and spot analyses from a to a' are shown in Figure 5.4**.** Four major zones of garnet growth were assigned based on Mn zoning (Figure 5.4A): core, mantle 1 (M1), mantle 2 (M2) and rim. A simplified sketch of the location of these regions is shown in Figure 5.5. The garnet core is characterized by high Mn (Figure 5.4E) characteristic of prograde zoning (Hollister, 1966). The transition between the garnet core and M1 is indicated by a gradual decrease in Mn concentration. M2 is indicated by a sharp transition from normal prograde zoning to oscillatory zoning. The garnet rim is characterized by a sharp decrease in Mn concentration. Ca exhibits sector zoning in the core and mantle regions of the garnet, with high-Ca sectors generally following {112} crystal faces (Figure 5.4C). Within M2, Ca exhibits oscillatory zoning, followed by an increase in concentration at the garnet rim. Fe is weakly sector zoned following Ca (Figure 5.4B). Fe concentration decreases towards the garnet rim. Mg is weakly zoned (Figure 5.4D) showing a slight increase in concentration from within M1 followed by a decrease in concentration towards the garnet rim. Non-systematic variations in X_{Pyp} in M2 reflect oscillatory zoning, which is weakly visible in the Mg X-ray map.

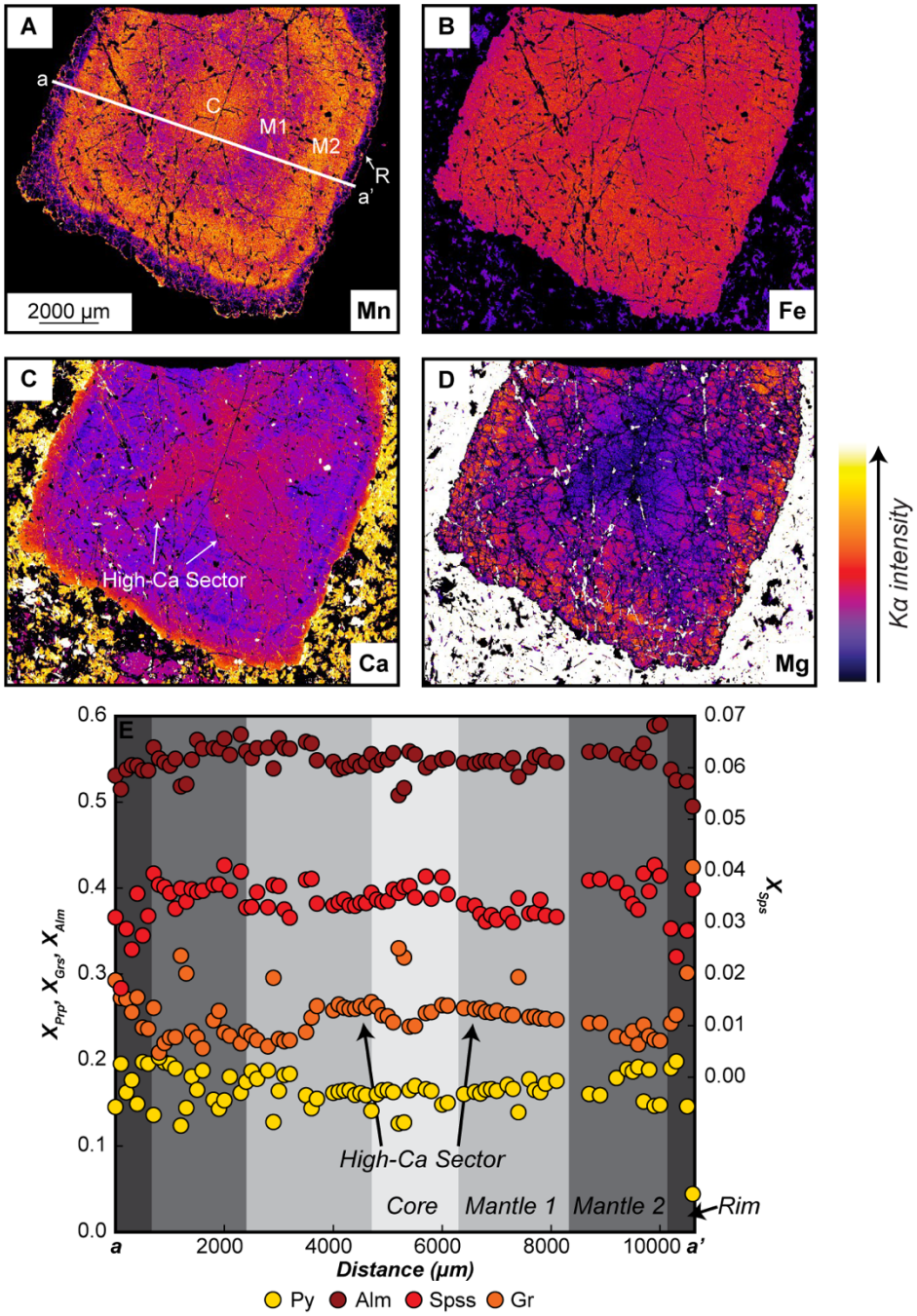

Figure 5.4. X-ray maps and WDS traverse of Garnet 1 from sample 25-228 showing changes in major element zoning. (A) Mn X-ray map showing transition from normal prograde zoning in the core (C) and mantle 1 (M1) to oscillatory zoning in mantle 2 (M2) followed by a sharp decrease in concentration at the rim (R). a to a' shows location of WDS traverse. (B) Fe X-ray map showing sector zoning between the garnet core and mantle followed by a decrease in concentration at the garnet rim. (C) Ca X-ray map showing sector zoning between C and M1 followed by oscillatory zoning in M2 and an increase in concentration at R. (D) Mg X-ray map showing little change in concentration from core to rim. (E) Major element traverse from a to a' showing changes in the mole fractions of the garnet end-member compositions. Alm = almandine, Grs = grossular, Pyp = pyrope, Sps = spessartine.

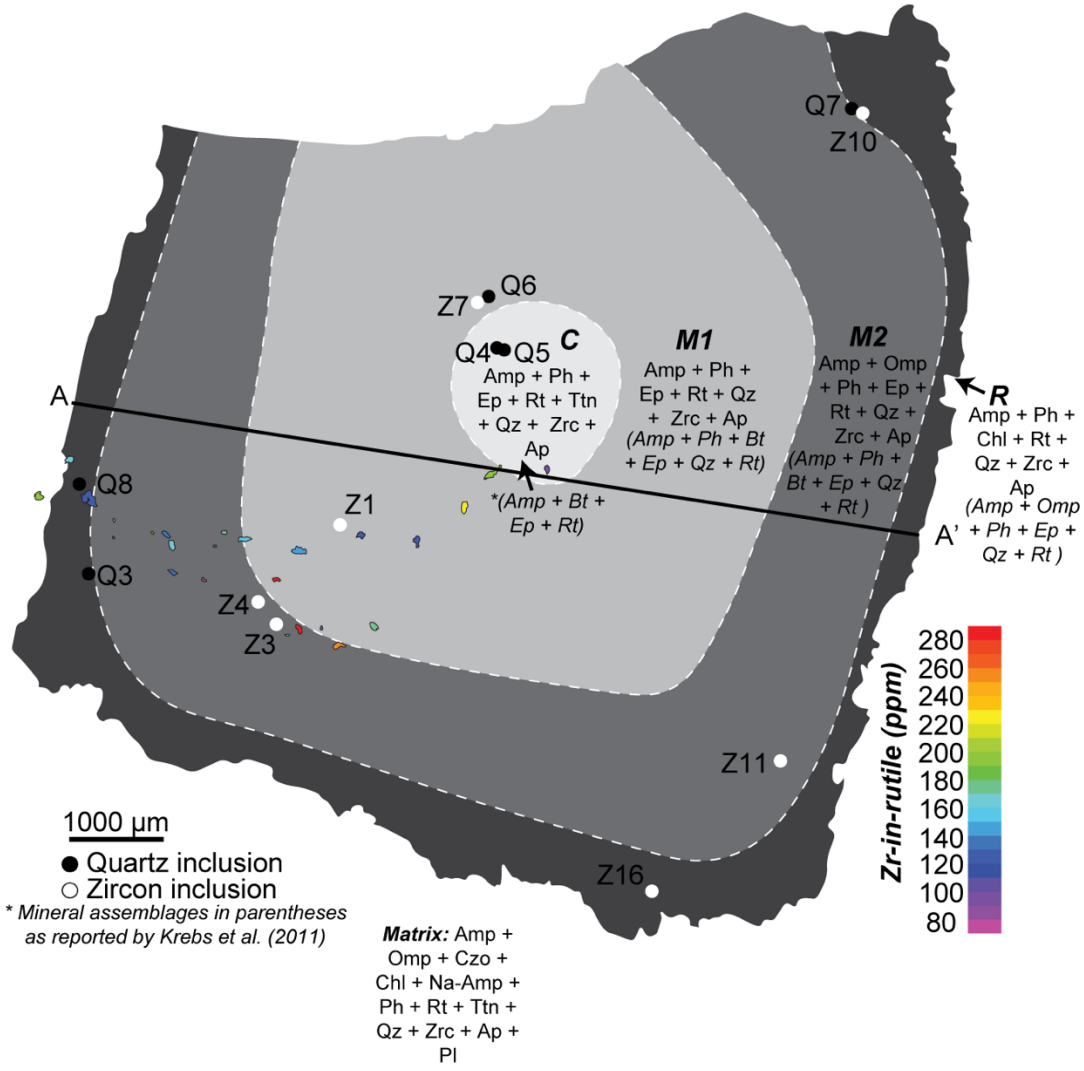

Figure 5.5. Cartoon sketch of Garnet 1 from sample 25-228 showing the four zones defined by Mn zoning. The locations of quartz inclusions and zircon inclusions are shown as black and white circles respectively. Rutile inclusions are colored based on Zr concentration. Mineral abbreviations follow Whitney and Evans (2010).

5.5.2 Petrography

Inclusion assemblages in garnet were characterized by SEM and are summarized in Figure 5.5. The core assemblage includes calcic-sodic amphibole, epidote, phengite, rutile, titanite, apatite, quartz and zircon. The mantle largely consists of the same assemblage, with the exception of titanite which is only observed in the core. Omphacite is not observed in the core or M1 but appears in M2. The garnet rim is characterized by the

presence of chlorite, which was not observed throughout the core or mantle. Omphacite and epidote were also not observed in the rim. Biotite was not observed. These mineral assemblages are somewhat different than those reported by Krebs et al. (2011) for the sample and are shown in parentheses in Figure 5.5. The Krebs et al. (2011) study did not observe phengite, quartz or titanite in the garnet core but do report chlorite and biotite throughout both the garnet core and mantle. The study also reports omphacite inclusions in the garnet rim rather than in the garnet mantle, although mantle/rim boundaries may have been defined differently.

The matrix mineral assemblage includes calcic-sodic amphibole, omphacite, clinozoisite, chlorite, sodic amphibole, phengite, rutile, titanite, quartz, zircon, apatite and albite. Sodic amphibole is found replacing calcic amphibole suggesting that it is a late phase. Similarly, titanite is generally found replacing rutile and, more rarely, as an inclusion in rutile. Clinozoisite occurs as mm-scale subhedral porphroblasts commonly associated with sodic amphibole.

5.5.3 Phase equilibria modeling

Pseudosection models constructed for the bulk rock and matrix compositions are shown in Figures 5.6 and 5.7 respectively. The intersection of garnet compositional isopleths was used to define the conditions of garnet core and rim growth. A core

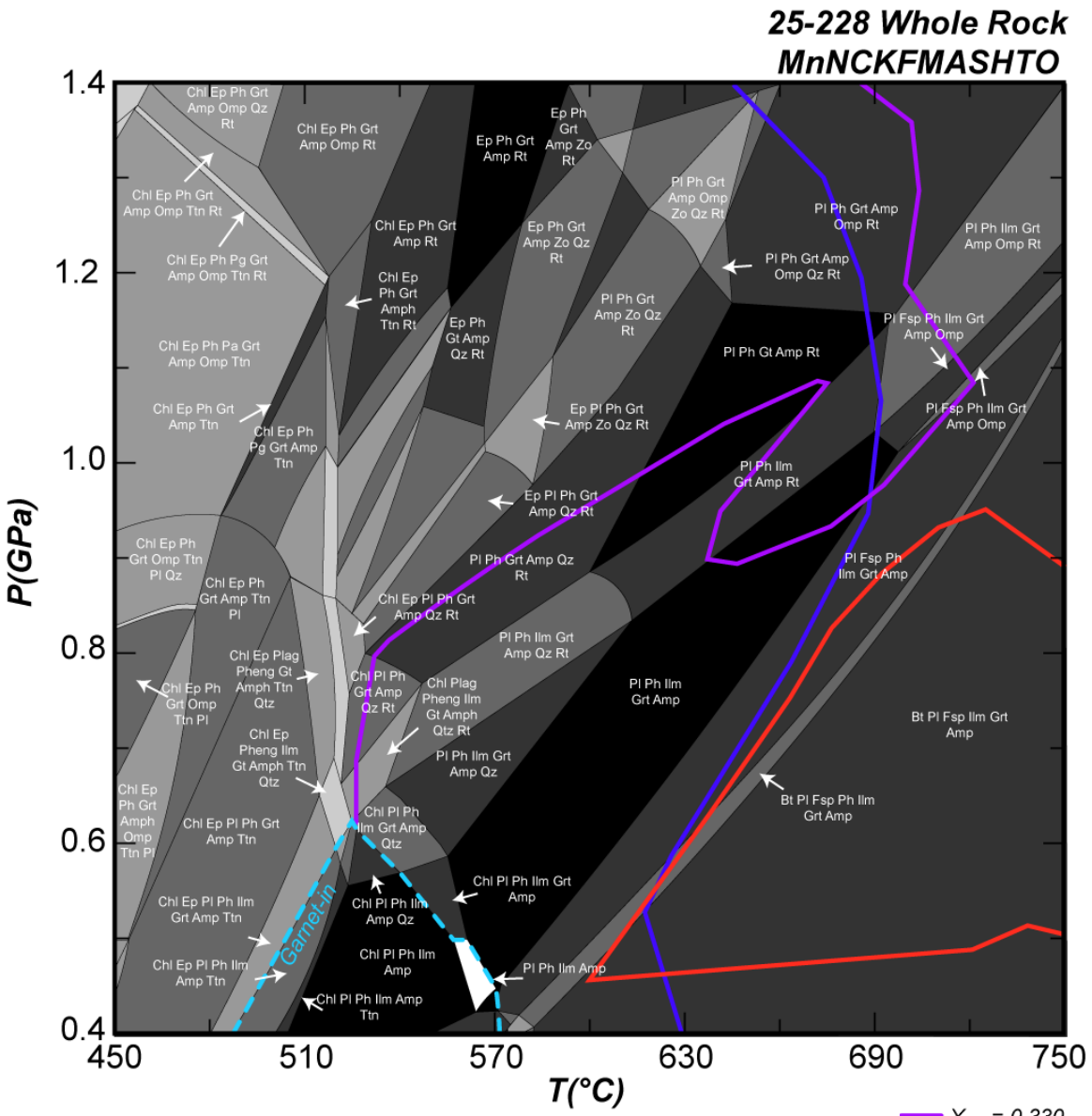

Figure 5.6. Whole rock pseudosection for sample 25-228 showing predicted stable mineral assemblages associated with garnet core nucleation. Garnet-in isograd is shown as a dashed line. Garnet core isopleths are shown for X_{Grs} = 0.330 (purple), X_{Pyp} = 0.126 (blue) and X_{Alm} = 0.508 (red). All amphibole is Ca-Na unless otherwise indicated. Mineral abbreviations follow Whitney and Evans (2010).

composition of X_{Alm} = 0.508, X_{Prp} = 0.126 and X_{Grs} = 0.330 was used to define the *P-T* conditions of garnet nucleation in the whole rock model. These garnet composition isopleths are shown in Figure 5.6. Because Mn is the fastest-diffusing major element in garnet (e.g., Carlson, 2006; Chakraborty and Ganguly, 1992) and the core Mn composition

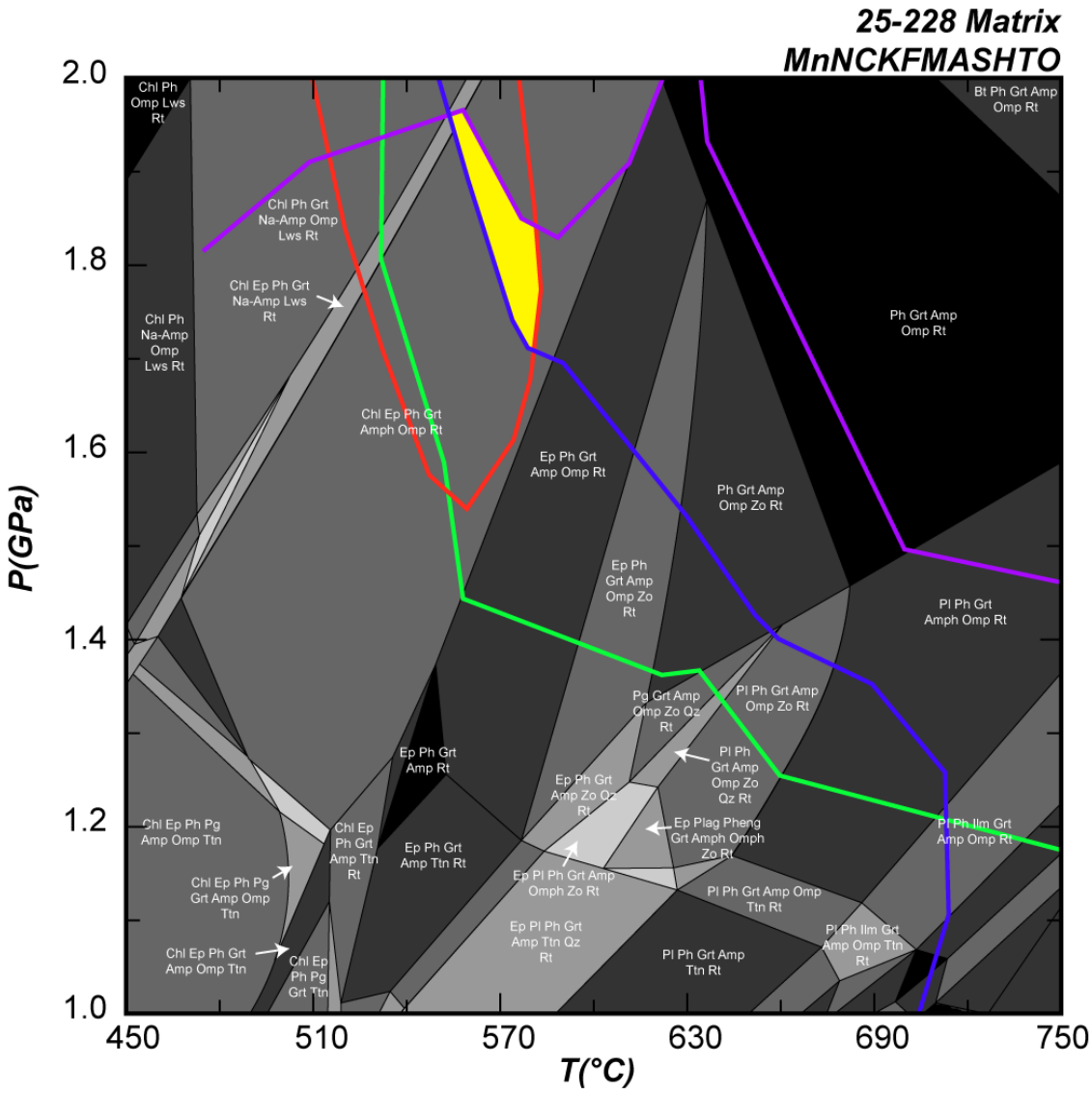

Figure 5.7. Matrix pseudosection for sample 25-228 showing predicted stable mineral assemblages associated with garnet mantle and rim growth and post-peak metamorphic conditions. Garnet rim isopleths are shown for X_{Grs} = 0.321 (purple), X_{Sps} = 0.032 (green), X_{Pyp} = 0.124 (blue) and X_{Alm} = 0.515 (red). All amphibole is Ca-Na unless otherwise indicated. The intersection of the grossular, pyrope and almandine isopleths is shown in yellow. Mineral abbreviations follow Whitney and Evans (2010).

was likely diffusively reset, spessartine was not considered. The intersection of the grossular and pyrope isopleths occurs at c. 670°C and 0.95 GPa, while pyrope and almandine isopleths intersect at c. 615°C and 0.45-0.52 GPa. Almandine and grossular

isopleths do not intersect. Grossular intersects with the garnet-in isograd at c. 515°C and 0.6 GPa.

The conditions of garnet rim growth in the matrix model were defined by the composition of X_{Alm} = 0.515, X_{Prp} = 0.124 and X_{Grs} = 0.321 and X_{Sps} = 0.032. These isopleths are shown in Figure 5.7. Pyrope, almandine and grossular isopleths intersect between 540 and 570°C and 1.7 to 1.9 GPa within the field chlorite + epidote + phengite + garnet + amphibole + omphacite + rutile. The spessartine isopleth intersects with almandine and grossular at colder conditions between c. 515 and 540°C at 1.5 to 1.9 GPa, although it again may be influenced by back-diffusion of Mn into garnet.

5.5.4 Zr-in-rutile thermometry

Maximum Zr concentrations in rutile inclusions in garnet range from 89 to 301 (± 11-23) ppm. The location of each inclusion and its corresponding maximum Zr concentration is shown in Figure 5.5. There is no obvious monotonic variation in Zr concentration with radial distance of the inclusion from the garnet core (Figure 5.8). Matrix rutile grains record Zr concentrations between 164 and 237 (± 7-15) ppm. Mean maximum Zr concentration were determined for the whole rock and each garnet zone following Penniston-Dorland et al. (2018) and Harvey et al. (in revision) and are listed in Table 5.2 (full results can be found in Appendix S4.2). The mean maximum Zr concentration determined using all analyzed rutile grains in the sample (whole rock) is 271 ± 61 ppm and is considered representative of the peak conditions. Only one inclusion from the core was analyzed which records a concentration of 107 ± 11 ppm. M1 records a higher mean

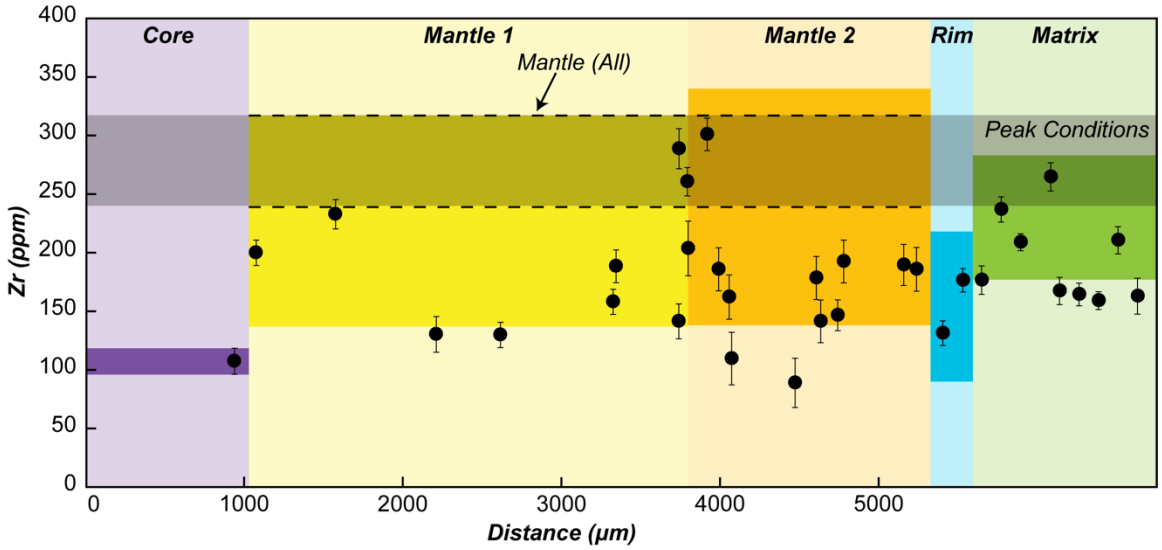

Figure 5.8. Concentration of Zr in rutile shown as a function of radial distance from the garnet core. Peak conditions, estimated using the whole rock mean maximum Zr concentration, are shown as a grey band. Mean maximum Zr concentrations for each region of Garnet 1 and the matrix are shown as colored bands. The mean maximum Zr concentration for all inclusions in the garnet mantle is shown as dashed lines.

Table 5.2. Mean maximum Zr-in-rutile concentrations for 25-228

Location	*Mean Maximum Zr (ppm)*
Whole Rock	271 ± 61
Core	107 ± 11
Mantle 1 (M1)	227 ± 90
Mantle 2 (M2)	239 ± 101
Rim	154 ± 64

maximum Zr concentration of 227 ± 90 ppm (n = 7), M2 records a concentration of 239 ± 101 ppm (n = 12) and the garnet rim records a concentration of 154 ± 64 ppm (n = 2). Because the two mantle regions do not record resolvable differences in mean maximum Zr concentration it is likely that they grew around the same metamorphic conditions. As such, they were combined into a single data set for all subsequent analyses. Combined, the two mantle regions record a mean maximum Zr concentration of 278 ± 39 ppm. It is important to note that the majority of inclusions in the mantle region with high Zr concentrations occur at the boundary between M1 and M2. It is possible that this reflects a temperature perturbation associated with the shift to oscillatory zoning and that the true temperature

conditions at which the majority of the mantle grew are much lower. It may be appropriate to reconsider how the garnet zones were assigned; however, this requires higher data density than currently available. Temperature isopleths for the peak conditions and each garnet zone were calculated using the calibration of Kohn (2020) and are shown in Figure 5.9.

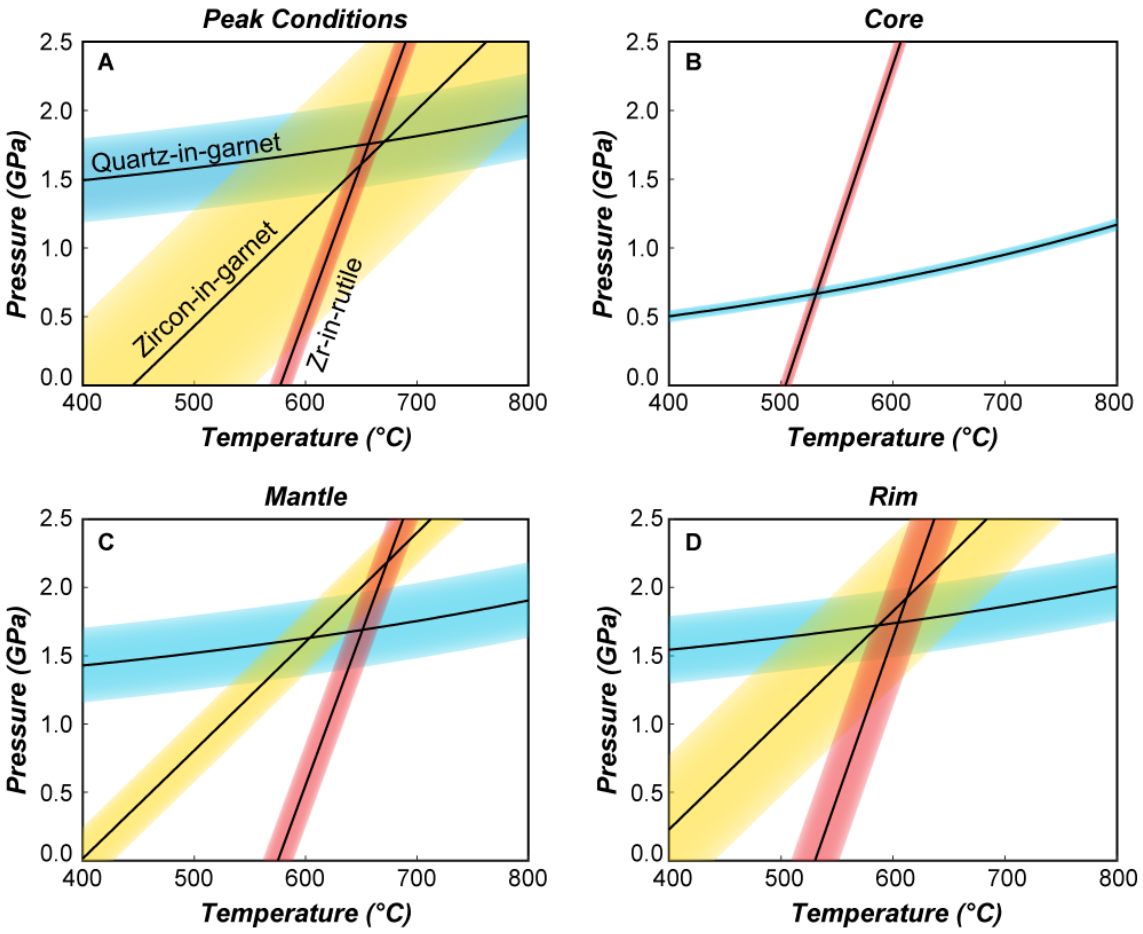

Figure 5.9. Pressure-temperature estimates and associated uncertainties using Zr-in-rutile thermometry (red), quartz-in-garnet barometry (blue) and zircon-in-garnet barometry (yellow) defining the *P-T* conditions associated with (A) peak metamorphism, (B) garnet core nucleation, (C) garnet mantle growth and (D) garnet rim growth.

5.5.5 Quartz-in-garnet barometry

Six quartz inclusions in garnet suitable for elastic barometry were analyzed. Their locations are shown in Figure 5.5. Raman shifts and calculated strains for each inclusion are shown in Appendix S4.3. Inclusion pressures (P_{inc}) are shown in Figure 5.10 and Table 5.3 and range from 0.11 to 0.76 (±0.03-0.26) GPa. Two inclusions in the garnet core record

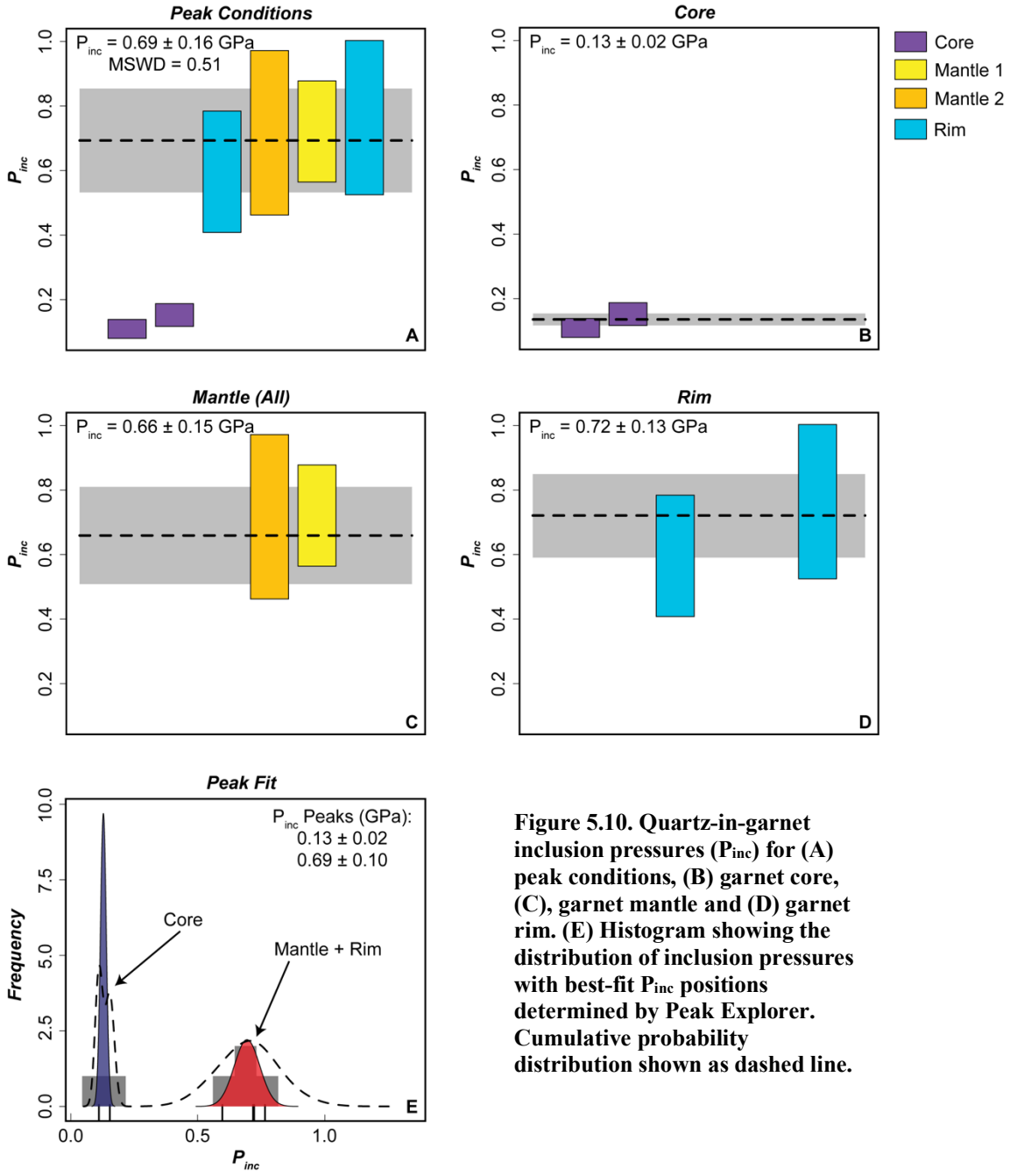

Figure 5.10. Quartz-in-garnet inclusion pressures (P_{inc}) for (A) peak conditions, (B) garnet core, (C), garnet mantle and (D) garnet rim. (E) Histogram showing the distribution of inclusion pressures with best-fit P_{inc} positions determined by Peak Explorer. Cumulative probability distribution shown as dashed line.

significantly lower inclusion pressures than inclusions in both the mantle and rim (Figure 5.10E), with a best-fit P_{inc} for the core of 0.13 ± 0.02 GPa (95%). Only two inclusions were observed in the garnet mantle –one in M1 and one in M2. The two inclusions record nearly identical inclusion pressures and are therefore treated as a single group. The two mantle inclusions define a best-fit P_{inc} of 0.66 ± 0.15 GPa. Similarly, two inclusions from the rim

Table 5.3. Inclusion pressures (P_{inc}) recorded by quartz and zircon inclusions in Garnet 1 from sample 25-228.

Inclusion Number	*Location*	*P_{inc} (GPa)*
Quartz		
Q4	Core	0.15 ± 0.04
Q5	Core	0.11 ± 0.03
Q6	Rim	0.72 ± 0.26
Q3	M2	0.76 ± 0.25
Q8	M1	0.60 ± 0.19
Q7	Rim	0.72 ± 0.16
Zircon		
Z10	M2	0.37 ± 0.06
Z7	M1	0.42 ± 0.08
Z16	Rim	0.42 ± 0.08
Z11	M2	0.46 ± 0.05
Z4	M1	0.47 ± 0.07
Z1	M1	0.50 ± 0.08
Z3	M1	0.52 ± 0.06

define a best-fit P_{inc} of 0.72 ± 0.13 GPa. There are no resolvable differences between inclusions in the garnet mantle and rim. A weighted mean of inclusions from these regions defines a best-fit peak P_{inc} of 0.693 ± 0.161 GPa (95%; MSWD = 0.51; n = 4). Quartz-in-garnet isomekes were calculated using the equations of state for quartz (Angel et al., 2017) and pyrope (Milani et al., 2015) and are shown in Figure 5.9.

5.5.6 Zircon-in-garnet barometry

Seven zircon inclusions in garnet were analyzed and their locations are shown in Figure 5.5. Of these seven inclusions, six are located in the mantle region of the garnet and one is located in the rim. No zircon inclusions were observed in the garnet core. Raman

shifts and calculated strains for each inclusion are shown in Appendix S4.4. Inclusion pressures are shown in Table 5.3 and Figure 5.11 and range from 0.37 to 0.52 (±0.06-0.08) GPa. Three potential best-fit P_{inc} values were statistically identified (Figure 5.11F). All

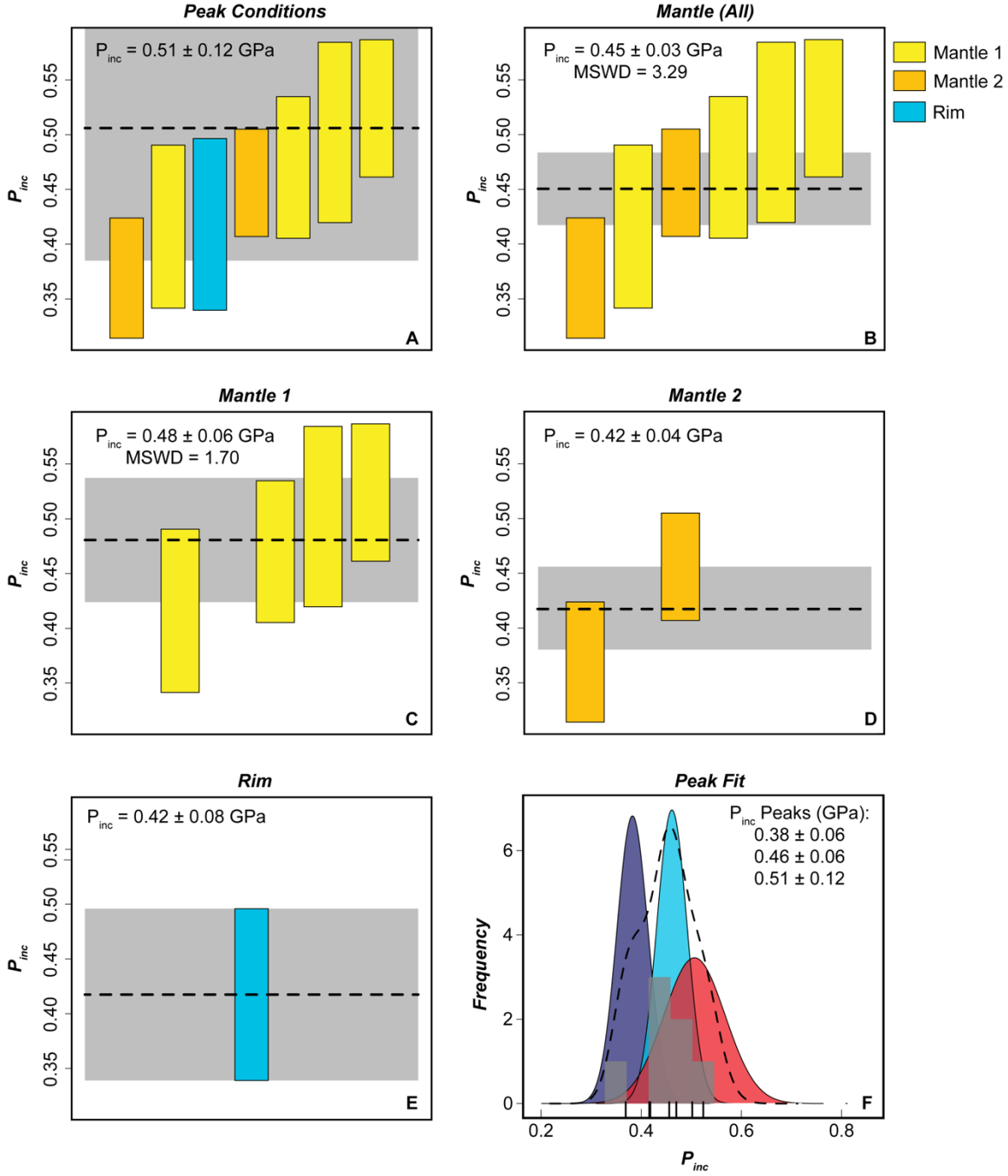

Figure 5.11. Zircon-in-garnet inclusion pressures (P_{inc}) for (A) peak conditions, (B) garnet mantle (combined M1 and M2), (C) M1, (D) M2 and (e) garnet rim (E) Histogram showing the distribution of inclusion pressures with best-fit P_{inc} positions determined by Peak Explorer. Cumulative probability distribution shown as dashed line.

three P_{inc} values overlap so it is not possible to identify which inclusions contributed to each. The highest-pressure value of 0.51 ± 0.12 GPa is considered representative of the peak conditions. Zircon inclusions in the two mantle regions were considered both as a single population and as two distinct populations. A weighted mean of all mantle inclusions (n = 6) gives an inclusion pressure of 0.45 ± 0.03 GPa (MSWD = 3.29). When treated separately, P_{inc} values for M1 and M2 do not appear to be resolvably different. A weighted mean of inclusions from M1 (n = 4) gives a P_{inc} of 0.48 ± 0.06 GPa (MSWD = 1.70). Inclusions from M2 record a slightly lower P_{inc} of 0.42 ± 0.04 GPa (n = 2). As such, the combined mantle P_{inc} was used for subsequent calculations. A single inclusion from the garnet rim records an inclusion pressure of 0.42 ± 0.08 GPa. Zircon-in-garnet isomekes were calculated using the most recent equations of state for zircon (Ehlers et al., in prep) and pyrope (Milani et al., 2015) and are shown in Figure 5.9.

Table 5.4. Pressure-temperature conditions for sample 25-228 defined by quartz-in-garnet (QuiG) barometry, zircon-in-garnet (ZiG) barometry and Zr-in-rutile thermometry.

	Peak Conditions		*Core*		*Mantle*		*Rim*	
Method	***T (°C)***	***P (GPa)***	***T (°C)***	***P (GPa)***	***T (°C)***	***P (GPa)***	***T (°C)***	***P (GPa)***
QuiG + Zr-in-rutile	657 ± 24	1.76 ± 0.33	532 ± 6	0.67 ± 0.04	651 ± 29	1.69 ± 0.31	605 ± 36	1.74 ± 0.30
QuiG + ZiG	670 ± 165	1.77 ± 0.48			604 ± 72	1.63 ± 0.34	587 ± 117	1.72 ± 0.37
ZiG + Zr-in-rutile	650 ± 67	1.61 ± 1.31			674 ± 39	2.19 ± 0.54	612 ± 68	1.92 ± 1.08

5.5.7 Defining *P-T* conditions

Pressure-temperature conditions associated with peak metamorphism and individual garnet growth zones were defined in three ways: by the intersection of the quartz-in-garnet isomeke and Zr-in-rutile isopleth, the intersection of the quartz-in-garnet and zircon-in-garnet isomekes and by the intersection of the zircon-in-garnet isomeke and Zr-in-rutile isopleth. The results are reported in Table 5.4. All three

approaches define overlapping peak metamorphic conditions, although the associated uncertainties are highly variable. Uncertainties in temperature range from 6 to 165°C and in pressure from 0.30 to 1.31 GPa depending on which thermobarometer pair was used. The approach with the lowest uncertainty, Zr-in-rutile + quartz-in-garnet, was used to define a *P-T* path for comparison to pseudosection modeling and prior studies. These data indicate that garnet core nucleation occurred at 532 ± 6°C and 0.67 ± 0.04 GPa. The mantle region of the garnet records metamorphic conditions of 651 ± 29°C and 1.69 ± 0.31 GPa, which overlap with the peak metamorphic conditions recorded by the sample of 657 ± 24°C at 1.76 ± 0.33 GPa. The garnet rim records a slightly lower temperature of 605 ± 36°C at a similar pressure of 1.74 ± 0.30 GPa. While this temperature is not statistically resolvable from the mantle conditions, it is resolvably lower than the peak metamorphic conditions.

5.6 Discussion

5.6.1 Resolving a prograde metamorphic history using single phase thermobarometers

In theory, single phase thermobarometers such as the Zr-in-rutile trace element thermometer and quartz-in-garnet and zircon-in-garnet elastic barometers should be applicable to resolving both the prograde and peak metamorphic history of a sample by utilizing inclusions in prograde porphyroblasts such as garnet. However, there are a number of challenges associated with this approach which have largely prevented application of these thermobarometers to estimating prograde metamorphic conditions. The challenges for each method and strategies for mitigating these challenges are discussed below.

5.6.1.1 Zr-in-rutile trace element thermometry

Historically, the Zr-in-rutile thermometer has only been applied to estimate the peak metamorphic conditions of a rock. Although rutile is expected to be present during prograde metamorphism (e.g., Kohn et al., 2015), multiple processes limit our ability to accurately define the entire range of temperatures over which rutile in a sample crystalized. First, although diffusion of Zr in rutile is slow (Ewing et al., 2018), there is some potential to diffusively reset a rutile grain that equilibrated at higher temperatures. Second, recrystallization of rutile at peak or post-peak metamorphic conditions greatly reduces the probability that the prograde metamorphic conditions are recoverable. Third, sluggish matrix diffusion kinetics at moderately low-temperatures (<450-500°C) may cause the observed concentration of Zr in rutile to deviate from the expected concentration (Zack and Kooijman, 2017). And finally, changes in the activity of zircon or quartz as a result of variations in or changes to the local or whole rock effective bulk compositions may cause the observable Zr concentration to be either lower (if $a_{ZrSiO4} < 1$) or higher (if $a_{SiO2} < 1$) than expected. The Mean Maximum Zirconium method (Penniston-Dorland et al., 2018) was designed specifically to account for these processes. By averaging grains with the highest Zr concentration within a population, this method mitigates effects relating to diffusive resetting or changes in a_{ZrSiO4}. Additionally, this averaging technique reduces the probability of overestimating the peak metamorphic conditions, unlike simply using the highest Zr concentration recorded by the sample which could be affected by local variations in a_{SiO2} or kinetic effects related to matrix diffusion of Zr.

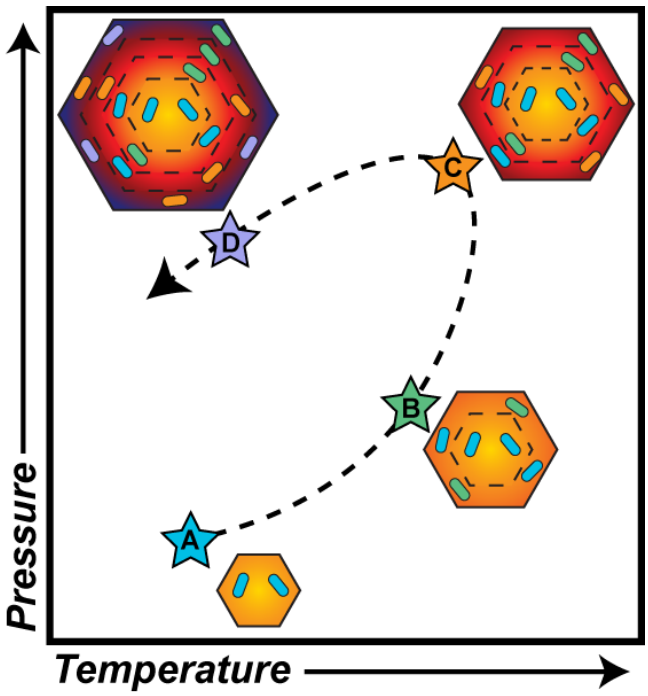

Figure 5.12. Conceptual sketch showing how the concentration of Zr in rutile inclusions in garnet change during prograde, peak and retrograde metamorphism. Throughout prograde and peak metamorphism, rutile inclusions with the highest Zr concentration in a garnet region are associated with the *P-T* conditions at which that region grew. However, this is not the case for retrograde garnet overgrowths, which may encapsulate rutile from earlier/higher-*T* metamorphic events.

Analyzing rutile inclusions in garnet is advantageous for reconstructing a prograde metamorphic history of the sample. Inclusions are unlikely to reequilibrate during prograde metamorphism because they are effectively isolated from the system once they become encapsulated in garnet. However, inclusions within a single zone of a garnet may still record a range of conditions. For example, inclusions in the mantle of a garnet are expected to record both conditions at the time that the mantle grew and earlier conditions given that the rate of metamorphism was sufficiently fast that rutile did not entirely recrystallize. If garnet grows along a typical prograde metamorphic path, where temperature increases as the garnet grows, then the peak conditions recorded by rutile in each growth zone of the garnet should represent the conditions around the time of garnet crystallization. If, however, garnet continues to grow at post-peak metamorphic conditions (overgrowth) along a counter-clockwise *P-T* path then the peak conditions recorded by rutile in the overgrowth region of the garnet may reflect the earlier and higher-temperature peak

metamorphic conditions as opposed to the true conditions of garnet growth (Figure 5.12). Garnet growth at post-peak conditions is not necessarily expected if the system is cooling (i.e., along a counter-clockwise *P-T* path). However, there are multiple processes which may perturb the system and drive garnet crystallization. These processes include re-equilibration by infiltrating fluids (e.g., Cheng et al., 2009; Page et al., 2007), or partial re-subduction (e.g., Page et al., 2014; Rubatto et al., 2011). Either of these two processes are possible given the tectonic setting (see Krebs et al., 2008; 2011); however, the presence of hydrated phases (i.e., glaucophane, chlorite) at the expense of nominally anhydrous phases (omphacite) suggests that there was at least some degree of re-hydration.

While rutile inclusions in garnet may be useful for reconstructing a prograde metamorphic history, some prior studies have specifically avoided this approach because the effects of a_{SiO2} are difficult to account for (Penniston-Dorland et al., 2018). Textural relationships between minerals are generally not preserved when the minerals become entrapped in another phase. However, if rutile and quartz are found within the same compositional domains of the host phase then it is reasonable to assume that a_{SiO2} at the time of rutile growth was c. 1. In this sample, quartz is found as an inclusion throughout garnet. Combined, this evidence shows that, at least for this sample, rutile inclusions in garnet can be used to accurately estimate metamorphic conditions.

5.6.1.2 Elastic Barometry

Elastic barometers, similar to the Zr-in-rutile thermometer, have generally only been applied to estimate peak metamorphic conditions. The primary reason for this is that inclusions are prone to reequilibration at lower inclusion pressures unless the host

maintains an infinite volume relative to the inclusion (Enami et al., 2007). The assumption of an infinite volume is met if the inclusion is further than three times its radius to any free surface, including fractures, grain boundaries, other inclusions, or the surface of the thin section (e.g., Bonazzi et al., 2019; Campomenosi et al., 2018; Enami et al., 2007; Mazzucchelli et al., 2018; Rosenfeld and Chase, 1961; Van der Molen and Van Roermund, 1986; Zhang, 1998). While the distance between the inclusion and any free surface can easily be measured to verify that this assumption is met, fractures have the potential re-heal following a brittle deformation event (e.g., Broadwell et al., 2019). It is not always possible to identify re-healed fractures, especially using standard optical methods. For this reason, inclusions used for elastic barometry should always be statistically treated to identify the highest inclusion pressure within the population since it is most likely to represent a true metamorphic event as opposed to a later deformation event.

A second effect that may inhibit our ability to estimate prograde inclusion pressures is plastic deformation of the host at peak metamorphic conditions. Plastic deformation of garnet has the potential to viscously reset inclusions at higher-pressure conditions, even at moderate temperatures (c. 600-700°C; Zhong et al., 2020). This would have the greatest impact on resolving the early portions of the prograde metamorphic path, and specifically may limit our ability to identify overstepping of the garnet isograd as a function of reaction affinity (e.g., Castro and Spear, 2017; Pattison et al., 2011; Spear et al., 2014; Spear and Pattison, 2017). In the case of this sample, systematic differences between inclusions in the garnet core and mantle regions of the garnet support that plastic deformation did not significantly affect the garnet host. Quartz inclusions in the garnet core record resolvably

lower inclusion pressures than both the mantle and rim regions of the garnet (Figures 5.9 and 5.10) and are interpreted to represent the conditions associated with garnet nucleation.

Perhaps the greatest challenge associated with utilizing elastic barometers to estimate a *P-T* path is that by creating sub-populations based on the location of the inclusions the population size is greatly reduced. Because inclusions need to meet strict criteria for analysis, very few are suitable. In the sample considered here, a total of eight quartz inclusions were found within the entire garnet porphyroblast. Of those, one inclusion was excluded because it was not isolated and a second because the inclusion was fractured, leaving a total of six quartz inclusions suitable for elastic barometry. This small sample size even inhibits our ability to accurately define peak conditions, making accurately defining prograde conditions based on a subset of the data especially challenging. The relatively high uncertainty in best-fit inclusion pressures (14-23%) relative to results presented in earlier chapters (6-17%; Harvey et al., in revision; Chapter 2) likely reflects the smaller sample sizes. To offset this effect, it is important to increase the number of analyses, perhaps by preparing multiple thin sections for analysis. Regardless, this work has demonstrated that it is possible to resolve differences in metamorphic conditions within a single garnet porphyroblast using elastic barometry.

5.6.2 Successes and challenges with the zircon-in-garnet elastic barometer

The zircon-in-garnet elastic barometer shows promise for being applicable to subduction-related metamorphic rocks, especially when the required assemblage for other single phase thermobarometers such as Zr-in-rutile or quartz-in-garnet is not present. However, there are still two challenges which inhibit our ability to rely on the accuracy of

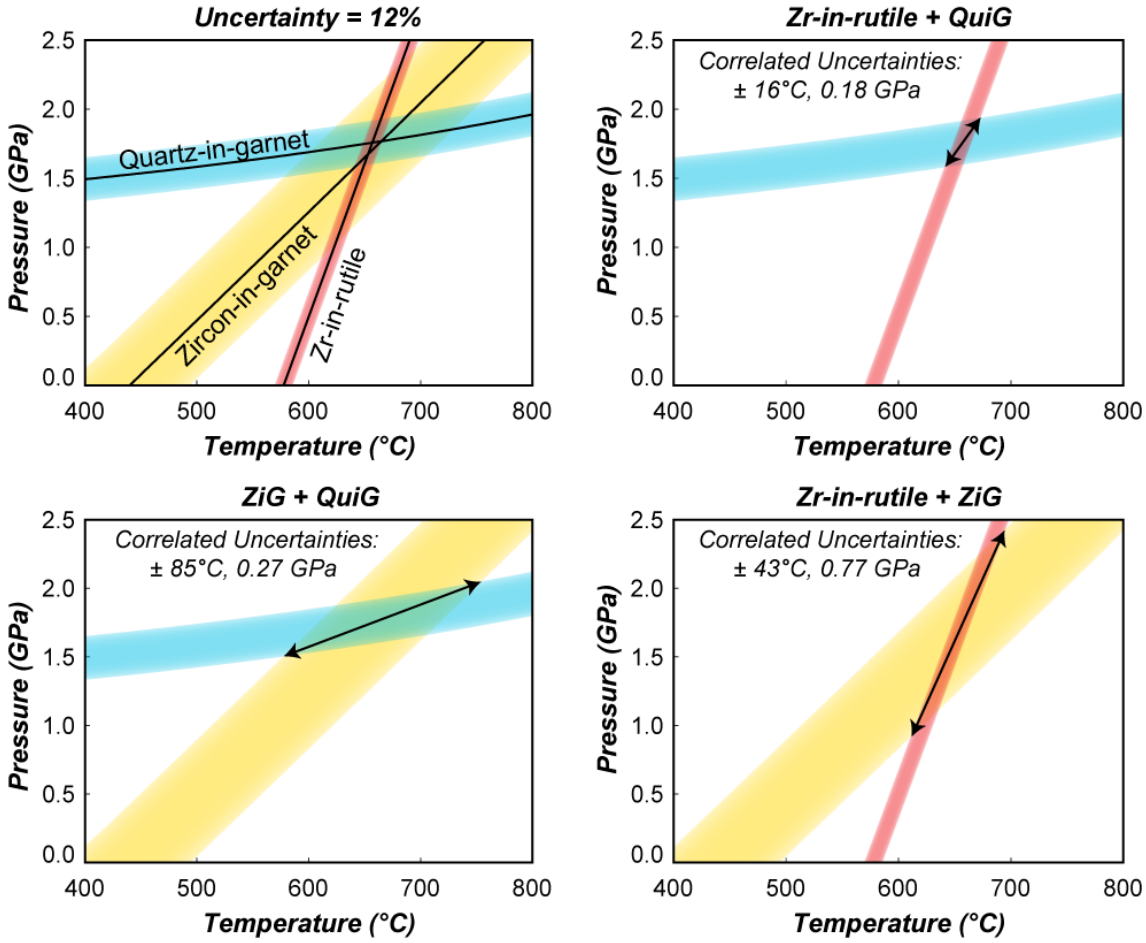

Figure 5.13. Example *P-T* plot showing how the slopes of the thermobarometers used to define a *P-T* point impact the positively-correlated uncertainties in pressure and temperature. All three thermobarometers are shown with error envelopes associated with 12% uncertainty in either Zr concentration (for Zr-in-rutile) or P_{inc} (for quartz-in-garnet/QuiG and zircon-in-garnet/ZiG).

the barometer without external constraints. The first is uncertainty in the EOS. While the conditions predicted by quartz-in-garnet and Zr-in-rutile were reproduced using the EOS for pyrope (Milani et al., 2015), the EOS for almandine (Milani et al., 2015) systematically overpredicts temperature conditions by upwards of 200°C (Figure 5.3). This is especially troubling for subduction-related metamafic rocks, where the primary component in garnet is typically almandine. The disparity between the two equations of state could be explained in one of three ways. Either the EOS for almandine needs to be refined with additional

experimental data, the EOS for zircon still needs refining, or the methodology for estimating P_{inc} from Raman shifts needs refining to specifically account for solid solution between zircon and hafnon ($HfSiO_4$), which affects the Raman shift (Grüneberger et al., 2016). Because the barometer is more sensitive to changes in host EOS, it may be necessary to also account for variations in the thermoelastic properties of garnet when the end-membmer components are mixed. The thermoelastic properties of garnet within the pyralspite solid solution series can be reasonably well approximated (within 1-2%) by linear mixing of the end-member components (e.g., Duffy and Anderson, 1989; Yeganeh-Haeri et al., 1990; Erba et al., 2014; Isaak and Grahm, 1976; Milani et al., 2015); however, this would likely still over-estimate temperature for sample 25-228 given the relatively large almandine component. These questions would be best addressed with additional experimental data, both to refine the equations of state for almandine and zircon and to test the validity of zircon-in-garnet barometer using different inclusion compositions following the methods of Thomas and Spear (2018) and Bonazzi et al. (2019).

The second challenge currently inhibiting our ability to rely on the zircon-in-garnet barometer is prohibitively large uncertainties. Because the slope of the isomeke is relatively shallow but not horizontal and because the barometer is far more sensitive to changes in P_{inc} than the quartz-in-garnet barometer, the positively-correlated uncertainty between the zircon-in-garnet barometer and either Zr-in-rutile thermometer or quartz-in-garnet barometer (see Chapter 2; Harvey et al., in review) will always be larger than the uncertainty between Zr-in-rutile and quartz-in-garnet, even if the analytical uncertainty is the same (Figure 5.13). In this study, the analytical uncertainty for zircon-in-garnet

propagated to an uncertainty in P_{inc} between 11 and 19% (2σ). This was reduced by statistical averaging to 7% (95% confidence) for the mantle; however, the final uncertainty for the peak conditions estimated using Peak Explorer was 24% at the 95% confidence interval. This higher uncertainty likely reflects scatter in the data and could be reduced by increasing the sample size.

The results from this study suggest that, in its current state, the best approach for using the zircon-in-garnet elastic barometer is to estimate an isomeke using the equations of state for zircon (Ehlers et al., in prep) and pyrope (Milani et al., 2015). Using any other equations of state for the garnet host result in erroneous *P-T* estimates. It is also necessary to analyze an adequate number of inclusions so that the final uncertainties in *P* and *T* are not prohibitively large.

5.6.3 Comparison to other constraints and implications for the tectonic history of the Rio San Juan Complex

Sample 25-228 was previously characterized as following a counter-clockwise *P-T* path from amphibolite to eclogite facies with an isobaric blueschist-facies overprint following peak conditions (Krebs et al., 2011). This type of *P-T* path is commonly associated with subduction initiation, where the subduction interface rapidly cools as the hanging wall is progressively serpentinized (e.g., Plunder et al., 2015; Wakabayashi and Dilek, 2003) and has been predicted for similar rock types in other localities including the Franciscan Complex (e.g., Krogh et al., 1994; Wakabayashi, 1990). Evidence for a counter-clockwise *P-T* path includes an amphibolite-facies inclusion assemblage (Amp + Ep + Ph + Rt + Qtz + Zrc + Ap ± Ttn) in the core and M1 regions of the garnet. The appearance of

omphacite in the M2 region of garnet suggests that peak conditions approached eclogite-facies conditions. The blueschist-facies overprint is indicated by replacement of Ca-amphibole by Na-amphibole in the matrix.

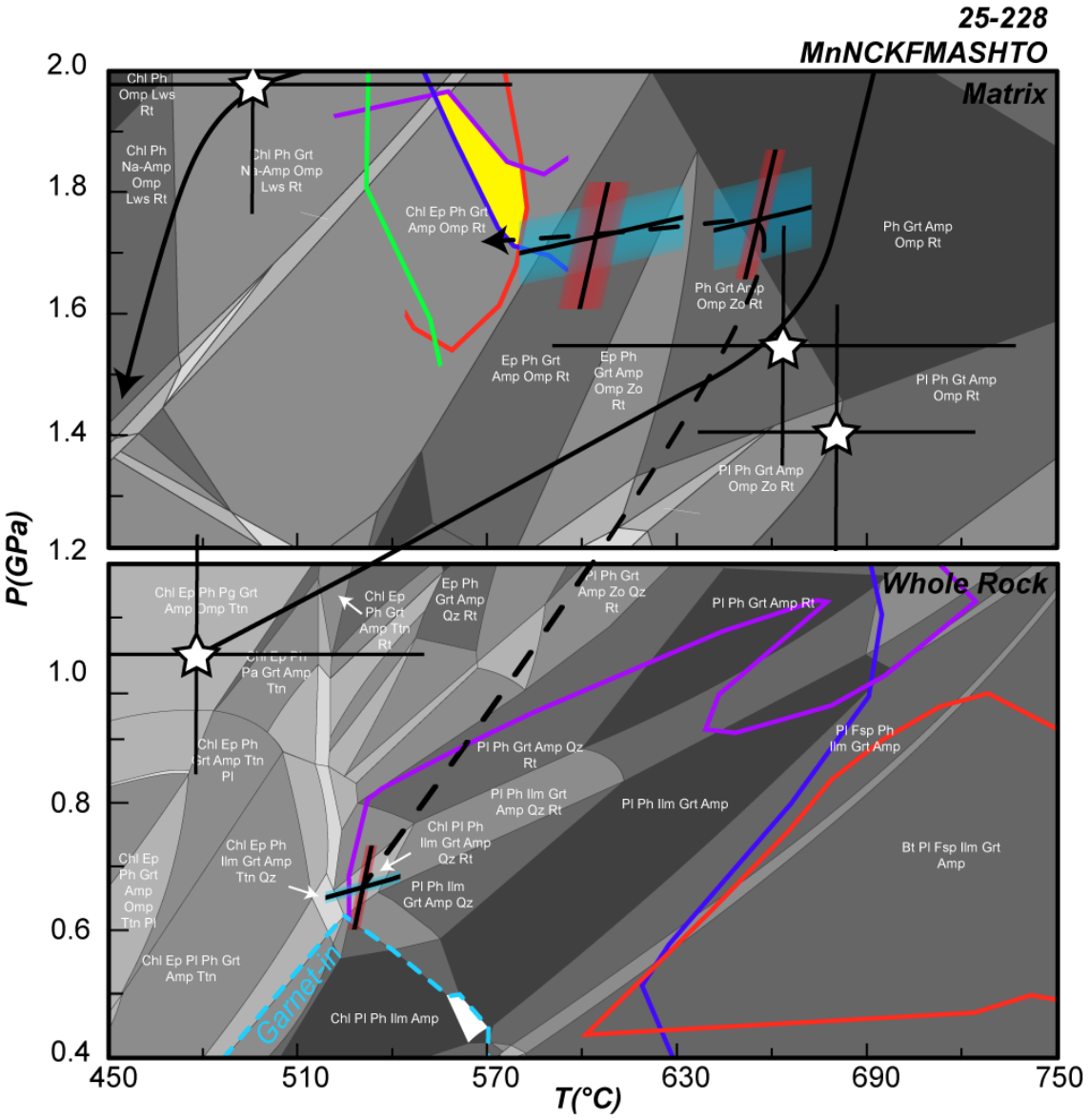

Figure 5.14. Comparison of *P-T* estimates using major element thermobarometry (white stars with uncertainties; Krebs et al., 2011), single phase thermobarometers (red/blue isopleths and isomekes) and whole rock/matrix phase equilibria models for sample 25-228. Pseudosection symbology follows Figures 6 and 7. Single phase thermobarometry symbology follows Figure 9. Solid black *P-T* path from Krebs et al. (2011). Dashed black path interpreted from single phase thermobarometry and validated by phase equilibria modeling.

While the results of this study suggests that the rock followed a counter-clockwise *P-T* path, the predicted conditions of prograde and peak metamorphism are somewhat different than those predicted by Krebs et al. (2011). The first appearance of garnet in the Krebs et al. (2011) model occurs at 477 ± 66°C at 1.0 ± 0.2 GPa within the field Chl + Ep + Ph + Pg + Grt + Amp + Omp + Ttn of the whole rock pseudosection for 25-228 (Figure 5.14). This is well above the predicted garnet-in isograd and not consistent with the inclusion assemblage in the garnet core (Pg + Amp + Rt + Qz + Ttn). In contrast, the intersection of the quartz-in-garnet isomeke and Zr-in-rutile isopleth from the garnet core suggest that nucleation occurred at 532 ± 6°C and 0.67 ± 0.04 GPa within the field Chl + Pl + Ph + Ilm + Grt + Amp + Qz + Rt. It is likely that because Krebs et al. (2011) did not model Mn and used higher concentrations of Fe^{3+} and Ca, their model underpredicts garnet stability in favor of other Fe-Mg phases such as biotite or chlorite. The intersection of the quartz-in-garnet isomeke and Zr-in-rutile isopleth also shows good agreement with the grossular isopleth and garnet-in isograd; however, the almandine and pyrope isopleths predict significantly higher temperatures. It is possible that the core composition was poorly constrained because the EPMA traverse from a to a' (Figure 5.6) did not intersect the geometric center of the core, or that the core composition was modified by diffusion. Additionally, the core and M1 regions of the garnet display sector zoning in Ca, Fe and Mg, which is likely indicative of fast disequilibrium garnet growth (e.g., Kohn, 2004; Spandler and Hermann, 2006). In this case, it is not necessarily surprising or troubling that the garnet composition isopleths do not intersect. The predicted mineral assemblage at garnet core nucleation is close to the observed mineral assemblage, with the exceptions of chlorite (which was reported by Krebs et al., 2011), plagioclase and ilmenite, which were

not observed. Additionally, titanite was observed but not predicted; however, titanite destabilizes in this region of the pseudosection at c. 515°C and 0.67 GPa, so it is conceivable that it would still be present at the time of garnet nucleation.

Peak conditions estimated by Krebs et al. (2011) were defined at 701 ± 66°C and 2.3 ± 0.2 GPa. This estimate is higher-pressure than the peak conditions defined by quartz-in-garnet/Zr-in-rutile of 657 ± 24°C and 1.76 ± 0.33 GPa, which overlaps with the matrix pseudosection phase fields Ph + Grt + Amp + Omp + Zo + Rt and Ph + Grt + Amp + Omp + Rt (Figure 5.14). The intersection of the single phase thermobarometers agrees well with the observed mineral assemblage in M2, although epidote was observed in place of zoisite. It is not immediately obvious why there is such a large pressure discrepancy between peak conditions estimated by this study and Krebs et al. (2011). It is possible that quartz-in-garnet inclusion pressures were partially reset, or that the analyzed phases (garnet, phengite, omphacite) used to estimate the peak conditions by Krebs et al. (2011) were not in equilibrium. This would be best assessed with additional elastic barometry data to ensure the peak metamorphic pressure is recovered.

Krebs et al. (2011) did not report conditions associated with a retrograde garnet rim. However, it appears that the outermost c. 200 μm of the garnet grew at post-peak metamorphic conditions, perhaps as the result of late stage reequilibration with fluid or a late thermal pulse. Zr-in-rutile thermometry with quartz-in-garnet barometry places this garnet overgrowth event at 605 ± 36°C and 1.74 ± 0.30 GPa within the field Ep + Ph + Grt + Amp + Omp + Rt. The garnet rim isopleths intersect at slightly lower temperatures

between 540 and 570°C (Figure 5.14) within the field Chl + Ep + Ph + Grt + Am + Omp + Rt. It is likely that these conditions overlap within uncertainty of the methods; however, it is possible that that Zr-in-rutile thermometry is slightly overestimating the conditions of garnet rim growth for reasons discussed in Section 5.6.1.1 and shown in Figure 5.12.

5.7 Recommendations for application of single phase thermobarometers

Collectively, the results of this study demonstrate that single phase thermobarometers can be utilized to constrain prograde, peak, and post-peak metamorphic conditions. Results for sample 25-228 using the Zr-in-rutile trace element thermometry and the quartz-in-garnet and zircon-in-garnet elastic barometers are both self-consistent (i.e., all three intersect around the same *P-T* conditions) and largely consistent with the updated phase equilibria modeling presented in this study. There are some discrepancies between these results and prior constraints by Krebs et al. (2011) that warrant further investigation to ensure that the peak metamorphic pressure was truly recovered using elastic barometry.

While these results demonstrate the applicability of single phase thermobarometers, they simultaneously highlight several important considerations. First, utilizing these thermobarometers to resolve the *P-T* conditions of individual growth zones in garnet greatly reduces the sample size for each estimate which increases the uncertainty. This is especially problematic for elastic barometers, where strict criteria for suitable inclusions already reduces the number of useable analyses. To circumvent this problem, it may be necessary to prepare multiple thin sections for analysis, especially for relatively inclusion-poor samples. Second, although the zircon-in-garnet barometer could reproduce conditions estimated by Zr-in-rutile thermometer and quartz-in-garnet barometer, this was only

possible by estimating the *P-T* conditions using the pyrope EOS. Even though the garnet considered in this study is predominately almandine, the EOS for almandine consistently over-estimated temperature by upwards of 200°C. This may simply reflect greater uncertainty in the almandine EOS, which has fewer experimental constraints than pyrope, or more likely reflects uncertainty in the EOS for zircon and compositional variations in zircon affecting the Raman peak positions. Until there are additional empirical observations of and experimental constraints on the zircon-in-garnet elastic barometer, it is recommended that the barometer only be applied using the EOS for pyrope and preferably where the results can be externally validated. Finally, although it appears that the Zr-in-rutile thermometer is suitable for constraining the prograde and peak metamorphic history of a sample when applied to inclusions in garnet, it may over-estimate post-peak metamorphic conditions because of incorporation of earlier/higher-*T* inclusions. In this case, elastic barometers are better-suited for constraining the post-peak *P-T* path. In order to apply the Zr-in-rutile thermometer to inclusions in garnet it is also necessary to ensure that zircon, quartz and rutile all coexist throughout garnet in order to reduce any uncertainty related to estimating the activities of quartz and zircon.

5.8 Acknowledgements

The work presented in this chapter was funded by NSF grant EAR-1850786 to SPD. Sample 25-228 was provided by Hans Peter-Schertel at Ruhr-Universität Bochum. Thank you to Besim Dragovic (University of South Carolina) for providing pseudosection models and to Phil Piccoli (UMD), Emma Bullock (Carnegie Institution for Science) and Karen Gaskell (UMD) for assistance with EPMA, SEM and Raman spectroscopy, respectively.

Chapter 6: Summary and closing remarks

6.1 Thermal and Structural Evolution of the Catalina Schist

Exhumed subduction terranes provide a unique opportunity to directly study processes occurring at depth within subduction zones. The Catalina Schist, best exposed on Santa Catalina Island (California, U.S.A), in particular provides unparalleled exposures of tectonic mélange, a block-in-matrix structure which is thought to be an important constituent of the interface between the downgoing slab and overriding plate (see Bebout and Penniston-Dorland, 2016). The composition and rheologic behavior of mélange at the subduction interface controls a number of geophysical and geochemical processes, including deformation, seismicity, melt generation and geochemical cycling. Mixing and metasomatism within mélange fundamentally change both its composition and its rheology, affecting both mass transfer and deformation processes. The Catalina Schist has been the subject of numerous petrologic and geochemical studies to understand fluid flow, metasomatism and tectonic mixing at the subduction interface (e.g., Bebout and Barton, 1989; Bebout, 1997; Bebout and Barton, 2002; King et al., 2006; 2007; Sorensen and Barton, 1987; Sorensen and Grossman, 1989; Penniston-Dorland et al., 2012, 2014, 2018). The work presented in this dissertation builds on this prior knowledge by placing spatial and temporal constraints on mélange formation and mixing processes as well as temporal constraints on the thermotectonic history of the terrane. The results are summarized briefly below.

Although mélange zones throughout the Catalina Schist record evidence for tectonic mixing, both the spatial and temporal scales of mixing are smaller than other exhumed terranes. Some terranes, such as the Rio San Juan Complex (Dominican Republic) or regions of the Franciscan Complex (California, U.S.A.), record temperature and age variations amongst mélange blocks as high as 400°C and 40 million years (e.g., Krebs et al., 2008, 2011; Mulcahy et al., 2018). These variations have been interpreted by some studies as evidence for large-scale tectonic mixing during subduction (e.g., Gerya et al., 2002). In contrast, blocks within the amphibolite-facies mélange zone of the Catalina Schist record up to 90°C differences in peak metamorphic temperature (Penniston-Dorland et al., 2018), indicating that the blocks were likely sourced from a somewhat smaller (ca. 12 km) region of the subduction interface. Temperature variations throughout the mélange zone appear to be non-systematic, favoring a model whereby blocks were juxtaposed by tectonic mixing and mélange flow during subduction. The limited scale of mixing relative to other exhumed terranes was attributed to development of rheologically stiff matrix phases, such as amphiboles and pyroxenes, which inhibited mixing between mélange components. The blocks record Sm-Nd garnet ages between 115 and 108 Ma, indicating that the mélange zone developed over at least 7 Myr (Chapter 3). Differences in peak metamorphic age do not correlate with peak metamorphic temperature, further supporting that the mélange zone developed by progressive tectonic mixing. The unit was underplated between c. 108 and 105 Ma, which likely occurred in conjunction with partial exhumation of the structurally lower and older coherent amphibolite (c. 115 Ma; Anczkiewicz et al., 2003). $^{39}Ar/^{40}Ar$ cooling ages from hornblende and white mica suggest that both

amphibolite units then rapidly cooled to <400-425°C by 100 Ma at a rate between 30 and 40°C/Myr (Grove, 1993; Grove and Bebout, 1995; Suppe and Armstrong, 1972).

Larger scales of mixing are recorded by "exotic" garnet-bearing amphibolite-facies blocks found within the structurally lower epidote amphibolite and lawsonite blueschist units (Harvey et al., in revision; Chapter 2). Exotic blocks within the epidote amphibolite unit record peak temperatures between 579 and 735°C and peak pressures between 1.16 and 1.47 GPa, suggesting that the blocks were sourced from a 20-30 km region of the subduction interface. Variations in the scale of tectonic mixing observed throughout the terrane were attributed to mineralogic heterogeneities within the matrix, which affect the rheologic behavior of the matrix and, therefore, the length-scales of deformation. This is supported by field observations, where sheet silicate- and chain silicate-dominated matrix compositions are intercalated at sub-km scales (see Bebout and Barton, 2002).

Exotic blocks also provide the earliest records of metamorphism within the terrane. A garnet-bearing blueschist block within the lawsonite blueschist unit, which reached eclogite-facies peak metamorphic conditions of 635°C at 1.65 GPa (Harvey et al., in revision), records an Sm-Nd garnet age of c. 186 Ma (Chapter 4). The block records a subsequent blueschist-facies overprint between 160 and 145 Ma (Awalt et al., 2013; Grove and Bebout, 1995; Grove et al., 2008). This suggests that subduction in the region was underway well before amphibolite-facies metamorphism of the Catalina Schist. Two amphibolite-facies exotic blocks within the epidote amphibolite unit record ages of c. 120 and 115 Ma respectively. This provides new constraints on the timing of amphibolite-facies

metamorphism, which appears to have begun at least 5 million years prior to the oldest record of peak metamorphism within the amphibolite-facies mélange zone. Collectively, these results demonstrate that amphibolite-facies metamorphism of the Catalina Schist occurred for at least 12 million years and post-dates subduction initiation in the region.

6.2 Applicability of trace element thermometry and elastic barometry to reconstructing the tectonometamorphic history of the Rio San Juan Complex

Trace element and elastic thermobarometers are useful tools for precisely reconstructing the metamorphic history, and in particular the peak pressure-temperature conditions, of subduction-related rocks. While both the Zr-in-rutile trace element thermometer and quartz-in-garnet elastic barometer have been successfully applied to estimate peak *P-T* conditions for a number of exhumed terranes, there is interest in applying these thermobarometers on inclusions within zoned garnet porphyroblasts to reconstruct prograde *P-T* paths. These methods, in addition to the more recently-calibrated zircon-in-garnet elastic barometer, were applied to inclusions within a ca. 1 cm garnet porphyroblast in an eclogite from the Rio San Juan Complex (Dominican Republic) and the results were compared to phase equilibria models for the sample (Chapter 5).

For regions of the garnet where all three thermobarometers were applied together, the thermobarometers all intersect at broadly the same *P-T* conditions. The single phase thermobarometers predict garnet core nucleation at 530°C and 0.67 GPa. This was

followed by peak conditions, recorded by the mantle region of the garnet, of 660°C at 1.76 GPa. A post-peak overgrowth garnet rim records colder conditions of 600°C at 1.74 GPa, consistent with a counter-clockwise *P-T* path proposed by prior studies (Krebs et al., 2011) and with petrologic observations. Phase equilibria models for the whole rock and matrix (whole rock minus garnet) compositions show good agreement with estimates from the single phase thermobarometers, suggesting that single phase thermobarometers can be applied to define a large portion of the metamorphic history of a sample.

6.3 Closing Remarks

The work presented in this dissertation highlights a number of interesting questions that could be addressed by future studies. In particular, the age relationship between the coherent amphibolite and amphibolite-facies mélange zone of the Catalina Schist suggests that the two units may have formed at different depths within the subduction zone and were later juxtaposed by partial exhumation of the coherent amphibolite. However, there are currently few constraints on the metamorphic history of the coherent amphibolite. Additional constraints on the *P-T-t* history of the unit would provide valuable insight into the tectonometamorphic evolution of the Catalina Schist, setting a framework for future geochemical, petrologic and structural studies of the terrane.

The work presented in Chapter 5 also highlights the potential for elastic barometry and trace element thermometry to be combined in order to reconstruct the prograde metamorphic history of a sample by analyzing inclusions in zoned garnet porphyroblasts. This work demonstrates numerous advantageous and challenges with the approach, many

of which are avenues for future exploration. There is still a significant amount of work to be done to fully refine the zircon-in-garnet elastic barometer, although it appears to be a promising tool for future petrologic studies. Current challenges with the barometer include its higher sensitivity to lattice strain and the host equation of state, which both amplify uncertainty, as well as uncertainty regarding how to effectively account for variations in zircon composition. Additional empirical observations in addition to experimental constraints will likely improve our understanding of these effects and increase the reliability of the barometer.

Appendix S1

The material presented in Appendix S1 supplements the research presented in Chapter 2. Sections S1.1-S1.7 provide additional details about analytical methods and field observations. Sections S1.8-1.15 provide sample locations and all data used for calculations in Chapter 2.

S1.1 Secondary Standard K13-02

A natural rutile, K13-02, was used as a secondary standard for all rutile analyses by electron probe microanalysis (EPMA). The concentration of Zr in the standard was

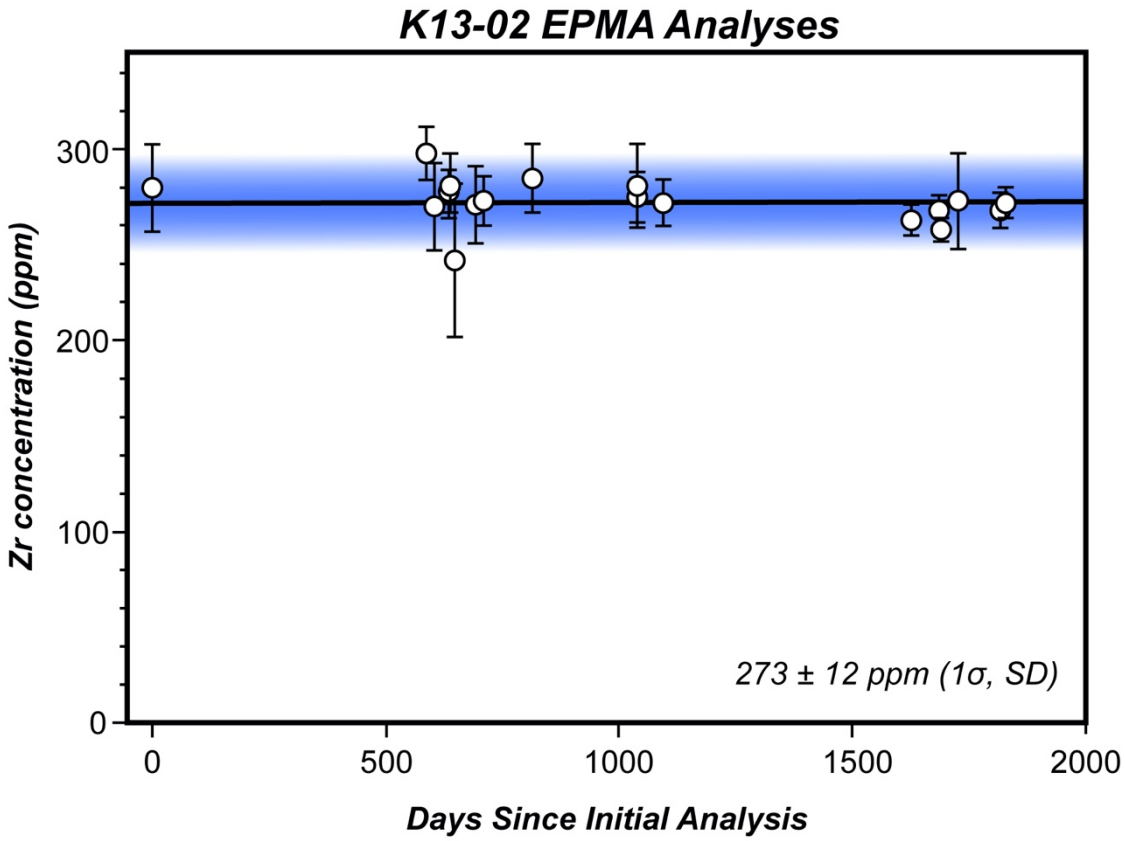

Figure S1.1. EPMA analyses of zirconium in secondary standard K13-02. The long-term average concentration is 273 ± 12 ppm (1σ, SD). Uncertainties represent variability of measurements across the grain within a single analytical session.

determined to be 273 ± 12 ppm (1σ, SD, n = 18) by EPMA. The long-term reproducibility of Zr concentration in K13-02 is shown in Figure S1.

S1.2 LA-ICP-MS Rutile Analyses

Sample EA13-7g was analyzed by laser ablation inductively coupled plasma mass spectrometry (LA-ICP-MS) in addition to EPMA. Spot sizes ranged from 40-80μm, using a repetition rate of 5-10 Hz, a fluence of 5-6 J/cm^2, and a dwell time of 30 seconds. Analyses were standardized using R10 rutile (Luvizotto et al., 2009) and the Rietfontein rutile megacryst (see Penniston-Dorland, Kohn, & Piccoli, 2018), and normalized to a concentration of Ti of 599340 ppm. Data were processed using Iolite 2.5 (Paton, Hellstrom, Woodhead, & Hergt, 2011), and filtered by excluding any analyses with high uncertainties in Zr due to possible incorporation of zircon microinclusions. Zr concentrations are reported in Appendix A1 (Grain numbers with "LA" prefix). Other isotopes that were analyzed include ^{49}Ti, ^{29}Si, ^{51}V, ^{52}Cr, ^{57}Fe, ^{91}Zr, ^{93}Nb, ^{177}Hf, ^{181}Ta, ^{204}Hg+Pb, ^{206}Pb, ^{207}Pb, ^{208}Pb, ^{232}Th, and ^{238}U.

S1.3 Comparability of EPMA and LA-ICP-MS Data

EPMA and LA-ICP-MS analyses for Zr-in-rutile have already been shown to be comparable for amphibolite-facies rocks from Catalina (Penniston-Dorland et al., 2018). The analytical methods were additionally compared for the epidote amphibolite facies sample EA13-7g. The mean maximum Zr content for the sample is indistinguishable when calculated using the EPMA data, the LA-ICP-MS data, and the combined data set (see Figure S2).

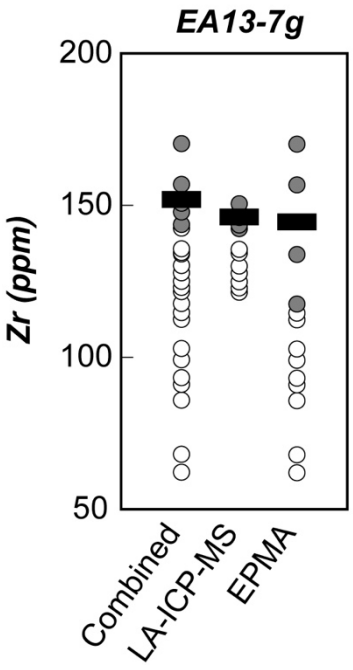

Figure S1.2. Comparison of EPMA and LA-ICP-MS results for sample EA13-7g. The combined data set does not predict a significantly different mean maximum Zr concentration than either individual data set. Symbology follows Figure 2.6 from the main text.

S1.4 Intra- and inter-grain variations in Zr concentration in rutile

Systematic variations of Zr within rutile grains varies from sample to sample. In most samples, there is no obvious systematic change from core-to-rim that would reflect either growth zoning or diffusion of Zr into or out of a crystal. Figure S3 shows a typical traverse across a rutile grain where there is no significant change in concentration. Some samples, on the other hand, show evidence for significant out-diffusion of Zr. These samples typically record the highest peak metamorphic temperatures (>700°C). Figure S4 shows a decreasing trend of Zr from core to rim in a rutile grain from sample LB15-03B ($T = 754 \pm 18$°C).

Similarly, systematic variations from matrix rutile populations versus inclusions within garnet are not consistent for all samples. In some samples, rutile inclusions in garnet record higher Zr concentrations than matrix rutile, whereas in others there is no systematic variation. For example, some rutile inclusions in garnet in WB16-03A (Figure S5) record

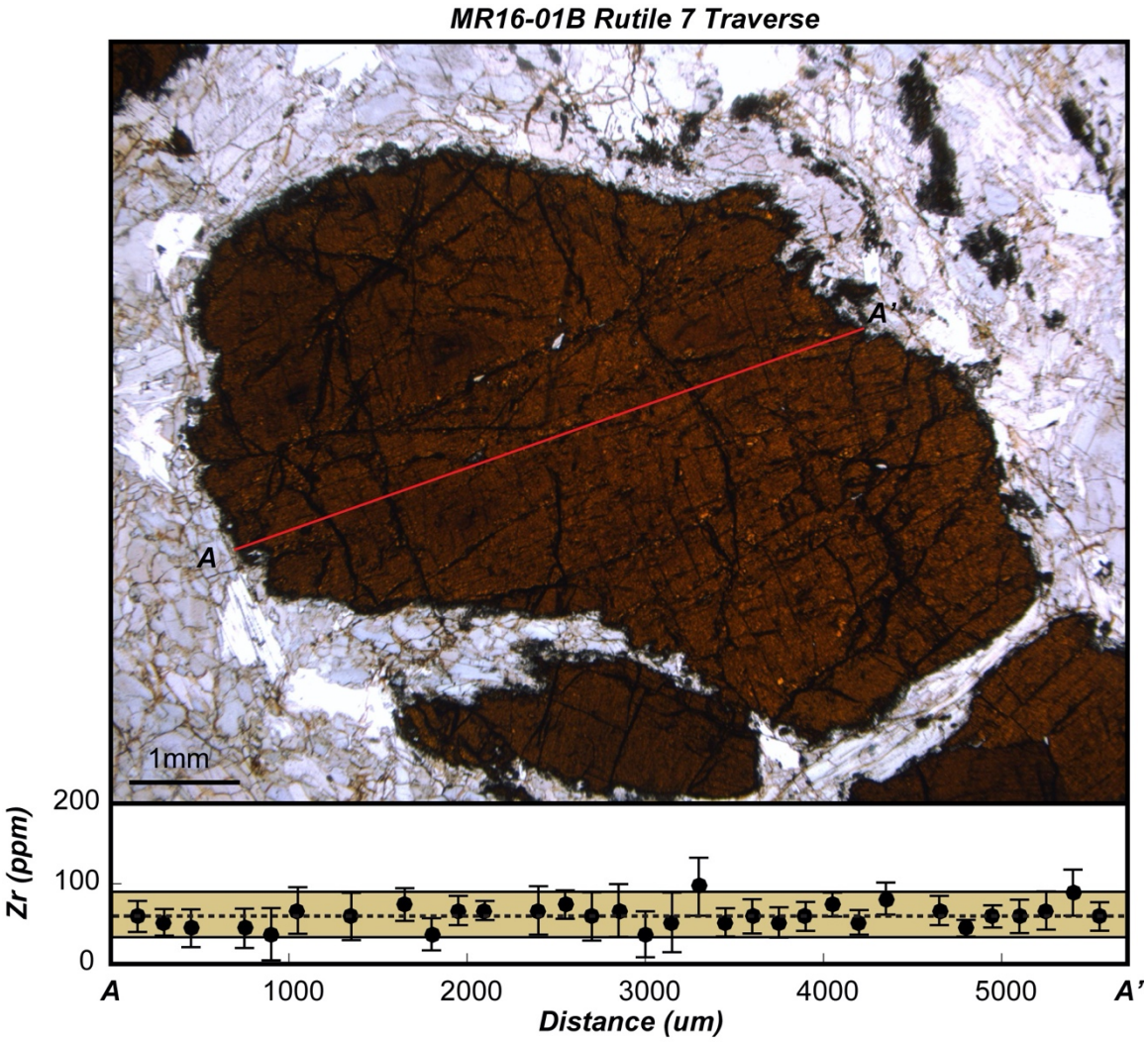

Figure S1.3. Variation in Zr concentration (*lower*) across a rutile megablast from sample MR16-01 from A to A' as shown in the photomicrograph (*upper*). The average concentration is shown as a dashed line with upper and lower quantiles (gold band).

higher concentrations than the matrix population. In contrast, there is no systematic variation observed in sample EA15-10A, also shown in Figure S5.

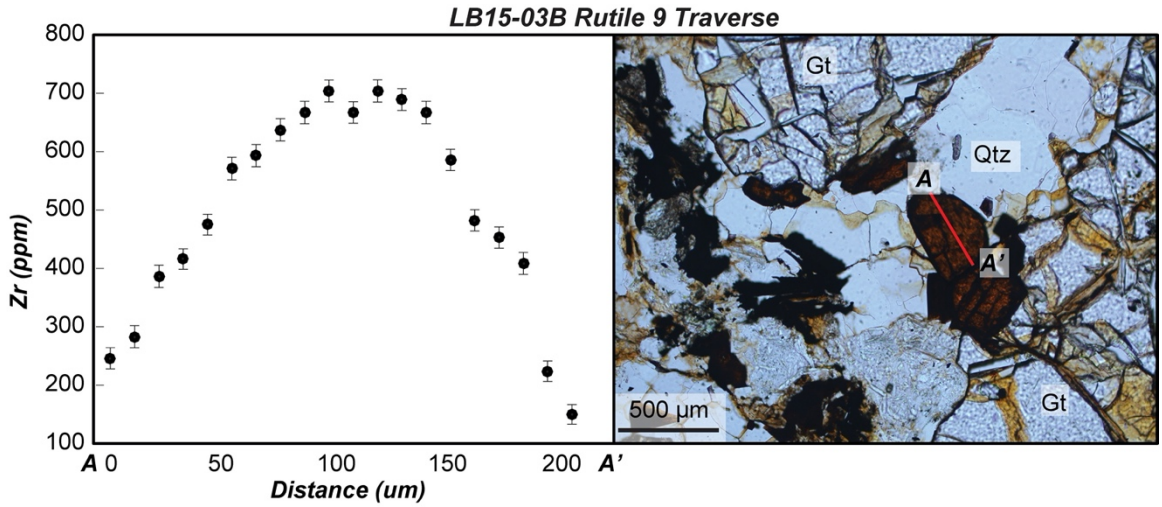

Figure S1.4. Variation in Zr concentration (*left*) across a matrix rutile grain from sample LB15-03B showing a decreasing trend in Zr concentration from core to rim. The profile is from A to A' as shown in the photomicrograph (*right*).

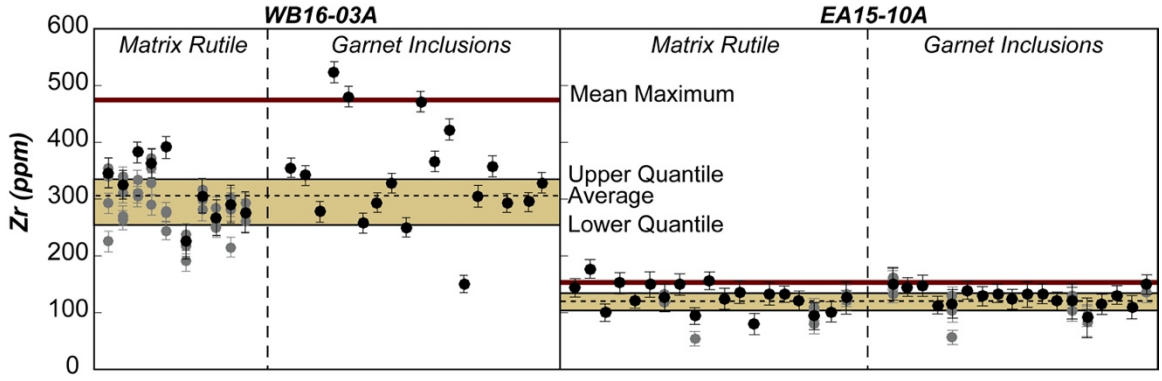

Figure S1.5. Variation in Zr concentration between matrix rutile grains and rutile inclusions in garnet for samples WB16-03A (*left*) and EA15-10A (*right)*. Maximum concentration in each grain shown as black circle. All other analyses shown as grey circles.

S.1.5 Determining "best-fit" P_{inc}

The best-fit maximum inclusion pressure (P_{inc}) used to calculate an entrapment pressure for each sample was determined as described in section 2.3.2.3. Figures S6 and

S7 show the results of this fitting procedure for each exotic blocks and amphibolite-facies mélange blocks respectively.

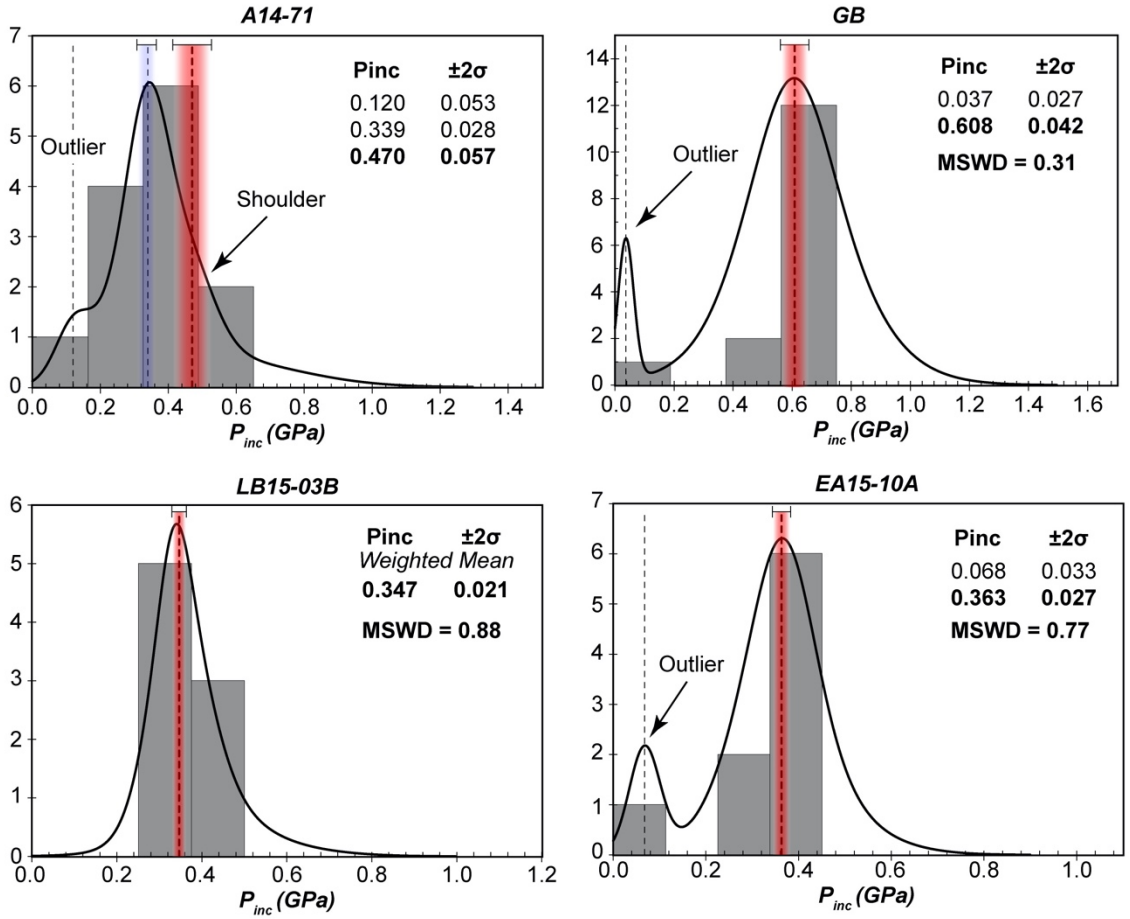

Figure S1.6. Histogram showing distribution of P_{inc} for each exotic block with probability density function (black line) and the "best-fit" P_{inc} (red band). Fits for lower-*P* inclusion populations shown as purple bands.

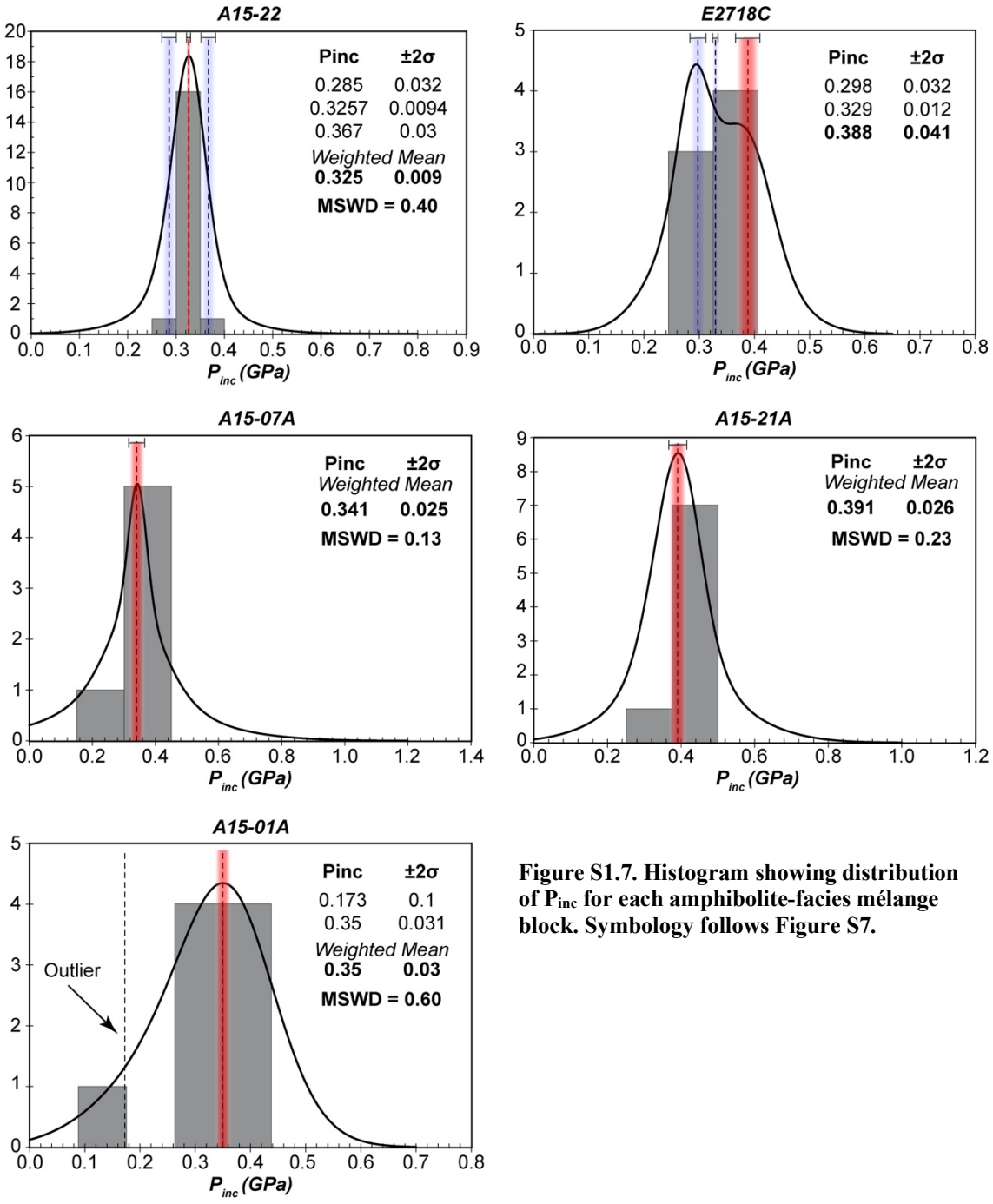

Figure S1.7. Histogram showing distribution of P_{inc} for each amphibolite-facies mélange block. Symbology follows Figure S7.

S1.6 Outcrop description of exotic block LB/A14-01

Outcrop LB/A14-01 occurs within the lawsonite blueschist unit along Middle Ranch Road just south of Little Harbor. The outcrop consists of a garnet-bearing amphibolite encapsulated by mélange matrix and metasedimentary rock. The matrix that occurs above

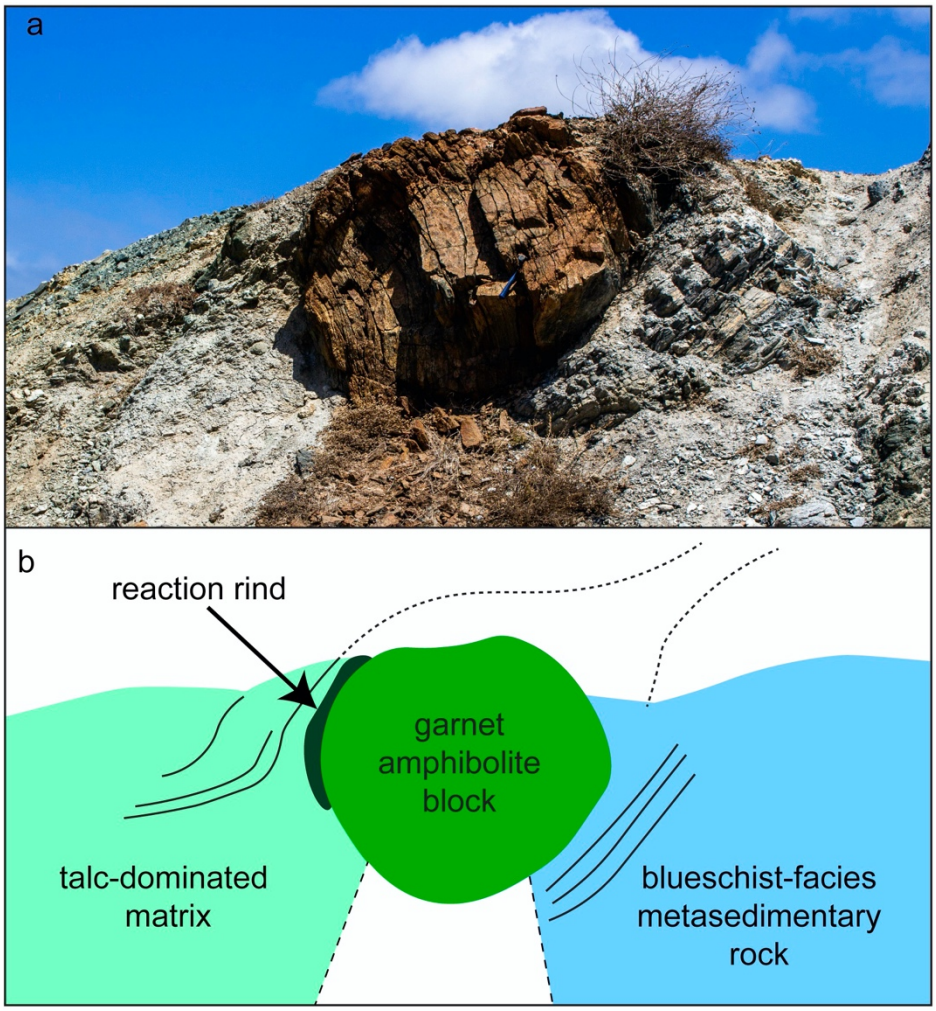

Figure S1.8. (a) field photo of outcrop LB/A14-01 showing garnet amphibolite block juxtaposed with blueschist-facies metasedimentary rock and mélange matrix. (b) cartoon sketch of the outcrop showing the relationship between the block, the matrix and the metasedimentary rock. Material directly below the block is talus.

and to the east of the block is talc-dominated and likely represents a mix of mafic and ultramafic components. The foliated rock below the block in contrast is a glaucophane-bearing metasedimentary rock. The relationship between these two lithologies is obscured by weathering. Figure S8 shows a field photo of the outcrop with a simplified cartoon depicting the general matrix and metasedimentary rock foliation and the location of the actinolite + chlorite reaction rind separating the matrix from the block.S1.7 Outcrop description of the epidote blueschist-facies rocks at the footwall of the ollas fault

The Ollas fault between the amphibolite and epidote blueschist units locally outcrops in Cottonwood Canyon. A simplified cross-section is shown in Figure S9. The hanging wall consists of green foliated amphibolite (garnet-absent) characteristic of the coherent amphibolite unit. Two matrix compositions were observed at the base of the unit: an actinolite + biotite matrix (CC16-14C) at the contact between the coherent amphibolite and the fault zone and a talc + biotite matrix (CC16-14E) with several m-scale mafic blocks composed of either biotite + hornblende or garnet + hornblende. The high-strain epidote blueschist-facies metachert footwall (CC16-15) of the fault outcrops ~140m southwest of the hanging wall. There are no outcrops between the two described above. The metachert is composed dominantly of quartz + muscovite with small garnet porphyroblasts, glaucophane, and feldspar. The metachert is underlain by a foliated mafic blueschist with epidote porphyroblasts (EBS12A-1). Field photos and photomicrographs of both the metachert and epidote blueschist are shown in Figure S10.

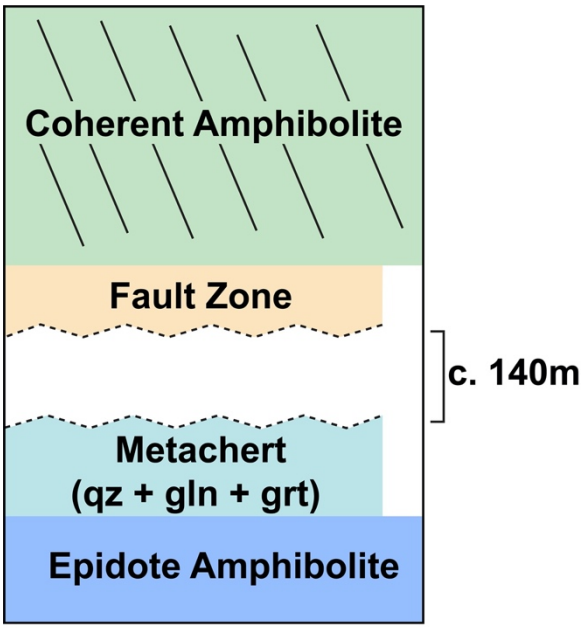

Figure S1.9. Simplified cross section sketch of the Ollas fault zone exposed in Cottonwood Canyon.

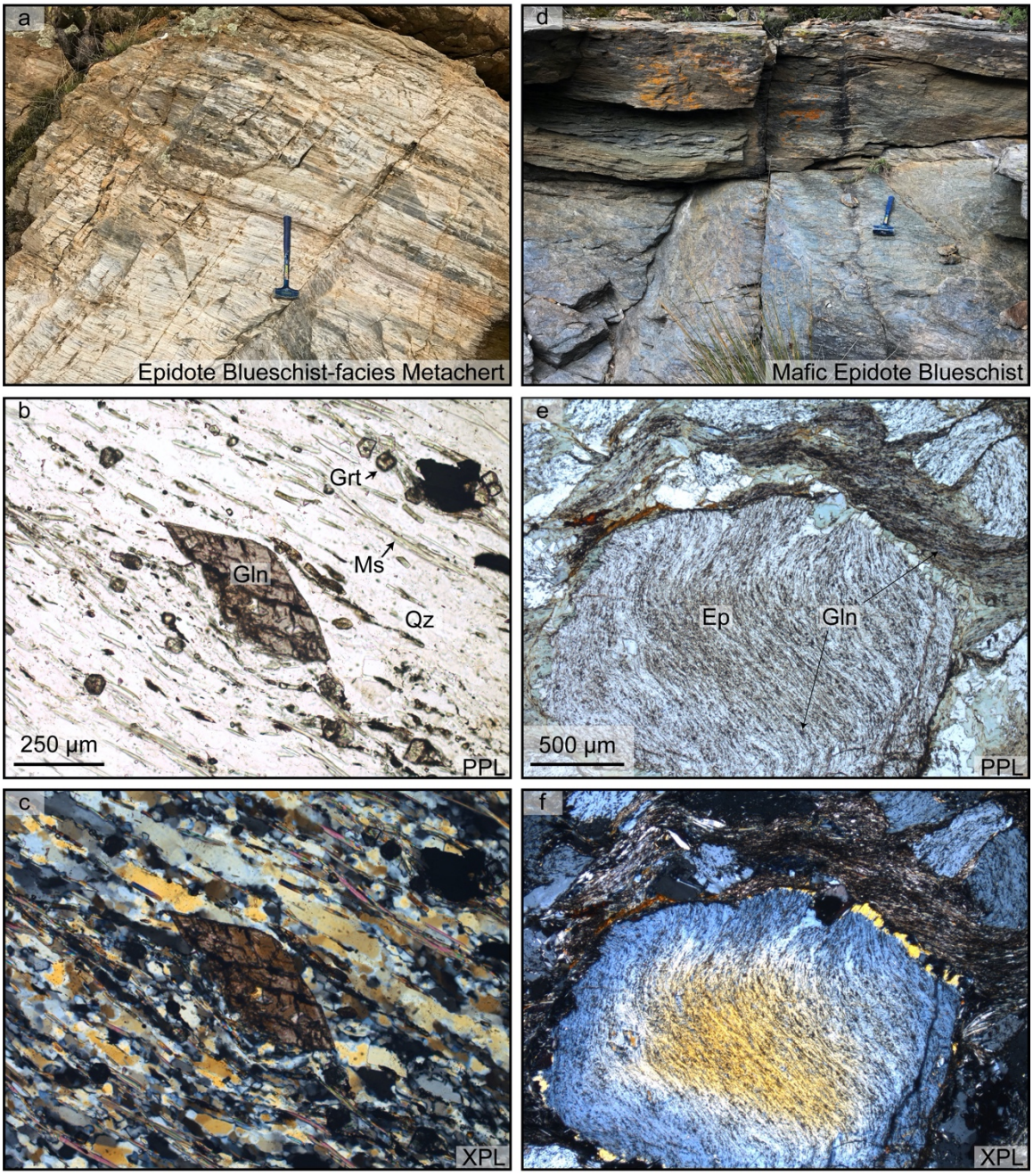

Figure S1.10. (a) field photo of outcrop CC16-15 showing garnet and glaucophane-bearing metachert. (b) plain-polarized light photomicrograph of sample CC16-15 showing glaucophane, quartz, muscovite and garnet. (c) cross-polarized light photomicrograph of CC16-15. (d) field photo of outcrop EBS12A-1 just below CC16-15. (e) plain-polarized light photomicrograph of epidote porphyroblast in sample EB12A-1 with s-type glaucophane inclusion trails. (f) cross-polarized light photomicrograph of EB12A-1.

S1.8 Location of rocks

Table S1.8.1 Sample locations. Symbology follows table 2.1.

Location in Fig. 2.1	*Sample Number*	*Latitude*	*Longitude*
Region A: Amphibolite Facies Exotic Blocks in Epidote-Amphibolite Facies Unit			
1	LB15-03B	33.388	-118.4676
2	LB18-04*	33.3891	-118.4666
3	LB18-10*	33.3897	-118.4657
Region B: Amphibolite Facies Exotic Blocks in Epidote-Amphibolite Facies Unit			
4	EA15-10A	33.4085	-118.4726
5	EA15-05B*	33.4098	-118.4754
6	EA15-01A*	33.4089	-118.4689
Region B: Epidote-Amphibolite Facies Blocks in Epidote-Amphibolite Facies Unit			
i	EA15-02Ba*	33.4092	-118.4691
Other Epidote-Amphibolite Facies Blocks in Epidote-Amphibolite Facies Unit			
ii	79841A*	N/A	N/A
iii	77842*	N/A	N/A
iv	EA13-07g	33.3546	-118.4642
v	EA13-12*+	33.3546	-118.4564
Other Exotic Blocks in Lawsonite-Blueschist Facies Unit			
12	WB16-03A*	33.4003	-118.4569
13	LB/A14-01	33.3841	-118.4705
14	GB	33.3735	-118.4782
15	A14-71	33.3699	-118.47
16	MR16-01*	33.3623	-118.4555
Ollas Fault Zone Blocks (Amphibolite Facies)			
17	CC16-14B*	33.393	-118.418
18	CC16-14D*	33.393	-118.418
Ollas Fault Zone Matrix (Amphibolite Facies)			
19	CC16-14C*	33.393	-118.418
20	CC16-14E*	33.393	-118.418
Amphibolite Facies Blocks in Amphibolite Facies Mélange Zone			
a	E2718C**	33.4152	-118.4422
b	A15-01A	33.4102	-118.4307
c	A15-22	33.3999	-118.4108
d	A15-21A	33.3972	-118.4122
e	A15-07A***	33.4069	-118.4293
Coherent Amphibolite			
f	CA15-06*	33.4092	-118.4434

S1.9 EPMA rutile analyses

Table S1.9.1 Zirconium concentrations in rutile

* Uncertainties reported as 2σ. Grain numbers used for mean maximum concentration highlighted in grey.

LB15-03B

Grain Number	Max Zr	Unc	Mean Max Grain	Unc
1	427	14	757	94
2	809	14		
3	404	19		
4	421	19		
5	570	20		
6	225	17		
7	410	19		
8	775	14		
9	404	9		
10	531	10		
11	595	18		
12	743	11		
13	488	13		
14	373	19		
15	581	18		
16	523	19		
17	699	11		
18	380	18		
19	326	19		
20	346	9		
21	433	9		
22	370	11		
23	383	19		

LB18-10

Grain Number	Max Zr	Unc	Mean Max Grain	Unc
1	327	20	452	82
2	296	19		
3	317	13		
4	403	13		
5	372	13		
6	349	13		
8	218	12		
9	356	18		
10	235	14		
11	167	18		
12	452	18		
13	315	19		
14	321	19		

15	195	20
17	263	9
18	417	17
19	221	16
20	429	20
21	343	17
23	410	18
24	392	20
25	400	18
26	411	13
27	509	14
28	267	18
29	362	14
30	310	19

LB18-04

Grain Number	Max Zr	Unc	Mean Max Grain	Unc
1	264	13	388	108
2	452	19		
3	360	17		
4	411	18		
5	220	18		
9	225	18		
10	218	13		
12	266	17		
13	258	17		
14	253	20		
18	130	10		
19	155	16		
20	160	20		
21	171	13		
22	151	10		
24	189	19		
26	169	21		
27	140	21		
28	329	18		
29	156	22		
31	203	18		
32	184	17		

EA15-05B

Grain Number	Max Zr	Unc	Mean Max Grain	Unc
1	144	12	219	32
2	161	17		
3	108	15		
4	144	21		
5	130	20		
6	175	18		

7	67	29
8	58	46
9	125	17
10	127	26
11	191	18
12	186	12
13	127	13
14	118	10
15	212	18
16	203	19
17	180	19
18	170	20
19	141	11
20	173	10
21	157	9
22	58	23
23	128	18
24	182	19
25	115	12
26	126	16
27	151	9
28	191	12
29	170	12
30	140	9
31	156	8
32	222	10
33	199	10
34	154	10
35	201	9
36	197	14
37	160	11
38	184	9
39	241	18
40	171	16
41	188	13
42	149	19
43	165	16
44	150	22

EA15-01A

Grain Number	Max Zr	Unc	Mean Max Grain	Unc
1	148	36	185	61
2	126	36		
3	141	29		
4	155	30		
5	133	28		
6	163	30		
7	170	34		
8	148	23		

9	192	37
10	200	39
11	126	36
12	200	48
13	148	43
14	222	46
15	178	40
16	163	40
17	215	48
18	252	74
19	185	56

EA15-10A

Grain Number	Max Zr	Unc	Mean Max Grain	Unc
1	144	16	153	20
2	177	16		
3	100	15		
4	152	19		
5	121	14		
6	150	22		
7	126	12		
8	150	19		
9	94	15		
10	156	16		
11	124	19		
12	136	20		
13	80	19		
14	133	20		
15	133	14		
16	121	18		
17	94	12		
18	151	10		
19	145	16		
20	147	19		
21	113	16		
22	115	13		
26	124	17		
27	132	22		
28	133	17		
29	120	16		
30	120	10		
31	91	12		
32	115	18		
33	131	16		
34	110	21		
35	150	17		
36	101	18		
37	126	9		

WB16-03A

Grain Number	Max Zr	Unc	Mean Max Grain	Unc
1	346	13	475	83
2	325	13		
3	382	19		
4	363	13		
5	391	19		
6	295	17		
8	225	10		
9	329	18		
12	306	10		
13	268	10		
14	291	11		
15	277	9		
16	355	17		
17	341	17		
18	278	18		
19	523	19		
20	480	18		
21	258	18		
22	294	17		
23	328	17		
24	250	17		
25	472	18		
26	366	18		
27	423	19		
28	150	15		
29	305	19		
30	358	19		
31	293	17		

MR16-01

Grain Number	Max Zr	Unc	Mean Max Grain	Unc
1	299	19	243	77
2	166	18		
3	213	18		
4	193	22		
5	168	18		
6	128	19		
7	201	17		
8	85	20		
9	171	20		
11	203	17		
13	225	18		
14	233	12		
15	203	11		
16	147	18		

17	190	16
18	207	17
19	181	18
20	166	17
21	192	15
22	201	20
23	186	18
24	117	19
25	209	18
26	212	18
27	187	19
28	175	21

CC16-14B

Grain Number	Max Zr	Unc	Mean Max Grain	Unc
1	334	6	325	20
2	298	12		
3	313	10		
4	319	9		
5	299	10		
6	276	12		
7	233	13		
8	193	20		
9	332	17		

CC16-14D

Grain Number	Max Zr	Unc	Mean Max Grain	Unc
1	293	9	297	15
2	298	17		
3	297	12		
4	246	8		
5	258	10		
6	294	13		
7	311	18		
8	181	12		
9	259	18		
10	222	18		
11	200	20		
13	192	17		
14	289	19		
15	215	18		
16	170	15		
18	178	16		
19	259	18		
20	192	19		
21	178	19		
22	207	19		

CC16-14C

Grain Number	Max Zr	Unc	Mean Max Grain	Unc
1	312	19	344	24
2	301	13		
3	323	19		
4	298	13		
5	363	19		
6	326	12		
7	362	13		
8	210	19		
9	257	19		
10	233	16		
11	215	13		
12	248	17		
13	249	18		
14	252	18		
15	232	18		
16	255	18		
17	201	18		
19	284	13		
20	291	13		
21	310	12		
22	252	13		
23	159	12		
24	324	18		

CC16-14E

Grain Number	Max Zr	Unc	Mean Max Grain	Unc
1	50	32	129	17
2	130	21		
4	121	14		
5	142	14		
6	68	11		
7	71	12		
8	99	10		
9	128	11		
10	78	12		
11	104	18		
13	122	9		
14	75	10		
15	75	12		

A14-71

Grain Number	Max Zr	Unc	Mean Max Grain	Unc
1	169	11	255	22
2	184	12		
3	166	11		
4	221	18		

5	205	8
6	180	9
7	157	9
8	151	9
9	174	13
10	200	19
11	244	16
12	267	18
13	204	13
14	215	13
15	107	12
16	178	19
17	192	18
18	215	18
19	215	13
21	244	18
22	267	18
23	252	16
24	207	18
25	152	13

GB

Grain Number	Max Zr	Unc	Mean Max Grain	Unc
1	155	17	173	34
2	115	15		
4	163	17		
9	126	19		
14	74	27		
15	126	24		
16	119	21		
17	68	15		
18	96	13		
19	113	18		
20	148	13		
21	170	18		
22	163	16		
23	198	18		
24	109	25		
25	155	18		
27	154	20		
28	98	21		
29	81	12		

EA15-02Ba

Grain Number	Max Zr	Unc	Mean Max Grain	Unc
1	104	31	95	36
2	89	32		
3	104	51		

4	96	30
5	59	41
6	126	74
7	104	66
8	89	30
9	89	46

EA13-12

Grain Number	Max Zr	Unc	Mean Max Grain	Unc
1	124	18	144	19
2	89	18		
3	79	18		
4	95	18		
5	77	18		
6	160	18		
7	147	18		
8	138	18		
9	102	18		
10	143	18		
11	140	18		
12	153	18		
13	141	18		
14	144	18		
15	142	18		
16	158	19		
17	141	19		

EA13-7g

Grain Number	Max Zr	Unc	Mean Max Grain	Unc
E1	157	18	152	26
E2	99	18	*E = analysis by EPMA	
E3	103	18	*LA = analysis by LA-ICP-MS	
E4	115	18		
E5	62	18		
E6	68	18		
E7	170	18		
E8	118	18		
E9	134	18		
E10	113	18		
E11	91	18		
E12	93	18		
E13	86	19		
LA1	144	7		
LA2	151	5		
LA3	148	6		
LA4	136	6		
LA5	135	7		
LA6	122	4		

LA7	125	5
LA8	123	4
LA9	128	6
LA10	143	5
LA11	130	4

79841A

Grain Number	Max Zr	Unc	Mean Max Grain	Unc
1	172	18	167	22
2	184	18		
3	176	18		
4	128	18		
7	117	18		
9	139	18		
10	166	18		
12	163	18		
13	173	18		
14	116	18		
15	155	18		
16	150	18		
18	135	18		
19	112	18		
20	103	18		

77842

Grain Number	Max Zr	Unc	Mean Max Grain	Unc
1	105	18	98	23
2	101	18		
3	111	18		
4	88	18		
5	58	18		
6	84	18		

A15-01A

Grain Number	Max Zr	Unc	Mean Max Grain	Unc
1	427	13	417	22
2	405	11		
3	400	18		
4	372	14		
5	424	19		
6	424	19		
7	415	9		
8	340	12		
9	394	12		
10	405	13		
11	363	13		
12	387	11		
13	399	10		

14	410	11		
15	428	11		

A15-21A

Grain Number	Max Zr	Unc	Mean Max Grain	Unc
1	461	8	493	48
2	526	11		
3	484	18		
4	449	8		
5	451	9		
6	469	13		
7	449	10		
8	470	13		
9	455	9		
10	490	8		
11	450	9		
12	463	9		
13	451	10		

A15-22

Grain Number	Max Zr	Unc	Mean Max Grain	Unc
1	487	9	567	66
2	487	9		
3	341	13		
4	531	13		
5	541	10		
6	557	13		
7	340	18		
8	488	13		
9	554	18		
11	509	19		
13	504	11		
14	615	13		
15	486	10		

CA15-06

Grain Number	Max Zr	Unc	Mean Max Grain	Unc
1	449	9	470	21
2	433	9		
3	453	10		
4	488	11		
5	458	14		
6	442	10		
7	458	10		
8	470	13		
9	444	8		
10	479	20		
11	428	18		

12	438	18
13	298	19
14	460	20
15	435	19
16	462	19
17	481	19
18	372	18
19	439	17
20	429	19
21	458	20
22	479	18
23	465	18
24	230	17
25	235	17
26	352	18
27	445	20
28	287	17
29	403	17
30	170	17
31	110	15
33	410	18
34	409	19
35	196	19
36	190	17
37	370	11
38	419	13
39	460	18
40	437	14
41	457	20
42	412	13
44	322	17

E2718C

Grain Number	Max Zr	Unc	Mean Max Grain	Unc
1	487	39	461	39
2	472	27		
3	471	28		
4	468	19		
5	466	39		
6	467	28		
7	464	39		
8	461	28		
9	439	38		
10	420	27		
11	416	38		
12	389	27		
13	374	38		
14	328	38		

15	316	38

Table S1.9.2 Electron probe microanalyzer data for rutile

LB15-03B

Grain	TiO2	ZrO2	Al2O3	FeO	Nb2O5	SiO2	MnO	Ta2O5	V2O3	Total	Zr Unc (%)	Zr (ppm)	Zr Unc (ppm)	Si (ppm)
16	99.36	0.0706	0.01	0.10	0.24	0.00	0.00	0.03	N/A	99.81	3.7	523	19	0
16	98.99	0.0495	0.01	0.11	0.25	0.00	0.00	0.00	N/A	99.41	5.0	366	18	0
16	99.94	0.0590	0.01	0.12	0.22	0.01	0.00	0.00	N/A	100.37	4.3	437	19	44
16	98.77	0.0549	0.01	0.11	0.25	0.00	0.00	0.02	N/A	99.22	4.5	406	18	14
17	99.28	0.0893	0.02	0.11	0.24	0.00	0.03	0.00	N/A	99.76	2.9	661	19	1
17	98.63	0.0903	0.01	0.09	0.23	0.01	0.00	0.00	N/A	99.06	2.7	669	18	24
17	98.79	0.0601	0.01	0.11	0.22	0.00	0.01	0.00	N/A	99.21	4.1	445	18	21
17	99.29	0.0686	0.01	0.09	0.25	0.00	0.00	0.00	N/A	99.71	3.6	508	18	0
18	98.92	0.0324	0.02	0.08	0.24	0.00	0.02	0.02	N/A	99.35	7.9	240	19	0
18	99.25	0.0311	0.02	0.13	0.23	0.00	0.01	0.00	N/A	99.67	7.8	230	18	0
18	98.78	0.0324	0.01	0.12	0.22	0.00	0.00	0.00	N/A	99.16	7.1	240	17	0
18	99.03	0.0513	0.01	0.10	0.19	0.00	0.00	0.13	N/A	99.51	4.9	380	18	0
19	99.22	0.0319	0.01	0.11	0.21	0.00	0.01	0.07	N/A	99.66	7.3	236	17	0
19	98.47	0.0440	0.01	0.11	0.21	0.00	0.02	0.02	N/A	98.89	5.7	326	19	0
19	99.07	0.0343	0.01	0.11	0.22	0.00	0.00	0.07	N/A	99.52	7.0	254	18	16
19	99.53	0.0281	0.01	0.10	0.20	0.01	0.00	0.01	N/A	99.88	8.2	208	17	57
20	99.37	0.0481	0.02	0.12	0.24	0.00	0.01	0.06	N/A	99.88	5.1	356	18	0
20	99.67	0.0457	0.02	0.15	0.22	0.00	0.00	0.00	N/A	100.10	4.9	338	17	13
20	99.35	0.0461	0.02	0.15	0.24	0.01	0.00	0.00	N/A	99.80	5.4	341	19	25
20	99.17	0.0473	0.02	0.10	0.21	0.00	0.00	0.00	N/A	99.55	5.1	350	18	0
21	99.61	0.0598	0.01	0.14	0.23	0.00	0.01	0.02	N/A	100.08	4.1	443	18	0
21	99.45	0.0556	0.01	0.16	0.24	0.00	0.00	0.01	N/A	99.93	4.6	412	19	9
21	99.21	0.0595	0.01	0.16	0.21	0.00	0.02	0.00	N/A	99.68	4.0	440	18	0
21	99.21	0.0592	0.02	0.19	0.21	0.01	0.00	0.00	N/A	99.70	4.2	438	19	41
22	99.18	0.0408	0.01	0.15	0.19	0.00	0.00	0.00	N/A	99.57	5.9	302	18	0
22	98.88	0.0496	0.01	0.11	0.20	0.00	0.00	0.02	N/A	99.28	5.1	367	19	0
22	99.31	0.0492	0.02	0.09	0.21	0.00	0.02	0.00	N/A	99.71	5.4	364	20	0
22	98.68	0.0511	0.02	0.12	0.22	0.00	0.00	0.00	N/A	99.10	4.7	378	18	0

23	98.32	0.0405	0.02	0.12	0.21	0.00	0.03	0.00	N/A	98.75	6.0	300	18	0
23	99.37	0.0448	0.01	0.12	0.19	0.01	0.00	0.04	N/A	99.78	5.9	332	20	33
23	98.78	0.0517	0.00	0.12	0.24	0.00	0.00	0.08	N/A	99.27	5.0	383	19	0
23	98.73	0.0440	0.00	0.10	0.24	0.01	0.03	0.03	N/A	99.19	5.5	326	18	36
17	99.41	0.0326	0.01	0.23	0.25	0.01	0.01	0.00	N/A	99.96	7.5	241	18	43
17	99.26	0.0375	0.01	0.16	0.28	0.01	0.00	0.01	N/A	99.77	6.8	278	19	52
17	99.32	0.0523	0.01	0.11	0.24	0.00	0.00	0.01	N/A	99.74	5.0	387	19	14
17	99.17	0.0562	0.01	0.09	0.21	0.00	0.02	0.00	N/A	99.56	4.2	416	18	0
17	99.81	0.0639	0.02	0.11	0.22	0.01	0.01	0.00	N/A	100.24	3.8	473	18	54
17	99.58	0.0770	0.02	0.12	0.25	0.00	0.00	0.03	N/A	100.08	3.4	570	19	9
17	98.93	0.0800	0.00	0.14	0.23	0.00	0.00	0.02	N/A	99.40	3.2	592	19	0
17	99.11	0.0856	0.02	0.10	0.24	0.00	0.00	0.00	N/A	99.55	3.0	634	19	0
17	99.36	0.0895	0.01	0.08	0.25	0.01	0.00	0.00	N/A	99.80	2.9	663	19	31
17	99.20	0.0946	0.03	0.09	0.25	0.00	0.00	0.00	N/A	99.67	2.7	700	19	0
17	99.81	0.0896	0.02	0.12	0.24	0.00	0.00	0.00	N/A	100.28	2.8	663	18	14
17	99.37	0.0954	0.03	0.09	0.23	0.00	0.00	0.00	N/A	99.81	2.7	706	19	0
17	99.62	0.0932	0.01	0.12	0.23	0.00	0.00	0.07	N/A	100.15	2.7	690	19	20
17	99.32	0.0896	0.01	0.10	0.25	0.01	0.00	0.04	N/A	99.82	2.9	663	19	28
17	99.31	0.0793	0.02	0.10	0.25	0.01	0.00	0.00	N/A	99.77	3.1	587	18	25
17	99.10	0.0650	0.01	0.08	0.26	0.00	0.01	0.02	N/A	99.55	3.8	481	18	20
17	99.43	0.0608	0.01	0.08	0.26	0.01	0.00	0.00	N/A	99.85	4.1	450	18	53
17	99.59	0.0547	0.01	0.10	0.28	0.02	0.03	0.00	N/A	100.08	4.6	405	19	105
17	99.41	0.0299	0.00	0.06	0.11	0.04	0.01	0.05	N/A	99.71	7.9	221	17	176
1	98.59	0.0512	0.10	0.14	0.25	0.00	0.00	0.00	0.39	99.51	4.7	379	18	0
1	97.84	0.0577	0.12	0.15	0.20	0.00	0.00	0.00	0.44	98.82	4.5	427	19	0
1	98.23	0.0577	0.14	0.12	0.24	0.00	0.02	0.00	0.45	99.26	4.7	427	20	0
1	98.69	0.0512	0.13	0.10	0.30	0.00	0.00	0.00	0.45	99.72	5.2	379	20	0
2	97.65	0.1084	0.14	0.32	0.31	0.00	0.00	0.00	0.78	99.31	2.4	803	19	0
2	97.54	0.1102	0.14	0.31	0.26	0.00	0.00	0.00	0.67	99.03	2.4	816	20	0
2	97.77	0.1016	0.13	0.35	0.31	0.00	0.00	0.00	0.72	99.39	2.5	752	19	0
2	97.26	0.0853	0.17	0.47	0.27	0.00	0.00	0.00	0.76	99.02	2.9	631	18	0
3	97.47	0.0546	0.17	0.83	0.27	0.00	0.03	0.00	0.72	99.56	4.7	404	19	0

4	97.88	0.0568	0.14	0.08	0.20	0.00	0.01	0.01	0.63	99.00	4.6	421	19	0
4	97.93	0.0475	0.13	0.08	0.20	0.00	0.04	0.00	0.61	99.04	4.8	352	17	0
4	98.38	0.0508	0.13	0.10	0.20	0.00	0.00	0.00	0.58	99.45	4.6	376	17	0
4	98.23	0.0501	0.13	0.09	0.19	0.00	0.02	0.00	0.64	99.34	5.1	371	19	0
5	97.58	0.0770	0.14	0.26	0.28	0.00	0.00	0.05	0.71	99.09	3.6	570	20	0
5	97.35	0.0660	0.14	0.24	0.24	0.00	0.02	0.01	0.70	98.78	3.8	489	18	0
5	97.48	0.0606	0.13	0.52	0.29	0.00	0.00	0.04	0.69	99.22	4.3	449	19	0
5	97.57	0.0701	0.14	0.34	0.27	0.00	0.01	0.00	0.60	99.00	3.6	519	19	0
6	98.58	0.0182	0.14	0.09	0.19	0.00	0.00	0.01	0.52	99.54	12.8	135	17	0
6	98.74	0.0256	0.14	0.18	0.17	0.01	0.01	0.02	0.60	99.90	11.0	190	21	42
6	98.01	0.0282	0.14	0.08	0.25	0.00	0.00	0.00	0.50	99.01	10.9	209	23	0
6	99.60	0.0326	0.13	0.07	0.26	0.00	0.02	0.05	0.51	100.68	10.3	241	25	0
7	98.98	0.0554	0.14	0.19	0.20	0.00	0.00	0.00	0.30	99.86	4.5	410	19	0
7	98.85	0.0452	0.14	0.16	0.22	0.00	0.00	0.00	0.31	99.72	4.8	335	16	0
7	98.57	0.0460	0.14	0.17	0.20	0.00	0.00	0.00	0.27	99.40	4.6	341	16	0
7	98.91	0.0402	0.13	0.15	0.18	0.00	0.00	0.00	0.34	99.75	7.0	298	21	0
8	98.48	0.0997	0.15	0.45	0.31	0.00	0.00	0.04	0.56	100.09	2.5	738	18	0
8	98.28	0.1064	0.14	0.50	0.31	0.00	0.01	0.00	0.60	99.95	2.6	788	20	0
8	99.11	0.1031	0.16	0.48	0.32	0.00	0.00	0.00	0.59	100.76	2.6	763	20	0
9	98.34	0.0546	0.15	0.14	0.23	0.00	0.00	0.02	0.69	99.63	4.7	404	19	0
9	98.24	0.0543	0.13	0.13	0.22	0.00	0.00	0.06	0.79	99.62	4.0	402	16	0
9	98.55	0.0560	0.14	0.10	0.21	0.01	0.00	0.00	0.75	99.81	4.3	415	18	37
9	97.87	0.0535	0.15	0.17	0.22	0.04	0.00	0.00	0.70	99.19	4.7	396	19	170
10	98.24	0.0688	0.14	0.20	0.29	0.00	0.01	0.00	0.58	99.52	3.4	509	17	0
10	98.09	0.0659	0.14	0.24	0.28	0.00	0.02	0.04	0.64	99.51	3.7	488	18	0
10	98.21	0.0728	0.15	0.23	0.27	0.00	0.02	0.07	0.63	99.66	3.4	539	18	0
10	98.53	0.0735	0.14	0.32	0.24	0.00	0.00	0.03	0.61	99.94	3.5	544	19	0
11	97.74	0.0804	0.18	0.46	0.42	0.00	0.02	0.00	0.53	99.43	3.0	595	18	0
12	98.56	0.1004	0.15	0.13	0.22	0.00	0.01	0.02	0.77	99.97	2.6	743	19	0
12	98.78	0.0985	0.15	0.16	0.23	0.00	0.00	0.00	0.65	100.07	2.7	729	19	0
12	98.28	0.0948	0.16	0.18	0.21	0.00	0.00	0.04	0.72	99.68	2.6	702	18	0
12	98.59	0.0907	0.16	0.21	0.28	0.00	0.00	0.00	0.68	100.02	2.7	671	18	0

12	98.71	0.1023	0.15	0.16	0.22	0.00	0.00	0.00	0.77	100.11	2.6	757	19	0
12	98.12	0.0799	0.15	0.16	0.23	0.00	0.00	0.00	0.70	99.44	3.0	592	18	0
12	98.35	0.0650	0.14	0.13	0.22	0.00	0.01	0.00	0.72	99.65	3.7	481	18	0
12	98.58	0.0453	0.15	0.08	0.24	0.00	0.03	0.00	0.73	99.85	4.9	335	16	0
13	97.91	0.0674	0.15	0.36	0.24	0.00	0.00	0.00	0.68	99.41	3.8	499	19	0
13	97.53	0.0645	0.16	0.29	0.27	0.00	0.01	0.00	0.71	99.02	3.6	478	17	0
13	97.35	0.0610	0.23	0.24	0.26	0.00	0.00	0.00	0.67	98.82	4.1	452	18	0
13	97.23	0.0471	0.15	0.22	0.25	0.00	0.00	0.00	0.72	98.62	5.6	349	19	0
14	98.24	0.0504	0.15	0.57	0.43	0.00	0.01	0.00	0.38	99.81	5.0	373	19	0
15	98.01	0.0785	0.18	0.65	0.23	0.00	0.04	0.00	0.57	99.75	3.1	581	18	0

LB18-10

Grain	TiO2	ZrO2	Al2O3	FeO	Nb2O5	SiO2	MnO	Ta2O5	V2O3	Total	Zr Unc (%)	Zr (ppm)	Zr Unc (ppm)	Si (ppm)
1	98.75	0.0442	0.05	0.50	0.34	0.03	0.02	0.02	0.51	100.26	6.1	327	20	137
2	98.31	0.0400	0.07	0.12	0.20	0.00	0.00	0.03	0.79	99.55	6.6	296	19	0
3	99.00	0.0407	0.14	0.12	0.19	0.00	0.00	0.00	0.69	100.18	5.9	301	18	0
3	99.00	0.0450	0.09	0.11	0.18	0.00	0.00	0.00	0.69	100.10	5.4	333	18	0
3	99.08	0.0347	0.06	0.08	0.16	0.01	0.00	0.02	0.75	100.19	6.0	257	16	47
4	98.92	0.0551	0.03	0.42	0.37	0.01	0.01	0.00	0.79	100.60	4.7	408	19	25
4	98.54	0.0537	0.05	0.45	0.38	0.00	0.01	0.05	0.80	100.33	4.8	398	19	0
5	98.82	0.0524	0.04	0.12	0.27	0.00	0.03	0.01	0.68	100.04	4.9	388	19	0
5	98.58	0.0481	0.04	0.12	0.29	0.00	0.02	0.00	0.61	99.71	5.1	356	18	0
6	99.21	0.0455	0.03	0.08	0.21	0.02	0.00	0.00	0.71	100.28	5.5	337	18	72
6	99.60	0.0488	0.04	0.08	0.23	0.04	0.04	0.00	0.72	100.80	4.8	361	17	167
8	98.75	0.0279	0.03	0.22	0.41	0.00	0.00	0.07	0.82	100.32	7.8	207	16	2
8	99.30	0.0309	0.05	0.16	0.34	0.00	0.00	0.00	0.74	100.62	7.8	229	18	0
8	98.94	0.0257	0.03	0.13	0.31	0.00	0.03	0.00	0.77	100.24	9.1	190	17	0
9	98.90	0.0481	0.08	0.62	0.22	0.03	0.00	0.00	0.20	100.10	4.9	356	18	132
10	99.84	0.0324	0.05	0.15	0.27	0.00	0.03	0.00	0.62	101.01	9.1	240	22	0
10	99.42	0.0310	0.09	0.19	0.26	0.00	0.01	0.02	0.63	100.66	7.1	229	16	0
10	99.22	0.0256	0.06	0.29	0.33	0.00	0.00	0.01	0.63	100.57	9.9	190	19	16

11	98.29	0.0225	0.05	0.08	0.35	0.04	0.00	0.02	0.58	99.44	11.0	167	18	198
12	98.32	0.0610	0.07	0.46	0.41	0.00	0.00	0.07	0.55	99.94	3.9	452	18	0
13	98.09	0.0426	0.13	0.45	0.44	0.00	0.00	0.00	0.60	99.76	5.9	315	19	0
14	98.92	0.0434	0.04	0.59	0.18	0.00	0.01	0.00	0.29	100.09	5.8	321	19	14
15	98.11	0.0263	0.03	0.18	0.14	0.01	0.00	0.00	0.63	99.13	10.3	195	20	66
17	98.24	0.0344	0.02	0.07	0.25	0.01	0.00	0.00	0.83	99.46	6.9	255	18	62
17	98.52	0.0363	0.02	0.09	0.25	0.01	0.00	0.01	0.84	99.77	6.8	269	18	23
17	99.02	0.0335	0.01	0.10	0.26	0.00	0.03	0.00	0.80	100.25	7.4	248	18	6
17	98.58	0.0381	0.02	0.08	0.27	0.00	0.02	0.03	0.83	99.86	5.8	282	16	17
18	99.75	0.0563	0.04	0.68	0.20	0.01	0.00	0.00	0.27	101.01	4.2	417	17	57
19	98.73	0.0299	0.08	0.93	0.18	0.02	0.02	0.04	0.36	100.40	7.4	221	16	79
20	99.10	0.0580	0.06	0.68	0.51	0.01	0.00	0.03	0.51	100.96	4.6	429	20	52
21	99.17	0.0350	0.03	0.44	0.36	0.02	0.00	0.00	0.60	100.66	6.6	259	17	113
21	98.93	0.0463	0.04	0.43	0.35	0.02	0.03	0.01	0.61	100.45	5.0	343	17	106
23	98.02	0.0554	0.04	0.84	0.28	0.01	0.00	0.01	0.59	99.85	4.5	410	18	54
24	98.21	0.0530	0.06	0.78	0.41	0.02	0.01	0.04	0.66	100.24	5.0	392	20	94
25	98.78	0.0540	0.11	0.55	0.33	0.00	0.01	0.00	0.61	100.44	4.4	400	18	0
26	98.48	0.0546	0.07	0.61	0.31	0.00	0.01	0.01	0.72	100.27	4.5	404	18	6
26	98.60	0.0564	0.08	0.66	0.29	0.00	0.02	0.02	0.74	100.46	4.5	418	19	0
27	98.65	0.0663	0.09	0.44	0.43	0.00	0.00	0.00	0.72	100.40	3.8	491	18	0
27	98.47	0.0713	0.05	0.46	0.46	0.00	0.02	0.03	0.82	100.40	3.8	528	20	18
28	98.70	0.0361	0.03	0.28	0.22	0.05	0.04	0.00	0.73	100.08	6.8	267	18	230
29	99.72	0.0500	0.03	0.14	0.25	0.00	0.00	0.00	0.65	100.85	5.5	370	20	0
29	99.12	0.0477	0.06	0.16	0.22	0.01	0.00	0.00	0.68	100.29	5.4	353	19	29
29	99.75	0.0260	0.03	0.18	0.13	0.00	0.01	0.09	0.70	100.92	8.4	192	16	15
30	99.75	0.0419	0.03	0.12	0.18	0.03	0.00	0.00	0.72	100.88	6.3	310	19	154
30	100.21	0.0365	0.03	0.10	0.25	0.02	0.01	0.00	0.68	101.33	7.2	270	20	84
30	99.53	0.0295	0.03	0.13	0.23	0.03	0.00	0.00	0.65	100.63	8.2	218	18	151

LB18-04

Grain	TiO2	ZrO2	Al2O3	FeO	Nb2O5	SiO2	MnO	Ta2O5	V2O3	Total	Zr Unc (%)	Zr (ppm)	Zr Unc (ppm)	Si (ppm)
1	99.86	0.0286	0.07	0.54	0.07	0.01	0.02	0.00	0.25	100.84	8.7	212	18	30
1	99.83	0.0338	0.06	0.59	0.08	0.01	0.01	0.00	0.27	100.88	7.8	250	20	37
1	100.36	0.0374	0.04	0.57	0.06	0.01	0.01	0.05	0.35	101.48	6.2	277	17	53
2	99.17	0.0610	0.05	0.71	0.09	0.01	0.04	0.00	0.23	100.37	4.2	452	19	53
3	99.39	0.0486	0.05	0.62	0.39	0.02	0.00	0.00	0.22	100.73	4.9	360	17	88
4	99.11	0.0555	0.03	0.79	0.25	0.01	0.01	0.00	0.29	100.55	4.5	411	18	48
5	100.43	0.0297	0.04	0.66	0.05	0.02	0.01	0.00	0.30	101.53	8.1	220	18	96
9	99.65	0.0304	0.02	0.70	0.08	0.02	0.00	0.01	0.26	100.77	7.8	225	18	85
10	100.52	0.0251	0.03	0.50	0.04	0.02	0.01	0.00	0.33	101.48	10.1	186	19	90
10	100.17	0.0306	0.03	0.49	0.06	0.01	0.00	0.00	0.27	101.07	8.0	227	18	60
10	100.33	0.0284	0.02	0.47	0.09	0.02	0.01	0.05	0.33	101.35	9.2	210	19	103
12	99.78	0.0359	0.04	0.54	0.05	0.00	0.01	0.00	0.20	100.65	6.6	266	17	0
12	100.30	0.0212	0.04	0.55	0.10	0.00	0.01	0.00	0.25	101.27	11.5	157	18	7
12	99.63	0.0224	0.05	0.47	0.04	0.00	0.00	0.00	0.21	100.42	10.8	166	18	0
12	99.83	0.0279	0.03	0.55	0.06	0.00	0.00	0.05	0.29	100.84	8.7	207	18	0
13	98.54	0.0348	0.07	0.65	0.15	0.03	0.00	0.00	0.28	99.75	6.7	258	17	125
14	98.14	0.0342	0.04	0.32	0.05	0.05	0.02	0.03	0.36	99.04	8.0	253	20	223
18	99.74	0.0170	0.03	0.60	0.06	0.01	0.00	0.01	0.27	100.74	14.8	126	19	58
18	99.98	0.0180	0.02	0.59	0.04	0.00	0.01	0.00	0.27	100.93	10.3	133	14	20
18	99.71	0.0178	0.02	0.65	0.08	0.00	0.00	0.00	0.20	100.69	15.4	132	20	14
19	99.64	0.0210	0.03	0.68	0.04	0.01	0.01	0.00	0.27	100.70	10.4	155	16	48
20	99.55	0.0216	0.04	0.76	0.08	0.00	0.00	0.00	0.25	100.71	12.5	160	20	23
21	99.91	0.0218	0.02	0.51	0.09	0.01	0.00	0.00	0.28	100.84	11.3	161	18	59
21	99.83	0.0244	0.03	0.48	0.16	0.02	0.01	0.04	0.30	100.88	10.5	181	19	89
22	99.97	0.0203	0.03	0.48	0.04	0.00	0.01	0.00	0.20	100.74	11.4	150	17	0
22	100.23	0.0220	0.02	0.51	0.02	0.00	0.02	0.02	0.27	101.11	10.9	163	18	0
22	99.41	0.0190	0.02	0.49	0.01	0.00	0.00	0.00	0.26	100.19	12.7	141	18	0
24	99.07	0.0255	0.05	0.74	0.06	0.00	0.01	0.00	0.35	100.31	9.9	189	19	0
24	98.86	0.0184	0.03	0.58	0.07	0.00	0.00	0.02	0.37	99.94	12.4	136	17	0
24	98.66	0.0194	0.03	0.55	0.08	0.01	0.00	0.00	0.41	99.75	12.5	144	18	26
26	99.40	0.0228	0.04	0.70	0.02	0.01	0.01	0.00	0.23	100.44	12.7	169	21	58

27	98.93	0.0189	0.05	0.63	0.00	0.02	0.03	0.00	0.38	100.07	14.7	140	21	85
28	98.78	0.0445	0.05	0.73	0.44	0.01	0.00	0.00	0.33	100.40	5.4	329	18	63
29	99.35	0.0211	0.04	0.50	0.00	0.03	0.00	0.00	0.22	100.16	13.8	156	22	131
31	98.91	0.0274	0.03	0.55	0.05	0.04	0.02	0.00	0.28	99.91	9.1	203	18	173
32	99.31	0.0248	0.05	0.57	0.00	0.01	0.00	0.00	0.16	100.12	9.2	184	17	45

EA15-05B

Grain	TiO2	ZrO2	Al2O3	FeO	Nb2O5	SiO2	MnO	Ta2O5	V2O3	Total	Zr Unc (%)	Zr (ppm)	Zr Unc (ppm)	Si (ppm)
1	97.54	0.0212	0.14	0.18	0.25	0.00	0.00	0.00	0.14	98.27	10.9	157	17	0
1	97.87	0.0150	0.14	0.20	0.23	0.00	0.00	0.00	0.13	98.59	15.5	111	17	0
1	97.46	0.0177	0.14	0.17	0.28	0.00	0.00	0.04	0.15	98.26	12.6	131	16	0
2	97.53	0.0217	0.15	0.20	0.29	0.00	0.00	0.00	0.03	98.23	10.8	161	17	20
3	98.06	0.0138	0.15	0.24	0.27	0.00	0.00	0.00	0.07	98.81	24.2	102	25	0
3	97.90	0.0153	0.15	0.22	0.23	0.00	0.00	0.00	0.13	98.64	13.4	113	15	0
4	98.02	0.0195	0.14	0.17	0.26	0.00	0.00	0.03	0.13	98.76	14.2	144	21	0
5	97.95	0.0176	0.14	0.18	0.29	0.00	0.02	0.06	0.14	98.81	15.4	130	20	0
6	99.68	0.0112	0.15	0.20	0.26	0.00	0.04	0.00	0.18	100.51	18.3	83	15	0
6	97.64	0.0150	0.14	0.22	0.26	0.00	0.00	0.00	0.11	98.39	14.4	111	16	0
7	97.29	0.0042	0.14	0.19	0.21	0.00	0.00	0.00	0.08	97.91	38.2	31	12	0
7	97.66	0.0139	0.14	0.15	0.19	0.00	0.00	0.00	0.12	98.28	15.6	103	16	0
7	97.26	0.0043	0.15	0.22	0.20	0.00	0.00	0.00	0.03	97.86	178.0	32	57	0
8	98.49	0.0078	0.14	0.26	0.18	0.00	0.00	0.00	0.11	99.18	80.0	58	46	0
9	98.55	0.0169	0.15	0.24	0.18	0.00	0.01	0.00	0.12	99.27	13.2	125	17	0
10	98.08	0.0171	0.14	0.21	0.19	0.00	0.01	0.07	0.17	98.88	20.2	127	26	0
11	98.38	0.0201	0.15	0.20	0.19	0.00	0.02	0.12	0.11	99.18	12.1	149	18	0
11	97.71	0.0258	0.15	0.18	0.22	0.00	0.00	0.01	0.15	98.44	9.5	191	18	0
12	98.18	0.0264	0.16	0.23	0.26	0.00	0.01	0.04	0.15	99.05	9.4	195	18	0
12	98.36	0.0239	0.15	0.24	0.27	0.00	0.00	0.04	0.14	99.22	9.1	177	16	0
13	98.28	0.0185	0.15	0.27	0.26	0.00	0.00	0.06	0.16	99.20	12.6	137	17	0
13	98.30	0.0159	0.14	0.31	0.26	0.00	0.00	0.09	0.17	99.29	16.2	118	19	0
14	97.35	0.0142	0.14	0.15	0.24	0.00	0.02	0.00	0.16	98.08	14.0	105	15	0

14	97.73	0.0178	0.14	0.17	0.21	0.00	0.00	0.00	0.16	98.44	11.0	132	15	0
15	97.84	0.0286	0.15	0.25	0.27	0.00	0.00	0.06	0.15	98.74	8.3	212	18	0
16	98.61	0.0274	0.16	0.23	0.24	0.00	0.02	0.00	0.16	99.45	9.6	203	19	0
6	98.80	0.0237	0.16	0.21	0.26	0.00	0.00	0.00	0.07	99.52	10.3	175	18	0
16	99.36	0.0066	0.14	0.19	0.23	0.00	0.00	0.02	0.08	100.03	33.8	49	17	0
16	99.26	0.0115	0.15	0.22	0.21	0.00	0.00	0.00	0.12	99.96	32.7	85	28	0
17	97.35	0.0243	0.16	0.16	0.25	0.00	0.00	0.04	0.14	98.13	10.7	180	19	0
18	97.69	0.0230	0.16	0.17	0.26	0.00	0.01	0.00	0.10	98.40	11.6	170	20	0
19	97.39	0.0192	0.15	0.19	0.26	0.00	0.01	0.07	0.21	98.29	11.6	142	16	0
19	97.33	0.0188	0.14	0.19	0.26	0.00	0.01	0.07	0.18	98.18	11.1	139	15	0
19	97.52	0.0097	0.16	0.17	0.26	0.00	0.00	0.09	0.19	98.39	33.1	72	24	0
20	97.58	0.0099	0.15	0.19	0.24	0.00	0.00	0.00	0.13	98.29	27.9	73	20	0
20	97.53	0.0254	0.14	0.15	0.31	0.00	0.00	0.10	0.16	98.42	10.3	188	19	0
20	97.65	0.0208	0.15	0.20	0.28	0.00	0.00	0.01	0.13	98.43	11.6	154	18	0
20	97.41	0.0239	0.14	0.19	0.27	0.00	0.01	0.00	0.09	98.15	8.0	177	14	0
21	97.77	0.0216	0.15	0.19	0.27	0.00	0.00	0.00	0.13	98.55	11.4	160	18	0
21	97.63	0.0195	0.15	0.24	0.28	0.00	0.00	0.03	0.14	98.48	11.6	144	17	0
21	97.91	0.0213	0.15	0.20	0.28	0.00	0.00	0.00	0.08	98.64	11.0	158	17	0
21	97.44	0.0226	0.16	0.19	0.26	0.00	0.01	0.04	0.15	98.26	10.0	167	17	0
22	95.99	0.0078	0.16	0.20	0.21	0.00	0.01	0.03	0.15	96.75	39.0	58	23	0
23	96.42	0.0173	0.15	0.18	0.22	0.00	0.01	0.00	0.18	97.19	14.4	128	18	0
24	96.51	0.0246	0.15	0.17	0.22	0.00	0.00	0.03	0.10	97.19	10.7	182	19	0
25	95.68	0.0164	0.14	0.22	0.27	0.00	0.00	0.02	0.13	96.47	14.7	121	18	0
25	95.85	0.0146	0.15	0.18	0.29	0.00	0.01	0.14	0.10	96.74	14.3	108	15	0
26	94.66	0.0088	0.15	0.17	0.20	0.00	0.00	0.00	0.12	95.30	59.4	65	39	0
26	95.32	0.0170	0.14	0.16	0.19	0.00	0.01	0.09	0.13	96.06	12.7	126	16	0
26	94.85	0.0107	0.15	0.21	0.22	0.00	0.02	0.00	0.04	95.49	21.3	79	17	0
26	95.27	0.0047	0.15	0.13	0.22	0.00	0.00	0.00	0.08	95.84	41.1	35	14	0
27	99.53	0.0217	0.15	0.34	0.31	0.00	0.01	0.00	0.20	100.56	11.3	161	18	0
27	99.44	0.0201	0.15	0.30	0.30	0.00	0.01	0.07	0.26	100.56	9.6	149	14	0
27	99.21	0.0197	0.15	0.23	0.26	0.00	0.00	0.00	0.19	100.05	13.9	146	20	0
27	99.23	0.0200	0.16	0.33	0.29	0.00	0.01	0.00	0.26	100.31	11.2	148	17	0

28	99.69	0.0269	0.15	0.38	0.22	0.00	0.02	0.04	0.21	100.73	8.8	199	17	0
28	99.17	0.0247	0.16	0.30	0.24	0.00	0.00	0.00	0.24	100.13	9.6	183	18	0
28	100.12	0.0190	0.16	0.32	0.33	0.00	0.03	0.00	0.23	101.20	10.6	141	15	0
29	100.15	0.0238	0.15	0.30	0.32	0.00	0.00	0.00	0.21	101.15	10.1	176	18	0
29	99.91	0.0222	0.17	0.29	0.26	0.00	0.00	0.03	0.27	100.96	10.2	164	17	0
30	99.62	0.0182	0.16	0.39	0.42	0.00	0.02	0.01	0.27	100.90	12.6	135	17	0
30	100.01	0.0190	0.15	0.35	0.42	0.00	0.00	0.00	0.18	101.13	13.4	141	19	0
30	99.46	0.0179	0.15	0.36	0.43	0.00	0.00	0.02	0.20	100.62	13.0	133	17	0
30	99.58	0.0206	0.15	0.37	0.38	0.00	0.00	0.04	0.22	100.75	14.6	153	22	0
31	99.31	0.0222	0.15	0.31	0.30	0.00	0.02	0.05	0.23	100.39	10.3	164	17	0
31	99.32	0.0206	0.15	0.33	0.30	0.00	0.01	0.05	0.23	100.40	11.3	153	17	0
31	99.33	0.0198	0.16	0.35	0.30	0.00	0.00	0.00	0.24	100.40	10.8	147	16	0
31	99.64	0.0215	0.15	0.30	0.28	0.00	0.00	0.00	0.20	100.60	11.0	159	18	0
32	100.25	0.0306	0.16	0.48	0.23	0.00	0.00	0.02	0.13	101.30	7.9	227	18	0
32	99.83	0.0254	0.16	0.50	0.25	0.04	0.00	0.00	0.19	100.99	9.3	188	18	171
32	99.78	0.0282	0.17	0.46	0.26	0.00	0.03	0.03	0.15	100.91	7.5	209	16	0
32	100.24	0.0313	0.15	0.46	0.27	0.00	0.01	0.00	0.08	101.25	7.5	232	17	0
33	99.29	0.0261	0.16	0.39	0.24	0.00	0.00	0.05	0.18	100.34	10.2	193	20	0
33	99.55	0.0285	0.16	0.41	0.23	0.00	0.00	0.00	0.15	100.53	9.8	211	21	3
33	99.73	0.0255	0.14	0.41	0.27	0.00	0.00	0.00	0.16	100.73	9.3	189	17	0
33	99.51	0.0276	0.15	0.42	0.26	0.02	0.00	0.00	0.10	100.49	8.9	204	18	80
34	99.80	0.0212	0.15	0.28	0.29	0.00	0.03	0.00	0.22	100.80	12.9	157	20	0
34	100.01	0.0231	0.15	0.35	0.27	0.00	0.03	0.00	0.11	100.93	9.8	171	17	0
34	99.33	0.0206	0.15	0.25	0.29	0.00	0.00	0.05	0.31	100.40	11.7	153	18	0
34	99.43	0.0181	0.16	0.26	0.26	0.00	0.00	0.07	0.38	100.57	15.6	134	21	0
35	99.58	0.0277	0.15	0.32	0.24	0.01	0.00	0.04	0.16	100.52	7.6	205	16	32
35	100.09	0.0251	0.15	0.38	0.26	0.00	0.00	0.00	0.17	101.08	8.0	186	15	0
35	99.63	0.0286	0.16	0.35	0.26	0.00	0.00	0.00	0.15	100.57	8.7	212	18	13
36	99.55	0.0220	0.15	0.46	0.27	0.00	0.00	0.03	0.17	100.64	9.3	163	15	0
36	99.48	0.0271	0.15	0.39	0.25	0.00	0.01	0.07	0.22	100.61	10.8	201	22	0
36	99.79	0.0204	0.15	0.35	0.27	0.00	0.03	0.02	0.30	100.92	9.8	151	15	0
36	99.69	0.0260	0.16	0.39	0.26	0.00	0.02	0.08	0.23	100.85	9.8	192	19	0

37	99.72	0.0240	0.14	0.39	0.25	0.00	0.01	0.00	0.16	100.69	10.0	178	18	0
37	99.33	0.0159	0.15	0.39	0.24	0.00	0.00	0.02	0.21	100.35	16.7	118	20	0
37	99.23	0.0214	0.15	0.37	0.29	0.00	0.01	0.13	0.22	100.42	11.1	158	18	0
37	98.99	0.0194	0.14	0.36	0.25	0.00	0.00	0.01	0.18	99.96	14.7	144	21	0
38	99.61	0.0268	0.15	0.40	0.36	0.00	0.00	0.00	0.23	100.78	8.6	198	17	0
38	99.48	0.0239	0.16	0.38	0.42	0.00	0.00	0.03	0.25	100.74	10.1	177	18	0
38	100.06	0.0248	0.14	0.34	0.38	0.00	0.00	0.00	0.23	101.18	10.9	184	20	0
38	99.86	0.0241	0.15	0.36	0.39	0.00	0.02	0.00	0.20	101.00	11.6	178	21	0
39	99.48	0.0325	0.15	0.42	0.25	0.00	0.00	0.05	0.28	100.66	7.5	241	18	0
40	99.27	0.0231	0.15	0.45	0.22	0.00	0.04	0.00	0.12	100.27	9.6	171	16	0
41	99.26	0.0236	0.15	0.42	0.24	0.03	0.00	0.00	0.20	100.33	10.3	175	18	158
41	99.31	0.0271	0.15	0.46	0.26	0.02	0.00	0.11	0.26	100.57	9.2	201	18	79
42	99.37	0.0201	0.15	0.41	0.26	0.02	0.02	0.00	0.10	100.35	12.8	149	19	116
43	99.45	0.0223	0.15	0.39	0.26	0.00	0.01	0.03	0.11	100.43	9.9	165	16	0
44	99.36	0.0202	0.15	0.34	0.27	0.00	0.00	0.00	0.15	100.28	14.4	150	22	0

EA15-01

Grain	TiO2	ZrO2	Al2O3	FeO	Nb2O5	SiO2	MnO	Ta2O5	V2O3	Total	Zr Unc (%)	Zr (ppm)	Zr Unc (ppm)	Si (ppm)
1	97.834	0.02	0.01	0.18	0.05	0.022	0.019	0	0.39	98.528	24.6	148	36	103
2	99.375	0.017	0.009	0.295	0.005	0.023	0.002	0	0.48	100.205	28.8	126	36	108
3	98.291	0.019	0.006	0.232	0.021	0.011	0	0	0.46	99.041	20.7	141	29	51
4	99.383	0.021	0.017	0.27	0.018	0	0	0.055	0.37	100.131	19.5	155	30	0
5	97.934	0.018	0.003	0.206	0.008	0.002	0.029	0	0.42	98.618	20.9	133	28	9
6	96.785	0.022	0.007	0.219	0.015	0	0	0	0.28	97.331	18.6	163	30	0
7	95.743	0.023	0.008	0.166	0.02	0	0.019	0	0.43	96.406	20.2	170	34	0
8	96.449	0.02	0.017	0.249	0.024	0.006	0.017	0.004	0.42	97.205	15.6	148	23	28
9	95.758	0.026	0.002	0.274	0.008	0.007	0	0	0.44	96.517	19.1	192	37	33
10	94.549	0.027	0.003	0.286	0.034	0.015	0	0	0.48	95.398	19.4	200	39	70
11	98.67	0.017	0.018	0.24	0.047	0.018	0.03	0	0.50	99.542	28.7	126	36	84
12	98.401	0.027	0.009	0.255	0.017	0.004	0	0	0.48	99.198	23.9	200	48	19
13	98.97	0.02	0.012	0.332	0.015	0.004	0	0	0.35	99.7	28.8	148	43	19

14	99.705	0.03	0	0.196	0	0.015	0	0	0.50	100.45	20.7	222	46	70
15	98.377	0.024	0.013	0.214	0.009	0	0	0	0.37	99.011	22.4	178	40	0
16	98.661	0.022	0.01	0.153	0.035	0.021	0.016	0	0.45	99.364	24.7	163	40	98
17	98.268	0.029	0.004	0.268	0.013	0.036	0	0	0.40	99.02	22.5	215	48	168
18	98.386	0.034	0.011	0.169	0.058	0.014	0	0.044	0.47	99.185	29.3	252	74	65
19	99.005	0.025	0.009	0.261	0.096	0.023	0	0.017	0.22	99.653	30.0	185	56	108

EA15-10A

Grain	TiO2	ZrO2	Al2O3	FeO	Nb2O5	SiO2	MnO	Ta2O5	V2O3	Total	Zr Unc (%)	Zr (ppm)	Zr Unc (ppm)	Si (ppm)
1	99.12	0.0194	0.02	0.24	0.02	0.05	0.02	0.00	0.38	99.88	11.3	144	16	216
2	99.94	0.0239	0.01	0.20	0.03	0.04	0.01	0.00	0.43	100.68	9.3	177	16	169
3	98.92	0.0135	0.01	0.21	0.01	0.03	0.01	0.00	0.41	99.63	15.3	100	15	137
4	99.53	0.0205	0.01	0.24	0.04	0.01	0.00	0.00	0.49	100.35	12.3	152	19	67
5	98.94	0.0164	0.02	0.31	0.04	0.02	0.00	0.00	0.46	99.80	11.3	121	14	93
6	98.37	0.0202	0.01	0.29	0.00	0.03	0.00	0.00	0.40	99.12	15.0	150	22	130
7	99.24	0.0160	0.01	0.19	0.00	0.02	0.00	0.00	0.42	99.90	14.5	118	17	98
7	99.15	0.0180	0.01	0.17	0.02	0.01	0.00	0.00	0.41	99.78	12.4	133	17	38
8	99.67	0.0202	0.01	0.23	0.04	0.01	0.00	0.00	0.42	100.40	12.6	150	19	46
9	100.06	0.0127	0.00	0.22	0.00	0.02	0.00	0.04	0.42	100.77	15.7	94	15	88
9	99.85	0.0073	0.02	0.21	0.00	0.03	0.00	0.00	0.37	100.48	23.6	54	13	133
10	100.08	0.0211	0.02	0.14	0.01	0.02	0.04	0.05	0.40	100.78	10.0	156	16	73
11	99.85	0.0168	0.02	0.20	0.01	0.06	0.00	0.00	0.37	100.53	15.0	124	19	289
12	100.22	0.0184	0.02	0.22	0.00	0.01	0.01	0.00	0.37	100.86	14.8	136	20	42
13	99.83	0.0108	0.02	0.23	0.00	0.04	0.01	0.00	0.29	100.42	23.4	80	19	169
14	99.96	0.0180	0.01	0.20	0.01	0.02	0.00	0.02	0.30	100.55	15.0	133	20	104
15	99.68	0.0179	0.02	0.17	0.00	0.02	0.00	0.00	0.39	100.30	10.9	133	14	79
16	99.79	0.0163	0.01	0.13	0.02	0.01	0.03	0.00	0.44	100.44	14.5	121	18	66
17	99.71	0.0146	0.03	0.20	0.00	0.05	0.01	0.04	0.41	100.46	15.7	108	17	241
17	99.53	0.0107	0.03	0.17	0.00	0.06	0.00	0.05	0.39	100.24	20.8	79	17	281
18	99.71	0.0217	0.02	0.44	0.02	0.02	0.01	0.00	0.36	100.60	10.5	161	17	100
18	99.62	0.0213	0.02	0.31	0.02	0.00	0.00	0.00	0.39	100.39	10.4	158	16	22

18	100.25	0.0181	0.03	0.37	0.01	0.00	0.00	0.00	0.43	101.11	12.3	134	16	0
19	99.71	0.0196	0.03	0.66	0.02	0.01	0.00	0.00	0.42	100.88	11.3	145	16	54
20	99.87	0.0199	0.03	0.72	0.03	0.05	0.00	0.00	0.44	101.17	12.7	147	19	229
21	98.05	0.0153	0.02	0.60	0.01	0.01	0.03	0.00	0.31	99.05	13.7	113	16	65
22	99.75	0.0138	0.02	0.58	0.03	0.01	0.03	0.00	0.31	100.74	18.6	102	19	50
22	100.02	0.0076	0.02	0.63	0.00	0.01	0.00	0.07	0.36	101.10	22.3	56	13	32
22	100.29	0.0174	0.02	0.55	0.03	0.02	0.00	0.00	0.30	101.24	12.8	129	17	110
26	99.42	0.0167	0.01	0.69	0.01	0.03	0.00	0.00	0.41	100.59	14.1	124	17	130
27	99.41	0.0178	0.03	0.67	0.01	0.03	0.00	0.04	0.40	100.60	17.0	132	22	142
28	99.56	0.0180	0.02	0.53	0.02	0.00	0.01	0.00	0.40	100.56	13.1	133	17	0
29	99.71	0.0162	0.03	0.61	0.04	0.01	0.06	0.00	0.31	100.79	13.5	120	16	64
30	99.99	0.0171	0.02	0.42	0.09	0.01	0.04	0.04	0.36	100.98	14.9	127	19	45
30	100.14	0.0141	0.03	0.46	0.09	0.00	0.01	0.00	0.31	101.04	18.7	104	20	21
30	99.82	0.0174	0.02	0.42	0.07	0.02	0.02	0.00	0.31	100.69	12.0	129	15	77
31	100.32	0.0129	0.01	0.49	0.00	0.01	0.02	0.00	0.33	101.19	16.8	96	16	51
31	100.44	0.0128	0.02	0.46	0.02	0.02	0.02	0.00	0.33	101.32	20.3	95	19	87
31	100.93	0.0111	0.02	0.46	0.00	0.01	0.01	0.00	0.33	101.76	29.8	82	24	69
32	99.36	0.0155	0.03	0.96	0.01	0.04	0.00	0.00	0.34	100.76	15.5	115	18	200
33	98.82	0.0177	0.03	0.75	0.05	0.02	0.02	0.00	0.33	100.03	12.5	131	16	107
34	98.52	0.0148	0.01	0.81	0.03	0.02	0.00	0.03	0.34	99.79	18.7	110	21	95
35	99.48	0.0202	0.01	0.49	0.02	0.01	0.04	0.02	0.29	100.39	11.4	150	17	62
36	98.73	0.0137	0.02	0.33	0.02	0.01	0.05	0.02	0.34	99.53	17.7	101	18	60
37	99.21	0.0163	0.01	0.07	0.01	0.02	0.04	0.00	0.37	99.76	14.8	121	18	115
37	99.19	0.0178	0.01	0.12	0.00	0.02	0.04	0.00	0.43	99.82	12.9	132	17	73
37	99.03	0.0169	0.02	0.13	0.03	0.02	0.00	0.00	0.43	99.67	11.4	125	14	73

CC16-14B

Grain	TiO2	ZrO2	Al2O3	FeO	Nb2O5	SiO2	MnO	Ta2O5	V2O3	Total	Zr Unc (%)	Zr (ppm)	Zr Unc (ppm)	Si (ppm)
1	99.20	0.0265	0.13	0.49	0.51	0.00	0.00	0.06	0.00	100.41	9.9	196	19	0
1	99.59	0.0478	0.13	0.31	0.13	0.00	0.02	0.06	0.00	100.29	5.2	354	18	0
1	99.67	0.0450	0.13	0.33	0.11	0.00	0.00	0.00	0.00	100.28	5.6	333	19	0

1	99.39	0.0460	0.14	0.27	0.07	0.00	0.00	0.00	0.00	99.92	5.8	341	20	0
1	99.35	0.0440	0.14	0.31	0.07	0.00	0.01	0.06	0.00	99.98	5.4	326	18	0
1	99.50	0.0428	0.14	0.30	0.09	0.00	0.02	0.00	0.00	100.09	5.7	317	18	0
1	99.53	0.0401	0.14	0.27	0.11	0.00	0.00	0.00	0.00	100.09	5.7	297	17	0
1	99.45	0.0368	0.14	0.32	0.09	0.00	0.00	0.00	0.00	100.03	6.2	272	17	0
1	99.49	0.0398	0.14	0.30	0.11	0.00	0.00	0.00	0.00	100.07	6.2	295	18	0
1	99.61	0.0432	0.15	0.29	0.09	0.00	0.02	0.00	0.00	100.20	5.4	320	17	0
1	99.68	0.0471	0.15	0.29	0.12	0.00	0.00	0.00	0.00	100.29	5.0	349	18	0
1	100.03	0.0441	0.15	0.31	0.08	0.00	0.00	0.00	0.00	100.61	5.3	326	17	0
1	99.61	0.0444	0.15	0.28	0.08	0.00	0.00	0.00	0.00	100.15	5.3	329	17	0
1	99.64	0.0444	0.16	0.29	0.08	0.00	0.00	0.00	0.01	100.22	5.3	329	17	0
1	99.78	0.0455	0.16	0.33	0.21	0.00	0.01	0.01	0.00	100.55	5.3	337	18	0
2	99.53	0.0425	0.14	0.40	0.16	0.00	0.00	0.00	0.01	100.28	5.6	315	18	0
2	99.82	0.0345	0.16	0.38	0.12	0.00	0.01	0.02	0.01	100.55	5.9	255	15	0
2	100.05	0.0381	0.14	0.36	0.14	0.00	0.00	0.00	0.00	100.73	5.7	282	16	0
2	99.65	0.0366	0.14	0.36	0.14	0.00	0.01	0.00	0.00	100.33	6.4	271	17	0
3	99.47	0.0426	0.14	0.40	0.12	0.00	0.01	0.05	0.01	100.24	5.4	315	17	0
3	99.81	0.0405	0.14	0.35	0.14	0.00	0.02	0.00	0.00	100.50	5.7	300	17	0
3	99.78	0.0439	0.16	0.38	0.14	0.00	0.00	0.00	0.00	100.50	5.8	325	19	0
3	99.06	0.0356	0.15	0.36	0.16	0.00	0.00	0.00	0.00	99.77	6.7	264	18	0
4	99.95	0.0448	0.13	0.38	0.12	0.00	0.00	0.03	0.00	100.65	5.6	332	18	0
4	99.84	0.0434	0.15	0.37	0.09	0.00	0.00	0.00	0.00	100.49	5.4	321	17	0
4	99.43	0.0433	0.13	0.40	0.09	0.00	0.00	0.00	0.00	100.09	5.1	321	16	0
4	99.46	0.0409	0.14	0.42	0.13	0.00	0.02	0.02	0.00	100.22	5.8	303	17	0
5	98.31	0.0405	0.16	0.45	0.52	0.00	0.00	0.09	0.01	99.58	5.4	300	16	0
5	99.21	0.0398	0.13	0.46	0.49	0.00	0.00	0.09	0.01	100.43	6.3	295	18	0
5	98.58	0.0410	0.14	0.43	0.45	0.00	0.00	0.08	0.00	99.72	6.2	304	19	0
5	99.61	0.0346	0.13	0.42	0.53	0.00	0.01	0.11	0.01	100.85	8.2	256	21	0
6	100.01	0.0372	0.01	0.42	0.32	0.00	0.03	0.00	0.29	101.11	6.5	275	18	0
6	99.97	0.0374	0.01	0.41	0.32	0.00	0.00	0.00	0.24	100.99	6.2	277	17	5
7	98.94	0.0211	0.01	0.40	0.42	0.00	0.00	0.05	0.28	100.12	10.2	156	16	0
7	98.95	0.0330	0.01	0.38	0.41	0.00	0.00	0.00	0.18	99.96	7.0	244	17	0

7	98.66	0.0299	0.01	0.45	0.48	0.00	0.00	0.04	0.27	99.93	8.4	221	19	0
8	99.50	0.0261	0.01	0.40	0.53	0.00	0.00	0.04	0.25	100.75	10.1	193	20	0
8	99.83	0.0152	0.01	0.41	0.54	0.00	0.00	0.00	0.26	101.07	16.4	113	18	0
9	100.14	0.0449	0.03	0.32	0.10	0.00	0.00	0.05	0.22	100.91	5.1	332	17	0
9	100.47	0.0400	0.03	0.28	0.09	0.00	0.00	0.00	0.17	101.08	5.8	296	17	0

CC16-14D

Grain	TiO2	ZrO2	Al2O3	FeO	Nb2O5	SiO2	MnO	Ta2O5	V2O3	Total	Zr Unc (%)	Zr (ppm)	Zr Unc (ppm)	Si (ppm)
9	99.07	0.0350	0.05	0.40	0.09	0.00	0.00	0.00	0.61	100.25	6.9	259	18	0
10	98.58	0.0300	0.05	0.71	0.09	0.02	0.01	0.00	0.47	99.96	8.2	222	18	93
11	98.29	0.0270	0.04	0.69	0.11	0.01	0.01	0.00	0.44	99.62	10.1	200	20	47
13	98.89	0.0180	0.01	0.57	0.08	0.00	0.00	0.00	0.50	100.07	16.3	133	22	0
13	98.10	0.0260	0.02	0.52	0.11	0.00	0.00	0.01	0.54	99.33	8.7	192	17	0
14	99.29	0.0390	0.02	0.39	0.10	0.00	0.02	0.00	0.27	100.13	6.5	289	19	0
15	97.93	0.0290	0.08	0.72	0.11	0.04	0.03	0.00	0.47	99.41	8.4	215	18	187
16	98.03	0.0230	0.03	0.68	0.09	0.01	0.02	0.00	0.44	99.32	8.9	170	15	47
18	98.68	0.0240	0.05	0.89	0.07	0.03	0.04	0.00	0.47	100.25	9.2	178	16	140
19	98.61	0.0350	0.05	0.57	0.06	0.00	0.02	0.00	0.41	99.75	6.8	259	18	0
20	98.10	0.0260	0.06	1.03	0.09	0.03	0.06	0.00	0.49	99.89	9.8	192	19	140
21	99.25	0.0240	0.03	0.42	0.08	0.01	0.00	0.00	0.47	100.28	11.0	178	19	47
22	98.89	0.0280	0.02	0.48	0.12	0.00	0.01	0.00	0.40	99.95	9.1	207	19	0
1	99.78	0.0363	0.15	0.29	0.11	0.00	0.00	0.00	0.00	100.36	6.5	269	18	0
1	99.49	0.0390	0.14	0.26	0.11	0.00	0.00	0.01	0.00	100.05	6.3	289	18	0
1	100.08	0.0337	0.14	0.28	0.10	0.00	0.00	0.08	0.01	100.72	7.2	249	18	0
1	99.82	0.0310	0.14	0.26	0.10	0.00	0.03	0.03	0.00	100.40	6.9	229	16	0
1	99.54	0.0417	0.15	0.25	0.06	0.00	0.00	0.00	0.00	100.04	5.8	309	18	0
1	99.16	0.0385	0.14	0.23	0.07	0.00	0.00	0.03	0.00	99.66	5.9	285	17	0
1	99.44	0.0302	0.14	0.21	0.08	0.00	0.00	0.00	0.00	99.90	8.0	224	18	0
1	99.47	0.0335	0.13	0.28	0.09	0.00	0.00	0.00	0.01	100.01	7.0	248	17	0
1	99.13	0.0332	0.14	0.26	0.09	0.00	0.02	0.00	0.01	99.68	6.9	246	17	0
1	98.62	0.0316	0.13	0.27	0.12	0.00	0.03	0.00	0.00	99.20	7.8	234	18	0

1	99.23	0.0367	0.14	0.26	0.09	0.00	0.00	0.00	0.00	99.76	6.4	272	17	0
1	98.91	0.0341	0.14	0.26	0.09	0.00	0.00	0.01	0.00	99.44	7.4	252	19	0
1	99.27	0.0390	0.14	0.23	0.11	0.00	0.00	0.00	0.00	99.78	6.4	289	19	0
2	99.36	0.0403	0.14	0.21	0.08	0.00	0.00	0.00	0.00	99.84	5.9	298	17	0
2	100.10	0.0288	0.13	0.22	0.09	0.00	0.00	0.00	0.00	100.56	8.2	213	18	0
2	100.20	0.0318	0.14	0.23	0.07	0.00	0.00	0.02	0.00	100.68	6.9	235	16	0
2	99.85	0.0347	0.14	0.21	0.07	0.00	0.00	0.00	0.01	100.31	6.8	257	17	0
3	100.45	0.0355	0.14	0.30	0.10	0.00	0.00	0.00	0.00	101.02	6.6	263	17	0
3	99.15	0.0336	0.14	0.38	0.08	0.00	0.03	0.00	0.01	99.82	7.1	249	18	0
3	99.39	0.0400	0.14	0.35	0.09	0.00	0.00	0.00	0.01	100.02	5.8	296	17	0
3	98.53	0.0403	0.15	0.41	0.08	0.03	0.00	0.00	0.01	99.25	5.9	298	18	140
4	99.22	0.0350	0.14	0.28	0.11	0.00	0.01	0.00	0.02	99.81	6.8	259	18	0
4	99.78	0.0332	0.14	0.30	0.11	0.00	0.00	0.02	0.00	100.37	6.5	246	16	0
4	99.69	0.0318	0.13	0.34	0.10	0.00	0.03	0.02	0.00	100.34	6.6	235	16	0
4	99.37	0.0330	0.13	0.32	0.08	0.00	0.00	0.02	0.02	99.97	6.3	244	15	0
5	99.02	0.0378	0.13	0.31	0.10	0.00	0.00	0.00	0.00	99.60	6.5	280	18	0
5	99.85	0.0306	0.13	0.33	0.07	0.00	0.00	0.00	0.00	100.41	6.4	227	14	0
5	99.54	0.0336	0.14	0.27	0.09	0.00	0.00	0.00	0.01	100.08	6.4	249	16	0
5	98.33	0.0333	0.15	0.24	0.10	0.01	0.00	0.00	0.01	98.87	6.3	247	15	47
6	99.64	0.0383	0.01	0.35	0.10	0.00	0.01	0.01	0.31	100.46	6.6	284	19	0
6	99.39	0.0410	0.01	0.36	0.08	0.00	0.00	0.00	0.31	100.19	5.5	304	17	0
6	99.38	0.0325	0.01	0.35	0.09	0.00	0.00	0.07	0.31	100.25	7.0	241	17	14
7	99.13	0.0340	0.01	0.32	0.09	0.00	0.01	0.00	0.36	99.95	7.1	252	18	0
7	98.50	0.0262	0.02	0.34	0.11	0.00	0.00	0.07	0.32	99.39	8.8	194	17	0
7	99.33	0.0294	0.01	0.41	0.10	0.00	0.00	0.02	0.35	100.25	9.0	218	20	9
7	98.93	0.0367	0.02	0.31	0.12	0.01	0.01	0.00	0.31	99.75	6.5	272	18	28
7	98.49	0.0420	0.02	0.32	0.07	0.01	0.00	0.00	0.24	99.18	5.8	311	18	28
8	98.06	0.0250	0.04	0.40	0.09	0.02	0.01	0.01	0.27	98.93	9.8	185	18	112
8	97.75	0.0240	0.01	0.40	0.10	0.00	0.00	0.00	0.20	98.48	9.5	178	17	9

CC16-14C

Grain	TiO2	ZrO2	Al2O3	FeO	Nb2O5	SiO2	MnO	Ta2O5	V2O3	Total	Zr Unc (%)	Zr (ppm)	Zr Unc (ppm)	Si (ppm)
1	99.18	0.0422	0.01	0.31	0.20	0.01	0.01	0.00	0.23	99.99	6.2	312	19	38
1	98.58	0.0334	0.01	0.40	0.52	0.03	0.02	0.00	0.29	99.88	6.9	247	17	136
2	98.91	0.0425	0.02	0.31	0.19	0.00	0.02	0.05	0.27	99.81	5.8	315	18	0
2	98.80	0.0389	0.01	0.32	0.25	0.00	0.00	0.00	0.25	99.66	6.4	288	19	0
3	99.24	0.0436	0.01	0.29	0.11	0.00	0.00	0.00	0.28	99.96	5.8	323	19	0
3	99.44	0.0375	0.02	0.33	0.15	0.00	0.00	0.00	0.21	100.19	6.1	278	17	0
4	98.97	0.0397	0.01	0.32	0.10	0.00	0.00	0.00	0.18	99.62	6.1	294	18	0
4	99.19	0.0409	0.01	0.34	0.15	0.00	0.00	0.00	0.27	99.99	6.4	303	19	0
5	98.70	0.0390	0.01	0.32	0.10	0.00	0.01	0.02	0.31	99.52	6.4	289	19	0
5	97.91	0.0490	0.01	0.33	0.13	0.00	0.00	0.06	0.28	98.76	5.3	363	19	0
6	98.24	0.0443	0.03	0.30	0.08	0.00	0.00	0.00	0.28	98.97	5.3	328	17	0
6	98.89	0.0438	0.01	0.30	0.08	0.00	0.00	0.03	0.24	99.60	5.3	324	17	0
7	99.07	0.0501	0.02	0.29	0.08	0.00	0.01	0.00	0.21	99.73	5.1	371	19	1
7	99.06	0.0476	0.01	0.30	0.06	0.00	0.00	0.05	0.27	99.80	5.0	352	17	0
8	97.11	0.0284	0.01	0.42	0.49	0.01	0.02	0.00	0.36	98.45	8.9	210	19	59
9	97.87	0.0347	0.00	0.48	0.57	0.02	0.01	0.02	0.37	99.38	7.4	257	19	84
10	98.55	0.0315	0.02	0.44	0.53	0.00	0.01	0.06	0.34	99.99	7.0	233	16	22
10	98.20	0.0232	0.02	0.48	0.55	0.00	0.02	0.04	0.37	99.72	8.9	172	15	18
11	97.98	0.0251	0.01	0.44	0.35	0.00	0.00	0.10	0.39	99.29	9.6	186	18	0
11	97.81	0.0290	0.01	0.42	0.34	0.00	0.00	0.05	0.30	98.97	9.4	215	20	0
12	98.22	0.0335	0.02	0.37	0.42	0.00	0.01	0.00	0.29	99.36	6.7	248	17	0
13	99.14	0.0337	0.02	0.37	0.30	0.00	0.01	0.00	0.25	100.13	7.1	249	18	0
14	98.78	0.0340	0.00	0.40	0.28	0.00	0.00	0.00	0.29	99.79	7.3	252	18	12
15	98.94	0.0313	0.02	0.34	0.28	0.00	0.00	0.04	0.27	99.91	7.7	232	18	0
16	98.89	0.0345	0.01	0.40	0.33	0.00	0.00	0.00	0.29	99.96	6.9	255	18	0
16	98.76	0.0216	0.02	0.39	0.36	0.00	0.01	0.00	0.32	99.89	9.6	160	15	3
17	98.76	0.0271	0.02	0.37	0.47	0.00	0.00	0.00	0.35	100.00	9.1	201	18	13
19	99.24	0.0336	0.00	0.43	0.29	0.00	0.00	0.00	0.29	100.29	7.3	249	18	0
19	99.03	0.0384	0.02	0.44	0.36	0.00	0.00	0.09	0.33	100.30	6.4	284	18	0
20	98.97	0.0386	0.01	0.39	0.19	0.00	0.01	0.00	0.31	99.92	6.1	286	17	12

20	98.89	0.0401	0.01	0.41	0.18	0.00	0.04	0.00	0.33	99.90	6.4	297	19	0
21	99.04	0.0424	0.02	0.37	0.15	0.00	0.00	0.00	0.30	99.91	5.3	314	17	0
21	98.30	0.0413	0.01	0.48	0.21	0.00	0.00	0.00	0.28	99.32	6.0	306	18	7
22	98.67	0.0343	0.02	0.40	0.30	0.00	0.00	0.01	0.35	99.78	7.8	254	20	0
22	98.05	0.0338	0.02	0.41	0.20	0.00	0.00	0.00	0.35	99.05	7.0	250	18	0
23	98.53	0.0211	0.02	0.40	0.47	0.00	0.00	0.07	0.34	99.86	11.8	156	18	0
23	98.84	0.0218	0.02	0.41	0.52	0.00	0.00	0.02	0.35	100.19	10.1	161	16	3
24	99.28	0.0390	0.02	0.34	0.14	0.00	0.00	0.00	0.32	100.15	5.9	289	17	0
24	99.48	0.0438	0.01	0.34	0.10	0.00	0.01	0.08	0.29	100.37	5.5	324	18	0

CC16-14E

Grain	TiO2	ZrO2	Al2O3	FeO	Nb2O5	SiO2	MnO	Ta2O5	V2O3	Total	Zr Unc (%)	Zr (ppm)	Zr Unc (ppm)	Si (ppm)
1	98.53	0.0067	0.01	0.29	0.36	0.02	0.01	0.01	0.32	99.55	63.8	50	32	89
2	97.76	0.0094	0.02	0.33	0.47	0.02	0.01	0.05	0.28	98.96	20.3	70	14	79
2	97.41	0.0175	0.02	0.36	0.64	0.00	0.00	0.03	0.25	98.73	16.5	130	21	5
4	98.15	0.0159	0.01	0.33	0.56	0.02	0.00	0.06	0.26	99.41	18.2	118	21	98
4	94.34	0.0108	0.02	0.36	0.53	0.02	0.01	0.03	0.28	95.61	16.8	80	13	112
4	97.07	0.0169	0.01	0.36	0.58	0.01	0.01	0.04	0.27	98.36	14.3	125	18	61
5	97.37	0.0130	0.02	0.39	0.67	0.02	0.01	0.10	0.32	98.91	15.2	96	15	108
5	98.62	0.0199	0.02	0.32	0.68	0.01	0.02	0.06	0.27	100.02	15.0	147	22	47
5	98.14	0.0185	0.02	0.40	0.60	0.01	0.00	0.04	0.29	99.51	12.6	137	17	65
6	99.13	0.0103	0.02	0.23	0.08	0.02	0.00	0.00	0.15	99.64	26.9	76	21	70
6	99.51	0.0090	0.01	0.21	0.08	0.02	0.04	0.00	0.17	100.05	30.4	67	20	93
6	99.10	0.0083	0.02	0.19	0.03	0.02	0.01	0.01	0.20	99.59	22.5	61	14	79
7	98.22	0.0085	0.02	0.32	0.17	0.03	0.00	0.01	0.20	98.97	26.4	63	17	122
7	97.54	0.0118	0.02	0.31	0.18	0.03	0.01	0.00	0.21	98.31	30.2	87	26	140
7	98.01	0.0086	0.01	0.28	0.14	0.04	0.00	0.05	0.21	98.74	24.8	64	16	187
8	98.40	0.0166	0.02	0.34	0.39	0.02	0.02	0.06	0.34	99.59	14.9	123	18	75
8	97.51	0.0123	0.03	0.35	0.41	0.03	0.00	0.00	0.29	98.63	18.4	91	17	117
8	99.62	0.0127	0.02	0.36	0.40	0.01	0.03	0.02	0.29	100.76	24.4	94	23	65
8	99.65	0.0121	0.02	0.39	0.39	0.01	0.00	0.01	0.31	100.80	19.8	90	18	61

9	98.72	0.0150	0.01	0.35	0.49	0.00	0.00	0.04	0.28	99.91	14.8	111	16	19
9	98.90	0.0186	0.02	0.35	0.47	0.01	0.02	0.04	0.32	100.15	13.5	138	19	56
9	98.62	0.0181	0.02	0.36	0.49	0.02	0.00	0.00	0.25	99.78	15.3	134	20	70
10	99.43	0.0102	0.02	0.26	0.14	0.01	0.00	0.00	0.20	100.06	21.7	76	16	65
10	99.04	0.0108	0.02	0.21	0.13	0.01	0.01	0.00	0.21	99.65	22.0	80	18	65
11	99.16	0.0140	0.01	0.39	0.41	0.04	0.00	0.03	0.27	100.31	17.1	104	18	164
13	99.14	0.0171	0.02	0.27	0.57	0.00	0.01	0.00	0.30	100.32	20.0	127	25	0
13	99.08	0.0147	0.02	0.19	0.54	0.01	0.02	0.01	0.31	100.20	16.0	109	17	61
13	98.41	0.0162	0.01	0.29	0.50	0.00	0.00	0.09	0.29	99.62	12.3	120	15	0
13	99.17	0.0180	0.01	0.23	0.46	0.00	0.00	0.05	0.27	100.21	11.1	133	15	0
14	97.67	0.0119	0.02	0.33	0.15	0.04	0.01	0.00	0.18	98.41	19.5	88	17	192
14	99.00	0.0095	0.02	0.33	0.21	0.02	0.00	0.01	0.19	99.80	26.7	70	19	108
14	99.14	0.0089	0.02	0.27	0.19	0.03	0.00	0.04	0.21	99.91	24.2	66	16	154
15	100.19	0.0087	0.02	0.32	0.13	0.03	0.00	0.00	0.21	100.91	36.6	64	24	145
15	99.97	0.0123	0.01	0.31	0.21	0.03	0.02	0.00	0.14	100.69	22.2	91	20	122
15	99.81	0.0092	0.02	0.30	0.18	0.02	0.00	0.03	0.22	100.58	28.7	68	20	98

WB16-03A

Grain	TiO2	ZrO2	Al2O3	FeO	Nb2O5	SiO2	MnO	Ta2O5	V2O3	Total	Zr Unc (%)	Zr (ppm)	Zr Unc (ppm)	Si (ppm)
1	97.51	0.0395	0.04	0.49	0.59	0.01	0.00	0.01	0.42	99.11	6.1	292	18	43
1	97.76	0.0304	0.03	0.48	0.56	0.02	0.01	0.00	0.42	99.30	8.1	225	18	77
1	97.72	0.0477	0.03	0.45	0.53	0.01	0.00	0.00	0.43	99.22	5.4	353	19	45
1	97.43	0.0458	0.04	0.45	0.53	0.01	0.04	0.00	0.40	98.94	5.4	339	18	27
2	96.41	0.0421	0.05	0.61	0.76	0.02	0.00	0.00	0.46	98.35	5.9	312	18	79
2	96.28	0.0366	0.06	0.61	0.87	0.02	0.00	0.07	0.48	98.43	6.2	271	17	92
2	96.34	0.0355	0.06	0.65	0.98	0.02	0.04	0.00	0.48	98.60	6.4	263	17	78
2	96.33	0.0458	0.06	0.61	0.83	0.02	0.02	0.05	0.48	98.44	5.2	339	17	96
3	97.81	0.0411	0.05	0.54	0.77	0.01	0.00	0.10	0.46	99.78	6.0	304	18	66
3	97.48	0.0450	0.06	0.50	0.76	0.02	0.00	0.06	0.44	99.35	5.4	333	18	95
3	97.24	0.0516	0.24	0.39	0.67	0.02	0.01	0.00	0.42	99.04	4.9	382	19	77
3	97.69	0.0419	0.04	0.43	0.72	0.01	0.00	0.05	0.38	99.37	5.5	310	17	54
4	97.83	0.0442	0.07	0.55	0.85	0.03	0.00	0.04	0.44	99.85	5.8	327	19	129

4	97.73	0.0390	0.25	0.47	0.93	0.02	0.02	0.00	0.40	99.87	6.0	289	17	84
4	97.63	0.0478	0.10	0.56	0.94	0.01	0.00	0.09	0.45	99.84	5.0	354	18	66
4	97.39	0.0502	0.06	0.57	0.93	0.02	0.01	0.03	0.43	99.50	4.8	372	18	93
5	97.61	0.0330	0.05	0.51	0.63	0.02	0.04	0.11	0.40	99.40	6.6	244	16	70
5	97.43	0.0375	0.05	0.52	0.81	0.02	0.02	0.02	0.45	99.37	5.9	278	16	94
5	97.31	0.0528	0.07	0.59	0.84	0.02	0.02	0.00	0.44	99.35	5.0	391	19	110
5	98.07	0.0374	0.05	0.51	0.82	0.02	0.02	0.00	0.50	100.03	6.2	277	17	72
6	96.97	0.0398	0.07	0.83	0.89	0.03	0.01	0.00	0.21	99.05	5.7	295	17	140
16	97.07	0.0480	0.05	0.89	0.78	0.03	0.02	0.08	0.19	99.15	4.8	355	17	117
17	97.80	0.0461	0.02	0.97	0.77	0.03	0.00	0.04	0.18	99.86	5.1	341	17	135
18	98.02	0.0375	0.04	0.78	0.67	0.01	0.01	0.04	0.19	99.81	6.6	278	18	69
19	98.52	0.0707	0.03	0.63	0.51	0.02	0.00	0.02	0.27	100.07	3.6	523	19	88
20	98.29	0.0649	0.04	0.77	0.55	0.03	0.05	0.00	0.24	100.03	3.8	480	18	135
8	99.51	0.0320	0.03	0.36	0.31	0.02	0.02	0.00	0.40	100.68	7.5	237	18	91
8	99.31	0.0300	0.03	0.37	0.28	0.01	0.01	0.06	0.36	100.46	8.4	222	19	36
8	99.19	0.0292	0.03	0.36	0.31	0.01	0.00	0.03	0.44	100.40	7.8	216	17	67
8	99.09	0.0258	0.03	0.39	0.35	0.02	0.00	0.00	0.39	100.29	9.5	191	18	81
9	98.12	0.0444	0.07	0.63	0.73	0.02	0.03	0.00	0.32	99.97	5.5	329	18	113
21	98.26	0.0348	0.02	0.77	0.75	0.02	0.00	0.08	0.28	100.22	6.9	258	18	112
22	98.07	0.0397	0.06	0.86	0.77	0.04	0.00	0.04	0.23	100.12	5.8	294	17	200
23	97.44	0.0443	0.10	0.71	0.82	0.02	0.00	0.08	0.26	99.47	5.3	328	17	107
24	98.58	0.0338	0.10	0.62	0.62	0.02	0.00	0.00	0.25	100.22	6.8	250	17	102
25	98.11	0.0637	0.08	0.57	0.54	0.01	0.00	0.00	0.28	99.66	3.9	472	18	61
26	98.23	0.0495	0.04	0.72	0.58	0.02	0.02	0.03	0.23	99.93	5.0	366	18	99
27	98.89	0.0571	0.01	0.56	0.60	0.02	0.01	0.00	0.29	100.44	4.4	423	19	93
15	98.10	0.0370	0.04	0.46	0.54	0.02	0.00	0.00	0.41	99.61	6.4	274	18	109
15	97.46	0.0378	0.07	0.37	0.45	0.01	0.00	0.00	0.41	98.81	7.0	280	19	35
15	97.77	0.0351	0.05	0.48	0.32	0.02	0.00	0.04	0.43	99.13	6.9	260	18	85
15	98.20	0.0396	0.03	0.45	0.35	0.01	0.00	0.05	0.37	99.50	6.0	293	18	56
28	96.66	0.0203	0.10	0.60	0.78	0.02	0.02	0.00	0.23	98.42	10.2	150	15	101
29	97.86	0.0412	0.09	0.69	0.69	0.02	0.03	0.05	0.19	99.65	6.3	305	19	96
30	98.18	0.0483	0.05	0.72	0.60	0.03	0.00	0.00	0.20	99.84	5.2	358	19	123

31	97.55	0.0396	0.10	0.64	0.72	0.02	0.00	0.05	0.31	99.44	5.6	293	17	102
14	98.20	0.0291	0.03	0.38	0.54	0.01	0.01	0.00	0.38	99.59	8.1	215	18	60
14	97.86	0.0379	0.04	0.39	0.55	0.01	0.01	0.02	0.43	99.34	6.9	281	19	56
14	98.09	0.0392	0.03	0.40	0.46	0.02	0.00	0.00	0.35	99.39	7.2	290	21	90
14	98.18	0.0409	0.05	0.41	0.38	0.02	0.01	0.00	0.35	99.44	5.6	303	17	72
12	98.02	0.0379	0.03	0.45	0.60	0.02	0.00	0.03	0.40	99.57	6.7	281	19	100
12	97.76	0.0407	0.04	0.49	0.59	0.01	0.01	0.00	0.36	99.29	6.2	301	19	67
12	98.28	0.0429	0.03	0.47	0.57	0.01	0.01	0.01	0.41	99.83	5.4	318	17	64
12	97.77	0.0404	0.04	0.49	0.58	0.02	0.00	0.00	0.45	99.40	5.6	299	17	84
13	98.25	0.0385	0.02	0.41	0.59	0.02	0.00	0.07	0.36	99.77	6.5	285	19	87
13	98.50	0.0358	0.03	0.40	0.37	0.01	0.01	0.02	0.35	99.73	6.9	265	18	60
13	98.25	0.0337	0.04	0.41	0.32	0.02	0.03	0.04	0.39	99.53	6.8	249	17	82
13	98.52	0.0341	0.03	0.45	0.38	0.02	0.03	0.00	0.38	99.85	6.8	252	17	91

MR16-01

Grain	TiO2	ZrO2	Al2O3	FeO	Nb2O5	SiO2	MnO	Ta2O5	V2O3	Total	Zr Unc (%)	Zr (ppm)	Zr Unc (ppm)	Si (ppm)
1	98.14	0.0404	0.03	0.74	0.21	0.05	0.02	0.02	0.27	99.51	6.2	299	19	230
2	98.66	0.0224	0.01	0.62	0.14	0.02	0.00	0.00	0.35	99.83	10.6	166	18	116
3	98.14	0.0288	0.03	0.88	0.15	0.05	0.04	0.00	0.37	99.68	8.3	213	18	219
4	98.70	0.0261	0.01	0.67	0.13	0.04	0.03	0.00	0.35	99.96	11.6	193	22	184
5	98.24	0.0227	0.03	0.55	0.14	0.01	0.00	0.00	0.33	99.34	10.7	168	18	61
6	98.32	0.0173	0.01	0.35	0.18	0.01	0.01	0.06	0.24	99.19	14.6	128	19	43
7	98.56	0.0272	0.02	0.32	0.20	0.02	0.05	0.00	0.26	99.46	8.4	201	17	87
8	98.58	0.0115	0.03	0.32	0.18	0.01	0.02	0.00	0.25	99.42	23.2	85	20	62
9	98.74	0.0231	0.02	0.31	0.18	0.01	0.04	0.00	0.27	99.59	11.7	171	20	50
11	98.16	0.0274	0.02	0.47	0.12	0.05	0.02	0.00	0.60	99.47	8.4	203	17	249
13	98.49	0.0155	0.02	0.43	0.15	0.02	0.00	0.10	0.37	99.59	12.3	115	14	92
13	98.28	0.0224	0.01	0.48	0.16	0.02	0.00	0.04	0.37	99.38	10.9	166	18	81
13	98.01	0.0304	0.03	0.52	0.15	0.02	0.03	0.00	0.39	99.18	8.0	225	18	84
14	98.08	0.0337	0.03	0.47	0.11	0.03	0.00	0.03	0.21	98.99	7.7	249	19	147
14	97.74	0.0293	0.04	0.48	0.09	0.02	0.00	0.00	0.22	98.62	7.4	217	16	109

15	97.50	0.0288	0.01	0.53	0.09	0.02	0.02	0.03	0.28	98.52	9.6	213	21	95
15	97.30	0.0270	0.01	0.53	0.12	0.02	0.00	0.00	0.25	98.26	8.7	200	17	100
15	97.52	0.0265	0.02	0.57	0.11	0.02	0.00	0.00	0.26	98.52	9.0	196	18	97
16	98.72	0.0199	0.02	0.91	0.14	0.03	0.01	0.00	0.26	100.11	12.5	147	18	140
17	97.81	0.0256	0.03	0.91	0.23	0.04	0.00	0.00	0.34	99.38	8.5	190	16	208
18	98.01	0.0280	0.02	0.80	0.16	0.04	0.03	0.00	0.29	99.38	8.1	207	17	210
19	97.62	0.0244	0.02	0.84	0.22	0.04	0.01	0.00	0.30	99.08	9.8	181	18	177
20	97.84	0.0224	0.03	0.89	0.20	0.02	0.01	0.00	0.23	99.25	10.4	166	17	106
21	98.63	0.0260	0.03	0.56	0.11	0.03	0.01	0.00	0.27	99.67	7.5	192	15	162
22	98.37	0.0271	0.01	0.53	0.12	0.02	0.00	0.05	0.23	99.36	10.2	201	20	94
23	98.78	0.0251	0.03	0.61	0.12	0.02	0.03	0.01	0.25	99.87	9.6	186	18	105
24	97.99	0.0158	0.03	0.77	0.14	0.05	0.01	0.03	0.26	99.29	15.8	117	19	219
25	98.78	0.0282	0.01	0.44	0.21	0.03	0.00	0.00	0.43	99.93	8.5	209	18	136
26	98.08	0.0286	0.02	0.52	0.21	0.02	0.00	0.00	0.40	99.27	8.6	212	18	108
26	97.92	0.0162	0.02	0.66	0.22	0.02	0.00	0.00	0.38	99.24	14.1	120	17	116
27	97.98	0.0252	0.02	0.46	0.14	0.02	0.03	0.10	0.23	99.00	10.0	187	19	101
28	97.89	0.0237	0.02	0.56	0.17	0.02	0.02	0.00	0.29	99.00	11.9	175	21	101

A14-71

Grain	TiO2	ZrO2	Al2O3	FeO	Nb2O5	SiO2	MnO	Ta2O5	V2O3	Total	Zr Unc (%)	Zr (ppm)	Zr Unc (ppm)	Si (ppm)
9	98.69	0.0210	0.03	0.22	0.01	0.00	0.01	0.00	0.59	99.57	11.5	155	18	0
9	98.87	0.0260	0.03	0.27	0.03	0.01	0.01	0.00	0.51	99.76	10.0	192	19	47
10	98.56	0.0270	0.02	0.39	0.07	0.01	0.00	0.00	0.59	99.67	9.7	200	19	47
11	98.84	0.0330	0.05	0.51	0.03	0.02	0.00	0.00	0.39	99.87	6.7	244	16	93
12	99.27	0.0190	0.09	0.42	0.02	0.02	0.01	0.00	0.44	100.29	13.7	141	19	93
12	99.14	0.0360	0.04	0.44	0.01	0.01	0.00	0.00	0.47	100.15	6.8	267	18	47
13	98.63	0.0260	0.02	0.55	0.04	0.01	0.01	0.00	0.26	99.55	9.6	192	19	47
13	98.99	0.0290	0.03	0.54	0.01	0.01	0.01	0.00	0.30	99.92	8.1	215	17	47
14	99.15	0.0290	0.03	0.40	0.04	0.01	0.01	0.00	0.40	100.07	8.8	215	19	47
14	99.05	0.0290	0.02	0.41	0.04	0.02	0.00	0.03	0.39	99.99	8.2	215	18	93
15	99.31	0.0160	0.06	0.25	0.08	0.02	0.01	0.00	0.42	100.17	14.3	118	17	93
15	99.51	0.0130	0.08	0.31	0.05	0.01	0.00	0.00	0.42	100.39	16.4	96	16	47

16	98.02	0.0240	0.04	0.39	0.06	0.01	0.01	0.00	0.55	99.10	10.8	178	19	47
17	98.39	0.0260	0.08	0.76	0.02	0.02	0.01	0.00	0.42	99.73	9.6	192	18	93
18	98.62	0.0290	0.04	0.56	0.01	0.02	0.00	0.00	0.38	99.66	8.4	215	18	93
19	98.64	0.0280	0.05	0.39	0.03	0.01	0.01	0.00	0.42	99.58	9.6	207	20	47
19	97.42	0.0300	0.03	0.52	0.05	0.00	0.00	0.00	0.40	98.45	8.1	222	18	0
21	97.25	0.0330	0.81	0.59	0.03	0.01	0.00	0.06	0.58	99.36	7.4	244	18	47
22	98.39	0.0360	0.05	0.38	0.02	0.00	0.00	0.01	0.56	99.45	6.8	267	18	0
22	98.43	0.0170	0.05	0.41	0.05	0.00	0.00	0.02	0.60	99.58	14.2	126	18	0
23	99.12	0.0340	0.02	0.35	0.06	0.01	0.02	0.00	0.55	100.16	6.2	252	16	47
24	99.37	0.0280	0.02	0.43	0.03	0.02	0.00	0.00	0.33	100.23	8.8	207	18	93
25	98.85	0.0200	0.04	0.35	0.05	0.01	0.04	0.00	0.39	99.75	13.9	148	21	47
25	99.55	0.0210	0.03	0.39	0.03	0.00	0.02	0.00	0.35	100.39	10.2	155	16	0
1	100.37	0.0179	0.04	0.32	0.03	0.00	0.00	0.00	N/A	100.79	13.1	133	17	12
1	99.46	0.0230	0.05	0.31	0.03	0.00	0.00	0.00	N/A	99.88	11.6	170	20	0
1	98.98	0.0232	0.03	0.30	0.03	0.01	0.00	0.00	N/A	99.37	11.7	172	20	37
1	97.68	0.0221	0.03	0.32	0.05	0.01	0.00	0.00	N/A	98.12	11.9	164	20	46
2	84.69	0.0206	0.40	0.61	0.06	0.05	0.00	0.10	N/A	85.93	19.8	153	30	225
2	96.48	0.0209	0.05	0.29	0.04	0.02	0.00	0.02	N/A	96.93	13.7	155	21	103
2	96.65	0.0249	0.03	0.31	0.05	0.01	0.02	0.00	N/A	97.09	11.8	184	22	29
2	99.27	0.0263	0.02	0.32	0.04	0.02	0.01	0.00	N/A	99.71	10.2	195	20	84
2	98.80	0.0274	0.05	0.33	0.03	0.02	0.00	0.06	N/A	99.32	10.5	203	21	99
2	98.88	0.0211	0.10	0.21	0.04	0.02	0.00	0.00	N/A	99.27	11.9	156	19	78
2	98.78	0.0217	0.03	0.30	0.06	0.02	0.00	0.13	N/A	99.35	11.1	161	18	99
2	98.39	0.0187	0.02	0.31	0.05	0.01	0.00	0.00	N/A	98.80	14.3	138	20	65
2	99.08	0.0202	0.03	0.27	0.07	0.02	0.00	0.00	N/A	99.49	12.7	150	19	91
2	99.30	0.0196	0.03	0.28	0.04	0.03	0.00	0.00	N/A	99.70	13.1	145	19	126
2	99.19	0.0093	0.02	0.23	0.04	0.02	0.03	0.00	N/A	99.54	78.2	69	54	83
2	99.01	0.0134	0.03	0.30	0.02	0.03	0.00	0.00	N/A	99.40	18.9	99	19	117
3	98.85	0.0200	0.03	0.22	0.07	0.00	0.02	0.00	N/A	99.23	10.2	148	15	0
3	99.54	0.0167	0.04	0.22	0.06	0.01	0.00	0.00	N/A	99.88	11.8	124	15	28
3	99.27	0.0231	0.03	0.26	0.01	0.00	0.01	0.00	N/A	99.60	12.6	171	22	0
3	99.38	0.0243	0.03	0.28	0.01	0.01	0.00	0.00	N/A	99.72	12.3	180	22	56

4	98.69	0.0298	0.03	0.27	0.03	0.01	0.02	0.00	N/A	99.07	8.3	221	18	24
4	99.18	0.0247	0.04	0.25	0.04	0.01	0.01	0.06	N/A	99.60	8.9	183	16	40
4	99.91	0.0236	0.03	0.30	0.04	0.00	0.00	0.00	N/A	100.30	9.9	175	17	14
4	99.46	0.0244	0.04	0.26	0.05	0.00	0.00	0.00	N/A	99.84	11.8	181	21	6
5	99.83	0.0279	0.02	0.33	0.07	0.03	0.00	0.00	N/A	100.31	8.7	207	18	135
5	99.53	0.0297	0.03	0.23	0.03	0.00	0.00	0.00	N/A	99.84	8.8	220	19	4
5	99.28	0.0277	0.04	0.21	0.01	0.00	0.00	0.00	N/A	99.57	11.6	205	24	0
5	100.06	0.0267	0.04	0.24	0.05	0.00	0.00	0.03	N/A	100.44	9.0	198	18	7
5	99.30	0.0243	0.04	0.22	0.04	0.00	0.01	0.00	N/A	99.64	10.0	180	18	18
5	100.07	0.0232	0.04	0.21	0.03	0.00	0.01	0.00	N/A	100.38	12.1	172	21	9
5	99.90	0.0271	0.03	0.22	0.03	0.00	0.02	0.00	N/A	100.22	11.2	201	22	18
5	99.67	0.0258	0.03	0.21	0.01	0.00	0.00	0.05	N/A	100.01	10.2	191	19	21
5	99.60	0.0229	0.03	0.25	0.05	0.00	0.00	0.05	N/A	100.01	10.2	170	17	2
5	99.92	0.0289	0.04	0.22	0.03	0.01	0.01	0.04	N/A	100.28	9.0	214	19	27
5	99.42	0.0235	0.05	0.18	0.03	0.01	0.01	0.00	N/A	99.72	10.6	174	18	43
6	99.93	0.0176	0.04	0.33	0.04	0.00	0.00	0.00	N/A	100.35	11.8	130	15	0
6	99.40	0.0249	0.04	0.29	0.07	0.00	0.00	0.00	N/A	99.82	8.5	184	16	0
6	99.88	0.0247	0.04	0.33	0.04	0.00	0.00	0.00	N/A	100.31	11.6	183	21	0
6	100.03	0.0254	0.04	0.27	0.06	0.01	0.00	0.00	N/A	100.43	10.0	188	19	31
6	100.03	0.0220	0.04	0.29	0.10	0.00	0.00	0.00	N/A	100.48	10.8	163	18	19
7	99.55	0.0206	0.05	0.28	0.07	0.00	0.01	0.06	N/A	100.03	15.0	153	23	22
7	99.16	0.0208	0.04	0.30	0.03	0.00	0.04	0.00	N/A	99.59	10.7	154	17	0
7	99.77	0.0209	0.03	0.33	0.04	0.00	0.04	0.10	N/A	100.34	14.4	155	22	2
7	99.38	0.0227	0.05	0.31	0.05	0.00	0.02	0.00	N/A	99.84	9.3	168	16	0
7	99.61	0.0207	0.04	0.30	0.01	0.00	0.00	0.00	N/A	99.98	11.6	153	18	0
8	100.24	0.0227	0.04	0.30	0.02	0.00	0.00	0.00	N/A	100.63	12.1	168	20	0
8	99.99	0.0223	0.03	0.32	0.03	0.00	0.00	0.00	N/A	100.40	11.4	165	19	0
8	99.68	0.0176	0.03	0.33	0.03	0.00	0.02	0.02	N/A	100.13	14.5	130	19	18
8	99.81	0.0193	0.05	0.30	0.08	0.00	0.01	0.00	N/A	100.27	16.6	143	24	2
8	99.42	0.0202	0.04	0.30	0.04	0.01	0.00	0.01	N/A	99.83	10.4	150	15	35

GB

Grain	TiO2	ZrO2	Al2O3	FeO	Nb2O5	SiO2	MnO	Ta2O5	V2O3	Total	Zr Unc (%)	Zr (ppm)	Zr Unc (ppm)	Si (ppm)
1	96.96	0.0210	0.02	1.10	0.15	0.02	0.06	0.00	N/A	98.33	11.2	155	17	108
2	99.28	0.0150	0.01	0.81	0.17	0.02	0.06	0.02	N/A	100.38	17.8	111	20	89
2	98.96	0.0160	0.02	1.21	0.18	0.05	0.08	0.00	N/A	100.51	18.1	118	21	220
4	98.40	0.0220	0.08	0.88	0.07	0.05	0.03	0.00	N/A	99.53	10.6	163	17	224
9	97.56	0.0170	0.02	1.00	0.17	0.03	0.01	0.04	N/A	98.84	15.1	126	19	159
14	98.89	0.0100	0.02	0.68	0.08	0.03	0.03	0.00	N/A	99.74	36.8	74	27	140
15	99.31	0.0170	0.02	0.83	0.10	0.03	0.08	0.00	N/A	100.39	18.9	126	24	150
16	99.23	0.0161	0.14	0.83	0.13	0.00	0.00	0.00	0.08	100.42	17.3	119	21	0
17	96.89	0.0092	0.27	1.00	0.04	0.01	0.01	0.00	0.23	98.46	22.2	68	15	50
18	96.20	0.0130	0.15	1.43	0.12	0.01	0.12	0.03	0.23	98.30	13.2	96	13	50
19	96.63	0.0152	0.15	0.58	0.05	0.01	0.02	0.00	0.24	97.70	16.2	113	18	67
20	97.32	0.0218	0.15	0.61	0.04	0.01	0.03	0.00	0.21	98.41	11.6	161	19	69
20	97.39	0.0181	0.14	0.55	0.09	0.00	0.05	0.00	0.22	98.46	13.9	134	19	0
21	97.13	0.0229	0.14	0.64	0.09	0.05	0.06	0.00	0.21	98.35	10.8	170	18	220
22	96.93	0.0220	0.15	0.70	0.05	0.02	0.03	0.06	0.23	98.19	10.0	163	16	82
23	97.16	0.0207	0.17	0.74	0.10	0.00	0.00	0.00	0.17	98.37	11.3	153	17	0
23	96.92	0.0114	0.18	0.84	0.07	0.00	0.01	0.00	0.22	98.24	12.9	84	11	0
23	96.98	0.0268	0.17	0.93	0.09	0.00	0.09	0.00	0.14	98.44	9.0	198	18	0
24	97.46	0.0147	0.16	0.57	0.12	0.01	0.04	0.00	0.33	98.71	22.6	109	25	63
25	96.83	0.0209	0.16	1.14	0.08	0.01	0.04	0.00	0.12	98.40	11.6	155	18	62
27	97.01	0.0208	0.22	0.73	0.02	0.01	0.03	0.00	0.31	98.36	12.7	154	20	66
28	97.41	0.0132	0.15	0.76	0.01	0.00	0.01	0.00	0.30	98.65	21.3	98	21	0
29	96.68	0.0109	0.21	0.95	0.02	0.01	0.05	0.05	0.28	98.25	14.7	81	12	32

EA15-2Ba

Grain	TiO2	ZrO2	Al2O3	FeO	Nb2O5	SiO2	MnO	Ta2O5	V2O3	Total	Zr Unc (%)	Zr (ppm)	Zr Unc (ppm)	Si (ppm)
1	99.48	0.0140	0.00	0.21	0.16	0.00	0.00	0.59	N/A	100.45	29.9	104	31	19
2	99.22	0.0120	0.01	0.24	0.10	0.04	0.00	0.44	N/A	100.06	36.3	89	32	201
3	98.36	0.0140	0.01	0.30	0.09	0.00	0.00	0.51	N/A	99.42	49.3	104	51	0

4	98.73	0.0130	0.00	0.15	0.26	0.01	0.00	0.46	N/A	99.64	31.3	96	30	65
5	98.49	0.0080	0.00	0.19	0.15	0.03	0.00	0.47	N/A	99.43	69.0	59	41	131
6	97.72	0.0170	0.02	0.26	0.20	0.04	0.04	0.32	N/A	98.61	58.7	126	74	182
7	98.44	0.0140	0.01	0.30	0.10	0.01	0.00	0.52	N/A	99.46	63.5	104	66	47
8	99.25	0.0120	0.02	0.17	0.12	0.02	0.00	0.46	N/A	100.06	33.7	89	30	112
9	97.23	0.0120	0.00	0.15	0.06	0.06	0.00	0.54	N/A	98.10	51.3	89	46	257

79841A

Grain	TiO2	ZrO2	Al2O3	FeO	Cr2O3	SiO2	MnO	V2O3	Total	Zr Unc (%)	Zr (ppm)	Zr Unc (ppm)	Si (ppm)
1	98.52	0.0233	0.01	0.35	0.05	0.02	0.02	0.28	99.27	10.5	172	18	78
2	99.02	0.0248	0.01	0.36	0.04	0.01	0.00	0.30	99.76	10.0	184	18	51
3	99.39	0.0238	0.00	0.39	0.03	0.01	0.00	0.27	100.11	10.3	176	18	28
4	99.17	0.0173	0.01	0.30	0.03	0.05	0.00	0.25	99.83	14.2	128	18	223
7	99.52	0.0158	0.01	0.30	0.05	0.02	0.00	0.33	100.25	15.4	117	18	93
9	99.15	0.0188	0.02	0.34	0.06	0.05	0.00	0.29	99.93	13.2	139	18	216
10	98.88	0.0224	0.01	0.27	0.04	0.01	0.00	0.34	99.59	11.0	166	18	65
12	99.36	0.0220	0.01	0.33	0.04	0.03	0.00	0.31	100.10	11.2	163	18	122
13	98.95	0.0234	0.01	0.35	0.03	0.01	0.00	0.30	99.68	10.6	173	18	53
14	98.95	0.0157	0.01	0.30	0.02	0.04	0.00	0.28	99.62	15.6	116	18	182
15	98.39	0.0209	0.01	0.36	0.07	0.03	0.00	0.30	99.18	11.8	155	18	153
16	99.01	0.0203	0.02	0.32	0.05	0.01	0.00	0.27	99.70	12.0	150	18	44
18	99.58	0.0183	0.01	0.34	0.04	0.01	0.01	0.31	100.32	13.4	135	18	59
19	100.10	0.0151	0.02	0.27	0.04	0.02	0.00	0.29	100.75	16.2	112	18	89
20	99.54	0.0139	0.02	0.32	0.02	0.02	0.00	0.27	100.19	17.6	103	18	95

77842

Grain	TiO2	ZrO2	Al2O3	FeO	Cr2O3	SiO2	MnO	V2O3	Total	Zr Unc (%)	Zr (ppm)	Zr Unc (ppm)	Si (ppm)
1	99.75	0.0142	0.02	0.32	0.07	0.01	0.00	0.30	100.49	17.2	105	18	45
2	99.76	0.0137	0.02	0.31	0.06	0.00	0.01	0.34	100.51	17.7	101	18	16
3	99.47	0.0150	0.02	0.31	0.07	0.02	0.00	0.34	100.24	16.2	111	18	73
4	100.65	0.0119	0.01	0.32	0.12	0.01	0.00	0.29	101.41	20.3	88	18	58
5	99.69	0.0079	0.02	0.36	0.09	0.02	0.01	0.28	100.47	30.7	58	18	80

6	100.46	0.0114	0.03	0.32	0.12	0.06	0.00	0.29	101.29		21.3	84	18	269

A15-01A

Grain	TiO2	ZrO2	Al2O3	FeO	Nb2O5	SiO2	MnO	Ta2O5	V2O3	Total	Zr Unc (%)	Zr (ppm)	Zr Unc (ppm)	Si (ppm)
1	98.98	0.0597	0.03	0.24	0.24	0.04	0.00	0.07	0.51	100.16	4.3	442	19	200
1	97.88	0.0557	0.03	0.23	0.22	0.03	0.03	0.00	0.54	99.01	4.3	412	18	131
2	97.91	0.0532	0.05	0.17	0.23	0.02	0.03	0.04	0.60	99.09	4.6	394	18	73
2	98.78	0.0542	0.05	0.10	0.24	0.01	0.01	0.02	0.66	99.93	4.6	401	18	36
2	99.14	0.0569	0.05	0.10	0.23	0.02	0.00	0.00	0.60	100.21	4.7	421	20	103
3	98.35	0.0540	0.02	0.11	0.25	0.06	0.00	0.00	0.70	99.54	4.5	400	18	281
4	99.40	0.0520	0.03	0.11	0.30	0.00	0.00	0.00	0.63	100.53	4.9	385	19	0
4	99.32	0.0469	0.05	0.17	0.34	0.01	0.00	0.00	0.62	100.56	5.2	347	18	55
4	99.29	0.0467	0.05	0.19	0.36	0.00	0.00	0.00	0.64	100.57	5.7	346	20	0
4	100.42	0.0485	0.05	0.20	0.40	0.00	0.01	0.00	0.62	101.75	5.5	359	20	0
5	98.86	0.0430	0.06	0.18	0.39	0.00	0.01	0.00	0.67	100.22	5.8	318	18	0
5	95.87	0.0465	0.04	3.20	0.40	0.00	0.00	0.17	0.62	100.36	5.3	344	18	22
5	99.25	0.0470	0.07	0.20	0.46	0.00	0.00	0.14	0.72	100.90	5.0	348	17	15
5	99.24	0.0573	0.06	0.19	0.31	0.01	0.00	0.00	0.64	100.51	4.5	424	19	33
6	99.24	0.0573	0.03	0.15	0.24	0.02	0.00	0.00	0.66	100.39	4.4	424	19	72
7	99.29	0.0584	0.03	0.16	0.24	0.02	0.00	0.04	0.67	100.52	4.3	432	19	115
7	98.94	0.0563	0.05	0.15	0.25	0.01	0.00	0.00	0.66	100.10	4.3	417	18	27
7	98.74	0.0552	0.05	0.11	0.22	0.00	0.00	0.00	0.62	99.79	4.7	409	19	0
7	98.86	0.0544	0.05	0.12	0.23	0.00	0.02	0.00	0.61	99.94	4.7	403	19	0
8	99.55	0.0446	0.02	0.16	0.23	0.00	0.00	0.05	0.57	100.62	5.2	330	17	0
8	99.40	0.0369	0.11	0.12	0.24	0.00	0.00	0.00	0.60	100.50	6.3	273	17	0
8	98.86	0.0472	0.31	0.14	0.25	0.00	0.01	0.00	0.57	100.19	5.1	349	18	0
9	99.15	0.0531	0.04	0.16	0.23	0.01	0.00	0.07	0.60	100.29	4.2	393	17	41
9	99.10	0.0534	0.03	0.23	0.20	0.01	0.04	0.00	0.58	100.25	4.4	395	17	59
10	98.55	0.0522	0.16	0.13	0.33	0.01	0.00	0.00	0.61	99.85	4.6	386	18	32
10	98.23	0.0513	0.09	0.11	0.34	0.00	0.00	0.00	0.57	99.39	5.0	380	19	4
10	98.90	0.0571	0.04	0.10	0.29	0.01	0.00	0.06	0.62	100.07	4.6	423	19	38

11	98.59	0.0472	0.06	0.16	0.34	0.02	0.01	0.09	0.64	99.96	5.6	349	19	87
11	98.42	0.0508	0.06	0.19	0.46	0.01	0.00	0.00	0.65	99.84	4.7	376	18	36
11	98.17	0.0440	0.06	0.18	0.49	0.02	0.00	0.04	0.69	99.69	6.1	326	20	109
12	98.59	0.0509	0.06	0.15	0.31	0.00	0.00	0.00	0.55	99.71	5.1	377	19	0
12	98.69	0.0523	0.05	0.12	0.33	0.00	0.01	0.00	0.59	99.85	4.8	387	18	14
12	98.48	0.0535	0.05	0.13	0.29	0.00	0.00	0.06	0.60	99.65	4.6	396	18	0
13	98.46	0.0521	0.05	0.12	0.23	0.01	0.01	0.01	0.67	99.60	4.6	386	18	38
13	99.02	0.0529	0.05	0.16	0.26	0.01	0.00	0.00	0.67	100.21	4.8	392	19	65
13	98.79	0.0566	0.05	0.13	0.25	0.01	0.03	0.00	0.69	100.01	4.4	419	18	50
14	98.45	0.0526	0.05	0.12	0.20	0.00	0.02	0.02	0.59	99.50	4.6	389	18	0
14	98.93	0.0475	0.05	0.15	0.25	0.00	0.00	0.04	0.64	100.12	5.1	352	18	0
14	98.82	0.0560	0.04	0.14	0.19	0.01	0.00	0.01	0.60	99.86	4.4	415	18	30
14	98.06	0.0575	0.06	0.37	0.23	0.02	0.01	0.00	0.62	99.43	4.5	426	19	112
15	98.55	0.0593	0.12	0.08	0.21	0.00	0.00	0.00	0.56	99.59	4.5	439	20	0
15	98.52	0.0558	0.05	0.10	0.22	0.02	0.00	0.00	0.61	99.58	4.3	413	18	84
15	98.86	0.0584	0.06	0.14	0.23	0.01	0.00	0.00	0.61	99.96	4.4	432	19	59

A15-21A

Grain	TiO2	ZrO2	Al2O3	FeO	Nb2O5	SiO2	MnO	Ta2O5	V2O3	Total	Zr Unc (%)	Zr (ppm)	Zr Unc (ppm)	Si (ppm)
1	99.00	0.0602	0.06	0.37	0.23	0.00	0.00	0.07	0.40	100.18	4.1	446	18	2
1	98.47	0.0591	0.06	0.36	0.27	0.00	0.00	0.00	0.36	99.57	4.2	438	18	7
1	98.93	0.0571	0.06	0.38	0.30	0.01	0.01	0.00	0.40	100.14	4.1	423	17	42
1	98.68	0.0630	0.05	0.43	0.23	0.00	0.01	0.00	0.41	99.88	3.9	466	18	0
1	98.78	0.0641	0.07	0.41	0.23	0.00	0.00	0.11	0.39	100.05	4.2	475	20	0
1	98.83	0.0616	0.05	0.46	0.28	0.00	0.01	0.00	0.41	100.11	4.0	456	18	5
2	98.65	0.0717	0.04	0.37	0.34	0.00	0.00	0.00	0.43	99.90	3.5	531	18	0
2	98.94	0.0592	0.06	0.40	0.30	0.00	0.00	0.00	0.41	100.17	4.3	438	19	0
2	98.91	0.0693	0.05	0.37	0.33	0.01	0.00	0.10	0.38	100.22	3.6	513	19	55
2	98.81	0.0721	0.06	0.39	0.34	0.00	0.02	0.00	0.42	100.12	3.5	534	19	0
3	98.55	0.0654	0.02	0.44	0.30	0.02	0.01	0.00	0.36	99.77	3.7	484	18	86
4	98.98	0.0632	0.03	0.39	0.39	0.00	0.00	0.06	0.37	100.29	4.2	468	20	14

4	99.31	0.0562	0.04	0.38	0.24	0.00	0.03	0.00	0.45	100.50	4.3	416	18	0
4	98.95	0.0589	0.04	0.39	0.28	0.00	0.00	0.01	0.37	100.10	4.5	436	20	19
4	98.71	0.0624	0.04	0.39	0.34	0.00	0.01	0.00	0.39	99.95	3.9	462	18	21
4	99.22	0.0597	0.05	0.34	0.25	0.00	0.00	0.00	0.42	100.34	4.3	442	19	0
4	98.72	0.0589	0.05	0.34	0.31	0.00	0.02	0.00	0.40	99.89	4.1	436	18	19
5	99.15	0.0602	0.03	0.36	0.35	0.00	0.00	0.00	0.36	100.30	4.0	446	18	0
5	99.35	0.0630	0.04	0.47	0.36	0.01	0.03	0.00	0.36	100.69	4.0	466	18	50
5	99.39	0.0596	0.03	0.33	0.33	0.01	0.00	0.05	0.37	100.56	4.5	441	20	50
5	99.28	0.0610	0.03	0.33	0.35	0.02	0.00	0.00	0.33	100.41	4.2	452	19	79
6	99.24	0.0581	0.02	0.35	0.38	0.01	0.02	0.01	0.39	100.46	4.5	430	19	35
6	98.90	0.0585	0.03	0.37	0.37	0.00	0.01	0.05	0.43	100.22	4.4	433	19	13
6	99.09	0.0627	0.02	0.34	0.35	0.02	0.02	0.00	0.41	100.31	3.8	464	18	73
6	96.97	0.0641	0.03	0.38	0.34	0.02	0.02	0.00	0.38	98.20	4.0	475	19	86
7	98.56	0.0615	0.04	0.27	0.36	0.01	0.00	0.00	0.45	99.76	3.9	455	18	59
7	98.82	0.0616	0.01	0.28	0.36	0.01	0.02	0.00	0.38	99.95	4.0	456	18	57
7	98.83	0.0589	0.04	0.27	0.30	0.03	0.00	0.00	0.41	99.94	4.1	436	18	136
8	97.78	0.0600	0.04	0.34	0.39	0.01	0.01	0.01	0.39	99.02	4.4	444	19	26
8	98.07	0.0615	0.04	0.32	0.34	0.00	0.00	0.08	0.43	99.34	4.0	455	18	0
8	98.02	0.0589	0.03	0.26	0.34	0.03	0.00	0.00	0.41	99.15	4.3	436	19	118
8	98.78	0.0585	0.03	0.33	0.36	0.02	0.00	0.04	0.36	99.98	4.1	433	18	72
8	98.52	0.0655	0.05	0.34	0.38	0.00	0.00	0.04	0.39	99.78	3.9	485	19	3
9	97.30	0.0623	0.03	0.35	0.38	0.00	0.01	0.13	0.42	98.70	4.2	461	19	12
9	97.68	0.0594	0.03	0.35	0.38	0.00	0.01	0.00	0.43	98.95	4.1	440	18	0
9	97.69	0.0607	0.04	0.40	0.41	0.00	0.01	0.03	0.45	99.09	3.9	449	18	0
9	97.66	0.0635	0.04	0.38	0.33	0.01	0.02	0.08	0.41	99.00	3.9	470	18	40
10	98.67	0.0638	0.03	0.35	0.38	0.00	0.00	0.00	0.35	99.85	3.8	472	18	7
10	98.94	0.0677	0.03	0.30	0.36	0.00	0.00	0.00	0.34	100.04	3.6	501	18	1
10	98.81	0.0596	0.04	0.30	0.34	0.00	0.00	0.00	0.36	99.92	4.2	441	18	15
10	98.74	0.0649	0.03	0.32	0.33	0.01	0.00	0.00	0.43	99.92	3.9	480	19	33
10	98.60	0.0664	0.03	0.39	0.37	0.00	0.00	0.00	0.36	99.83	3.8	492	19	0
10	98.78	0.0684	0.03	0.31	0.35	0.00	0.00	0.00	0.38	99.92	3.7	506	19	0
11	99.34	0.0593	0.04	0.35	0.34	0.01	0.02	0.01	0.35	100.53	4.4	439	19	42

11	99.17	0.0496	0.04	0.31	0.34	0.00	0.00	0.10	0.36	100.37	5.2	367	19	0
11	99.10	0.0622	0.04	0.34	0.37	0.00	0.00	0.00	0.34	100.25	3.9	460	18	0
11	99.33	0.0625	0.05	0.36	0.33	0.02	0.00	0.15	0.37	100.65	4.3	463	20	74
11	99.21	0.0592	0.05	0.33	0.37	0.00	0.00	0.06	0.33	100.40	4.2	438	18	0
12	98.45	0.0642	0.04	0.30	0.33	0.01	0.00	0.00	0.35	99.54	3.8	475	18	38
12	98.57	0.0580	0.05	0.36	0.31	0.01	0.00	0.03	0.35	99.75	3.8	429	16	50
12	98.46	0.0624	0.04	0.31	0.35	0.02	0.00	0.00	0.31	99.55	4.0	462	19	87
12	97.85	0.0607	0.05	0.36	0.30	0.01	0.00	0.00	0.40	99.04	4.2	449	19	58
12	98.73	0.0627	0.05	0.34	0.26	0.00	0.00	0.01	0.34	99.79	4.1	464	19	22
13	98.38	0.0597	0.05	0.29	0.33	0.03	0.00	0.05	0.34	99.53	4.3	442	19	121
13	98.30	0.0616	0.06	0.29	0.31	0.00	0.02	0.02	0.33	99.39	4.3	456	20	0
13	97.83	0.0605	0.05	0.32	0.32	0.00	0.01	0.00	0.33	98.91	4.4	448	20	0
13	98.01	0.0620	0.05	0.26	0.33	0.02	0.02	0.00	0.34	99.09	4.1	459	19	94

A15-22

Grain	TiO2	ZrO2	Al2O3	FeO	Nb2O5	SiO2	MnO	Ta2O5	V2O3	Total	Zr Unc (%)	Zr (ppm)	Zr Unc (ppm)	Si (ppm)
1	98.63	0.0657	0.02	0.20	0.16	0.03	0.02	0.00	0.65	99.76	3.9	486	19	117
1	98.93	0.0645	0.02	0.21	0.15	0.03	0.00	0.02	0.61	100.03	3.8	478	18	140
1	98.71	0.0668	0.02	0.22	0.16	0.02	0.00	0.00	0.62	99.82	3.9	495	19	108
1	98.54	0.0662	0.01	0.29	0.15	0.02	0.05	0.00	0.65	99.77	3.7	490	18	73
2	98.78	0.0650	0.02	0.24	0.14	0.01	0.01	0.00	0.73	100.01	3.9	481	19	33
2	98.17	0.0665	0.02	0.18	0.13	0.01	0.00	0.00	0.73	99.32	3.7	492	18	67
2	97.57	0.0655	0.03	0.20	0.13	0.00	0.00	0.00	0.74	98.74	3.7	485	18	22
2	97.49	0.0661	0.03	0.22	0.16	0.01	0.00	0.00	0.69	98.67	3.6	489	18	44
13	97.33	0.0698	0.01	0.19	0.14	0.02	0.01	0.02	0.78	98.58	3.8	517	20	77
13	97.70	0.0673	0.03	0.20	0.16	0.02	0.01	0.00	0.77	98.96	3.9	498	19	109
13	98.42	0.0671	0.03	0.23	0.15	0.02	0.02	0.01	0.79	99.74	3.7	497	18	88
3	99.10	0.0461	0.02	0.41	0.16	0.06	0.03	0.00	0.61	100.43	5.1	341	18	266
3	99.49	0.0308	0.05	0.35	0.14	0.04	0.03	0.00	0.51	100.64	7.9	228	18	184
3	98.89	0.0381	0.03	0.35	0.17	0.04	0.04	0.00	0.59	100.13	7.1	282	20	184
3	98.92	0.0461	0.03	0.59	0.12	0.03	0.02	0.02	0.58	100.36	5.4	341	19	153
11	98.70	0.0687	0.03	0.45	0.13	0.02	0.03	0.00	0.46	99.89	3.7	509	19	103

9	99.42	0.0658	0.03	0.41	0.15	0.00	0.00	0.03	0.48	100.59	3.6	487	18	18
9	99.26	0.0696	0.03	0.29	0.12	0.00	0.01	0.00	0.45	100.24	3.6	515	19	0
9	99.22	0.0670	0.03	0.29	0.12	0.00	0.00	0.00	0.47	100.21	3.7	496	18	0
9	99.03	0.0749	0.02	0.25	0.13	0.00	0.00	0.00	0.51	100.01	3.3	554	18	7
4	98.82	0.0707	0.03	0.30	0.11	0.03	0.01	0.00	0.48	99.85	3.5	523	18	139
4	98.98	0.0727	0.03	0.28	0.13	0.01	0.01	0.00	0.52	100.04	3.6	538	19	65
4	98.95	0.0668	0.02	0.28	0.13	0.01	0.02	0.00	0.56	100.03	3.4	495	17	33
4	98.77	0.0655	0.03	0.31	0.11	0.01	0.00	0.02	0.52	99.84	3.7	485	18	61
8	99.23	0.0583	0.05	0.34	0.12	0.00	0.01	0.00	0.43	100.23	4.2	432	18	20
8	99.20	0.0619	0.05	0.30	0.14	0.02	0.00	0.04	0.48	100.29	4.0	458	18	85
8	99.06	0.0671	0.03	0.31	0.13	0.02	0.00	0.07	0.42	100.11	3.7	497	18	84
8	98.76	0.0648	0.03	0.29	0.14	0.01	0.00	0.03	0.45	99.77	3.7	480	18	54
5	96.60	0.0720	0.03	0.30	0.11	0.01	0.01	0.04	0.55	97.74	3.4	533	18	64
5	97.44	0.0749	0.02	0.26	0.12	0.01	0.00	0.04	0.59	98.55	3.3	554	18	26
5	97.36	0.0725	0.03	0.24	0.11	0.01	0.00	0.02	0.52	98.38	3.3	537	18	68
5	97.35	0.0654	0.03	0.25	0.13	0.03	0.02	0.03	0.58	98.49	3.6	484	17	117
6	98.62	0.0691	0.04	0.35	0.10	0.02	0.05	0.00	0.40	99.65	3.5	512	18	99
6	98.68	0.0737	0.05	0.29	0.10	0.01	0.00	0.00	0.37	99.58	3.5	546	19	57
6	98.66	0.0768	0.05	0.33	0.13	0.02	0.00	0.00	0.41	99.68	3.2	569	18	81
6	98.73	0.0659	0.05	0.36	0.15	0.02	0.00	0.01	0.44	99.83	3.7	488	18	77
15	98.91	0.0533	0.06	0.35	0.13	0.01	0.01	0.01	0.36	99.89	4.6	395	18	69
15	99.02	0.0655	0.05	0.35	0.13	0.01	0.00	0.00	0.33	99.97	3.8	485	18	54
15	99.15	0.0670	0.06	0.36	0.11	0.01	0.04	0.00	0.37	100.16	3.7	496	18	39
15	98.49	0.0644	0.05	0.39	0.13	0.03	0.01	0.05	0.35	99.57	3.7	477	18	159
14	98.90	0.0637	0.04	0.33	0.08	0.01	0.00	0.02	0.39	99.84	3.9	472	18	36
14	98.90	0.0755	0.05	0.36	0.05	0.00	0.00	0.10	0.38	99.91	3.2	559	18	15
14	99.10	0.0809	0.11	0.29	0.05	0.01	0.00	0.00	0.36	100.00	3.1	599	18	35
14	99.13	0.0853	0.04	0.32	0.03	0.00	0.00	0.00	0.39	99.99	3.0	631	19	6
7	98.16	0.0459	0.03	0.27	0.14	0.02	0.00	0.03	0.48	99.17	5.3	340	18	100
7	98.06	0.0379	0.04	0.23	0.13	0.04	0.00	0.05	0.49	99.07	6.9	281	19	184
7	98.40	0.0216	0.04	0.24	0.11	0.02	0.04	0.00	0.52	99.37	10.6	160	17	72

CA15-06

Grain	TiO2	ZrO2	Al2O3	FeO	Nb2O5	SiO2	MnO	Ta2O5	V2O3	Total	Zr Unc (%)	Zr (ppm)	Zr Unc (ppm)	Si (ppm)
1	99.89	0.0608	0.03	0.28	0.17	0.02	0.00	0.00	N/A	100.44	4.3	450	19	77
1	99.97	0.0624	0.05	0.29	0.17	0.00	0.00	0.00	N/A	100.54	4.0	462	19	0
1	99.63	0.0591	0.03	0.28	0.19	0.00	0.03	0.00	N/A	100.21	4.1	438	18	13
1	100.23	0.0602	0.03	0.28	0.20	0.01	0.00	0.00	N/A	100.80	4.4	446	20	28
2	99.92	0.0600	0.04	0.35	0.16	0.00	0.00	0.00	N/A	100.53	4.3	444	19	6
2	99.99	0.0600	0.02	0.36	0.14	0.00	0.00	0.00	N/A	100.57	4.0	444	18	18
2	99.79	0.0552	0.03	0.37	0.20	0.00	0.00	0.00	N/A	100.44	4.4	409	18	1
2	99.74	0.0585	0.02	0.31	0.12	0.00	0.01	0.00	N/A	100.26	4.1	433	18	3
3	99.39	0.0603	0.08	0.30	0.19	0.00	0.01	0.00	N/A	100.03	4.3	446	19	17
3	99.85	0.0620	0.03	0.40	0.16	0.00	0.00	0.00	N/A	100.50	4.2	459	19	12
3	99.78	0.0602	0.04	0.31	0.15	0.01	0.00	0.00	N/A	100.34	4.4	446	20	38
3	98.50	0.0623	0.03	0.34	0.15	0.01	0.04	0.02	N/A	99.15	4.2	461	19	43
4	99.22	0.0637	0.05	0.44	0.14	0.00	0.02	0.00	N/A	99.94	4.0	472	19	0
4	99.37	0.0655	0.05	0.44	0.13	0.00	0.00	0.04	N/A	100.09	4.0	485	19	5
4	99.33	0.0684	0.04	0.45	0.11	0.01	0.00	0.00	N/A	100.02	3.8	506	19	65
4	99.90	0.0632	0.03	0.51	0.19	0.00	0.01	0.04	N/A	100.74	4.1	468	19	0
5	100.02	0.0635	0.02	0.36	0.15	0.00	0.01	0.00	N/A	100.63	3.9	470	19	0
5	99.39	0.0571	0.01	0.34	0.14	0.01	0.01	0.00	N/A	99.95	4.4	423	19	23
5	99.83	0.0601	0.03	0.36	0.12	0.00	0.00	0.00	N/A	100.40	4.5	445	20	0
5	100.00	0.0579	0.03	0.38	0.12	0.00	0.02	0.05	N/A	100.66	4.1	429	17	0
6	99.92	0.0582	0.03	0.33	0.21	0.00	0.00	0.00	N/A	100.55	4.3	431	19	1
6	99.24	0.0600	0.02	0.36	0.24	0.00	0.01	0.01	N/A	99.93	4.4	444	20	4
6	99.45	0.0581	0.03	0.38	0.25	0.00	0.00	0.02	N/A	100.20	4.7	430	20	23
6	99.28	0.0623	0.03	0.37	0.35	0.01	0.00	0.12	N/A	100.23	4.3	461	20	42
7	99.84	0.0612	0.02	0.32	0.23	0.00	0.00	0.00	N/A	100.46	4.2	453	19	4
7	100.00	0.0615	0.02	0.32	0.20	0.00	0.00	0.02	N/A	100.63	4.0	455	18	0
7	99.46	0.0621	0.02	0.35	0.20	0.01	0.00	0.04	N/A	100.14	4.2	460	19	43
7	99.36	0.0628	0.03	0.32	0.20	0.00	0.03	0.00	N/A	99.99	4.3	465	20	0
8	99.09	0.0556	0.02	0.33	0.16	0.02	0.00	0.00	N/A	99.68	4.5	412	19	72
8	99.51	0.0574	0.03	0.33	0.13	0.01	0.00	0.07	N/A	100.13	4.2	425	18	46

8	99.65	0.0650	0.03	0.30	0.12	0.01	0.00	0.00	N/A	100.17	4.2	481	20	42
8	99.94	0.0620	0.02	0.28	0.13	0.00	0.00	0.00	N/A	100.44	3.7	459	17	7
9	98.48	0.0619	0.02	0.29	0.23	0.05	0.00	0.70	N/A	99.82	3.8	458	18	217
9	97.91	0.0552	0.04	0.32	0.21	0.03	0.02	0.70	N/A	99.28	4.2	409	17	132
9	98.20	0.0603	0.03	0.33	0.20	0.03	0.00	0.70	0.02	99.56	4.2	446	19	117
9	98.23	0.0617	0.02	0.32	0.24	0.00	0.00	0.71	0.01	99.59	4.2	457	19	1
9	98.81	0.0579	0.02	0.37	0.23	0.02	0.00	0.69	0.00	100.21	4.1	429	18	86
9	98.69	0.0600	0.03	0.28	0.27	0.02	0.00	0.67	0.00	100.02	4.2	444	19	102
9	98.26	0.0580	0.03	0.31	0.25	0.03	0.00	0.67	0.04	99.65	4.3	429	18	119
10	98.54	0.0647	0.03	0.34	0.11	0.01	0.01	0.00	0.73	99.82	4.1	479	20	36
11	98.20	0.0578	0.02	0.28	0.12	0.01	0.00	0.06	0.69	99.44	4.1	428	18	38
12	98.03	0.0591	0.03	0.37	0.32	0.02	0.00	0.10	0.72	99.65	4.1	438	18	98
13	97.94	0.0402	0.02	0.31	0.37	0.02	0.00	0.02	0.91	99.64	6.5	298	19	91
14	98.36	0.0622	0.02	0.26	0.31	0.01	0.01	0.00	0.86	99.89	4.3	460	20	48
15	97.55	0.0587	0.01	0.27	0.34	0.01	0.00	0.00	0.79	99.04	4.3	435	19	64
16	98.01	0.0624	0.02	0.26	0.31	0.02	0.00	0.00	0.86	99.53	4.1	462	19	72
17	97.91	0.0650	0.01	0.28	0.32	0.01	0.02	0.00	0.93	99.54	3.9	481	19	25
18	98.52	0.0503	0.01	0.34	0.37	0.01	0.00	0.04	0.84	100.18	4.7	372	18	34
19	98.22	0.0593	0.02	0.35	0.15	0.00	0.01	0.00	0.62	99.42	3.9	439	17	21
20	98.59	0.0579	0.02	0.38	0.13	0.00	0.00	0.10	0.62	99.90	4.4	429	19	0
21	98.39	0.0618	0.04	0.30	0.16	0.01	0.03	0.02	0.59	99.59	4.4	458	20	44
22	98.46	0.0647	0.03	0.32	0.17	0.01	0.00	0.01	0.62	99.68	3.8	479	18	36
23	97.07	0.0628	0.01	0.36	0.35	0.00	0.02	0.06	0.58	98.52	3.9	465	18	21
24	98.64	0.0311	0.00	0.33	0.17	0.01	0.00	0.00	0.66	99.85	7.2	230	17	52
25	99.85	0.0318	0.01	0.22	0.15	0.01	0.02	0.00	0.70	100.99	7.4	235	17	35
26	98.41	0.0475	0.00	0.28	0.29	0.01	0.00	0.00	0.70	99.73	5.2	352	18	54
27	97.88	0.0601	0.01	0.35	0.35	0.00	0.00	0.05	0.62	99.32	4.4	445	20	22
28	98.08	0.0388	0.00	0.33	0.32	0.00	0.00	0.04	0.64	99.45	5.8	287	17	0
29	98.07	0.0544	0.01	0.36	0.36	0.00	0.00	0.00	0.49	99.33	4.2	403	17	0
30	98.39	0.0230	0.01	0.28	0.17	0.00	0.00	0.00	0.64	99.51	9.9	170	17	19
31	97.76	0.0149	0.01	0.24	0.23	0.04	0.01	0.00	0.58	98.88	13.2	110	15	187
33	97.91	0.0554	0.01	0.31	0.37	0.02	0.03	0.00	0.75	99.46	4.3	410	18	75

34	97.69	0.0553	0.01	0.31	0.39	0.02	0.01	0.08	0.70	99.26	4.5	409	19	95
35	98.12	0.0265	0.00	0.35	0.25	0.00	0.00	0.00	0.71	99.46	9.6	196	19	18
36	97.88	0.0257	0.01	0.24	0.21	0.06	0.00	0.00	0.68	99.11	8.8	190	17	258
37	100.26	0.0110	0.02	0.47	0.12	0.03	0.00	0.00	N/A	100.90	23.0	81	19	122
37	99.60	0.0440	0.00	0.48	0.20	0.02	0.00	0.00	N/A	100.35	5.8	326	19	84
37	99.76	0.0510	0.02	0.41	0.25	0.01	0.01	0.01	N/A	100.51	4.5	378	17	56
37	99.44	0.0510	0.00	0.40	0.28	0.02	0.02	0.00	N/A	100.21	5.1	378	19	103
37	99.26	0.0480	0.00	0.38	0.25	0.02	0.00	0.02	N/A	99.97	5.2	355	18	70
37	100.01	0.0370	0.01	0.33	0.24	0.01	0.00	0.08	N/A	100.71	6.4	274	17	23
37	99.67	0.0280	0.01	0.35	0.21	0.01	0.00	0.00	N/A	100.27	8.1	207	17	23
37	99.57	0.0330	0.01	0.38	0.23	0.01	0.02	0.00	N/A	100.24	7.0	244	17	42
37	99.69	0.0390	0.01	0.43	0.24	0.00	0.02	0.00	N/A	100.44	6.2	289	18	14
37	99.76	0.0380	0.01	0.40	0.26	0.01	0.00	0.05	N/A	100.52	6.2	281	17	47
37	99.64	0.0360	0.00	0.41	0.21	0.02	0.00	0.00	N/A	100.31	7.5	267	20	75
37	99.65	0.0260	0.02	0.41	0.18	0.04	0.00	0.07	N/A	100.40	11.3	192	22	178
37	99.69	0.0140	0.01	0.61	0.18	0.05	0.00	0.04	N/A	100.59	15.0	104	15	238
38	98.97	0.0387	0.01	0.33	0.27	0.02	0.00	0.04	N/A	99.68	6.2	287	18	89
38	99.59	0.0566	0.00	0.32	0.31	0.01	0.00	0.01	N/A	100.31	4.4	419	19	58
38	100.35	0.0444	0.01	0.37	0.34	0.02	0.00	0.00	N/A	101.13	5.8	329	19	74
38	99.76	0.0567	0.00	0.32	0.31	0.04	0.00	0.04	N/A	100.53	4.4	420	19	208
37	99.35	0.0316	0.02	0.37	0.20	0.00	0.01	0.05	N/A	100.02	7.3	234	17	12
37	98.73	0.0442	0.00	0.33	0.23	0.00	0.00	0.03	N/A	99.37	5.8	327	19	7
37	98.82	0.0442	0.00	0.36	0.24	0.01	0.00	0.01	N/A	99.49	5.6	327	18	65
37	99.40	0.0296	0.00	0.40	0.21	0.01	0.00	0.01	N/A	100.06	8.4	219	18	27
39	99.03	0.0564	0.02	0.39	0.42	0.00	0.00	0.02	N/A	99.94	4.4	418	18	0
39	98.58	0.0492	0.01	0.34	0.34	0.01	0.00	0.01	N/A	99.34	5.0	364	18	29
39	98.77	0.0622	0.01	0.31	0.40	0.02	0.00	0.03	N/A	99.60	3.8	460	18	98
39	98.94	0.0537	0.01	0.29	0.31	0.01	0.00	0.04	N/A	99.65	4.7	398	18	55
40	99.77	0.0615	0.01	0.36	0.44	0.01	0.00	0.03	N/A	100.68	4.3	455	20	31
40	99.34	0.0556	0.01	0.42	0.37	0.00	0.00	0.08	N/A	100.28	4.5	412	18	11
40	99.09	0.0502	0.01	0.39	0.30	0.01	0.01	0.00	N/A	99.88	4.5	372	17	56
40	98.97	0.0566	0.01	0.40	0.38	0.00	0.00	0.00	N/A	99.83	4.6	419	19	16

41	100.12	0.0538	0.01	0.34	0.36	0.00	0.01	0.00	N/A	100.90	4.6	398	18	0
41	99.56	0.0617	0.01	0.43	0.45	0.01	0.01	0.00	N/A	100.53	4.3	457	20	30
41	99.47	0.0517	0.01	0.36	0.41	0.00	0.02	0.00	N/A	100.33	4.9	383	19	0
41	99.83	0.0298	0.00	0.25	0.16	0.00	0.00	0.00	N/A	100.28	8.3	221	18	0
42	99.03	0.0548	0.01	0.30	0.31	0.00	0.03	0.03	N/A	99.76	4.5	406	18	0
42	98.85	0.0566	0.01	0.31	0.40	0.00	0.00	0.00	N/A	99.64	4.6	419	19	16
42	99.11	0.0479	0.01	0.22	0.33	0.01	0.02	0.00	N/A	99.75	5.4	355	19	63
42	98.61	0.0217	0.02	0.20	0.15	0.03	0.00	0.00	N/A	99.04	12.6	161	20	156
44	99.24	0.0359	0.00	0.25	0.41	0.00	0.03	0.00	N/A	99.98	6.2	266	16	4
44	98.95	0.0199	0.01	0.24	0.37	0.01	0.00	0.01	N/A	99.60	12.1	147	18	32
44	99.16	0.0435	0.01	0.31	0.40	0.01	0.00	0.02	N/A	99.94	5.4	322	17	41
44	98.98	0.0373	0.01	0.25	0.29	0.02	0.00	0.00	N/A	99.58	7.4	276	21	91

S1.10 Updated temperature estimates for the amphibolite-facies mélange zone

Table S1.10.1 Comparison of previously reported and updated temperature estimates for the amphibolite-facies mélange zone

		Pressure Thermometer	1.0 Gpa Tomkins et al. (2007)		1.4 Gpa Tomkins et al. (2007)		***1.4 Gpa Kohn (2020)***	
Sample	***Zr (ppm)***	***Unc (2σ)***	***T°C (Tomkins et al., 2007)***	***Unc (2σ)***	***T°C (Tomkins et al., 2007)***	***Unc (2σ)***	***T°C (Kohn, 2020)***	***Unc (2σ)***
A14-29	722	73	726	7	745	7	**735**	**8**
A14-55	634	92	714	10	732	10	**721**	**11**
A14-32	621	46	712	5	730	5	**719**	**6**
A14-08A	558	72	702	8	720	9	**707**	**10**
A14-22	530	166	698	20	716	21	**702**	**23**
A15-20A	529	43	698	5	716	5	**702**	**6**
A12A-5	524	49	697	6	715	6	**701**	**7**
A14-57B	515	53	695	7	713	7	**699**	**8**
A14-15	511	192	694	24	712	24	**698**	**28**
A14-28	500	63	693	8	711	8	**696**	**9**
A15-14	496	87	692	11	710	11	**695**	**13**

A15-18A	470	49	687	6	705	7	**690**	**8**
E2718C	457	45	685	6	703	6	**687**	**7**
A12A-3	452	35	684	5	702	5	**686**	**6**
A14-27A	442	36	682	5	700	5	**684**	**6**
A15-02A	442	41	682	6	700	6	**684**	**7**
A15-27C	436	60	681	8	698	9	**683**	**10**
A14-61A	426	26	679	4	696	4	**680**	**4**
A14-13	422	57	678	8	696	8	**679**	**9**
A14-45C	419	64	677	9	695	10	**679**	**11**
A15-17	445	45	682	6	700	6	**685**	**7**
A15-25A	403	42	674	6	692	6	**675**	**7**
A15-23B	397	45	673	7	690	7	**673**	**8**
A15-12A	388	46	671	7	688	7	**671**	**8**
A15-09	357	92	664	15	681	16	**663**	**17**
A10-7A	332	41	658	7	675	7	**656**	**8**
A14-25A	327	33	656	6	674	6	**655**	**7**
A14-50C	286	26	646	5	663	5	**643**	**6**
A14-64B	470	45	687	6	705	6	**690**	**7**
A14-64C	458	36	685	5	703	5	**687**	**6**
A14-64D	439	48	681	7	699	7	**683**	**8**
A14-64G	355	71	663	12	681	12	**663**	**13**
A14-64E	410	42	675	6	693	6	**677**	**7**

**Reported by Penniston-Dorland et al. (2018)* **Used in this study*

S1.11 Quartz-in-garnet elastic barometry

Table S1.11.1 Quartz-in-garnet Raman peak positions

A14-71

Analysis Number	Type	128	STD	%RSD	206	STD	%RSD	464	STD	%RSD
01Std_A_01	Standard	127.809	0.0065	0.0048	206.224	0.0711	0.0345	464.305	0.0077	0.0017
02A14-71_Gt1_Q1_01	Sample	129.850	0.0114	0.0088	217.800	0.0926	0.0425	467.112	0.0067	0.0014
04Std_A_02	Standard	127.875	0.0078	0.0061	206.297	0.0447	0.0217	464.352	0.0075	0.0016
06A14-71_Gt1_Q2_01	Sample	129.710	0.0198	0.0152	217.534	0.1177	0.0541	467.003	0.0083	0.0018
15Std_A_03	Standard	127.847	0.0090	0.0070	206.283	0.0238	0.0116	464.298	0.0065	0.0014
17A14-71_Gt4_Q1_01	Sample	128.020	0.0077	0.0060	208.505	0.0032	0.0015	464.819	0.0114	0.0024
19Std_A_04	Standard	127.651	0.0053	0.0041	206.079	0.0304	0.0148	464.128	0.0053	0.0011
21A14-71_Gt4_Q2_01	Sample	129.070	0.0143	0.0111	213.090	0.0028	0.0013	466.441	0.0093	0.0020
23Std_A_05	Standard	127.782	0.0081	0.0063	206.501	0.0058	0.0028	464.242	0.0047	0.0010
25A14-71_Gt4_Q3_01	Sample	129.804	0.0073	0.0057	215.760	0.0039	0.0018	467.424	0.0081	0.0017
01Std_B_01	Standard	127.983	0.0096	0.0075	207.070	0.0114	0.0055	464.431	0.0091	0.0020
03A14-71_Gt11_Q1_01	Sample	129.646	0.0075	0.0058	214.402	0.0025	0.0012	467.098	0.0054	0.0012
05Std_B_02	Standard	127.923	0.0063	0.0049	207.019	0.0099	0.0048	464.354	0.0105	0.0023
07A14-71_Gt11_Q2_01	Sample	129.458	0.0075	0.0058	213.611	0.0031	0.0015	466.535	0.0099	0.0021
09Std_B_03	Standard	127.904	0.0063	0.0049	206.779	0.0071	0.0034	464.341	0.0078	0.0017
11A14-71A_Gt11_Q3_01	Sample	129.466	0.0066	0.0051	213.716	0.0052	0.0025	466.633	0.0078	0.0017
13Std_B_04	Standard	128.008	0.0073	0.0057	206.969	0.0090	0.0044	464.447	0.0074	0.0016
15A14-71_Gt11_Q4_01	Sample	129.417	0.0122	0.0095	213.341	0.0031	0.0015	466.475	0.0108	0.0023
17Std_B_05	Standard	127.918	0.0099	0.0077	206.844	0.0076	0.0037	464.343	0.0076	0.0016
19A14-71_Gt11_Q5_01	Sample	129.514	0.0100	0.0077	213.720	0.0051	0.0024	466.811	0.0098	0.0021
21Std_B_06	Standard	128.029	0.0097	0.0076	207.154	0.0109	0.0053	464.476	0.0074	0.0016
23A14-71_Gt11_Q6_01	Sample	129.715	0.0146	0.0112	214.800	0.0259	0.0120	467.175	0.0057	0.0012
25Std_B_07	Standard	127.936	0.0071	0.0056	207.139	0.0099	0.0048	464.372	0.0072	0.0016
27A14-71_Gt11_Q7_01	Sample	130.118	0.0156	0.0120	215.823	0.0039	0.0018	467.463	0.0103	0.0022
29Std_B_09	Standard	127.822	0.0022	0.0018	206.750	0.0061	0.0030	464.271	0.0061	0.0013

31A14-71_Gt12_Q1_01	Sample	130.003	0.0052	0.0040	216.926	0.0028	0.0013	467.850	0.0073	0.0016

LB15-03B

Analysis Number	**Type**	**128**	**STD**	**%RSD**	**206**	**STD**	**%RSD**	**464**	**STD**	**%RSD**
02Std_B_01	Standard	127.761	0.0082	0.0064	206.591	0.0050	0.0024	464.22	0.0056	0.0012
04LB15-03B__Gt1_Q1_01	Sample	129.770	0.0066	0.0051	215.167	0.0024	0.0011	467.35	0.0061	0.0013
10Std_B_02	Standard	127.890	0.0055	0.0043	206.685	0.0075	0.0036	464.31	0.0051	0.0011
12LB15-03B_Gt5_Q1_01	Sample	129.900	0.0059	0.0045	214.836	0.0046	0.0022	467.29	0.0061	0.0013
18Std_B_02	Standard	127.825	0.0069	0.0054	206.603	0.0060	0.0029	464.27	0.0043	0.0009
20LB15-03B_Gt3_Q1_01	Sample	129.770	0.0236	0.0182	216.478	0.0412	0.0190	466.89	0.0060	0.0013
22Std_B_03	Standard	127.869	0.0092	0.0072	206.793	0.0083	0.0040	464.34	0.0055	0.0012
24LB15-03B_Gt6_Q1_01	Sample	129.483	0.0050	0.0038	213.977	0.0021	0.0010	466.87	0.0062	0.0013
26Std_B_05	Standard	127.617	0.0076	0.0060	206.545	0.0078	0.0038	464.10	0.0077	0.0017
28LB15-03B_Gt6_Q2_01	Sample	129.289	0.0079	0.0061	214.052	0.0024	0.0011	466.68	0.0115	0.0025
30Std_B_07	Standard	127.826	0.0087	0.0068	206.659	0.0069	0.0033	464.28	0.0044	0.0009
32LB15-03B_Gt6_Q3_01	Sample	129.263	0.0102	0.0079	213.861	0.0038	0.0018	466.70	0.0080	0.0017
34Std_B_08	Standard	127.727	0.0064	0.0050	206.638	0.0065	0.0031	464.19	0.0075	0.0016
36LB15-03B_Gt6_Q4_01	Sample	129.377	0.0084	0.0065	215.525	0.0524	0.0243	466.70	0.0071	0.0015
38Std_B_09	Standard	127.630	0.0050	0.0039	206.425	0.0058	0.0028	464.11	0.0072	0.0015
40LB15-03B_Gt6_Q5_01	Sample	129.321	0.0413	0.0319	214.009	0.0049	0.0023	466.73	0.0081	0.0017

GB

Analysis Number	**Type**	**128**	**STD**	**%RSD**	**206**	**STD**	**%RSD**	**464**	**STD**	**%RSD**
01Std_A_01	Standard	128.007	0.0066	0.0052	206.686	0.0054	0.0026	464.428	0.0053	0.0011
03GB12-01A_Gt1_Q1_01	Sample	131.841	0.0045	0.0034	221.874	0.0039	0.0018	470.049	0.0086	0.0018
06Std_A_02	Standard	128.223	0.0076	0.0059	207.406	0.0090	0.0043	464.630	0.0061	0.0013
08GB12-01A_Gt1_Q2_01	Sample	131.726	0.0116	0.0088	221.635	0.0065	0.0029	469.817	0.0115	0.0024
10Std_A_03	Standard	128.123	0.0080	0.0062	207.054	0.0076	0.0037	464.549	0.0065	0.0014
12GB12-01A_Gt1_Q3_01	Sample	131.314	0.0085	0.0064	220.131	0.0049	0.0022	469.073	0.0105	0.0022
14Std_A_04	Standard	128.127	0.0043	0.0034	207.001	0.0054	0.0026	464.530	0.0062	0.0013
16GB12-01A_Gt2_Q1_01	Sample	131.993	0.0056	0.0042	221.731	0.0034	0.0015	469.794	0.0050	0.0011
18Std_A_05	Standard	128.141	0.0053	0.0042	207.213	0.0081	0.0039	464.520	0.0090	0.0019

20GB12-01A_Gt2_Q2_01	Sample	131.524	0.0058	0.0044	221.343	0.0033	0.0015	469.795	0.0052	0.0011
22Std_A_06	Standard	128.016	0.0076	0.0060	206.819	0.0126	0.0061	464.413	0.0065	0.0014
24GB12-01A_Gt5_Q1_01	Sample	127.721	0.0090	0.0070	207.178	0.0047	0.0022	464.184	0.0062	0.0013
01Std_B_01	Standard	127.498	0.0049	0.0039	206.810	0.0122	0.0059	463.964	0.0074	0.0016
03GB15-01A_Gt6_Q1_01	Sample	131.487	0.0038	0.0029	220.190	0.0025	0.0011	468.783	0.0052	0.0011
06Std_B_02	Standard	127.460	0.0080	0.0063	206.373	0.0065	0.0032	463.921	0.0070	0.0015
08GB15-01A_Gt6B_Q1_01	Sample	132.131	0.0090	0.0068	223.749	0.0055	0.0025	470.444	0.0073	0.0015
10Std_B_04	Standard	127.467	0.0071	0.0055	206.645	0.0123	0.0059	463.934	0.0081	0.0017
12GB15-01A_Gt6C_Q1_01	Sample	130.387	0.0192	0.0147	219.306	0.0055	0.0025	468.377	0.0074	0.0016
18Std_B_05	Standard	127.373	0.0068	0.0053	206.578	0.0088	0.0043	463.806	0.0062	0.0013
20GB15-01A_Gt7_Q1_01	Sample	130.844	0.0105	0.0080	219.784	0.0054	0.0025	468.622	0.0060	0.0013
22Std_B_06	Standard	127.302	0.0083	0.0065	206.313	0.0078	0.0038	463.781	0.0066	0.0014
24GB15-01A_Gt7_Q2_01	Sample	131.006	0.0177	0.0135	220.908	0.0065	0.0029	468.808	0.0125	0.0027
26Std_B_07	Standard	127.276	0.0072	0.0057	206.344	0.0128	0.0062	463.728	0.0065	0.0014
28GB15-01A_Gt15B_Q1_01	Sample	130.604	0.0053	0.0040	219.500	0.0036	0.0017	468.625	0.0066	0.0014
30Std_B_08	Standard	127.152	0.0042	0.0033	206.301	0.0118	0.0057	463.582	0.0056	0.0012
32GB15-01A_Gt9_Q1_01	Sample	131.391	0.0096	0.0073	222.467	0.0030	0.0014	469.668	0.0063	0.0013
34Std_B_10	Standard	127.135	0.0093	0.0073	206.088	0.0066	0.0032	463.619	0.0044	0.0010
36GB15-01A_Gt11_Q1_01	Sample	130.661	0.0152	0.0116	219.966	0.0052	0.0023	468.605	0.0064	0.0014
38Std_B_11	Standard	127.132	0.0057	0.0045	206.118	0.0078	0.0038	463.612	0.0080	0.0017
40GB15-01A_Gt11_Q2_01	Sample	130.665	0.0084	0.0064	220.122	0.0271	0.0123	468.734	0.0090	0.0019

EA15-10A

Analysis Number	**Type**	**128**	**STD**	**%RSD**	**206**	**STD**	**%RSD**	**464**	**STD**	**%RSD**
01Std_B_01	Standard	128.240	0.0155	0.0120	207.312	0.0086	0.0041	464.647	0.0068	0.0015
03EA15-10A_Gt1_Q1_01	Sample	128.561	0.0046	0.0036	208.852	0.0032	0.0015	465.040	0.0107	0.0023
05Std_B_02	Standard	128.322	0.0065	0.0051	206.982	0.0102	0.0049	464.735	0.0047	0.0010
07EA15-10A_Gt1_Q2_01	Sample	130.093	0.0071	0.0054	215.139	0.0035	0.0016	467.562	0.0078	0.0017
09EA15-10A_Gt1_Q3_01	Sample	130.099	0.0080	0.0061	214.800	0.0026	0.0012	467.383	0.0074	0.0016
11Std_B_03	Standard	127.907	0.0157	0.0122	206.677	0.0036	0.0017	464.342	0.0059	0.0013
13EA15-10A_Gt2_Q1_01	Sample	129.428	0.0063	0.0048	213.410	0.0049	0.0023	466.553	0.0049	0.0011
21StdC_02	Standard	127.250	0.0038	0.0030	205.953	0.0065	0.0031	463.687	0.0076	0.0016

23EA15-10A_Gt7_Q1_01	Sample	129.163	0.0147	0.0114	214.513	0.0296	0.0138	466.684	0.0052	0.0011
25Std_C_L_02	Standard	127.251	0.0090	0.0071	205.794	0.0046	0.0022	463.710	0.0064	0.0014
27EA15-10A_Gt8_Q1_02	Sample	129.451	0.0091	0.0070	214.732	0.0052	0.0024	466.635	0.0134	0.0029
31Std_C_04	Standard	127.242	0.0104	0.0082	205.738	0.0039	0.0019	463.694	0.0053	0.0011
33EA15-10A_Gt8_Q2_01	Sample	129.518	0.0086	0.0066	214.969	0.0027	0.0013	466.833	0.0119	0.0026
35Std_C_05	Standard	127.324	0.0056	0.0044	206.157	0.0060	0.0029	463.766	0.0064	0.0014
37EA15-10A_Gt8_Q3_01	Sample	129.359	0.0083	0.0064	215.218	0.0039	0.0018	466.876	0.0147	0.0031
40Std_C_06	Standard	127.322	0.0106	0.0083	206.143	0.0060	0.0029	463.753	0.0043	0.0009
44EA15-10A_Gt8_Q4_03	Sample	129.132	0.0108	0.0084	213.688	0.0041	0.0019	466.500	0.0087468	0.001875

A15-22

Analysis Number	**Type**	**128**	**STD**	**%RSD**	**206**	**STD**	**%RSD**	**464**	**STD**	**%RSD**
01Std_A_01	Standard	128.346	0.0117	0.0091	206.976	0.0047	0.0023	464.758	0.0061	0.0013
03A15-22_Gt7_Q1_01	Sample	130.011	0.0136	0.0105	214.282	0.0049	0.0023	467.283	0.0063	0.0013
05Std_A_02	Standard	128.624	0.0096	0.0075	207.438	0.0048	0.0023	464.981	0.0054	0.0012
08A15-22_Gt8_Q1_02	Sample	129.879	0.0182	0.0140	214.024	0.0416	0.0194	467.183	0.0084	0.0018
11Std_A_04	Standard	128.451	0.0071	0.0055	207.110	0.0049	0.0024	464.894	0.0051	0.0011
12A15-22_Gt9_Q1_01	Sample	129.875	0.0100	0.0077	214.154	0.0058	0.0027	467.324	0.0072	0.0015
14A15-22_Gt9_Q2_01	Sample	129.923	0.0136	0.0105	214.228	0.0045	0.0021	467.559	0.0061	0.0013
16A15-22_Gt9_Q3_01	Sample	130.325	0.0099	0.0076	214.395	0.0053	0.0025	467.529	0.0099	0.0021
20Std_A_05	Standard	128.414	0.0063	0.0049	207.089	0.0047	0.0023	464.813	0.0054	0.0012
22A15-22_Gt9_Q4_01	Sample	130.034	0.0086	0.0066	213.910	0.0045	0.0021	467.291	0.0068	0.0015
23Std_A_04	Standard	128.452	0.0064	0.0049	207.192	0.0054	0.0026	464.847	0.0041	0.0009
25A15-22_Gt20_Q1_01	Sample	129.926	0.0211	0.0163	214.443	0.0149	0.0070	467.361	0.0055	0.0012
26Std_A_06	Standard	128.348	0.0058	0.0045	207.055	0.0045	0.0022	464.777	0.0035	0.0007
28A15-22_Gt20_Q2_01	Sample	129.830	0.0132	0.0102	213.807	0.0083	0.0039	467.234	0.0107	0.0023
29A15-22_Gt20_Q3_01	Sample	129.769	0.0104	0.0080	214.127	0.0088	0.0041	467.398	0.0093	0.0020
30Std_A_08	Standard	128.402	0.0059	0.0046	207.044	0.0038	0.0018	464.800	0.0052	0.0011
32A15-22_Gt20b_Q1_01	Sample	129.994	0.0070	0.0054	214.137	0.0073	0.0034	467.548	0.0116	0.0025
34Std_A_10	Standard	128.295	0.0086	0.0067	207.129	0.0079	0.0038	464.688	0.0061	0.0013
37A15-22_Gt3_Q1_02	Sample	129.458	0.0052	0.0040	213.093	0.0050	0.0024	466.784	0.0066	0.0014
39Std_A_12	Standard	128.236	0.0035	0.0027	207.017	0.0056	0.0027	464.648	0.0063	0.0014

41A15-22_Gt3_Q2_01	Sample	130.072	0.0268	0.0206	214.314	0.0049	0.0023	467.289	0.0101	0.0022
43Std_A_14	Standard	128.356	0.0070	0.0054	207.069	0.0062	0.0030	464.751	0.0044	0.0010
45A15-22_Gt3_Q3_01	Sample	129.455	0.0137	0.0106	213.759	0.0125	0.0059	467.088	0.0089	0.0019
47Std_A_15	Standard	128.406	0.0043	0.0033	207.067	0.0062	0.0030	464.839	0.0034	0.0007
49A15-22_Gt6_Q1_01	Sample	130.323	0.0104	0.0080	214.510	0.0047	0.0022	467.497	0.0126	0.0027
53Std_B_01	Standard	129.271	0.0042	0.0033	207.955	0.0028	0.0013	465.651	0.0058	0.0012
55A15-22_Gt2b_Q1_01	Sample	131.276	0.0132	0.0101	215.542	0.0077	0.0036	468.220	0.0073	0.0016
57Std_B_02	Standard	129.431	0.0049	0.0038	208.035	0.0031	0.0015	465.809	0.0047	0.0010
59A15-22_Gt6_Q1_03	Sample	131.044	0.0064	0.0049	215.934	0.0021	0.0010	468.768	0.0071	0.0015
61Std_B_03	Standard	129.213	0.0028	0.0021	207.943	0.0048	0.0023	465.594	0.0050	0.0011
63A15-22_Gt6_Q2_03	Sample	130.468	0.0062	0.0048	214.756	0.0057	0.0027	467.940	0.0057	0.0012
65Std_B_04	Standard	129.230	0.0052	0.0040	207.758	0.0034	0.0017	465.611	0.0053	0.0011
67A15-22_Gt7_Q1_03	Sample	130.686	0.0108	0.0083	214.975	0.0060	0.0028	467.985	0.0096	0.0021

E2718C

Analysis Number	**Type**	**128.000**	**STD**	**%RSD**	**206**	**STD**	**%RSD**	**464**	**STD**	**%RSD**
01Std_C_01	Standard	129.394	0.0078	0.0060	208.226	0.0058	0.0028	465.727	0.0069	0.0015
03E2718C_Gt5_Q1_01	Sample	131.143	0.0051	0.0039	216.800	0.0059	0.0027	468.668	0.0064	0.0014
05Std_C_02	Standard	129.401	0.0097	0.0075	208.005	0.0053	0.0025	465.762	0.0054	0.0012
07E2718C_Gt5_Q2_01	Sample	130.646	0.0076	0.0058	214.171	0.0034	0.0016	467.886	0.0078	0.0017
09Std_D_01	Standard	128.275	0.0117	0.0091	206.732	0.0035	0.0017	464.666	0.0064	0.0014
13E2718C_Gt5_Q3_03	Sample	129.951	0.0161	0.0124	213.656	0.0099	0.0047	467.104	0.0043	0.0009
14Std_D_02	Standard	128.239	0.0091	0.0071	206.794	0.0039	0.0019	464.703	0.0100	0.0021
16E2718C_Gt5_Q4_01	Sample	129.658	0.0210	0.0162	214.175	0.0132	0.0062	466.847	0.0059	0.0013
18Std_D_03	Standard	128.154	0.0062	0.0048	206.902	0.0041	0.0020	464.576	0.0073	0.0016
20E2718C_Gt7_Q1_01	Sample	129.956	0.0106	0.0082	214.148	0.0092	0.0043	467.273	0.0074	0.0016
21Std_D_04	Standard	128.314	0.0055	0.0043	206.827	0.0035	0.0017	464.718	0.0120	0.0026
23E2718C_Gt7_Q2_01	Sample	129.967	0.0135	0.0104	214.330	0.0059	0.0028	467.155	0.0060	0.0013
27Std_D_06	Standard	128.305	0.0074	0.0058	206.856	0.0054	0.0026	464.705	0.0060	0.0013
30E2718C_Gt1B_Q1_02	Sample	130.009	0.0143	0.0110	214.725	0.0152	0.0071	467.221	0.0083	0.0018

A15-07A

Analysis Number	Type	128	STD	%RSD	206	STD	%RSD	464	STD	%RSD
01Std_1_01	Standard	127.576	0.0123	0.0096	206.127	0.0050	0.0024	464.054	0.0040	0.0009
02A15-07A_Gt12_Q1	Sample	129.370	0.0068	0.0053	213.549	0.0056	0.0026	466.369	0.0045	0.0010
04Std_2_01	Standard	127.449	0.0073	0.0058	206.198	0.0045	0.0022	463.937	0.0039	0.0008
03A15-07A_Gt12_Q2	Sample	128.930	0.0156	0.0121	213.425	0.0042	0.0020	466.191	0.0065	0.0014
07Std_01	Standard	127.192	0.0094	0.0074	205.593	0.0117	0.0057	463.701	0.0074	0.0016
05A15-07A_Gt12_Q3_01	Sample	129.478	0.0116	0.0089	212.612	0.0051	0.0024	465.958	0.0064	0.0014
06A15-07A_Gt12_Q4_01	Sample	128.712	0.0147	0.0114	213.005	0.0040	0.0019	466.286	0.0092	0.0020
08Std_A_01	Standard	126.778	0.0149	0.0118	205.307	0.0086	0.0042	463.267	0.0053	0.0012
09A15-07A_Gt11_Q1_01	Sample	126.761	0.0133	0.0105	211.008	0.0064	0.0030	465.301	0.0068	0.0015
10Std_A_02	Standard	126.872	0.0061	0.0048	205.408	0.0049	0.0024	463.363	0.0056	0.0012
11A15-07A_Gt5_Q1_01	Sample	127.553	0.0080	0.0062	211.885	0.0047	0.0022	465.511	0.0088	0.0019

A15-21A

Analysis Number	Type	128	STD	%RSD	206	STD	%RSD	464	STD	%RSD
01Std_A_03_01	Standard	128.128	0.0095	0.0074	206.856	0.0086	0.0042	464.562	0.0094	0.0020
05A15-21A_Gt7_Q1_04_ND100	Sample	130.112	0.0186	0.0143	215.383	0.0131	0.0061	467.529	0.0101	0.0022
07Std_A_01	Standard	128.253	0.0117	0.0092	206.309	0.0067	0.0032	464.642	0.0040	0.0009
08A15-21A_Gt10_Q1_01	Sample	130.571	0.0223	0.0171	215.681	0.0206	0.0095	467.552	0.0047	0.0010
09Std_A_02	Standard	128.117	0.0041	0.0032	206.906	0.0066	0.0032	464.507	0.0063	0.0014
10A15-21A_Gt10_Q2_01	Sample	130.818	0.0122	0.0093	216.754	0.0104	0.0048	468.111	0.0084	0.0018
11Std_A_03	Standard	128.002	0.0043	0.0034	206.524	0.0053	0.0025	464.387	0.0037	0.0008
12A15-21A_Gt12_Q1_01	Sample	130.117	0.0050	0.0038	215.612	0.0025	0.0011	467.626	0.0067	0.0014
13Std_A_04	Standard	127.933	0.0073	0.0057	206.508	0.0070	0.0034	464.353	0.0034	0.0007
14A15-21A_Gt20B_Q1_01	Sample	130.413	0.0072	0.0055	215.586	0.0032	0.0015	467.641	0.0060	0.0013
15A15-21A_Gt20B_Q2_01	Sample	130.061	0.0037	0.0029	215.582	0.0037	0.0017	467.773	0.0068	0.0015
16Std_A_05	Standard	127.999	0.0033	0.0026	206.622	0.0041	0.0020	464.444	0.0047	0.0010
17A15-21A_Gt21_Q1_01	Sample	129.943	0.0086	0.0066	215.271	0.0026	0.0012	467.538	0.0103	0.0022
18Std_A_06	Standard	127.978	0.0071	0.0055	206.607	0.0037	0.0018	464.368	0.0047	0.0010
19A15-21A_Gt23_Q1_01	Sample	130.025	0.0126	0.0097	214.917	0.0050	0.0023	467.535	0.0074	0.0016

A15-01A

Analysis Number	Type	128	STD	%RSD	206	STD	%RSD	464	STD	%RSD
02Std_B_01	Standard	126.170	0.0151	0.0120	204.897	0.0065	0.0032	462.669	0.0046	0.0010
03A15-01A_Gt5_Q1_01	Sample	128.325	0.0309	0.0241	213.054	0.0070	0.0033	465.692	0.0079	0.0017
06Std_B_02	Standard	126.094	0.0055	0.0044	204.794	0.0055	0.0027	462.601	0.0075	0.0016
05A15-01A_Gt8_Q1_01	Sample	127.945	0.0349	0.0273	212.865	0.0072	0.0034	465.335	0.0073	0.0016
07Std_B_05	Standard	126.095	0.0067	0.0053	204.843	0.0055	0.0027	462.646	0.0067	0.0014
08A15-01A_Gt10_Q1_01	Sample	128.009	0.0121	0.0095	212.171	0.0080	0.0038	465.353	0.0088	0.0019
11A15-01A_Gt10_Q2_02	Sample	127.998	0.0224	0.0175	211.678	0.0124	0.0059	465.266	0.0072	0.0015
12Std_B_06	Standard	126.164	0.0120	0.0095	205.119	0.0070	0.0034	462.688	0.0052	0.0011
13A15-01A_Gt11_Q1_01	Sample	127.167	0.0145	0.0114	209.114	0.0062	0.0030	463.864	0.0092	0.0020
16Std_C_02	Standard	126.098	0.0063	0.0050	204.897	0.0030	0.0015	462.597	0.0062	0.0013
17A15-01A_Gt13_Q1_03	Sample	127.941	0.0120	0.0094	213.519	0.0625	0.0293	465.440	0.0153	0.0033
18Std_C_03	Standard	126.056	0.0070	0.0055	204.650	0.0037	0.0018	462.592	0.0064	0.0014
19A15_01A_Gt15_Q1_01	Sample	127.972	0.0073	0.0057	212.964	0.0083	0.0039	465.547	0.0066	0.0014
21Std_C_01(2)	Standard	126.010	0.0068	0.0054	204.882	0.0056	0.0027	462.551	0.0060	0.0013
22A15-01A_Gt16_Q1_01	Sample	128.069	0.0100	0.0078	213.139	0.0039	0.0018	465.455	0.0076	0.0016
23Std_C_02(2)	Standard	126.062	0.0061	0.0048	204.732	0.0038	0.0018	462.577	0.0049	0.0011
25A15-01A_Gt16_Q3_01	Sample	127.986	0.0108	0.0084	212.550	0.0045	0.0021	465.439	0.0070	0.0015

Table S1.11.2 Quartz-in-garnet peak shifts

A14-71

Analysis Number	d464	esd	misfit	d206	esd	misfit	d128	esd	misfit
02A14-71_Gt1_Q1_01	2.807	0.141	-0.407	11.576	0.212	0.105	2.041	0.141	0.507
06A14-71_Gt1_Q2_01	2.651	0.141	-0.354	11.237	0.212	0.091	1.836	0.141	0.441
17A14-71_Gt4_Q1_01	0.522	0.141	0.021	2.222	0.212	-0.005	0.173	0.141	-0.026
21A14-71_Gt4_Q2_01	2.313	0.141	-0.098	7.010	0.212	0.025	1.420	0.141	0.122
25A14-71_Gt4_Q3_01	3.183	0.141	-0.150	9.258	0.212	0.039	2.022	0.141	0.188
03A14-71_Gt11_Q1_01	2.667	0.141	-0.092	7.332	0.212	0.024	1.663	0.141	0.115
07A14-71_Gt11_Q2_01	2.181	0.141	-0.186	6.592	0.212	0.048	1.535	0.141	0.232
11A14-71A_Gt11_Q3_01	2.292	0.141	-0.171	6.937	0.212	0.044	1.562	0.141	0.214
15A14-71_Gt11_Q4_01	2.028	0.141	-0.174	6.372	0.212	0.045	1.408	0.141	0.217
19A14-71_Gt11_Q5_01	2.468	0.141	-0.117	6.876	0.212	0.030	1.596	0.141	0.146
23A14-71_Gt11_Q6_01	2.699	0.141	-0.105	7.646	0.212	0.027	1.687	0.141	0.131
27A14-71_Gt11_Q7_01	3.091	0.141	-0.238	8.684	0.212	0.061	2.181	0.141	0.296
31A14-71_Gt12_Q1_01	3.580	0.141	-0.114	10.175	0.212	0.029	2.181	0.141	0.142

LB15-03B

Analysis Number	d464	esd	misfit	d206	esd	misfit	d128	esd	misfit
04LB15-03B__Gt1_Q1_01	3.124	0.141	-0.339	8.576	0.212	0.087	2.009	0.014	0.004
12LB15-03B_Gt5_Q1_01	2.983	0.141	-0.428	8.151	0.212	0.110	2.009	0.014	0.005
20LB15-03B_Gt3_Q1_01	2.621	0.141	-0.884	9.874	0.212	0.227	1.944	0.014	0.011
24LB15-03B_Gt6_Q1_01	2.531	0.141	-0.284	7.184	0.212	0.073	1.614	0.014	0.004
28LB15-03B_Gt6_Q2_01	2.576	0.141	-0.345	7.507	0.212	0.089	1.672	0.014	0.004
32LB15-03B_Gt6_Q3_01	2.415	0.141	-0.186	7.202	0.212	0.048	1.437	0.014	0.002
36LB15-03B_Gt6_Q4_01	2.510	0.141	-0.533	8.888	0.212	0.137	1.651	0.014	0.007
40LB15-03B_Gt6_Q5_01	2.620	0.141	-0.334	7.584	0.212	0.086	1.691	0.014	0.004

GB

Analysis Number	d464	esd	misfit	d206	esd	misfit	d128	esd	misfit
03GB12-01A_Gt1_Q1_01	5.621	0.141	-0.845	15.188	0.212	0.217	3.834	0.014	0.010
08GB12-01A_Gt1_Q2_01	5.187	0.141	-0.761	14.229	0.212	0.195	3.503	0.014	0.009
12GB12-01A_Gt1_Q3_01	4.524	0.141	-0.897	13.076	0.212	0.230	3.190	0.014	0.011
16GB12-01A_Gt2_Q1_01	5.265	0.141	-1.176	14.730	0.212	0.301	3.867	0.014	0.014
20GB12-01A_Gt2_Q2_01	5.275	0.141	-0.524	14.130	0.212	0.135	3.384	0.014	0.006
24GB12-01A_Gt5_Q1_01	-0.229	0.141	0.094	0.358	0.212	-0.024	-0.295	0.014	-0.001
03GB15-01A_Gt6_Q1_01	4.819	0.141	-1.601	13.380	0.212	0.411	3.989	0.014	0.020
08GB15-01A_Gt6B_Q1_01	6.523	0.141	-1.219	17.376	0.212	0.313	4.672	0.014	0.015
12GB15-01A_Gt6C_Q1_01	4.443	0.141	-0.608	12.660	0.212	0.156	2.921	0.014	0.008
20GB15-01A_Gt7_Q1_01	4.816	0.141	-0.966	13.206	0.212	0.248	3.470	0.014	0.012
24GB15-01A_Gt7_Q2_01	5.027	0.141	-1.195	14.595	0.212	0.307	3.705	0.014	0.015
28GB15-01A_Gt15B_Q1_01	4.898	0.141	-0.712	13.156	0.212	0.183	3.328	0.014	0.009
32GB15-01A_Gt9_Q1_01	6.086	0.141	-0.990	16.166	0.212	0.254	4.239	0.014	0.012
36GB15-01A_Gt11_Q1_01	4.986	0.141	-0.942	13.878	0.212	0.242	3.525	0.014	0.012
40GB15-01A_Gt11_Q2_01	5.122	0.141	-0.835	14.005	0.212	0.214	3.533	0.014	0.010

EA15-10A

Analysis Number	d464	esd	misfit	d206	esd	misfit	d128	esd	misfit
03EA15-10A_Gt1_Q1_01	0.393	0.141	-0.174	1.540	0.212	0.045	0.321	0.014	0.002
07EA15-10A_Gt1_Q2_01	2.827	0.141	-0.293	8.156	0.212	0.075	1.771	0.014	0.004
09EA15-10A_Gt1_Q3_01	2.648	0.141	-0.434	7.818	0.212	0.111	1.776	0.014	0.005
13EA15-10A_Gt2_Q1_01	2.211	0.141	-0.430	6.733	0.212	0.110	1.521	0.014	0.005
23EA15-10A_Gt7_Q1_01	2.996	0.141	-0.345	8.560	0.212	0.089	1.913	0.014	0.004
27EA15-10A_Gt8_Q1_02	2.925	0.141	-0.796	8.938	0.212	0.204	2.199	0.014	0.010
33EA15-10A_Gt8_Q2_01	3.139	0.141	-0.713	9.232	0.212	0.183	2.275	0.014	0.009
37EA15-10A_Gt8_Q3_01	3.110	0.141	-0.436	9.062	0.212	0.112	2.035	0.014	0.005
44EA15-10A_Gt8_Q4_03	2.746	0.141	-0.352	7.545	0.212	0.090	1.811	0.014	0.004

A15-22

Analysis Number	d464	esd	misfit	d206	esd	misfit	d128	esd	misfit
03A15-22_Gt7_Q1_01	2.526	0.141	-0.363	7.306	0.212	0.093	1.665	0.014	0.005
08A15-22_Gt8_Q1_02	2.202	0.141	-0.105	6.586	0.212	0.027	1.255	0.014	0.001
12A15-22_Gt9_Q1_01	2.430	0.141	-0.139	7.044	0.212	0.036	1.424	0.014	0.002
14A15-22_Gt9_Q2_01	2.665	0.141	0.021	7.117	0.212	-0.005	1.472	0.014	0.000
16A15-22_Gt9_Q3_01	2.635	0.141	-0.506	7.285	0.212	0.130	1.874	0.014	0.006
22A15-22_Gt9_Q4_01	2.478	0.141	-0.302	6.821	0.212	0.078	1.620	0.014	0.004
25A15-22_Gt20_Q1_01	2.514	0.141	-0.140	7.251	0.212	0.036	1.474	0.014	0.002
28A15-22_Gt20_Q2_01	2.457	0.141	-0.150	6.752	0.212	0.039	1.482	0.014	0.002
29A15-22_Gt20_Q3_01	2.621	0.141	0.045	7.072	0.212	-0.011	1.421	0.014	-0.001
32A15-22_Gt20b_Q1_01	2.748	0.141	-0.040	7.093	0.212	0.010	1.592	0.014	0.001
37A15-22_Gt3_Q1_02	2.096	0.141	-0.029	5.964	0.212	0.008	1.163	0.014	0.000
41A15-22_Gt3_Q2_01	2.642	0.141	-0.456	7.297	0.212	0.117	1.837	0.014	0.006
45A15-22_Gt3_Q3_01	2.337	0.141	0.199	6.690	0.212	-0.051	1.099	0.014	-0.002
49A15-22_Gt6_Q1_01	2.658	0.141	-0.551	7.443	0.212	0.141	1.916	0.014	0.007
55A15-22_Gt2b_Q1_01	2.569	0.141	-0.758	7.587	0.212	0.195	2.005	0.014	0.009
59A15-22_Gt6_Q1_03	2.959	0.141	0.049	7.900	0.212	-0.013	1.613	0.014	-0.001
63A15-22_Gt6_Q2_03	2.346	0.141	0.009	6.813	0.212	-0.002	1.254	0.014	0.000
67A15-22_Gt7_Q1_03	2.373	0.141	-0.250	7.218	0.212	0.064	1.456	0.014	0.003

E2718C

Analysis Number	d464	esd	misfit	d206	esd	misfit	d128	esd	misfit
03E2718C_Gt5_Q1_01	2.941	0.141	-0.204	8.574	0.212	0.052	1.749	0.014	0.003
07E2718C_Gt5_Q2_01	2.124	0.141	-0.122	6.166	0.212	0.031	1.245	0.014	0.002
13E2718C_Gt5_Q3_03	2.439	0.141	-0.418	6.924	0.212	0.107	1.676	0.014	0.005
16E2718C_Gt5_Q4_01	2.144	0.141	-0.443	7.381	0.212	0.114	1.419	0.014	0.006
20E2718C_Gt7_Q1_01	2.698	0.141	-0.355	7.246	0.212	0.091	1.802	0.014	0.004
23E2718C_Gt7_Q2_01	2.437	0.141	-0.455	7.503	0.212	0.117	1.653	0.014	0.006
30E2718C_Gt1B_Q1_02	2.516	0.141	-0.480	7.869	0.212	0.123	1.704	0.014	0.006

A15-07A

Analysis Number	d464	esd	misfit	d206	esd	misfit	d128	esd	misfit
02A15-07A_Gt12_Q1	2.315	0.141	-0.731	7.422	0.212	0.188	1.794	0.014	0.009
03A15-07A_Gt12_Q2	2.254	0.141	-0.395	7.227	0.212	0.101	1.481	0.014	0.005
05A15-07A_Gt12_Q3_01	2.257	0.141	-1.330	7.019	0.212	0.341	2.286	0.014	0.016
06A15-07A_Gt12_Q4_01	2.585	0.141	-0.145	7.412	0.212	0.037	1.520	0.014	0.002
09A15-07A_Gt11_Q1_01	2.033	0.141	1.347	5.702	0.212	-0.346	-0.017	0.014	-0.017
11A15-07A_Gt5_Q1_01	2.149	0.141	0.542	6.477	0.212	-0.139	0.680	0.014	-0.007

A15-21A

Analysis Number	d464	esd	misfit	d206	esd	misfit	d128	esd	misfit
05A15-21A_Gt7_Q1_04	2.967	0.141	-0.454	8.527	0.212	0.117	1.984	0.014	0.006
08A15-21A_Gt10_Q1_01	2.910	0.141	-0.999	9.372	0.212	0.256	2.318	0.014	0.012
10A15-21A_Gt10_Q2_01	3.605	0.141	-0.843	9.848	0.212	0.216	2.701	0.014	0.010
12A15-21A_Gt12_Q1_01	3.238	0.141	-0.413	9.088	0.212	0.106	2.116	0.014	0.005
14A15-21A_Gt20B_Q1_01	3.287	0.141	-0.798	9.078	0.212	0.205	2.479	0.014	0.010
15A15-21A_Gt20B_Q2_01	3.420	0.141	-0.250	9.074	0.212	0.064	2.127	0.014	0.003
17A15-21A_Gt21_Q1_01	3.094	0.141	-0.298	8.648	0.212	0.076	1.944	0.014	0.004
19A15-21A_Gt23_Q1_01	3.167	0.141	-0.314	8.310	0.212	0.081	2.047	0.014	0.004

A15-01A

Analysis Number	d464	esd	misfit	d206	esd	misfit	d128	esd	misfit
03A15-01A_Gt5_Q1_01	3.024	0.141	-0.563	8.158	0.212	0.145	2.155	0.014	0.007
05A15-01A_Gt8_Q1_01	2.734	0.141	-0.470	8.071	0.212	0.121	1.852	0.014	0.006
08A15-01A_Gt10_Q1_01	2.707	0.141	-0.490	7.328	0.212	0.126	1.915	0.014	0.006
11A15-01A_Gt10_Q2_02	2.620	0.141	-0.506	6.835	0.212	0.130	1.903	0.014	0.006
13A15-01A_Gt11_Q1_01	1.175	0.141	-0.508	3.995	0.212	0.130	1.004	0.014	0.006
17A15-01A_Gt13_Q1_03	2.843	0.141	-0.416	8.622	0.212	0.107	1.844	0.014	0.005
19A15_01A_Gt15_Q1_01	2.955	0.141	-0.360	8.313	0.212	0.092	1.915	0.014	0.004
22A15-01A_Gt16_Q1_01	2.904	0.141	-0.574	8.257	0.212	0.148	2.059	0.014	0.007

25A15-01A_Gt16_Q3_01	2.863	0.141	-0.405	7.818	0.212	0.104	1.924	0.014	0.005

Table S1.11.3 Quartz-in-garnet calculated strains, stresses and inclusion pressures. All values reported in GPa.

A14-71

Analysis Number	e1+e2	esd	e3	esd	Vs	esd	10E6cv	corr%	chi2	Sigma 1	Sigma 2	Sigma 3	Pinc	Unc (2σ)
02A14-71_Gt1_Q1_01	-0.0250	0.0065	0.0068	0.0040	-0.0182	0.0027	-25.633	-98.6	21.5	-1.082	-1.082	0.414	0.584	0.238
06A14-71_Gt1_Q2_01	-0.0254	0.0057	0.0074	0.0035	-0.0180	0.0023	-19.343	-98.6	16.2	-1.094	-1.094	0.472	0.572	0.209
17A14-71_Gt4_Q1_01	-0.0060	0.0014	0.0021	0.0009	-0.0039	0.0006	-1.191	-98.6	0.06	-0.254	-0.254	0.149	0.120	0.053
21A14-71_Gt4_Q2_01	-0.0109	0.0016	0.0011	0.0010	-0.0098	0.0007	-1.483	-98.6	1.25	-0.495	-0.495	-0.018	0.336	0.059
25A14-71_Gt4_Q3_01	-0.0129	0.0024	0.0005	0.0015	-0.0124	0.0010	-3.501	-98.6	2.94	-0.596	-0.596	-0.107	0.433	0.089
03A14-71_Gt11_Q1_01	-0.0091	0.0015	-0.0004	0.0009	-0.0095	0.0006	-1.318	-98.6	1.11	-0.430	-0.430	-0.155	0.338	0.054
07A14-71_Gt11_Q2_01	-0.0092	0.0030	0.0003	0.0018	-0.0088	0.0012	-5.362	-98.6	4.5	-0.426	-0.426	-0.082	0.311	0.109
11A14-71A_Gt11_Q3_01	-0.0099	0.0028	0.0006	0.0017	-0.0094	0.0011	-4.544	-98.6	3.82	-0.455	-0.455	-0.059	0.323	0.102
15A14-71_Gt11_Q4_01	-0.0097	0.0028	0.0009	0.0017	-0.0088	0.0012	-4.707	-98.6	3.95	-0.442	-0.442	-0.025	0.303	0.102
19A14-71_Gt11_Q5_01	-0.0086	0.0019	-0.0004	0.0012	-0.0089	0.0008	-2.117	-98.6	1.78	-0.406	-0.406	-0.149	0.321	0.071
23A14-71_Gt11_Q6_01	-0.0102	0.0017	0.0001	0.0010	-0.0101	0.0007	-1.715	-98.6	1.44	-0.475	-0.475	-0.116	0.355	0.061
27A14-71_Gt11_Q7_01	-0.0101	0.0038	-0.0009	0.0023	-0.0110	0.0016	-8.732	-98.6	7.33	-0.483	-0.483	-0.221	0.395	0.138
31A14-71_Gt12_Q1_01	-0.0140	0.0018	0.0004	0.0011	-0.0136	0.0008	-2.003	-98.6	1.68	-0.648	-0.648	-0.131	0.476	0.066

LB15-03B

Analysis Number	e1+e2	esd	e3	esd	Vs	esd	10E6cv	corr%	chi2	Sigma 1	Sigma 2	Sigma 3	Pinc	Unc
04LB15-03B__Gt1_Q1_01	-0.0081	0.0020	-0.0022	0.0009	-0.0103	0.0011	-1.821	-99.4	6.03	-0.405	-0.405	-0.335	0.382	0.064
12LB15-03B_Gt5_Q1_01	-0.0065	0.0025	-0.0029	0.0012	-0.0094	0.0014	-2.901	-99.4	9.61	-0.339	-0.339	-0.389	0.356	0.081
20LB15-03B_Gt3_Q1_01	-0.0134	0.0052	0.0004	0.0024	-0.0130	0.0028	-12.393	-99.4	41	-0.620	-0.620	-0.124	0.455	0.167
24LB15-03B_Gt6_Q1_01	-0.0076	0.0017	-0.0012	0.0008	-0.0089	0.0009	-1.278	-99.4	4.23	-0.370	-0.370	-0.222	0.320	0.055
28LB15-03B_Gt6_Q2_01	-0.0081	0.0020	-0.0012	0.0009	-0.0093	0.0011	-1.889	-99.4	6.26	-0.393	-0.393	-0.228	0.338	0.064
32LB15-03B_Gt6_Q3_01	-0.0099	0.0011	0.0003	0.0005	-0.0096	0.0006	-0.547	-99.4	1.81	-0.458	-0.458	-0.091	0.336	0.035
36LB15-03B_Gt6_Q4_01	-0.0134	0.0031	0.0013	0.0015	-0.0122	0.0017	-4.512	-99.4	14.9	-0.609	-0.609	-0.028	0.415	0.101
40LB15-03B_Gt6_Q5_01	-0.0082	0.0020	-0.0012	0.0009	-0.0094	0.0011	-1.770	-99.4	5.86	-0.398	-0.398	-0.229	0.342	0.064

GB

Analysis Number	e1+e2	esd	e3	esd	Vs	esd	10E6cv	corr%	chi2	Sigma 1	Sigma 2	Sigma 3	Pinc	Unc
03GB12-01A_Gt1_Q1_01	-0.0109	0.0050	-0.0062	0.0023	-0.0171	0.0027	-11.325	-99.4	37.5	-0.586	-0.586	-0.795	0.655	0.160
08GB12-01A_Gt1_Q2_01	-0.0113	0.0045	-0.0051	0.0021	-0.0164	0.0024	-9.191	-99.4	30.4	-0.591	-0.591	-0.683	0.621	0.145
12GB12-01A_Gt1_Q3_01	-0.0106	0.0053	-0.0045	0.0024	-0.0151	0.0029	-12.765	-99.4	42.3	-0.551	-0.551	-0.610	0.570	0.169
16GB12-01A_Gt2_Q1_01	-0.0085	0.0069	-0.0073	0.0032	-0.0159	0.0037	-21.915	-99.4	72.6	-0.487	-0.487	-0.882	0.619	0.222

20GB12-01A_Gt2_Q2_01	-0.0126	0.0031	-0.0042	0.0014	-0.0167	0.0017	-4.358	-99.4	14.4	-0.640	-0.640	-0.603	0.628	0.099
24GB12-01A_Gt5_Q1_01	-0.0049	0.0008	0.0031	0.0004	-0.0019	0.0004	-0.302	-99.4	0.46	-0.190	-0.190	0.269	0.037	0.027
03GB15-01A_Gt6_Q1_01	-0.0016	0.0094	-0.0108	0.0044	-0.0124	0.0051	-40.673	-99.4	135	-0.209	-0.209	-1.169	0.529	0.303
08GB15-01A_Gt6B_Q1_01	-0.0089	0.0072	-0.0095	0.0033	-0.0184	0.0039	-23.584	-99.4	78.1	-0.533	-0.533	-1.121	0.729	0.230
12GB15-01A_Gt6C_Q1_01	-0.0125	0.0036	-0.0029	0.0017	-0.0153	0.0019	-5.871	-99.4	19.4	-0.619	-0.619	-0.464	0.567	0.117
20GB15-01A_Gt7_Q1_01	-0.0077	0.0057	-0.0066	0.0026	-0.0143	0.0031	-14.797	-99.4	49	-0.441	-0.441	-0.798	0.560	0.182
24GB15-01A_Gt7_Q2_01	-0.0099	0.0070	-0.0062	0.0033	-0.0162	0.0038	-22.661	-99.4	75.1	-0.539	-0.539	-0.782	0.620	0.226
28GB15-01A_Gt15B_Q1_01	-0.0094	0.0042	-0.0054	0.0019	-0.0148	0.0023	-8.051	-99.4	26.7	-0.506	-0.506	-0.691	0.567	0.134
32GB15-01A_Gt9_Q1_01	-0.0097	0.0058	-0.0079	0.0027	-0.0176	0.0031	-15.529	-99.4	51.4	-0.551	-0.551	-0.961	0.687	0.187
36GB15-01A_Gt11_Q1_01	-0.0096	0.0055	-0.0059	0.0026	-0.0155	0.0030	-14.068	-99.4	46.6	-0.521	-0.521	-0.747	0.596	0.178
40GB15-01A_Gt11_Q2_01	-0.0101	0.0049	-0.0057	0.0023	-0.0158	0.0027	-11.057	-99.4	36.6	-0.542	-0.542	-0.732	0.605	0.158

EA15-10A

Analysis Number	**e1+e2**	**esd**	**e3**	**esd**	**Vs**	**esd**	**10E6cv**	**corr%**	**chi2**	**Sigma 1**	**Sigma 2**	**Sigma 3**	**Pinc**	**Unc**
03EA15-10A_Gt1_Q1_01	-0.0018	0.0010	-0.0001	0.0005	-0.0019	0.0006	-0.481	-99.4	1.59	-0.085	-0.085	-0.033	0.068	0.033
07EA15-10A_Gt1_Q2_01	-0.0094	0.0017	-0.0009	0.0008	-0.0103	0.0009	-1.366	-99.4	4.53	-0.450	-0.450	-0.212	0.371	0.055
09EA15-10A_Gt1_Q3_01	-0.0080	0.0026	-0.0016	0.0012	-0.0095	0.0014	-2.989	-99.4	9.9	-0.393	-0.393	-0.269	0.352	0.083
13EA15-10A_Gt2_Q1_01	-0.0069	0.0025	-0.0013	0.0012	-0.0082	0.0014	-2.936	-99.4	9.73	-0.338	-0.338	-0.224	0.300	0.081
23EA15-10A_Gt7_Q1_01	-0.0092	0.0020	-0.0014	0.0009	-0.0106	0.0011	-1.889	-99.4	6.26	-0.447	-0.447	-0.263	0.385	0.064

27EA15-10A_Gt8_Q1_02	-0.0069	0.0047	-0.0033	0.0022	-0.0101	0.0025	-10.037	-99.4	33.2	-0.363	-0.363	-0.437	0.388	0.152
33EA15-10A_Gt8_Q2_01	-0.0071	0.0042	-0.0034	0.0019	-0.0105	0.0023	-8.070	-99.4	26.7	-0.374	-0.374	-0.450	0.399	0.134
37EA15-10A_Gt8_Q3_01	-0.0096	0.0026	-0.0016	0.0012	-0.0112	0.0014	-3.017	-99.4	9.99	-0.468	-0.468	-0.289	0.408	0.083
44EA15-10A_Gt8_Q4_03	-0.0066	0.0021	-0.0023	0.0010	-0.0089	0.0011	-1.970	-99.4	6.52	-0.337	-0.337	-0.327	0.333	0.068

A15-22

Analysis Number	**e1+e2**	**esd**	**e3**	**esd**	**Vs**	**esd**	**10E6cv**	**corr%**	**chi2**	**Sigma 1**	**Sigma 2**	**Sigma 3**	**Pinc**	**Unc**
03A15-22_Gt7_Q1_01	-0.0074	0.0021	-0.0015	0.0010	-0.0089	0.0012	-2.088	-99.4	6.92	-0.364	-0.364	-0.251	0.326	0.068
08A15-22_Gt8_Q1_02	-0.0098	0.0008	0.0008	0.0004	-0.0090	0.0004	-0.302	-99.4	0.58	-0.447	-0.447	-0.036	0.310	0.027
12A15-22_Gt9_Q1_01	-0.0095	0.0008	0.0001	0.0004	-0.0094	0.0004	-0.305	-99.4	1.01	-0.442	-0.442	-0.107	0.330	0.027
14A15-22_Gt9_Q2_01	-0.0093	0.0008	-0.0001	0.0004	-0.0094	0.0004	-0.302	-99.4	0.02	-0.435	-0.435	-0.126	0.332	0.027
16A15-22_Gt9_Q3_01	-0.0047	0.0030	-0.0033	0.0014	-0.0080	0.0016	-4.055	-99.4	13.4	-0.260	-0.260	-0.409	0.310	0.097
22A15-22_Gt9_Q4_01	-0.0062	0.0018	-0.0019	0.0008	-0.0081	0.0010	-1.450	-99.4	4.8	-0.313	-0.313	-0.279	0.302	0.057
25A15-22_Gt20_Q1_01	-0.0097	0.0008	0.0001	0.0004	-0.0096	0.0005	-0.312	-99.4	1.03	-0.451	-0.451	-0.110	0.338	0.027
28A15-22_Gt20_Q2_01	-0.0077	0.0009	-0.0008	0.0004	-0.0085	0.0005	-0.358	-99.4	1.19	-0.369	-0.369	-0.181	0.306	0.028
29A15-22_Gt20_Q3_01	-0.0098	0.0008	0.0003	0.0004	-0.0095	0.0004	-0.302	-99.4	0.11	-0.454	-0.454	-0.090	0.332	0.027
32A15-22_Gt20b_Q1_01	-0.0078	0.0008	-0.0011	0.0004	-0.0089	0.0004	-0.302	-99.4	0.08	-0.378	-0.378	-0.214	0.323	0.027
37A15-22_Gt3_Q1_02	-0.0086	0.0008	0.0005	0.0004	-0.0081	0.0004	-0.302	-99.4	0.05	-0.395	-0.395	-0.053	0.281	0.027
41A15-22_Gt3_Q2_01	-0.0053	0.0027	-0.0030	0.0012	-0.0082	0.0015	-3.299	-99.4	10.9	-0.285	-0.285	-0.385	0.318	0.085

45A15-22_Gt3_Q3_01	-0.0123	0.0012	0.0023	0.0005	-0.0100	0.0006	-0.626	-99.4	2.08	-0.546	-0.546	0.092	0.333	0.037
49A15-22_Gt6_Q1_01	-0.0048	0.0032	-0.0034	0.0015	-0.0082	0.0018	-4.814	-99.4	15.9	-0.266	-0.266	-0.421	0.318	0.103
55A15-22_Gt2b_Q1_01	-0.0041	0.0045	-0.0039	0.0021	-0.0081	0.0024	-9.113	-99.4	30.2	-0.240	-0.240	-0.466	0.315	0.145
59A15-22_Gt6_Q1_03	-0.0106	0.0008	0.0001	0.0004	-0.0105	0.0004	-0.302	-99.4	0.13	-0.493	-0.493	-0.121	0.369	0.027
63A15-22_Gt6_Q2_03	-0.0108	0.0008	0.0012	0.0004	-0.0096	0.0004	-0.302	-99.4	0	-0.489	-0.489	-0.006	0.328	0.027
67A15-22_Gt7_Q1_03	-0.0097	0.0015	0.0001	0.0007	-0.0095	0.0008	-0.993	-99.4	3.29	-0.451	-0.451	-0.110	0.338	0.048

E2718C

Analysis Number	**e1+e2**	**esd**	**e3**	**esd**	**Vs**	**esd**	**10E6cv**	**corr%**	**chi2**	**Sigma 1**	**Sigma 2**	**Sigma 3**	**Pinc**	**Unc**
03E2718C_Gt5_Q1_01	-0.0113	0.0012	0.00003	0.0006	-0.0113	0.0007	-0.66	-99.4	2.18	-0.527	-0.527	-0.137	0.397	0.040
07E2718C_Gt5_Q2_01	-0.0083	0.0008	0.0001	0.0004	-0.0082	0.0004	-0.30	-99.4	0.79	-0.386	-0.386	-0.092	0.288	0.027
13E2718C_Gt5_Q3_03	-0.0058	0.0025	-0.0022	0.0011	-0.0081	0.0013	-2.77	-99.4	9.17	-0.298	-0.298	-0.306	0.301	0.079
16E2718C_Gt5_Q4_01	-0.0106	0.0026	0.0007	0.0012	-0.0099	0.0014	-3.11	-99.4	10.3	-0.486	-0.486	-0.057	0.343	0.083
20E2718C_Gt7_Q1_01	-0.0056	0.0021	-0.0027	0.0010	-0.0083	0.0011	-2.00	-99.4	6.63	-0.295	-0.295	-0.357	0.315	0.068
23E2718C_Gt7_Q2_01	-0.0082	0.0027	-0.0011	0.0012	-0.0093	0.0014	-3.29	-99.4	10.9	-0.396	-0.396	-0.219	0.337	0.085
30E2718C_Gt1B_Q1_02	-0.0090	0.0028	-0.0009	0.0013	-0.0099	0.0015	-3.66	-99.4	12.1	-0.431	-0.431	-0.207	0.357	0.090

A15-07A

Analysis Number	**e1+e2**	**esd**	**e3**	**esd**	**Vs**	**esd**	**10E6cv**	**corr%**	**chi2**	**Sigma 1**	**Sigma 2**	**Sigma 3**	**Pinc**	**Unc**

02A15-07A_Gt12_Q1	-0.0060	0.0043	-0.0025	0.0020	-0.0085	0.0023	-8.485	-99.4	28.1	-0.311	-0.311	-0.340	0.321	0.138
03A15-07A_Gt12_Q2	-0.0093	0.0023	-0.0001	0.0011	-0.0094	0.0013	-2.475	-99.4	8.2	-0.435	-0.435	-0.126	0.332	0.075
05A15-07A_Gt12_Q3_01	0.0019	0.0078	-0.0074	0.0036	-0.0056	0.0042	-28.072	-99.4	93	-0.003	-0.003	-0.764	0.257	0.250
06A15-07A_Gt12_Q4_01	-0.0097	0.0009	-0.00003	0.0004	-0.0098	0.0005	-0.332	-99.4	1.1	-0.453	-0.453	-0.123	0.343	0.028
09A15-07A_Gt11_Q1_01	-0.0228	0.0079	0.0103	0.0037	-0.0126	0.0043	-28.781	-99.4	95.3	-0.936	-0.936	0.813	0.353	0.255
11A15-07A_Gt5_Q1_01	-0.0168	0.0032	0.0056	0.0015	-0.0112	0.0017	-4.659	-99.4	15.4	-0.715	-0.715	0.388	0.347	0.103

A15-21A

Analysis Number	**e1+e2**	**esd**	**e3**	**esd**	**Vs**	**esd**	**10E6cv**	**corr%**	**chi2**	**Sigma 1**	**Sigma 2**	**Sigma 3**	**Pinc**	**Unc**
05A15-21A_Gt7_Q1_04	-0.0082	0.0027	-0.0021	0.0012	-0.0102	0.0014	-3.270	-99.4	10.8	-0.409	-0.409	-0.325	0.381	0.085
08A15-21A_Gt10_Q1_01	-0.0069	0.0059	-0.0036	0.0027	-0.0105	0.0032	-15.832	-99.4	52.4	-0.367	-0.367	-0.469	0.401	0.189
10A15-21A_Gt10_Q2_01	-0.0043	0.0049	-0.0059	0.0023	-0.0102	0.0027	-11.259	-99.4	37.3	-0.274	-0.274	-0.681	0.410	0.158
12A15-21A_Gt12_Q1_01	-0.0087	0.0024	-0.0022	0.0011	-0.0109	0.0013	-2.706	-99.4	8.96	-0.433	-0.433	-0.342	0.403	0.077
14A15-21A_Gt20B_Q1_01	-0.0041	0.0047	-0.0053	0.0022	-0.0094	0.0025	-10.109	-99.4	33.5	-0.257	-0.257	-0.615	0.376	0.152
15A15-21A_Gt20B_Q2_01	-0.0087	0.0015	-0.0023	0.0007	-0.0109	0.0008	-0.995	-99.4	3.29	-0.435	-0.435	-0.353	0.407	0.048
17A15-21A_Gt21_Q1_01	-0.0092	0.0018	-0.0015	0.0008	-0.0107	0.0010	-1.407	-99.4	4.66	-0.448	-0.448	-0.274	0.390	0.057
19A15-21A_Gt23_Q1_01	-0.0067	0.0018	-0.0029	0.0009	-0.0096	0.0010	-1.565	-99.4	5.18	-0.349	-0.349	-0.392	0.363	0.060

A15-01A

Analysis Number	e1+e2	esd	e3	esd	Vs	esd	10E6cv	corr%	chi2	Sigma 1	Sigma 2	Sigma 3	Pinc	Unc
03A15-01A_Gt5_Q1_01	-0.0046	0.0033	-0.0042	0.0015	-0.0088	0.0018	-5.035	-99.4	16.7	-0.267	-0.267	-0.504	0.346	0.105
05A15-01A_Gt8_Q1_01	-0.0080	0.0028	-0.0018	0.0013	-0.0098	0.0015	-3.504	-99.4	11.6	-0.396	-0.396	-0.291	0.361	0.090
08A15-01A_Gt10_Q1_01	-0.0044	0.0029	-0.0036	0.0013	-0.0080	0.0016	-3.813	-99.4	12.6	-0.250	-0.250	-0.438	0.313	0.092
11A15-01A_Gt10_Q2_02	-0.0027	0.0030	-0.0043	0.0014	-0.0070	0.0016	-4.056	-99.4	13.4	-0.179	-0.179	-0.491	0.283	0.097
13A15-01A_Gt11_Q1_01	-0.0027	0.0030	-0.0017	0.0014	-0.0044	0.0016	-4.085	-99.4	13.5	-0.147	-0.147	-0.214	0.170	0.097
17A15-01A_Gt13_Q1_03	-0.0102	0.0024	-0.0007	0.0011	-0.0110	0.0013	-2.744	-99.4	9.09	-0.485	-0.485	-0.201	0.390	0.077
19A15_01A_Gt15_Q1_01	-0.0083	0.0021	-0.0018	0.0010	-0.0101	0.0011	-2.054	-99.4	6.81	-0.410	-0.410	-0.294	0.371	0.068
22A15-01A_Gt16_Q1_01	-0.0062	0.0034	-0.0032	0.0016	-0.0093	0.0018	-5.235	-99.4	17.3	-0.329	-0.329	-0.417	0.358	0.110
25A15-01A_Gt16_Q3_01	-0.0062	0.0024	-0.0028	0.0011	-0.0090	0.0013	-2.601	-99.4	8.61	-0.324	-0.324	-0.375	0.341	0.077

Appendix S2

S2.1 Field observations of high-strain features

High-strain features observed within the amphibolite-facies mélange zone provide an indication that the zone was actively deforming during subduction and support the tectonic mixing model proposed for the terrane. There are multiple examples of high-strain features within the mélange zone, including folding and crenulation of mélange matrix and mylonitization of blocks. Figure S2.1 shows one example of a sheared contact between a mélange block and associated matrix with an interpretive sketch of the relationship.

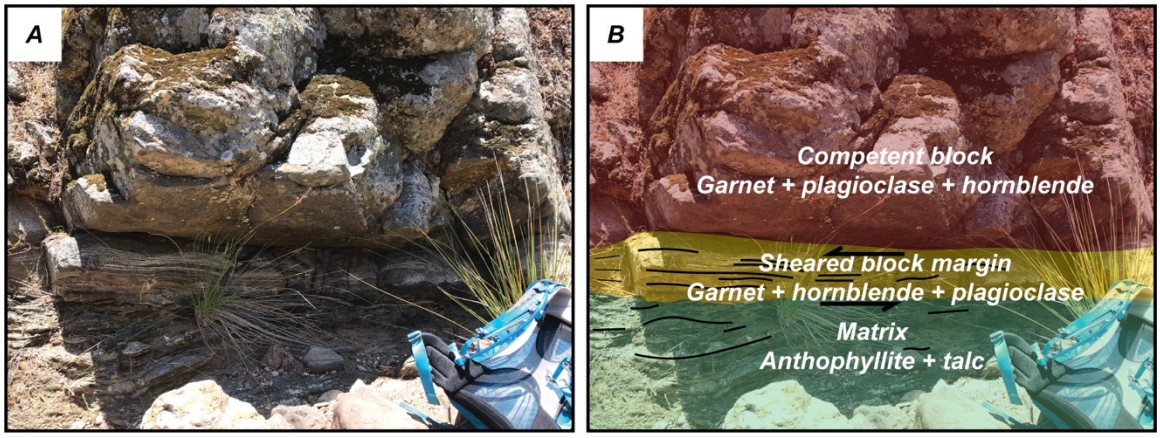

Figure S2.1. Example of mylonitized mafic block (garnet + plagioclase + hornblende) in contact with an anothophyllite + talc matrix. The base of the block is sheared, indicated by strong foliation, reduction of grain size and change in mineral modes. A) Field photo of outcrop. B) Interpretive sketch of the field relationship with shear sense indicators.

S2.2 EPMA and ICP-MS garnet analyses

Table S2.2.1 EPMA traverses across garnet

A14-50C

Number	Distance (µm)	MgO	MnO	CaO	Al2O3	FeO	SiO2	Total
1	0	5.12	10.30	5.09	21.95	20.16	38.36	100.98
2	14	5.22	10.26	5.22	22.03	19.97	38.16	100.86
3	28	5.47	10.76	4.00	21.61	21.02	38.27	101.13
4	41	5.63	10.87	3.51	21.58	21.44	38.13	101.16
5	55	5.64	11.03	3.68	21.71	21.17	37.89	101.12
7	83	5.37	10.86	4.77	21.45	20.45	38.33	101.23
8	97	5.44	10.98	4.19	21.20	20.97	38.36	101.14
9	110	5.41	11.04	4.40	21.30	20.89	38.24	101.28
11	138	5.32	11.06	4.47	20.99	20.90	38.20	100.94
12	152	5.29	10.84	4.76	20.96	20.33	38.21	100.39
13	165	5.44	10.85	4.39	21.11	21.15	38.24	101.18
14	179	5.42	10.88	4.20	21.24	21.05	38.14	100.93
16	207	5.75	10.90	3.59	21.47	20.83	38.39	100.93
17	221	5.74	10.98	3.34	21.18	21.44	37.87	100.55
18	234	5.50	10.70	4.08	21.46	21.11	38.43	101.28
19	248	5.38	10.48	4.57	21.78	20.70	38.27	101.18
20	262	5.04	10.34	5.13	22.02	20.22	38.18	100.93

A14-25A

Number	Distance (µm)	MgO	MnO	CaO	Al2O3	FeO	SiO2	Total
1	0	4.22	1.15	8.24	21.97	26.30	38.24	100.12
2	14	4.63	0.64	9.98	21.83	23.73	38.38	99.19
3	28	4.81	0.55	10.00	21.61	24.01	38.46	99.44
4	41	4.71	0.57	10.05	21.68	23.65	38.13	98.79

5	55	4.56	0.65	10.36	21.63	24.00	38.36	99.56
6	69	4.27	0.81	10.11	21.46	24.12	38.23	99.00
7	83	3.66	1.19	8.78	21.36	25.87	37.71	98.57
9	110	3.72	0.95	9.78	21.49	24.81	38.06	98.81
10	124	3.87	1.18	9.21	21.37	25.69	38.28	99.60
11	138	3.74	1.30	9.38	21.34	26.21	37.95	99.92
12	152	3.52	1.30	9.63	21.42	25.59	37.95	99.41
13	165	3.42	1.62	9.61	21.30	25.73	37.91	99.59
14	179	2.87	1.68	10.34	21.21	25.62	37.79	99.51
15	193	3.13	1.58	10.18	21.25	25.61	38.02	99.77
16	207	2.88	1.64	10.27	21.23	25.77	37.79	99.58
17	221	2.98	1.56	9.55	21.27	26.34	37.87	99.57
18	234	2.98	1.46	9.45	21.11	26.56	37.64	99.20
19	248	2.78	1.28	9.53	20.72	26.98	37.47	98.76
20	262	2.97	1.29	9.58	21.31	26.63	37.87	99.65
21	276	2.76	1.30	9.08	21.01	27.35	37.71	99.21
22	290	2.73	1.33	9.51	21.22	27.22	37.59	99.60
23	303	2.77	1.15	9.47	21.18	26.84	37.73	99.14
24	317	2.63	1.33	9.99	21.22	26.64	37.73	99.54
25	331	2.99	1.38	9.37	21.05	26.45	37.90	99.14
26	345	3.10	1.40	9.49	21.24	26.58	37.97	99.78
27	359	3.23	1.26	9.42	21.11	26.44	37.70	99.16
28	372	3.16	1.31	9.62	21.56	26.04	37.63	99.32
29	386	3.29	1.36	9.38	20.98	26.16	37.61	98.78
30	400	3.17	1.32	9.45	21.06	26.30	37.99	99.29
31	414	3.23	1.37	9.25	21.24	26.27	37.76	99.12
32	427	3.18	1.26	9.59	21.16	26.35	37.71	99.25
33	441	3.41	1.36	9.23	21.00	26.41	37.94	99.35
34	455	3.59	1.25	9.18	21.33	26.38	38.03	99.76
35	469	3.26	1.23	9.50	21.14	26.05	37.89	99.07
36	483	3.34	1.27	9.31	21.15	26.30	37.89	99.26
37	496	3.10	1.20	9.68	21.27	26.06	37.92	99.23

38	510	3.04	1.27	9.68	21.18	26.65	37.88	99.70
39	524	3.56	1.24	9.72	21.10	25.70	37.89	99.21
40	538	3.40	1.30	8.91	21.54	26.45	37.70	99.30
41	552	3.22	1.27	10.13	21.16	25.67	37.90	99.35
42	565	3.12	1.43	9.96	21.17	25.93	37.74	99.35
43	579	3.51	1.24	9.19	21.04	26.27	37.73	98.98
44	593	3.74	1.29	9.08	21.45	26.40	37.63	99.59
45	607	3.70	1.35	9.27	21.37	25.66	37.87	99.22
46	621	3.21	1.56	9.87	21.28	25.59	37.87	99.38
47	634	3.87	1.47	9.52	21.39	25.42	38.18	99.85
48	648	3.95	1.13	10.05	21.52	24.78	37.85	99.28
49	662	4.01	1.00	9.59	21.50	25.38	38.00	99.48
50	676	4.05	1.06	9.37	21.56	25.06	38.21	99.31
52	703	4.04	1.00	9.06	21.73	25.63	38.58	100.04
53	717	4.31	0.83	9.74	21.66	24.59	38.29	99.42
54	731	4.23	0.81	9.88	21.66	24.47	38.02	99.07
55	745	4.28	0.69	10.58	21.60	23.67	38.19	99.01
56	758	4.37	0.62	10.67	21.66	23.51	38.11	98.94
57	772	4.49	0.63	9.90	21.38	24.22	37.97	98.59
58	786	4.49	0.66	10.11	21.54	24.19	38.12	99.11
60	814	3.95	0.98	9.12	21.51	25.75	37.75	99.06

A15-14

Number	**Distance (µm)**	**MgO**	**MnO**	**CaO**	**Al2O3**	**FeO**	**SiO2**	**Total**
1	0	6.93	0.97	4.73	22.04	26.35	38.65	99.67
2	14	7.44	0.86	4.76	21.92	25.98	38.50	99.46
3	28	7.55	0.94	4.88	21.93	25.49	38.77	99.56
4	41	7.61	0.97	4.75	21.97	25.79	38.29	99.38
5	55	7.49	0.89	4.97	21.83	25.75	38.43	99.36
6	69	7.63	0.94	4.77	21.96	25.93	38.55	99.78
7	83	7.51	0.97	4.96	21.82	25.69	38.58	99.53
8	97	7.12	0.98	4.82	21.68	26.48	38.46	99.54

9	110	7.52	0.92	4.90	21.69	25.61	38.28	98.92
10	124	7.41	0.86	4.96	21.95	26.04	38.74	99.96
11	138	7.40	0.95	4.86	21.78	25.83	38.52	99.34
12	152	7.61	0.88	4.91	21.74	25.98	38.21	99.33
13	165	7.54	0.90	4.88	21.90	25.87	38.43	99.52
14	179	7.55	0.96	4.84	21.64	26.06	38.28	99.33
15	193	7.48	0.86	4.86	21.46	25.82	38.47	98.95
16	207	7.56	0.94	4.63	21.93	25.49	38.29	98.84
17	221	6.78	1.00	4.79	21.71	27.05	38.14	99.47
18	234	7.28	0.96	4.57	21.99	26.17	38.47	99.44
19	248	7.43	0.93	4.71	21.46	26.19	38.14	98.86
20	262	7.00	0.96	4.91	22.00	26.47	38.39	99.73
21	276	7.29	0.90	4.81	21.96	26.28	38.26	99.50
22	290	7.54	0.90	4.91	21.69	25.79	38.37	99.20
23	303	7.51	0.95	4.85	21.83	26.17	38.49	99.80
25	331	7.03	0.92	4.95	21.88	25.93	38.56	99.27
26	345	7.17	0.97	4.92	21.89	26.23	38.11	99.29
27	359	7.09	0.94	4.61	21.83	26.50	38.09	99.06
28	372	7.01	0.95	5.24	21.87	25.79	38.29	99.15
29	386	7.29	0.89	5.32	22.01	25.70	38.47	99.68
30	400	7.43	0.88	5.02	22.01	25.49	38.53	99.36
31	414	7.29	0.89	5.62	21.85	25.15	38.34	99.14
32	427	7.50	0.90	5.30	21.92	25.40	38.70	99.72
33	441	7.50	0.83	5.35	21.83	25.56	38.45	99.52
34	455	7.36	0.90	5.41	21.68	25.51	38.68	99.54
35	469	7.27	0.92	5.26	21.82	25.28	38.40	98.95
36	483	7.02	0.93	4.87	21.79	26.05	38.29	98.95
37	496	7.13	0.89	4.50	21.95	26.50	38.53	99.50
38	510	7.31	0.94	4.59	21.84	26.40	38.09	99.17
39	524	7.45	0.89	4.77	21.91	25.76	38.35	99.13
40	538	6.94	0.96	5.15	21.72	26.07	38.17	99.01

A14-55

Number	Distance (µm)	MgO	MnO	CaO	Al2O3	FeO	SiO2	Total
1	0	4.29	1.15	8.33	21.63	26.66	37.87	99.93
2	14	4.55	1.07	7.74	21.60	26.93	38.25	100.14
3	28	4.62	0.98	8.05	21.59	26.86	38.27	100.37
4	41	4.37	0.84	8.19	21.68	26.97	38.20	100.25
5	55	4.34	0.75	8.43	21.56	27.12	38.28	100.48
6	69	4.37	0.69	8.35	21.61	27.15	37.98	100.15
7	83	4.39	0.67	8.25	21.56	27.34	38.23	100.44
8	97	4.47	0.79	8.02	21.58	27.24	38.14	100.24
9	110	4.45	0.86	8.30	21.53	27.01	38.12	100.27
10	124	4.42	0.75	8.56	21.55	26.97	38.06	100.31
11	138	4.44	0.82	8.01	21.61	27.38	38.35	100.61
12	152	4.29	0.74	8.22	21.52	27.16	38.30	100.23
13	165	4.32	0.77	8.13	21.24	27.20	38.12	99.78
14	179	4.36	0.84	8.16	21.16	27.12	38.29	99.93
15	193	4.33	0.86	8.14	21.50	27.32	38.44	100.59
16	207	4.40	1.06	8.10	21.42	26.85	37.74	99.57
19	248	4.41	1.05	8.36	21.67	26.85	38.36	100.70
20	262	4.55	1.04	7.99	21.70	27.33	38.12	100.73
21	276	4.60	1.07	8.16	21.67	26.91	38.39	100.80
23	303	3.72	1.22	8.05	21.23	28.19	37.99	100.40
24	317	4.35	1.13	8.13	21.53	27.23	38.06	100.43
25	331	4.49	1.06	7.88	21.25	27.16	38.37	100.21
26	345	4.20	1.08	8.14	21.29	27.56	38.15	100.42
27	359	4.51	0.97	7.85	21.29	27.31	38.33	100.26
28	372	3.69	1.18	7.67	21.62	28.35	38.05	100.56
29	386	3.74	1.12	7.81	21.39	28.43	38.24	100.73
30	400	3.90	1.11	7.54	21.29	27.24	37.76	98.84
31	414	3.96	1.12	7.69	21.59	27.97	37.95	100.28
32	427	4.40	1.05	8.27	21.32	27.14	38.04	100.22
33	441	3.86	1.14	8.07	21.08	27.58	37.54	99.27

35	469	4.14	1.10	8.06	21.48	27.60	38.34	100.72
36	483	3.84	1.09	8.15	21.31	27.66	38.18	100.23
38	510	4.37	0.95	8.34	21.26	26.73	38.21	99.86
39	524	4.44	1.04	8.14	21.24	27.40	38.16	100.42
41	552	4.08	0.95	8.43	21.24	26.96	38.30	99.96
42	565	4.30	0.94	8.35	21.62	26.97	38.29	100.47
43	579	4.29	0.94	8.34	21.28	27.11	38.31	100.27
44	593	4.40	0.93	8.23	21.20	26.93	37.85	99.54
45	607	4.28	0.92	8.23	21.19	27.19	38.15	99.96
46	621	4.05	0.79	8.73	21.34	27.04	38.08	100.03
47	634	3.92	0.75	8.79	21.36	27.29	38.22	100.33
48	648	3.81	0.67	8.54	21.11	27.70	38.02	99.85
49	662	3.69	0.62	8.84	21.08	27.97	38.17	100.37
50	676	3.50	0.57	9.51	21.20	27.16	37.95	99.89
51	690	3.55	0.50	9.00	21.30	27.66	37.93	99.94
52	703	3.55	0.45	8.77	21.25	27.95	38.20	100.17
53	717	3.67	0.44	8.69	21.33	28.07	38.17	100.37
54	731	3.71	0.44	8.56	21.40	28.26	38.13	100.50
55	745	3.83	0.43	8.33	21.46	28.28	38.07	100.40
56	758	3.81	0.59	8.54	21.45	27.73	38.18	100.30
57	772	4.15	0.74	8.82	21.59	26.67	38.17	100.14
58	786	4.27	0.89	8.87	21.84	26.23	38.23	100.33
59	800	4.37	1.11	8.33	21.62	26.88	38.47	100.78
60	814	3.97	1.26	7.33	21.95	28.09	38.20	100.80

A14-29

Number	Distance (µm)	MgO	MnO	CaO	Al2O3	FeO	SiO2	Total
1	0	4.54	0.72	8.05	22.12	27.15	38.71	101.32
2	14	4.77	0.70	8.15	22.16	26.94	38.46	101.24
3	28	4.74	0.72	8.31	22.09	26.63	38.45	101.00
4	41	4.87	0.68	8.51	21.95	26.45	38.65	101.17
5	55	4.86	0.71	8.38	21.92	26.76	38.75	101.43

6	69	4.86	0.71	8.43	22.05	26.59	38.60	101.30
7	83	4.90	0.70	8.47	21.93	26.53	38.66	101.20
8	97	4.91	0.71	8.37	21.92	26.77	38.42	101.21
9	110	4.85	0.68	8.20	21.98	26.78	38.78	101.37
10	124	4.80	0.69	8.12	21.96	26.71	38.61	100.97
11	138	4.99	0.70	8.19	22.05	26.36	38.54	100.94
12	152	5.02	0.71	8.21	21.91	26.63	38.78	101.39
13	165	4.94	0.67	8.26	21.97	26.75	38.74	101.42
14	179	4.99	0.66	8.45	21.97	26.26	38.92	101.34
15	207	4.92	0.67	8.28	21.88	25.96	38.62	100.40
16	221	4.84	0.71	8.77	21.59	26.47	38.72	101.20
17	234	4.75	0.68	8.48	21.79	26.53	38.59	100.94
18	248	4.66	0.68	8.95	21.81	25.87	38.58	100.66
19	276	4.75	0.69	9.35	21.96	25.23	38.92	101.01
20	303	4.77	0.75	9.39	21.97	25.80	38.73	101.47
21	345	4.74	0.67	9.55	21.86	25.52	38.85	101.36
22	372	4.68	0.69	9.70	21.86	25.27	38.65	100.95
23	386	4.71	0.70	9.42	22.07	25.34	38.37	100.72
24	400	4.59	0.69	9.89	21.99	25.41	38.42	101.14
25	414	4.72	0.66	9.55	21.89	25.74	38.59	101.28
26	427	4.72	0.66	9.20	22.23	25.63	38.59	101.10
27	441	4.60	0.69	9.66	22.09	25.22	38.74	101.08
28	455	4.73	0.69	9.29	21.94	26.05	38.65	101.43
29	496	4.65	0.67	9.09	21.78	26.17	38.63	101.26
30	524	4.86	0.67	8.95	21.98	26.11	38.76	101.42
31	538	4.92	0.67	8.84	21.90	26.27	38.66	101.31
32	552	4.98	0.67	8.56	21.73	26.68	38.54	101.26
33	565	4.86	0.65	8.47	21.41	26.61	38.57	100.71
34	579	4.98	0.70	8.36	21.81	26.83	38.65	101.45
35	593	4.99	0.71	8.21	21.89	26.75	38.67	101.34
36	607	4.97	0.70	8.28	21.65	27.02	38.50	101.23
37	634	4.89	0.67	8.04	21.95	27.04	38.81	101.49

38	648	4.81	0.72	7.79	21.87	26.99	38.67	100.93
39	676	4.98	0.73	7.81	22.08	27.01	38.54	101.26
40	717	5.00	0.71	7.88	22.02	27.25	38.54	101.44
41	731	5.00	0.71	7.80	21.61	27.10	38.57	100.92
42	772	5.02	0.68	7.93	21.95	27.24	38.54	101.45
43	786	4.91	0.71	8.15	21.92	27.04	38.73	101.50
44	800	4.98	0.72	8.17	21.81	27.07	38.30	101.17
45	814	4.81	0.71	8.03	21.74	26.94	38.57	100.94
46	841	4.81	0.72	8.08	21.92	27.05	38.51	101.17
47	855	4.87	0.72	8.05	22.07	27.04	38.55	101.36
48	869	4.74	0.70	8.54	21.96	26.55	38.68	101.20
49	883	4.75	0.73	8.10	21.86	27.09	38.67	101.28
50	896	4.28	0.77	7.83	21.91	27.45	38.32	100.61

Trace element concentrations in garnet were determined by laser ablation inductively coupled plasma mass spectrometry using the Thermo-Fisher Element 2 magnetic sector mass spectrometer coupled to a Nu-Wave UP213 solid state Nd:YAG laser ablation system housed in the Plasma Laboratory at the University of Maryland. Data were standardized using the glass reference material NIST-610 (Jochum et al., 2011) and the secondary standard BHVO-2g (Jochum, 2005). Data for the secondary standard and for each sample are reported in Tables S2.2.2-7.

Table S2.2.2 Reproducibility of secondary standard BHVO-2g for 6/10/2019 analytical session (n=3). Concentrations reported in ppm.

BHVO-2g

Element	Reported	Measured (Ave.)	STD	%RSD	Δ (%)
Rb	8.89	8.57	0.70	8.2	3.7
Sr	389	382.6	47.78	12.5	1.6
Zr	175	165.4	17.72	10.7	5.5
Ba	127	125.3	15.92	12.7	1.3
La	15.8	14.99	1.41	9.4	5.1
Ce	36.0	35.08	5.07	14.5	2.6
Pr	5.16	5.06	0.69	13.6	1.8
Nd	24.3	23.29	1.81	7.8	4.2
Sm	6.07	5.74	0.15	2.6	5.4
Eu	2.10	1.81	0.24	13.3	13.8
Gd	6.35	6.76	1.65	24.3	-6.5
Tb	0.96	0.84	0.15	17.8	12.8
Dy	5.47	5.02	0.26	5.1	8.2
Ho	1.03	0.89	0.13	14.3	13.9
Er	2.56	2.44	0.63	25.7	4.6
Tm	0.339	0.31	0.03	9.6	8.4
Yb	2.13	1.94	0.24	12.2	9.0
Lu	0.293	0.26	0.01	3.6	11.3
Hf	4.60	4.41	0.31	7.0	4.0

Table S2.2.3 LA-ICP-MS analysis of A14-25A Grt1. Concentrations reported in ppm. Uncertainties are 2σ.

A14-25A

Spot Number	Distance (µm)	Rb	Unc	Sr	Unc	Zr	Unc	Ba	Unc	La	Unc
1	113	0.08	0.06	0.18	0.05	7.88	0.53	0.28	0.13	0.00	0.00
2	243	0.39	0.10	5.90	0.44	14.46	0.92	7.14	0.87	0.05	0.02
3	600	0.00	0.05	0.10	0.04	9.21	0.61			0.00	0.00
4	751			0.17	0.04	14.97	0.90			0.00	0.00
5	1151	0.97	0.15	10.13	0.90	8.25	0.69	21.40	1.80	0.06	0.02
Matrix Ring Start	1280										
Matrix Ring End	1423										
6	1586	0.06	0.06	0.04	0.02	4.18	0.36	0.02	0.04	0.00	0.00
7	1738	0.05	0.05	0.08	0.03	3.92	0.38			0.00	0.00
8	2009	0.03	0.05	0.06	0.02	1.11	0.18	0.48	0.22	0.00	0.00
15	4899	0.07	0.06	1.42	0.36	17.70	4.80			0.00	0.00
16	5211	0.05	0.06	0.28	0.08	3.38	0.44			0.12	0.05
18	5940	0.04	0.05	0.05	0.02	2.43	0.26			0.00	0.00
19	6023	0.07	0.05	0.04	0.02	2.26	0.29			0.00	0.00
20	6311	0.10	0.06	0.08	0.03	4.89	0.39			0.00	0.00
21	6456	0.02	0.04	0.07	0.03	4.86	0.42			0.00	0.00
22	6781	0.10	0.06	0.07	0.04	2.02	0.25	0.63	0.23	0.00	0.00
Matrix Ring Start	6299										
Matrix Ring End	7100										
23	7237	0.02	0.04	0.10	0.04	9.50	0.70	0.02	0.03	0.00	0.00
24	7457	0.06	0.05	0.02	0.01	7.12	0.64			0.00	0.00
25	7564	0.03	0.04	0.08	0.04	10.50	1.10			0.00	0.00
26	7674	0.02	0.04	0.10	0.04	10.07	0.91	0.14	0.13	0.00	0.00
27	7795	0.04	0.05	0.04	0.02	8.79	0.70	0.01	0.02	0.00	0.00

A14-25A (cont.)

Spot Number		Distance (µm)	Ce	Unc	Pr	Unc	Nd	Unc	Sm	Unc	Eu	Unc
	1	113	0.01	0.01	0.01	0.00	0.21	0.04	0.80	0.09	0.90	0.13
	2	243	0.22	0.05	0.02	0.01	0.35	0.06	0.65	0.08	0.46	0.09
	3	600					0.17	0.04	0.51	0.09	0.36	0.07
	4	751	0.01	0.01			0.21	0.04	0.55	0.07	0.55	0.10
	5	1151	0.31	0.06	0.06	0.02	0.48	0.08	0.70	0.09	0.39	0.07
Matrix Ring Start		1280										
Matrix Ring End		1423										
	6	1586	0.01	0.01			0.10	0.03	0.55	0.07	0.47	0.08
	7	1738					0.08	0.02	0.32	0.07	0.37	0.07
	8	2009					0.00	0.00	0.06	0.02	0.04	0.03
	15	4899	0.03	0.02			0.09	0.03	0.14	0.04	0.18	0.05
	16	5211	0.54	0.16	0.08	0.03	0.42	0.11	0.19	0.04	0.16	0.05
	18	5940					0.02	0.01	0.06	0.02	0.08	0.03
	19	6023					0.00	0.01	0.06	0.02	0.06	0.03
	20	6311					0.03	0.01	0.27	0.05	0.33	0.07
	21	6456					0.08	0.03	0.41	0.07	0.50	0.10
	22	6781					0.02	0.01	0.15	0.04	0.16	0.05
Matrix Ring Start		6299										
Matrix Ring End		7100										
	23	7237					0.19	0.05	0.50	0.08	0.57	0.11
	24	7457					0.14	0.03	0.53	0.09	0.47	0.10
	25	7564					0.38	0.07	0.92	0.12	0.99	0.20
	26	7674	0.02	0.01			0.16	0.03	0.57	0.07	0.58	0.11
	27	7795					0.17	0.04	0.48	0.08	0.36	0.08

A14-25A (cont.)

Spot Number	Distance (µm)	Gd	Unc	Tb	Unc	Dy	Unc	Ho	Unc	Er	Unc
1	113	3.79	0.38	1.60	0.14	13.62	0.75	3.19	0.22	8.75	0.62
2	243	2.38	0.36	1.04	0.09	8.48	0.68	1.91	0.16	5.78	0.47
3	600	1.96	0.29	0.95	0.09	8.68	0.65	2.10	0.17	6.09	0.48
4	751	2.72	0.36	0.91	0.09	7.61	0.54	1.81	0.14	5.16	0.39
5	1151	2.64	0.31	1.26	0.11	12.28	0.78	3.38	0.21	10.95	0.73
Matrix Ring Start	1280										
Matrix Ring End	1423										
6	1586	3.29	0.39	1.87	0.15	24.10	1.40	6.83	0.40	21.50	1.40
7	1738	1.84	0.34	1.44	0.13	21.10	1.50	7.68	0.50	27.80	1.50
8	2009	0.38	0.14	0.34	0.05	4.40	0.40	1.49	0.11	5.96	0.53
15	4899	1.23	0.26	0.91	0.10	15.10	1.00	6.89	0.57	31.00	2.30
16	5211	0.76	0.19	0.72	0.09	12.92	0.96	5.94	0.43	29.80	2.40
18	5940	0.53	0.15	0.42	0.07	7.13	0.53	3.18	0.21	16.80	1.10
19	6023	0.78	0.20	0.48	0.07	8.30	0.78	3.85	0.29	22.00	1.50
20	6311	2.33	0.36	1.48	0.14	26.70	1.70	10.47	0.60	40.70	2.20
21	6456	3.38	0.44	2.05	0.18	28.10	1.90	9.37	0.59	30.00	1.70
22	6781	1.09	0.23	0.81	0.09	11.70	1.10	4.11	0.33	13.19	0.99
Matrix Ring Start	6299										
Matrix Ring End	7100										
23	7237	3.00	0.43	0.86	0.10	7.52	0.78	1.57	0.18	3.76	0.49
24	7457	3.35	0.49	1.17	0.16	10.70	1.10	2.54	0.25	6.68	0.83
25	7564	4.55	0.67	1.45	0.21	11.00	1.50	2.06	0.29	4.43	0.65
26	7674	3.57	0.58	1.08	0.16	8.90	1.30	1.95	0.25	4.96	0.66
27	7795	2.73	0.43	0.81	0.12	7.50	1.00	1.80	0.21	5.19	0.58

A14-25A (cont.)

Spot Number	Distance (µm)	Tm	Unc	Yb	Unc	Lu	Unc	Hf	Unc
1	113	1.19	0.11	8.12	0.71	1.08	0.10	0.01	0.02
2	243	0.82	0.09	5.30	0.52	0.80	0.08	0.07	0.06
3	600	0.78	0.07	5.14	0.52	0.76	0.09	0.01	0.02
4	751	0.68	0.07	4.42	0.46	0.59	0.07	0.13	0.07
5	1151	1.57	0.12	10.28	0.76	1.61	0.11	0.13	0.08
Matrix Ring Start	1280								
Matrix Ring End	1423								
6	1586	2.68	0.20	16.30	1.10	1.93	0.13	0.03	0.03
7	1738	4.18	0.29	25.50	1.90	2.94	0.18		
8	2009	0.89	0.09	5.19	0.55	0.52	0.06	0.01	0.02
15	4899	5.58	0.40	43.40	2.60	5.88	0.39	0.19	0.11
16	5211	5.31	0.39	42.50	3.30	6.02	0.51	0.03	0.04
18	5940	3.44	0.26	29.10	1.80	4.31	0.23		
19	6023	4.29	0.29	35.80	2.30	5.75	0.38		
20	6311	6.45	0.38	40.50	2.00	4.74	0.28		
21	6456	3.97	0.31	21.90	1.50	2.51	0.18	0.13	0.09
22	6781	1.60	0.11	8.88	0.91	1.13	0.12	0.01	0.02
Matrix Ring Start	6299								
Matrix Ring End	7100								
23	7237	0.42	0.07	2.86	0.42	0.34	0.06	0.06	0.05
24	7457	0.77	0.11	4.66	0.51	0.69	0.09	0.04	0.04
25	7564	0.44	0.07	2.64	0.40	0.33	0.07	0.03	0.03
26	7674	0.62	0.08	3.71	0.58	0.47	0.08	0.03	0.03
27	7795	0.75	0.09	4.81	0.61	0.67	0.08		

Table S2.2.4 LA-ICP-MS analysis of A14-55 Grt2 and Grt2. Concentrations reported in ppm. Uncertainties are 2σ.

A14-55

Spot Number	Distance (μm)	Rb	Unc	Sr	Unc	Zr	Unc	Ba	Unc	La	Unc
Garnet 1											
1	101	0.29	0.09	0.20	0.06	3.02	0.32	0.50	0.25		
2	259	0.02	0.05	0.05	0.04	7.97	0.99			0.08	0.05
5	579	0.10	0.06	0.03	0.02	13.00	2.90				
6	754	0.10	0.06	2.10	0.41	56.70	7.70			0.01	0.01
7	1137	0.14	0.06	0.22	0.09	3.80	0.42	0.29	0.29	0.01	0.01
8	1323	0.06	0.07	0.32	0.11	6.80	1.40				
9	1527	0.05	0.06	0.06	0.03	5.12	0.64				
10	1651	0.19	0.08	0.32	0.09	185.00	28.00	0.10	0.08	0.02	0.01
11	1777	0.22	0.12	2.26	0.75	85.00	12.00			0.02	0.02
12	1904	0.21	0.11	0.08	0.04	24.00	4.10				
13	2213	0.00	0.04	0.08	0.04	112.00	17.00			0.00	0.00
15	2570	0.02	0.06	0.07	0.05	11.10	2.40				
16	2751	0.20	0.09	0.06	0.04	4.32	0.72				
17	2852	0.19	0.12	0.10	0.08	67.00	17.00				
18	2957	0.00	0.04	0.04	0.02	5.04	0.49				
19	3010			0.02	0.02	3.19	0.34				
Garnet 2											
21	137			2.72	0.40	1.75	0.24	0.11	0.10	0.00	0.00
22	277	0.06	0.06	0.39	0.11	5.47	0.58				
23	1782	0.05	0.06	0.93	0.26	3.50	0.63	0.03	0.05	0.62	0.17
24	1914	0.02	0.05	0.12	0.05	3.75	0.60			0.01	0.01
25	2252	0.89	0.30	1.36	0.34	6.10	1.20	5.30	1.40	0.25	0.10
26	2449	0.11	0.07	0.05	0.03	111.00	17.00			0.01	0.01
27	3008	0.13	0.09	0.07	0.04	3.88	0.76			0.00	0.00

A14-55 (cont.)

Spot Number	Distance (µm)	Ce	Unc	Pr	Unc	Nd	Unc	Sm	Unc	Eu	Unc
Garnet 1											
1	101	0.00	0.01			0.27	0.05	1.64	0.19	1.14	0.17
2	259	0.18	0.08	0.04	0.03	0.42	0.12	0.77	0.15	0.37	0.12
5	579	0.00	0.00			0.06	0.02	0.47	0.08	0.52	0.10
6	754	0.10	0.04	0.04	0.02	0.39	0.07	0.70	0.11	0.62	0.13
7	1137	0.05	0.03	0.01	0.01	0.42	0.09	1.45	0.16	1.08	0.15
8	1323	0.00	0.00			0.23	0.08	1.12	0.15	0.66	0.22
9	1527	0.01	0.01			0.20	0.05	0.98	0.15	0.50	0.13
10	1651	0.25	0.09	0.08	0.03	0.71	0.12	1.35	0.17	0.75	0.15
11	1777	0.13	0.07	0.04	0.03	0.58	0.17	1.12	0.19	0.52	0.13
12	1904	0.00	0.01	0.01	0.01	0.26	0.07	0.82	0.12	0.47	0.13
13	2213	0.02	0.01			0.09	0.02	0.48	0.09	0.44	0.11
15	2570	0.00	0.00			0.08	0.03	0.36	0.10	0.39	0.14
16	2751	0.00	0.00	0.00	0.00	0.24	0.06	1.37	0.18	1.47	0.23
17	2852	0.00	0.00			0.40	0.11	1.84	0.41	1.65	0.37
18	2957	0.00	0.00	0.02	0.01	0.37	0.05	1.13	0.14	0.66	0.11
19	3010	0.00	0.00	0.00	0.00	0.33	0.05	0.84	0.10	0.63	0.12
Garnet 2											
21	137	0.07	0.03	0.03	0.02	0.47	0.07	0.66	0.10	0.48	0.11
22	277	0.01	0.01	0.01	0.01	0.28	0.06	0.95	0.13	0.59	0.12
23	1782	2.90	0.63	0.58	0.16	4.32	0.96	1.76	0.36	0.99	0.22
24	1914	0.07	0.04	0.01	0.01	0.25	0.06	0.38	0.08	0.25	0.07
25	2252	0.87	0.25	0.22	0.09	1.26	0.36	0.77	0.18	0.49	0.14
26	2449	0.05	0.02	0.02	0.02	0.24	0.06	0.55	0.09	0.48	0.10
27	3008	0.00	0.01	0.01	0.01	0.28	0.07	0.90	0.17	0.65	0.12

A14-55 (cont.)

Spot Number	Distance (µm)	Gd	Unc	Tb	Unc	Dy	Unc	Ho	Unc	Er	Unc
Garnet 1											
1	101	12.10	1.30	3.40	0.28	30.30	2.30	6.36	0.50	18.10	1.70
2	259	4.59	0.76	1.13	0.14	10.00	1.10	2.19	0.28	5.25	0.82
5	579	6.03	0.74	3.59	0.33	40.30	3.10	9.65	0.74	28.20	2.50
6	754	7.41	0.84	3.76	0.29	42.40	2.70	10.65	0.76	30.50	2.40
7	1137	11.30	1.30	4.62	0.37	53.20	3.10	16.20	1.00	57.60	3.40
8	1323	7.30	1.60	2.73	0.35	34.30	4.90	10.00	1.50	34.50	3.80
9	1527	6.53	0.98	2.87	0.25	33.40	2.80	10.97	0.86	48.80	4.60
10	1651	6.84	0.78	3.16	0.31	35.60	3.00	11.48	0.87	48.10	3.70
11	1777	6.40	1.60	2.50	0.31	30.60	3.10	10.05	0.87	45.50	4.60
12	1904	5.34	0.70	2.25	0.22	29.40	2.50	10.25	0.95	42.90	3.10
13	2213	4.96	0.63	2.24	0.18	22.60	2.00	6.07	0.47	19.00	1.40
15	2570	5.37	0.78	2.64	0.32	26.40	3.10	6.54	0.69	19.20	2.00
16	2751	13.80	1.60	5.28	0.55	53.80	4.50	14.70	1.60	51.70	5.20
17	2852	14.70	2.20	5.76	0.65	59.90	8.60	16.30	2.40	47.60	5.40
18	2957	4.97	0.62	1.29	0.13	10.98	0.96	2.52	0.23	8.04	0.68
19	3010	5.17	0.70	1.26	0.13	11.25	0.92	2.97	0.28	10.82	0.94
Garnet 2											
21	137	2.85	0.43	1.08	0.12	9.39	0.77	2.53	0.22	8.88	0.79
22	277	5.19	0.67	1.64	0.15	15.50	1.30	4.15	0.35	13.10	1.10
23	1782	3.77	0.83	1.03	0.16	11.20	1.50	3.45	0.43	15.10	1.60
24	1914	1.82	0.39	1.17	0.12	15.10	1.30	4.73	0.37	17.30	1.50
25	2252	2.63	0.69	1.38	0.19	18.80	1.90	6.88	0.68	35.10	3.80
26	2449	5.08	0.75	2.03	0.20	20.80	1.50	5.46	0.40	17.30	1.30
27	3008	5.24	0.66	1.43	0.25	12.60	2.00	2.85	0.46	8.90	1.20

A14-55 (cont.)

Spot Number	Distance (µm)	Tm	Unc	Yb	Unc	Lu	Unc	Hf	Unc
Garnet 1									
1	101	2.30	0.20	16.10	1.20	2.35	0.22	0.01	0.02
2	259	0.56	0.09	3.59	0.75	0.49	0.11	0.02	0.04
5	579	3.37	0.31	20.00	1.80	2.55	0.24	0.35	0.17
6	754	3.99	0.26	23.30	1.80	2.90	0.21	1.72	0.36
7	1137	8.10	0.46	56.10	3.60	8.73	0.51	0.03	0.04
8	1323	5.92	0.56	47.50	5.90	6.93	0.87	0.09	0.10
9	1527	8.96	0.71	74.40	6.10	11.73	0.99	0.03	0.04
10	1651	8.78	0.78	73.30	5.90	11.47	0.93	5.00	1.10
11	1777	7.75	0.68	71.20	7.10	11.24	0.94	2.08	0.74
12	1904	8.23	0.72	68.90	6.10	11.37	0.89	0.66	0.26
13	2213	2.74	0.22	19.90	1.60	2.69	0.21	3.04	0.59
15	2570	2.75	0.32	14.50	1.60	1.83	0.23	0.11	0.11
16	2751	7.28	0.75	51.20	4.80	7.27	0.64	0.01	0.03
17	2852	6.23	0.90	40.20	5.70	5.65	0.76	2.19	0.97
18	2957	1.10	0.11	7.37	0.83	1.13	0.12	0.02	0.03
19	3010	1.71	0.16	12.00	1.20	1.91	0.17	0.00	0.00
Garnet 2									
21	137	1.34	0.14	8.68	0.82	1.30	0.13	0.00	0.00
22	277	2.04	0.18	13.80	1.20	2.21	0.20	0.04	0.05
23	1782	3.76	0.46	37.00	4.00	7.60	0.88	0.06	0.06
24	1914	2.85	0.26	19.50	1.60	3.06	0.24	0.01	0.01
25	2252	6.97	0.71	58.80	6.00	7.13	0.65	0.10	0.09
26	2449	2.69	0.24	18.00	1.60	2.66	0.23	2.43	0.61
27	3008	1.39	0.21	9.60	1.70	1.32	0.14	0.00	0.00

Table S2.2.5 LA-ICP-MS analysis of A14-50C Grt1, Grt2 and Grt3. Concentrations reported in ppm. Uncertainties are 2σ.

A14-50C

Spot Number	Distance (µm)	Rb	Unc	Sr	Unc	Zr	Unc	Ba	Unc	La	Unc
Garnet 1											
1	36	0.13	0.14	0.09	0.05	3.27	0.59				
2	106	0.27	0.17	0.05	0.04	1.09	0.25				
3	178	0.14	0.11	0.01	0.02	1.15	0.25				
4	247	0.12	0.10	0.06	0.04	2.48	0.36				
Garnet 2											
1	49	0.02	0.07	0.12	0.05	4.27	0.52				
2	118	0.35	0.21	0.06	0.05	1.67	0.39				
3	186	0.22	0.15	4.50	1.80	6.70	1.20			0.31	0.14
4	268	0.04	0.09	0.02	0.01	5.72	0.60				
Garnet 3											
1	46	0.14	0.10	0.11	0.05	1.38	0.31	0.06	0.09		
2	120	0.08	0.07	0.05	0.03	5.58	0.79	0.12	0.13		

A14-50C (cont.)

Spot Number	Distance (µm)	Ce	Unc	Pr	Unc	Nd	Unc	Sm	Unc	Eu	Unc
Garnet 1											
1	36	0.02	0.02	0.01	0.01	0.80	0.18	3.44	0.46	2.56	0.70
2	106	0.03	0.02	0.01	0.01	0.61	0.13	4.40	0.55	3.33	0.64
3	178	0.01	0.01	0.00	0.00	0.37	0.08	3.54	0.35	3.06	0.40
4	247	0.00	0.01	0.01	0.01	0.71	0.12	3.90	0.44	2.51	0.32
Garnet 2											
1	49	0.04	0.03	0.02	0.01	0.98	0.17	4.21	0.43	2.58	0.36
2	118	0.02	0.02	0.01	0.01	0.65	0.17	4.57	0.62	4.43	0.86
3	186	1.16	0.36	0.18	0.10	2.15	0.41	5.30	0.77	4.51	0.82
4	268	0.05	0.03	0.01	0.01	0.76	0.13	4.02	0.46	2.77	0.42
Garnet 3											
1	46	0.02	0.02	0.00	0.01	0.51	0.09	4.25	0.48	4.31	0.56
2	120	0.02	0.02	0.02	0.02	0.71	0.11	4.00	0.58	2.51	0.46

A14-50C (cont.)

Spot Number	Distance (µm)	Gd	Unc	Tb	Unc	Dy	Unc	Ho	Unc	Er	Unc
Garnet 1											
1	36	19.30	4.20	4.54	0.71	27.90	3.10	6.40	1.10	19.40	2.80
2	106	35.20	4.70	10.10	1.10	66.10	8.00	12.80	1.50	31.40	3.80
3	178	28.40	2.90	7.98	0.70	52.70	4.20	8.92	0.81	22.50	2.00
4	247	21.10	2.60	4.88	0.46	31.60	3.00	6.89	0.71	18.60	2.00
Garnet 2											
1	49	21.40	2.70	5.01	0.61	29.20	2.90	5.17	0.48	14.00	1.70
2	118	42.20	6.70	13.70	2.00	92.00	13.00	18.20	2.50	50.60	6.70
3	186	43.50	6.30	11.70	1.60	85.00	11.00	17.80	2.50	48.00	7.00
4	268	19.80	2.20	4.20	0.45	23.00	2.40	3.46	0.37	7.71	0.84
Garnet 3											
1	46	36.90	3.60	11.40	1.10	81.70	7.80	15.40	1.50	39.90	3.70
2	120	18.20	2.80	3.81	0.48	18.30	2.20	2.20	0.28	5.02	0.88

A14-50C (cont.)

Spot Number	Distance (µm)	Tm	Unc	Yb	Unc	Lu	Unc	Hf	Unc
Garnet 1									
1	36	2.95	0.37	23.80	4.20	3.65	0.66		
2	106	4.20	0.56	27.40	3.70	4.03	0.45		
3	178	3.05	0.28	21.10	2.00	3.37	0.32	0.01	0.02
4	247	3.32	0.36	20.30	2.00	3.28	0.37		
Garnet 2									
1	49	2.09	0.26	14.80	1.70	2.18	0.24	0.01	0.02
2	118	6.90	0.88	46.20	6.30	7.00	1.00		
3	186	7.10	1.20	47.30	7.00	7.30	1.10	0.32	0.23
4	268	1.21	0.17	7.19	0.99	1.06	0.15	0.02	0.03
Garnet 3									
1	46	5.13	0.49	37.60	3.60	5.50	0.53		
2	120	0.56	0.10	3.40	0.62	0.57	0.11	0.01	0.03

Table S2.2.6 LA-ICP-MS analysis of A15-14 Grt1, Grt2 and Grt3. Concentrations reported in ppm. Uncertainties are 2σ.

A15-14

Spot Number	Distance (µm)	Rb	Unc	Sr	Unc	Zr	Unc	Ba	Unc	La	Unc
Garnet 1											
1	120	0.16	0.06	0.23	0.09	3.82	0.40	0.96	0.29	0.04	0.02
2	205	0.06	0.07	0.02	0.02	5.81	0.75				
3	338	0.08	0.18	0.02	0.02	3.24	0.68	0.02	0.04		
5	559			0.03	0.02	9.25	0.88				
6	599			0.06	0.04	3.94	0.60				
7	949	0.08	0.07	0.13	0.07	5.93	0.93	0.49	0.26		
8	983	0.56	0.23	0.20	0.07	2.50	0.36	0.03	0.05		
9	1277	1.95	0.75	0.07	0.05	1.28	0.35	0.34	0.23	0.01	0.01
10	1607	0.03	0.06	0.02	0.02	0.80	0.17				
11	1811	0.00	0.04	0.01	0.01	1.58	0.34				
Garnet 2											
12	75			0.04	0.04	1.43	0.26				
13	304			0.02	0.02	1.63	0.30	0.02	0.03		
14	526			0.03	0.02	1.48	0.27				
15	652			0.02	0.02	1.79	0.31				
16	729			0.03	0.03	6.56	0.83				
17	851	0.00	0.05	0.01	0.01	18.40	1.90				
18	1031	0.02	0.06	0.00	0.01	18.20	1.70	0.02	0.03		
19	1125	0.02	0.06	0.21	0.08	3.83	0.63	0.02	0.03		
Garnet 3											
20	100	1.17	0.42	0.10	0.06	2.04	0.79	1.29	0.60		
21	194	0.10	0.12	0.06	0.04	1.38	0.26	0.01	0.03		
22	508	0.02	0.06	0.02	0.02	1.08	0.23				
23	649			0.10	0.07	1.37	0.31				
24	904	0.04	0.07	0.06	0.05	15.10	1.70				
25	1024	0.02	0.07	0.05	0.03	6.50	0.83				
26	1162	0.00	0.05	0.03	0.02	2.79	0.37				
27	1378	0.20	0.09	0.05	0.03	1.76	0.31	0.05	0.05		

A15-14 (cont.)

Spot Number	Distance (µm)	Ce	Unc	Pr	Unc	Nd	Unc	Sm	Unc	Eu	Unc
Garnet 1											
1	120	0.41	0.09	0.08	0.02	0.42	0.06	0.69	0.10	0.64	0.12
2	205	0.00	0.00	0.01	0.01	0.09	0.04	0.83	0.17	0.49	0.18
3	338	0.01	0.01			0.10	0.04	0.71	0.21	0.70	0.16
5	559	0.00	0.00			0.22	0.05	1.10	0.14	0.93	0.14
6	599	0.03	0.02			0.12	0.05	0.59	0.10	0.51	0.15
7	949	0.04	0.02			0.18	0.05	0.61	0.10	0.40	0.10
8	983	0.02	0.02			0.17	0.05	0.71	0.11	0.54	0.17
9	1277	0.12	0.05			0.26	0.06	0.64	0.11	0.73	0.20
10	1607	0.00	0.00			0.11	0.03	0.64	0.13	0.58	0.13
11	1811	0.00	0.00			0.20	0.05	0.91	0.16	0.70	0.15
Garnet 2											
12	75	0.00	0.01			0.22	0.05	0.87	0.14	0.67	0.13
13	304					0.20	0.05	0.89	0.11	0.77	0.15
14	526	0.00	0.00			0.21	0.05	0.70	0.10	0.60	0.11
15	652					0.14	0.03	0.67	0.11	0.52	0.11
16	729					0.19	0.04	0.79	0.13	0.80	0.18
17	851			0.01	0.01	0.44	0.07	2.05	0.27	1.72	0.28
18	1031	0.01	0.01	0.00	0.00	0.42	0.08	1.91	0.22	1.72	0.28
19	1125	0.01	0.01	0.01	0.01	0.16	0.05	0.70	0.15	0.54	0.12
Garnet 3											
20	100	0.01	0.01			0.16	0.06	0.88	0.22	0.80	1.00
21	194	0.03	0.03			0.21	0.06	0.96	0.21	0.69	0.13
22	508	0.01	0.01			0.18	0.04	0.72	0.12	0.71	0.12
23	649	0.01	0.01	0.01	0.01	0.22	0.06	0.81	0.10	0.54	0.11
24	904	0.01	0.01			0.24	0.05	1.25	0.23	1.20	0.22
25	1024	0.00	0.00			0.21	0.06	0.91	0.17	1.02	0.19
26	1162	0.00	0.00			0.16	0.05	0.70	0.13	0.69	0.16
27	1378	0.03	0.02	0.01	0.01	0.13	0.04	0.53	0.10	0.51	0.12

A15-14 (cont.)

Spot Number	Distance (µm)	Gd	Unc	Tb	Unc	Dy	Unc	Ho	Unc	Er	Unc
Garnet 1											
1	120	2.97	0.47	0.96	0.10	8.78	0.72	2.31	0.20	9.24	0.82
2	205	4.08	0.79	1.45	0.17	10.80	1.20	2.51	0.24	8.36	0.99
3	338	3.96	0.86	1.17	0.29	10.10	1.40	2.52	0.61	9.00	2.40
5	559	6.14	0.69	1.64	0.14	12.32	0.85	3.05	0.25	9.92	0.85
6	599	2.77	0.48	0.99	0.18	8.74	0.98	2.53	0.31	10.20	1.10
7	949	3.49	0.60	0.97	0.10	8.95	0.75	2.72	0.25	11.00	1.30
8	983	3.26	0.63	1.12	0.17	11.60	1.40	3.45	0.40	15.30	1.70
9	1277	2.89	0.61	1.17	0.25	9.20	1.60	2.30	0.33	8.50	1.20
10	1607	3.27	0.68	0.97	0.16	9.10	1.50	2.39	0.33	9.60	1.20
11	1811	4.49	0.76	1.36	0.18	10.90	1.30	2.78	0.34	9.37	0.90
Garnet 2											
12	75	4.07	0.68	1.37	0.17	11.00	1.50	2.52	0.32	8.20	1.10
13	304	4.59	0.75	1.41	0.20	11.70	1.40	2.49	0.28	8.22	0.98
14	526	5.86	0.78	1.57	0.19	12.20	1.20	3.14	0.31	9.90	1.00
15	652	4.22	0.55	1.28	0.14	12.10	1.30	3.03	0.32	10.20	1.00
16	729	6.60	1.00	1.95	0.25	18.00	1.90	4.67	0.63	15.30	2.00
17	851	11.50	1.40	2.68	0.28	20.10	2.40	4.16	0.47	13.70	1.40
18	1031	12.60	1.70	2.91	0.33	21.20	2.40	4.50	0.51	14.60	1.70
19	1125	3.81	0.62	1.32	0.23	11.70	1.40	3.12	0.34	11.10	1.30
Garnet 3											
20	100	4.30	1.10	1.16	0.44	11.40	4.80	2.20	1.00	7.60	2.90
21	194	4.90	1.00	1.61	0.30	14.20	2.20	4.04	0.57	16.70	3.20
22	508	5.06	0.73	1.47	0.17	14.90	1.70	4.85	0.57	20.90	2.30
23	649	5.06	0.83	1.53	0.22	13.50	1.50	4.15	0.42	16.20	1.90
24	904	8.40	1.30	1.88	0.25	14.60	2.10	3.59	0.44	11.90	1.40
25	1024	7.60	0.95	2.12	0.35	16.00	2.10	4.04	0.44	13.50	1.60
26	1162	5.16	0.74	1.65	0.21	15.50	1.90	3.97	0.40	14.00	1.70
27	1378	3.11	0.43	1.22	0.17	10.50	1.20	3.10	0.33	10.80	1.10

A15-14 (cont.)

Spot Number	Distance (µm)	Tm	Unc	Yb	Unc	Lu	Unc	Hf	Unc
Garnet 1									
1	120	1.54	0.14	12.00	1.20	1.96	0.18	0.02	0.03
2	205	1.33	0.18	10.34	0.79	1.38	0.18	0.12	0.14
3	338	1.65	0.36	13.40	1.90	1.80	0.50		
5	559	1.54	0.15	11.64	0.95	1.79	0.14	0.06	0.04
6	599	1.73	0.21	13.30	1.30	2.05	0.26	0.01	0.03
7	949	1.98	0.26	14.90	1.70	2.28	0.23	0.11	0.07
8	983	3.31	0.35	31.80	3.40	6.19	0.70	0.02	0.03
9	1277	1.43	0.24	10.50	1.50	1.50	0.24		
10	1607	1.53	0.21	12.70	2.20	1.98	0.34		
11	1811	1.76	0.23	12.60	1.60	1.81	0.22		
Garnet 2									
12	75	1.19	0.17	8.10	1.20	1.37	0.18		
13	304	1.29	0.19	8.80	1.30	1.38	0.17	0.02	0.03
14	526	1.50	0.18	10.70	1.30	1.61	0.21		
15	652	1.71	0.19	11.30	1.20	1.57	0.18		
16	729	2.49	0.29	16.60	1.90	2.64	0.38	0.11	0.10
17	851	1.80	0.18	12.70	1.50	1.78	0.17	0.24	0.11
18	1031	2.17	0.27	15.60	1.80	2.13	0.26	0.17	0.10
19	1125	1.69	0.23	12.00	1.50	1.79	0.21	0.03	0.04
Garnet 3									
20	100	1.18	0.35	8.20	2.40	1.26	0.73		
21	194	3.24	0.57	23.20	3.50	4.35	0.84		
22	508	3.93	0.40	34.70	3.90	6.39	0.62		
23	649	2.74	0.33	19.90	2.20	3.46	0.37		
24	904	1.76	0.24	11.70	1.80	2.27	0.30	0.13	0.08
25	1024	2.02	0.26	15.30	2.20	2.27	0.29		
26	1162	2.21	0.27	15.10	1.80	2.49	0.27		
27	1378	1.89	0.25	13.70	1.50	2.17	0.27	0.00	0.00

Table S2.2.7 LA-ICP-MS analysis of A14-29 Grt1 and Grt2. Concentrations reported in ppm. Uncertainties are 2σ.

A14-29

Spot Number	Distance (µm)	Rb	Unc	Sr	Unc	Zr	Unc	Ba	Unc	La	Unc
Garnet 1											
5	59	0.10	0.14	0.26	0.10	2.36	0.51	0.00	0.00	0.00	0.00
6	266	0.13	0.12	0.27	0.13	3.21	0.56	0.00	0.00	0.00	0.00
7	641	0.17	0.14	0.26	0.11	3.36	0.76	0.00	0.00	0.00	0.00
8	805	0.06	0.12	0.15	0.10	3.36	0.53	0.00	0.00	0.00	0.00
9	921	0.43	0.16	0.76	0.19	1.20	0.33	0.00	0.00	0.00	0.00
10	1000	0.37	0.18	0.52	0.12	0.98	0.27	0.00	0.00	0.00	0.00
Garnet 2											
1	84	0.06	0.09	0.15	0.07	5.02	0.67	0.00	0.00	0.00	0.00
2	145	0.30	0.15	0.16	0.06	1.67	0.36	0.00	0.00	0.00	0.00
3	207	0.13	0.12	0.17	0.08	2.39	0.41	0.00	0.00	0.00	0.00
5	329	0.09	0.10	1.41	0.76	1.83	0.35	0.00	0.00	0.00	0.00
6	396	0.15	0.16	0.11	0.09	1.68	0.61	0.00	0.00	0.00	0.00
7	454	0.25	0.13	0.18	0.09	1.58	0.30	0.00	0.00	0.00	0.00
8	522	0.12	0.11	0.22	0.09	1.76	0.36	0.00	0.00	0.00	0.00
9	611	0.07	0.10	0.18	0.10	2.06	0.42	0.00	0.00	0.00	0.00

A14-29 (cont.)

Spot Number	Distance (µm)	Ce	Unc	Pr	Unc	Nd	Unc	Sm	Unc	Eu	Unc
Garnet 1											
5	59	0.00	0.00	0.00	0.00	0.07	0.07	0.42	0.24	0.41	0.17
6	266	0.02	0.02	0.00	0.00	0.20	0.14	0.88	0.36	0.54	0.20
7	641	0.00	0.00	0.00	0.00	0.00	1.00	0.39	0.23	0.24	0.13
8	805	0.00	0.00	0.00	0.00	0.02	0.03	0.41	0.23	0.35	0.18
9	921	0.00	0.00	0.00	0.00	0.00	1.00	0.06	0.07	0.16	0.11
10	1000	0.00	0.00	0.00	0.00	0.07	0.06	0.24	0.15	0.16	0.10
Garnet 2											
1	84	0.00	0.00	0.01	0.01	0.09	0.04	0.56	0.13	0.46	0.16
2	145	0.00	0.01	0.00	0.00	0.07	0.04	0.55	0.14	0.53	0.16
3	207	0.00	0.00	0.00	0.00	0.04	0.03	0.20	0.09	0.30	0.11
5	329	0.00	0.00	0.00	0.01	0.08	0.06	0.16	0.07	0.10	0.05
6	396	0.00	0.00	0.00	0.00	0.08	0.06	0.17	0.10	0.19	0.10
7	454	0.00	0.00	0.00	0.00	0.00	0.00	0.19	0.10	0.14	0.09
8	522	0.00	0.00	0.00	0.00	0.02	0.02	0.12	0.07	0.09	0.06
9	611	0.00	0.01	0.00	0.00	0.06	0.04	0.12	0.07	0.12	0.09

A14-29 (cont.)

Spot Number	Distance (µm)	Gd	Unc	Tb	Unc	Dy	Unc	Ho	Unc	Er	Unc
Garnet 1											
5	59	3.11	0.86	1.17	0.17	11.10	1.30	2.56	0.33	7.80	1.10
6	266	4.90	1.10	1.54	0.24	12.60	1.40	2.59	0.33	7.60	1.00
7	641	2.94	0.90	1.01	0.19	8.50	1.00	1.83	0.26	5.83	0.93
8	805	2.38	0.81	0.64	0.13	5.50	1.00	1.11	0.17	4.17	0.81
9	921	1.25	0.48	0.44	0.09	3.51	0.77	1.47	0.19	9.00	1.10
10	1000	0.88	0.35	0.37	0.10	3.51	0.64	1.33	0.18	6.61	0.84
Garnet 2											
1	84	3.80	0.77	1.53	0.19	11.57	0.89	2.51	0.24	6.94	0.75
2	145	6.90	1.10	3.25	0.25	34.10	2.10	9.27	0.56	24.60	1.60
3	207	3.51	0.73	1.20	0.17	13.70	1.20	4.14	0.36	10.76	0.90
5	329	1.07	0.34	0.78	0.14	9.06	0.73	3.21	0.25	13.90	1.20
6	396	0.46	0.34	0.71	0.14	8.30	1.20	2.84	0.35	12.20	1.90
7	454	1.45	0.48	0.61	0.12	7.63	0.79	2.81	0.23	12.80	1.10
8	522	0.70	0.33	0.27	0.08	4.86	0.69	2.20	0.22	10.10	1.00
9	611	0.62	0.39	0.52	0.12	8.90	1.20	3.42	0.31	15.20	1.60

A14-29 (cont.)

Spot Number	Distance (µm)	Tm	Unc	Yb	Unc	Lu	Unc	Hf	Unc	Th	Unc	U	Unc
Garnet 1													
5	59	1.01	0.15	7.60	1.40	1.07	0.18	0.00	1.00	0.00	1.00	0.00	1.00
6	266	1.12	0.16	9.70	1.40	0.89	0.15	0.00	1.00	0.00	1.00	0.00	0.01
7	641	0.83	0.14	6.70	1.10	0.90	0.18	0.03	0.06	0.00	1.00	0.00	1.00
8	805	0.64	0.15	5.20	1.10	0.78	0.16	0.00	1.00	0.00	1.00	0.00	1.00
9	921	2.66	0.35	29.60	3.50	6.48	0.84	0.00	1.00	0.00	1.00	0.00	1.00
10	1000	1.51	0.20	17.70	2.00	3.70	0.48	0.00	1.00	0.00	1.00	0.00	1.00
Garnet 2													
1	84	0.99	0.14	5.42	0.66	0.65	0.10	0.05	0.06	0.00	0.00	0.00	0.00
2	145	3.33	0.27	21.20	1.50	2.50	0.20	0.00	0.00	0.00	0.00	0.00	0.00
3	207	1.49	0.18	9.04	0.98	1.26	0.14	0.00	0.00	0.00	0.00	0.00	0.00
5	329	2.37	0.20	19.50	1.40	2.91	0.24	0.00	0.00	0.00	0.00	0.01	0.01
6	396	2.02	0.31	15.80	2.40	2.33	0.28	0.00	0.00	0.00	0.00	0.01	0.01
7	454	2.24	0.20	19.20	2.00	3.07	0.30	0.00	0.00	0.00	0.00	0.00	0.00
8	522	2.20	0.21	20.00	2.00	3.79	0.36	0.00	0.00	0.00	0.00	0.00	0.00
9	611	3.09	0.34	24.90	2.80	4.01	0.35	0.00	0.00	0.00	0.00	0.00	0.00

S2.3 Comparison of TIMS and LA-ICP-MS garnet analyses

Concentrations of Sm and Nd determined by thermal ionization mass spectrometry (TIMS) were compared to concentrations determined by laser ablation inductively coupled plasma mass spectrometry (LA-ICP-MS) to assess the effectiveness of chemical preparation of the garnet separates. Averages and ranges for TIMS and LA-ICP-MS concentrations for each sample are reported in Table S2.3.1.

Table S2.3.1 Comparison of average Sm and Nd concentrations in garnet as determined by LA-ICP-MS and TIMS. Ranges reported in parentheses.

Sample	*Sm (ppm; LA-ICP-MS)*	*Sm (ppm; TIMS)*	*Nd (ppm; LA-ICP-MS)*	*Nd (ppm; TIMS)*
A14-25A	0.42 (0.06-0.92)	0.60 (0.55-0.63)	0.16 (0-0.48)	0.20 (0.17-0.24)
A14-50C	4.16 (3.44-5.30)	4.90 (3.69-5.50)	0.83 (0.51-2.15)	1.82 (1.64-1.95)
A14-55	0.92 (0.36-1.64)	0.78 (0.66-0.85)	0.34 (0.06-1.26)	0.35 (0.30-0.38)
A15-14	0.88 (0.53-2.05)	0.81 (0.59-1.02)	0.21 (0.09-0.44)	0.43 (0.31-0.51)
A14-29	0.32 (0.06-0.88)	0.71 (0.43-0.81)	0.06 (0-0.20)	0.58 (0.49-0.64)

S2.4 Whole rock solution ICP-MS analyses

Whole rock powders were prepared for analysis at the University of Maryland. Each was hand-crushed using a steal mortar and pestle and then powdered using a ceramic ball mill. Samples were dissolved in a combination of concentrated HNO_3, HF and HCl. An aliquot of each whole rock fraction was diluted in 2% HNO_3 to 60-71 ppm of material prior to spiking with 100 ppm In. Samples were analyzed using the Thermo-Fisher Element 2 magnetic sector mass spectrometer housed in the Plasma Laboratory at the University of Maryland. Prior to each analysis, the instrument was washed out for 2 minutes with 2% HNO_3. Unknowns were bracketed by analysis of the primary standard BHVO-2g (Jochum et al., 2005) and secondary standard BCR-2g (Jochum et al., 2011). Reproducibility of the BCR-2g is reported in Table S2.4.1. Data for samples A14-25A, A15-14, A14-55 and A14-50C are reported in Table S2.4.2.

Table S2.4.1 Standard reproducibility of BCR-2g for 3/12/2020 analytical session. Concentrations reported in ppm.

	Reported	Unc	Measured	STD	% Difference
Li	9	1	8	0.4	11
B	6	1	4	2.5	37
Sc	33	2	29	0.2	12
V	425	18	368	9	13
Cr	17	2	18	0.4	-6
Co	38	2	33	0.9	13
Ni	13	2	17	2.3	-32
Cu	21	5	17	0.39	17
Zn	125	5	113	2	10
Rb	47	0.5	43	5	9
Sr	342	4	300	9	12
Y	35	3	31	0.1	12
Zr	184	15	159	4	14
Nb	12.5	1	10.1	0.5	19
Mo	270	30	208	4	23
Sb	0.35	0.08	1.20	0.05	-244
Cs	1.16	0.07	1.02	0.1	12
Ba	683	7	588	25	14
La	24.7	0.3	21.6	0.01	12
Ce	53.3	0.5	45.7	0.60	14
Pr	6.7	0.4	5.9	0.04	12
Nd	28.9	0.3	24.9	0.02	14
Sm	6.59	0.07	5.70	0.05	13
Eu	1.97	0.02	1.72	0.002	13
Gd	6.71	0.07	6.07	0.08	10
Tb	1.02	0.08	0.90	0.001	12
Dy	6.44	0.06	5.57	0.03	13
Ho	1.27	0.08	1.12	0.002	12
Er	3.7	0.04	3.18	0.02	14
Tm	0.51	0.04	0.45	0.01	11
Yb	3.39	0.03	2.94	0.002	13
Lu	0.503	0.005	0.42	0.004	16
Hf	4.84	0.28	4.24	0.01	12
Ta	0.78	0.06	0.53	0.06	32
W	0.5	0.07	0.30	0.003	40
Pb	11	1	7.89	0.38	28
Th	5.9	0.3	5.15	0.01	13
U	1.69	0.12	1.22	0.01	28

Table S2.4.2 Whole rock trace element abundances for A14-25A, A15-14, A14-55 and A14-50C in ppm.

	A14-25A WR2	*A15-14 WR2*	*A14-55 WR2*	*A14-50C WR2*
Li	5.17	6.02	3.78	2.28
B	2.79	3.33	2.49	2.72
Sc	37.91	39.92	40.82	76.59
V	255.71	512.26	351.05	195.94
Cr	189.21	246.56	71.77	154.16
Co	37.77	47.76	27.24	160.76
Ni	100.45	99.69	31.77	372.00
Cu	51.39	18.41	23.13	2.19
Zn	87.84	102.97	90.84	158.15
Rb	2.53	0.75	1.72	0.88
Sr	109.90	104.29	45.30	34.12
Y	65.36	38.28	73.45	229.95
Zr	15.38	18.93	16.73	38.01
Nb	36.89	37.66	8.69	2.26
Mo	1.44	2.08	1.17	0.85
Sb	0.09	0.10	0.08	0.09
Cs	0.09	0.05	0.02	0.15
Ba	43.81	21.44	30.26	3.28
La	8.37	243.69	18.34	194.42
Ce	29.33	497.60	52.49	526.16
Pr	5.21	54.61	9.47	48.42
Nd	**28.03**	**221.14**	**46.86**	**202.91**
Sm	**10.34**	**37.74**	**13.30**	**37.19**
Eu	4.21	8.36	2.74	6.16
Gd	11.87	26.68	12.81	32.24
Tb	2.10	2.13	2.03	4.59
Dy	12.69	8.12	12.91	31.63
Ho	2.47	1.41	2.83	7.47
Er	6.51	4.22	8.28	22.78
Tm	0.92	0.61	1.27	3.48
Yb	5.65	4.14	8.20	22.98
Lu	0.73	0.58	1.08	3.11
Hf	0.60	0.76	0.75	1.07
Ta	2.74	2.12	0.39	0.21
W	1.07	0.47	1.10	0.43
Pb	1.21	1.45	0.85	1.06
Th	0.98	43.46	1.69	36.53
U	1.45	2.98	1.40	1.89

Appendix S3

S3.1 EPMA garnet analyses

Table S3.1.1 EPMA traverses across garnet

GB12-01A

Number	Distance (µm)	Na2O	FeO	TiO2	CaO	Al2O3	MgO	MnO	K2O	SiO2	Cr2O3	Total
1	0	0.00	26.46	0.04	9.20	21.94	2.95	1.43	0.01	38.56	0.00	100.56
2	25	0.04	26.47	0.05	8.89	21.29	2.84	2.03	0.00	38.19	0.00	99.73
6	124	0.00	25.65	0.48	10.10	21.88	2.51	1.75	0.00	38.79	0.10	101.18
8	174	0.03	26.55	0.25	9.41	22.03	1.99	2.24	0.00	38.39	0.02	100.90
9	198	0.03	26.18	0.19	9.39	21.80	1.71	2.53	0.00	38.45	0.00	100.26
10	223	0.14	25.89	0.26	9.87	21.73	1.75	2.62	0.01	38.08	0.01	100.37
11	248	0.00	25.83	0.26	9.35	21.51	1.78	2.83	0.00	38.05	0.13	99.73
13	298	0.13	25.76	0.28	9.36	20.69	1.84	3.11	0.00	38.33	0.00	99.50
14	322	0.09	25.25	0.29	9.31	21.77	1.88	3.16	0.01	38.97	0.07	100.80
15	347	0.00	25.70	0.22	9.50	21.64	1.71	3.52	0.00	38.30	0.00	100.55
16	372	0.16	25.19	0.34	9.47	21.71	1.71	3.95	0.00	38.14	0.00	100.65
17	397	0.04	25.04	0.27	9.54	21.47	1.51	4.29	0.00	38.56	0.00	100.68
18	422	0.00	25.11	0.23	9.37	21.41	1.36	4.25	0.02	37.95	0.07	99.77
19	446	0.00	25.00	0.30	9.28	21.62	1.49	4.46	0.01	38.04	0.04	100.25
20	471	0.00	25.22	0.31	9.47	21.45	1.30	4.44	0.00	37.64	0.06	99.86
21	496	0.23	25.19	0.19	9.19	21.22	1.12	4.42	0.01	37.89	0.00	99.45
22	521	0.04	25.16	0.25	9.24	21.47	1.09	4.34	0.00	37.48	0.00	99.01
23	546	0.04	25.16	0.28	9.00	21.68	1.46	4.22	0.01	38.05	0.00	99.87
24	570	0.05	25.27	0.28	9.48	21.68	1.65	3.86	0.00	37.99	0.02	100.28
25	595	0.12	25.45	0.23	9.44	21.54	1.63	3.69	0.00	37.97	0.00	100.05
28	670	0.08	26.22	0.09	8.68	22.33	1.81	2.91	0.01	37.69	0.00	99.75
29	694	0.28	25.36	0.22	8.81	23.48	1.90	2.56	0.00	36.85	0.00	99.45

30	719	0.00	25.96	0.23	9.68	21.66	1.88	2.43	0.00	38.06	0.01	99.89
31	744	0.15	26.28	0.20	9.67	21.68	1.90	2.18	0.00	38.06	0.09	100.19
32	769	0.34	25.78	0.33	10.21	21.31	2.02	2.06	0.01	38.12	0.02	100.19
33	794	0.01	26.59	0.17	9.59	21.83	2.10	1.96	0.01	38.46	0.05	100.76
34	818	0.00	26.08	0.16	9.96	21.83	1.89	1.77	0.01	38.19	0.01	99.83
35	843	0.13	25.31	0.16	9.38	23.01	2.32	1.91	0.00	37.71	0.00	99.89
37	893	0.35	24.77	0.13	9.44	23.39	2.72	1.76	0.00	37.42	0.17	100.13
38	918	0.18	26.00	0.14	9.52	21.84	2.68	1.45	0.00	38.46	0.00	100.26
39	942	0.00	26.16	0.12	9.51	21.77	2.77	1.35	0.03	38.28	0.11	100.07
40	967	0.00	25.98	0.13	9.75	21.74	2.72	1.20	0.00	38.38	0.03	99.91

A14-71

Number	**Distance (µm)**	**Na2O**	**FeO**	**TiO2**	**CaO**	**Al2O3**	**MgO**	**MnO**	**K2O**	**SiO2**	**Cr2O3**	**Total**
232	0	0.03	23.95	0.36	11.66	21.70	3.98	0.63	0.00	38.40	0.00	100.71
233	25	0.06	22.94	0.29	11.95	21.99	4.62	0.38	0.00	38.67	0.00	100.90
234	50	0.05	23.75	0.24	10.65	21.76	4.78	0.44	0.01	38.75	0.00	100.43
235	75	0.02	23.43	0.16	9.63	21.95	6.35	0.23	0.00	38.71	0.00	100.48
236	100	0.05	22.93	0.20	9.58	22.02	6.55	0.27	0.00	38.81	0.00	100.42
237	125	0.06	22.29	0.19	9.69	22.21	6.54	0.23	0.01	38.75	0.00	99.96
238	151	0.05	23.02	0.10	9.53	22.11	6.59	0.22	0.00	38.88	0.00	100.50
239	176	0.06	23.00	0.17	9.43	22.25	6.61	0.21	0.02	39.03	0.00	100.78
240	201	0.02	23.35	0.07	8.93	22.14	6.53	0.26	0.02	38.97	0.00	100.28
241	226	0.08	23.58	0.21	9.34	21.95	6.37	0.24	0.01	38.94	0.00	100.71
242	251	0.07	24.03	0.10	9.04	21.82	6.27	0.34	0.00	39.02	0.00	100.69
243	276	0.05	24.75	0.06	9.00	21.99	5.95	0.34	0.01	38.99	0.00	101.13
244	301	0.05	24.58	0.11	9.00	22.09	5.87	0.34	0.01	38.69	0.00	100.74
245	326	0.08	24.54	0.12	9.10	21.85	5.86	0.35	0.01	38.85	0.00	100.75
246	351	0.04	24.62	0.03	9.02	22.05	5.76	0.40	0.00	38.87	0.00	100.79
247	376	0.00	24.65	0.13	8.99	21.76	5.58	0.42	0.00	38.55	0.00	100.07
248	401	0.02	25.31	0.03	9.01	21.97	5.37	0.47	0.00	38.73	0.00	100.90
249	427	0.03	25.65	0.07	8.62	21.92	5.07	0.34	0.00	38.68	0.00	100.38
250	452	0.04	26.46	0.04	9.00	21.84	4.43	0.33	0.00	38.35	0.00	100.50

251	477	0.03	26.56	0.09	9.38	21.93	4.15	0.35	0.00	38.38	0.00	100.86
252	502	0.02	26.25	0.11	9.34	21.82	4.43	0.33	0.00	38.45	0.00	100.75
253	527	0.04	26.07	0.06	9.18	21.76	4.55	0.35	0.02	38.62	0.00	100.64
254	552	0.04	25.64	0.06	9.58	22.19	4.69	0.48	0.00	38.68	0.00	101.36
255	577	0.07	25.75	0.16	9.90	21.93	4.26	0.48	0.02	38.58	0.00	101.14
257	627	0.04	25.88	0.14	9.98	21.83	3.92	0.61	0.00	38.39	0.00	100.78
258	652	0.04	25.20	0.09	9.62	21.58	3.98	0.95	0.00	38.07	0.00	99.52
259	677	0.04	26.26	0.14	9.21	21.50	3.90	1.02	0.01	38.12	0.00	100.21
260	703	0.01	26.26	0.06	9.69	21.88	3.64	1.11	0.00	38.31	0.00	100.96
261	728	0.06	26.33	0.11	9.51	21.62	3.80	1.09	0.00	38.00	0.00	100.52
262	753	0.04	25.90	0.14	9.82	21.87	3.68	0.98	0.00	38.46	0.00	100.89
263	778	0.04	25.67	0.16	10.01	21.78	3.70	1.05	0.01	38.36	0.00	100.78
264	803	0.06	25.40	0.14	10.39	21.74	3.61	1.11	0.01	38.35	0.00	100.81
265	828	0.02	25.54	0.23	10.04	21.44	3.57	1.17	0.01	38.07	0.00	100.09
266	853	0.03	25.43	0.16	10.54	21.72	3.34	1.16	0.00	38.20	0.00	100.58
267	878	0.05	25.86	0.12	9.99	21.85	3.45	1.31	0.01	38.28	0.00	100.93
268	903	0.06	25.63	0.19	9.99	21.53	3.42	1.36	0.01	38.41	0.00	100.59
269	928	0.06	25.58	0.26	10.20	21.26	3.22	1.34	0.02	37.88	0.00	99.83
270	953	0.06	26.01	0.11	9.78	21.68	3.21	1.57	0.01	37.95	0.00	100.38
271	979	0.05	26.03	0.13	9.73	21.53	3.15	1.67	0.00	38.03	0.00	100.32
272	1004	0.06	25.61	0.12	10.26	21.51	3.15	1.76	0.00	37.98	0.00	100.46
273	1029	0.02	25.27	0.17	10.80	21.47	3.05	1.58	0.02	38.16	0.00	100.54
274	1054	0.07	25.25	0.14	10.58	21.52	2.94	1.80	0.01	38.21	0.00	100.52
275	1079	0.07	25.38	0.18	10.30	21.42	3.05	1.82	0.01	38.26	0.00	100.48
276	1104	0.05	25.48	0.19	10.67	21.38	3.04	1.81	0.01	37.91	0.00	100.54
277	1129	0.05	25.42	0.17	10.70	21.33	2.93	1.77	0.01	37.92	0.00	100.30
278	1154	0.10	25.40	0.22	10.68	20.62	2.86	1.97	0.01	37.48	0.00	99.34
279	1179	0.14	25.41	0.22	10.21	21.10	2.56	2.48	0.02	37.86	0.00	100.00
280	1204	0.09	25.68	0.21	10.40	21.14	2.47	2.47	0.00	37.89	0.00	100.35
281	1229	0.06	24.59	0.12	11.12	21.90	2.40	2.17	0.01	38.60	0.00	100.97
282	1255	0.05	25.53	0.25	10.75	21.23	2.55	2.17	0.00	38.20	0.00	100.73
283	1280	0.07	25.54	0.26	10.84	21.05	2.37	2.41	0.01	37.75	0.00	100.30

285	1330	0.05	26.02	0.17	10.43	21.28	2.45	2.38	0.01	37.64	0.00	100.44
286	1355	0.04	25.66	0.26	10.69	20.96	2.31	2.40	0.00	37.91	0.00	100.23
287	1380	0.04	25.94	0.27	10.39	21.23	2.28	2.78	0.00	37.87	0.00	100.80
288	1405	0.04	25.66	0.14	11.01	21.39	2.22	2.44	0.00	37.93	0.00	100.84
290	1455	0.06	26.23	0.16	10.67	21.15	2.24	2.60	0.01	37.54	0.00	100.66
291	1480	0.07	26.01	0.20	10.85	21.05	2.27	2.48	0.01	38.24	0.00	101.17
292	1505	0.03	26.10	0.18	10.68	21.13	2.27	2.45	0.01	38.34	0.00	101.19
294	1556	0.03	26.14	0.18	10.38	21.14	2.21	2.54	0.00	37.95	0.00	100.57
295	1581	0.05	25.72	0.17	11.28	21.26	2.20	2.34	0.00	38.16	0.00	101.18
296	1606	0.03	25.76	0.31	11.25	20.94	2.15	2.35	0.00	37.87	0.00	100.66
297	1631	0.05	26.34	0.23	10.38	21.06	2.03	2.93	0.00	38.10	0.00	101.12
298	1656	0.03	24.16	0.06	12.59	21.97	1.76	2.30	0.00	37.94	0.00	100.81
299	1681	0.06	26.16	0.22	10.70	20.90	2.04	2.63	0.01	38.19	0.00	100.91
300	1706	0.04	25.81	0.28	10.79	21.12	2.05	2.62	0.00	37.92	0.00	100.63
301	1731	0.05	25.48	0.28	11.10	21.08	2.16	2.28	0.00	37.66	0.00	100.09
302	1756	0.06	26.33	0.23	10.61	21.16	2.15	2.43	0.00	37.78	0.00	100.75
303	1781	0.06	26.14	0.19	10.45	21.08	1.90	2.92	0.00	37.99	0.00	100.72
304	1806	0.02	26.32	0.20	10.67	21.28	1.91	2.86	0.00	37.98	0.00	101.24
305	1832	0.03	26.23	0.16	10.39	21.19	2.03	2.64	0.00	37.83	0.00	100.49
306	1857	0.03	26.25	0.21	10.68	21.27	2.25	2.14	0.01	38.04	0.00	100.89
307	1882	0.08	26.45	0.22	10.55	21.14	2.04	2.42	0.00	37.62	0.00	100.52
308	1907	0.05	25.59	0.15	11.30	21.23	2.40	1.76	0.00	38.30	0.00	100.78
309	1932	0.00	26.42	0.14	10.32	21.30	2.54	1.78	0.00	37.92	0.00	100.42
310	1957	0.01	26.30	0.13	10.46	21.73	2.67	1.64	0.00	38.10	0.00	101.04
311	1982	0.07	26.14	0.24	10.92	21.52	2.65	1.54	0.00	38.13	0.00	101.21
312	2007	0.07	26.64	0.09	10.24	21.45	2.55	1.62	0.00	38.22	0.00	100.88
313	2032	0.05	26.09	0.20	10.71	21.49	2.67	1.41	0.00	37.94	0.00	100.56
316	2108	0.04	26.24	0.20	10.39	21.41	2.82	1.17	0.00	38.07	0.00	100.34
317	2133	0.03	26.61	0.10	10.17	21.73	3.00	1.17	0.00	38.50	0.00	101.31
318	2158	0.04	25.58	0.08	11.12	21.70	2.81	1.00	0.00	38.45	0.00	100.77
319	2183	0.06	26.87	0.16	9.87	21.76	3.20	0.94	0.00	38.27	0.00	101.13
320	2208	0.03	27.04	0.15	9.61	21.82	3.26	0.78	0.01	38.14	0.00	100.84

322	2258	0.07	26.98	0.19	9.50	21.81	3.28	0.79	0.01	38.50	0.00	101.13
323	2283	0.04	27.06	0.13	9.37	21.85	3.39	0.72	0.01	38.37	0.00	100.93
326	2358	0.03	25.32	0.07	11.44	22.23	2.80	0.71	0.00	38.73	0.00	101.33
327	2384	0.05	26.46	0.13	10.14	21.70	3.33	0.72	0.02	37.99	0.00	100.54
328	2409	0.07	26.88	0.12	9.69	21.83	3.47	0.65	0.01	38.48	0.00	101.19
329	2434	0.04	27.44	0.12	9.14	21.51	3.63	0.54	0.01	38.27	0.00	100.70
330	2459	0.05	26.45	0.12	9.59	21.86	3.56	0.46	0.00	38.53	0.00	100.62
331	2484	0.04	26.98	0.10	9.40	21.80	3.80	0.46	0.00	38.33	0.00	100.91
332	2509	0.03	27.01	0.13	9.68	21.60	3.55	0.41	0.00	38.46	0.00	100.87
333	2534	0.04	27.60	0.13	9.19	21.72	3.65	0.43	0.02	38.31	0.00	101.08
334	2559	0.06	27.49	0.08	9.36	21.90	3.40	0.37	0.01	38.09	0.00	100.76
335	2584	0.06	27.38	0.08	9.15	21.90	3.73	0.36	0.00	38.58	0.00	101.25
336	2609	0.03	26.79	0.13	9.31	21.88	3.97	0.36	0.01	38.55	0.00	101.03
337	2634	0.04	27.41	0.09	9.05	21.96	3.80	0.35	0.00	38.42	0.00	101.11
338	2660	0.03	26.63	0.13	9.12	21.75	3.91	0.35	0.00	38.50	0.00	100.41
339	2685	0.01	27.23	0.11	9.07	21.93	4.01	0.30	0.02	38.51	0.00	101.19
340	2710	0.05	26.87	0.10	9.13	21.75	4.17	0.25	0.00	38.43	0.00	100.75
341	2735	0.05	26.55	0.12	9.18	22.02	4.43	0.28	0.00	38.77	0.00	101.39
342	2760	0.04	25.11	0.02	8.87	22.12	5.42	0.40	0.00	38.67	0.00	100.66
343	2785	0.04	24.76	0.17	9.04	22.06	5.46	0.36	0.00	38.97	0.00	100.86
344	2810	0.03	23.85	0.13	9.29	21.78	6.10	0.25	0.00	38.90	0.00	100.33
345	2835	0.04	22.92	0.26	11.49	21.74	4.67	0.43	0.00	38.67	0.00	100.23
346	2860	0.03	23.53	0.31	11.43	21.90	4.55	0.43	0.00	38.48	0.00	100.66
347	2885	0.06	22.53	0.30	12.43	21.68	4.47	0.36	0.01	38.60	0.00	100.43
348	2910	0.09	23.65	0.27	11.17	21.90	4.87	0.35	0.00	38.78	0.00	101.08
349	2936	0.06	23.88	0.20	10.59	22.08	4.98	0.38	0.00	38.31	0.00	100.49

LB15-03B

Number	Distance (µm)	Na2O	FeO	TiO2	CaO	Al2O3	MgO	MnO	K2O	SiO2	Cr2O3	Total
35	25	0.01	26.82	0.02	4.67	21.92	6.97	0.68	0.00	38.59	0.00	99.67
36	50	0.01	27.37	0.01	4.50	21.75	7.22	0.69	0.00	38.54	0.00	100.10
37	75	0.01	26.65	0.04	4.65	21.98	7.37	0.68	0.00	38.49	0.00	99.87

38	100	0.00	26.76	0.00	4.65	22.08	7.16	0.69	0.00	38.59	0.00	99.93
39	125	0.01	26.90	0.00	4.44	22.18	7.37	0.74	0.00	38.79	0.00	100.43
41	176	0.01	26.64	0.00	4.51	22.06	7.27	0.70	0.00	38.60	0.00	99.79
42	201	0.00	26.76	0.04	4.75	22.13	7.28	0.71	0.00	38.48	0.00	100.15
43	226	0.00	26.63	0.02	5.17	22.16	7.25	0.66	0.00	38.60	0.00	100.48
44	251	0.03	26.74	0.00	4.89	22.00	7.25	0.69	0.00	38.79	0.00	100.38
45	276	0.01	26.73	0.01	4.97	22.21	7.29	0.70	0.00	38.30	0.00	100.22
46	301	0.01	26.88	0.01	4.70	21.98	7.15	0.70	0.00	38.46	0.00	99.89
48	351	0.00	26.76	0.00	4.95	22.11	7.25	0.71	0.01	38.67	0.00	100.45
49	376	0.00	26.56	0.00	4.88	22.32	7.28	0.73	0.00	38.67	0.00	100.44
50	401	0.00	26.65	0.03	4.96	22.26	7.30	0.71	0.01	38.54	0.00	100.46
51	427	0.02	26.87	0.00	4.92	22.29	7.35	0.72	0.00	38.58	0.00	100.75
52	452	0.00	26.83	0.00	4.84	22.29	7.30	0.70	0.00	38.79	0.00	100.75
53	477	0.02	26.39	0.00	5.04	22.03	7.15	0.70	0.01	38.50	0.00	99.84
54	502	0.02	26.47	0.01	4.61	22.24	7.44	0.66	0.00	38.73	0.00	100.18
55	527	0.02	26.31	0.00	5.02	22.20	7.35	0.70	0.00	38.82	0.00	100.42
56	552	0.03	26.35	0.01	5.31	22.25	7.20	0.71	0.00	38.73	0.00	100.58
57	577	0.03	26.54	0.00	4.56	22.32	7.56	0.71	0.01	38.60	0.00	100.33
58	602	0.02	26.54	0.02	4.70	22.07	7.52	0.68	0.00	38.78	0.00	100.34
60	652	0.01	26.64	0.01	4.67	22.09	7.50	0.65	0.02	38.66	0.00	100.25
61	677	0.01	26.89	0.01	4.75	21.94	7.20	0.66	0.00	38.42	0.00	99.88
71	928	0.00	26.90	0.00	4.74	22.20	7.35	0.70	0.00	38.96	0.00	100.85
72	953	0.01	26.76	0.00	4.88	22.11	7.38	0.70	0.00	38.75	0.00	100.59
74	1004	0.02	26.95	0.00	5.01	22.18	7.47	0.76	0.00	38.95	0.00	101.34
75	1029	0.01	27.15	0.05	4.68	22.25	7.33	0.72	0.00	39.02	0.00	101.21
78	1104	0.01	27.11	0.00	4.94	22.10	6.96	0.69	0.00	38.41	0.00	100.22
79	1129	0.02	27.67	0.04	5.13	21.88	6.57	0.75	0.01	38.61	0.00	100.67
95	1530	0.04	26.75	0.00	4.75	22.47	7.38	0.77	0.00	39.07	0.00	101.24
97	1581	0.00	26.82	0.02	5.06	22.39	7.04	0.74	0.00	39.17	0.00	101.24
98	1606	0.01	26.86	0.00	5.05	22.20	7.03	0.67	0.00	38.70	0.00	100.51
99	1631	0.00	27.17	0.03	4.94	22.18	7.16	0.72	0.00	38.77	0.00	100.97
100	1656	0.01	26.94	0.01	4.99	22.25	7.14	0.72	0.00	38.73	0.00	100.79

107	1832	0.02	26.93	0.02	4.83	21.89	7.00	0.69	0.00	38.77	0.00	100.14
108	1857	0.00	27.07	0.03	4.89	22.16	6.98	0.77	0.00	38.71	0.00	100.61
110	1907	0.02	26.92	0.01	4.82	22.20	7.18	0.73	0.00	38.87	0.00	100.75
111	1932	0.00	27.03	0.01	4.79	22.12	7.18	0.76	0.00	38.50	0.00	100.39
112	1957	0.04	27.14	0.02	4.71	22.16	7.25	0.70	0.00	38.76	0.00	100.77
113	1982	0.03	26.81	0.03	4.73	22.08	7.28	0.71	0.00	38.72	0.00	100.39
114	2007	0.02	26.94	0.04	4.87	22.18	7.17	0.73	0.00	38.67	0.00	100.62
115	2032	0.00	27.16	0.04	4.66	22.27	7.23	0.73	0.00	38.66	0.00	100.74
116	2057	0.04	26.95	0.02	4.99	22.23	6.86	0.73	0.00	38.61	0.00	100.43
119	2133	0.00	27.22	0.00	5.13	22.34	6.89	0.73	0.00	38.64	0.00	100.95
120	2158	0.01	27.51	0.01	4.75	22.20	6.95	0.72	0.01	38.74	0.00	100.90
121	2183	0.02	27.32	0.00	4.99	22.20	6.71	0.78	0.00	38.37	0.00	100.39
125	2283	0.01	26.82	0.01	5.49	22.26	6.65	0.72	0.00	38.55	0.00	100.51
126	2308	0.00	27.10	0.04	5.21	22.13	6.91	0.68	0.00	38.59	0.00	100.66
128	2358	0.00	26.74	0.03	4.96	22.24	7.08	0.68	0.00	38.80	0.00	100.52
129	2384	0.02	27.14	0.00	4.93	22.14	7.12	0.70	0.00	38.54	0.00	100.59
130	2409	0.00	27.36	0.01	4.77	22.31	6.98	0.74	0.00	38.97	0.00	101.15
138	2609	0.00	27.22	0.00	5.02	22.14	6.99	0.77	0.01	38.98	0.00	101.13
139	2634	0.01	27.27	0.00	4.91	22.11	7.03	0.74	0.01	38.82	0.00	100.90
140	2660	0.01	27.01	0.04	5.12	22.06	6.78	0.74	0.00	38.80	0.00	100.56
147	2835	0.01	26.94	0.00	4.92	22.04	6.78	0.72	0.00	38.28	0.00	99.70
148	2860	0.00	27.03	0.04	4.80	21.74	6.89	0.77	0.00	38.02	0.00	99.29
149	2885	0.01	27.14	0.01	5.06	22.01	6.71	0.72	0.01	38.29	0.00	99.97
150	2910	0.00	27.01	0.00	4.60	21.87	6.89	0.74	0.00	38.36	0.00	99.47
152	2961	0.00	26.27	0.00	5.19	21.80	6.79	0.75	0.00	38.38	0.00	99.18
153	2986	0.00	26.85	0.00	4.88	21.90	6.98	0.68	0.00	38.44	0.00	99.73
154	3011	0.01	27.11	0.00	4.62	21.96	7.22	0.72	0.00	38.49	0.00	100.13
155	3036	0.01	27.28	0.02	4.33	22.06	7.26	0.74	0.00	38.42	0.00	100.12
156	3061	0.01	26.44	0.03	4.84	21.87	7.07	0.70	0.00	38.51	0.00	99.46
157	3086	0.01	26.72	0.04	4.67	22.02	7.28	0.73	0.00	38.56	0.00	100.02
158	3111	0.00	27.13	0.00	4.69	21.99	7.06	0.73	0.00	38.43	0.00	100.03
160	3161	0.00	26.74	0.03	5.38	21.99	6.72	0.69	0.01	38.79	0.00	100.35

166	3312	0.00	26.80	0.23	4.70	22.04	7.15	0.71	0.00	38.51	0.00	100.14
167	3337	0.00	26.69	0.07	4.89	21.98	7.32	0.66	0.00	38.61	0.00	100.22
168	3362	0.00	26.80	0.05	4.73	22.09	7.36	0.68	0.00	38.25	0.00	99.96
169	3387	0.00	26.58	0.02	4.81	22.00	7.41	0.72	0.00	38.53	0.00	100.06
170	3412	0.00	26.22	0.14	5.06	22.17	7.43	0.69	0.00	38.39	0.00	100.10
171	3437	0.02	26.39	0.09	4.75	22.02	7.11	0.71	0.01	38.60	0.00	99.70
172	3462	0.01	26.98	0.07	4.60	22.32	7.23	0.74	0.00	38.65	0.00	100.60
176	3563	0.01	26.78	0.00	4.90	21.82	7.13	0.66	0.00	38.54	0.00	99.84
177	3588	0.04	26.40	0.00	5.01	22.00	7.23	0.69	0.00	38.47	0.00	99.84
178	3613	0.01	26.81	0.00	4.95	22.05	7.31	0.68	0.01	38.59	0.00	100.41
181	3688	0.02	26.51	0.03	5.13	22.12	7.21	0.71	0.00	38.64	0.00	100.36
182	3713	0.00	26.89	0.03	4.69	21.98	7.35	0.69	0.00	38.44	0.00	100.07
183	3738	0.02	26.69	0.06	4.75	21.96	7.45	0.72	0.01	38.68	0.00	100.34
184	3764	0.04	26.92	0.03	4.74	22.04	7.28	0.68	0.01	38.58	0.00	100.32
185	3789	0.04	26.59	0.00	4.74	22.08	7.41	0.72	0.00	38.60	0.00	100.17
189	3889	0.00	26.78	0.02	4.71	21.97	7.44	0.70	0.00	38.53	0.00	100.15
190	3914	0.01	26.76	0.02	4.69	22.22	7.43	0.68	0.00	38.41	0.00	100.21
191	3939	0.00	26.61	0.02	4.75	21.90	7.48	0.71	0.01	38.37	0.00	99.85
192	3964	0.00	26.68	0.02	4.61	22.18	7.47	0.73	0.00	38.79	0.00	100.48
193	3989	0.00	26.58	0.01	4.61	22.08	7.39	0.74	0.00	38.61	0.00	100.02
194	4014	0.04	26.25	0.02	4.41	22.23	7.53	0.70	0.00	38.39	0.00	99.56
195	4039	0.01	26.87	0.01	4.53	21.99	7.50	0.70	0.00	38.56	0.00	100.17
196	4065	0.02	26.84	0.00	4.77	22.02	7.46	0.70	0.00	38.65	0.00	100.45
198	4115	0.01	26.66	0.01	4.91	21.80	7.15	0.70	0.01	38.36	0.00	99.61
203	4240	0.00	26.16	0.00	4.92	21.94	7.06	0.75	0.00	38.10	0.00	98.93
205	4290	0.01	26.56	0.02	4.85	21.94	7.23	0.69	0.00	38.61	0.00	99.91
206	4315	0.02	26.68	0.00	4.69	21.97	7.47	0.76	0.00	38.54	0.00	100.13
207	4341	0.01	29.27	0.04	4.72	22.24	5.50	0.79	0.00	38.50	0.00	101.06
208	4366	0.02	26.54	0.03	4.70	21.59	7.52	0.70	0.01	38.69	0.00	99.79
210	4416	0.01	27.27	0.01	4.65	21.93	7.00	0.77	0.01	38.54	0.00	100.19
211	4441	0.03	26.77	0.01	4.82	22.05	7.47	0.68	0.00	38.56	0.00	100.38
213	4491	0.00	26.77	0.05	4.63	21.95	7.48	0.74	0.00	38.62	0.00	100.24

214	4516	0.00	26.86	0.03	4.51	22.01	7.62	0.69	0.00	38.43	0.00	100.15
215	4541	0.03	26.75	0.00	4.69	22.12	7.31	0.74	0.01	38.55	0.00	100.20
216	4566	0.00	26.23	0.00	4.96	22.27	7.01	0.72	0.01	38.58	0.00	99.78
219	4642	0.02	26.96	0.00	5.16	22.23	6.88	0.75	0.02	38.92	0.00	100.94
220	4667	0.00	27.07	0.01	4.85	22.27	7.16	0.73	0.00	38.87	0.00	100.96
221	4692	0.00	26.76	0.00	4.94	22.02	7.01	0.68	0.00	38.81	0.00	100.22
222	4717	0.00	26.61	0.00	4.88	22.16	7.29	0.73	0.00	39.03	0.00	100.70
223	4742	0.00	26.74	0.00	4.81	22.16	7.44	0.73	0.00	38.77	0.00	100.65
224	4767	0.01	26.46	0.00	4.94	22.29	7.34	0.69	0.01	38.89	0.00	100.64
225	4792	0.00	26.70	0.01	5.09	21.99	7.21	0.70	0.00	38.57	0.00	100.27
226	4817	0.01	26.68	0.02	5.16	22.42	7.29	0.70	0.00	39.03	0.00	101.31
227	4842	0.02	26.41	0.00	5.28	22.12	7.16	0.71	0.00	38.61	0.00	100.30
228	4867	0.01	27.07	0.01	4.77	22.29	7.29	0.73	0.01	38.56	0.00	100.74
229	4893	0.03	28.46	0.00	4.39	21.18	6.55	0.70	0.03	37.28	0.00	98.61
230	4918	0.04	27.51	0.02	4.97	22.09	6.90	0.73	0.01	38.62	0.00	100.88
231	4943	0.01	27.83	0.02	4.83	21.98	6.43	0.82	0.00	38.64	0.00	100.57

S3.2 Data sources for early-Farallon terranes age compilation

The following data sources were included in the age compilation for early-Farallon subduction presented in Figure 4.6. Additional details on the rock types, methods and uncertainties can be found in Mulcahy et al. (2018).

Oregon
Coleman and Lanphere (1971): K-Ar (white mica, sodic amphibole, actinolite, hornblende)

Northern Franciscan
Anczkiewicz et al. (2004): Sm-Nd, Lu-Hf (garnet, hornblende, clinopyroxene, whole rock)
Catlos and Sorensen (2003): Ar-Ar (white mica)
Coleman and Lanphere (1971): K-Ar (hornblende)
Firsov and Dobretsov (1970): K-Ar (clinopyoxene, white mica, chlorite)
Lee et al. (1964): K-Ar (white mica)
McDowell et al. (1984): K-Ar (white mica, sodic amphibole, actinolite)
Mulcahy et al. (2014): Lu-Hf (lawsonite, garnet, sodic amphibole, whole rock), Ar-Ar (white mica)
Mulcahy et al. (2018): Lu-Hf (lawsonite, garnet, sodic amphibole, epidote, whole rock), U-Pb (zircon); Ar-Ar (white mica)
Page et al. (2014): U-Pb (zircon)
Page et al. (2003): U-Pb (zircon)
Shervais et al. (2011): Ar-Ar (hornblende)
Suppe (1969): K-Ar (white mica)
Suppe and Armstrong (1972): K-Ar (sodic amphibole)
Wakabayashi and Deino (1989): Ar-Ar (white mica)
Wakabayashi and Dimitru (2007): Ar-Ar (hornblende)

Southern Franciscan
Anczkiewicz et al. (2004): Lu-Hf (garnet, whole rock)
Brown (1971): K-Ar (white mica)
Catlos and Sorensen (2003): Ar-Ar (white mica)
Page et al. (2014): U-Pb (zircon)
Ross and Sharp (1986): Sm-Nd (garnet, hornblende)
Ross and Sharp (1988): Ar-Ar (hornblende)
Suppe and Armstrong (1972): K-Ar (white mica)
Suppe and Foland (1978): K-Ar (sodic amphibole, hornblende, white mica); Rb-Sr (lawsonite, titanite, amphibole, white mica, whole rock)
Ukar (2012): Ar-Ar (white mica)
Wakabayashi and Dimitru (2007): Ar-Ar (white mica)

Catalina Schist
Anczkiewicz et al. (2004): Lu-Hf (garnet, clinopyroxene)
Awalt et al. (2013): U-Pb (titanite)
Grove and Bebout (1995): Ar-Ar (white mica)
Harvey et al. (in prep): Sm-Nd (garnet, whole rock)
Harvey et al. (this study): Sm-Nd (garnet, whole rock)
Mattinson (1986): U-Pb (garnet, amphibole, titanite, apatite)
Suppe and Armstrong (1972): K-Ar (hornblende, white mica, sodic amphibole)

Baja Californmia
Gonzalez and Baldwin (2019): Ar-Ar (white mica)
Suppe and Armstrong (1972): K-Ar (sodic amphibole, hornblende)

Appendix S4

S4.1 Peak Explorer (in prep.)

Peak Explorer is an R-based application for statistically identifying subpopulations within a group of data. The program is still in preparation and was designed by Buchanan Kerswell (Boise State University) in collaboration with Matt Kohn (Boise State University) and Kayleigh Harvey (University of Maryland). Peak Explorer utilizes the "peakfit" R function available with the application IsoplotR (Vermeesch, 2018), although it is not currently part of the online IsoplotR GUI. Peakfit is a finite mixture modelling algorithm that has been historically used by the geochronology community to model mixed geochronology (e.g., U-Pb, ^{39}Ar-^{40}Ar) datasets (after Galbraith and Laslett, 1993); however, it is applicable to any dataset with associated uncertainty.

While Peak Explorer has the utility to be applied to any number of datasets, it is particularly advantageous to use for elastic barometry data. When applying elastic barometry, researchers are typically focused on determining a "best-fit" maximum inclusion pressure to use for calculating the peak metamorphic conditions of a sample.

Historically, researchers have simply used the maximum inclusion pressure or the average of some subset of "maximum" inclusion pressures. However, because inclusion pressures within a given group of data often have significantly different uncertainties (e.g., uncertainties presented in Chapter 2 range from 7-97%) as a result of how Raman shifts are converted to strain, simply picking the maximum inclusion pressure or averaging a subset of the data without weighting the data is not necessarily appropriate. Because the finite mixture modeling algorithm weights analyses by uncertainty, Peak Explorer is an ideal tool to use for estimating a "best-fit" maximum inclusion pressure while simultaneously reducing uncertainty by statistical averaging.

S4.2 EPMA Data

Table S4.1.1 Major element EPMA traverse across 25-228 Garnet 1

Distance (µm)	Na2O	CaO	TiO2	MnO	Al2O3	MgO	K2O	FeO	SiO2	Total
0	0.02	10.53	0.10	1.41	21.74	3.76	0.00	24.46	37.41	99.43
100	0.00	9.83	0.06	0.79	21.96	5.08	0.01	23.84	37.89	99.46
200	0.04	9.68	0.10	1.30	21.84	4.17	0.00	24.62	37.62	99.37
300	0.03	9.22	0.09	1.13	22.01	4.58	0.00	25.08	37.83	99.97
400	0.04	9.76	0.11	1.61	21.94	3.83	0.00	24.84	37.61	99.74
500	0.02	8.60	0.07	1.26	21.94	5.14	0.01	24.88	37.35	99.26
600	0.01	8.48	0.06	1.42	21.97	5.05	0.00	24.68	37.44	99.11
700	0.03	9.19	0.07	1.76	21.55	3.45	0.00	25.44	37.51	99.00
800	0.04	7.47	0.15	1.69	21.73	5.23	0.00	25.25	37.66	99.22
900	0.00	7.92	0.09	1.68	21.96	5.11	0.01	25.21	37.71	99.69
1000	0.04	8.17	0.20	1.63	21.86	5.08	0.00	25.10	37.37	99.45
1100	0.04	8.17	0.20	1.49	21.71	4.93	0.00	25.41	37.79	99.74
1200	0.01	11.59	0.04	1.67	21.81	3.21	0.00	23.95	37.67	99.95
1300	0.04	10.75	0.12	1.54	21.59	3.71	0.00	23.85	37.49	99.09
1400	0.04	8.46	0.18	1.67	21.82	4.71	0.00	25.50	37.53	99.91
1500	0.05	8.07	0.12	1.62	21.70	4.24	0.00	26.14	37.43	99.37
1600	0.03	7.66	0.19	1.64	21.60	4.84	0.00	25.82	37.70	99.48
1800	0.05	8.77	0.09	1.68	21.64	3.94	0.00	25.67	37.41	99.25
1900	0.03	9.19	0.16	1.69	21.46	3.68	0.00	25.73	37.50	99.45
2000	0.08	8.22	0.20	1.84	21.65	3.90	0.01	26.03	37.15	99.08
2100	0.04	8.18	0.20	1.64	21.72	4.65	0.00	25.47	37.74	99.63
2300	0.06	7.79	0.20	1.79	21.70	4.13	0.00	26.31	37.43	99.41
2400	0.07	8.35	0.46	1.49	21.77	4.50	0.00	25.67	37.79	100.10
2500	0.06	8.10	0.24	1.48	21.64	4.77	0.00	25.04	37.59	98.91
2600	0.05	8.02	0.20	1.63	21.50	4.60	0.00	25.89	37.22	99.11
2800	0.06	7.72	0.23	1.49	21.58	4.83	0.00	25.80	37.24	98.95
2900	0.06	10.54	0.14	1.68	21.78	3.28	0.02	24.62	37.37	99.48

3000	0.07	8.05	0.19	1.68	21.68	4.23	0.00	26.36	37.64	99.90
3100	0.04	7.93	0.23	1.47	21.63	4.69	0.01	25.76	37.50	99.25
3200	0.04	7.98	0.23	1.40	21.61	4.73	0.01	25.76	37.73	99.48
3500	0.07	8.26	0.21	1.72	21.46	4.06	0.00	25.94	37.01	98.74
3600	0.04	8.87	0.22	1.73	21.81	3.68	0.00	25.89	37.53	99.77
3700	0.04	9.32	0.28	1.51	21.48	3.95	0.00	24.92	37.32	98.82
4000	0.06	9.18	0.25	1.50	21.63	4.14	0.00	24.93	37.32	99.01
4100	0.05	9.38	0.30	1.52	21.45	4.16	0.00	24.44	37.40	98.70
4200	0.08	9.40	0.26	1.57	21.52	4.26	0.00	24.92	37.29	99.29
4300	0.04	9.30	0.30	1.51	21.75	4.25	0.01	24.90	37.42	99.48
4400	0.06	9.33	0.31	1.51	21.61	4.12	0.00	25.21	37.58	99.73
4500	0.08	9.40	0.30	1.53	21.46	4.15	0.00	24.82	37.61	99.35
4600	0.04	9.34	0.31	1.53	21.60	4.10	0.00	25.08	37.50	99.50
4700	0.11	9.52	0.24	1.61	21.51	3.61	0.01	25.34	37.04	98.99
4800	0.04	9.32	0.32	1.55	21.60	4.10	0.00	24.76	37.47	99.16
4900	0.04	9.02	0.29	1.54	21.53	4.24	0.00	25.17	37.48	99.31
5000	0.07	8.88	0.29	1.53	21.58	4.20	0.00	24.91	37.62	99.09
5100	0.03	8.64	0.23	1.63	21.42	4.14	0.00	25.26	37.31	98.66
5200	0.02	11.82	0.12	1.62	21.62	3.25	0.00	23.31	37.23	98.99
5300	0.00	11.22	0.07	1.64	21.72	3.22	0.00	23.24	37.50	98.61
5400	0.03	8.66	0.22	1.70	21.70	4.30	0.00	25.95	37.38	99.94
5500	0.07	8.54	0.20	1.57	21.56	4.35	0.01	25.34	37.28	98.92
5700	0.06	9.21	0.24	1.78	21.53	4.32	0.00	25.03	37.36	99.53
5800	0.07	9.11	0.28	1.56	21.51	4.20	0.00	24.89	37.40	99.02
6000	0.04	9.46	0.24	1.76	21.54	3.82	0.04	25.23	37.21	99.35
6100	0.08	9.33	0.29	1.59	21.45	3.83	0.00	25.01	37.18	98.76
6400	0.05	9.26	0.25	1.51	21.59	4.10	0.00	24.84	37.41	99.01
6600	0.07	9.25	0.29	1.50	21.62	4.18	0.00	24.88	37.21	99.00
6700	0.04	9.24	0.30	1.42	21.34	4.11	0.00	24.88	37.28	98.61
6800	0.06	9.12	0.24	1.36	21.51	4.24	0.00	25.01	37.07	98.60
6900	0.06	9.12	0.26	1.42	21.47	4.27	0.00	25.03	37.42	99.05
7000	0.05	9.20	0.23	1.38	21.52	4.22	0.00	25.09	37.20	98.90
7200	0.07	9.04	0.26	1.43	21.56	4.40	0.00	24.92	37.04	98.72
7300	0.08	9.02	0.24	1.36	21.47	4.28	0.00	25.25	37.08	98.77
7400	0.03	10.54	0.15	1.56	21.41	3.56	0.00	24.11	37.31	98.67
7600	0.07	8.91	0.27	1.43	21.49	4.55	0.00	24.69	37.36	98.77
7700	0.06	8.89	0.27	1.43	21.60	4.21	0.00	25.09	37.22	98.77
7800	0.03	8.80	0.22	1.54	21.65	4.14	0.00	25.16	37.27	98.80
7900	0.06	8.88	0.24	1.42	21.59	4.44	0.01	25.15	37.21	99.00
8100	0.05	8.79	0.27	1.40	21.52	4.50	0.00	24.90	37.23	98.66
8700	0.06	8.61	0.25	1.71	21.48	4.09	0.01	25.35	36.97	98.53
8900	0.05	8.71	0.26	1.74	21.17	4.10	0.01	25.67	37.08	98.79
9200	0.00	8.17	0.21	1.71	21.46	4.62	0.00	25.52	37.03	98.72
9400	0.03	8.10	0.19	1.62	21.63	4.89	0.00	25.24	36.95	98.65
9500	0.02	8.31	0.10	1.51	21.60	4.77	0.00	24.88	37.38	98.57
9600	0.04	7.75	0.14	1.46	21.73	4.90	0.00	25.35	37.22	98.59
9700	0.04	8.54	0.12	1.77	21.49	3.87	0.00	25.79	37.44	99.07
9800	0.06	8.11	0.16	1.62	21.73	4.82	0.00	24.89	37.63	99.01
9900	0.05	7.87	0.10	1.83	21.50	3.71	0.00	26.53	37.23	98.82
10000	0.04	7.79	0.13	1.73	21.52	3.72	0.03	26.49	37.09	98.54
10200	0.03	8.72	0.10	1.31	21.64	4.92	0.00	24.74	37.32	98.78
10300	0.05	9.08	0.08	1.06	21.84	5.13	0.00	24.20	37.32	98.76
10500	0.01	10.73	0.05	1.28	21.84	3.74	0.00	23.90	37.43	98.98
10600	0.02	14.92	0.06	1.62	21.52	1.12	0.00	22.30	37.45	99.01

Table S4.2.2 Zr concentrations in rutile

*Grain numbers used for mean maximum concentration highlighted in grey.

25-228

Grain Number	Max Zr	Unc (2σ)	Mean Max Grain	Unc (2σ)
1	107	11	279	39
2	200	11		
3	233	13		
4	130	15		
5	130	11		
6	188	14		
7	261	12		
8	141	15		
9	158	11		
10	301	14		
11	289	17		
12	162	19		
13	204	23		
14	186	18		
15	110	22		
16	89	21		
17	147	13		
18	178	18		
19	141	18		
20	192	18		
21	186	19		
22	190	18		
23	131	11		
24	176	10		
25	177	12		
26	237	11		
27	209	7		
28	265	12		
29	167	12		
30	164	10		
31	159	8		
32	211	12		
33	163	15		

Table S4.2.3 Rutile EPMA analyses with radial distance of inclusions from the garnet core

25-228

Grain	Distance (μm)	TiO2	ZrO2	Al2O3	FeO	Nb2O5	SiO2	MnO	Ta2O5	V2O3	Total	Zr Unc (%)	Zr (ppm)	Zr Unc (ppm, 2σ)	Si (ppm)
1	929	98.85	0.02	0.15	1.17	0.00	0.00	0.03	0.35	0.35	100.55	13	120	15	0
1	929	98.76	0.01	0.15	0.98	0.01	0.00	0.01	0.39	0.39	100.28	17	95	16	0
2	1066	99.20	0.03	0.15	0.63	0.02	0.00	0.01	0.35	0.35	100.45	7	204	15	0
2	1066	99.23	0.03	0.15	0.63	0.03	0.00	0.00	0.33	0.33	100.33	8	196	16	0
2	1066	99.44	0.02	0.15	0.63	0.01	0.00	0.00	0.35	0.35	100.58	12	153	19	0
3	1572	99.67	0.02	0.19	0.56	0.02	0.00	0.01	0.33	0.33	100.80	9	170	16	0
3	1572	99.60	0.03	0.17	0.63	0.02	0.00	0.04	0.29	0.29	100.77	7	232	17	0
3	1572	99.88	0.03	0.17	0.63	0.03	0.00	0.01	0.28	0.28	100.96	8	234	18	0
4	2202	99.59	0.02	0.20	0.49	0.01	0.00	0.01	0.36	0.36	100.65	12	130	15	22
5	2622	98.60	0.02	0.13	0.86	0.04	0.00	0.03	0.38	0.38	100.02	14	121	17	0
5	2622	99.27	0.02	0.14	0.62	0.01	0.00	0.01	0.35	0.35	100.47	11	150	16	0
5	2622	99.09	0.02	0.14	0.65	0.00	0.00	0.00	0.36	0.36	100.25	19	118	22	0
6	3349	99.21	0.02	0.15	0.53	0.03	0.00	0.00	0.39	0.39	100.30	13	150	19	0
6	3349	99.47	0.02	0.14	0.59	0.04	0.00	0.01	0.43	0.43	100.63	10	172	17	0
6	3349	99.21	0.03	0.15	0.63	0.02	0.00	0.04	0.38	0.38	100.46	11	205	22	0
7	3785	98.91	0.04	0.16	0.61	0.03	0.00	0.00	0.36	0.36	100.16	6	277	16	0
7	3785	98.48	0.02	0.16	0.69	0.00	0.00	0.00	0.40	0.40	99.69	11	152	17	0
7	3785	98.15	0.03	0.15	0.62	0.00	0.00	0.04	0.44	0.44	99.40	7	244	18	0
8	3734	98.11	0.02	0.16	0.87	0.03	0.00	0.02	0.31	0.31	99.45	11	141	15	0
9	3330	98.94	0.02	0.20	0.55	0.02	0.00	0.01	0.35	0.35	100.02	11	144	16	0
9	3330	98.50	0.02	0.16	0.60	0.00	0.00	0.02	0.36	0.36	99.60	9	172	15	0

10	3934	97.98	0.04	0.15	0.70	0.00	0.00	0.00	0.42	0.42	99.27	6	301	18	0
10	3934	98.27	0.04	0.16	0.67	0.00	0.00	0.00	0.43	0.43	99.50	7	301	21	0
10	3934	98.34	0.03	0.15	0.64	0.00	0.00	0.01	0.42	0.42	99.55	9	196	18	0
11	3739	98.71	0.04	0.17	0.69	0.01	0.00	0.00	0.33	0.33	99.94	6	289	17	0
12	4074	98.42	0.02	0.17	0.86	0.02	0.00	0.01	0.38	0.38	99.88	12	162	19	0
13	3795	99.13	0.03	0.15	0.73	0.02	0.00	0.03	0.30	0.30	100.37	11	204	23	0
13	3795	99.43	0.02	0.16	0.74	0.05	0.00	0.03	0.27	0.27	100.68	12	140	16	0
13	3795	99.40	0.02	0.16	0.84	0.00	0.00	0.01	0.33	0.33	100.79	14	151	22	0
14	3986	99.62	0.03	0.15	0.68	0.01	0.00	0.02	0.37	0.37	100.86	10	186	18	0
14	3986	99.35	0.02	0.15	0.77	0.02	0.00	0.01	0.31	0.31	100.62	12	118	14	0
15	4148	99.06	0.01	0.15	1.00	0.04	0.00	0.01	0.34	0.34	100.62	20	110	22	0
16	4471	98.68	0.01	0.18	0.84	0.01	0.00	0.03	0.35	0.35	100.05	24	89	21	0
17	4740	99.20	0.02	0.17	0.61	0.03	0.00	0.01	0.34	0.34	100.35	13	122	16	0
17	4740	99.34	0.02	0.16	0.81	0.03	0.00	0.00	0.39	0.39	100.68	13	162	21	0
17	4740	98.83	0.02	0.16	0.63	0.01	0.00	0.00	0.33	0.33	100.00	12	131	16	0
18	4622	98.40	0.02	0.18	0.55	0.01	0.00	0.02	0.40	0.40	99.58	16	136	22	0
18	4622	98.54	0.02	0.16	0.61	0.03	0.00	0.02	0.38	0.38	99.70	10	178	18	0
19	4633	98.32	0.02	0.15	0.56	0.02	0.00	0.04	0.35	0.35	99.50	13	141	18	0
20	4776	99.02	0.03	0.15	0.80	0.03	0.00	0.04	0.44	0.44	100.46	9	192	18	0
21	5237	99.06	0.03	0.15	0.77	0.05	0.00	0.04	0.45	0.45	100.53	10	186	19	0
22	5159	99.22	0.03	0.15	0.83	0.01	0.00	0.03	0.52	0.52	100.76	9	190	18	0
23	5395	99.80	0.02	0.17	0.48	0.01	0.00	0.00	0.32	0.32	100.81	14	127	18	0
23	5395	99.54	0.02	0.17	0.50	0.03	0.00	0.01	0.31	0.31	100.60	14	127	18	0
23	5395	99.46	0.02	0.16	0.51	0.00	0.00	0.01	0.31	0.31	100.39	14	141	19	0
24	5528	99.82	0.02	0.16	0.41	0.00	0.00	0.00	0.36	0.36	100.71	12	175	21	0
24	5528	99.72	0.03	0.16	0.42	0.03	0.00	0.01	0.39	0.39	100.71	9	188	16	0

24	5528	100.00	0.02	0.17	0.48	0.03	0.00	0.00	0.35	0.35	101.08	9	166	14	0
25	matrix	99.00	0.02	0.15	0.37	0.02	0.00	0.01	0.36	0.36	99.82	9	173	16	0
25	matrix	99.68	0.02	0.15	0.36	0.01	0.00	0.00	0.35	0.35	100.55	10	180	19	0
26	matrix	99.87	0.03	0.15	0.43	0.03	0.00	0.00	0.35	0.35	100.78	7	247	18	0
26	matrix	99.31	0.03	0.15	0.41	0.00	0.00	0.01	0.35	0.35	100.20	8	246	20	0
26	matrix	99.63	0.03	0.15	0.40	0.02	0.00	0.00	0.37	0.37	100.52	8	218	18	0
27	matrix	99.52	0.02	0.16	0.42	0.02	0.00	0.01	0.43	0.43	100.61	11	176	19	0
27	matrix	99.19	0.03	0.17	0.45	0.00	0.00	0.01	0.43	0.43	100.23	9	218	19	0
27	matrix	99.20	0.03	0.17	0.46	0.02	0.00	0.02	0.35	0.35	100.22	9	208	19	0
27	matrix	99.22	0.03	0.15	0.45	0.02	0.00	0.00	0.38	0.38	100.17	9	204	18	0
27	matrix	99.35	0.03	0.16	0.48	0.01	0.00	0.00	0.37	0.37	100.33	8	204	15	0
27	matrix	99.54	0.03	0.16	0.45	0.02	0.00	0.00	0.35	0.35	100.47	8	224	18	0
27	matrix	99.36	0.03	0.16	0.43	0.01	0.00	0.00	0.36	0.36	100.37	9	197	18	0
28	matrix	99.55	0.04	0.14	0.37	0.01	0.00	0.01	0.34	0.34	100.37	6	280	16	0
28	matrix	99.60	0.03	0.14	0.35	0.02	0.00	0.00	0.37	0.37	100.40	7	249	18	0
28	matrix	99.25	0.03	0.15	0.32	0.00	0.00	0.02	0.36	0.36	100.09	8	208	16	0
28	matrix	99.85	0.03	0.14	0.32	0.01	0.00	0.00	0.37	0.37	100.68	9	202	18	0
29	matrix	99.52	0.02	0.14	0.36	0.01	0.00	0.01	0.38	0.38	100.45	14	128	17	0
29	matrix	99.40	0.02	0.15	0.38	0.02	0.00	0.03	0.38	0.38	100.36	11	141	16	0
29	matrix	98.81	0.02	0.16	0.36	0.04	0.00	0.00	0.37	0.37	99.69	10	153	16	0
29	matrix	99.10	0.02	0.16	0.40	0.00	0.00	0.00	0.40	0.40	100.01	10	181	17	0
30	matrix	98.99	0.02	0.16	0.36	0.02	0.00	0.00	0.45	0.45	99.94	12	163	19	0
30	matrix	99.50	0.02	0.15	0.27	0.01	0.00	0.00	0.40	0.40	100.32	11	155	16	0
30	matrix	98.98	0.02	0.14	0.34	0.01	0.00	0.01	0.40	0.40	99.89	11	172	19	0
30	matrix	99.00	0.02	0.15	0.39	0.02	0.00	0.00	0.40	0.40	99.98	13	167	22	0
31	matrix	99.39	0.02	0.16	0.40	0.00	0.00	0.01	0.36	0.36	100.29	12	161	19	0

31	matrix	99.06	0.02	0.16	0.46	0.00	0.00	0.00	0.30	0.30	99.98	10	181	18	0
31	matrix	99.60	0.02	0.16	0.46	0.00	0.00	0.02	0.39	0.39	100.65	14	154	21	0
31	matrix	99.15	0.02	0.17	0.46	0.03	0.00	0.00	0.31	0.31	100.12	11	158	17	0
31	matrix	99.58	0.02	0.17	0.48	0.01	0.00	0.01	0.34	0.34	100.54	13	147	18	0
31	matrix	99.57	0.02	0.18	0.45	0.02	0.00	0.02	0.35	0.35	100.62	11	153	17	0
32	matrix	99.63	0.03	0.15	0.32	0.01	0.00	0.02	0.40	0.40	100.56	7	221	16	0
33	matrix	99.21	0.02	0.14	0.33	0.02	0.00	0.00	0.40	0.40	100.07	9	163	15	0
32	matrix	98.79	0.03	0.14	0.36	0.00	0.00	0.00	0.43	0.43	99.68	8	200	17	0

S4.3 Raman shifts and strains in quartz

Table S4.3.1 Quartz-in-garnet Raman peak positions

25-228

Analysis Number	Type	128	STD	%RSD	206	STD	%RSD	464	STD	%RSD
Gt1_Q4	Sample	127.753	0.025	0.019	209.247	0.062	0.030	465.401	0.011	0.002
Gt1_Q4_Std	Standard	127.113	0.094	0.074	206.031	0.224	0.109	464.445	0.046	0.010
Gt1_Q5	Sample	127.758	0.038	0.030	208.654	0.038	0.018	465.296	0.014	0.003
Gt1_Q5_Std	Standard	127.125	0.025	0.019	206.168	0.025	0.012	464.395	0.011	0.002
Gt1_Q6	Sample	131.541	0.050	0.038	222.480	0.043	0.019	470.264	0.021	0.004
Gt1_Q6_Std	Standard	127.166	0.023	0.018	206.000	0.024	0.012	464.422	0.071	0.020
Gt1_Q3	Sample	132.057	0.021	0.016	223.900	0.067	0.030	471.102	0.011	0.002
Gt1_Q3_Std	Standard	127.174	0.031	0.025	206.107	0.026	0.013	464.393	0.010	0.002
Gt1_Q8	Sample	130.777	0.036	0.028	219.761	0.024	0.011	469.332	0.008	0.002
Gt1_Q8_Std	Standard	127.188	0.023	0.018	206.107	0.023	0.011	464.410	0.009	0.002
Gt1_Q7	Sample	131.298	0.017	0.013	222.411	0.019	0.008	470.475	0.008	0.002
Gt1_Q7_Std	Standard	127.186	0.016	0.012	206.084	0.021	0.010	464.409	0.010	0.002

Table S4.3.1 Quartz-in-garnet Raman peak shifts

25-228

Analysis Number	d464	esd	misfit	d206	esd	misfit	d128	esd	misfit
Gt1_Q4	0.956	0.11	-0.17	3.216	0.1	0.016	0.64	0.04	0.028
Gt1_Q5	0.901	0.11	-0.14	2.485	0.1	0.0131	0.633	0.04	0.0231
Gt1_Q6	5.842	0.11	-1.219	16.48	0.1	0.1144	4.375	0.04	0.201
Gt1_Q3	6.709	0.11	-1.151	17.793	0.1	0.1079	4.884	0.04	0.1897
Gt1_Q8	4.921	0.11	-0.907	13.654	0.1	0.0851	3.589	0.04	0.1495
Gt1_Q7	6.066	0.11	-0.751	16.327	0.1	0.0705	4.112	0.04	0.1238

Table S4.3.2 Quartz-in-garnet strains, stresses and inclusion pressures. All values reported in GPa.

25-228

Analysis Number	e1+e2	esd	e3	esd	Vs	esd	10E6cv	corr%	chi2	S1	S2	S3	Pinc	Unc (2σ)
Gt1_Q4	-0.005	0.001	0.000	0.001	-0.004	0.000	-0.588	-98.1	2.91	-0.218	-0.218	-0.020	0.152	0.036
Gt1_Q5	-0.002	0.001	-0.001	0.000	-0.003	0.000	-0.398	-98.1	1.97	-0.107	-0.107	-0.115	0.109	0.030
Gt1_Q6	-0.012	0.007	-0.007	0.004	-0.019	0.003	-30.222	-98.1	149.00	-0.644	-0.644	-0.863	0.717	0.259
Gt1_Q3	-0.011	0.007	-0.009	0.004	-0.020	0.003	-26.917	-98.1	133.00	-0.612	-0.612	-1.067	0.764	0.245
Gt1_Q8	-0.010	0.005	-0.005	0.003	-0.016	0.002	-16.727	-98.1	82.70	-0.543	-0.543	-0.700	0.596	0.193
Gt1_Q7	-0.014	0.004	-0.005	0.003	-0.019	0.002	-11.471	-98.1	56.70	-0.711	-0.711	-0.742	0.721	0.160

S4.4 Raman shifts and strains in zircon

Table S4.4.1 Zircon-in-garnet Raman peak shifts

25-228

Sample Number	Type	202	STD	%RSD	214	STD	%RSD	224	STD	%RSD	354	STD	%RSD
Gt1_Z1	Sample	200.455	0.005	0.003	213.531	0.004	0.002	223.485	0.003	0.001	357.460	0.007	0.002
Gt1_Z1_Std	Standard	200.902	0.008	0.004	212.837	0.003	0.001	223.767	0.006	0.003	355.770	0.002	0.000

Gt1_Z3	Sample	200.562	0.010	0.005	214.061	0.020	0.009	223.718	0.003	0.001	357.817	0.003	0.001
Gt1_Z3_Std	Standard	200.660	0.008	0.004	212.671	0.004	0.002	223.572	0.004	0.002	355.498	0.004	0.001
Gt1_Z4	Sample	200.468	0.007	0.004	214.043	0.016	0.008	223.594	0.003	0.001	357.333	0.003	0.001
Gt1_Z4_Std	Standard	200.782	0.008	0.004	212.803	0.004	0.002	223.673	0.003	0.001	355.752	0.003	0.001
Gt1_Z5	Sample	200.281	0.009	0.004	-	-	-	223.371	0.003	0.001	359.155	0.003	0.001
Gt1_Z5_Std	Standard	200.795	0.006	0.003	212.703	0.003	0.002	223.620	0.004	0.002	355.607	0.002	0.001
Gt1_Z7	Sample	200.743	0.009	0.004	214.180	0.044	0.021	223.844	0.004	0.002	357.738	0.005	0.001
Gt1_Z7_Std	Standard	200.932	0.012	0.006	212.887	0.004	0.002	223.840	0.004	0.002	355.830	0.003	0.001
Gt1_Z10	Sample	200.849	0.005	0.002	213.799	0.003	0.001	223.921	0.003	0.001	356.978	0.005	0.001
Gt1_Z10_Std	Standard	201.122	0.008	0.004	213.161	0.003	0.001	224.003	0.005	0.002	356.009	0.003	0.001
Gt1_Z11	Sample	200.404	0.009	0.005	213.737	0.005	0.002	223.514	0.003	0.002	357.226	0.003	0.001
Gt1_Z11_Std	Standard	200.753	0.007	0.004	212.674	0.003	0.001	223.631	0.004	0.002	355.641	0.002	0.001
Gt1_Z16	Sample	200.510	0.007	0.004	213.408	0.004	0.002	223.606	0.003	0.001	357.352	0.002	0.001
Gt1_Z16_Std	Standard	200.677	0.010	0.005	212.713	0.003	0.002	223.573	0.005	0.002	355.589	0.003	0.001

Table S.4.4.1 cont.

Sample Number	Type	440	STD	%RSD	975	STD	%RSD	1008	STD	%RSD
Gt1_Z1	Sample	439.174	0.004	0.001	976.296	0.004	0.000	1010.075	0.003	0.0003
Gt1_Z1_Std	Standard	438.250	0.003	0.001	973.671	0.004	0.000	1007.232	0.004	0.0004
Gt1_Z3	Sample	438.962	0.005	0.001	976.141	0.005	0.001	1009.895	0.003	0.0003
Gt1_Z3_Std	Standard	438.041	0.004	0.001	973.594	0.004	0.000	1007.139	0.003	0.0003
Gt1_Z4	Sample	439.242	0.005	0.001	976.032	0.008	0.001	1009.881	0.003	0.0003
Gt1_Z4_Std	Standard	438.032	0.002	0.000	973.745	0.004	0.000	1007.302	0.004	0.0032
Gt1_Z5	Sample	439.043	0.006	0.001	977.312	0.009	0.001	1011.050	0.012	0.0012
Gt1_Z5_Std	Standard	438.116	0.003	0.001	973.581	0.003	0.000	1007.143	0.003	0.0003
Gt1_Z7	Sample	439.045	0.003	0.001	975.714	0.010	0.001	1009.485	0.006	0.0005
Gt1_Z7_Std	Standard	438.273	0.002	0.000	973.773	0.004	0.000	1007.307	0.004	0.0004
Gt1_Z10	Sample	439.449	0.004	0.001	975.858	0.005	0.001	1009.730	0.003	0.0003
Gt1_Z10_Std	Standard	438.485	0.002	0.000	974.006	0.004	0.000	1007.559	0.004	0.0004
Gt1_Z11	Sample	438.904	0.004	0.001	975.779	0.007	0.001	1009.703	0.004	0.0004
Gt1_Z11_Std	Standard	438.081	0.002	0.001	973.542	0.004	0.000	1007.104	0.004	0.0003

Gt1_Z16	Sample	439.381	0.011	0.002	975.686	0.003	0.000	1009.435	0.003	0.0003
Gt1_Z16_Std	Standard	438.068	0.002	0.000	973.641	0.004	0.000	1007.227	0.004	0.0004

Table S4.4.2 Zircon 1008 cm^{-1} peak heights and widths

Sample Number	Type	Height (intensity)	Width (cm^{-1})
Gt1_Z1	Sample	22839	4.32
Gt1_Z1_Std	Standard	49954	4.09
Gt1_Z3	Sample	2796.8	4.28
Gt1_Z3_Std	Standard	30331	4.13
Gt1_Z4	Sample	2750	4.37
Gt1_Z4_Std	Standard	38138	3.99
Gt1_Z5	Sample	240.48	4.65
Gt1_Z5_Std	Standard	43570	4.10
Gt1_Z7	Sample	447.91	4.52
Gt1_Z7_Std	Standard	45801	4.11
Gt1_Z10	Sample	19692	4.30
Gt1_Z10_Std	Standard	36978	4.06
Gt1_Z11	Sample	7858.1	4.11
Gt1_Z11_Std	Standard	45653	4.12
Gt1_Z16	Sample	15237	4.31
Gt1_Z16_Std	Standard	42995	4.04

Table S4.4.3 Zircon-in-garnet Raman peak shifts

25-228

Analysis	1008.7	esd	misfit	974.8	esd	misfit	438.8	esd	misfit
Gt1_Z10	2.171	0.127	-0.023	1.852	0.113	0.120	0.965	0.141	0.132
Gt1_Z7	2.178	0.127	-0.162	1.941	0.113	-0.059	0.771	0.141	0.056
Gt1_Z16	2.207	0.127	-0.196	2.045	0.113	0.040	1.313	0.141	0.524
Gt1_Z11	2.599	0.127	-0.024	2.237	0.113	0.060	0.824	0.141	-0.052
Gt1_Z4	2.578	0.127	-0.180	2.288	0.113	0.073	1.210	0.141	0.206

Gt1_Z1	2.843	0.127	0.002	2.624	0.113	0.206	0.923	0.141	0.043
Gt1_Z3	2.756	0.127	-0.193	2.546	0.113	0.018	0.921	0.141	0.028

Table S4.4.3 cont.

Analysis	356	esd	misfit	224	esd	misfit	213.4	esd	misfit
Gt1_Z10	0.969	0.17	-0.187	-0.082	0.141	-0.321	0.638	0.141	-0.178
Gt1_Z7	1.908	0.17	0.1898	0.004	0.141	-0.131	1.293	0.141	0.5274
Gt1_Z16	1.763	0.17	0.1533	0.033	0.141	-0.144	0.695	0.141	-0.125
Gt1_Z11	1.584	0.17	-0.134	-0.117	0.141	-0.32	1.063	0.141	0.1596
Gt1_Z4	1.581	0.17	0.0064	-0.079	0.141	-0.349	1.24	0.141	0.2404
Gt1_Z1	1.69	0.17	-0.363	-0.282	0.141	-0.455	0.694	0.141	-0.243
Gt1_Z3	2.319	0.17	0.1301	0.146	0.141	-0.019	1.39	0.141	0.4301

Table S4.4.4 Zircon-in-garnet strains, stresses and inclusion pressures. All values reported in GPa.

25-228

Analysis	e1+e2	esd	e3	esd	Vs	esd	10E6cv	corr%	chi2	Sigma 1	Sigma 2	Sigma 3	Pinc	Unc (2σ)
Gt1_Z10	-0.0005	0.0002	-0.0009	0.0002	-0.0015	0.0001	-0.032	-87.8	2.5	-0.281	-0.280	-0.545	0.369	0.057
Gt1_Z7	-0.0010	0.0003	-0.0007	0.0002	-0.0017	0.0001	-0.057	-87.8	4.5	-0.372	-0.370	-0.507	0.416	0.077
Gt1_Z16	-0.0009	0.0003	-0.0008	0.0002	-0.0017	0.0001	-0.060	-87.8	4.7	-0.357	-0.355	-0.541	0.418	0.080
Gt1_Z11	-0.0010	0.0002	-0.0009	0.0002	-0.0019	0.0001	-0.024	-87.8	1.9	-0.386	-0.383	-0.599	0.456	0.050
Gt1_Z4	-0.0008	0.0002	-0.0011	0.0002	-0.0019	0.0001	-0.043	-87.8	3.4	-0.373	-0.371	-0.667	0.470	0.066
Gt1_Z1	-0.0012	0.0003	-0.0008	0.0003	-0.0021	0.0002	-0.067	-87.8	5.3	-0.446	-0.443	-0.617	0.502	0.084
Gt1_Z3	-0.0013	0.0002	-0.0008	0.0002	-0.0022	0.0001	-0.039	-87.8	3.1	-0.471	-0.468	-0.633	0.524	0.063

Bibliography

Abers, G.A., van Keken, P.E., Kneller, E.A., Ferris, A., Stachnik, J.C., 2006. The thermal structure of subduction zones constrained by seismic imaging: Implications for slab dehydration and wedge flow. Earth and Planetary Science Letters 241, 387–397. https://doi.org/10.1016/j.epsl.2005.11.055

Abratis, M., Wörner, G., 2001. Ridge collision, slab-window formation, and the flux of Pacific asthenosphere into the Caribbean realm. Geology 29, 127–130. https://doi.org/10.1130/0091-7613(2001)029<0127:RCSWFA>2.0.CO;2

Agard, P., Plunder, A., Angiboust, S., Bonnet, G., Ruh, J., 2018. The subduction plate interface: rock record and mechanical coupling (from long to short timescales). Lithos 320–321, 537–566. https://doi.org/10.1016/j.lithos.2018.09.029

Agard, P., Yamato, P., Jolivet, L., Burov, E., 2009. Exhumation of oceanic blueschists and eclogites in subduction zones: Timing and mechanisms. Earth-Science Reviews 92, 53–79. https://doi.org/10.1016/j.earscirev.2008.11.002

Ague, J.J., Baxter, E.F., 2007. Brief thermal pulses during mountain building recorded by Sr diffusion in apatite and multicomponent diffusion in garnet. Earth and Planetary Science Letters 261, 500–516. https://doi.org/10.1016/j.epsl.2007.07.017

Ague, J.J., Carlson, W.D., 2013. Metamorphism as Garnet Sees It: The Kinetics of Nucleation and Growth, Equilibration, and Diffusional Relaxation. Elements 9, 439–445. https://doi.org/10.2113/gselements.9.6.439

Ague, J.J., Nicolescu, S., 2014. Carbon dioxide released from subduction zones by fluid-

mediated reactions. Nature Geoscience 7, 355–360. https://doi.org/10.1038/ngeo2143

Alder-Ivanbrook, B., Hampton, S.K., Esparaza Limon, J.P., Lackey, J.S., Page, F.Z., 2018. An investigation of the Catalina garnet-blueschist: Major and trace element composition and zoning in garnet and lawsonite from a multiply subducted block. Presented at the 2018 American Geophysical Union Fall Meeting, Washington D.C.

Alt, J.C., Schwarzenbach, E.M., Früh-Green, G.L., Shanks, W.C., Bernasconi, S.M., Garrido, C.J., Crispini, L., Gaggero, L., Padrón-Navarta, J.A., Marchesi, C., 2013. The role of serpentinites in cycling of carbon and sulfur: Seafloor serpentinization and subduction metamorphism. Lithos 178, 40–54. https://doi.org/10.1016/j.lithos.2012.12.006

Alvaro, M., Mazzucchelli, M.L., Angel, R.J., Murri, M., Campomenosi, N., Scambelluri, M., Nestola, F., Korsakov, A., Tomilenko, A.A., Marone, F., Morana, M., 2020. Fossil subduction recorded by quartz from the coesite stability field. Geology 48, 24–28. https://doi.org/10.1130/G46617.1

Anczkiewicz, R., Platt, J.P., Thirlwall, M.F., Wakabayashi, J., 2004. Franciscan subduction off to a slow start: evidence from high-precision Lu–Hf garnet ages on high grade-blocks. Earth and Planetary Science Letters 225, 147–161. https://doi.org/10.1016/j.epsl.2004.06.003

Angel, R.J., Alvaro, M., Miletich, R., Nestola, F., 2017a. A simple and generalised P–T–

V EoS for continuous phase transitions, implemented in EosFit and applied to quartz. Contributions to Mineralogy and Petrology 172, 29. https://doi.org/10.1007/s00410-017-1349-x

Angel, R.J., Mazzucchelli, M.L., Alvaro, M., Nestola, F., 2017b. EosFit-Pinc: A simple GUI for host-inclusion elastic thermobarometry. American Mineralogist 102, 1957–1960. https://doi.org/10.2138/am-2017-6190

Angel, R.J., Murri, M., Mihailova, B., Alvaro, M., 2019. Stress, strain and Raman shifts. Zeitschrift für Kristallographie - Crystalline Materials 234, 129–140. https://doi.org/10.1515/zkri-2018-2112

Angiboust, S., Agard, P., Raimbourg, H., Yamato, P., Huet, B., 2011. Subduction interface processes recorded by eclogite-facies shear zones (Monviso, W. Alps). Lithos 127, 222–238. https://doi.org/10.1016/j.lithos.2011.09.004

Angiboust, S., Glodny, J., Oncken, O., Chopin, C., 2014. In search of transient subduction interfaces in the Dent Blanche–Sesia Tectonic System (W. Alps). Lithos 205, 298–321. https://doi.org/10.1016/j.lithos.2014.07.001

Angiboust, S., Langdon, R., Agard, P., Waters, D., Chopin, C., 2012. Eclogitization of the Monviso ophiolite (W. Alps) and implications on subduction dynamics: Monviso eclogites and subduction dynamics. Journal of Metamorphic Geology 30, 37–61. https://doi.org/10.1111/j.1525-1314.2011.00951.x

Armstrong, J.T., 1988. Quantitative analysis of silicate and oxide minerals: comparison of Monte Carlo, ZAF and phi-rho-z procedures, in: Newbury, D.E. (Ed.), Microbeam Analysis. San Francisco Press, San Francisco, CA, pp. 239–246.

Audet, P., Bürgmann, R., 2014. Possible control of subduction zone slow-earthquake

periodicity by silica enrichment. Nature 510, 389–392. https://doi.org/10.1038/nature13391

Auzanneau, E., Schmidt, M.W., Vielzeuf, D., D Connolly, J.A., 2010. Titanium in phengite: a geobarometer for high temperature eclogites. Contrib Mineral Petrol 159, 1–24. https://doi.org/10.1007/s00410-009-0412-7

Awalt, M.B., Page, F.Z., Walsh, E.O., Kylander-Clark, A., Wirth, K.R., 2013. New evidence for old subduction in the Catalina Schist, Santa Catalina Island, CA. Presented at the 2013 Geological Society of America Annual Meeting, Denver, CO, p. 798.

Bachmann, R., Glodny, J., Oncken, O., Seifert, W., 2009. Abandonment of the South Penninic–Austroalpine palaeosubduction zone, Central Alps, and shift from subduction erosion to accretion: constraints from Rb/Sr geochronology. Journal of the Geological Society 166, 217–231. https://doi.org/10.1144/0016-76492008-024

Baldwin, S.L., Harrison, T.M., Gerald, J.D.F., 1990. Diffusion of 40Ar in metamorphic hornblende. Contributions to Mineralogy and Petrology 105, 691–703. https://doi.org/10.1007/BF00306534

Baxter, E.F., Ague, J.J., Depaolo, D.J., 2002. Prograde temperature–time evolution in the Barrovian type–locality constrained by Sm/Nd garnet ages from Glen Clova, Scotland. Journal of the Geological Society 159, 71–82. https://doi.org/10.1144/0016-76901013

Baxter, E.F., Scherer, E.E., 2013. Garnet Geochronology: Timekeeper of Tectonometamorphic Processes. Elements 9, 433–438. https://doi.org/10.2113/gselements.9.6.433

Beall, A., Fagereng, Å., Ellis, S., 2019. Strength of Strained Two-Phase Mixtures: Application to Rapid Creep and Stress Amplification in Subduction Zone Mélange. Geophysical Research Letters 46, 169–178. https://doi.org/10.1029/2018GL081252

Beall, A.P., Moresi, L., Stern, T., 2017. Dripping or delamination? A range of mechanisms for removing the lower crust or lithosphere. Geophysical Journal International 210, 671–692. https://doi.org/10.1093/gji/ggx202

Bebout, G.E., 1997. Nitrogen isotope tracers of high-temperature fluid-rock interactions: Case study of the Catalina Schist, California. Earth and Planetary Science Letters 151, 77–90. https://doi.org/10.1016/S0012-821X(97)00117-9

Bebout, G.E., Barton, M.D., 2002. Tectonic and metasomatic mixing in a high-T, subduction-zone mélange—insights into the geochemical evolution of the slab–mantle interface. Chemical Geology 187, 79–106. https://doi.org/10.1016/S0009-2541(02)00019-0

Bebout, G.E., Barton, M.D., 1993. Metasomatism during subduction: products and possible paths in the Catalina Schist, California. Chemical Geology 108, 61–92.

Bebout, G.E., Barton, M.D., 1989. Fluid flow and metasomatism in a subduction zone hydrothermal system: Catalina Schist terrane, California. Geology 17, 976–980. https://doi.org/10.1130/0091-7613(1989)017<0976:FFAMIA>2.3.CO;2

Bebout, G.E., Penniston-Dorland, S.C., 2016. Fluid and mass transfer at subduction interfaces—The field metamorphic record. Lithos 240–243, 228–258. https://doi.org/10.1016/j.lithos.2015.10.007

Behn, M.D., Kelemen, P.B., Hirth, G., Hacker, B.R., Massonne, H.-J., 2011. Diapirs as

the source of the sediment signature in arc lavas. Nature Geoscience 4, 641–646. https://doi.org/10.1038/ngeo1214

Behr, W.M., Kotowski, A.J., Ashley, K.T., 2018. Dehydration-induced rheological heterogeneity and the deep tremor source in warm subduction zones. Geology 46, 475–478. https://doi.org/10.1130/G40105.1

Billen, M.I., Hirth, G., 2007. Rheologic controls on slab dynamics. Geochemistry, Geophysics, Geosystems 8(8), https://doi.org/10.1029/2007GC001597

Bloch, E., Ganguly, J., 2015. 176Lu–176Hf geochronology of garnet II: numerical simulations of the development of garnet–whole-rock 176Lu–176Hf isochrons and a new method for constraining the thermal history of metamorphic rocks. Contributions to Mineralogy and Petrology 169, 14. https://doi.org/10.1007/s00410-015-1115-x

Bloch, E., Ganguly, J., Hervig, R., Cheng, W., 2015. 176Lu–176Hf geochronology of garnet I: experimental determination of the diffusion kinetics of Lu3+ and Hf4+ in garnet, closure temperatures and geochronological implications. Contributions to Mineralogy and Petrology 169, 12. https://doi.org/10.1007/s00410-015-1109-8

Bloch, E.M., Jollands, M.C., Devoir, A., Bouvier, A.-S., Ibañez-Mejia, M., Baumgartner, L.P., 2020. Multispecies diffusion of yttrium, rare earth elements and hafnium in garnet. Journal of Petrology. https://doi.org/10.1093/petrology/egaa055

Bonazzi, M., Tumiati, S., Thomas, J.B., Angel, R.J., Alvaro, M., 2019. Assessment of the reliability of elastic geobarometry with quartz inclusions. Lithos 350–351, 105201. https://doi.org/10.1016/j.lithos.2019.105201

Bonnet, G., Agard, P., Angiboust, S., Monié, P., Jentzer, M., Omrani, J., Whitechurch,

H., Fournier, M., 2018. Tectonic slicing and mixing processes along the subduction interface: The Sistan example (Eastern Iran). Lithos 310–311, 269–287. https://doi.org/10.1016/j.lithos.2018.04.016

Broadwell, K.S., Locatelli, M., Verlaguet, A., Agard, P., Caddick, M.J., 2019. Transient and periodic brittle deformation of eclogites during intermediate-depth subduction. Earth and Planetary Science Letters 521, 91–102. https://doi.org/10.1016/j.epsl.2019.06.008

Brown, K., Tryon, M., Deshon, H., Dorman, L., Schwartz, S., 2005. Correlated transient fluid pulsing and seismic tremor in the Costa Rica subduction zone. Earth and Planetary Science Letters 238, 189–203. https://doi.org/10.1016/j.epsl.2005.06.055

Brown, M., Johnson, T., 2018. Secular change in metamorphism and the onset of global plate tectonics. American Mineralogist 103, 181–196. https://doi.org/10.2138/am-2018-6166

Bürgmann, R., Dresen, G., 2008. Rheology of the Lower Crust and Upper Mantle: Evidence from Rock Mechanics, Geodesy, and Field Observations. Annual Review of Earth and Planetary Sciences 36, 531–567. https://doi.org/10.1146/annurev.earth.36.031207.124326

Bystricky, M., Mackwell, S., 2001. Creep of dry clinopyroxene aggregates. Journal of Geophysical Research: Solid Earth 106, 13443–13454.

Caddick, M.J., Konopásek, J., Thompson, A.B., 2010. Preservation of Garnet Growth Zoning and the Duration of Prograde Metamorphism. Journal of Petrology 51, 2327–2347. https://doi.org/10.1093/petrology/egq059

Calvert, A.J., 2004. Seismic reflection imaging of two megathrust shear zones in the northern Cascadia subduction zone. Nature, 428(6979), 163-167. https://doi.org/10.1038/nature02372

Campomenosi, N., Mazzucchelli, M.L., Mihailova, B., Scambelluri, M., Angel, R.J., Nestola, F., Reali, A., Alvaro, M., 2018. How geometry and anisotropy affect residual strain in host-inclusion systems: Coupling experimental and numerical approaches. American Mineralogist 103, 2032–2035. https://doi.org/10.2138/am-2018-6700CCBY

Carlson, W.D., 2012. Rates and mechanism of Y, REE, and Cr diffusion in garnet. American Mineralogist 97, 1598–1618. https://doi.org/10.2138/am.2012.4108

Carlson, W.D., 2006. Rates of Fe, Mg, Mn, and Ca diffusion in garnet. American Mineralogist 91, 1–11. https://doi.org/10.2138/am.2006.2043

Carlson, W.D., 2002. Scales of disequilibrium and rates of equilibration during metamorphism. American Mineralogist 87, 185–204. https://doi.org/10.2138/am-2002-2-301

Carlson, W.D., Gordon, C.L., 2004. Effects of matrix grain size on the kinetics of intergranular diffusion. Journal of Metamorphic Geology 22, 733–742. https://doi.org/10.1111/j.1525-1314.2004.00545.x

Carlson, W.D., Pattison, D.R.M., Caddick, M.J., 2015. Beyond the equilibrium paradigm: How consideration of kinetics enhances metamorphic interpretation. American Mineralogist 100, 1659–1667. https://doi.org/10.2138/am-2015-5097

Castro, A.E., Spear, F.S., 2017. Reaction overstepping and re-evaluation of peak P–T

conditions of the blueschist unit Sifnos, Greece: implications for the Cyclades subduction zone. International Geology Review 59, 548–562. https://doi.org/10.1080/00206814.2016.1200499

Catlos, E.J., Sorensen, S.S., 2003. Phengite-Based Chronology of K- and Ba-Rich Fluid Flow in Two Paleosubduction Zones. Science 299, 92–95. https://doi.org/10.1126/science.1076977

Chakraborty, S., Ganguly, J., 1992. Cation diffusion in aluminosilicate garnets: experimental determination in spessartine-almandine diffusion couples, evaluation of effective binary diffusion coefficients, and applications. Contributions to Mineralogy and Petrology 111, 74–86. https://doi.org/10.1007/BF00296579

Chalmers, P., Spear, F.S., & Cheney, J.T., 2007. Zr-in-rutile thermometry in blueschists of Syros, Greece. Geological Society of America Abstracts with Program, 39, 86.

Cheng, H., DuFrane, S.A., Vervoort, J.D., Nakamura, E., Zheng, Y.-F., Zhou, Z., 2010. Protracted oceanic subduction prior to continental subduction: New Lu-Hf and Sm-Nd geochronology of oceanic-type high-pressure eclogite in the western Dabie orogen. American Mineralogist 95, 1214–1223. https://doi.org/10.2138/am.2010.3307

Cheng, H., King, R.L., Nakamura, E., Vervoort, J.D., Zhou, Z., 2008. Coupled Lu-Hf and Sm-Nd geochronology constrains garnet growth in ultra-high-pressure eclogites from the Dabie orogen. Journal of Metamorphic Geology 26, 741–758. https://doi.org/10.1111/j.1525-1314.2008.00785.x

Cheng, H., Nakamura, E., Zhou, Z., 2009. Garnet Lu–Hf dating of retrograde fluid

activity during ultrahigh-pressure metamorphic eclogites exhumation. Mineralogy and Petrology 95, 315–326. https://doi.org/10.1007/s00710-008-0030-5

Cheng, H., Vervoort, J.D., Dragovic, B., Wilford, D., Zhang, L., 2018. Coupled Lu–Hf and Sm–Nd geochronology on a single eclogitic garnet from the Huwan shear zone, China. Chemical Geology 476, 208–222. https://doi.org/10.1016/j.chemgeo.2017.11.018

Čížková, H., Bina, C.R., 2013. Effects of mantle and subduction-interface rheologies on slab stagnation and trench rollback. Earth and Planetary Science Letters 379, 95–103. https://doi.org/10.1016/j.epsl.2013.08.011

Cloos, M., 1993. Lithospheric buoyancy and collisional orogenesis: Subduction of oceanic plateaus, continental margins, island arcs, spreading ridges, and seamounts. GSA Bulletin 105, 715–737. https://doi.org/10.1130/0016-7606(1993)105<0715:LBACOS>2.3.CO;2

Cloos, M., 1986. Blueschists in the Franciscan Complex of California: Petrotectonic constraints on uplift mechanisms, in: Blueschists and Eclogites. Geological Society of America Memoir, pp. 77–93.

Cloos, M., 1982. Flow melanges: Numerical modeling and geologic constraints on their origin in the Franciscan subduction complex, California. Geological Society of America Bulletin 93, 330–345.

Cloos, M., Shreve, R.L., 1988a. Subduction-channel model of prism accretion, mélange formation, sediment subduction, and subduction erosion at convergent plate margins: 2. Implications and discussion. Pure and Applied Geophysics 128, 501–545.

Cloos, M., Shreve, R.L., 1988b. Subduction-channel model of prism accretion, melange formation, sediment subduction, and subduction erosion at convergent plate margins: 1. Background and description. Pure and Applied Geophysics 128, 455–500. https://doi.org/10.1007/BF00874548

Coggon, R., Holland, T.J.B., 2002. Mixing properties of phengitic micas and revised garnet-phengite thermobarometers. Journal of Metamorphic Geology 20, 683–696. https://doi.org/10.1046/j.1525-1314.2002.00395.x

Coleman, R.G., Lanphere, M.A., 1971. Distribution and Age of High-Grade Blueschists, Associated Eclogites, and Amphibolites from Oregon and California. Geological Society of America Bulletin 82, 2397. https://doi.org/10.1130/0016-7606(1971)82[2397:DAAOHB]2.0.CO;2

Connolly, J.A.D., 2009. The geodynamic equation of state: What and how: geodynamic equation of state-what and how. Geochemistry, Geophysics, Geosystems 10. https://doi.org/10.1029/2009GC002540

Connolly, J.A.D., 2005. Computation of phase equilibria by linear programming: A tool for geodynamic modeling and its application to subduction zone decarbonation. Earth and Planetary Science Letters 236, 524–541. https://doi.org/10.1016/j.epsl.2005.04.033

Cooper, L.B., Ruscitto, D.M., Plank, T., Wallace, P.J., Syracuse, E.M., Manning, C.E., 2012. Global variations in H_2O/Ce: 1. Slab surface temperatures beneath volcanic arcs: slab surface temperatures beneath volcanic arcs. Geochemistry Geophysics, Geosystems 13. https://doi.org/10.1029/2011GC003902

Cooperdock, E.H.G., Raia, N.H., Barnes, J.D., Stockli, D.F., Schwarzenbach, E.M., 2018.

Tectonic origin of serpentinites on Syros, Greece: Geochemical signatures of abyssal origin preserved in a HP/LT subduction complex. Lithos 296–299, 352–364. https://doi.org/10.1016/j.lithos.2017.10.020

Cowan, D.S., 1985. Structural styles in Mesozoic and Cenozoic melanges in the western Cordillera of North America. Geological Society of America Bulletin 96, 451–462. https://doi.org/10.1130/0016-7606(1985)96<451:SSIMAC>2.0.CO;2

Cruz-Uribe, A.M., Feineman, M.D., Zack, T., Jacob, D.E., 2018a. Assessing trace element (dis)equilibrium and the application of single element thermometers in metamorphic rocks. Lithos 314–315, 1–15. https://doi.org/10.1016/j.lithos.2018.05.007

Cruz-Uribe, A.M., Marschall, H.R., Gaetani, G.A., Le Roux, V., 2018b. Generation of alkaline magmas in subduction zones by partial melting of mélange diapirs—An experimental study. Geology 46, 343–346. https://doi.org/10.1130/G39956.1

de Capitani, C., Petrakakis, K., 2010. The computation of equilibrium assemblage diagrams with Theriak/Domino software. American Mineralogist 95, 1006–1016. https://doi.org/10.2138/am.2010.3354

DeCelles, P.G., 2004. Late Jurassic to Eocene evolution of the Cordilleran thrust belt and foreland basin system, western U.S.A. American Journal of Science 304, 105–168. https://doi.org/10.2475/ajs.304.2.105

DeLong, S.E., Schwarz, W.M., Anderson, R.N., 1979. Thermal effects of ridge subduction. Earth and Planetary Science Letters 44, 239–246. https://doi.org/10.1016/0012-821X(79)90172-9

Dickinson, W.R., & Gehrels, G.E., 2009. Use of U–Pb ages of detrital zircons to infer

maximum depositional ages of strata: A test against a Colorado Plateau Mesozoic database. Earth and Planetary Science Letters, 288(1-2), 115-125. https://doi.org/10.1016/j.epsl.2009.09.013

Diener, J.F.A., Powell, R., 2012. Revised activity-composition models for clinopyroxene and amphibole: Revised a-X models for CPX and amphibole. Journal of Metamorphic Geology 30, 131–142. https://doi.org/10.1111/j.1525-1314.2011.00959.x

Diener, J.F.A., Powell, R., White, R.W., Holland, T.J.B., 2007. A new thermodynamic model for clino- and orthoamphiboles in the system Na_2O-CaO-FeO-MgO-Al_2O_3-SiO_2-H_2O-O. Journal of Metamorphic Geology 25, 631–656. https://doi.org/10.1111/j.1525-1314.2007.00720.x

Dilek, Y., Altunkaynak, Ş., 2009. Geochemical and temporal evolution of Cenozoic magmatism in western Turkey: mantle response to collision, slab break-off, and lithospheric tearing in an orogenic belt. Geological Society, London, Special Publications 311, 213–233. https://doi.org/10.1144/SP311.8

Dragovic, B., Baxter, E.F., Caddick, M.J., 2015. Pulsed dehydration and garnet growth during subduction revealed by zoned garnet geochronology and thermodynamic modeling, Sifnos, Greece. Earth and Planetary Science Letters 413, 111–122. https://doi.org/10.1016/j.epsl.2014.12.024

Dragovic, B., Samanta, L.M., Baxter, E.F., Selverstone, J., 2012. Using garnet to constrain the duration and rate of water-releasing metamorphic reactions during subduction: An example from Sifnos, Greece. Chemical Geology 314–317, 9–22. https://doi.org/10.1016/j.chemgeo.2012.04.016

Draper, G., Nagle, F., 1991. Geology, structure, and tectonic development of the Rio San Juan Complex, northern Dominican Republic. Geologic and tectonic development of the North America-Caribbean plate boundary in Hispaniola. Geological Society of America Special Paper 262, 77–95.

Duffy, T.S., Anderson, D.L., 1989. Seismic velocities in mantle minerals and the mineralogy of the upper mantle. Journal of Geophysical Research 94, 1895. https://doi.org/10.1029/JB094iB02p01895

Dumitru, T.A., Wakabayashi, J., Wright, J.E., Wooden, J.L., 2010. Early Cretaceous transition from nonaccretionary behavior to strongly accretionary behavior within the Franciscan subduction complex: Accretion in the Franciscan Complex. Tectonics 29. https://doi.org/10.1029/2009TC002542

Enami, M., Nishiyama, T., Mouri, T., 2007. Laser Raman microspectrometry of metamorphic quartz: A simple method for comparison of metamorphic pressures. American Mineralogist 92, 1303–1315. https://doi.org/10.2138/am.2007.2438

Erba, A., Mahmoud, A., Orlando, R., Dovesi, R., 2014. Elastic properties of six silicate garnet end members from accurate ab initio simulations. Physics and Chemistry Minerals 41, 151–160. https://doi.org/10.1007/s00269-013-0630-4

Escuder-Viruete, J., Pérez-Estaún, A., 2013. Contrasting exhumation P–T paths followed by high-P rocks in the northern Caribbean subduction–accretionary complex: Insights from the structural geology, microtextures and equilibrium assemblage diagrams. Lithos 160–161, 117–144. https://doi.org/10.1016/j.lithos.2012.11.028

Escuder-Viruete, J., Valverde-Vaquero, P., Rojas-Agramonte, Y., Gabites, J., Castillo-

Carrión, M., Pérez-Estaún, A., 2013. Timing of deformational events in the Río San Juan complex: Implications for the tectonic controls on the exhumation of high-P rocks in the northern Caribbean subduction–accretionary prism. Lithos 177, 416–435. https://doi.org/10.1016/j.lithos.2013.07.006

Evans, T.P., 2004. A method for calculating effective bulk composition modification due to crystal fractionation in garnet-bearing schist: implications for isopleth thermobarometry: Garnet fractionation and P-T path calculation. Journal of Metamorphic Geology 22, 547–557. https://doi.org/10.1111/j.1525-1314.2004.00532.x

Ewing, T.A., Hermann, J., Rubatto, D., 2013. The robustness of the Zr-in-rutile and Ti-in-zircon thermometers during high-temperature metamorphism (Ivrea-Verbano Zone, northern Italy). Contributions to Mineralogy and Petrology 165, 757–779. https://doi.org/10.1007/s00410-012-0834-5

Fagereng, Å., Hillary, G.W.B., & Diener, J.F.A., 2014. Brittle-viscous deformation, slow slip and tremor. Geophysical Research Letters, 41(12), 4159-4167. https://doi.org/ 10.1002/2014GL060433

Fagereng, Å., & Sibson, R.H.. 2010. Mélange rheology and seismic cycle. Geology, 38(8), 751-754. https://doi.org/10.1130/G30868.1

Ferry, J.M., Spear, F.S., 1978. Experimental calibration of the partitioning of Fe and Mg between biotite and garnet. Contributions to Mineralogy and Petrology 66, 113–117. https://doi.org/10.1007/BF00372150

Festa, A., Pini, G.A., Dilek, Y., Codegone, G., 2010. Mélanges and mélange-forming

processes: a historical overview and new concepts. International Geology Review 52, 1040–1105. https://doi.org/10.1080/00206810903557704

Festa, A., Pini, G.A., Ogata, K., Dilek, Y., 2019. Diagnostic features and field-criteria in recognition of tectonic, sedimentary and diapiric mélanges in orogenic belts and exhumed subduction-accretion complexes. Gondwana Research 74, 7-30. https://doi.org/10.1016/j.gr.2019.01.003

Firsov, L.V., Dobretsov, N.L., 1970. Age of glaucophane metamorphism at the northwestern fringe of the Pacific Ocean. Doklady Akademii Nauk SSSR 185, 46–48.

Fisher, A.T., 2003. Abrupt thermal transition reveals hydrothermal boundary and role of seamounts within the Cocos Plate. Geophysical Research Letters 30, 1550. https://doi.org/10.1029/2002GL016766

Fisher, D., Byrne, T., 1990. The character and distribution of mineralized fractures in the Kodiak Formation, Alaska: Implications for fluid flow in an underthrust sequence. Journal of Geophysical Research 95, 9069. https://doi.org/10.1029/JB095iB06p09069

Fisher, D., Byrne, T., 1987. Structural evolution of underthrusted sediments, Kodiak Islands, Alaska. Tectonics 6, 775–793. https://doi.org/10.1029/TC006i006p00775

French, M.E., Condit, C.B., 2019. Slip partitioning along an idealized subduction plate boundary at deep slow slip conditions. Earth and Planetary Science Letters 528, 115828. https://doi.org/10.1016/j.epsl.2019.115828

French, M.E., Zhu, W., 2017. Slow fault propagation in serpentinite under conditions of

high pore fluid pressure. Earth and Planetary Science Letters 473, 131–140. https://doi.org/10.1016/j.epsl.2017.06.009

Freymueller, J.T., Woodard, H., Cohen, S.C., Cross, R., Elliott, J., Larsen, C.F., Hreinsdóttir, S., Zweck, C., 2013. Active Deformation Processes in Alaska, Based on 15 Years of GPS Measurements, in: Freymueller, J.T., Haeussler, P.J., Wesson, R.L., Ekström, G. (Eds.), Geophysical Monograph Series. American Geophysical Union, Washington, D. C, pp. 1–42. https://doi.org/10.1029/179GM02

Fuhrman, M.L., Lindsley, D.H., 1988. Ternary-feldspar modeling and thermometry. American Mineralogist 73, 201–215.

Gaidies, F., de Capitani, C., Abart, R., 2008. THERIA_G: a software program to numerically model prograde garnet growth. Contributions to Mineralogy and Petrology 155, 657–671. https://doi.org/10.1007/s00410-007-0263-z

Galbraith, R.F., Laslett, G.M., 1993. Statistical models for mixed fission track ages. Nuclear Tracks and Radiation Measurements 21, 459–470. https://doi.org/10.1016/1359-0189(93)90185-C

Garcia-Casco, A., Lazaro, C., Rojas-Agramonte, Y., Kroner, A., Torres-Roldan, R.L., Nunez, K., Neubauer, F., Millan, G., Blanco-Quintero, I., 2007. Partial Melting and Counterclockwise P T Path of Subducted Oceanic Crust (Sierra del Convento Melange, Cuba). Journal of Petrology 49, 129–161. https://doi.org/10.1093/petrology/egm074

Gerrits, A.R., Inglis, E.C., Dragovic, B., Starr, P.G., Baxter, E.F., Burton, K.W., 2019.

Release of oxidizing fluids in subduction zones recorded by iron isotope zonation in garnet. Nature Geoscience 12, 1029–1033. https://doi.org/10.1038/s41561-019-0471-y

Gerya, T.V., Stöckhert, B., Perchuk, A.L., 2002. Exhumation of high-pressure metamorphic rocks in a subduction channel: A numerical simulation: Exhumation of high-pressure rocks. Tectonics 21, 6-1-6–19. https://doi.org/10.1029/2002TC001406

Göğüş, O.H., Pysklywec, R.N., 2008. Near-surface diagnostics of dripping or delaminating lithosphere. Journal of Geophysical Research 113, B11404. https://doi.org/10.1029/2007JB005123

Gonzalez, J.P., Baldwin, S.L., 2019. Modelling white mica pressure-temperature-time (P-T-t) paths using thermobarometric and ^{40}Ar/^{39}Ar thermochronologic data. Terra Nova 31, 169–178. https://doi.org/10.1111/ter.12381

Green, E., Holland, T., Powell, R., 2007. An order-disorder model for omphacitic pyroxenes in the system jadeite-diopside-hedenbergite-acmite, with applications to eclogitic rocks. American Mineralogist 92, 1181–1189. https://doi.org/10.2138/am.2007.2401

Grove, M., 1993. Thermal histories of southern California basement terranes (Ph.D. Thesis). University of California, Los Angeles.

Grove, M., Bebout, G.E., 1995. Cretaceous tectonic evolution of coastal southern California: insights from the Catalina Schist. Tectonics 14, 1290–1308.

Grove, M., Bebout, G.E., Jacobson, C.E., Barth, A.P., Kimbrough, D.L., King, R.L., Zou,

H., Lovera, O.M., Mahoney, B.J., Gehrels, G.E., 2008. The Catalina Schist: Evidence for middle Cretaceous subduction erosion of southwestern North America. Special Paper 436: Formation and Applications of the Sedimentary Record in Arc Collision Zones 436, 335–361. https://doi.org/10.1130/2008.2436(15)

Grove, T.L., Till, C.B., Krawczynski, M.J., 2012. The Role of H_2O in Subduction Zone Magmatism. Annual Reviews of Earth and Planetary Science 40, 413–439. https://doi.org/10.1146/annurev-earth-042711-105310

Grüneberger, A.M., Schmidt, C., Jahn, S., Rhede, D., Loges, A., Wilke, M., 2016. Interpretation of Raman spectra of the zircon–hafnon solid solution. European Journal of Mineralogy 28, 721–733. https://doi.org/10.1127/ejm/2016/0028-2551

Hacker, B.R., Abers, G.A., Peacock, S.M., 2003. Subduction factory 1. Theoretical mineralogy, densities, seismic wave speeds, and H_2O contents: Eubduction zone mineralogy and physical properties. Journal of Geophysical Research 108. https://doi.org/10.1029/2001JB001127

Harrison, T.M., Célérier, J., Aikman, A.B., Hermann, J., Heizler, M.T., 2009. Diffusion of ^{40}Ar in muscovite. Geochimica et Cosmochimica Acta 73, 1039–1051. https://doi.org/10.1016/j.gca.2008.09.038

Harvey, J., Baxter, E.F., 2009. An improved method for TIMS high precision neodymium isotope analysis of very small aliquots (1–10 ng). Chemical Geology 258, 251–257. https://doi.org/10.1016/j.chemgeo.2008.10.024

Hayden, L.A., Watson, E.B., Wark, D.A., 2008. A thermobarometer for sphene (titanite).

Contributions to Mineralogy and Petrology 155, 529–540. https://doi.org/10.1007/s00410-007-0256-y

Hayes, G.P., Wald, D.J., & Johnson, R.L., 2012. Slab 1.0: A three-dimensional model of global subduction zone geometries. Journal of Geophysical Research: Solid Earth, 117(B1). https://doi.org/10.1029/ 2011JB008524

Hayman, N.W., Lavier, L.L., 2014. The geologic record of deep episodic tremor and slip. Geology 42, 195–198. https://doi.org/10.1130/G34990.1

Hirschmann, M.M., 2006. Water, melting, and the deep earth H_2O cycle. Annual Reviews of Earth and Planetary Science 34, 629–653. https://doi.org/10.1146/annurev.earth.34.031405.125211

Holdaway, M.J., 2001. Recalibration of the GASP geobarometer in light of recent garnet and plagioclase activity models and versions of the garnet-biotite geothermometer. American Mineralogist 86, 1117–1129. https://doi.org/10.2138/am-2001-1001

Holdaway, M.J., Mukhopadhyay, B., Dyar, M.D., Guidotti, C.V., Dutrow, B.L., 1997. Garnet-biotite geothermometry revised; new Margules parameters and a natural specimen data set from Maine. American Mineralogist 82, 582–595. https://doi.org/10.2138/am-1997-5-618

Holder, R.M., Viete, D.R., Brown, M., Johnson, T.E., 2019. Metamorphism and the evolution of plate tectonics. Nature 572, 378–381. https://doi.org/10.1038/s41586-019-1462-2

Holland, T., Powell, R., 2011. An improved and extended internally consistent

thermodynamic dataset for phases of petrological interest, involving a new equation of state for solids. Journal of Metamorphic Geology 29, 333–383. https://doi.org/10.1111/j.1525-1314.2010.00923.x

Holland, T., Powell, R., 2003. Activity-composition relations for phases in petrological calculations: an asymmetric multicomponent formulation. Contributions to Mineralogy and Petrology 145, 492–501. https://doi.org/10.1007/s00410-003-0464-z

Holland, T., Powell, R., 1998. An internally consistent thermodynamic data set for phases of petrological interest. Journal of metamorphic Geology 16, 309–343.

Hollister, L.S., 1966. Garnet Zoning: An Interpretation Based on the Rayleigh Fractionation Model. Science 154, 1647. https://doi.org/10.1126/science.154.3757.1647

Hsü, K.J., 1968. Principles of melanges and their bearing on the Franciscan-Knoxville paradox. Geological Society of America Bulletin 79, 1063–1074.

Huang, R., Audétat, A., 2012. The titanium-in-quartz (TitaniQ) thermobarometer: A critical examination and re-calibration. Geochimica et Cosmochimica Acta 84, 75–89. https://doi.org/10.1016/j.gca.2012.01.009

Isaak, D.G., Graham, E.K., 1976. The elastic properties of an almandine-spessartine garnet and elasticity in the garnet solid solution series. Journal of Geophysical Research 81, 2483–2489. https://doi.org/10.1029/JB081i014p02483

Ishizuka, O., Tani, K., Reagan, M.K., Kanayama, K., Umino, S., Harigane, Y., Sakamoto,

I., Miyajima, Y., Yuasa, M., Dunkley, D.J., 2011. The timescales of subduction initiation and subsequent evolution of an oceanic island arc. Earth and Planetary Science Letters 306, 229–240. https://doi.org/10.1016/j.epsl.2011.04.006

Iwamori, H., 2000. Thermal effects of ridge subduction and its implications for the origin of granitic batholith and paired metamorphic belts. Earth and Planetary Science Letters 181, 131–144. https://doi.org/10.1016/S0012-821X(00)00182-5

Jochum, K.P., Weis, U., Stoll, B., Kuzmin, D., Yang, Q., Raczek, I., Jacob, D.E., Stracke, A., Birbaum, K., Frick, D.A., Günther, D., Enzweiler, J., 2011. Determination of Reference Values for NIST SRM 610-617 Glasses Following ISO Guidelines. Geostandards and Geoanalytical Research 35, 397–429. https://doi.org/10.1111/j.1751-908X.2011.00120.x

Jochum, K.P., Willbold, M., Raczek, I., Stoll, B., Herwig, K., 2005. Chemical Characterisation of the USGS Reference Glasses GSA-1G, GSC-1G, GSD-1G, GSE-1G, BCR-2G, BHVO-2G and BIR-1G Using EPMA, ID-TIMS, ID-ICP-MS and LA-ICP-MS. Geostandards and Geoanalytical Research 29, 285–302. https://doi.org/10.1111/j.1751-908X.2005.tb00901.x

John, T., Gussone, N., Podladchikov, Y.Y., Bebout, G.E., Dohmen, R., Halama, R., Klemd, R., Magna, T., Seitz, H.-M., 2012. Volcanic arcs fed by rapid pulsed fluid flow through subducting slabs. Nature Geoscience 5, 489–492. https://doi.org/10.1038/ngeo1482

Kano, M., Kato, A., Ando, R., Obara, K., 2018. Strength of tremor patches along deep transition zone of a megathrust. Scientific Reports 8, 3655. https://doi.org/10.1038/s41598-018-22048-8

Kay, R.W., Mahlburg Kay, S., 1993. Delamination and delamination magmatism. Tectonophysics 219, 177–189. https://doi.org/10.1016/0040-1951(93)90295-U

Keiter, M., Piepjohn, K., Ballhaus, C., Lagos, M., Bode, M., 2004. Structural development of high-pressure metamorphic rocks on Syros island (Cyclades, Greece). Journal of Structural Geology 26, 1433–1445. https://doi.org/10.1016/j.jsg.2003.11.027

Kelemen, P.B., Hanghøj, K., Greene, A.R., 2007. One View of the Geochemistry of Subduction-Related Magmatic Arcs, with an Emphasis on Primitive Andesite and Lower Crust, in: Treatise on Geochemistry. Elsevier, pp. 1–70. https://doi.org/10.1016/B0-08-043751-6/03035-8

Kelemen, P.B., Rilling, J.L., Parmentier, E.M., Mehl, L., Hacker, B.R., 2003. Thermal structure due to solid-state flow in the mantle wedge beneath arcs, in: Eiler, J. (Ed.), Geophysical Monograph Series. American Geophysical Union, Washington, D. C., pp. 293–311. https://doi.org/10.1029/138GM13

Kimura, G., Hina, S., Hamada, Y., Kameda, J., Tsuji, T., Kinoshita, M., Yamaguchi, A., 2012. Runaway slip to the trench due to rupture of highly pressurized megathrust beneath the middle trench slope: The tsunamigenesis of the 2011 Tohoku earthquake off the east coast of northern Japan. Earth and Planetary Science Letters 339–340, 32–45. https://doi.org/10.1016/j.epsl.2012.04.002

Kincaid, C., Griffiths, R.W., 2004. Variability in flow and temperatures within mantle subduction zones: Flow and temperature in mantle subduction zones. Geochemistry, Geophysics, Geosystems 5. https://doi.org/10.1029/2003GC000666

King, R., Bebout, G., Moriguti, T., Nakamura, E., 2006. Elemental mixing systematics and Sr–Nd isotope geochemistry of mélange formation: Obstacles to identification of fluid sources to arc volcanics. Earth and Planetary Science Letters 246, 288–304. https://doi.org/10.1016/j.epsl.2006.03.053

King, R.L., Bebout, G.E., Grove, M., Moriguti, T., Nakamura, E., 2007. Boron and lead isotope signatures of subduction-zone mélange formation: Hybridization and fractionation along the slab–mantle interface beneath volcanic arcs. Chemical Geology 239, 305–322. https://doi.org/10.1016/j.chemgeo.2007.01.009

Király, Á., Portner, D.E., Haynie, K.L., Chilson-Parks, B.H., Ghosh, T., Jadamec, M., Makushkina, A., Manga, M., Moresi, L., O'Farrell, K.A., 2020. The effect of slab gaps on subduction dynamics and mantle upwelling. Tectonophysics 785, 228458. https://doi.org/10.1016/j.tecto.2020.228458

Kodolányi, J., Pettke, T., Spandler, C., Kamber, B.S., Gméling, K., 2012. Geochemistry of Ocean Floor and Fore-arc Serpentinites: Constraints on the Ultramafic Input to Subduction Zones. Journal of Petrology 53, 235–270. https://doi.org/10.1093/petrology/egr058

Kouketsu, Y., Nishiyama, T., Ikeda, T., & Enami, M., 2014. Evaluation of residual pressure in an inclusion-host system using negative frequency shift of quartz Raman spectra. American Mineralogist, 99, 433-442. https://doi.org/10.2138/am.2014.4427

Kohn, M.J., 2017. Titanite Petrochronology. Reviews in Mineralogy and Geochemistry, 83, 419-441. https://doi.org/10.2138/rmg.2017.83.13

Kohn, M.J., 2020. A refined zirconium-in-rutile thermometer. American Mineralogist

105(6), 963-971. https://doi.org/10.2138/am-2020-7091

Kohn, M.J., 2014. “Thermoba-Raman-try”: Calibration of spectroscopic barometers and thermometers for mineral inclusions. Earth and Planetary Science Letters 388, 187–196. https://doi.org/10.1016/j.epsl.2013.11.054

Kohn, M.J., 2009. Models of garnet differential geochronology. Geochimica et Cosmochimica Acta 73, 170–182. https://doi.org/10.1016/j.gca.2008.10.004

Kohn, M.J., 2004. Oscillatory- and sector-zoned garnets record cyclic (?) rapid thrusting in central Nepal: Oscillatory- and sector-zoned garnets. Geochemistry, Geophysics, Geosystems 5. https://doi.org/10.1029/2004GC000737

Kohn, M.J., Castro, A.E., Kerswell, B.C., Ranero, C.R., Spear, F.S., 2018. Shear heating reconciles thermal models with the metamorphic rock record of subduction. Proceedings of the National Academy of Sciences USA 115, 11706–11711. https://doi.org/10.1073/pnas.1809962115

Kohn, M.J., Corrie, S.L., Markley, C., 2015. The fall and rise of metamorphic zircon. American Mineralogist 100, 897–908. https://doi.org/10.2138/am-2015-5064

Kohn, M.J., Penniston-Dorland, S.C., 2017. Diffusion: Obstacles and Opportunities in Petrochronology. Reviews in Mineralogy and Geochemistry 83, 103–152. https://doi.org/10.2138/rmg.2017.83.4

Kohn, M.J., Penniston-Dorland, S.C., Ferreira, J.C.S., 2016a. Implications of near-rim compositional zoning in rutile for geothermometry, geospeedometry, and trace element equilibration. Contributions to Mineralogy and Petrology 171, 78. https://doi.org/10.1007/s00410-016-1285-1

Kohn, M.J., 2016b. Metamorphic chronology—a tool for all ages: Past achievements and

future prospects. American Mineralogist 101, 25–42. https://doi.org/10.2138/am-2016-5146

Kohn, M.J., Spear, F., 2000. Retrograde net transfer reaction insurance for pressure-temperature estimates. Geology 28, 1127–1130. https://doi.org/10.1130/0091-7613(2000)28<1127:RNTRIF>2.0.CO;2

Konrad-Schmolke, M., O'Brien, P.J., de Capitani, C., Carswell, D.A., 2008a. Garnet growth at high- and ultra-high pressure conditions and the effect of element fractionation on mineral modes and composition. Lithos 103, 309–332. https://doi.org/10.1016/j.lithos.2007.10.007

Konrad-Schmolke, M., Zack, T., O'Brien, P.J., Jacob, D.E., 2008b. Combined thermodynamic and rare earth element modelling of garnet growth during subduction: Examples from ultrahigh-pressure eclogite of the Western Gneiss Region, Norway. Earth and Planetary Science Letters 272, 488–498. https://doi.org/10.1016/j.epsl.2008.05.018

Krebs, M., Maresch, W.V., Schertl, H.-P., Münker, C., Baumann, A., Draper, G., Idleman, B., Trapp, E., 2008. The dynamics of intra-oceanic subduction zones: A direct comparison between fossil petrological evidence (Rio San Juan Complex, Dominican Republic) and numerical simulation. Lithos 103, 106–137. https://doi.org/10.1016/j.lithos.2007.09.003

Krebs, M., Schertl, H.-P., Maresch, W.V., Draper, G., 2011. Mass flow in serpentinite-hosted subduction channels: P–T–t path patterns of metamorphic blocks in the Rio San Juan mélange (Dominican Republic). Journal of Asian Earth Sciences 42, 569–595. https://doi.org/10.1016/j.jseaes.2011.01.011

Krogh, E.J., Oh, C.W., Liou, J.C., 1994. Polyphase and anticlockwise P-T evolution for Franciscan eclogites and blueschists from Jenner, California, USA. Journal of Metamorphic Geology 12, 121–134. https://doi.org/10.1111/j.1525-1314.1994.tb00008.x

Krohe, A., 2017. The Franciscan Complex (California, USA) – The model case for return-flow in a subduction channel put to the test. Gondwana Research 45, 282–307. https://doi.org/10.1016/j.gr.2017.02.003

Kronenberg, A.K., Kirby, S.H., Pinkston, J., 1990. Basal slip and mechanical anisotropy of biotite. J. Geophys. Res. 95, 19257. https://doi.org/10.1029/JB095iB12p19257

Lagos, M., Scherer, E.E., Tomaschek, F., Münker, C., Keiter, M., Berndt, J., Ballhaus, C., 2007. High precision Lu–Hf geochronology of Eocene eclogite-facies rocks from Syros, Cyclades, Greece. Chemical Geology 243, 16–35. https://doi.org/10.1016/j.chemgeo.2007.04.008

Lanari, P., Duesterhoeft, E., 2019. Modeling Metamorphic Rocks Using Equilibrium Thermodynamics and Internally Consistent Databases: Past Achievements, Problems and Perspectives. Journal of Petrology 60, 19–56. https://doi.org/10.1093/petrology/egy105

Lanari, P., Engi, M., 2017. Local Bulk Composition Effects on Metamorphic Mineral Assemblages. Reviews in Mineralogy and Geochemistry 83, 55–102. https://doi.org/10.2138/rmg.2017.83.3

Lanari, P., Ferrero, S., Goncalves, P., Grosch, E.G., 2019. Metamorphic geology: progress and perspectives. Geological Society, London, Special Publications 478, 1–12. https://doi.org/10.1144/SP478-2018-186

Lapen, T.J., Johnson, C.M., Baumgartner, L.P., Mahlen, N.J., Beard, B.L., Amato, J.M., 2003. Burial rates during prograde metamorphism of an ultra-high-pressure terrane: an example from Lago di Cignana, western Alps, Italy. Earth and Planetary Science Letters 215, 57–72. https://doi.org/10.1016/S0012-821X(03)00455-2

Lee, D.E., Thomas, H.H., Marvin, R.F., Coleman, R.G., 1964. Isotopic ages of glaucophane schists from the area of Cazadero, California. U.S. Geological Survey Professional Paper 475-D, D105-107.

Lister, G.S., Baldwin, S.L., 1996. Modelling the effect of arbitrary P-T-t histories on argon diffusion in minerals using the MacArgon program for the Apple Macintosh. Tectonophysics 253, 83–109. https://doi.org/10.1016/0040-1951(95)00059-3

Ludwig, K.R., 2012. User's Manual for Isoplot 3.75. Berkeley Geochronology Center Special Publications 5, 75p.

Luvizotto, G.L., Zack, T., Meyer, H.P., Ludwig, T., Triebold, S., Kronz, A., Münker, C., Stockli, D.F., Prowatke, S., Klemme, S., Jacob, D.E., von Eynatten, H., 2009. Rutile crystals as potential trace element and isotope mineral standards for microanalysis. Chemical Geology 261, 346–369. https://doi.org/10.1016/j.chemgeo.2008.04.012

Marmo, B.A., Clarke, G.L., Powell, R., 2002. Fractionation of bulk rock composition due to porphyroblast growth: effects on eclogite facies mineral equilibria, Pam Peninsula, New Caledonia: Fractionation of bulk rock composition. Journal of

Metamorphic Geology 20, 151–165. https://doi.org/10.1046/j.0263-4929.2001.00346.x

Marocchi, M., Hermann, J., Tropper, P., Bargossi, G.M., Mair, V., 2010. Amphibole and phlogopite in "hybrid" metasomatic bands monitor trace element transfer at the interface between felsic and ultramafic rocks (Eastern Alps, Italy). Lithos 117, 135–148. https://doi.org/10.1016/j.lithos.2010.02.011

Marschall, H.R., Schumacher, J.C., 2012. Arc magmas sourced from mélange diapirs in subduction zones. Nature Geoscience 5, 862–867. https://doi.org/10.1038/ngeo1634

Massonne, H.-J.W., Willner, A.P., 2008. Phase relations and dehydration behaviour of psammopelite and mid-ocean ridge basalt at very-low-grade to low-grade metamorphic conditions. European Journal of Mineralogy 20, 867–879. https://doi.org/10.1127/0935-1221/2008/0020-1871

Mattinson, J.M., 1986. Geochronology of high-pressure–low-temperature Franciscan metabasites: A new approach using the U-Pb system, in: Blueschists and Eclogites. Geological Society of America, pp. 95–105.

Mazzucchelli, M.L., Burnley, P., Angel, R.J., Morganti, S., Domeneghetti, M.C., Nestola, F., Alvaro, M., 2018. Elastic geothermobarometry: Corrections for the geometry of the host-inclusion system. Geology 46, 231–234. https://doi.org/10.1130/G39807.1

McDowell, F.W., Lehman, D.H., Gucwa, P.R., Fritz, D., Maxwell, J.C., 1984. Glaucophane schists and ophiolites of the northern California Coast Ranges: Isotopic ages and their tectonic implications. Geological Society of America

Bulletin 95, 1373–1382. https://doi.org/10.1130/0016-7606(1984)95<1373:GSAOOT>2.0.CO;2

Menant, A., Sternai, P., Jolivet, L., Guillou-Frottier, L., Gerya, T., 2016. 3D numerical modeling of mantle flow, crustal dynamics and magma genesis associated with slab roll-back and tearing: The eastern Mediterranean case. Earth and Planetary Science Letters 442, 93–107. https://doi.org/10.1016/j.epsl.2016.03.002

Meth, C.E., Carlson, W.D., 2005. Diffusion-controlled synkinematic growth of garnet from a heterogeneous precursor at Passo Del Sole, Switzerland. The Canadian Mineralogist 43, 157–182. https://doi.org/10.2113/gscanmin.43.1.157

Milani, S., Angel, R.J., Scandolo, L., Mazzucchelli, M.L., Ballaran, T.B., Klemme, S., Domeneghetti, M.C., Miletich, R., Scheidl, K.S., Derzsi, M., Tokár, K., Prencipe, M., Alvaro, M., Nestola, F., 2017. Thermo-elastic behavior of grossular garnet at high pressures and temperatures. American Mineralogist 102, 851–859. https://doi.org/10.2138/am-2017-5855

Milani, S., Nestola, F., Alvaro, M., Pasqual, D., Mazzucchelli, M.L., Domeneghetti, M.C., Geiger, C.A., 2015. Diamond–garnet geobarometry: The role of garnet compressibility and expansivity. Lithos 227, 140–147. https://doi.org/10.1016/j.lithos.2015.03.017

Morton, D.M., Miller, F.K., Kistler, R.W., Premo, W.R., Lee, C.-T.A., Langenheim, V.E., Wooden, J.L., Snee, L.W., Clausen, B.L., Cossette, P., 2014. Framework and petrogenesis of the northern Peninsular Ranges batholith, southern California, in: Peninsular Ranges Batholith, Baja California and Southern California. Geological Society of America. https://doi.org/10.1130/2014.1211(03)

Mulcahy, S.R., Starnes, J.K., Day, H.W., Coble, M.A., Vervoort, J.D., 2018. Early Onset of Franciscan Subduction. Tectonics 37, 1194–1209. https://doi.org/10.1029/2017TC004753

Mulcahy, S.R., Vervoort, J.D., Renne, P.R., 2014. Dating subduction-zone metamorphism with combined garnet and lawsonite Lu-Hf geochronology. Journal of Metamorphic Geology 32, 515–533. https://doi.org/10.1111/jmg.12092

Müller, R.D., Seton, M., Zahirovic, S., Williams, S.E., Matthews, K.J., Wright, N.M., Shephard, G.E., Maloney, K.T., Barnett-Moore, N., Hosseinpour, M., Bower, D.J., Cannon, J., 2016. Ocean Basin Evolution and Global-Scale Plate Reorganization Events Since Pangea Breakup. Annual Reviews of Earth and Planetary Science 44, 107–138. https://doi.org/10.1146/annurev-earth-060115-012211

Murri, M., Mazzucchelli, M.L., Campomenosi, N., Korsakov, A., Prencipe, M., Mihailova, B., Scamelluri, M., Angel, R., Alvaro, M., 2018. Raman Elastic Geobarometry For Anisotropic Mineral Inclusions. American Mineralogist 103, 1869–1872. https://doi.org/10.2138/am-2018-6625CCBY

Naif, S., Key, K., Constable, S., Evans, R.L., 2015. Water-rich bending faults at the Middle America Trench: Water-rich bending faults. Geochemistry, Geophysics, Geosystems 16, 2582–2597. https://doi.org/10.1002/2015GC005927

Newcombe, M.E., Plank, T., Barth, A., Asimow, P.D., Hauri, E., 2020. Water-in-olivine magma ascent chronometry: Every crystal is a clock. Journal of Volcanology and Geothermal Research 398, 106872. https://doi.org/10.1016/j.jvolgeores.2020.106872

Nielsen, S.G., Marschall, H.R., 2017. Geochemical evidence for mélange melting in global arcs. Science Advances 3, e1602402. https://doi.org/10.1126/sciadv.1602402

Page, B.M., 1978. Franciscan melanges compared with olistostromes of Taiwan and Italy. Tectonophysics 47, 223–246. https://doi.org/10.1016/0040-1951(78)90032-X

Page, F.Z., Armstrong, L.S., Essene, E.J., Mukasa, S.B., 2007. Prograde and retrograde history of the Junction School eclogite, California, and an evaluation of garnet–phengite–clinopyroxene thermobarometry. Contributions to Mineralogy and Petrology 153, 533–555. https://doi.org/10.1007/s00410-006-0161-9

Page, F.Z., Cameron, E.M., Flood, C.M., Dobbins, J.W., Spicuzza, M.J., Kitajima, K., Strickland, A., Ushikubo, T., Mattinson, C.G., Valley, J.W., 2019. Extreme oxygen isotope zoning in garnet and zircon from a metachert block in mélange reveals metasomatism at the peak of subduction metamorphism. Geology. https://doi.org/10.1130/G46135.1

Page, F.Z., Essene, E.J., Mukasa, S.B., Valley, J.W., 2014. A Garnet–Zircon Oxygen Isotope Record of Subduction and Exhumation Fluids from the Franciscan Complex, California. Journal of Petrology 55, 103–131. https://doi.org/10.1093/petrology/egt062

Page, F.Z., Makusa, S.B., Essene, E.J., Carrigan, C.W., 2003. Lu-Hf and U-Pb chronology of a possible Triassic high-grade block, Healdsburg, California, in: EOS, Transactions of the American Geophysical Union. p. F1567.

Palin, R.M., Santosh, M., Cao, W., Li, S.-S., Hernández-Uribe, D., Parsons, A., 2020.

Secular change and the onset of plate tectonics on Earth. Earth-Science Reviews 103172. https://doi.org/10.1016/j.earscirev.2020.103172

Paton, C., Hellstrom, J., Paul, B., Woodhead, J., Hergt, J., 2011. Iolite: Freeware for the visualisation and processing of mass spectrometric data. Journal of Analytical Atomic Spectrometry 26, 2508. https://doi.org/10.1039/c1ja10172b

Pattison, D.R.M., De Capitani, C., Gaidies, F., 2011. Petrological consequences of variations in metamorphic reaction affinity. Journal of Metamorphic Geology 29, 953–977. https://doi.org/10.1111/j.1525-1314.2011.00950.x

Pattison, D.R.M., Tinkham, D.K., 2009. Interplay between equilibrium and kinetics in prograde metamorphism of pelites: an example from the Nelson aureole, British Columbia. Journal of Metamorphic Geology 27, 249–279. https://doi.org/10.1111/j.1525-1314.2009.00816.x

Peacock, S.M., 1990. Numerical simulation of metamorphic pressure-temperature-time paths and fluid production in subducting slabs. Tectonics 9, 1197–1211. https://doi.org/10.1029/TC009i005p01197

Penniston-Dorland, S.C., Bebout, G.E., Pogge von Strandmann, P.A.E., Elliott, T., Sorensen, S.S., 2012. Lithium and its isotopes as tracers of subduction zone fluids and metasomatic processes: Evidence from the Catalina Schist, California, USA. Geochimica et Cosmochimica Acta 77, 530–545. https://doi.org/10.1016/j.gca.2011.10.038

Penniston-Dorland, S.C., Gorman, J.K., Bebout, G.E., Piccoli, P.M., Walker, R.J., 2014.

Reaction rind formation in the Catalina Schist: Deciphering a history of mechanical mixing and metasomatic alteration. Chemical Geology 384, 47–61. https://doi.org/10.1016/j.chemgeo.2014.06.024

Penniston-Dorland, S.C., Kohn, M.J., Manning, C.E., 2015. The global range of subduction zone thermal structures from exhumed blueschists and eclogites: Rocks are hotter than models. Earth and Planetary Science Letters 428, 243–254. https://doi.org/10.1016/j.epsl.2015.07.031

Penniston-Dorland, S.C., Kohn, M.J., Piccoli, P.M., 2018. A mélange of subduction temperatures: Evidence from Zr-in-rutile thermometry for strengthening of the subduction interface. Earth and Planetary Science Letters 482, 525–535. https://doi.org/10.1016/j.epsl.2017.11.005

Penniston-Dorland, S.C., Sorensen, S.S., Ash, R.D., Khadke, S.V., 2010. Lithium isotopes as a tracer of fluids in a subduction zone mélange: Franciscan Complex, CA. Earth and Planetary Science Letters 292, 181–190. https://doi.org/10.1016/j.epsl.2010.01.034

Plank, T., Langmuir, C.H., 1998. The chemical composition of subducting sediment and its consequences for the crust and mantle. Chemical Geology 145, 325–394. https://doi.org/10.1016/S0009-2541(97)00150-2

Platt, J., 1976. The significance of the Catalina Schist in the history of the southern California borderland. University of California Publications in Geological Sciences 112, 111p.

Platt, J., 1975. Metamorphic and deformational processes in the Franciscan Complex,

California: Some insights from the Catalina Schist terrane. Geological Society of America Bulletin 86, 1337–1347.

Platt, J.P., 2015. Origin of Franciscan blueschist-bearing mélange at San Simeon, central California coast. International Geology Review 57, 843–853. https://doi.org/10.1080/00206814.2014.902756

Plunder, A., Agard, P., Chopin, C., Pourteau, A., Okay, A.I., 2015. Accretion, underplating and exhumation along a subduction interface: From subduction initiation to continental subduction (Tavşanlı zone, W. Turkey). Lithos 226, 233–254. https://doi.org/10.1016/j.lithos.2015.01.007

Plunder, A., Thieulot, C., van Hinsbergen, D.J.J., 2018. The effect of obliquity on temperature in subduction zones: insights from 3-D numerical modeling. Solid Earth 9, 759–776. https://doi.org/10.5194/se-9-759-2018

Pollington, A.D., Baxter, E.F., 2011. High precision microsampling and preparation of zoned garnet porphyroblasts for Sm–Nd geochronology. Chemical Geology 281, 270–282. https://doi.org/10.1016/j.chemgeo.2010.12.014

Powell, R., Holland, T., 1994. Optimal geothermometry and geobarometry. American Mineralogist 79, 120–133.

Powell, R., Holland, T., Worley, B., 1998. Calculating phase diagrams involving solid solutions via non-linear equations, with examples using THERMOCALC. Journal of Metamorphic Geology 16, 577–588.

Powell, R., Holland, T.J.B., 1988. An internally consistent dataset with uncertainties and

correlations: 3. Applications to geobarometry, worked examples and a computer program. J Metamorphic Geology 6, 173–204. https://doi.org/10.1111/j.1525-1314.1988.tb00415.x

Ranero, C.R., Phipps Morgan, J., McIntosh, K., Reichert, C., 2003. Bending-related faulting and mantle serpentinization at the Middle America trench. Nature 425, 367–373. https://doi.org/10.1038/nature01961

Raymond, L.A., 2016. A metasomatic setting, the Russian River Arch, and gravitational emplacement in the history of eclogites at the classic eclogite locality of Jenner, California, USA. International Geology Review 1–22. https://doi.org/10.1080/00206814.2016.1213143

Rosenfeld, J.L., Chase, A.B., 1961. Pressure and temperature of crystallization from elastic effects around solid inclusions in minerals? American Journal of Science 259, 519–541. https://doi.org/10.2475/ajs.259.7.519

Ross, J.A., Sharp, W.D., 1988. The effects of sub-blocking temperature metamorphism on the K/Ar systematics of hornblendes: $^{40}Ar/^{39}Ar$ dating of polymetamorphic garnet amphibolite from the Franciscan Complex, California. Contributions to Mineralogy and Petrology 100, 213–221. https://doi.org/10.1007/BF00373587

Ross, J.A., Sharp, W.D., 1986. 40Ar/39Ar and Sm/Nd dating of garnet amphibolite in the Coast Ranges, California. Presented at the Eos, Transactions of the American Geophysical Union, p. 1249.

Rowe, C.D., Moore, J.C., Remitti, F., the IODP Expedition 343/343T Scientists, 2013. The thickness of subduction plate boundary faults from the seafloor into the seismogenic zone. Geology 41, 991–994. https://doi.org/10.1130/G34556.1

Rubatto, D., Angiboust, S., 2015. Oxygen isotope record of oceanic and high-pressure metasomatism: a P–T–time–fluid path for the Monviso eclogites (Italy). Contributions to Mineralogy and Petrology 170, 44. https://doi.org/10.1007/s00410-015-1198-4

Rubatto, D., Regis, D., Hermann, J., Boston, K., Engi, M., Beltrando, M., McAlpine, S.R.B., 2011. Yo-yo subduction recorded by accessory minerals in the Italian Western Alps. Nature Geoscience 4, 338–342. https://doi.org/10.1038/ngeo1124

Sakakibara, M., Umeki, M., Cartwright, I., 2007. Isotopic evidence for channeled fluid flow in low-grade metamorphosed Jurassic accretionary complex in the Northern Chichibu belt, western Shikoku, Japan. Journal of Metamorphic Geology 25, 383–400. https://doi.org/10.1111/j.1525-1314.2007.00701.x

Saleeby, J., 2003. Segmentation of the Laramide Slab—evidence from the southern Sierra Nevada region. Geological Society of America Bulletin 115(6), 655-668. https://doi.org/10.1130/0016-7606(2003)115<0655:SOTLSF>2.0.CO;2

Sambridge, M.S., Compston, W., 1994. Mixture modeling of multi-component data sets with application to ion-probe zircon ages. Earth and Planetary Science Letters 128, 373–390. https://doi.org/10.1016/0012-821X(94)90157-0

Santosh, M., Kusky, T., 2010. Origin of paired high pressure–ultrahigh-temperature orogens: a ridge subduction and slab window model. Terra Nova 22, 35–42. https://doi.org/10.1111/j.1365-3121.2009.00914.x

Sassi, R., Harte, B., Carswell, D.A., Yujing, H., 2000. Trace element distribution in

Central Dabie eclogites. Contributions to Mineralogy and Petrology 139, 298–315. https://doi.org/10.1007/s004100000133

Saumur, B.-M., Hattori, K.H., Guillot, S., 2010. Contrasting origins of serpentinites in a subduction complex, northern Dominican Republic. Geological Society of America Bulletin 122, 292–304. https://doi.org/10.1130/B26530.1

Scherer, E.E., Cameron, K.L., Blichert-Toft, J., 2000. Lu–hf garnet geochronology: closure temperature relative to the Sm–Nd system and the effects of trace mineral inclusions. Geochimica et Cosmochimica Acta 64, 3413–3432. https://doi.org/10.1016/S0016-7037(00)00440-3

Schmandt, B., Humphreys, E., 2010. Complex subduction and small-scale convection revealed by body-wave tomography of the western United States upper mantle. Earth and Planetary Science Letters 297, 435–445. https://doi.org/10.1016/j.epsl.2010.06.047

Schmidt, C., Ziemann, M.A., 2000. In-situ Raman spectroscopy of quartz: A pressure sensor for hydrothermal diamond-anvil cell experiments at elevated temperatures. American Mineralogist 85, 1725–1734. https://doi.org/10.2138/am-2000-11-1216

Shaw, S.E., Todd, V.R., Grove, M., 2003. Jurassic peraluminous gneissic granites in the axial zone of the Peninsular Ranges, southern California, in: Tectonic Evolution of Northwestern Mexico and the Southwestern USA. Geological Society of America. https://doi.org/10.1130/0-8137-2374-4.157

Shelton, G.L., Tullis, J., Tullis, T., 1981. Experimental high temperature and high pressure faults. Geophysical Research Letters 8, 55–58.

Shervais, J.W., Murchey, B.L., Kimbrough, D.L., Renne, P.R., Hanan, B., 2005.

Radioisotopic and biostratigraphic age relations in the Coast Range Ophiolite, northern California: Implications for the tectonic evolution of the Western Cordillera. Geological Society of America Bulletin 117, 633. https://doi.org/10.1130/B25443.1

Shreve, R.L., Cloos, M., 1986. Dynamics of sediment subduction, melange formation, and prism accretion. Journal of Geophysical Research: Solid Earth 91, 10229–10245.

Skora, S., Baumgartner, L.P., Mahlen, N.J., Johnson, C.M., Pilet, S., Hellebrand, E., 2006. Diffusion-limited REE uptake by eclogite garnets and its consequences for Lu–Hf and Sm–Nd geochronology. Contributions to Mineralogy and Petrology 152, 703–720. https://doi.org/10.1007/s00410-006-0128-x

Smit, M.A., Scherer, E.E., Mezger, K., 2013. Lu–Hf and Sm–Nd garnet geochronology: Chronometric closure and implications for dating petrological processes. Earth and Planetary Science Letters 381, 222–233. https://doi.org/10.1016/j.epsl.2013.08.046

Smye, A.J., Greenwood, L.V., Holland, T.J.B., 2010. Garnet-chloritoid-kyanite assemblages: eclogite facies indicators of subduction constraints in orogenic belts: Garnet-chloritoid-kyanite assemblages. Journal of Metamorphic Geology 28, 753–768. https://doi.org/10.1111/j.1525-1314.2010.00889.x

Sorensen, S.S., 1988. Petrology of amphibolite-facies mafic and ultramafic rocks from the Catalina Schist, southern California: metasomatism and migmatization in a subduction zone metamorphic setting. Journal of Metamorphic Geology 6, 405–435. https://doi.org/10.1111/j.1525-1314.1988.tb00431.x

Sorensen, S.S., 1984. Petrology of Basement Rocks of the California Continental Borderland and the Los Angeles Basin (Pd.D. Thesis). University of California, Los Angeles.

Sorensen, S.S., Barton, M.D., 1987. Metasomatism and partial melting in a subduction complex Catalina Schist, southern California. Geology 15, 115–118.

Sorensen, S.S., Grossman, J., 1989. Enrichment of trace elements in garnet amphibolites from a paleo-subduction zone: Catalina Schist, southern California. Geochimica et Cosmochimica Acta 53, 3155–3177.

Sorensen, S.S., Grossman, J.N., Perfit, M.R., 1997. Phengite-hosted LILE Enrichment in Eclogite and Related Rocks: Implications for Fluid-Mediated Mass Transfer in Subduction Zones and Arc Magma Genesis. Journal of Petrology 38, 3–34. https://doi.org/10.1093/petroj/38.1.3

Spandler, C., Hermann, J., 2006. High-pressure veins in eclogite from New Caledonia and their significance for fluid migration in subduction zones. Lithos 89, 135–153. https://doi.org/10.1016/j.lithos.2005.12.003

Spandler, C., Hermann, J., Faure, K., Mavrogenes, J.A., Arculus, R.J., 2008. The importance of talc and chlorite “hybrid” rocks for volatile recycling through subduction zones; evidence from the high-pressure subduction mélange of New Caledonia. Contributions to Mineralogy and Petrology 155, 181–198. https://doi.org/10.1007/s00410-007-0236-2

Spear, F.S., 1993. Metamorphic Phase Equilibria and Pressure-Temperature-Time Paths. Mineralogical Society of America, Washington D.C.

Spear, F.S., Pattison, D.R.M., 2017. The implications of overstepping for metamorphic

assemblage diagrams (MADs). Chemical Geology 457, 38–46. https://doi.org/10.1016/j.chemgeo.2017.03.011

Spear, F.S., Thomas, J.B., Hallett, B.W., 2014. Overstepping the garnet isograd: a comparison of QuiG barometry and thermodynamic modeling. Contributions to Mineralogy and Petrology 168, 1059. https://doi.org/10.1007/s00410-014-1059-6

Spinelli, G.A., Harris, R.N., 2011. Thermal effects of hydrothermal circulation and seamount subduction: Temperatures in the Nankai Trough Seismogenic Zone Experiment transect, Japan: Nankai subduction zone temperatures. Geochemistry, Geophysics, Geosystems 12. https://doi.org/10.1029/2011GC003727

Stangarone, C., Angel, R.J., Prencipe, M., Campomenosi, N., Mihailova, B., Alvaro, M., 2019. Measurement of strains in zircon inclusions by Raman spectroscopy. European Journal of Mineralogy 31, 685–694. https://doi.org/10.1127/ejm/2019/0031-2851

Stegman, D.R., Freeman, J., Schellart, W.P., Moresi, L., May, D., 2006. Influence of trench width on subduction hinge retreat rates in 3-D models of slab rollback: 3-D models of slab rollback. Geochemistry, Geophysics, Geosystems 7. https://doi.org/10.1029/2005GC001056

Suppe, J., 1969. Times of metamorphism in the Franciscan terrain of the northern Coast Ranges, California. Geological Society of America Bulletin 80, 135–142. https://doi.org/10.1130/0016-7606(1969)80%5B135:TOMITF%5D2.0.CO;2

Suppe, J., Armstrong, R.L., 1972. Potassium-argon dating of Franciscan metamorphic rocks. American Journal of Science 272, 217–233.

Suppe, J., Foland, K.A., 1978. The Goat Mountain schists and Pacific Ridge complex: A

redeformed but still-intact late Mesozoic Franciscan schuppen complex, in: Howell, D.G., McDougall, K. (Eds.), Pacific Coast Paleogeography Symposium, Pacific Section, Society of Economic Paleontologist and Mineralogists. pp. 431–451.

Syracuse, E.M., van Keken, P.E., Abers, G.A., 2010. The global range of subduction zone thermal models. Physics of the Earth and Planetary Interiors 183, 73–90. https://doi.org/10.1016/j.pepi.2010.02.004

Taetz, S., John, T., Bröcker, M., Spandler, C., Stracke, A., 2018. Fast intraslab fluid-flow events linked to pulses of high pore fluid pressure at the subducted plate interface. Earth and Planetary Science Letters 482, 33–43. https://doi.org/10.1016/j.epsl.2017.10.044

Tajčmanová, L., Connolly, J.A.D., Cesare, B., 2009. A thermodynamic model for titanium and ferric iron solution in biotite. Journal of Metamorphic Geology 27, 153–165. https://doi.org/10.1111/j.1525-1314.2009.00812.x

Tarling, M.S., Smith, S.A.F., Scott, J.M., 2019. Fluid overpressure from chemical reactions in serpentinite within the source region of deep episodic tremor. Nature Geoscience 12, 1034–1042. https://doi.org/10.1038/s41561-019-0470-z

Thomas, J.B., Spear, F.S., 2018. Experimental study of quartz inclusions in garnet at pressures up to 3.0 GPa: evaluating validity of the quartz-in-garnet inclusion elastic thermobarometer. Contributions to Mineralogy and Petrology 173, 42. https://doi.org/10.1007/s00410-018-1469-y

Thorkelson, D.J., Madsen, J.K., Sluggett, C.L., 2011. Mantle flow through the Northern

Cordilleran slab window revealed by volcanic geochemistry. Geology 39, 267–270. https://doi.org/10.1130/G31522.1

Tinkham, D.K., Zuluaga, C.A., Stowell, H.H., 2001. Metapelite phase equilibria modeling in MnNCkFMASH: The effect of variable Al2O3 and MgO/(MgO+FeO) on mineral stability. Geological Materials Research 3, 1–42.

Tirone, M., Ganguly, J., Dohmen, R., Langenhorst, F., Hervig, R., Becker, H.-W., 2005. Rare earth diffusion kinetics in garnet: Experimental studies and applications. Geochimica et Cosmochimica Acta 69, 2385–2398. https://doi.org/10.1016/j.gca.2004.09.025

Tomkins, H.S., Powell, R., Ellis, D.J., 2007. The pressure dependence of the zirconium-in-rutile thermometer. Journal of Metamorphic Geology 25, 703–713. https://doi.org/10.1111/j.1525-1314.2007.00724.x

Touret, J.L.R., 2001. Fluids in metamorphic rocks. Lithos 55, 1–25. https://doi.org/10.1016/S0024-4937(00)00036-0

Tsujimori, T., Sisson, V.B., Liou, J.G., Harlow, G.E., Sorensen, S.S., 2006. Petrologic characterization of Guatemalan lawsonite eclogite: Eclogitization of subducted oceanic crust in a cold subduction zone, in: Ultrahigh-Pressure Metamorphism: Deep Continental Subduction. Geological Society of America. https://doi.org/10.1130/2006.2403(09)

Ukar, E., 2012. Tectonic significance of low-temperature blueschist blocks in the Franciscan mélange at San Simeon, California. Tectonophysics 568–569, 154–169. https://doi.org/10.1016/j.tecto.2011.12.039

Ukar, E., Cloos, M., 2014. Low-temperature blueschist-facies mafic blocks in the

Franciscan mélange, San Simeon, California: Field relations, petrology, and counterclockwise *P* - *T* paths. Geological Society of America Bulletin 126, 831–856. https://doi.org/10.1130/B30876.1

Van der Molen, I., Van Roermund, H.L.M., 1986. The pressure path of solid inclusions in minerals: the retention of coesite inclusions during uplift. Lithos 19, 317–324. https://doi.org/10.1016/0024-4937(86)90030-7

van Keken, P.E., Hacker, B.R., Syracuse, E.M., Abers, G.A., 2011. Subduction factory: 4. Depth-dependent flux of H_2O from subducting slabs worldwide. Journal of Geophysical Research 116, B01401. https://doi.org/10.1029/2010JB007922

van Keken, P.E., Kiefer, B., Peacock, S.M., 2002. High-resolution models of subduction zones: Implications for mineral dehydration reactions and the transport of water into the deep mantle: High-resolution models of subduction zones. Geochemistry, Geophysics, Geosystems 3, 1 of 20–20 20. https://doi.org/10.1029/2001GC000256

van Keken, P.E., Wada, I., Abers, G.A., Hacker, B.R., Wang, K., 2018. Mafic High-Pressure Rocks Are Preferentially Exhumed From Warm Subduction Settings. Geochemistry, Geophysics, Geosystems 19, 2934–2961. https://doi.org/10.1029/2018GC007624

Vermeesch, P., 2018. IsoplotR: A free and open toolbox for geochronology. Geoscience Frontiers 9, 1479–1493. https://doi.org/10.1016/j.gsf.2018.04.001

Viete, D.R., Hacker, B.R., Allen, M.B., Seward, G.G.E., Tobin, M.J., Kelley, C.S.,

Cinque, G., Duckworth, A.R., 2018. Metamorphic records of multiple seismic cycles during subduction. Sci. Adv. 4, eaaq0234. https://doi.org/10.1126/sciadv.aaq0234

Vrolijk, P., Myers, G., Moore, J.C., 1988. Warm fluid migration along tectonic mélanges in the Kodiak Accretionary Complex, Alaska. Journal of Geophysical Research 93, 10313–10324. https://doi.org/10.1029/JB093iB09p10313

Wada, I., Wang, K., 2009. Common depth of slab-mantle decoupling: Reconciling diversity and uniformity of subduction zones: Common depth of slab-mantle decoupling. Geochemistry, Geophysics, Geosystems 10. https://doi.org/10.1029/2009GC002570

Wada, I., Behn, M.D., Shaw, A.M., 2012. Effects of heterogeneous hydration in the incoming plate, slab rehydration, and mantle wedge hydration on slab-derived H 2 O flux in subduction zones. Earth and Planetary Science Letters 353–354, 60–71. https://doi.org/10.1016/j.epsl.2012.07.025

Wada, I., He, J., Hasegawa, A., Nakajima, J., 2015. Mantle wedge flow pattern and thermal structure in Northeast Japan: Effects of oblique subduction and 3-D slab geometry. Earth and Planetary Science Letters 426, 76–88. https://doi.org/10.1016/j.epsl.2015.06.021

Wakabayashi, J., 2012. Subducted sedimentary serpentinite mélanges: Record of multiple burial–exhumation cycles and subduction erosion. Tectonophysics 568–569, 230–247. https://doi.org/10.1016/j.tecto.2011.11.006

Wakabayashi, J., 2011. Mélanges of the Franciscan Complex, California: Diverse

structural settings, evidence for sedimentary mixing, and their connection to subduction processes. Mélanges: processes of formation and societal significance: Geological Society of America Special Paper 480, 117–141.

Wakabayashi, J., 1999. Subduction and the rock record: Concepts developed in the Franciscan Complex, California, in: Classic Cordilleran Concepts: A View from California. Geological Society of America. https://doi.org/10.1130/0-8137-2338-8.123

Wakabayashi, J., 1990. Counterclockwise P-T-t Paths from Amphibolites, Franciscan Complex, California: Relics from the Early Stages of Subduction Zone Metamorphism. The Journal of Geology 98, 657–680. https://doi.org/10.1086/629432

Wakabayashi, J., Deino, A., 1989. Laser-probe 40Ar/39Ar ages from high grade blocks and coherent blueschists, Franciscan Complex, California: Preliminary results and implications for Franciscan tectonics. Presented at the Geological Society of America Abstracts and Programs, p. A267.

Wakabayashi, J., Dilek, Y., 2003. What constitutes 'emplacement' of an ophiolite?: Mechanisms and relationship to subduction initiation and formation of metamorphic soles. Geological Society, London, Special Publications 218, 427–447. https://doi.org/10.1144/GSL.SP.2003.218.01.22

Wakabayashi, J., Dumitru, T.A., 2007. ^{40}Ar/^{39}Ar Ages from Coherent, High-Pressure Metamorphic Rocks of the Franciscan Complex, California: Revisiting the Timing of Metamorphism of the World's Type Subduction Complex.

International Geology Review 49, 873–906. https://doi.org/10.2747/0020-6814.49.10.873

Walters, J.B., Cruz-Uribe, A.M., Marschall, H.R., 2020. Sulfur loss from subducted altered oceanic crust and implications for mantle oxidation. Geochemical Perspectives Letters 36–41. https://doi.org/10.7185/geochemlet.2011

Wang, J., Mao, Z., Jiang, F., Duffy, T.S., 2015. Elasticity of single-crystal quartz to 10 GPa. Physics and Chemistry of Minerals 42, 203–212. https://doi.org/10.1007/s00269-014-0711-z

Wark, D.A., Watson, E.B., 2006. TitaniQ: a titanium-in-quartz geothermometer. Contributions to Mineralogy and Petrology 152, 743–754. https://doi.org/10.1007/s00410-006-0132-1

Waters, D.J., Lovegrove, D.P., 2002. Assessing the extent of disequilibrium and overstepping of prograde metamorphic reactions in metapelites from the Bushveld Complex aureole, South Africa: Overstepping of prograde reactions in Bushveld metapelites. Journal of Metamorphic Geology 20, 135–149. https://doi.org/10.1046/j.0263-4929.2001.00350.x

Watson, E.B., Wark, D.A., Thomas, J.B., 2006. Crystallization thermometers for zircon and rutile. Contributions to Mineralogy and Petrology 151, 413–433. https://doi.org/10.1007/s00410-006-0068-5

Webber, S., Ellis, S., Fagereng, Å., 2018. “Virtual shear box” experiments of stress and slip cycling within a subduction interface mélange. Earth and Planetary Science Letters 488, 27–35. https://doi.org/10.1016/j.epsl.2018.01.035

Wells, M.L., Hoisch, T.D., 2008. The role of mantle delamination in widespread Late

Cretaceous extension and magmatism in the Cordilleran orogen, western United States. Geological Society of America Bulletin 120, 515–530. https://doi.org/10.1130/B26006.1

White, Powell, Holland, Worley, 2000. The effect of TiO_2 and Fe_2O_3 on metapelitic assemblages at greenschist and amphibolite facies conditions: mineral equilibria calculations in the system K_2O-FeO-MgO-Al_2O_3-SiO_2-H_2O-TiO_2-Fe_2O_3. J Journal of Metamorphic Geology 18, 497–511. https://doi.org/10.1046/j.1525-1314.2000.00269.x

Whitney, D.L., Evans, B.W., 2010. Abbreviations for names of rock-forming minerals. American Mineralogist 95, 185–187. https://doi.org/10.2138/am.2010.3371

Whitney, D.L., Teyssier, C., Seaton, N.C.A., Fornash, K.F., 2014. Petrofabrics of high-pressure rocks exhumed at the slab-mantle interface from the "point of no return" in a subduction zone (Sivrihisar, Turkey): Subduction petrofabrics. Tectonics 33, 2315–2341. https://doi.org/10.1002/2014TC003677

Wilbur, D.E., Ague, J.J., 2006. Chemical disequilibrium during garnet growth: Monte Carlo simulations of natural crystal morphologies. Geology 34, 689. https://doi.org/10.1130/G22483.1

Yeganeh-Haeri, A., Weidner, D.J., Ito, E., 1990. Elastic properties of the pyrope-majorite solid solution series. Geophysical Research Letters 17, 2453–2456. https://doi.org/10.1029/GL017i013p02453

Zack, T., Kooijman, E., 2017. Petrology and Geochronology of Rutile. Reviews in Mineralogy and Geochemistry 83, 443–467. https://doi.org/10.2138/rmg.2017.83.14

Zack, T., Moraes, R., Kronz, A., 2004. Temperature dependence of Zr in rutile: empirical calibration of a rutile thermometer. Contributions to Mineralogy and Petrology 148, 471–488. https://doi.org/10.1007/s00410-004-0617-8

Zaffiro, G., Angel, R., Alvaro, M., Prencipe, M., Stangarone, C., 2018. P-V-T-KS Equations of State for zircon and rutile, in: Geophysical Research Abstracts. Presented at the EGU General Assembly, p. 6952.

Zhang, Y., 1998. Mechanical and phase equilibria in inclusion–host systems. Earth and Planetary Science Letters 157, 209–222. https://doi.org/10.1016/S0012-821X(98)00036-3

Zhong, X., Andersen, N.H., Dabrowski, M., Jamtveit, B., 2019. Zircon and quartz inclusions in garnet used for complementary Raman thermobarometry: application to the Holsnøy eclogite, Bergen Arcs, Western Norway. Contributions to Mineralogy and Petrology 174, 50. https://doi.org/10.1007/s00410-019-1584-4

Zhong, X., Moulas, E., Tajčmanová, L., 2020. Post-entrapment modification of residual inclusion pressure and its implications for Raman elastic thermobarometry. Solid Earth 11, 223–240. https://doi.org/10.5194/se-11-223-2020